MCEER
EARTHQUAKE ENGINEERING TO EXTREME EVENTS

ISSN 1520-295X

Numerical and Experimental Studies of Self-Centering Post-Tensioned Steel Frames

by
Dong Wang and Andre Filiatrault

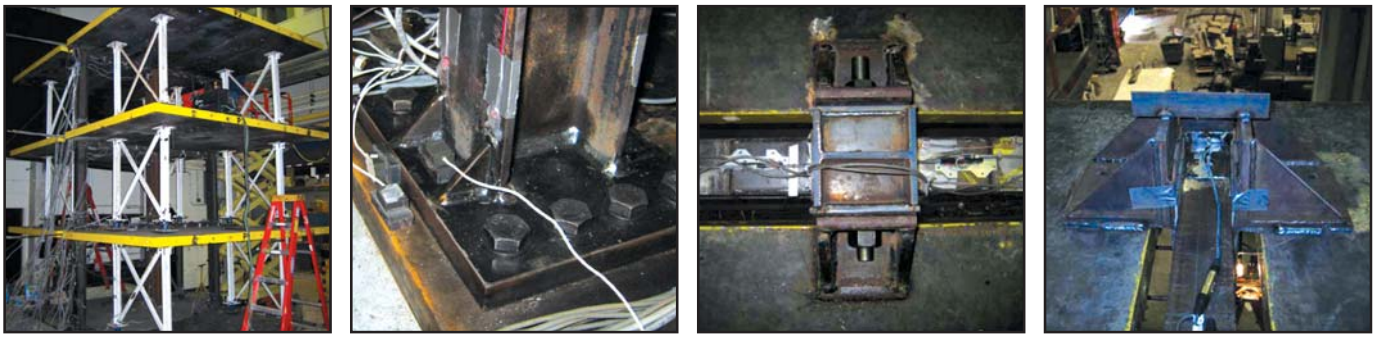

Technical Report MCEER-08-0017

May 12, 2008

This research was conducted at the University at Buffalo, State University of New York and was supported primarily by the Earthquake Engineering Research Centers Program of the National Science Foundation under award number EEC 9701471.

NOTICE

This report was prepared by the University at Buffalo, State University of New York as a result of research sponsored by MCEER through a grant from the Earthquake Engineering Research Centers Program of the National Science Foundation under NSF award number EEC-9701471 and other sponsors. Neither MCEER, associates of MCEER, its sponsors, the University at Buffalo, State University of New York, nor any person acting on their behalf:

a. makes any warranty, express or implied, with respect to the use of any information, apparatus, method, or process disclosed in this report or that such use may not infringe upon privately owned rights; or

b. assumes any liabilities of whatsoever kind with respect to the use of, or the damage resulting from the use of, any information, apparatus, method, or process disclosed in this report.

Any opinions, findings, and conclusions or recommendations expressed in this publication are those of the author(s) and do not necessarily reflect the views of MCEER, the National Science Foundation, or other sponsors.

MCEER
EARTHQUAKE ENGINEERING TO EXTREME EVENTS

Numerical and Experimental Studies of Self-Centering Post-Tensioned Steel Frames

by

Dong Wang[1] and Andre Filiatrault[2]

Publication Date: May 12, 2008
Submittal Date: January 3, 2008

Technical Report MCEER-08-0017

Task Number 10.2.4

NSF Master Contract Number EEC 9701471

1 Project Engineer, DCI-Engineers; former Graduate Student, Department of Civil, Structural and Environmental Engineering, University at Buffalo, State University of New York
2 Professor, Department of Civil, Structural and Environmental Engineering, University at Buffalo, State University of New York

MCEER
University at Buffalo, State University of New York
Red Jacket Quadrangle, Buffalo, NY 14261
Phone: (716) 645-3391; Fax (716) 645-3399
E-mail: *mceer@buffalo.edu*; WWW Site: *http://mceer.buffalo.edu*

Preface

The Multidisciplinary Center for Earthquake Engineering Research (MCEER) is a national center of excellence in advanced technology applications that is dedicated to the reduction of earthquake losses nationwide. Headquartered at the University at Buffalo, State University of New York, the Center was originally established by the National Science Foundation in 1986, as the National Center for Earthquake Engineering Research (NCEER).

Comprising a consortium of researchers from numerous disciplines and institutions throughout the United States, the Center's mission is to reduce earthquake losses through research and the application of advanced technologies that improve engineering, pre-earthquake planning and post-earthquake recovery strategies. Toward this end, the Center coordinates a nationwide program of multidisciplinary team research, education and outreach activities.

MCEER's research is conducted under the sponsorship of two major federal agencies: the National Science Foundation (NSF) and the Federal Highway Administration (FHWA), and the State of New York. Significant support is derived from the Federal Emergency Management Agency (FEMA), other state governments, academic institutions, foreign governments and private industry.

MCEER's NSF-sponsored research objectives are twofold: to increase resilience by developing seismic evaluation and rehabilitation strategies for the post-disaster facilities and systems (hospitals, electrical and water lifelines, and bridges and highways) that society expects to be operational following an earthquake; and to further enhance resilience by developing improved emergency management capabilities to ensure an effective response and recovery following the earthquake (see the figure below).

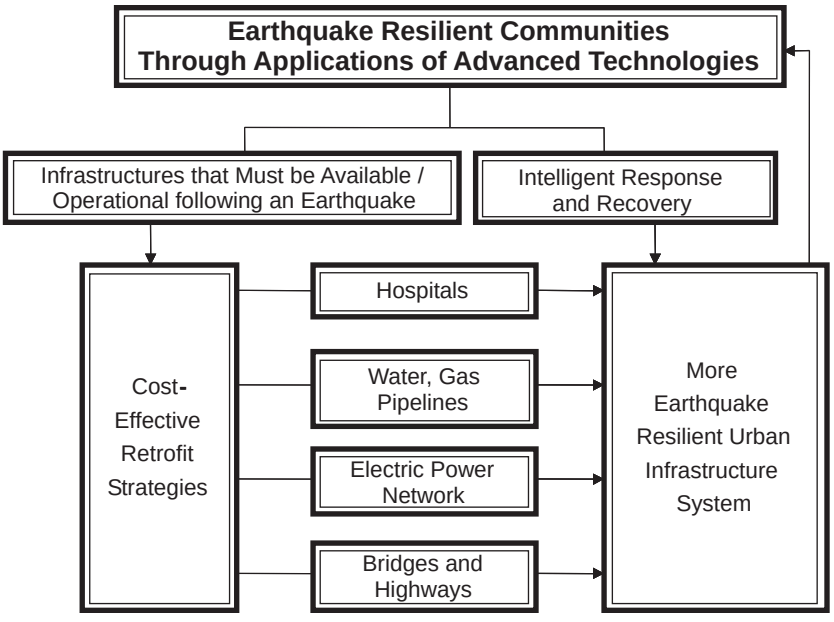

A cross-program activity focuses on the establishment of an effective experimental and analytical network to facilitate the exchange of information between researchers located in various institutions across the country. These are complemented by, and integrated with, other MCEER activities in education, outreach, technology transfer, and industry partnerships.

This report presents a numerical and experimental study to evaluate and compare the seismic performance of Self-Centering Post-Tensioned (SCPT) steel frames and conventional Steel Moment Resisting Frames (SMRF). A methodology for designing SCPT structures is developed and used to retrofit an existing four-story SMRF medical facility located in Northridge, California. A Relative Performance Index (RPI) is proposed to compare the enhancement in the seismic response of SCPT's to the SMRF's. Numerical simulations and shake table tests were carried out on two scaled 3-story 2-bay SCPT and SMRF building prototypes based on the medical facility. The study indicates that the seismic floor displacements of SCPT and SMRF are alike, while absolute floor accelerations are lower when self centering systems are implemented. Moreover, while yielding in the beam-to-column connections of the SMRF are observed, only yielding of the sacrificial devices in the self centering system of the SCPT occurred during the strongest ground motions considered.

ABSTRACT

In this research, numerical and experimental studies were conducted to evaluate the seismic performance of Self-Centering Post-Tensioned (SCPT) steel frames and Steel Moment Resisting Frames (SMRF).

Numerical analyses of Single-Degree-of-Freedom (SDOF) and Multiple-Degree-of-Freedom (MDOF) Self-Centering Systems (SCS) and Elasto-Plastic Systems (EPS) were conducted under simulated strong ground motions. A Relative Performance Index (RPI) was developed as an evaluation criterion of the seismic performance of both systems. A design procedure for SCPT frames was also developed. The results obtained from the numerical analyses indicated better seismic performances of the SCS/SCPT systems when compared to the EPS/SMRF systems. The MCEER Demonstration Hospital building was used as a prototype of a SMRF building in the numerical studies.

An experimental study was carried out on the five degrees-of-freedom shake table at the University at Buffalo. Two 3-story, 2-bay, steel plane frame models incorporating SCPT connections and conventional fully welded moment-resisting connections were used in this test. The SCPT frame, unlike traditional welded steel frames, incorporates high strength post-tensioned strands along with sacrificial yielding elements in each beam-to-column connection and is particularly appealing for hospital buildings from an initial investment stand point. These two test models were subjected to various ground motions of increasing intensities. The results of the tests indicated that the displacement response of the SCPT frame was very similar to the fully-welded SMRF and the acceleration response was reduced. While the beams of the SMRF yielded under the largest seismic excitations, the energy dissipation mechanism of the SCPT frame was limited to the Energy Dissipating (ED) bars without inelastic deformations of the beams and columns. The experimental results suggest that only the ED bars would need to be replaced in the SCPT frame as compared to the costly replacement of the damaged beams or columns sections in the SMRF building after a significant earthquake.

ACKNOWLEDGEMENT

This report was supported financially by the Earthquake Engineering Research Centers Program of the National Science Foundation (NSF) under Award Number EEC-9701471 to the Multidisciplinary Center for Earthquake Engineering Research (MCEER). Any opinions, findings, conclusions and recommendations presented in this report are those of the authors and do not necessarily reflect the views of the sponsor.

TABLE OF CONTENTS

TABLE OF CONTENTS (CONT'D)

TABLE OF CONTENTS (CONT'D)

LIST OF FIGURES

LIST OF FIGURES (CONT'D)

LIST OF FIGURES (CONT'D)

LIST OF FIGURES (CONT'D)

LIST OF FIGURES (CONT'D)

LIST OF TABLES

LIST OF TABLES (CONT'D)

CHAPTER I

INTRODUCTION

In the history of human kind, the construction technology has always been one of the most important and most practical technologies because any social, natural or engineering science cannot be developed without a safe and comfortable housing environment. Several thousands years ago, our ancestors used the natural construction materials for their houses. At that time, these primitive types of construction could only supply basic housing needs. The most obvious evidence of the evolution of the human civilization is the increased sophistication associated with housing structures. Before the 20^{th} century, wood and stones were widely used for the construction of mostly low-rise buildings not exceeding 3 to 4 stories. Nevertheless, these simple buildings did supply an adequate environment for the progress of technologies but were not constructed to resist some natural hazards like floods or earthquakes. In the last century, the engineering community has developed optimized construction materials, such as concrete and steel, which allowed the construction of much larger and higher buildings. But still due to the lack of knowledge about the effects of earthquakes on structures, these early engineered buildings could only survive small seismic events. This lack of proper earthquake-resistant design in buildings remained a significant design flaw until approximately fifty years ago. In the last thirty years, the development of computers and mechanics as well as the observations of the actual behavior of structures following large earthquakes in urban areas has allowed a much better understanding of the effects of earthquakes on structures. This improved understanding has been embodied by more stringent seismic design requirements in building codes. Engineers could then begin to

explicitly implement seismic requirements and detailing at the design stage. As a result, the seismic performance of newly constructed buildings was increased gradually. These traditional seismic design requirements that are still included in current building codes, concentrate mainly on maintaining the structural integrity of the structural system during a major seismic event in order to prevent loss of lives. Therefore, according to this life-safety design requirement approach, buildings may still be damaged beyond repair and may need to be demolished or rebuilt.

Because of the increased needs of space by expanding urban areas, an increase in mid- to high-rise buildings has been observed in the last thirty years. Steel Moment Resisting Frame (SMRF) constructions are most widely used in mid- and high-rise buildings in North America. Because of their widespread use, the seismic behavior of SMRF buildings has become one of the most important concerns in the mind of designers and owners. In this chapter the seismic behavior of SMRF and the applicability of the concept of Self-Centering Systems (SCS) to SMRF are discussed and the research objectives and organizations of this report are also presented.

1.1 Seismic Behavior of Steel Moment Resisting Frames (SMRF)

Prior to the 1994 Northridge earthquake in California, it was believed that SMRF represented one of the most adequate forms of earthquake-resistant construction, as evidenced by very few failures or severe damaged observed in SMRFs and steel structures in general after earthquakes. In fact, prior to 1994, the only severe damage reported in steel

structures, occurred in the Pio Suarez building in the 1985 Mexico City Earthquake (SAC 1995). Because of this apparent good seismic behavior of steel structures in general and SMRFs in particular, designers and owners believed that this type of building was one of the most seismic-resisting structures.

The other reason for the good reputation that SMRFs enjoyed is that SMRFs were considered to be a ductile framing system due to the ductile property along with the strength and reliability of structural steel. These apparent good material properties motivated engineers to push the envelope by designing larger and taller buildings. Indeed, many practicing engineers believed for years, albeit incorrectly, that steel structures were immune to earthquake-induced damage as a consequence of the material's inherent ductile properties (Bruneau et al. 1998). Welded SMRF connections were mostly applied in SMRF structures. Over the years, two major types of welded SMRF connections were developed. The first and earliest (pre-1970) type of connections involved welding the whole beam section to the column, as shown in Fig. 1-1. The other and more recent type of connections incorporate a shear tab welded to the flange of the column and bolted to the web of beams, while the flange of the beam is welded to the column with a full penetration grooved weld held in place by a backing bar, as shown in Fig. 1-2. Several experimental investigations on these two types of connections conducted by several investigators (Popov & Pinkney, 1969; Popov & Bertero, 1973; Popov et al. 1975) have concluded that both types of connections appear to possess a very good ductile behavior. It should be noted, however, that rare unacceptable behaviors like sudden fractures at the weld-to-column interface at the beam

bottom flange were also reported (Engelhardt & Husain, 1993). Based on these early experimental results, conducted mostly on small scale connection specimens, the earthquake engineering community considered SMRFs as excellent ductile lateral load-resisting systems, which lead to an increased numbers of SMRFs buildings, particularly in California.

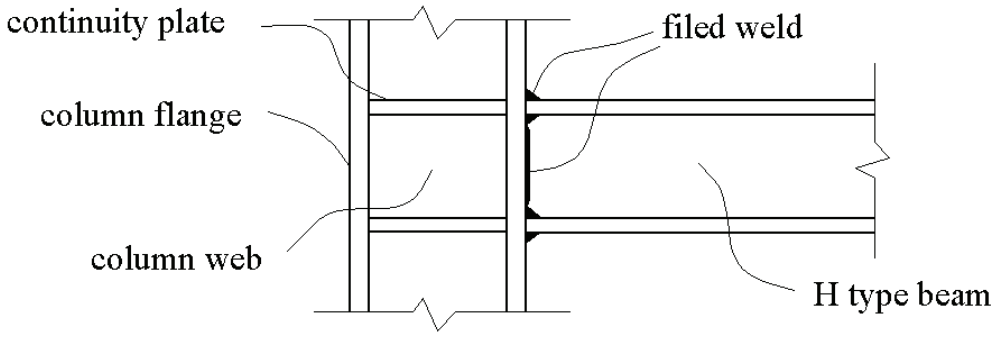

Figure 1-1 Earlier (pre-170) Type of Welded SMRF Connection

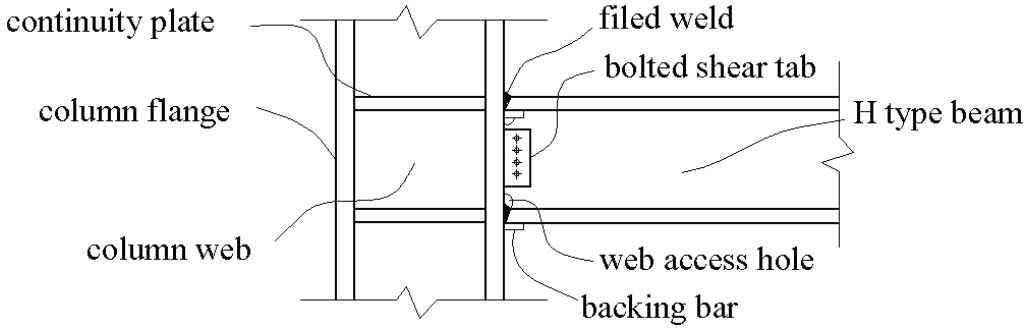

Figure 1-2 Recent (post-1970) Type of Welded SMRF Connection

However, the January 17th, 1994 Northridge Earthquake in Los Angeles, completely changed the perspective of the earthquake engineering community towards SMRFs. Over 100 SMRF structures experienced brittle beam-to-column connection fractures as a result of this Richter magnitude 6.8 seismic event (SAC 1995). The height of damaged structures covered a wide

range from one to 26 stories. The age of damaged buildings spanned from as old as 30 years to new. A typical connection damage observed in a SMRF after the Northridge earthquake is shown in Fig. 1-3, in which a crack was observed in the column flange connected to the weld of the beam bottom flange and propagated to the web of the column.

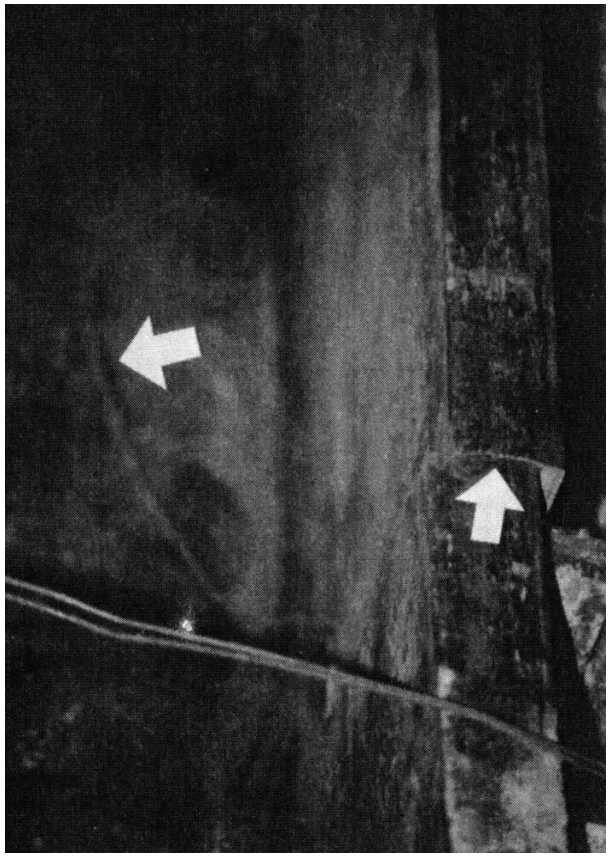

Figure 1-3 Typical Connection Damage in the Northridge Earthquake (Bruneau et al. 1998)

Figure 1-4 illustrates eight types of fractures observed in beam-to-column connections during the Northridge earthquake. Fractures and cracks were found to propagate around the fused zone in the flange and web of columns and beams. Causes of failures are complicated and include many aspects: inspection quality, weld design, fracture mechanics, base metal

elevated yield stress, welds stress condition, stress concentrations, effect of triaxial stress conditions, loading rate and presence of composite floor slab. More details on the cause of these observed fractures can be found in Bruneau et al. (1998).

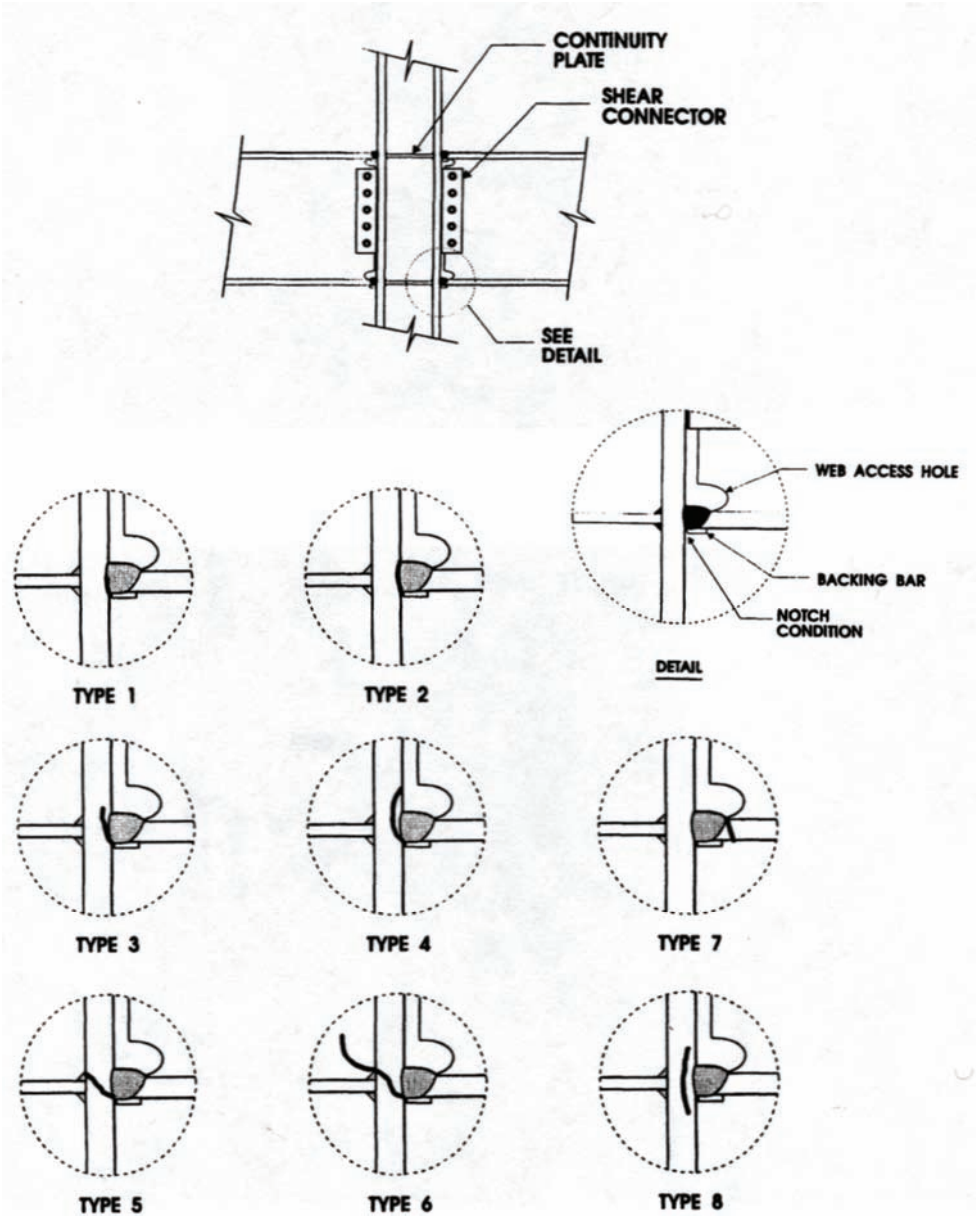

Figure 1-4 Eight Types of Fractures in Beam-Column Connections Identified as a Result of the Northridge Earthquake (Tremblay et al. 1995)

After the 1994 Northridge earthquake, a significant research effort was conducted by the SAC joint venture, which is a partnership of Structural Engineers Association of California (SEAOC), the Applied Technology Council (ATC) and the California Universities for Research in Earthquake Engineering (CUREe). Another parallel research was initialed by the Federal Emergency Management Agency (FEMA), which published several instructional documents: FEMA-350, FEMA-351, FEMA-352, FEMA-353, FEMA-354, FEMA-355 and FEMA-356. Those documents provided new design procedures and guidelines to insure a good seismic performance of SMRFs. As a result of this research effort, it is believed that the seismic performance of SMRF buildings has been increased to an acceptable level compared to that observed in the Northridge earthquake.

Although brittle fractures in beam-to-column connections were widespread in SMRF buildings during the Northridge earthquake, no SMRF structures collapsed and it can be assumed that SMRFs reached the life safety performance level. However, severe economic loss resulted. During the 1994 Northridge Earthquake, with the loss of approximately $18.5 billion due to building damage, nonstructural damage accounted for about 50% of this total (Kircher, 2003). From an economic point of view, not only the seismic properties of connections (inelastic response, yielding sections of beams, plastic rotations etc.) in earthquakes should be considered but also the seismic response (displacement, velocity and acceleration response) of buildings, local buckling, residual deformation and corresponding cost for recovering functions of post-earthquake buildings should be given more

considerations. Further discussions and potential solutions on these aspects will be presented in the following chapters.

1.2 Concepts of Elasto-Plastic Systems (EPS) and Self-Centering Systems (SCS)

Conventional buildings designed according to current seismic design requirements should have capacities for ductile inelastic response and for dissipating energy during earthquake shaking. Such structural systems are referred to as Elasto-Plastic Systems (EPS). Fig. 1-5 illustrates the idealized inelastic response of EPS during earthquake excitations.

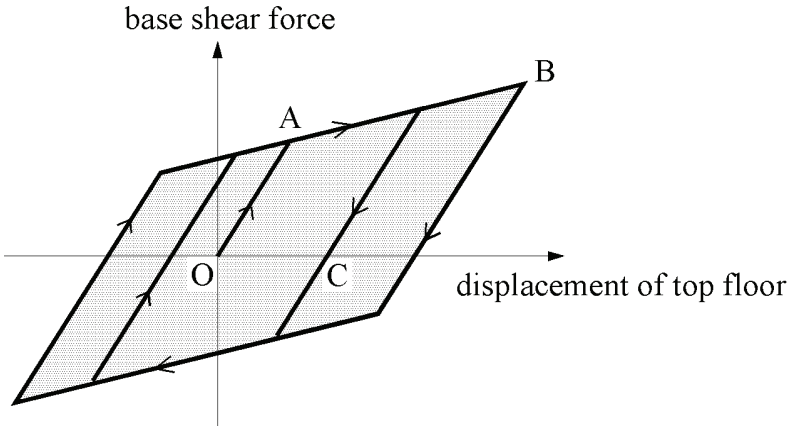

Figure 1-5 Ideal Inelastic Seismic Response of Elasto-Plastic Systems (EPS)

The portion OA in the hysteretic loop in Fig. 1-5 represents the elastic response of EPS. The structure yields at point A and reaches its maximum displacement at point B. The shaded area illustrates the energy dissipated through hysteretic yielding of the main structural elements: mainly the end of beams. A larger shaded area represents more energy dissipated,

an increase of the effective damping in the structural system and an increased probability that the EPS structure survives in the earthquakes. However, the hysteretic energy dissipated by EPS is also directly associated with structural damage to the structure and with potential large permanent inelastic deformations. The residual drift of the structure can be relatively large due to the large plastic deformation, as illustrated by point C in Fig. 1-5. Most SMRFs can be modeled as EPS systems. In SMRFs, the sections at the end of the beams develop plastic rotations or local buckling, which can lead to significant repair to the structure and associated costs to recover its normal operations. If a severe residual drift occurred, the cost of repairing the structure may be more than that of building a new one.

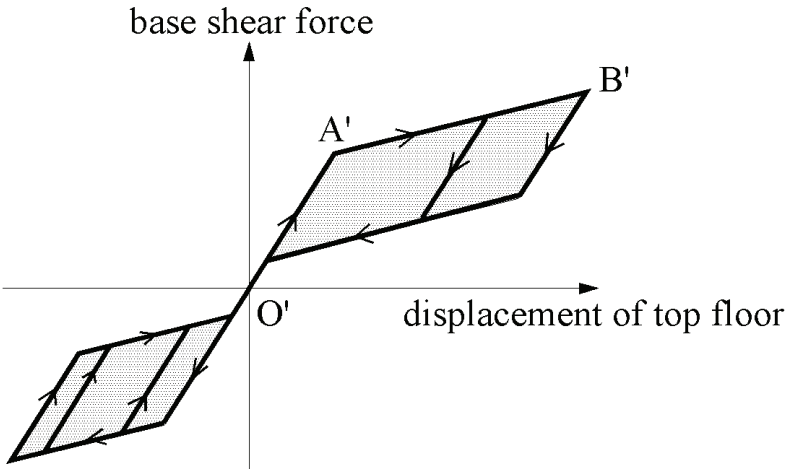

Figure 1-6 Ideal Seismic Response of Self-Centering Systems (SCS)

The idealized seismic response of a Self-Centering System (SCS) is shown in Fig. 1-6. There are two major differences between the seismic response of the EPS shown in Fig. 1-5 and that of the SCS shown in Fig. 1-6. First, the hysteretic loops are different which indicates that the energy dissipated in the SCS is less than that of the EPS. The reduced energy absorbed by the SCS “flows” into special devices rather than being dissipated hysteretically

by the main structural elements. Therefore, the damage to the structure is diminished or eliminated. Second, in Fig. 1-6, there is no point in the zero force axis except the original point, which means that the residual drift of the SCS is zero. The zero residual drift in the SCS can eliminate the cost to "return" the structure to its original position. After comparing the different properties, it can be argued that the SCS exhibits much better hysteretic properties than EPS, although special energy absorbing devices can be more costly in the initial construction. Self-centering properties in structural systems can be achieved using special dampers, control materials (like shape memory alloy) or special connections. More details on practical means of achieving self-centering properties are presented in Chapter II of this report. When compared to the cost of repairing a structure and recovering its operations, it is apparent that potentially the SCS can achieve a higher seismic performance at a reduced cost.

1.3 Research Objectives and Organizations

The objectives of this research are to numerically and experimentally investigate the properties and seismic performance of Self-Centering Systems (SCS) and apply the Self-Centering Post-Tensioned (SCPT) connections to the design of SMRF buildings.

Chapter I introduces the seismic performance of SMRF, the concepts of Elasto-Plastic Systems (EPS) and Self-Centering Systems, research objectives, and organizations.

The previous research on Self-Centering Systems is presented in Chapter II.

An analysis tool for Single-Degree-of-Freedom (SDOF) SCS excited by strong ground motions is developed in Chapter III. A full parametric dynamic analysis of SDOF EPS and SCS is conducted and the seismic performance is compared.

In Chapter IV, the redesign of the Multidisciplinary Center for Earthquake Engineering Research (MCEER) Demonstration Hospital incorporating SCPT connections is presented. Different numerical models of the structure are developed. Push-over analysis, seismic analysis and fragility analysis are also conducted.

Chapter V presents the design and scaling of the prototype structure and the design of the SCPT model used in the shake table testing.

In Chapter VI, the experimental procedure for the SMRF and SCPT models are presented. The selection of the ground motion used as the seismic excitation and the instrumentations are also discussed.

The experimental results are presented and compared in Chapter VII.

Chapter VIII describes the comparison of the results obtained from the initial numerical models, calibrated numerical models and experimental results.

The conclusions of both the numerical and experimental studies and suggestions for future work are presented in Chapter IX.

Through this report the SCS/SCPT systems are proved to have a better seismic performance and a reduced cost of repair after earthquakes than the most popular EPS/SMRF systems.

CHAPTER 2
PREVIOUS RESEARCH AND APPLICATIONS ON SELF-CENTERING SYSTEMS

Self-Centering Systems (SCS) have been studied analytically and experimentally mostly in the last fifteen years. As introduced in Chapter I, these systems, involving post-tensioned and energy dissipating elements or other special devices with self-centering property, also exhibit nonlinear softening behavior, ductility and energy dissipation. Re-centering forces are provided by post-tensioned systems or other special devices to return the structure to its original position and eliminate or diminish residual deformations.

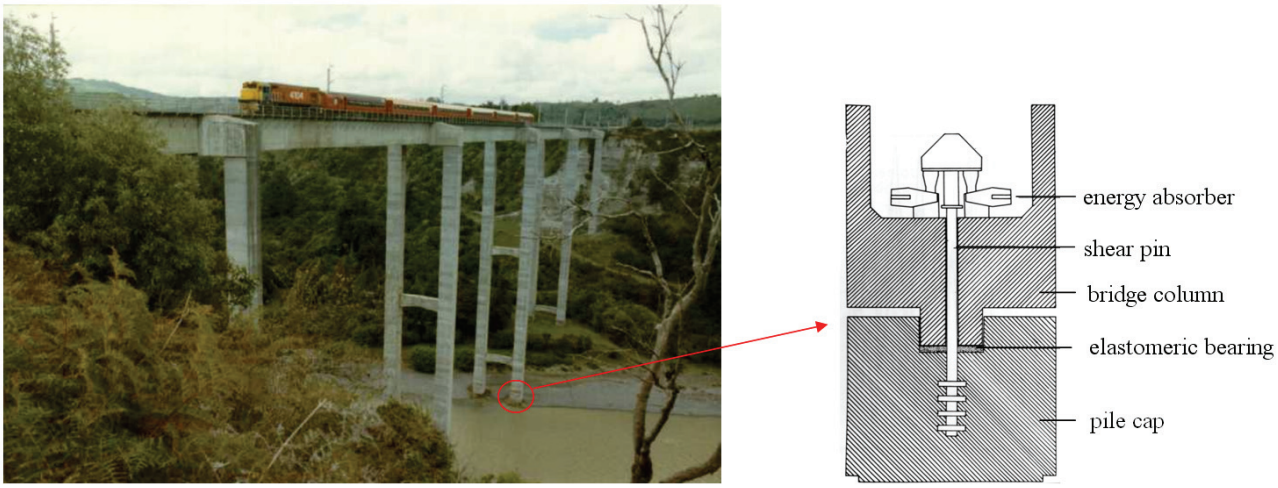

(a) (b)

Figure 2-1 Rangitikei Railway Bridge (a) Overall View (b) Rocking Pad (Cormack 1988)

The first practical application of SCS was the design of the “stepping” Rangitikei rail bridge in New Zealand in 1981. As shown in Fig. 2-1(a), this 70 m (230 ft) tall 315 m (1033 ft) long bridge was constructed with six spans of prestressed concrete hollow-box girders

(Cormack 1988). The self-centering property is exhibited by the rocking foundation system as shown in Fig. 2-1(b). The weight of the bridge allows the re-centering of the structure when there is a transverse displacement. Therefore, this bridge behaves as an inverted pendulum with its own weight providing the self-centering effect.

After this first application of SCS, more research efforts were conducted. To achieve the re-centering capability, two major methods were developed: self-centering dampers and special self-centering connections. These two methods are discussed in this chapter in order to present previous and recent research and applications on SCS.

2.1 Self-Centering Dampers

Structures designed with conventional dampers, such as viscous dampers, friction dampers or viscoelastic dampers, do not prevent residual drifts to occur after earthquakes. To eliminate or decrease these residual drifts, dampers can be improved to incorporate re-centering capabilities. These dampers with SCS properties are referred herein as “Self-Centering Dampers”.

2.1.1 Shape Memory Alloys (SMA) Dampers

Shape Memory Alloys (SMA) dampers are metallic dampers incorporating a special class of alloys, which produce the so-called supper elastic behavior as shown in Fig. 2-2.

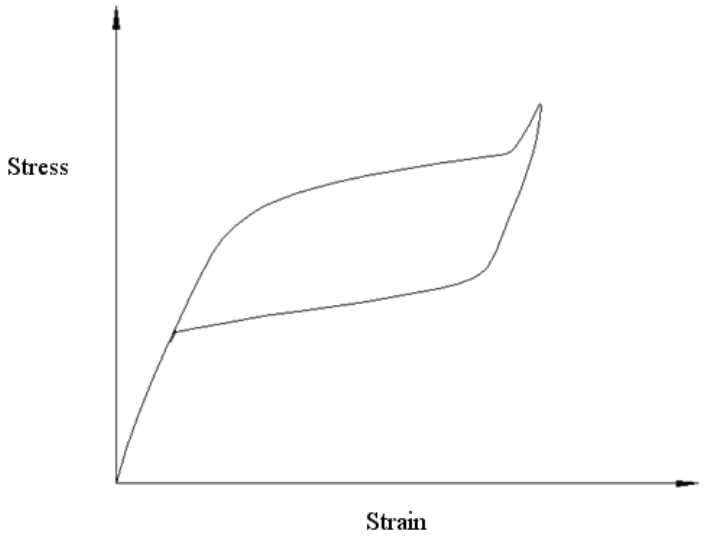

Figure 2-2 Super Elastic Hysteresis

There are five primary SMA systems that have been developed: the Nickel-Titanium family (often called Nitinol); two copper-based systems, Cu-Zn-Al and Cu-Al-Ni; Fe-Mn-Si alloys; and some special stainless steel compositions (Whittaker et al. 1995). The stress-strain relationship of SMAs depends on the alloying temperature. A high alloying temperature produces a fully austenite phase, which exhibits a linear elastic stress-strain relationship. A fully martensite phase occurs in a low alloying temperature and exhibits a viscoelastic stress-strain relationship. An intermediate alloying temperature produces a hybrid phase involving both phases, which displays the supper elastic behavior similar to the SCS. Aiken et al. (1992) conducted shake table tests on a small-scale three-story steel frame using SMA (Nitinol) dampers, which incorporated Nitinol wires at the end of the cross-bracing systems. Due to the large pre-load in the braces, the Nitinol wires were cycled in the range of martensite phase and lost the self-centering property. Another SMA (Cu-Zn-Al) damper test in a 2/5- scale five-story frame was conducted by Witting and Cozzarelli (1992). This test

result indicated that the SMA (Cu-Zn-Al) damper had a super elastic stress-strain relation for a very limited number of cycles and after a few cycles the damper performed an elastoplactic hysteretic behavior due to the increased internal friction.

Another experimental work of SMA in structures was conducted by Ocel et al. (2004). In this investigation, the SMA was used in two full scale steel beam-column connections as shown in Fig. 2-3. Results from cyclic loading and dynamic loading indicated that the connections with SMA exhibited a high level of energy dissipation, large ductility and no strength degradation. The recovery of residual shape by heating the SMA demonstrated the self-centering capability in this system.

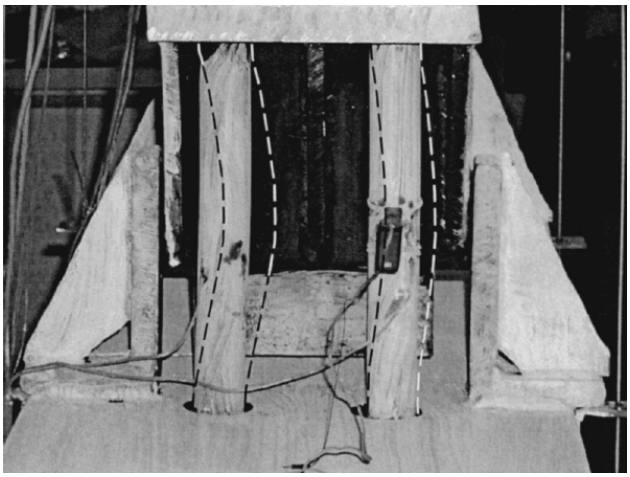

Figure 2-3 Recovered-deformation of Connections with SMA after Heating: dashed lines represent residual shape before heating (Ocel et al. 2004)

2.1.2 Energy Dissipating Restraint (EDR)

The Energy Dissipating Restraint (EDR) was originally designed as a seismic restraint device for the support of piping systems in nuclear power plants. The EDR is a damper

device, indicated in Fig. 2-4, which is based on a friction mechanism. In this device, as a result of the combination of wedges, internal stops and springs, a frictional force is produced and determined proportional to the relative displacement of two device ends. More details of the mechanism in this device can be found in Nims (1993).

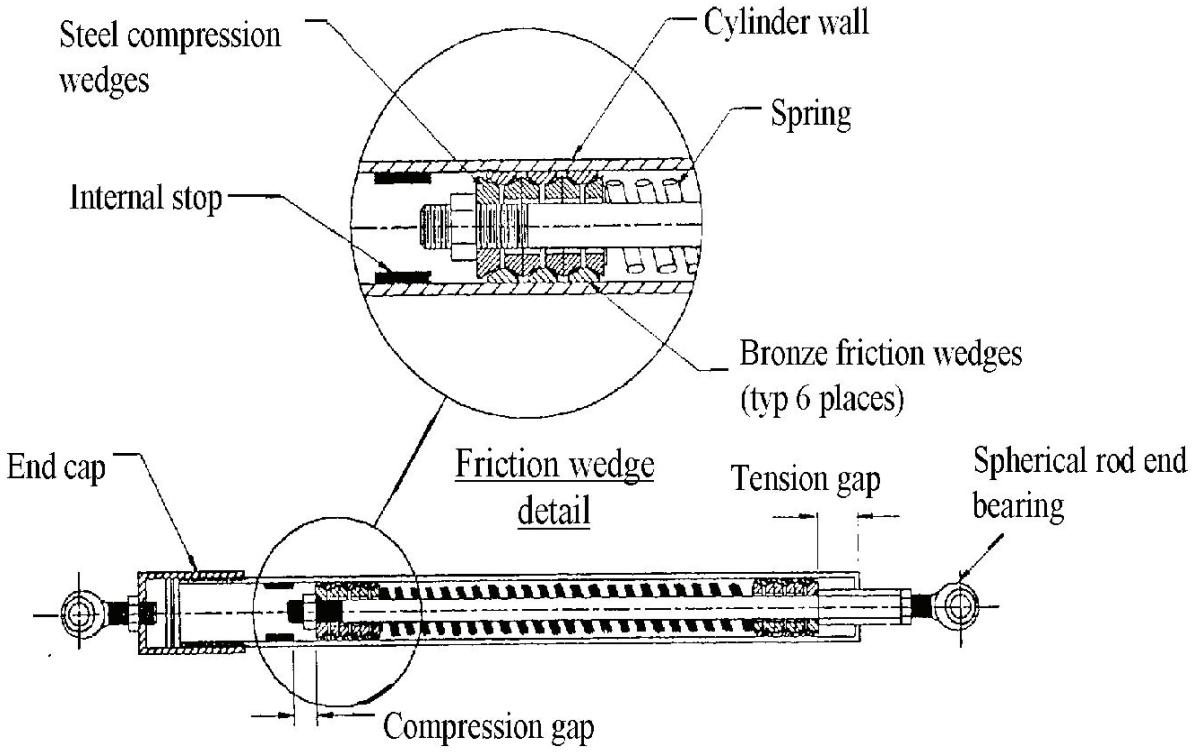

Figure 2-4 Internal View of Energy Dissipating Restraint (Nims et al. 1993)

The EDR can provide various self-centering hysteretic responses as shown in Fig. 2-5. An experimental shake table study of a small-scale 3-story EDR frame was conducted by Aiken et al. (1993), as shown in Fig. 2-6. The results of this test indicated that the effect of the EDR reduced the model deformations and interstory drifts.

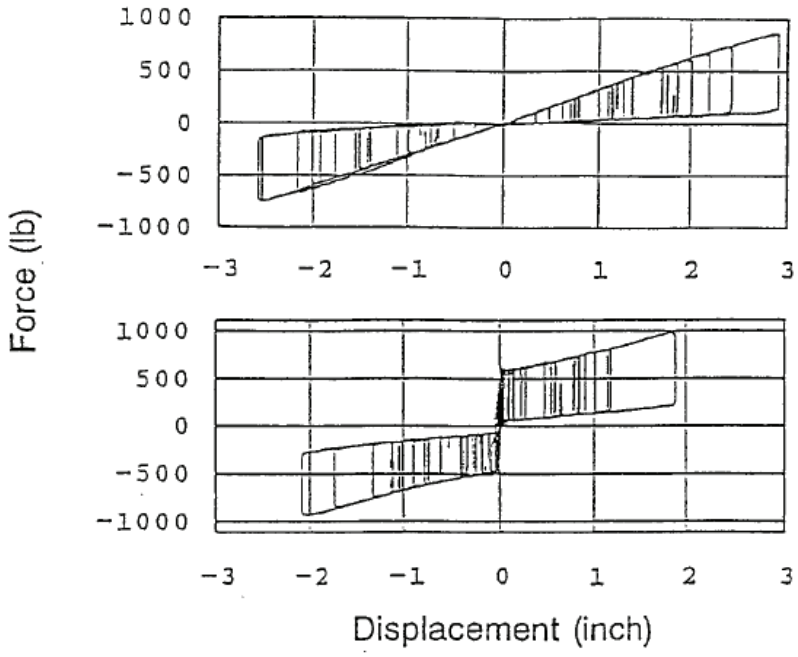

Figure 2-5 Various Self-Centering Hysteresis Loops Provided by the EDR Device (Aiken et al. 1993)

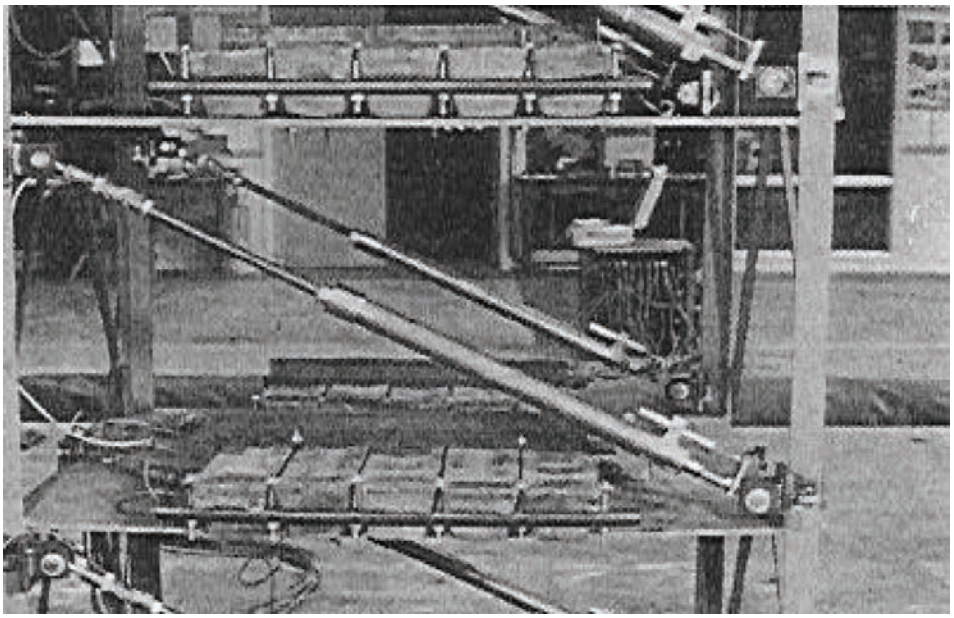

Figure 2-6 View of EDRs Installed at the Second Level of Test Frame (Aiken et al. 1993)

2.1.3 SHAPIA Damper

The SHAPIA damper is another damping device that exhibits the self-centering behavior. This damper uses a friction-based ring spring as the key component for the energy dissipation as shown in Fig. 2-7. Under compression load, the friction springs are compressed by the left and right cup while the tie bar moves toward the right. Under the tension load, the right cup is pulled by the tie bar toward to the left while the left cup is hold by the right sliding sleeve so that the friction springs are also compressed. This simple and effective mechanism makes the friction springs compressing and dissipating energy under both compression and tension external load.

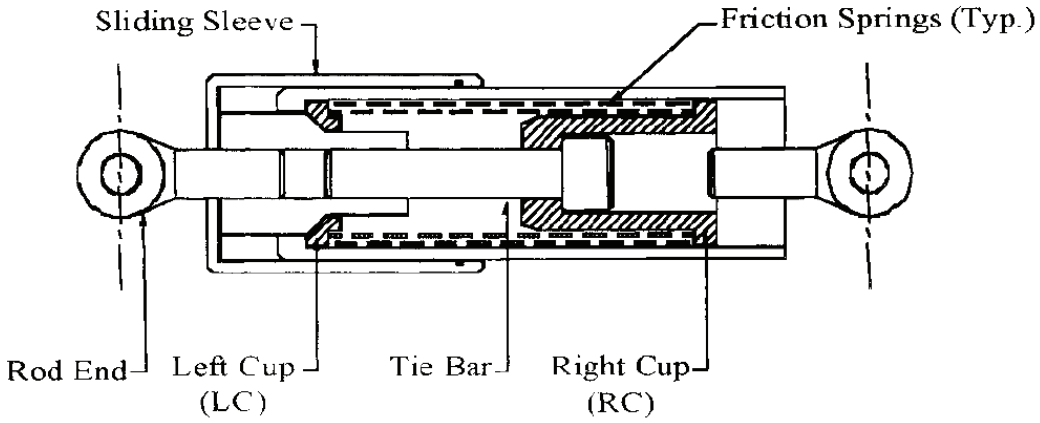

Figure 2-7 Diagrammatic View of the SHAPIA Damper (Filiatrault et al. 2000)

A seismic test on a single-story steel frame incorporating a SHAPIA damper was conducted by Filiatrault et al. (2000). The test demonstrated that the SHAPIA damper reduced the lateral displacement of the test structure through its self-centering characteristics as shown in Fig. 2-8.

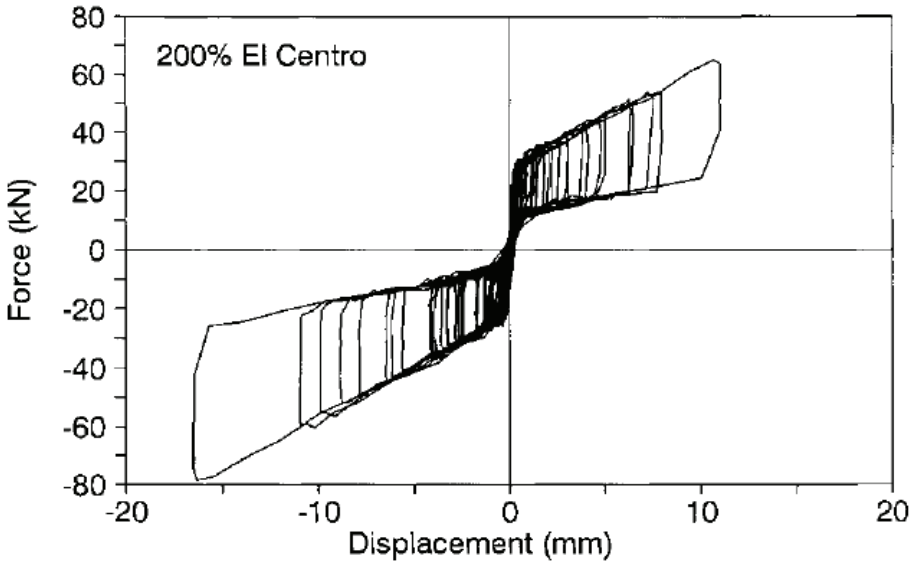

Figure 2-8 Force-Displacement Hysteresis loop of SHAPIA Damper Recorded during the Seismic Test (Filiatrault et al. 2000)

2.2 Self-Centering Connections

Self-Centering Systems (SCS) can also be achieved by special self-centering connections. Most of there connections use post-tensioned bars and tendons to provide the re-centering capability along with metallic devices, usually mild steel, to absorb the energy incurred by the excitation of earthquakes. The advantages of the self-centering connections are not only the re-centering capability but also the lower cost compared to the self-centering dampers. Depending on their orientation, self-centering connections in structures can be classified into two types: horizontal connections (beam to column) and vertical connections (wall to foundation or column to foundation).

2.2.1 Rocking Self-Centering Connections

Rocking self-centering connections can be implemented in bridge piers and in unbonded post-tensioned precast concrete walls in buildings. As introduced in the beginning of this chapter, the first application of these connections was the south Rangitikei Railway Bridge in New Zealand. Since then, several experimental investigations have been conducted in the United States using a similar concept. Mander and Cheng (1997) investigated the performance of unbonded post-tensioning in bridge piers under seismic loading.

Fig. 2-9(a) shows an unbonded post-tensioned precast concrete wall. The post-tensioned steel is anchored at the top of the wall and the foundation. A gap between the wall and the foundation develops due to the lateral deformation or the overturning moment. When unloading, the post-tensioned steel and the weight of the wall return the wall to its original position, thereby exhibiting a self-centering property as shown in Fig. 2-9(b).

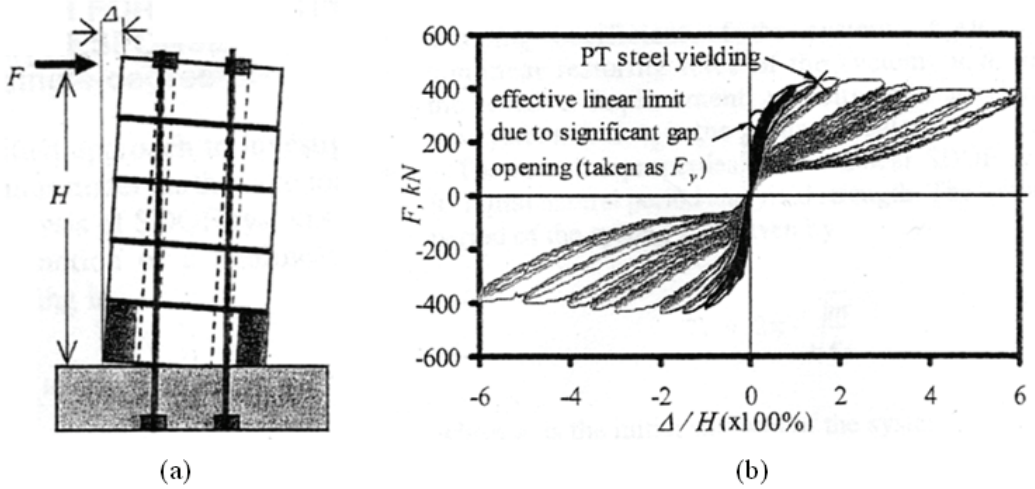

Figure 2-9 Post-Tensioned Precast Concrete Wall (a) Deformed Configuration of Unbonded PT Precast Concrete Wall (b) Experimental Cyclic lateral Load-Drift Behavior of Unbonded PT Precast Concrete Wall (Perez 2004)

Kurama et al. (1996, 1997, 1999 and 2004) and Shen et al. (2002) analytically investigated the seismic behavior and design of similar unbonded post-tensioned precast concrete walls. As a result of the analysis, unbonded post-tensioned precast walls had larger displacements than comparable monolithic cast-in-place reinforced concrete walls and had significantly smaller maximum residual displacements than the monolithic walls, which verified the self-centering capability of the walls. Stanton and Nakaki (2002) developed a post-tensioned split rocking wall system, in which wall panels are split to allow rocking of the individual panels. The re-centering force is provided mainly by post-tensioned tendons. Restrepo (2002) further developed these walls by adding conventional tapered mild steel bars between the foundation and the wall as energy dissipating devices. The advantage of the added steel is to absorb more energy and delay the yielding of post-tensioned tendons, which provide the large displacement and re-centering capability observed in this shake table tests. Figure 2-10 shows the experimental test of a rocking wall conducted by Holden et al. (2003). Results of conventional walls and rocking walls from this quasi-static test were compared and indicated the benefit of this hybrid wall system. Another rocking shear wall system was developed by Ajrab et al. (2004), who conducted also a parametric study. This analytical research verified that rocking wall structures with supplemental damping systems provided viable alternatives to conventional fixed-base ones.

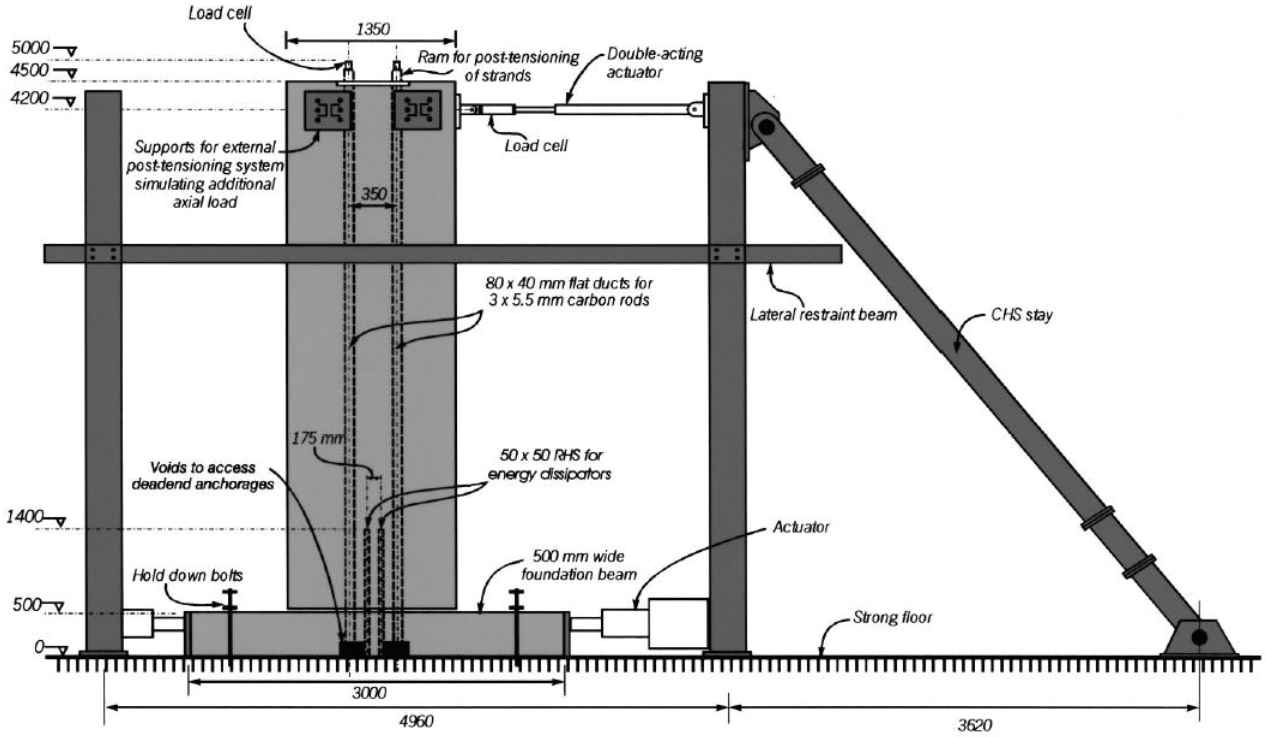

Figure 2-10 Loading Frame and Rocking Wall (Holden et al. 2003)

2.2.2 Self-Centering Connections in Concrete Structures

Priestley and Tao (1993) first proposed the use of partially unbonded post-tensioned tendons through beam-column joints as a design for precast concrete ductile connections. Figure 2-11 indicates the shear transfer mechanism in a typical partially unbonded post-tensioned beam-to-column connections. The horizontal shear force is transferred by a diagonal compression strut and the vertical shear force is transferred by the contact friction between the beam and column in the joint. The clamping force, provided by the unbonded post-tensioned tendons, produces a self-centering characteristic.

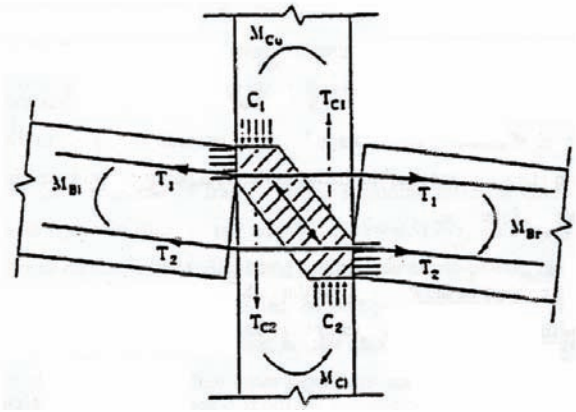

Figure 2-11 Shear Transfer Mechanism in the Joint Region with Unbonded Tendons (Priestley and Tao, 1993)

An experimental study on full-scale unbonded post-tensioned precast beam-column subassemblies was conducted by MacRae and Priestley (1994). These results demonstrated the good seismic performance of these new connections. A hybrid system was proposed by Stanton et al. (1997). This system involved the use of not only post-tensioned bars but also grouted reinforcing bars, which provided additional energy dissipation. As a result of the test, this hybrid system was demonstrated to have a good self-centering capability and exhibited essentially no residual drifts.

After the above self-centering connections in concrete structures were studied, a 60% scale five-story precast concrete building model was tested under simulated seismic loading as part of the PREcast Seismic Structural Systems (PRESSS) research program (Priestly et al. 1999). As shown in Fig. 2-12, the building was constructed with four different ductile structural frame systems involving different self-centering connections in one direction and a jointed structural wall system in the orthogonal direction. The pseudo-dynamic method was

used for the test using several different earthquakes records. Under the excitation of the scaled earthquake records, which is equivalent to 1.5 UBC Zone 4 loading, the behavior of the structure was extremely satisfactory. The self-centering connections of the structure led to a significant reduction of residual drifts. There was only minimal damage observed in the shear wall direction. Among the different connections used in the structure, the hybrid connections with energy dissipating bars exhibited the best performance including the capacities for large deformations and re-centering characteristics. A detailed report of the performance of self-centering connections and the analysis procedure used in this test is given by Pampanin et al. (2000).

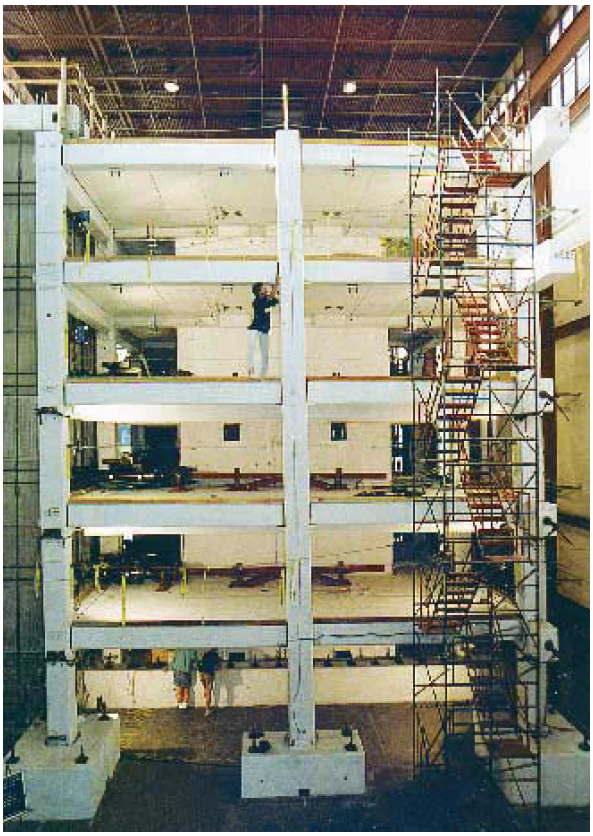

Figure 2-12 Overall View of Five-Story Building under Test (Priestley et al. 1999)

2.2.3 Self-Centering Connections in Steel Structures

Self-centering connections in steel structures have been studied mostly in the last five years. A Post-Tensioned (PT) connection was developed by Ricles et al. (2001, 2002). Another one was the Post-Tensioned Energy Dissipating (PTED) connection proposed by Christopoulos et al. (2002a, 2002b). An analytical research of another type of self-centering connections, the Post-tensioned Friction Damped Connection (PFDC), was conducted by Rojas et al. (2005). In this section, these three types of connections are discussed.

2.2.3.1 Post-Tensioned (PT) Connections

As shown in Fig. 2-13(a), the Post-Tensioned (PT) beam-column steel connection proposed by Ricles et al. (2001) uses post-tensioned strands, distributed along the depth of the beam to provide the self-centering capability, and bolted angles between the top/bottom flange of the beams and columns to provide the energy dissipation. Shear forces are transferred by the friction at the beam-column interface and bolted angles. One of the advantages in this configuration is no requirement for field welding.

A large-scale test program was conducted by Ricles et al. (2002). Fig. 2-13(b) illustrates the test setup. Loading was applied by displacing the top of the column through a series of increasing symmetric displacement cycles. As shown in Fig. 2-13(c), the test results indicated the several advantages of this PT connection: (1) the similar initial stiffness to conventional welded steel connections; (2) the self-centering capability; and (3) the energy dissipation by the bolted angles without evident damage to the beam and column. Another

full-scale PT connection was tested using inelastic cyclic loading by Garlock et al. (2005) and once again it demonstrated the benefits of this type of connection. A performance-based seismic design approach for this PT frame was outlined and evaluated by Garlock et al. (2007).

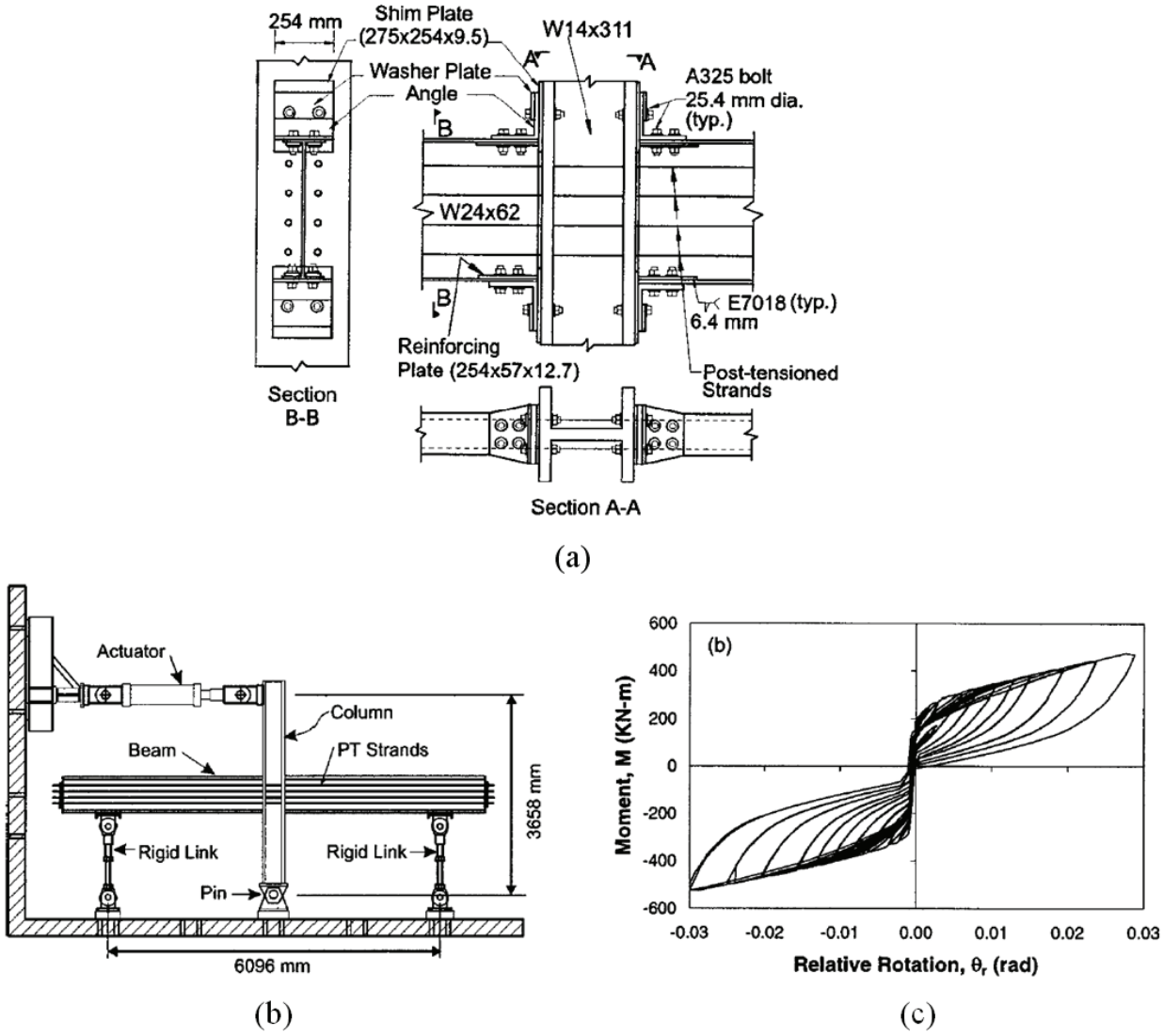

Figure 2-13 Post-Tensioned Connections Test (a) Post-Tensioned Specimen Connection (b) Post-Tensioned Connection Subassembly Setup (c) Moment-Rotation Response of a PT Connection (Ricles, et al. 2002)

2.2.3.2 Post-Tensioned Energy Dissipating (PTED) Connections

Another self-centering steel connection: the Post-Tensioned Energy Dissipating (PTED) connection was proposed by Christopoulos et al. (2002a, b). As shown in Fig. 2-14, the PTED connection incorporates two symmetric high strength Post-Tensioned (PT) tendons or bars at the mid-depth of the beam as re-centering components and four symmetric

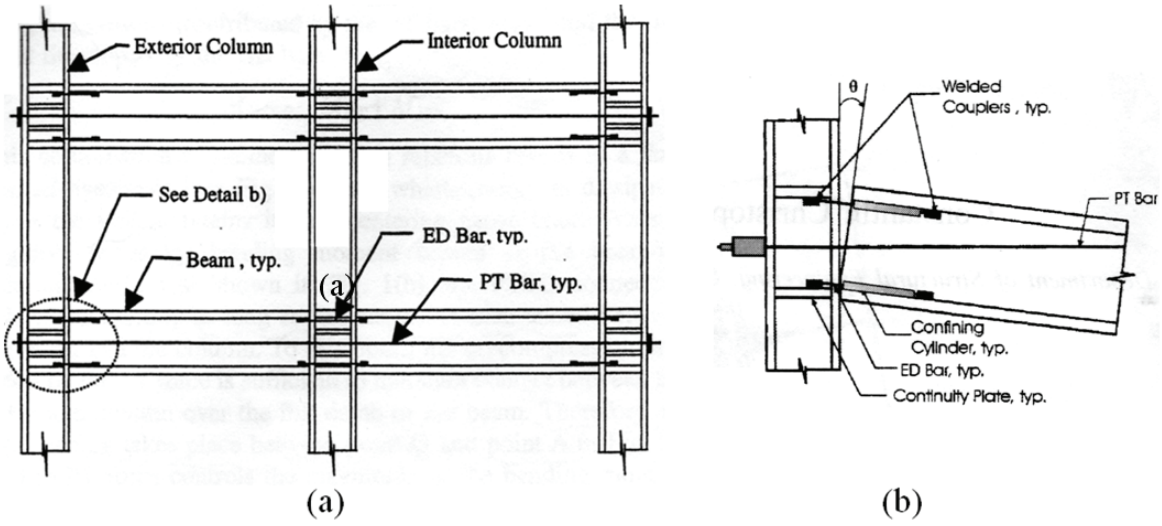

Figure 2-14 Concept of PTED connections (a) Steel Frame with PTED Connections (b) Geometric Configuration of Exterior PTED Connections (Christopoulos et al, 2002a)

Energy Dissipating (ED) bars per connection for dissipating energy. The PT bars are anchored at the flange of the exterior columns of the lateral load-resisting frame and the ED bars are welded to the inside face of the beam flanges and the continuity plates of the exterior columns. To prevent the buckling of the ED bars in compression, confining steel sleeves welded to the flanges of beams or the continuity plates of columns confine the ED bars. As shown in Fig. 2-15(a), cyclic testing of a PTED beam-to-column connection was conducted by using inelastic cyclic loading at the mid-length of the beam. Fig. 2-15(b)

indicates that the PTED connection exhibited very good self-centering characteristics and eliminated the residual drift without any damage in the beam and column. The experimental results were in good conformity to the predictions provided by a numerical study developed by the same authors.

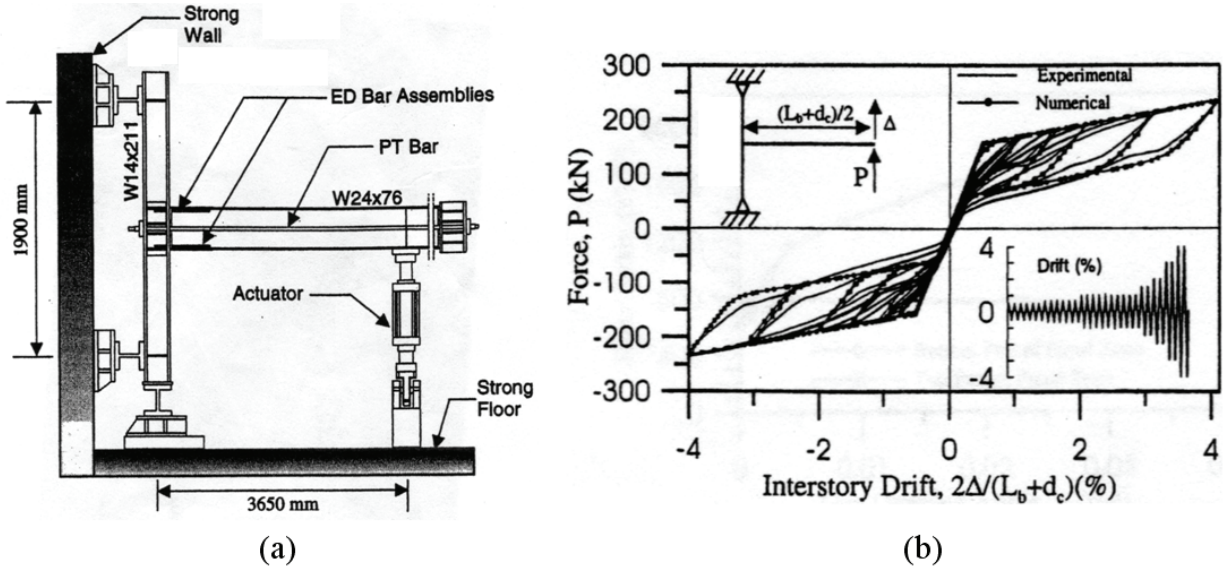

Figure 2-15 Cyclic Testing of a PTED connection (a) Experimental Setup (b) Experimental and Numerical Force-Interstory Drift Response (Christopoulos et al., 2002b)

Another experimental study was also conducted by Collins and Filiatrault (2003). The test model was a half-scale steel moment-resisting frame involving PTED connections along with a concrete floor slab. The test results demonstrated that the steel frame with PTED connections had the capacity for large deformations and self-centering capability without evident damage to the primary steel components. Although the concrete floor slab had uniform crack patterns at a 3% inter-story deformation, it didn't limit the performance of the PTED connections.

2.2.3.3 Post-tensioned Friction Damped Connections (PFDC)

Rojas et al. (2005) analytically investigated another self-centering steel connection: the Post-tensioned Friction Damped Connection (PFDC). As shown in Fig. 2-16, this type of connection includes friction plates bolted in the flanges of beams and columns for energy dissipation and high strength post-tensioned strands to provide the self-centering property. The shear force is transferred by the combination of the bolted shear tab, the friction between beams and columns, and the friction plate. Results from an inelastic analysis of a six-story, four-bay, Steel Moment-Resisting Frame (SMRF) with PFDC indicated that the system has good energy dissipation and self-centering capability and its seismic performance could exceed that of the SMRF with conventional welded connections.

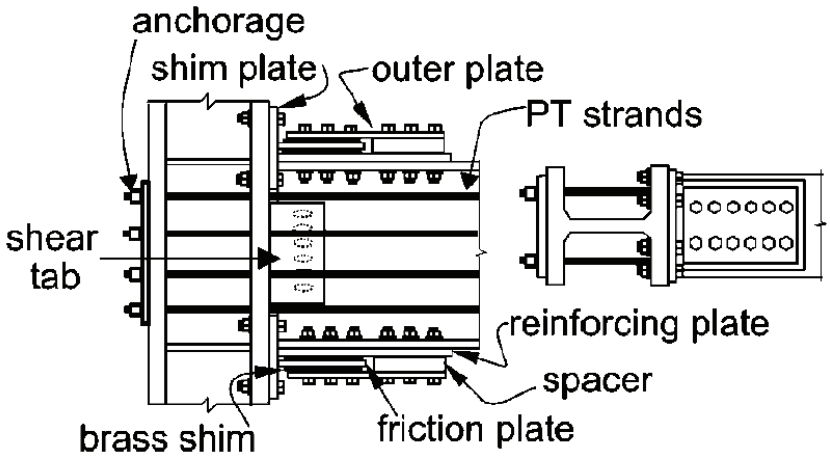

Figure 2-16 Post-tensioned Friction Damped Connection (PFDC) Details (Rojas et al. 2005)

2.3 Summary and Research Motivation

In this chapter, various Self-Centering Systems (SCS) were reviewed. The self-centering capability (i.e. no permanent deformation) and energy dissipation mechanism without major damage to structural components are the main benefits of SCS.

Up to now, the main applications of SCS have been as rocking systems in bridge structures. Although there have been several experimental studies of SCS on building models or subassemblies, there is lack of practical applications to real building structures. More research efforts focusing on the actual implementation of SCS in complete building systems are necessary for the development of these systems. To address this issue, this report investigates the use of SCS for the re-design of a real structure: the MCEER Demonstrated Hospital. To experimentally validate the analytical research, shake table testing was conducted on two 1/3 scale models of steel SCPT and SMRF structures.

The objectives of this study are to provide more experiences on the actual design methods of SCS in building structures and demonstrate the feasibility of SCS as a practical design alternative in complete structural systems.

CHAPTER 3
SEISMIC RESPONSE OF SINGLE-DEGREE OF-FREEDOM SELF-CENTERING SYSTEMS

In order to apply the concept of Self-Centering Systems (SCS) for the seismic design of actual Multi-Degree-of-Freedom (MDOF) structural systems, it is useful to consider the seismic response of Single-Degree-of-Freedom (SDOF) systems under strong ground motion excitations. This chapter describes the development of a Matlab-based computer code used to evaluate the seismic response of SDOF SCS and Elasto-Plastic Systems (EPS), which properties were introduced in Chapter I (see Fig. 1-5). The seismic performances of these two systems are also discussed. The main objective of this chapter is to develop insight and design aides to be used for the seismic design of MDOF equipped with SCS.

This chapter builds on similar analyses performed by Christopoulos et al. (2002a) under a more restricted set of ground motions. The approach taken herein is somewhat similar to the one used by Christopoulos but the computer codes are independently developed and the evaluation method is more complex and more integrated so that the results can be used more directly as a preliminary guideline for the seismic design of more complex structures equipped with SCS. This improved analysis of the results coupled with a more elaborated ensembles of ground motion excitations is the main advantage over the results obtained by Christopoulos et al. (2002a).

3.1 Hysteretic Models of Single-Degree-of-Freedom Self-Centering Systems and Elasto-Plastic Systems

A SDOF model with either SCS or EPS is considered in the numerical analysis as shown in Fig. 3-1 (a). An equivalent damping ratio of 5% of critical is introduced to consider other sources of energy dissipation in the structure that are not associated with hysteretic behavior of the structural elements after yielding. The global hysteretic characteristic of the structural system is considered by a nonlinear spring with initial stiffness k_0, as shown in Fig. 3-1 (b) and (c).

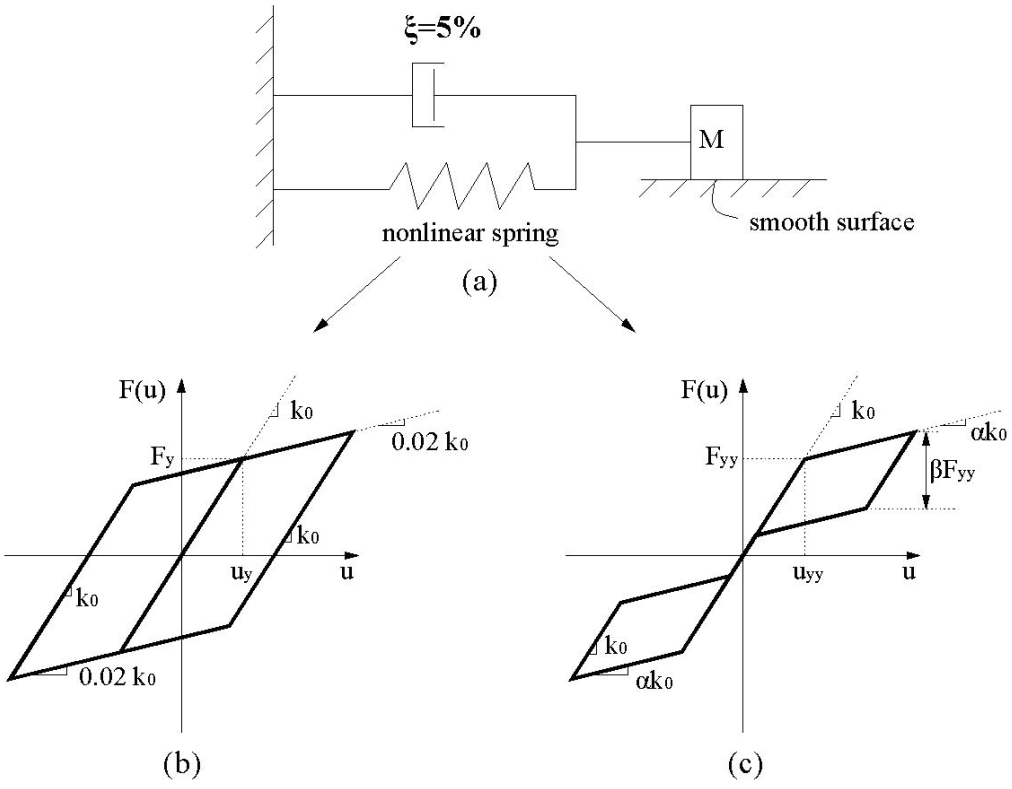

Figure 3-1 SDOF Numerical Model (a) SDOF system (b) Hysteretic Loop of Elasto-Plastic Systems (EPS) (c) Hysteretic Loop of Self-Centering Systems (SCS)

The bilinear elasto-plastic hysteretic behavior shown in Fig. 3-1 (b) for the nonlinear spring represents an idealized response of an EPS, which is representative of Steel Moment-Resisting Frames (SMRF) designed with post-Northridge welded connections (Gross et al. 1999). In this idealized loop, it is assumed that there is no strength degradation. The EPS yields at displacement u_Y under the yielding force F_Y and a post-yielding stiffness is assumed to be equal to 2% of the initial stiffness. The second nonlinear spring considered exhibits a self-centering behavior as shown in Fig. 3-1 (c). This model represents the SMRF incorporating the self-centering components. The initial stiffness is the same as that of the EPS and the post-yielding stiffness is variable and is controlled by the factor α, which ranges from 2% to 35%. Another controlling parameter is the energy dissipating factor β, which ranges from 0 to 1. The SCS model yields at the displacement u_{YY} under the force F_{YY}, which indicates that the yielding point in these two models can be different. This difference in yielding force between the SCS and EPS is controlled by the strength ratio factor η and yielding ratio factor ψ. Theses controlling parameters will be presented and discussed in details in Section 3.2.2.

3.2 Seismic Parametric Study of Single-Degree-of-Freedom (SDOF) Self-Centering Systems (SCS)

A numerical parametric study of the seismic response of SDOF SCS is conducted in this section using two ensembles of MCEER simulated earthquake ground motions, in which the 25 motions are strong ground motions having a probability of exceeding of 2% in 50 years in California and the other 25 motions have a 10% probability of exceedance in 50 years in CA.

The seismic responses of SDOF SCS and EPS are compared and the results are plotted in the form of design charts to estimate the optimum SCS parameters to guide the design of more complex MDOF structures equipped with SCS.

3.2.1 Definition of Earthquake Ground Motions

The MCEER simulated ground motions, developed by Wanitkorkul and Filiatrault (2005), were used as input in this parametric study. These ground motions were generated at an assumed hospital site located on the west-coast of the United States. A near-field site model was used in this simulation because the west-coast in the U.S. was considered to be in a near-fault region. The simulated ground motions were scaled to match the uniform hazard spectra in Northridge, CA, provided by the U.S. Geological Survey (USGS) as shown in Fig. 3-2. There were four different hazard levels (2%, 5%, 10%, 20% probability of exceedance

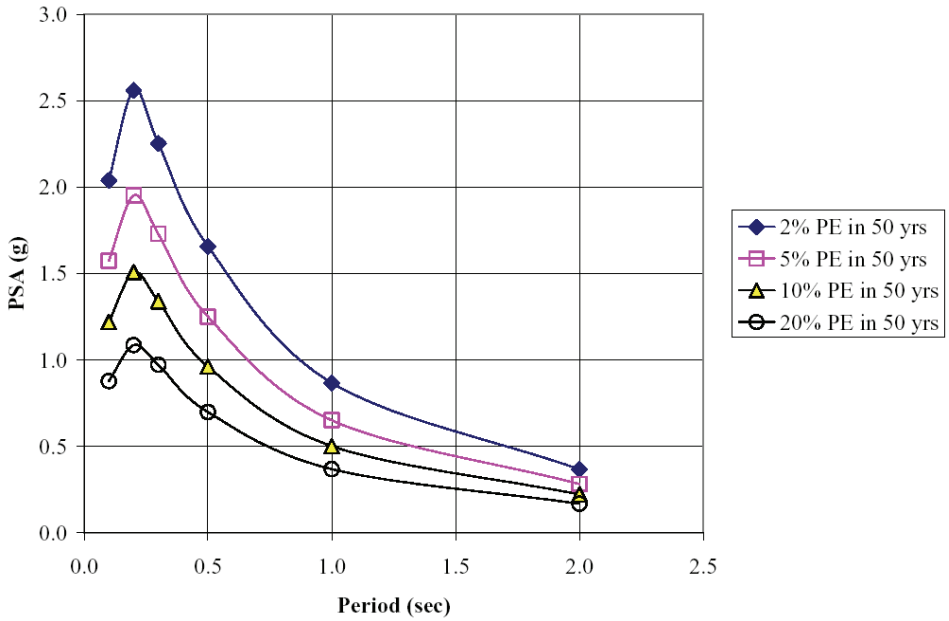

Figure 3-2 USGS Uniform Hazard Spectra: Northridge, CA
(Wanitkorkul and Filiatrault, 2005)

in 50 years) considered in this simulation. An ensemble of 25 earthquake motions for each probability level was generated by using a simulation methodology proposed by Mavroeidis and Papageorgiou (2003). More details about the simulation procedure and ground motions can be found in the report by Wanitkorkul and Filiatrault (2005). In order to analyze the seismic response of SDOF SCS and EPS under the excitations of earthquakes in severe and medium hazard levels, the two ensembles of 25 MCEER ground motions with 2% probability and 10% probability of exceedance in 50 years are selected.

3.2.2 Equations of Motion and Controlling Parameters

The equation of motion for a nonlinear SDOF system is given by:

$$m\ddot{u} + c\dot{u} + F(u,\dot{u}) = -m\ddot{u}_g \tag{3.1}$$

where m is the mass, c is the damping constant, u is the relative displacement, $\dot{u}$ is the relative velocity, $\ddot{u}$ is the relative acceleration of SDOF model and $F(u,\dot{u})$ is the nonlinear restoring force, which are also shown in Fig. 3-1. The restoring force $F(u,\dot{u})$ is dependent on not only the displacement but also the velocity due to the nonlinear properties of the SCS and EPS. The term $\ddot{u}_g$ is the ground acceleration and the mass, m, is representative of the total mass of a structure. The damping constant is defined by:

$$c = 2\xi\sqrt{mk_0} \tag{3.2}$$

where the damping ratio ξ is assumed to be 5% of critical and k_0 is the initial stiffness of the model, which can be calculated from:

$$k_0 = \frac{4\pi^2 m}{T_0^2} \tag{3.3}$$

where T_0 is the initial fundamental period of the structure. According to the prestandard and commentary for the seismic rehabilitation of buildings developed by the Federal Emergency Management Agency (FEMA 356), the fundamental period T_0 can be estimated by:

$$T_0 = C_t h_n^{\lambda} \tag{3.3}$$

where:

C_t = 0.035 for Steel Moment Resisting Frame (SMRF) systems

h_n = Height (in feet) above the base to roof level

λ = 0.8 for SMRF systems

It is assumed that the story height of typical SMRFs is 11ft and the number of stories ranges from one to fifteen. From Eq. (3.3) and the above assumption, the range of fundamental periods can be calculated as:

$$0.23\text{sec} < T_0 < 2.08\text{sec} \tag{3.4}$$

In order to consider the full range response of short-period systems, a lower bound value for T_0 is assumed at 0.01 second.

Another controlling factor is the strength factor η, which is defined by:

$$\eta = \frac{Fy}{W} \tag{3.5}$$

where F_Y is the yielding strength and W is the weight of the structure. This factor controls the yielding force, which is also the design shear, with the specific weight of the building.

This factor is assumed to be less than 1. In order to compare the results from EPS and SCS with different yielding strength, a yielding strength ratio factor ψ is given by:

$$\psi = \frac{(Fy)_{SCS}}{(Fy)_{EPS}} == \frac{\frac{(Fy)_{SCS}}{W}}{\frac{(Fy)_{EPS}}{W}} = \frac{\eta_{SCS}}{\eta_{EPS}} \tag{3.6}$$

To fully define the hysteretic properties of SCS, two supplemental factors, α and β, are incorporated as shown in Fig. 3-1. The range of post-yielding stiffness factor α is assumed to be from 0.02 to 0.35, which is mainly dependent on the initial PT force in the PT components of SCS. The energy dissipating factor β is assumed to range from 0 to 1. When β equals to 0, the SCS behaves as a bi-linear elastic system without energy dissipation. A value of β equal to 1 corresponds to the largest energy dissipating capacity that a SCS can exhibit while maintaining its self-centering characteristics. If β is larger than 1, the SCS loses its self-centering capability and a residual displacement occurs at the end of each cycle. Table 3-1 shows these controlling parameters, in which α and β are used for modeling the SDOF SCS, while in SDOF EPS model, α is assumed to be 0.02 and β actually equals to 2. After the permutation and combination of these four factors, there are 576 SDOF SCS models and 36 SDOF EPS models included in the parametric analysis.

Table 3-1 Controlling Parameters in SDOF SCS and EPS models

α	β	η	T_0 (sec)
0.02	0.0	0.05	0.01
0.10	0.3	0.10	0.25
0.20	0.6	0.20	0.50
0.35	1.0	0.30	1.00
		0.50	1.50
		1.00	2.00

3.2.3 Integration Algorithm for Nonlinear Time-History Dynamic Analysis

The Newmark's method (Newmark 1959) is used for integrating the second-order equation of motion in the time domain. This integration algorithm is based on solving the following equations at the end of each time-step:

$$m\ddot{u}_{i+1} + c\dot{u}_{i+1} + (f_s)_{i+1} = p_{i+1} \tag{3.7}$$

$$\dot{u}_{i+1} = \dot{u}_i + [(1-\gamma)\Delta t]\ddot{u}_i + (\gamma\Delta t)\ddot{u}_{i+1} \tag{3.8}$$

$$u_{i+1} = u_i + (\Delta t)\dot{u}_i + [(0.5-\Gamma)(\Delta t)^2]\ddot{u}_i + [\Gamma(\Delta t)^2]\ddot{u}_{i+1} \tag{3.9}$$

where γ and Γ determine the variation of acceleration over a time step and the stability and accuracy of this integration. These three equations (3.7, 3.8 and 3.9) are combined to compute the unknown displacement u_{i+1}, velocity $\dot{u}_{i+1}$ and acceleration $\ddot{u}_{i+1}$ at the time-step i+1 from the known u_i, $\dot{u}_i$ and $\ddot{u}_i$ at the time-step i through an iteration process; f_s is the restoring force and p is the external force such as earthquake excitations.

The Newmark's method applied to nonlinear systems introduces numerical errors, as shown in Fig. 3-3 (a). Those numerical errors are the results of using the tangent stiffness k_{ab} instead of the unknown secant stiffness $k_{ab'}$ in the numerical calculations. To minimize these errors, the Newton-Raphson iteration can be added to the Newmark's method as illustrated in Fig. 3-3 (b). This iteration is performed within one time step to make the numerical result at the end of a first iteration (point *B* in Fig. 3-3 (b)) closer to the exact point B' to an acceptable error level after 3 iterations. A full description of the Newmark's method with the Newton-Raphson iteration can be found in Chopra (2000).

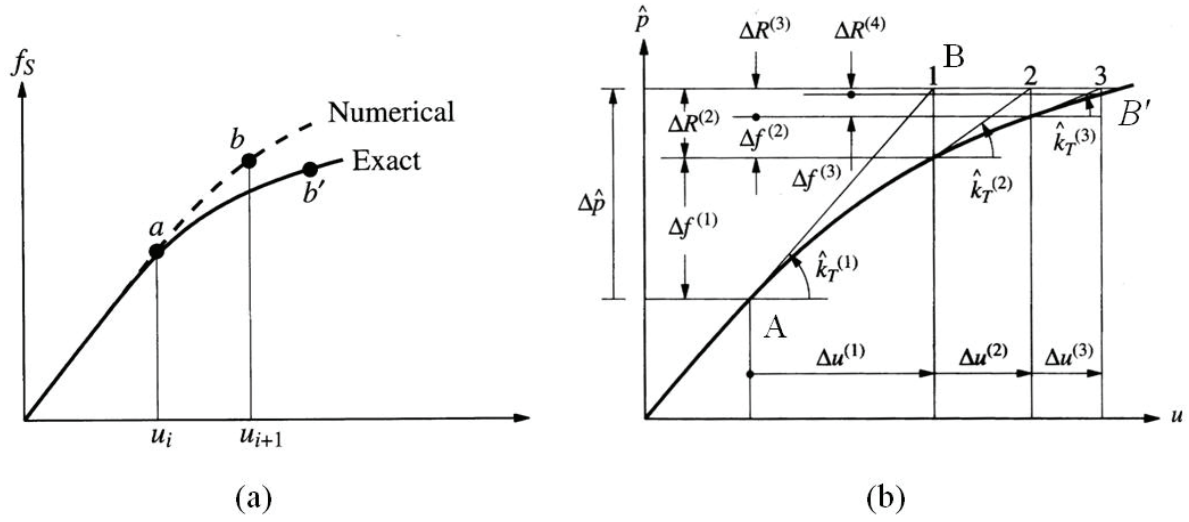

Figure 3-3 Error in Newmark's Method (a) Numerical Error in Newmark's method (b) Newton-Raphson Iteration (Chopra 2000)

The Newmark's method, assuming a constant average acceleration with $\gamma = \frac{1}{2}$ and $\Gamma = \frac{1}{4}$ in Eqs. 3.8 and 3.9, is used herein to develop a Matlab-based computer code to evaluate the seismic response of SDOF SCS and EPS. The Newton-Raphson iteration is implemented to decrease the error in the computation. The time step is set to about 0.005 second and 20 seconds of free vibration are added at the end of each earthquake ground motion in order to determine the residual displacement of these systems.

3.2.4 Performance Indices

The seismic responses of SDOF SCS and EPS can be evaluated by various performance indices including the mean displacement ductility, the mean maximum absolute acceleration and a new Relative Performance Index (RPI) defined herein.

3.2.4.1 Mean Displacement Ductility

The displacement ductility ratio is defined by:

$$\mu = \left| \frac{u_{\max}}{u_y} \right| \tag{3.10}$$

where $u_{\max}$ is the maximum relative displacement of the SDOF system and u_y is the corresponding yielding displacement. Based on the numerical results obatained from an ensemble of 25 ground motions, the mean displacement ductility $\bar{\mu}$ of a specific model is defined by:

$$\bar{\mu} = \frac{\sum_{i=1}^{25} \mu_i}{25} \tag{3.11}$$

where μ_i is the displacement ductility of a specific model under the ith earthquake in an ensemble of 25 ground motions.

The mean displacement ductility is an indicator of the deformation capacity in structures. It is also an indicator of the potential damage that a structure would experience under an ensemble of earthquakes.

3.2.4.2 Mean Maximum Absolute Acceleration

The mean maximum absolute acceleration $\bar{a}_{\max}$ is defined by:

$$\bar{a}_{\max} = \frac{\sum_{i=1}^{25} \max\left(\left| (\ddot{u} + \ddot{u}_g)_i \right| \right)}{25} \tag{3.12}$$

where $\ddot{u}$ is the relative acceleration response of the systems and $\ddot{u}_g$ is the ground acceleration. The maximum absolute acceleration is an indicator of the damage potential to acceleration-sensitive non-structural components. It also represents the maximum transient shear force transferred to the structure by the ground motion.

3.2.4.3 Relative Performance Index (RPI)

In this study, a new Relative Performance Index (RPI) is defined as follows:

$$RPI = b \cdot \frac{(\overline{u}_{\max})_{SCS}}{(\overline{u}_{\max})_{EPS}} + (1-b) \cdot \frac{(\overline{a}_{\max})_{SCS}}{(\overline{a}_{\max})_{EPS}} \tag{3.13}$$

where b is a coefficient with values between 0 and 1 (the values of 0, 0.3, 0.5, 0.7, 1.0 are used in this study); $(\overline{u}_{\max})_{SCS}$ and $(\overline{a}_{\max})_{SCS}$ are the mean response values of maximum displacement and absolute acceleration in Self-Centering Systems (SCS); $(\overline{u}_{\max})_{EPS}$ and $(\overline{a}_{\max})_{EPS}$ are the mean response values of maximum displacement and absolute acceleration in Elasto-Plastic Systems (EPS)

The RPI is a weighted index, which provides an indicator of the combined effect of the displacement and acceleration responses on the structure. When the RPI equals to 1, the seismic performances of the SCS and EPS are equivalent. When the RPI is less than 1, the seismic performance of the SCS is “better” than that of the EPS. Conversely, when the RPI is larger than 1, the seismic performance of the SCS is “worse” than that of the EPS. Therefore, the RPI can serve as a single numerical parameter to guide the choice of optimum SCS parameters in the design of more complex structures.

When b is less than 0.5 in Eq. (3.13), the numerical value of the RPI is mainly controlled by acceleration response. This range of values of b could be used for the design of structures incorporating acceleration sensitive nonstructural components. When b is larger than 0.5 in Eq. (3.13), the numerical value of the RPI is mainly controlled by displacement response. This range of values of b could be used for the design of structures in which damage to the structural components is of prime interest and/or for the design of structures incorporating drift-sensitive nonstructural components.

3.2.5 Numerical Evaluation of Seismic Response of SDOF SCS and EPS

In this section the results of the numerical parametric study conducted on the seismic response of SDOF SCS and EPS are presented along with the observed trends

3.2.5.1 Seismic Response of SDOF SCS

The mean displacement ductility ratios for the SCS excited by the ground motions corresponding to a 2% and 10% probability of exceedance in 50 years are shown in Figs. 3-4 and 3-5, respectively. The ductility ratio is reduced for increasing values of α and β especially in lower period systems ($T_0 \leq 0.5\text{sec}$) or for increasing the value of strength ratio η. The values of α and β have no impact on the ductility for η=1.0, where most of the responses remains in the elastic ranges and consequently μ_Δ remains under unity. As expected, the mean displacement ductility is larger for 2%-50 years ground motions than for 10%-50 years ground motions.

The mean maximum absolute acceleration for the SCS excited by the ground motions corresponding to a 2% and 10% probability of exceedence in 50 years are shown in Figs. 3-6 and 3-7, respectively. When α is increasing, the mean maximum absolute acceleration is also increasing. This increase in acceleration response is more significant for lower period systems ($T_0 \le 1.0\,\text{sec}$). As α is increasing, the mean maximum absolute acceleration is increasing more quickly for lower values of η. When β is increasing, the acceleration response is reduced for $T_0 \le 1.0\,\text{sec}$ and higher values of η, except η=1.0.

For other cases, the mean maximum acceleration is insensitive to values of β. For η=1.0, the values of $\bar{a}_{\max}$ have no change for different values of α and β with same period (T_0) because the relative high yielding strength and the acceleration responses tend to be in the elastic ranges.

It is noted again that the earthquakes in the highest hazard level (2% probability) causes the larger acceleration response by comparing the Fig. 3-6 and 3-7.

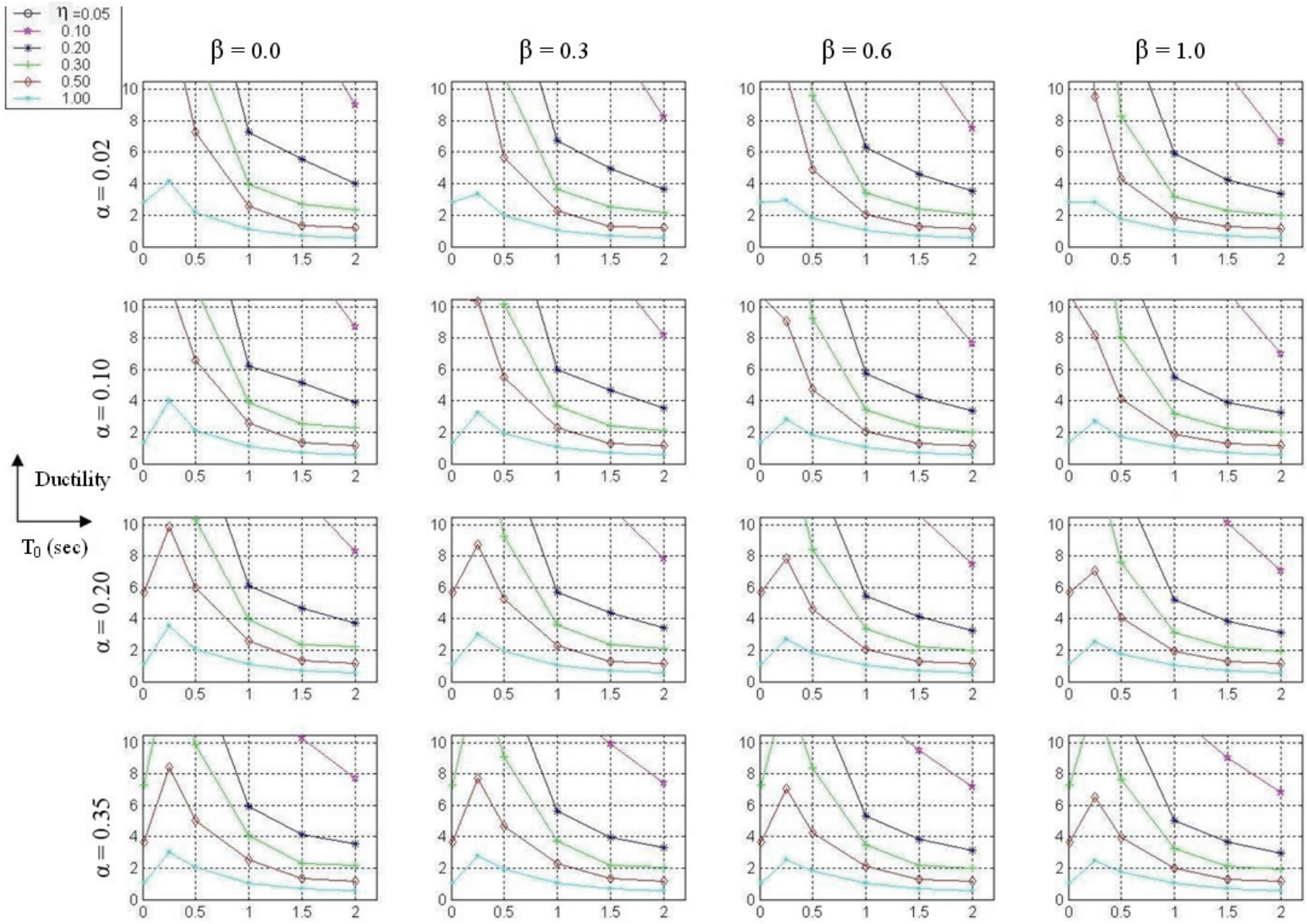

Figure 3-4 Mean Displacement Ductility of Self-Centering System (SCS) under Earthquakes with 2% probability of exceedance in 50 years

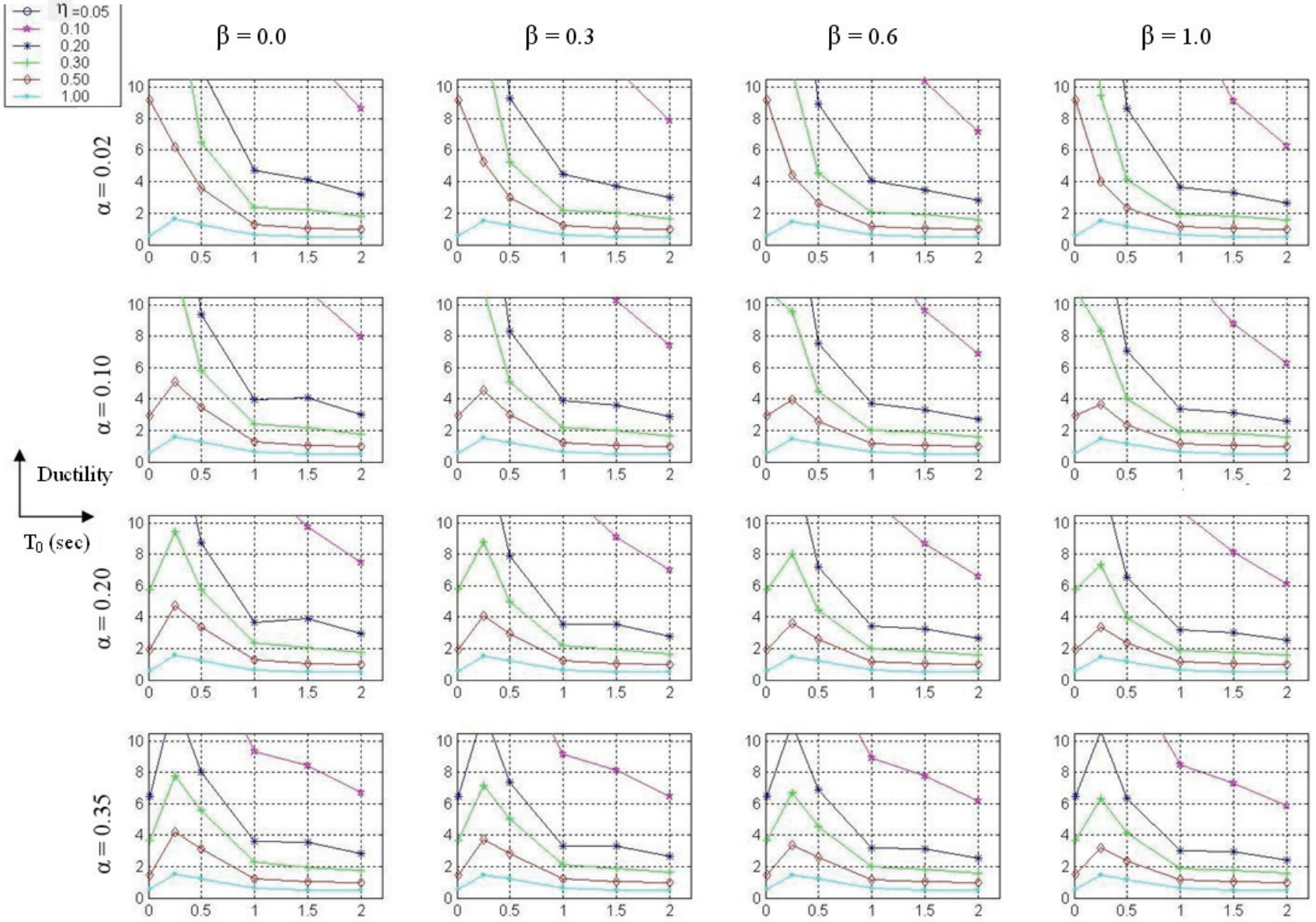

Figure 3-5 Mean Displacement Ductility of SCS
under Earthquakes with 10% probability of exceedance in 50 years

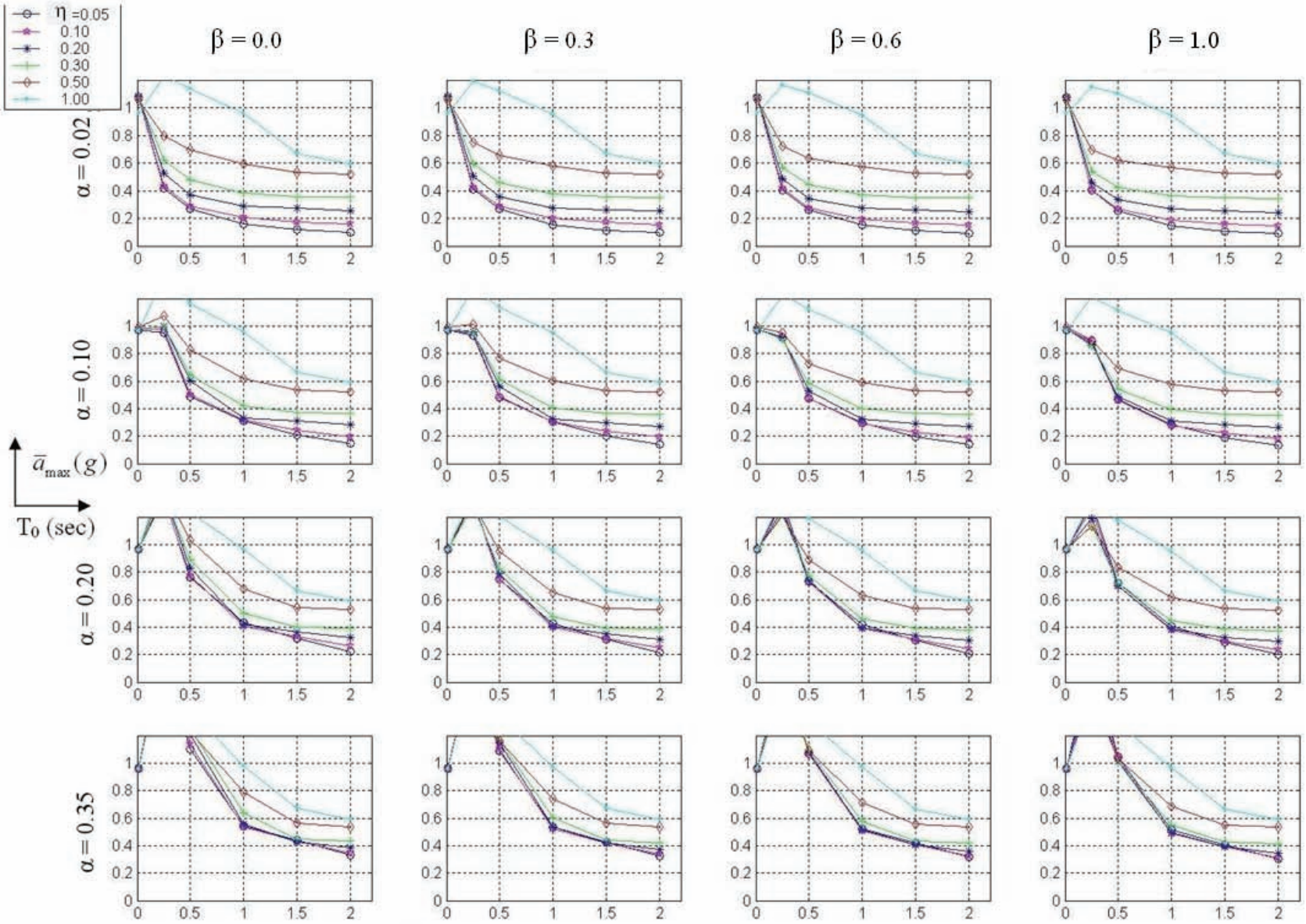

Figure 3-6 Mean Maximum Absolute Acceleration of SCS
under Earthquakes with 2% probability of exceedance in 50 years

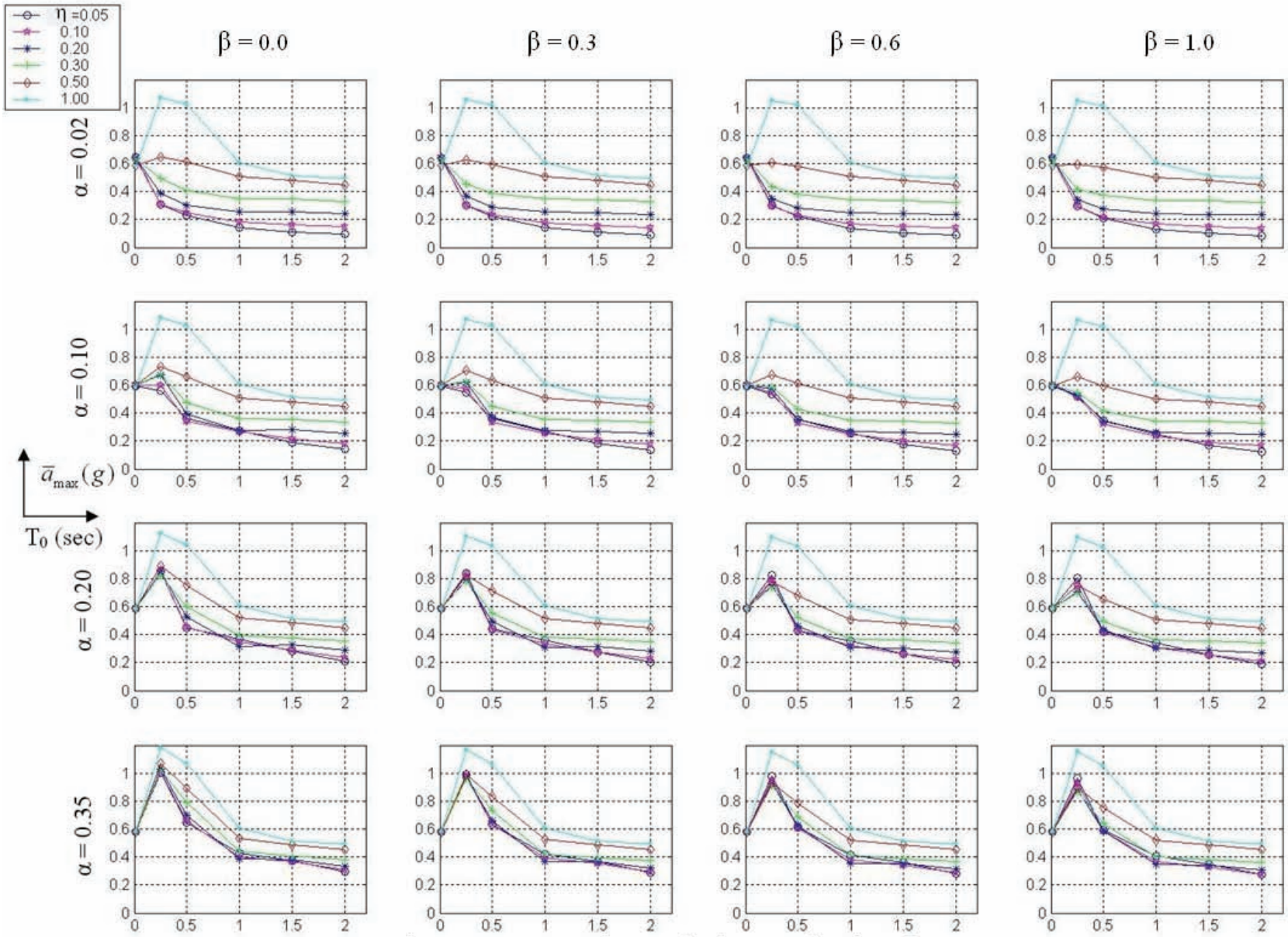

Figure 3-7 Mean Maximum Absolute Acceleration of SCS
under Earthquakes with 10% probability of exceedance in 50 years

3.2.5.2 Seismic Response of SDOF EPS

The seismic responses of SDOF EPS excited by the ground motions corresponding to a 2% and 10% probability of exceedance in 50 years are shown in Figs. 3-8 and 3-9, respectively.

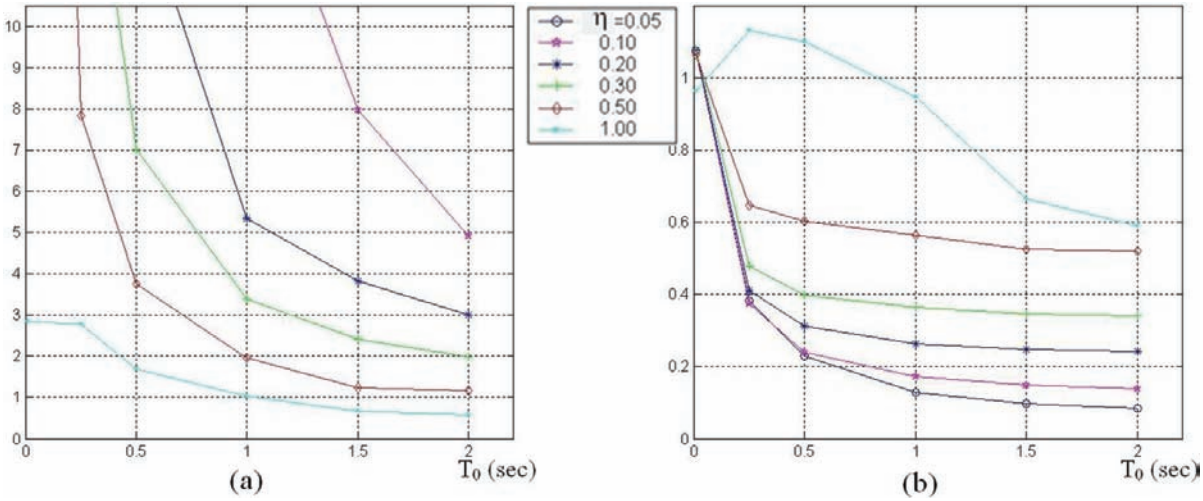

Figure 3-8 Seismic Responses of EPS under Ground Motions having 2% Probability of Exceedance in 50 years (a) Mean Displacement Ductility (b) Mean Maximum Absolute Acceleration (g)

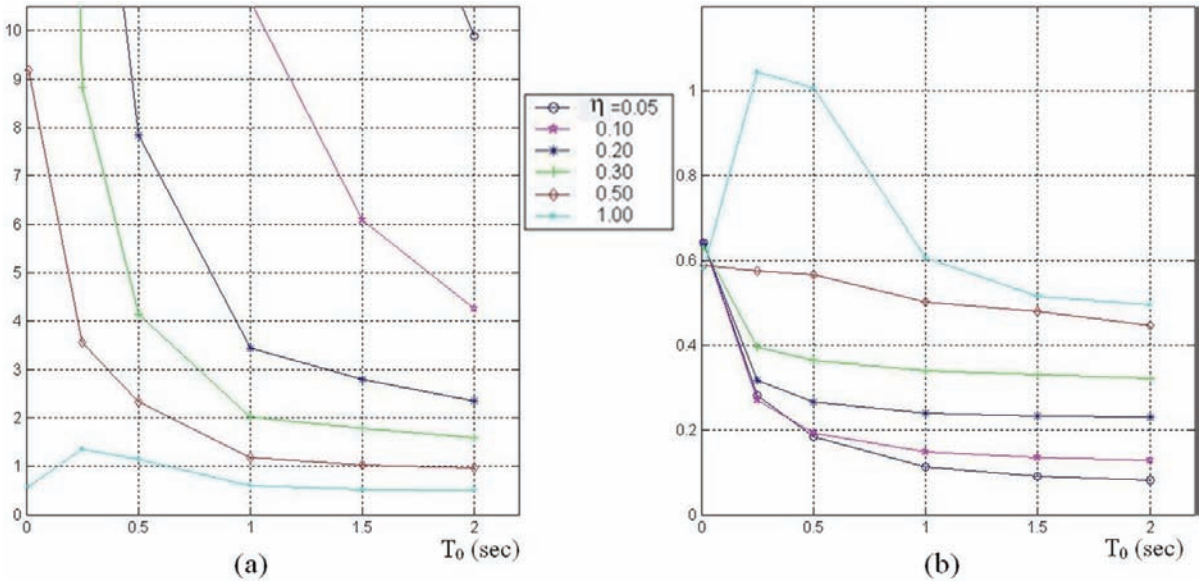

Figure 3-9 Seismic Responses of EPS under Ground Motions having 10% Probability of Exceedance in 50 years (a) Mean Displacement Ductility (b) Mean Maximum Absolute Acceleration (g)

From Fig. 3-8 (a) and 3-9 (a), the mean values of the displacement ductility ratio are increasing when the fundamental period or the strength factor is reduced. When the initial period of systems is less than one second, the mean ductility is increasing significantly when the strength factor is decreased. As shown in Fig. 3-8 (b) and 3-9 (b), the mean maximum absolute acceleration is increasing when the strength factor η increases. For short period systems (T_0<0.5sec), the acceleration values are increasing rapidly compared to that of long period systems (T_0>1sec).

Also, all responses of EPS are increased from lower hazard level to higher one. For the long period systems (T_0>1 sec) with larger values of η (>0.3), these responses are similar for both hazard levels.

3.2.6 Comparative Seismic Responses between SDOF Self-Centering Systems (SCS) and Elasto-Plastic Systems (EPS)

In order to compare the seismic responses of SDOF SCS and EPS, the Relative Performance Index (RPI) introduced in Section 3.2.4.4 is used to generate a series of total 70 comparative figures under two ensembles of 25 earthquakes records with 2% and 5% exceedance of 50 years, which are shown in Appendix A and B.

From Appendix A and B, it is found that, when RPI is completely based on maximum displacement response (i.e. the weighted factor of displacement ratio equals to 1), if α is increasing, the value of RPI decreases especially for shorter period systems ($T_0 \leq 1.0\,\text{sec}$)

and if β decreases, the value of RPI is increasing. But for longer period systems ($T_0 > 1.0\,\text{sec}$) with $\alpha \geq 0.1$, the RPI is insensitive to β.

When RPI is completely based on maximum absolute acceleration responses (i.e. the weighted factor of acceleration ratio is 1), if α is increasing, the value of RPI is increasing especially for lower ψ values and if β is increasing, the RPI is reduced especially for lower period systems $T_0 (\leq 1.0\,\text{sec})$ with lower ψ values. For $T_0 \geq 1.0$, the RPI is insensitive to β.

When the weighted factor is not equal to 0 or 1, the RPI represents a combined effect of the above two trends. When the weighted factor of the displacement ratio is larger than that of the acceleration ratio, the RPI tends to be close to the first one (i.e. weight factor of displacement ratio equals to 1). The reverse effect is also observed.

A final conclusion for the comparative response of the two systems is that to any reasonable specific EPS, there will be at least one SCS, in which the displacement response is less than that of EPS or the acceleration response is less than that of EPS or both of these two responses of SCS are reduced compared to that of EPS. In other words, the seismic performance of SCS can exceed that of EPS in respect of displacement responses or acceleration responses or both.

3.2.7 Recommended Use of Design Aid Charts

The Relative Performance Index (RPI) shown in Appendix A and B can be used as design aid charts to design SCS based on the existing EPS.

The weight factor in the design aid charts ranges from 0 to 1 and the values of SCS factors such as α, β, η, ψ and T_0 are shown in Table 3-1 (see Sec. 3.2.2). Based on the previous discussion in Sec. 3.2, the ranges of values of those factors in the design aid charts were determined by the physical condition and design code such as FEMA 356. Therefore, those values are rational so that an equivalent EPS of a real structure can be found and then the corresponding SCS with better seismic performance can also be determined. Based on the discussion in Sec. 3.2.5 and the observations for these design aid charts in Appendix A and B, it is believed that the RPI can be interpolated with the selected factors within the range of the existed values.

For the recommendations of the selection of the individual factors in SCS, the post-yielding factor α could be selected lower than 0.2, since to achieve higher value α, much more re-centering force (i.e. post-tensioned force) are needed which may lead to the yielding of the beam or other components. The energy dissipating factor β should be selected less than 1 to maintain the self-centering properties without residual drifts and may be selected around 0.6~0.8 since the larger β can lead to reduced seismic responses as a result of dissipating more energy while too large β (i.e. close to 1) may lead to lose part of the capability of eliminating the residual drifts in the condition that not all the connections are SCS (e.g. beam-to-column joints are SCS while the base column connections are EPS). The strength ratio factor ψ may be selected as low as 0.5 (i.e. $\eta_{SCS} = 0.5\eta_{EPS}$) since when a value less than 0.5 for ψ is selected, the displacement response of SCS is higher than that of EPS.

If a building has more displacement-sensitive non-structural components, the weight factor b should be selected larger than 50% while b should be considered less than 50% (i.e. 1-b>50%) to account for more acceleration-sensitive non-structural components existing in other types of buildings such as hospitals.

Since the design aid charts (i.e. RPI) in Appendix A were calculated based on the MCEER simulated earthquakes with 2% probability of exceedance in 50 years, it should be used when designing for the Maximum Considered Earthquake (MCE). When the Design Basis Earthquake (DBE) is considered, the design aid charts in Appendix B are recommended.

3.3 Summary

In this chapter, a numerical seismic nonlinear analysis of Single-Degree-of-Freedom (SDOF) Self-Centering Systems (SCS) and Elasto-Plastic Systems (EPS) was conducted by using the Newmark's integration method with the Newton-Raphson iteration. The comparative evaluation of the seismic responses of two systems was presented, which indicated that the seismic performance of SCS is better than that of EPS. The main advantage of SCS is that no permanent deformation and no inelastic action associated with damage to the main structural elements occur after earthquakes. The parametric comparative results in Appendix A and B were given and discussed, which can be used as design aid charts to the seismic design of actual structures incorporating SCS. The use of design aid charts (i.e. RPI) obtained will be discussed further in Chapter IV.

CHAPTER 4
SEISMIC PERFORMANCE OF MCEER DEMONSTRATION HOSPITAL WITH SELF-CENTERING SYSTEMS

As discussed in previous chapters, there has not been yet any practical implementation of Self-Centering Systems (SCS) in Steel Moment-Resisting Frames (SMRF). Before such implementation can take place, the seismic performance of SMRF equipped with SCS needs to be investigated. In this chapter, numerical investigations were carried out to obtain the seismic response of one of the steel buildings part of the MCEER West Coast Demonstration Hospital located in Southern California. This facility was designed in the 1970s and the WC70 design version of the building (Yang and Whittaker 2002) was considered in this study.

Two numerical studies are discussed in this Chapter. In the first study, the response of the original WC70 building model is compared to that of the same building in which ideal self-centering hysteretic properties are introduced at each beam-to-column connection. In the second numerical study, actual Self-Centering Post-Tensioned (SCPT) connections are designed and analyzed.

The structural properties and the numerical model of the WC70 hospital building are first introduced. Thereafter, based on the seismic response of the Single-Degree-of-Freedom (SDOF) SCS presented in Chapter II, the hospital was redesigned with ideal SCS and a comparation between the seismic performance of the original building and the redesigned

one is presented in terms of push-over analysis under cyclic loading, seismic analysis and fragility analysis under the MCEER strong ground motions (see Chapter III). A complete seismic design procedure for SCPT connections is then developed. Finally, this procedure is used to design a SCS with SCPT connections for the hospital building and the results from the push-over analysis, the seismic analysis and the fragility analysis are compared again to that of the original building.

4.1 Numerical Model of MCEER Demonstration Hospital

The steel building considered in this study is part of the MCEER West Coast Demonstration Hospital. This facility is located in Southern California and was constructed in the 1970s (hence the designation WC70). A conventional Steel Moment-Resisting Frame (SMRF) system was used in this 4-story building. As shown in Fig. 4-1, the lateral load-resisting system of this building is composed of 4 SMRFs in the North-South direction (lines B, F, J

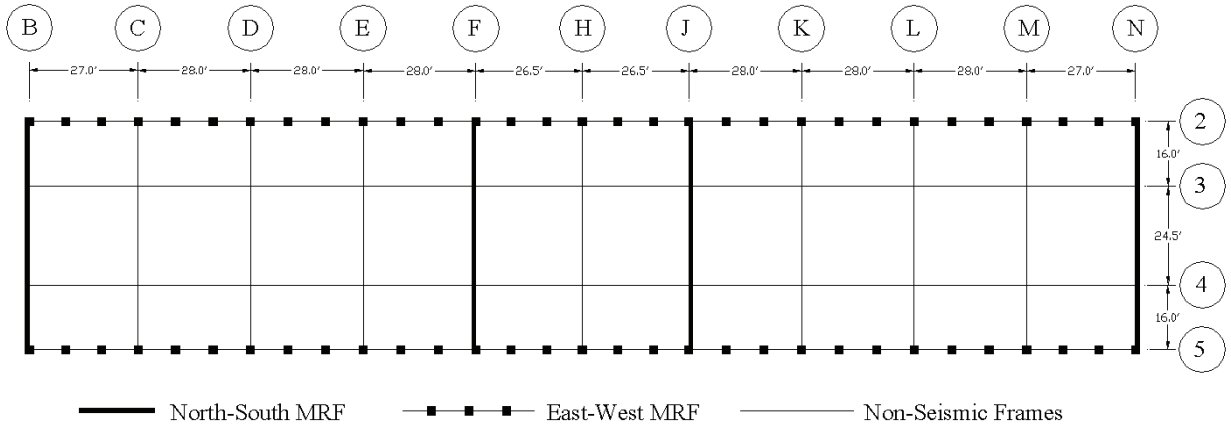

Figure 4-1 Plan View of WC70 Hospital Building Considered

and N) and 2 MRFs in the East-West direction (lines 2 and 5). The dimensions and sections of moment resisting frames on lines B, N, F and J in Fig. 4-1 are shown in Figs. 4-2 and 4-3.

The other frames in the structure were designed only to resist the gravity loads and are assumed not to contribute in resisting the lateral forces.

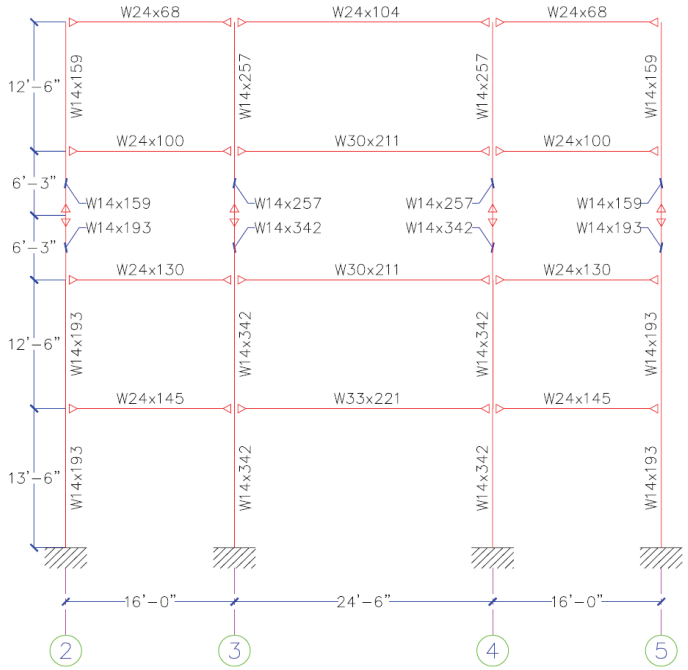

Figure 4-2 Elevation View of Exterior Moment Resisting Frame on lines B and N of WC70 (Yang and Whittaker 2002)

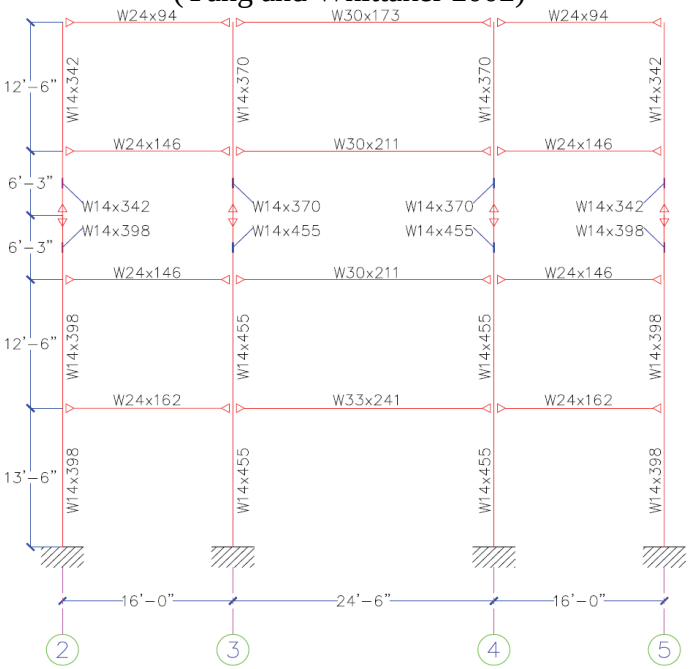

Figure 4-3 Elevation View of Interior Moment Resisting Frame on lines F and J of WC70 (Yang and Whittaker 2002)

In order to evaluate the seismic performance of this building, a two-dimension numerical model is developed in the RUAUMOKO-2D software (Carr 2004) to model the North-South MRFs as shown in Fig. 4-4. Due to the symmetry, only half of these 4 MRFs were used in this model: the exterior frames on line B or N and the interior frames on lines F or J. A pin-ended gravity column is introduced in the model to account for the second order (P-Δ) effect

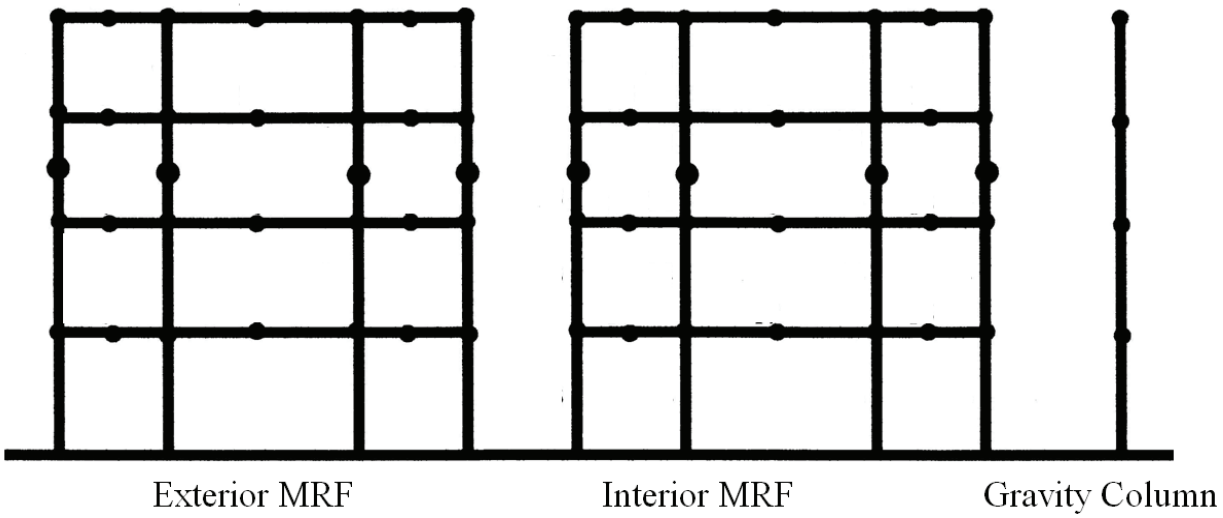

Figure 4-4 Numerical Model of WC Hospital

generated by those non-seismic frames on the lateral load-resisting frames. A frame element is utilized to represent all beams and columns. The inelastic response is assumed to be concentrated in the plastic hinges forming at the end of frame members. A bilinear moment-curvature hysteresis similar to that of Elasto-Plastic Systems (EPS) with a post-yielding stiffness equal to 0.02 is assigned to all frame numbers, as indicated in Fig. 4-5, where the k_0 is the initial flexural stiffness of the frame elements. All slab contributions are neglected. This model is defined as the original model of the building. The model the retrofitted with

ideal SCS and the model re-designed with SCPT systems are discussed in the following sections.

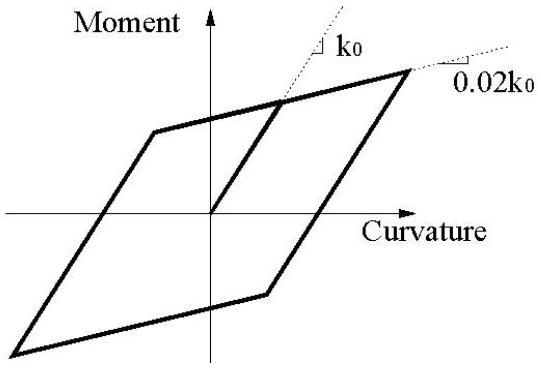

Figure 4-5 Bilinear Moment-Curvature Hysteresis

4.2 Re-Design Procedure and Numerical Model for Steel Moment Resisting Frames (SMRF) with Ideal Self-Centering Systems (SCS)

The ideal SCS represent structural components that exhibit complete self-centering properties by changing the elasto-plastic hysteretic properties to self-centering hysteresis at every beam-to-column connections but without considerations of installing actual self-centering devices such as those mentioned in Chapter II. The re-design objectives are to reduce the displacement and/or acceleration responses and to decrease or eliminate the residual drifts in the SCS frame compared to the SMRF structures so that the damage on the non-structural and structural components can be reduced after earthquakes. Based on the seismic performance of SDOF SCS in Chapter III, the redesign procedure for SMRF with ideal SCS can be conducted through the following steps:

(1) Determine the structural properties of the SMRF including the fundamental period, seismic weights, mode shapes, yielding strength.

(2) According to the modal contributions, the Multi-Degree-of-Freedom (MDOF) SMRF is reduced to be an equivalent SDOF system. For regular SMRF buildings, the first mode contribution to seismic response is considered to be dominant while the contributions from higher modes are neglected. In fact, it is assumed that all SCS joints in the structure experience the same rotation, thereby implying a linear (straight line) first modal shape. The parameters of the equivalent SDOF system can be determined by the first mode properties of the MDOF system. For particular conditions, where higher modal contributions need to be considered, the method for generating an equivalent SDOF system can be found in Chopra, 2000.

(3) Determine the original strength ratio factor $\eta_{original}$ of the SMRF based on its beam and column properties.

(4) According to the Relative Performance Index (RPI) values given in Appendix A or B, determine the parameters of the SCS including the post-yielding factor α, energy dissipating factor β, yielding ratio factor ψ and required strength ratio factor $\eta_{reqired}$. For different redesign objectives, the relative importance of displacement and acceleration response can be taken into account by the specific weighting factor b introduced in the RPI calculation, as described in Chapter III. If one is concerned with displacement-sensitive structural and nonstructural components, more weight

should be given to the displacement response than that of acceleration response in the RPI calculation, while more weight should be given to the acceleration response if one is concerned with acceleration-sensitive components.

(5) Establish a numerical model for the original SMRF buildings and implement the SCS with selected parameters to change the original model to a new one with SCS.

(6) Evaluate and compare the seismic performance of theses two models.

(7) If the performance of the SCS can not reach a satisfactory level, repeat the step (4), (5) and (6) until a good performance is achieved. Usually with the initial parameters, a relative good retrofit result can be obtained. In order to get better results, the procedure can be repeated by modifying the controlling parameters of the SCS.

Those steps in re-design procedure are also summarized in Fig. 4-6.

Since the WC70 building is a welded SMRF, the above procedure can also be used in the re-design process. The structural properties of this building are provided in Section 4.1. The total seismic weight of the WC70 building is 20881 kN and its modal properties are shown in Table 4-1.

Table 4-1 Modal Properties of the Original Model for WC70 Building

Mode	Period (sec)	Cumulative Mass
1st	0.760	85%
2nd	0.257	96%
3rd	0.148	99%
4th	0.100	100%

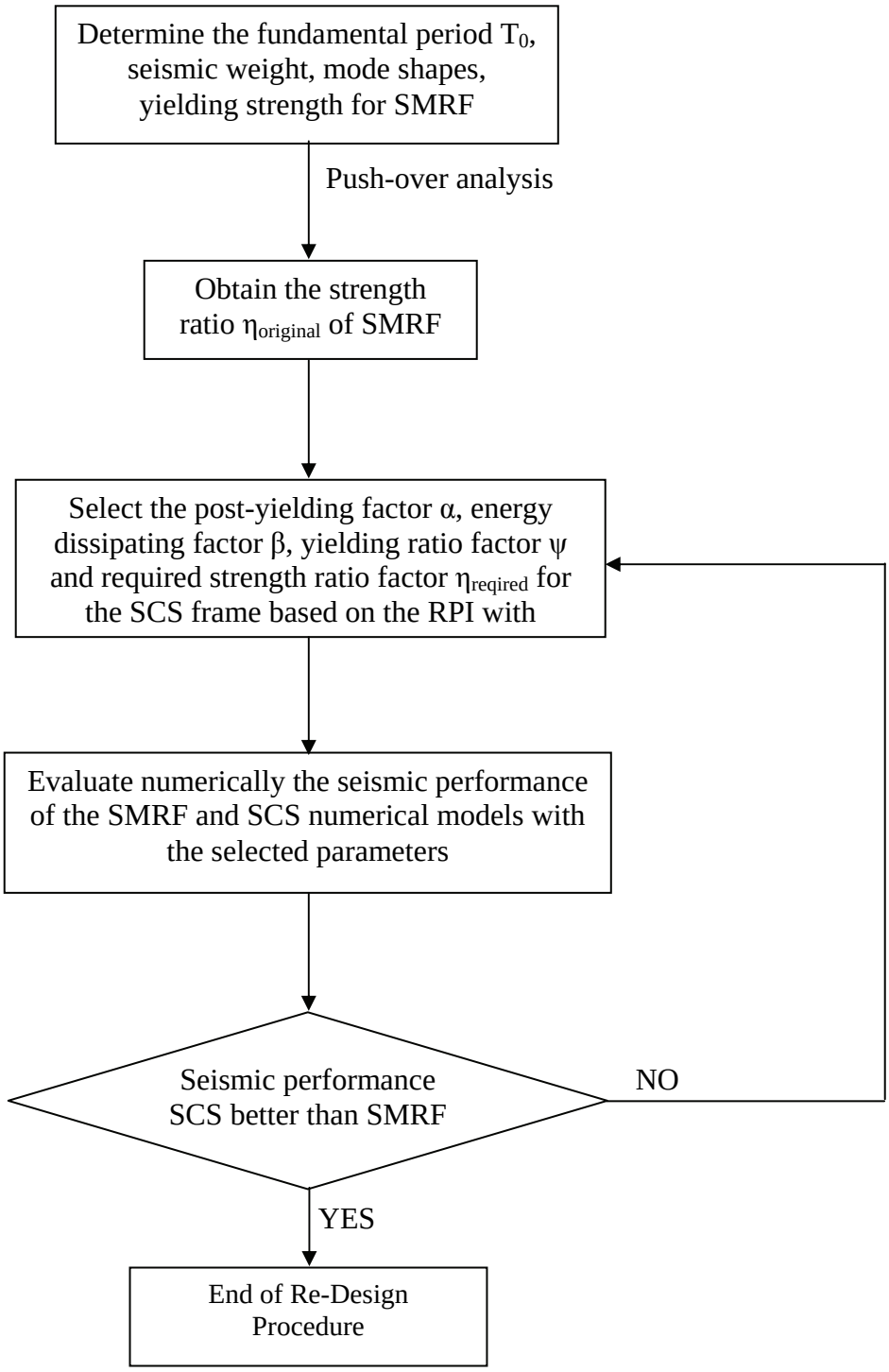

Figure 4-6 Flowchart of the Re-Design Procedure for Ideal SCS Frame

The results shown in Table 4-1 indicate that 85% of the total participating mass is associated with the 1st mode of vibration. Therefore, the seismic response of the building is mostly dominated by the first mode and the weight of the equivalent SDOF system used to model the building is made equal to the first mode weight:

$$W_{eq} = 85\% W_{total} = 85\% * 20881 = 17749 kN \tag{4.1}$$

Where W_{eq} is the weight of equivalent SDOF system and W_{total} is the total weight. In order to determine the strength ratio of the original building, $\eta_{original}$, a push-over analysis on the original building model is conducted using a set of lateral forces proportional to the 1st mode shape, as shown in Fig. 4-7. The structure yields at point A with a top displacement of 114 mm and a base shear of 10690 kN, as seen in Fig. 4-7 (a). The strength ratio $\eta_{original}$ is given by:

$$\eta_{original} = \frac{F_Y}{W_{eq}} = \frac{10690.1}{17749} = 0.60 \tag{4.2}$$

where F_Y is the yielding force.

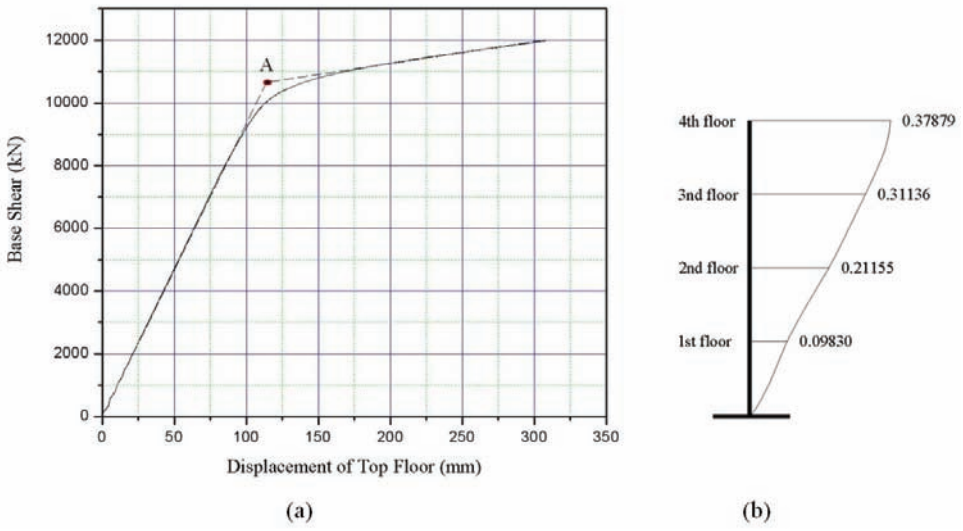

Figure 4-7 Pushover Analysis of the SMRF structure
(a) Pushover Curve (b) First Mode Shape

Because hospital buildings contain mainly sensitive medical equipments that are acceleration-sensitive, the calculations of the RPI should be based mainly on mimimizing acceleration response. With the original strength ratio $\eta_{original}$=0.6 and fundamental period T=0.7sec, the parameters of α, β and η_{scs} can be selected in Appendix A or B with RPI values based on b=0.3 (70% acceleration response and 30% displacement response). Although the results presented in Appendix A and B were not made specifically for $\eta_{original}$ equal to 0.6, $\eta_{original}$=0.5 is selected as the closest value. The initial values of α, β and ψ selected in Appendix B in page B-13 are listed in Table 4-2. With these three parameters, the RPI of the corresponding SCS is less than 1, which indicates that the performance of WC70 hospital with SCS should be better than that of original building.

Table 4-2 Parameters in self-centering systems

α	β	$\psi = \eta_{scs}/ \eta_{original}$
0.2	0.6	0.6

The original numerical model of the WC70 building described in Section 4.1 is then re-designed with ideal self-centering system incorporating the parameters shown in Table 4-2. For this purpose, the Elasto-Plastic (EP) properties of the moment-curvature relationship at the end of all beam elements in the original model are changed to incorporate the characteristics of SCS to generate a new SCS model. This process is illustrated in Fig. 4-8. The values of α and β in Fig. 4-8(c) are taken in Table 4-2. The yield moments in Fig. 4-8(b) and (c) have the following relation:

$$\frac{M_{Yscs}}{M_{Yoriginal}} = \frac{\frac{(F_Y)_{scs}}{W_{eq}}}{\frac{(F_Y)_{original}}{W_{eq}}} = \frac{\eta_{scs}}{\eta_{oringal}} = \psi = 0.60 \quad (4.3)$$

where:

F_Y: yielding force for the equivalent SDOF system

M_Y: yielding moment for the beams or columns

W_{eq}: the weight of equivalent SDOF system.

η: the strength ratio

ψ: the yielding ratio, the value of 0.60 is taken from Table 4-2.

In order to evaluate the complete performance of SCS, the base connections (i.e. the ends of columns connected to the foundation) of the SCS model are also changed to three types: fixed-base connections, pin-base connections and SCS-base connections. As shown in Fig. 4-8, the fixed-base connections are similar to that of the original model with the EP property and the ideal SCS-base connections lead base columns to have the ability of SCS, while the pin-based connections do not supply any moment resistance.

Therefore, a total of four numerical models are considered, as shown in Table 4-3. The first model represents the original WC70 building and the other three represent a re-design of the same building with ideal SCS incorporating three different base connections.

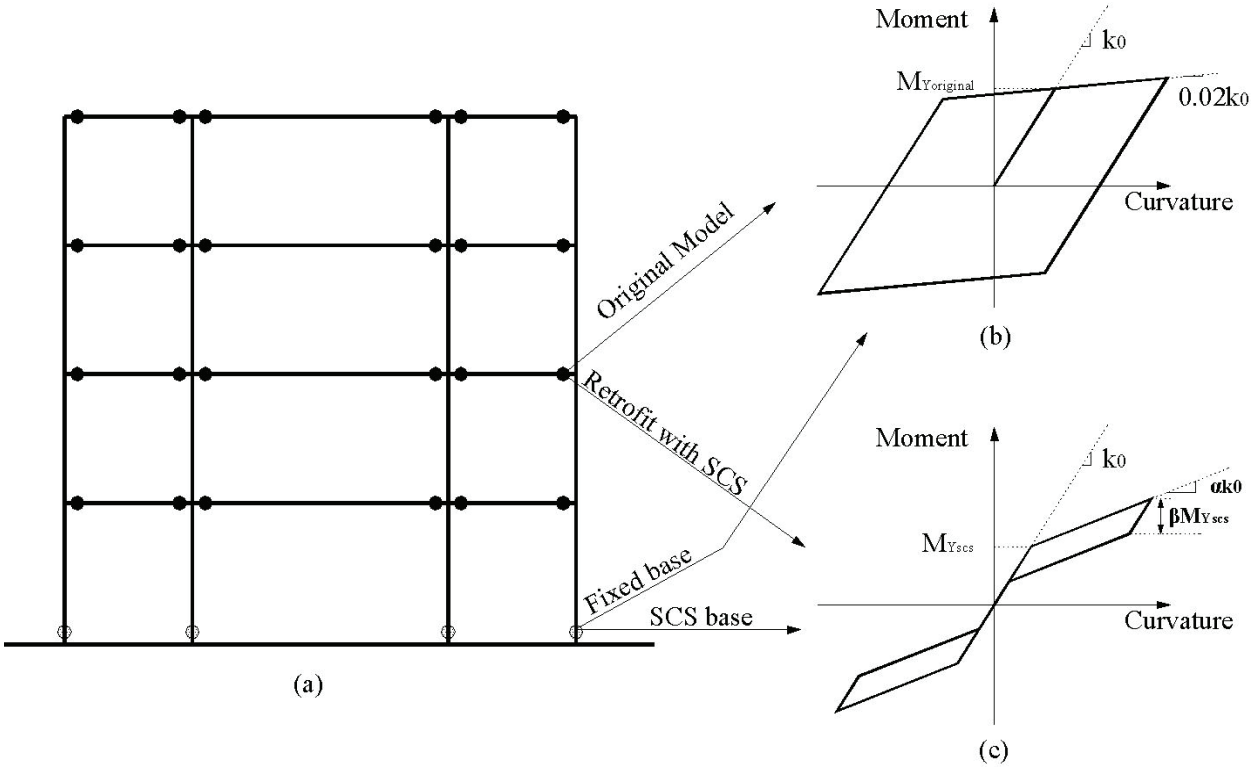

Figure 4-8 Numerical Models of EPS and SCS

(a) Frame in original model of WC70 hospital (b) Bilinear Hysteresis (c) SCS Hysteresis

Table 4-3 Moment-curvature Properties of the Original and SCS models

	Original Model (Elasto-Plastic System, EPS)	Self-Centering System (SCS) Model		
		Fixed-base	SCS-base	Pin-base
Moment-Curvature Property (MCP) of beam elements	EPS Hysteresis	SCS Hysteresis	SCS Hysteresis	SCS Hysteresis
MCP of column elements	EPS Hysteresis	EPS Hysteresis	EPS Hysteresis	EPS Hysteresis
MCP of base column elements	EPS Hysteresis	EPS Hysteresis	SCS Hysteresis	No moment resistance

4.3 Performance of the Original WC70 Hospital Model and the Models Re-Designed with Ideal Self-Centering Systems

In this section, the seismic performances of the original and re-designed WC70 building models are investigated using Cyclic nonlinear quasi-static and seismic analyses. The results obtained are also expressed in terms of fragility curves.

4.3.1 Cyclic Nonlinear Quasi-Static Analyses

Cyclic nonlinear quasi-static analyses were conducted under one cycle of loading to evaluate the global seismic performance of the four models described above. The results of these Cyclic nonlinear quasi-static analyses are shown in Fig. 4-9. Lateral loads are added at each floor and scaled to the first mode shape of the building (see Fig. 4-7(a)) until a total lateral force (base shear) of 12650kN is reached. This base shear level corresponds for the original building to a global top floor displacement ductility factor equal to 4. At this base shear level, the maximum top floor displacement is about 1000 mm for the SCS model with pin base. Obviously, this large displacement indicates that the building would have collapsed because the stiffness of the first floor is too low due to the pin base. As shown in Fig. 4-9, after retrofit with SCS with fixed and SCS base connections, the initial stiffness of the building is not changed substantially compared to the initial building but the first-yield force level is reduced significantly, as expected since the moment capacity of all SCS beam-to-column connections is only 60% of that of the original building. At the same base shear level, the maximum top floor displacements of the SCS models with fixed or SCS base connections are reduced substantially compared to that of the original building. The points A, B and C

identified in Fig. 4-9 are the residual drifts associated with the different building models, which indicates that the SCS model with SCS base connections possess the best performance. The residual drift of the SCS model with fixed base is also reduced largely compared to that of the original model. The possible residual drifts (point B and C) of SCS models are not zero as that of SDOF SCS discussed in the previous Chapter. In MDOF systems, the SCS are only added into the beam-to-column connections, which can not prevent the column ends to yield. From the results of these analyses, it is clear that the performance of SCS models exceeds that of original model except for the pin-base SCS model.

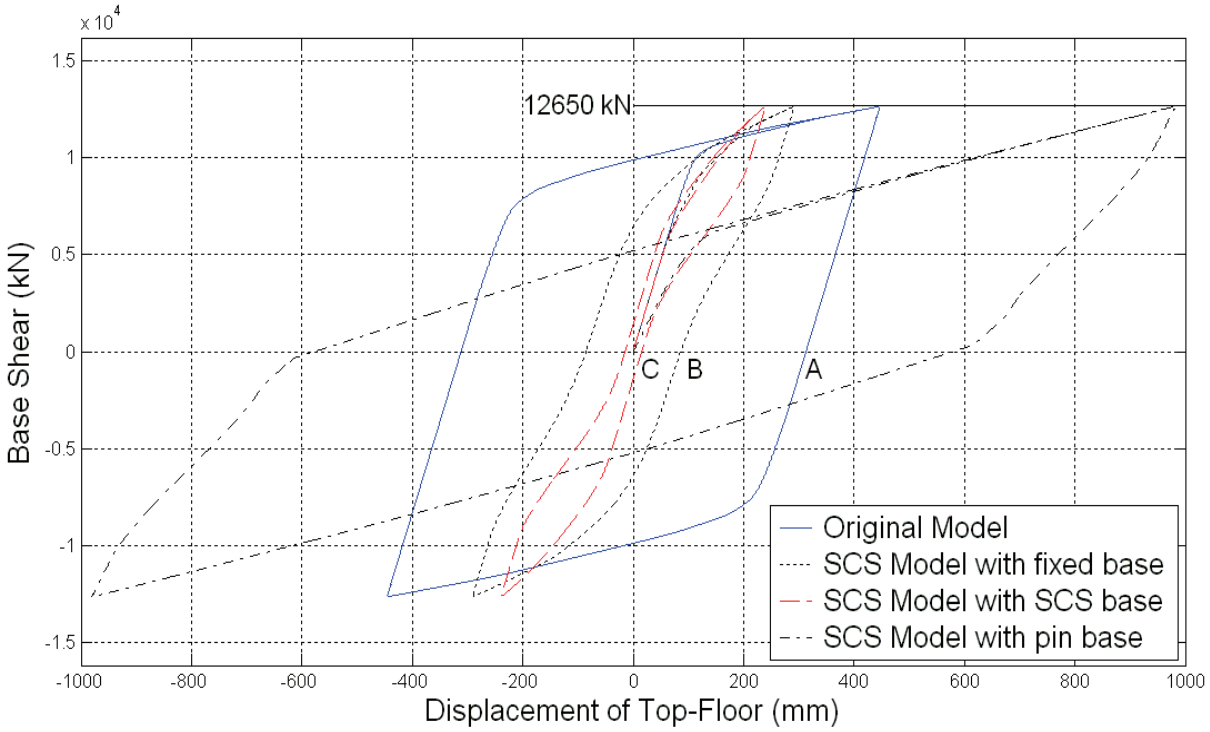

Figure 4-9 Hysteretic Loop in Push-over Analysis

4.3.2 Seismic Analyses under MCEER Ground Motions

Seismic analyses were conducted by using the 4 ensembles of 25 MCEER ground motions having 2%, 5%, 10% and 20% probabilities of exceedance in 50 years, as introduced in Section 3.2.1. Analysis results for mean values of various responses from each ensemble of ground motion are shown in Tables 4-4 to 4-7. Through comparing the results, it is found that:

(i) From these four tables, it is apparent that although the acceleration response of the SCS model with pin base is the lowest, the maximum first interstory displacement and column ductility are very large, which indicates that this pin-base model can not resist the strong ground motions due to the low stiffness of the first floor. Therefore, in the following discussion, the SCS model with pin base is neglected and the SCS model is referred to as the SCS model with fixed or SCS base.

(ii) By comparing the mean values of top floor maximum displacements and interstory drifts, it is found that the response of the SCS model is similar or slightly larger than that of the original model. The reason for this increase is that the determination of SCS parameters is mainly based on the acceleration response with a 70% weight and the non-SCS connections such as base columns also have a negative impact on the displacement response of the SCS model.

Table 4-4 Mean Values of response under 25 MCEER ground motions with 20% probability of exceedance in 50 years

Mean Values		Original Model		SCS Model with Fixed Base		SCS Model with SCS Base		SCS Model with Pin Base	
	unit	mm	%	mm	%	mm	%	mm	%
Maximum Displacement	top floor	130.14	0.84	136.63	0.88	142.71	0.92	186.82	1.20
Residual Displacement	top floor	12.48	0.08	3.00	0.02	0.59	0.00	26.55	0.17
Maximum Interstory Drift	1st floor	40.21	0.98	40.22	0.98	43.16	1.05	131.77	3.20*
	2nd	40.90	1.07*	42.72	1.12*	44.11	1.16*	32.92	0.86
	3rd	36.06	0.95	38.63	1.01	38.46	1.01	21.08	0.55
	4th	25.30	0.66	24.91	0.65	26.08	0.68	14.15	0.37
Residual Interstory Drift	1st	5.06	0.12*	2.53	0.06*	0.17	0.00	26.38	0.64*
	2nd	4.22	0.11	0.37	0.01	0.29	0.01*	0.19	0.00
	3rd	2.82	0.07	0.22	0.01	0.23	0.01	0.03	0.00
	4th	0.52	0.01	0.02	0.00	0.02	0.00	0.01	0.00
Acceleration Unit		g		g		g		g	
Maximum Absolute Acceleration	1st	0.68		0.64		0.65		0.46	
	2nd	0.74		0.70		0.69		0.42	
	3rd	0.79		0.81		0.73		0.44	
	4th	1.06*		0.93*		0.95*		0.59*	
Maximum Ductility of Beams		2.90		4.77 / 1.0**		4.93 / 1.0**		5.41 / 1.0**	
Maximum Ductility of Columns		2.03		1.90		4.17 / 1.0		4.65	

* Shaded values represent maximum and residual interstory drifts and maximum absolute accelerations.

**Ductility values in SCS energy dissipating components / ductility in structural members.

Table 4-5 Mean Values of response under 25 MCEER ground motions with 10% probability of exceedance in 50 years

Mean Values		Original Model		SCS Model with Fixed Base		SCS Model with SCS Base		SCS Model with Pin Base	
	unit	mm	%	mm	%	mm	%	mm	%
Maximum Displacement	top floor	143.38	0.92	156.99	1.01	169.95	1.09	203.55	1.31
Residual Displacement	top floor	13.46	0.09	4.37	0.03	1.65	0.01	32.43	0.21
Maximum Interstory Drift	1st floor	45.63	1.11	48.92	1.19	51.33	1.25	147.33	3.58*
	2nd	45.03	1.18*	48.36	1.27*	53.11	1.39*	35.19	0.92
	3rd	41.10	1.08	42.86	1.12	45.63	1.20	23.20	0.61
	4th	29.86	0.78	29.41	0.77	30.71	0.81	15.60	0.41
Residual Interstory Drift	1st	5.27	0.13*	3.65	0.09*	0.41	0.01	32.22	0.78*
	2nd	4.79	0.13	0.74	0.02	0.87	0.02*	0.19	0.01
	3rd	3.60	0.09	0.29	0.01	0.46	0.01	0.04	0.00
	4th	0.91	0.02	0.03	0.00	0.04	0.00	0.01	0.00
Acceleration Unit		g		g		g		g	
Maximum Absolute Acceleration	1st	0.83		0.83		0.78		0.51	
	2nd	0.88		0.85		0.83		0.46	
	3rd	0.88		0.88		0.80		0.48	
	4th	1.23*		1.07*		1.07*		0.65*	
Maximum Ductility of Beams		3.36		5.59 / 1.0**		5.97 / 1.0**		5.70 / 1.0**	
Maximum Ductility of Columns		2.81		2.78		5.05 / 1.0**		5.86	

* Shaded values represent maximum and residual interstory drifts and maximum absolute accelerations.

**Ductility values in SCS energy dissipating components / ductility in structural members.

Table 4-6 Mean Values of response under 25 MCEER ground motions with 5% probability of exceedance in 50 years

Mean Values		Original Model		SCS Model with Fixed Base		SCS Model with SCS Base		SCS Model with Pin Base	
	unit	mm	%	mm	%	mm	%	mm	%
Maximum Displacement	top floor	205.46	1.32	223.38	1.44	253.95	1.63	244.66	1.57
Residual Displacement	top floor	42.47	0.27	12.04	0.08	6.68	0.04	40.46	0.26
Maximum Interstory Drift	1st floor	73.52	1.78*	79.10	1.92*	74.12	1.80	178.96	4.34*
	2nd	67.14	1.76	68.40	1.80	84.63	2.22*	41.18	1.08
	3rd	53.66	1.41	58.28	1.53	68.12	1.79	29.14	0.76
	4th	34.55	0.91	40.10	1.05	42.59	1.12	19.28	0.51
Residual Interstory Drift	1st	16.34	0.40*	8.35	0.20*	1.27	0.03	40.27	0.98*
	2nd	14.15	0.37	3.29	0.09	3.79	0.10*	0.16	0.00
	3rd	10.30	0.27	0.98	0.03	1.72	0.05	0.05	0.00
	4th	2.56	0.07	0.11	0.00	0.28	0.01	0.01	0.00
Acceleration Unit		g		g		g		g	
Maximum Absolute Acceleration	1st	1.05		0.93		0.96		0.63	
	2nd	1.01		0.94		0.97		0.55	
	3rd	1.04		1.00		0.99		0.57	
	4th	1.41*		1.27*		1.25*		0.78*	
Maximum Ductility of Beams		5.42		7.97 / 1.0**		9.20 / 1.0**		6.35 / 1.0**	
Maximum Ductility of Columns		5.23		5.83		7.38 / 1.0**		7.96	

* Shaded values represent maximum and residual interstory drifts and maximum absolute accelerations.

**Ductility values in SCS energy dissipating components / ductility in structural members.

Table 4-7 Mean Values of response under 25 MCEER ground motions with 2% probability of exceedance in 50 years

Mean Values		Original Model		SCS Model with Fixed Base		SCS Model with SCS Base		SCS Model with Pin Base	
	unit	mm	%	mm	%	mm	%	mm	%
Maximum Displacement	top floor	235.06	1.51	246.25	1.58	281.77	1.81	308.82	1.99
Residual Displacement	top floor	51.98	0.33	17.00	0.11	10.19	0.07	45.89	0.30
Maximum Interstory Drift	1st floor	85.57	2.08*	92.72	2.25*	87.26	2.12	243.44	5.91*
	2nd	77.25	2.03	75.02	1.97	97.61	2.56*	44.52	1.17
	3rd	62.34	1.64	61.20	1.61	74.90	1.97	32.27	0.85
	4th	38.72	1.02	45.93	1.21	48.12	1.26	22.72	0.60
Residual Interstory Drift	1st	19.87	0.48*	12.22	0.30*	1.85	0.04	45.65	1.11*
	2nd	16.41	0.43	4.07	0.11	7.49	0.20*	0.31	0.01
	3rd	11.72	0.31	1.40	0.04	2.76	0.07	0.10	0.00
	4th	4.28	0.11	0.51	0.01	0.71	0.02	0.02	0.00
Acceleration Unit		g		g		g		g	
Maximum Absolute Acceleration	1st	1.18		1.10		1.20		0.72	
	2nd	1.13		1.14		1.12		0.63	
	3rd	1.15		1.09		1.06		0.66	
	4th	1.47*		1.41*		1.42*		0.90*	
Maximum Ductility of Beams		6.17		8.80 / 1.0**		10.33 / 1.0**		6.86 / 1.0**	
Maximum Ductility of Columns		6.38		7.12		8.63 / 1.0		11.57	

* Shaded values represent maximum and residual interstory drifts and maximum absolute accelerations.

**Ductility values in SCS energy dissipating components / ductility in structural members.

(iii) For the residual displacement and residual interstory drift, the SCS model shows a very good ability to largely reduce or even eliminate residual drifts. The SCS model with SCS base has extremely small residual displacements and residual inter-story drifts, which is because the self-centering ability of the SCS base is accounted for more reduction of residual displacements. This reduction of residual drifts in SCS model can reduce the cost to return the building to its own position after earthquakes.

(iv) The maximum floor acceleration is reduced by about 10% for the SCS building compared to the original building under the ground motions with 20%, 10% or 5% exceedance probability in 50 years. This indicates a better seismic performance of the SCS Model compared to that of the original model. As shown in Table 4-7, the 4% reduction in acceleration response indicates that under the ground motions with the high hazard level (2% exceedance probability in 50 years), the building re-designed with SCS has less impact on acceleration than that in lower hazard levels (5%, 10% or 20% exceedance in 50 years).

(v) For the ductility of columns and beams, the ductility associated with the value “1.0” (i.e. no yielding) in SCS model means that no yielding and no damage occurred in the beams or columns while those yieldings happened in the energy dissipating components of SCS. Under the ground motions with the lower hazard levels, the ductility of columns in the SCS model is similar to that of the original model while for the higher hazard level the ductility is increasing for the SCS model compared to the original model, which indicates that the SCS model with fixed base can not

protect the columns from yielding if the columns of the SMRF building yielded in severe earthquakes. Therefore, reinforcing the base columns in the SCS model with fixed base or changing them to SCS base connections is necessary if the original design of the SMRF building can not save the base column connections.

(vi) By comparing the responses between the SCS model with fixed base and SCS base, it is observed that the displacement and acceleration responses are similar in these two models. The SCS model with SCS base, however, has less residual drift than the SCS model with fixed base. Also, the residual drifts of these two models are much lower compared to that of the original model. Therefore, from this point of view, it is believed that the seismic performance of the SCS model with fixed base is similar to that of the SCS model with SCS base.

4.3.3 Fragility Analyses

Fragility is defined as the probability that a system exceeds a limit state as a function of some measures of seismic intensity. In this section, the mean return period corresponding to the different exceedance probabilities of MCEER ground motions is used as the measure of seismic intensity. In Section C1.6.1.2 of FEMA 356, the mean return period is defined by:

$$P_R = \frac{-Y}{\ln(1 - P_{EY})} \tag{4.4}$$

where P_R: Mean return period (years)

Y: Time (years) for the desired earthquake hazard level

P_{EY}: Probability of exceedance for the desired earthquake hazard level

Using the Eq. (4.4), the mean return period of the MCEER ground motions with 4 hazard levels having 20%, 10%, 5% and 2% exceedance probabilities in 50 years, is obtained as shown in Table 4-8.

Table 4-8 Mean Return Period

Hazard Level	20%/50years	10%/50years	5%/50years	2%/50years
Mean Return Period P_R (year)	224.1	474.6	974.8	2474.9

The structural performance levels are used as the limit state in the fragility analyses. This limit state is defined by table C1-3 in FEMA 356, part of which is shown in the following table 4-9. In this table, the 0.2% residual drift for immediate occupancy is added by the authors in order to determine the fragility in the low performance level.

Table 4-9 Limit State for Fragility Analysis (FEMA 356)

Structural Performance Level		Immediate Occupancy	Life Safety	Collapse Prevention
Steel Moment Frames	Maximum Interstory Drift (transient)	0.7%	2.5%	5%
	Residual Drift (permanent)	0.2%	1%	5%

A regression process was conducted to obtain the approximate function between the fragility probability and the mean return period using the data obtained from the seismic analyses. The regression equation is defined as:

$$P_{FRAGILITY} = a * \exp(c * \frac{-Y}{P_R}) \quad (4.5)$$

where:

a and c: regression coefficients

$P_{FRAGILITY}$: probability of exceeding

Y and P_R are defined in Eq. (4.4).

The results of the fragility analyses are shown in Figs. 4-10, 4-11, 4-12, 4-13 and 4-14. Note that the result for the probability of fragility in collapse prevention level with the criteria of 5% residual (permanent) drift is not presented since probabilities of the three models are all zero. In the structural performance of immediate occupancy, similar results are achieved in all three models as shown in Fig. 4-10, while as indicated in Fig. 4-11, the better results are obtained in two SCS models compared to those in the original model with the criteria of 0.7% residual drift. In the medium level (life safety), the similar or better performance are obtained in SCS models compared to those of original model as shown in Fig. 4-12 and 4-13. In collapse prevention level, as shown in Fig. 4-14, all 3 models can easily pass through the criteria of 5% transient drift, which indicates that no large transit drift occurred in the building after severe earthquakes. Since the better performance can be achieved in the SCS models based on the residual drift criteria, it is believed that SCS possesses the good ability to reduce or eliminate the residual drifts leading to save much in the cost of recovering the normal function of the hospital buildings.

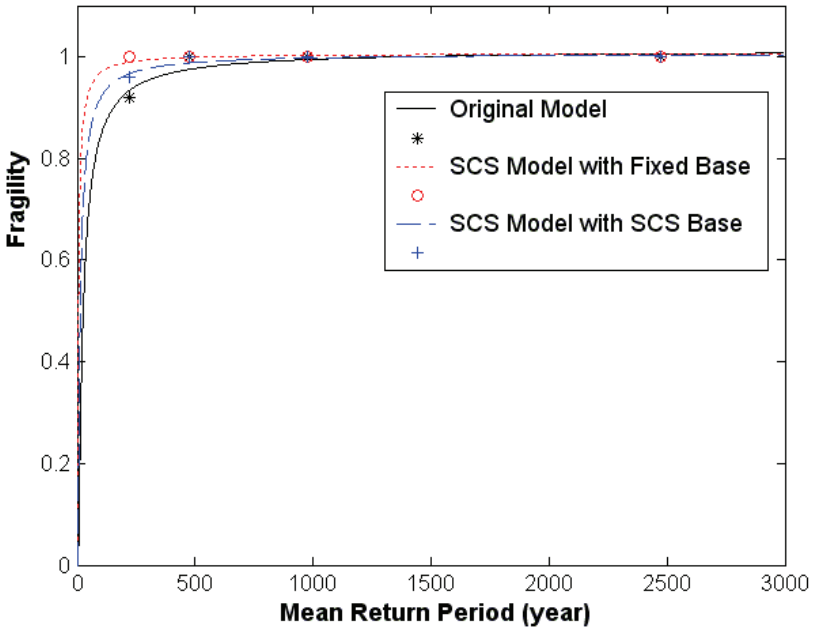

Figure 4-10 Fragility of Immediate Occupancy with 0.7% transient drift criteria

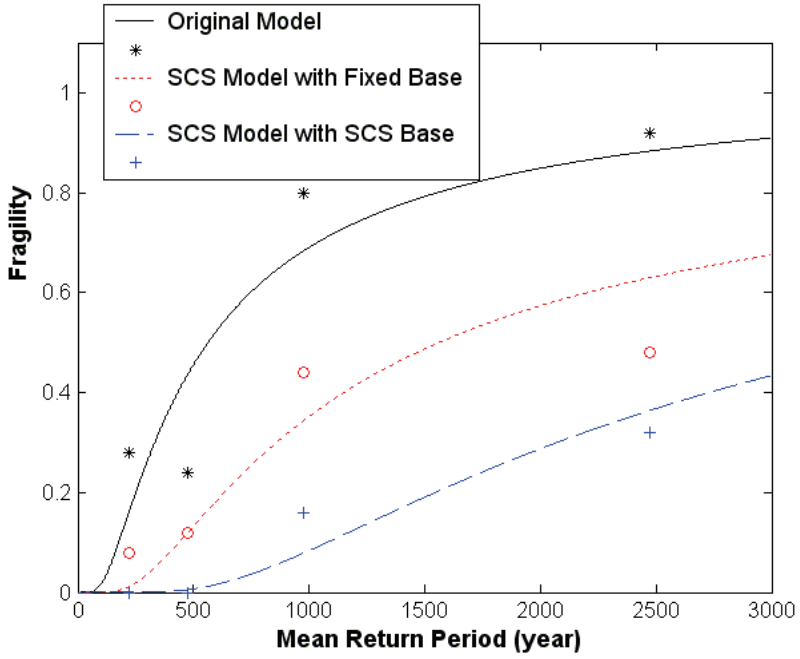

Figure 4-11 Fragility of Immediate Occupancy with 0.2% permanent drift criteria

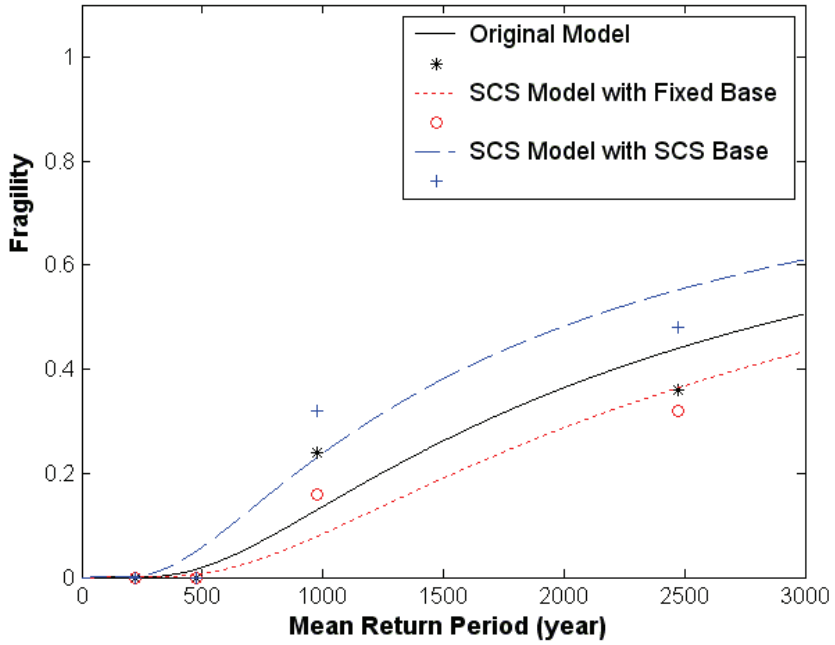

Figure 4-12 Fragility of Life Safety with 2.5% transient drift criteria

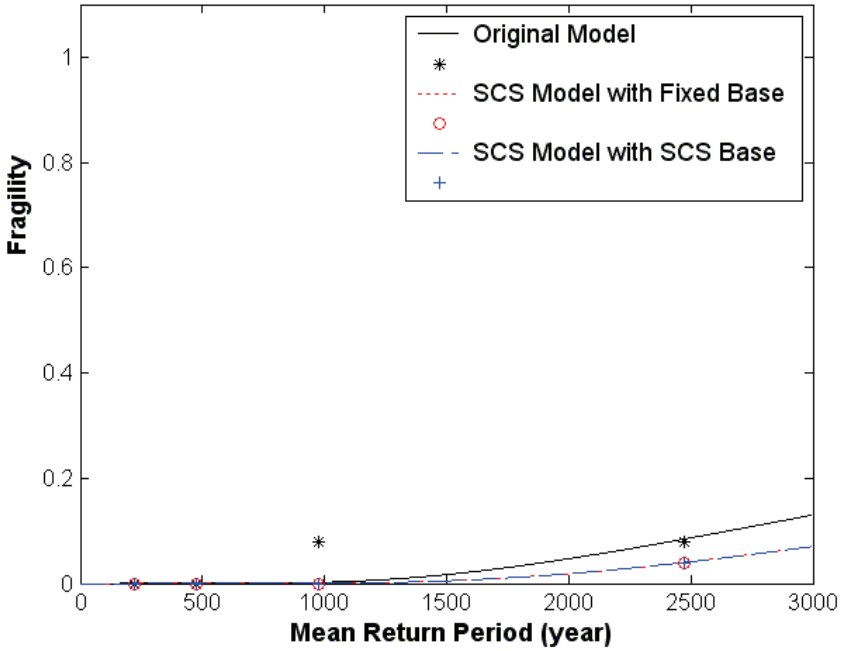

Figure 4-13 Fragility in Life Safety with 1% permanent drift criteria

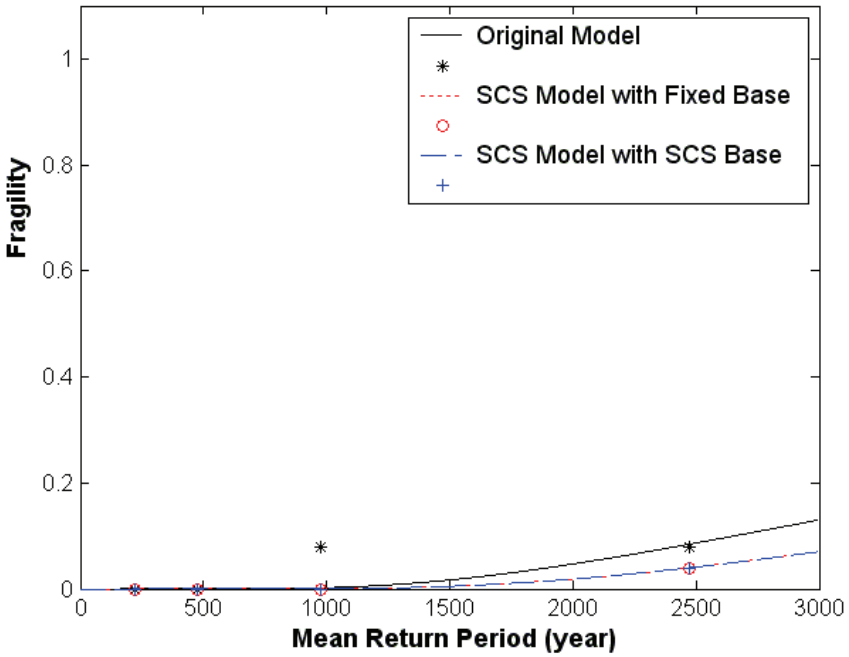

Figure 4-14 Fragility in Collapse Prevention with 5% transient drift criteria

4.4 Practical Re-Design Procedure for SCS with SCPT connections in SMRF Buildings

In order to implement the SCS behavior, it is necessary to use practical SCS devices in real buildings. Such devices should possess good self-centering abilities, relatively low cost and easy installation and replacement. Based on these criteria, the Self-Centering Post-Tensioned (SCPT) connections (i.e. PTED connections as introduced in Chapter II) were used for the practical re-design of the WC70 building. In this section, the relationship between the moment-curvature property and SCS parameters is presented and then the re-design procedure of SCS with SCPT connections is developed.

4.4.1 Relationship between Parameters of SCS and SCPT Connections

Following the procedure presented in Section 4.2, the SCS parameters α, β, ψ and η can be determined. Having these SCS parameters, the next step is to determine the physical properties of SCPT connections. As shown in Fig. 4-15, four parameters in the SCPT connections are required: the cross area of Energy Dissipating (ED) elements $A_{ED,}$, the cross area of Post-Tensioned (PT) elements A_{PT}, the thickness of the Reinforcing Plates (R-Plate) welded to the outside of the upper and lower flanges of the beams t_R and the initial PT force in the PT bars F_{PTin}. These four parameters can not be directly determined only by the SCS parameters but need to be estimated based from the properties of the beam-to-column connections. Once the physical parameters of the SCPT connections are estimated, the moment-curvature relationship of the SCPT connections can be determined to check whether the SCS parameters of the SCPT connections are consistent with the estimated A_{ED}, A_{PT}, t_R and F_{PTin}. If a large difference exists between the original set of SCS parameters and the ones calculated from the estimated A_{ED}, A_{PT}, t_R and F_{PTin}, those four SCS parameters need to be adjusted and the iteration should be continued until similar SCS parameters are achieved.

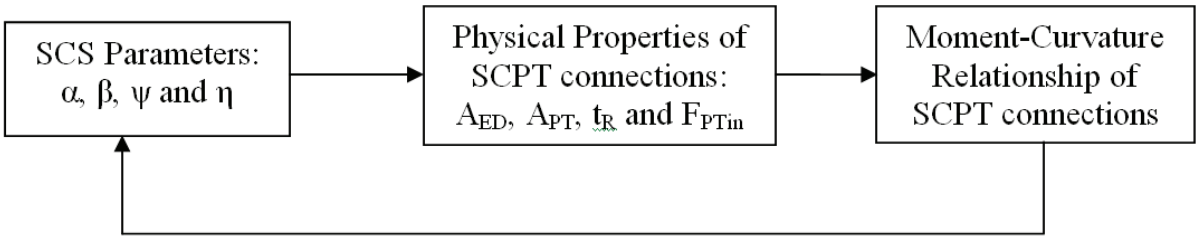

Figure 4-15 Relationship between parameters in SCS and SCPT connections

4.4.1.1 First Estimate of Design Parameters (A_{ED}, A_{PT}, t_R and F_{PTin}) of SCPT Connections

Parametric studies showed that a first estimate for the initial PT force F_{PTin} can be taken as 20% of axial yielding force of beams. The stress in the PT elements should remain in the elastic range, therefore:

$$F_{PT\max} < F_{yPT} \tag{4.6}$$

where F_{yPT} is the yielding force of the PT elements and F_{PTmax} is the max force developed in the PT elements, which occurs when the gap-opening angle of SCPT connections reaches the maximum designed value (assumed to equal to 0.03 rad):

$$F_{PT\max} = F_{PTin} + A_{PT}(\Delta\varepsilon_{PT})E \tag{4.7}$$

Where E is the Youngs' Modulus and $\Delta\varepsilon_{PT}$ is the increase in strain in the PT bars at the target gap-opening angle, which can be estimated by:

$$\Delta\varepsilon_{PT} = \frac{\Delta L_{PT}}{L_{PT}} \approx \frac{n(\theta_{target} d_c)}{L_{PT}} \tag{4.8}$$

where d_c is the distance from the position of the PT elements to the neutral axial (approximately assumed to be equal to half of the depth of the beams), θ_{target} is the target gap-opening angle, L_{PT} is the length of the PT elements and n is the number of gaps in the frame. Each gap opening will result in a similar strain increase in the PT elements.

The yielding force of the PT elements in Eq. (4.6) is given by:

$$F_{yPT} = A_{PT} f_{yPT} \tag{4.9}$$

where f_{yPT} is the yield strength of the PT elements.

From Eq. (4.6) to (4.9), A_{PT} should be meet the following cretiria:

$$A_{PT} > \frac{F_{PTin}}{f_{yPT} - \frac{n(\theta_{target} d_c)}{L_{PT}} E} \tag{4.10}$$

As proposed by Christopoulos et al. (2002c), the energy dissipating factor β can be estimated by:

$$\beta \approx \frac{2F_{ED}(d_b - t_f)}{F_{PTin}(d_b/2) + F_{ED}(d_b - t_f)} \tag{4.12}$$

where d_b is the depth of the beam, t_f is the thickness of the flange of beams and F_{ED} is the force developed in the ED elements at the target gap-opening angle, which can be estimated as 1.2 times the yielding force of the ED. The factor 1.2 is included to take into account the strain hardening effect in the ED bars. Therefore, the force in the ED elements is given by:

$$F_{ED} \approx 1.2 A_{ED} f_{yED} \tag{4.13}$$

where f_{yED} is the yield strength of ED bars. Substituting Eq (4.13) into Eq (4.12), a first estimate of the area of the ED elements A_{ED} can be obtained:

$$A_{ED} \approx \frac{F_{PTin}(d_b/2)}{(\frac{2}{\beta}-1)1.2\, f_{yED}(d_b - t_f)} \tag{4.14}$$

R-plates are used to reinforce the flange of the beams in order to avoid compression yielding when the gaps open. For this purpose, high strength (100ksi yielding stress) steel are used for the R-plates. A first estimate of the thickness of R-plates t_R can be taken in the range from 50% to 100% of the thickness of beam flanges.

4.4.1.2 Moment-Curvature Relationship of SCPT Connections

Since the designed parameters of SCPT connections are estimated, it is necessary to verify that the corresponding SCS parameters calculated for the SCPT connections with the designed parameters are in accordance with the originally selected SCS parameters. This verification is achieved by determining the moment-curvature relationship of each SCPT connection with the estimated SCS parameters.

As shown in Fig. 4-16, when the moment M applied to the connection reaches a critical value, the gap begins to open ($\theta>0$) and the contact point C in Fig. 4-16 (b), which moves from A to B, is assumed to be the neutral axis in the beam section. In order to determine the moment-curvature relationship, the force in the ED bars and the PT bars must be determined. The solution for these forces can be obtained for five distinct phases: (i) before gap opening ($h_C=d_b+2t_R$); (ii) point C is in the upper beam flange ($d_b+2t_R > h_C \geq d_b+t_R-t_f$); (iii) point C is between the upper flange and the upper half depth of the beam ($d_b+t_R-t_f > h_C \geq d_b/2+t_R$); (iv)

point C is between the lower half depth of the beam and the lower beam flange ($d_b/2+t_R > h_C \geq t_R+t_f$); (v) point C in the lower beam flange ($h_C < t_R+t_f$).

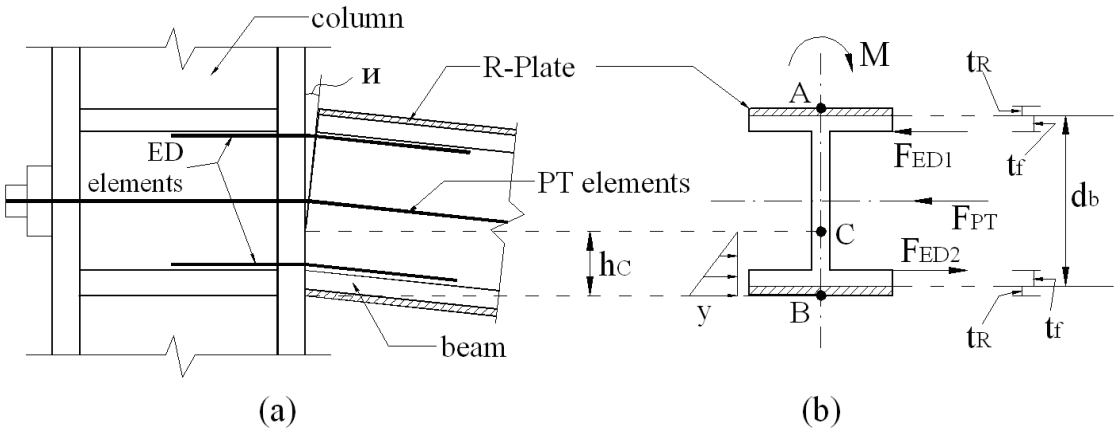

Figure 4-16 SCPT connection (a) beam-column connection (b) cross section of beam

Phase (i) $h_C = d_b+2t_R$

The beam section of the SCPT connection is in its initial position, as shown in Fig. 4-17(a). The parameters F_{ED1} and F_{ED2} are the upper and lower forces in the ED elements, F_{PT} is the force in the PT elements and ε_{b-in} is the initial strain in the beam section. Since the ED elements are installed after the installation and post-tension of the PT elements, there is no force in the ED bars. As shown in Fig. 4-17(b), the gap is beginning to open right after the critical moment is reached and the neutral point C will begin to move down. Through the horizontal force equilibrium in Fig. 4-17(a), the initial strain in the beam is given by:

$$\varepsilon_{b-in} = \frac{F_{PTin}}{E(A_b + 2A_R)} \tag{4.15}$$

where A_b is the area of beam section and A_R is the area of one R-plate section.

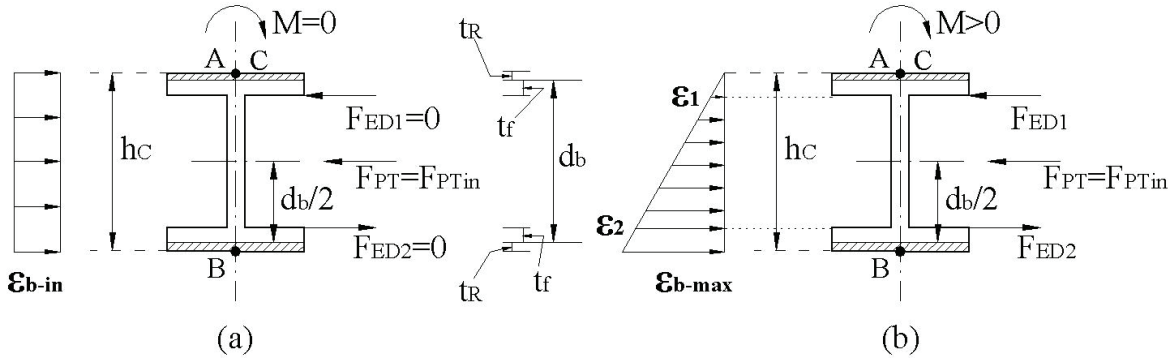

Figure 4-17 Onset of Gap-Opening, Phase i (a) beam cross section in initial position (b) beam cross section at the onset of gap-opening

From the Fig. 4-17 (a) to (b), the distribution of strains in the beam section is changed, which results in changes of the strains in the ED and PT elements without any gap-opening. Because the length of the PT elements is more than 10 to 20 times of the depth of the beam, which depends on the number of spans in one story, the change in the PT strain can be neglected and the force F_{PT} is assumed to be equal to the initial post-tensioned force F_{PTin}. For the same reason, as long as the neutral point C is higher than the position of the PT element (i.e. $h_C > d_b/2 + t_R$), F_{PT} is assumed to be the same as the initial PT force. However, since the length of the ED elements is similar to the depth of the beam, the changes of strains in ED bars can not be neglected. The change in strains in the ED bars can be approximated to the change of normal strains in the beam section at the same height:

$$\varepsilon_{ED1} = \varepsilon_{b-in} - \varepsilon_1 \tag{4.16}$$

$$\varepsilon_{ED2} = \varepsilon_2 - \varepsilon_{b-in} \tag{4.17}$$

where ε_{ED1} and ε_{ED2} are the strains in the upper and lower ED elements; ε_1 and ε_2 are the strains in the beam section at the same height as the upper and lower ED bars as shown in Fig. 4-17(b) and can be defined by:

$$\varepsilon_1 = \frac{h_C - (d_b + t_R - t_f)}{h_C} \varepsilon_{b-\max} \tag{4.18}$$

$$\varepsilon_2 = \frac{h_C - (t_R + t_f)}{h_C} \varepsilon_{b-\max} \tag{4.19}$$

where h_C is the distance between the neural point C and the bottom of the lower R-plate, d_b is the depth of beam, t_R is the thickness of the R-plate, t_f is the thickness of the beam flange and $\varepsilon_{b-\max}$ is the maximum strain in the beam section. Through horizontal force equilibrium, $\varepsilon_{b-\max}$ is given by:

$$\varepsilon_{b-\max} = \frac{F_{PTin} + 2A_{ED}E\varepsilon_{b-in}}{\frac{E}{2}\left[2A_{ED} + h_C b_f - (b_f - t_W)(d_b - 2t_f)\right]} \tag{4.20}$$

where b_f is the width of beam flange and t_W is the thickness of beam web.

From Eq. (4.15) to (4.20), the force in the ED and PT elements can be determined and the critical gap opening moment can also be obtained by moment equilibrium in Fig. 4-17(b).

Phase (ii) $d_b+2t_R > h_C \geq d_b+t_R-t_f$

In this phase the gap begins to open and the neutral point C is located in the upper beam flange, as shown in Fig. 4-18. Due to the gap opening, there is no strain in the upper beam flange located higher than the neutral point C. The height of the neutral axis h_C is

undetermined, which is the major difference compared to Phase (i). Therefore, $\varepsilon_{b-\max}$ can not be obtained from Eq. (4-20) but can be estimated by:

$$\varepsilon_{b-\max} = h_C \frac{\theta}{d_b + 2t_R} \tag{4.21}$$

where θ is the gap-opening angle. More details on this approximation can be found in Pampanin et al. (2000).

With Eqs. (4.15) to (4.21), the position of the neutral axis h_C can be determined by horizontal force equilibrium in Fig. 4-18. The moment corresponding to the gap opening angel θ can also be obtained by moment equilibrium.

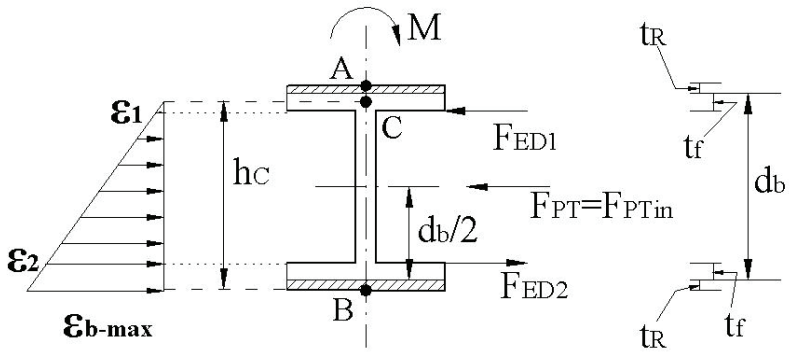

Figure 4-18 Beginning of Gap-Opening, Phase ii

Phase (iii) $d_b+t_R-t_f > h_C \geq d_b/2+t_R$

In this phase, the neutral axis is moving into the upper half of the beam web, as shown in Fig. 4-19. Comparing Fig. 4-19 with Fig. 4-18, the major difference is the disappearance of the strain ε_1 in the upper part of the beam, which is due to the increasing of gap-opening angle. Therefore the strain in the upper ED elements is given by:

$$\varepsilon_{ED1} = \frac{\theta(d_b - t_f - h_C)}{L_{ED}} + \varepsilon_{b-in} \tag{4.22}$$

where L_{ED} is the length of ED bars and assumed to be equal to the depth of beams and ε_{b-in} is defined in Eq. (4.15).

In Eq. (4.22), the first term represents the increased in strains due to the gap-opening and the second term indicates the effect of the initial post-tensioned force. The replacement of Eq.(4.16) by Eq. (4.22) is the only different step between Phase (ii) and (iii). Thereafter, the moment can be determined through moment equilibrium.

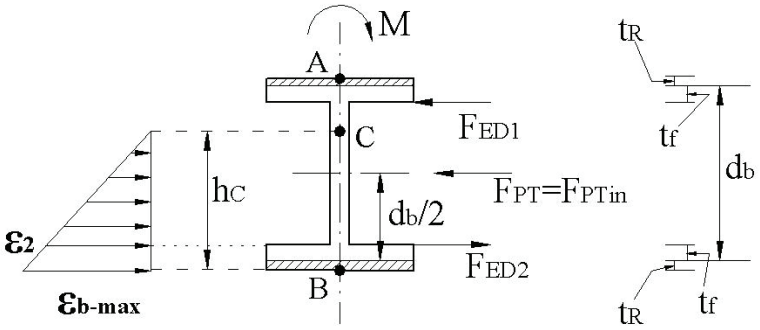

Figure 4-19 Gap-Opening Phase iii

Phase (iv) $d_b/2+t_R > h_C \geq t_R+t_f$

In this phase, the neutral axis moves under the PT elements, as shown in Fig. 4-20, which results in a relatively large increase in the PT force F_{PT}. In the previous three phases, the PT force did not change. Therefore, the strain in the PT elements ε_{PT} is given by:

$$\varepsilon_{PT} = \frac{\theta(\frac{d_b}{2} + t_R - h_C)}{L_{PT}} + \varepsilon_{PT-in} \tag{4.23}$$

where L_{PT} is the length of the PT elements and ε_{PT-in} is the initial post-tensioned strain.

With Eq. (4.23), the PT force F_{PT} can be obtained. The other steps to obtain the forces in the ED elements and moment M are the same as those in Phase (iii)..

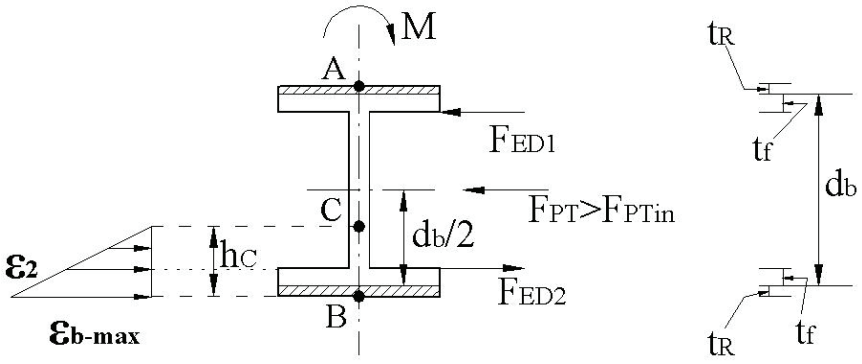

Figure 4-20 Gap-Opening, Phase iv

Phase (v) $h_C < t_R + t_f$

As shown in Fig. 4-21, in this phase, the neutral point C moves down to the lower beam flange due to the large gap-opening angle, which should reach or exceed the target angle of 0.03rad. The lower ED elements transit from compression in the previous phases to tension and the strain in the lower ED elements ε_{ED2} is given by:

$$\varepsilon_{ED2} = \frac{\theta(t_R + t_f - h_C)}{L_{ED}} + \varepsilon_{b-in} \tag{4.24}$$

From Eqs. 4.15, 21, 22, 23 and 24, the height of the neutral axis can be determined through horizontal force equilibrium in Fig. 4-21 and the forces in the PT and ED elements can also be obtained. Again through moment equilibrium, the moment M can be determined.

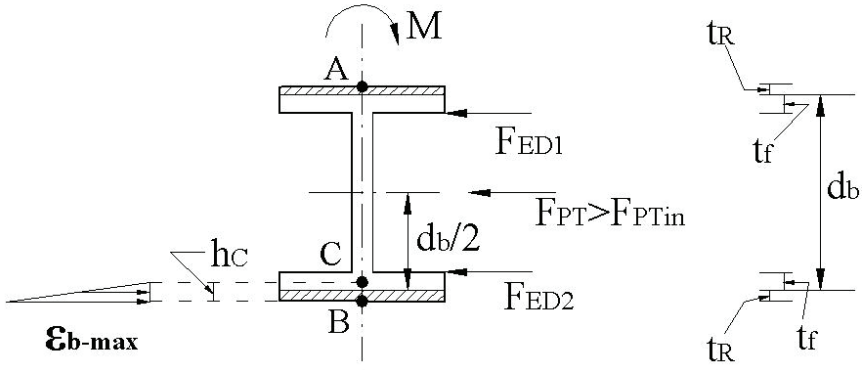

Figure 4-21 Gap-Opening, Phase v

For any specified gap-opening angle, the moment can be obtained in one of the five phases described above and the whole moment-curvature relationship can be established to verify whether the corresponding SCS parameters with the designed SCPT connections are similar to the SCS parameters. If there is an unacceptable difference between these two sets of SCS parameters, the physical parameters (A_{ED}, A_{PT}, t_R and F_{PTin}) of the SCPT connections should be modified and the iteration needs to be continued until the verification of conformity with the SCS parameters. Note also that at the target gap-opening angle (i.e. maximum designed angle 0.03) the beam and R-plates should remain elastic, which is another criteria to modify the designed parameters of the SCPT connections.

Based on a series of numerical iterations on the physical parameters (A_{ED}, A_{PT}, t_R and F_{PTin}) of SCPT connections, the following conclusions can be made:

1) It is difficult for the post-yielding factor α to reach values larger than 0.2 by increasing the area of the ED elements A_{ED} or the area of the PT elements A_{PT}.

2) It is relatively easy to get the normal range (0.5 to 1) of the energy dissipating factor β by adjusting A_{ED}.

3) Increasing the initial PT force F_{PTin} can increase the strength ratio η and yielding ratio factor ψ, but at the same time it may increase the possibility of yielding in the beam flange or R-plate before or at the target gap-opening angle.

4) When A_{ED} is increasing, the factors β, ψ and η are also increasing.

5) An increase of A_{PT} causes also an increase of the post-yielding factor α.

6) Increasing the thickness of the R-plates t_R can reduce the yielding in the beam or the R-plates.

When a iteration process for adjusting the physical parameters of the SCPT connections is conducted, the above conclusions can be used as a guideline to accelerate the iteration process.

4.4.2 Practical Re-Design Procedure of SMRF Buildings with SCPT Connections

There are three distinct steps in the practical re-design procedure of SMRF buildings with SCPT connections: preliminary design, intermediate design and final design. In the preliminary design, all the SCS parameters (α, β, η and ψ) and physical parameters (A_{ED}, A_{PT}, t_R and F_{PTin}) of the SCPT connections are first determined. Thereafter, in the intermediate design, the physical parameters (A_{ED}, A_{PT}, t_R and F_{PTin}) are modified in the same story and same joint. Finally, in the final design, the sections of R-plates, ED and PT elements are selected according to the modified parameters and available steel products.

4.4.2.1 Preliminary Design

The preliminary design phase described can be summarized as followed:

i) Determine the desirable SCS parameters (α, β, η and ψ) for the SMRF building by implementing the redesign procedure proposed in Chapter 4.2.

ii) Provide a first estimate of the physical parameters (A_{ED}, A_{PT}, t_R and F_{PTin}) to each beam-column joint in the whole buildings according to Section 4.4.1.1.

iii) Obtain the moment-curvature relationship of each joint to verify the desirable SCS parameters according to Section 4.4.1.2.

iv) Iterate on the values of the physical parameters until verification of the target SCS parameters according to Section 4.4.1.

v) Finally, form a preliminary set of physical parameters (A_{ED}, A_{PT}, t_R and F_{PTin}) for each beam-column joint.

4.4.2.2 Intermediate Design

In a real building, it is common that different beam sections exist in adjacent spans of a given story. However, following the preliminary design procedure, the different sets of physical SCPT parameters are selected for different beam sections. Therefore, a conflict arises because in one frame of a given story, the area of the PT elements and the initial PT force should be the same and so should the area of the ED elements in a joint connected to different beam sections. Therefore, the aim of the intermediate design step is to resolve this

conflict. The approach is to modify the parameters to an interpolated value so that the performance of the whole building approaches that of the ideal SCS frame with the target SCS parameters, although for each single joint the SCS property will deviate from the target one. The procedure is summarized as follows:

i) Modify the initial PT force F_{PTin} in the same frame of the same story.

for $(F_{PTin})_{\max} > \frac{3}{2}(F_{PTin})_{\min}$

$$(F_{PTin})_M = (F_{PTin})_{\min} + \frac{1}{4}[(F_{PTin})_{\max} - (F_{PTin})_{\min}] \quad (4.25)$$

for $(F_{PTin})_{\max} \le \frac{3}{2}(F_{PTin})_{\min}$

$$(F_{PTin})_M = (F_{PTin})_{\min} + \frac{1}{3}[(F_{PTin})_{\max} - (F_{PTin})_{\min}] \quad (4.26)$$

where $(F_{PTin})_{max}$ and $(F_{PTin})_{min}$ are the maximum and minimum of values of the initial PT force of one frame in the same story, respectively; $(F_{PTin})_M$ is the modified initial PT force. If there is a large difference between the maximum and minimum initial PT force, the modified one is set closer (1/4) to the minimum one in Eq. (4.25) than that (1/3) in Eq. (4.26). The criteria is to set a relatively low interpolated value since the large value of the initial PT force may result in yielding in the small beam sections at the target gap-opening angle.

ii) Modify the area of the PT elements A_{PT} in the same story.

$$(A_{PT})_M = (A_{PT})_{\min} + \frac{2}{3}[(A_{PT})_{\max} - (A_{PT})_{\min}] \quad (4.27)$$

where $(A_{PT})_{max}$ and $(A_{PT})_{min}$ are the maximum and minimum of values of the area of PT elements in one frame of the same story, respectively; $(A_{PT})_M$ is the modified area of the PT elements. The modified area is selected to be closer to the larger value ($(A_{PT})_{max}$), which represents the safety design idea.

iii) Re-calculate the area of the ED elements and the thickness of the R-plates for each joint according to Section 4.4.1.

iv) Finally, a new set of physical SCPT parameters is developed for each beam-column connection.

4.4.2.3 Final Design

Based on the modified SCPT parameters from the intermediate design step, the selection of real steel products is conducted in the final design.

i) Selection for PT elements.

Considering cost, the PT elements should be selected with readily used steel products such as the product manufactured by DYWIDAG Systems International (DSI). DYWIDAG mono-strand tendons are typically made from cold-drawn, low relaxation 7-wire strand conforming to ASTM A416, gr270 [1860MPa] and there are two sizes available: 0.5 and 0.6 in diameter, which are suitable for PT elements. High strength DSI bars can also be used as PT elements.

ii) Selection of ED elements

The ED elements can also be selected from DSI Thread Bar products, which conform to ASTM A615 (Grade 60 & 75) CAN/CSA(G3018-M1982) with 60 or 75 ksi yielding stress. The designation of DSI product is including #6, #7, #8, #9, #10, #11, #14 and #18, which has different cross section area. For a design value of A_{ED}, the DSI product can be machined down to the corresponding area.

iii) Selection of R-plates

R-plates are selected with high yield stress steel products conforming to A514 with 90 or 100 ksi yield stress. The size can be selected from Table 1-19 in LRFD 3rd Edition (LRFD, 2001).

4.5 Re-Design and Numerical Modeling of WC70 Hospital Building with SCPT connections

The re-design of the WC70 hospital building incorporating SCPT connections was conducted by following the practical re-design procedure given in Section 4.4.2. The SCPT connections were designed for each beam-column joint without changing the properties of the base column connection. The results of the preliminary design, intermediate design and final design are shown in Table 4-10, 4-11 and 4-12, respectively. To improve the performance of the Ideal SCS hospital model with α=0.2, β=0.6 and $\psi = \eta_{SCS}/\eta_{Original}$=0.6, these SCS parameters were modified as a target set: α=0.05, β=0.8 and $\psi = \eta_{SCS}/\eta_{Original}$=0.5 as shown in Table 4-10. It is noted that in these three tables, the maximum stresses in the beam flanges and R-plates are listed to verify that the beams and R-plates remain elastic.

Table 4-10 Preliminary Design for WC70 Hospital with SCPT Connections

* Target SCS parameters: α=0.05; β=0.8; $\psi = \eta_{SCS}/\eta_{Original}$=0.5;

	Beam Section	Initial PT force F_{PTin} (kips)	Area of PT bar A_{PT} (in^2)	Area of 2 ED bars A_{ED} (in^2)	Thickness of R plate t_R (in)	α	β	Ψ ($\eta_{SCS}/\eta_{Original}$)	Max Stress of R plate (ksi)	Max Stress of beam Flange (ksi)
1st floor (interior)	w33x241	759.70	7.43	3.01	0.98	0.04	0.80	0.50	78.97	49.72
	w24x162	505.62	5.93	2.04	0.98	0.05	0.80	0.50	85.83	48.05
1st floor (exterior)	w33x221	700.90	6.72	2.76	0.89	0.04	0.80	0.50	76.78	49.61
	w24x146	462.25	5.17	1.85	0.82	0.04	0.80	0.50	82.82	49.91
2nd floor (interior)	w30x211	681.09	5.87	2.70	0.86	0.03	0.80	0.50	78.32	49.60
	w24x146	462.25	5.17	1.85	0.82	0.04	0.80	0.50	82.82	49.91
2nd floor (exterior)	w30x211	681.09	5.87	2.70	0.86	0.03	0.80	0.50	78.32	49.60
	w24x131	413.88	4.53	1.64	0.72	0.04	0.80	0.50	79.09	49.34
3rd floor (interior)	w30x211	681.09	5.87	2.70	0.86	0.03	0.80	0.50	78.32	49.60
	w24x146	462.25	5.17	1.85	0.82	0.04	0.80	0.50	82.82	49.91
3rd floor (exterior)	w30x211	681.09	5.87	2.70	0.86	0.03	0.80	0.50	78.32	49.60
	w24x103	307.55	3.61	1.22	0.83	0.04	0.80	0.50	81.52	48.08
4th floor (interior)	w30x173	561.00	4.70	2.20	0.70	0.03	0.80	0.50	72.79	48.37
	w24x94	282.54	3.22	1.11	0.70	0.04	0.80	0.50	78.78	49.79
4th floor (exterior)	w24x104	341.19	2.38	1.33	0.45	0.02	0.80	0.50	67.00	46.19
	w24x68	202.01	2.22	0.78	0.50	0.04	0.80	0.50	70.51	48.52

Table 4-11 Intermediate Design for WC70 Hospital with SCPT Connections

* Target SCS parameters: α=0.05; β=0.8; $\psi = \eta_{SCS}/\eta_{Original}$=0.5;

	Position	Beam Section	Initial PT force F_{PTin} (kips)	Area of PT bar A_{PT} (in^2)	Area of 2 ED bars A_{ED} (in^2)	Thickness of R plate t_R (in)	α	β	Ψ ($\eta_{SCS}/\eta_{Original}$)	Max Stress of R plate (ksi)	Max Stress of beam Flange (ksi)
1st floor (interior)	End	w24x162	590.31	6.93	2.39	1.10	0.05	0.80	0.59	92.30	49.78
	Internal	w33x241			2.36	0.84	0.03	0.80	0.39	71.57	46.95
	Joint	w24x162			2.36	1.10	0.05	0.79	0.58	92.22	49.70
1st floor (exterior)	End	w24x146	541.80	6.20	2.18	1.04	0.05	0.80	0.59	89.20	48.10
	Internal	w33x221			2.15	0.76	0.03	0.80	0.39	69.21	46.40
	Joint	w24x146			2.15	1.04	0.05	0.79	0.59	89.13	48.02
2nd floor (interior)	End	w24x146	535.20	5.64	2.15	0.98	0.05	0.80	0.58	87.80	48.51
	Internal	w30x211			2.13	0.79	0.03	0.80	0.40	71.03	45.19
	Joint	w24x146			2.13	0.98	0.05	0.79	0.58	87.76	48.47
2nd floor (exterior)	End	w24x131	502.95	5.42	2.01	0.91	0.05	0.80	0.61	86.30	48.86
	Internal	w30x211			2.00	0.79	0.03	0.80	0.37	69.01	43.36
	Joint	w24x131			2.00	0.91	0.05	0.80	0.61	86.28	48.83
3rd floor (interior)	End	w24x146	535.20	5.64	2.15	0.98	0.05	0.80	0.58	87.80	48.51
	Internal	w30x211			2.13	0.79	0.03	0.80	0.40	71.03	45.19
	Joint	w24x146			2.13	0.98	0.05	0.79	0.58	87.76	48.47
3rd floor (exterior)	End	w24x103	400.94	5.12	1.61	1.13	0.06	0.80	0.66	93.09	48.50
	Internal	w30x211			1.60	0.79	0.03	0.80	0.30	63.14	38.18
	Joint	w24x103			1.60	1.13	0.06	0.79	0.66	93.04	48.45
4th floor (interior)	End	w24x94	352.16	4.21	1.40	0.92	0.05	0.80	0.63	87.66	49.98
	Internal	w30x173			1.39	0.64	0.03	0.80	0.32	59.64	38.36
	Joint	w24x94			1.39	0.92	0.05	0.79	0.63	87.61	49.93
4th floor (exterior)	End	w24x68	248.40	2.33	0.97	0.59	0.04	0.80	0.61	76.05	49.75
	Internal	w24x104			0.97	0.45	0.02	0.80	0.37	57.66	37.88
	Joint	w24x68			0.97	0.59	0.04	0.80	0.61	76.05	49.75

Table 4-12 Final Design for WC70 Hospital with SCPT Connections

* Target SCS parameters: α=0.05; β=0.8; $\psi = \eta_{SCS}/\eta_{Original}$=0.5;

	Position	Beam Section	Initial PT force F_{PTin} (kips)	Area of PT bar A_{PT} (in^2)	Area of 2 ED bars A_{ED} (in^2)	Thickness of R plate t_R (in)	α	β	ψ ($\eta_{SCS}/\eta_{Original}$)	Max Stress of R plate (ksi)	Max Stress of beam Flange (ksi)
1st floor (interior)	internal	w33x241	590	32@0.6in. 6.944	#10 @1.234 in. 2.39	0.875	0.033	0.809	0.38	71.53	45.99
	external	w24x162				1.25	0.053	0.795	0.56	91.89	44.46
1st floor (exterior)	internal	w33x221	540	4@0.5 in. 26@0.6 in. 6.254	#10 @1.178 in. 2.18	0.75	0.032	0.811	0.37	69.35	46.88
	external	w24x146				1	0.050	0.800	0.56	89.37	49.51
2nd floor (interior)	internal	w30x211	535	26@0.6in. 5.642	#10 @1.170 in. 2.15	0.875	0.029	0.804	0.38	70.87	42.63
	external	w24x146				1	0.047	0.798	0.56	87.73	47.79
2nd floor (exterior)	internal	w30x211	500	36@0.5in. 5.508	#9 @1.128 in. 2.00	0.875	0.028	0.801	0.36	68.87	40.86
	external	w24x131				1	0.050	0.798	0.59	85.83	45.37
3rd floor (interior)	internal	w30x211	535	26@0.6in. 5.642	#10 @1.170 in. 2.15	0.875	0.029	0.804	0.38	70.87	42.63
	external	w24x146				1	0.047	0.798	0.56	87.73	47.79
3rd floor (exterior)	internal	w30x211	400	24@0.6in. 5.208	#9 @1.012 in. 1.61	0.875	0.026	0.805	0.29	63.17	35.88
	external	w24x103				1.25	0.061	0.797	0.64	92.68	44.08
4th floor (interior)	internal	w30x173	350	28@0.5in. 4.284	#8 @0.944 in. 1.40	0.625	0.025	0.809	0.30	59.80	39.07
	external	w24x94				1	0.055	0.800	0.60	87.17	46.71
4th floor (exterior)	internal	w24x104	250	16@0.5in. 2.448	#7 @0.786 in. 0.97	0.5	0.020	0.797	0.36	57.88	36.13
	external	w24x68				0.625	0.044	0.798	0.60	76.26	48.40

A numerical model of the WC70 Hospital Building with SCPT connections was developed with the RUAUMOKO software (Carr 2004), as shown in Fig. 4-22. The gap-opening characteristic is modeled by a multi-spring gap element, which yields with zero tension force and remains rigid in compression. Each beam-to-column joint in the WC70 moment-resistant frame was modified with SCPT connections. The effect of the R-plates was added by increasing the beam section between the rigid bar and gap element. In the internal beam-column joint, the ED bars were connected to the beams but not to the columns.

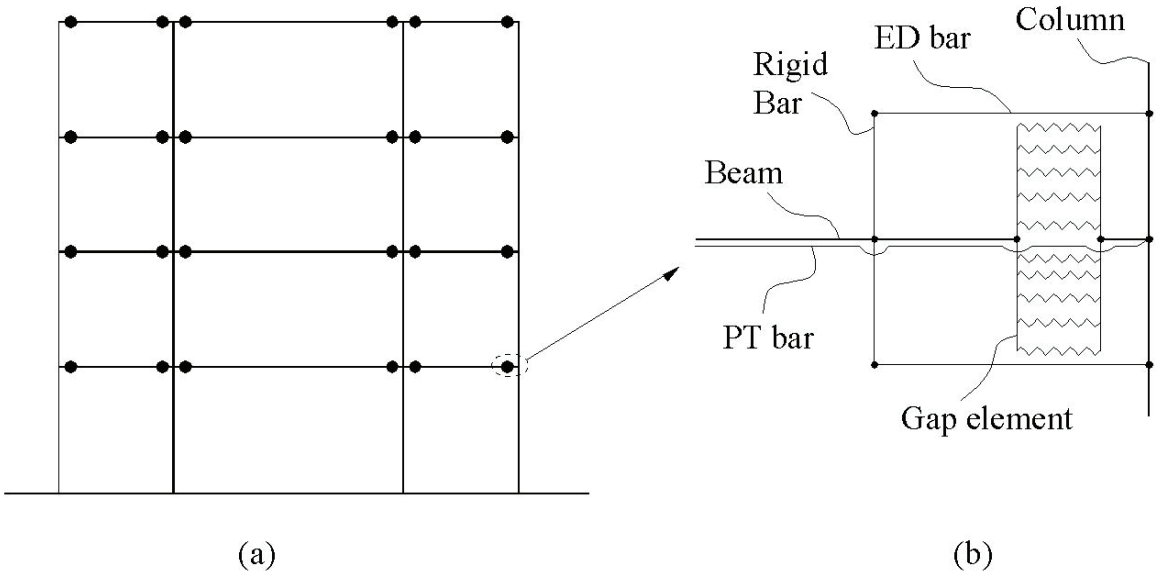

Figure 4-22 Numerical Model of WC70 Hospital Building with SCPT Connections
(a) WC70 Frame (b) Detail of External SCPT Connections

4.6 Performance of SCS WC70 Hospital Model with SCPT Connections

In this section, the seismic performances of the SCS Hospital Model equipped with SCPT connections is investigated through Cyclic nonlinear quasi-static analyses, seismic analyses and fragility analyses. The calculation methods used for these analyses are same as those in Section 4.3. Therefore, the methods are not discussed in the following presentation.

4.6.1 Cyclic nonlinear quasi-static Analyses

The result of the Cyclic nonlinear quasi-static analyses is shown in Fig. 4-23. In this figures, it is observed that the initial stiffness of the SCS model equipped with SCPT connections does not change, while the yield strength is reduced and the post-yielding stiffness is a slightly higher than that of the original model. Those observations validate the design procedure. The possible maximum residual displacement (point B in Fig. 4-23) in the SCS

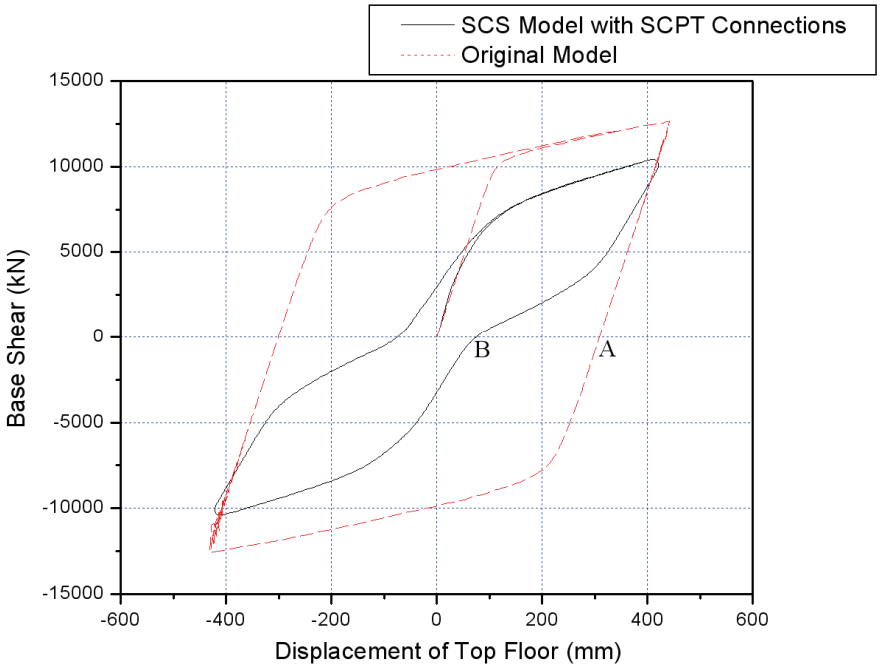

Figure 4-23 Push-Over Analysis for two models

model is reduced compared to that (point A) in the original model, which shows the good self-centering ability. The reason for non-zero residual drift is that column connections did not incorporate SCPT connections with self-centering properties.

4.6.2 Seismic Analyses

The seismic analyses were conducted under the same MCEER ground motion as mentioned in Section 4.3. In order to compare the performance of the different numerical models, the results obtained from the SCS model equipped with SCPT connections along with those of the original and ideal SCS models are listed in Table 4-13 to 4-16. The SCS model with SCPT connections is termed herein as new model.

From these tables, it is observed that the displacements and residual drifts of the new model are reduced, which shows that the performance of new model exceeds not only that of the original model but also that of the ideal SCS model. The acceleration responses of the new model are reduced by 15% to 30% compared to those of the original model, which largely exceeds the performance of the ideal SCS model. The ductility in the columns in new model is also reduced compared to the reduction in the ideal model, which indicates that the damage to the columns is reduced in the new model. All of the above observations show that the new model incorporating adjusted SCS parameters with SCPT connections can achieve much better performance than the previous ideal model, reduce the displacement responses and the acceleration responses at the same time and decrease or diminish the residual drifts, all of which shows the new re-designed SCS model with SCPT connections has a complete ability to improve the seismic performance.

Table 4-13 Mean Values of response under 25 MCEER ground motions having 20% probability of exceedance in 50 years

Mean Values		Original Model		SCS Model with SCPT connections (New Model) $\alpha = 0.05,\ \beta = 0.8$ $\psi = \eta_{SCS}/\ \eta_{Original} = 0.5$		Ideal SCS Model with fixed base $\alpha = 0.2,\ \beta = 0.6$ $\psi = \eta_{SCS}/\ \eta_{Original} = 0.6$	
	unit	mm	%	mm	%	mm	%
Maximum Displacement	top floor	130.14	0.84	112.64	0.72	136.63	0.88
Residual Displacement	top floor	12.48	0.08	1.49	0.01	3.00	0.02
Maximum Interstory Drift	1st floor	40.21	0.98	30.99	0.75	40.22	0.98
	2nd	40.90	1.07*	36.45	0.96*	42.72	1.12*
	3rd	36.06	0.95	30.26	0.79	38.63	1.01
	4th	25.30	0.66	18.61	0.49	24.91	0.65
Residual Interstory Drift	1st	5.06	0.12*	1.30	0.03*	2.53	0.06*
	2nd	4.22	0.11	0.15	0.00	0.37	0.01
	3rd	2.82	0.07	0.04	0.00	0.22	0.01
	4th	0.52	0.01	0.02	0.00	0.02	0.00
Acceleration Unit		g		g		g	
Maximum Absolute Acceleration	1st	0.68		0.55		0.64	
	2nd	0.74		0.56		0.70	
	3rd	0.79		0.60		0.81	
	4th	1.06*		0.75*		0.93*	
Maximum Ductility of Beams		2.90		1.0**		1.0**	
Maximum Ductility of Columns		2.03		0.78		1.90	

* Shaded values represent maximum and residual interstory drifts and maximum absolute accelerations.

**No yielding in beams of SCS Models.

Table 4-14 Mean Values of response under 25 MCEER ground motions having 10% probability of exceedance in 50 years

Mean Values		Original Model		SCS Model with SCPT connections (New Model) $\alpha = 0.05,\ \beta = 0.8$ $\psi = \eta_{SCS}/\ \eta_{Original} = 0.5$		Ideal SCS Model with fixed base $\alpha = 0.2,\ \beta = 0.6$ $\psi = \eta_{SCS}/\ \eta_{Original} = 0.6$	
	unit	mm	%	mm	%	mm	%
Maximum Displacement	top floor	143.38	0.92	133.81	0.86	156.99	1.01
Residual Displacement	top floor	13.46	0.09	2.44	0.02	4.37	0.03
Maximum Interstory Drift	1st floor	45.63	1.11	37.55	0.91	48.92	1.19
	2nd	45.03	1.18*	42.76	1.12*	48.36	1.27*
	3rd	41.10	1.08	35.81	0.94	42.86	1.12
	4th	29.86	0.78	21.50	0.56	29.41	0.77
Residual Interstory Drift	1st	5.27	0.13*	2.12	0.05*	3.65	0.09*
	2nd	4.79	0.13	0.24	0.01	0.74	0.02
	3rd	3.60	0.09	0.08	0.00	0.29	0.01
	4th	0.91	0.02	0.03	0.00	0.03	0.00
Acceleration Unit		g		g		g	
Maximum Absolute Acceleration	1st	0.83		0.64		0.83	
	2nd	0.88		0.67		0.85	
	3rd	0.88		0.67		0.88	
	4th	1.23*		0.85*		1.07*	
Maximum Ductility of Beams		3.36		1.0**		1.0**	
Maximum Ductility of Columns		2.81		1.18		2.78	

* Shaded values represent maximum and residual interstory drifts and maximum absolute accelerations.

**No yielding in beams of SCS Models.

Table 4-15 Mean Values of response under 25 MCEER ground motions having 5% probability of exceedance in 50 years

Mean Values		Original Model		SCS Model with SCPT connections (New Model) $\alpha = 0.05,\ \beta = 0.8$ $\psi = \eta_{SCS}/\ \eta_{Original} = 0.5$		Ideal SCS Model with fixed base $\alpha = 0.2,\ \beta = 0.6$ $\psi = \eta_{SCS}/\ \eta_{Original} = 0.6$	
	unit	mm	%	mm	%	mm	%
Maximum Displacement	top floor	205.46	1.32	189.14	1.22	223.38	1.44
Residual Displacement	top floor	42.47	0.27	6.17	0.04	12.04	0.08
Maximum Interstory Drift	1st floor	73.52	1.78*	59.35	1.44	79.10	1.92*
	2nd	67.14	1.76	58.71	1.54*	68.40	1.80
	3rd	53.66	1.41	47.70	1.25	58.28	1.53
	4th	34.55	0.91	29.10	0.76	40.10	1.05
Residual Interstory Drift	1st	16.34	0.40*	4.73	0.11*	8.35	0.20*
	2nd	14.15	0.37	0.88	0.02	3.29	0.09
	3rd	10.30	0.27	0.68	0.02	0.98	0.03
	4th	2.56	0.07	0.04	0.00	0.11	0.00
Acceleration Unit		g		g		g	
Maximum Absolute Acceleration	1st	1.05		0.76		0.93	
	2nd	1.01		0.76		0.94	
	3rd	1.04		0.82		1.00	
	4th	1.41*		1.06*		1.27*	
Maximum Ductility of Beams		5.42		1.0**		1.0**	
Maximum Ductility of Columns		5.23		3.69		5.83	

* Shaded values represent maximum and residual interstory drifts and maximum absolute accelerations.

**No yielding in beams of SCS Models.

Table 4-16 Mean Values of response under 25 MCEER ground motions having 2% probability of exceedance in 50 years

Mean Values		Original Model		SCS Model with SCPT connections (New Model) $\alpha = 0.05,\ \beta = 0.8$ $\psi = \eta_{SCS}/\ \eta_{Original} = 0.5$		Ideal SCS Model with fixed base $\alpha = 0.2,\ \beta = 0.6$ $\psi = \eta_{SCS}/\ \eta_{Original} = 0.6$	
	unit	mm	%	mm	%	mm	%
Maximum Displacement	top floor	235.06	1.51	208.47	1.34	246.25	1.58
Residual Displacement	top floor	51.98	0.33	8.22	0.05	17.00	0.11
Maximum Interstory Drift	1st floor	85.57	2.08*	71.30	1.73*	92.72	2.25
	2nd	77.25	2.03	64.31	1.69	75.02	1.97
	3rd	62.34	1.64	50.93	1.34	61.20	1.61
	4th	38.72	1.02	31.94	0.84	45.93	1.21
Residual Interstory Drift	1st	19.87	0.48*	7.04	0.17*	12.22	0.30*
	2nd	16.41	0.43	0.99	0.03	4.07	0.11
	3rd	11.72	0.31	0.48	0.01	1.40	0.04
	4th	4.28	0.11	0.05	0.00	0.51	0.01
Acceleration Unit		g		g		g	
Maximum Absolute Acceleration	1st	1.18		0.95		1.10	
	2nd	1.13		0.87		1.14	
	3rd	1.15		0.89		1.09	
	4th	1.47*		1.20*		1.41*	
Maximum Ductility of Beams		6.17		1.0**		1.0**	
Maximum Ductility of Columns		6.38		4.86		7.12	

* Shaded values represent maximum and residual interstory drifts and maximum absolute accelerations.

**No yielding in beams of SCS Models.

4.6.3 Seismic Fragility Analysis

As shown in Figs. 4-24 to 4-27, it is observed that for each performance level, the fragility of the SCS model equipped with SCPT connections is lower than that of the original model and ideal SCS model, especially with respect to permanent drifts (residual drifts). It is again apparent that the new model with the adjusted set of SCS parameters incorporating SCPT connections achieved a better performance than those of the original model and of the ideal SCS model.

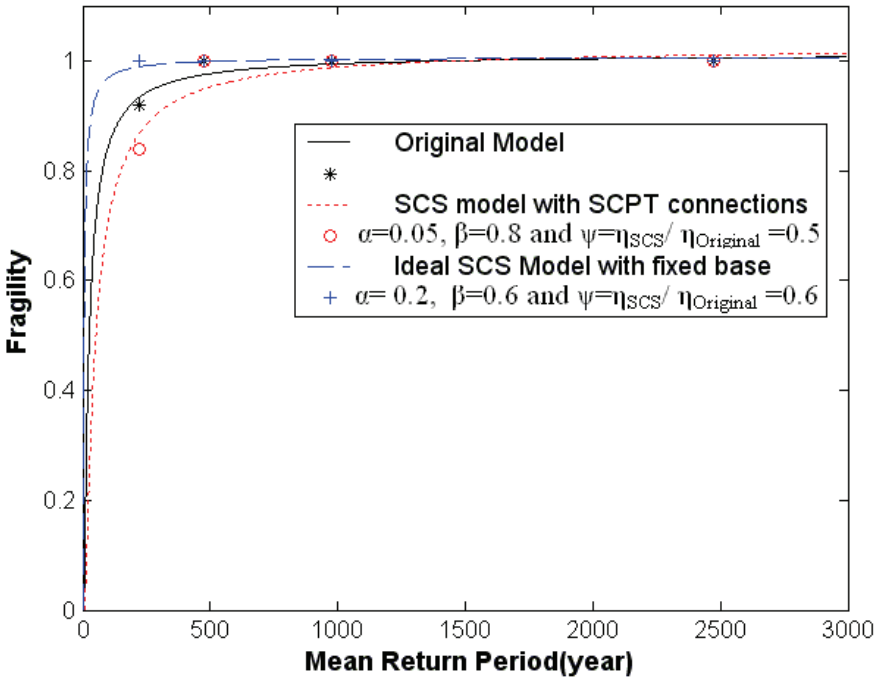

Figure 4-24 Fragility of Immediate Occupancy with the criteria of 0.7% transient drift

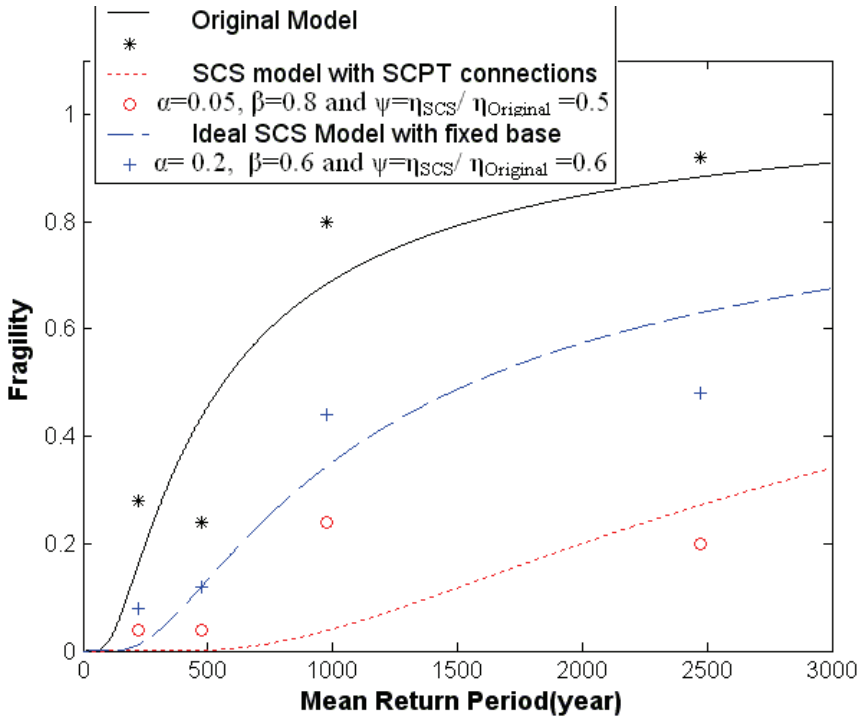

Figure 4-25 Fragility of Immediate Occupancy with the criteria of 0.2% permanent drift

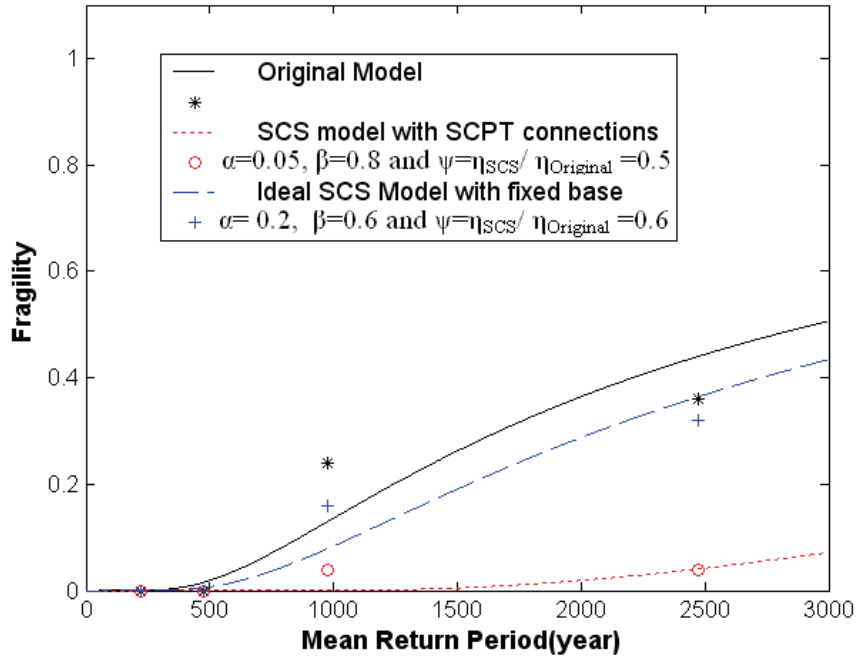

Figure 4-26 Fragility of Life Safety with the criteria of 2.5% transient drift

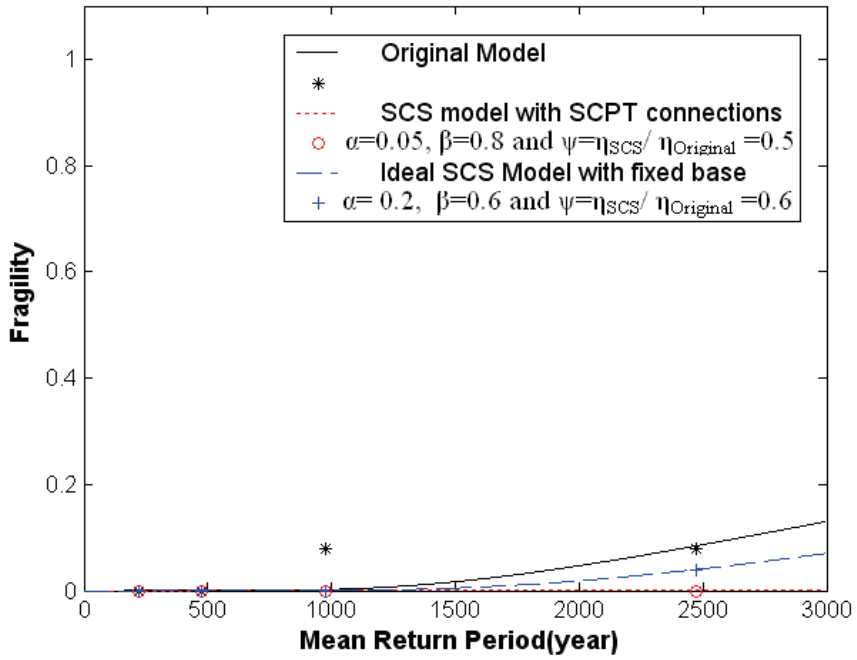

Figure 4-27 Fragility of Life Safety with the criteria of 1% permanent drift

CHAPTER 5
PROTOTYPES AND MODELS FOR SHAKE TABLE TESTING

The numerical research on the application of Self-Centering Systems (SCS) to steel framed structures was presented in previous parts of this report. From this chapter to the end of the report, the experimental testing of two steel frame specimens is reported.

To the knowledge of the authors, the experimental research of SCS implemented in an entire Steel Moment Resisting Frame (SMRF) has never been conducted. All of the previous experimental works associated with SCS in SMRF have been concentrated on subassemblies such as beam-column joints or base-column joints. There is a need to experimentally investigate the seismic performance of a complete steel frame using SCS. Therefore, the shake table testing with two steel frames: SMRF and SCS frame, is carried out to evaluate the seismic performance of each system and to validate the numerical study conducted in former chapters.

This chapter describes the procedure for designing the prototypes considered to define the models used in the shake table testing, in which the SAP 2000 computer program and the 2003 National Earthquake Hazards Reduction Program (NEHRP) Recommended Provisions (also called as FEMA 450) were utilized. Thereafter, the scaling of the prototypes leading to the test models is presented and verified numerically. Finally, according to the seismic

design procedure for Self-Centering Post-Tensioned (SCPT) frame developed in Chapter IV, the SCPT frame model is designed and detailed.

5.1 Prototype Design

To experimentally investigate the seismic performance of Steel Moment Resisting Frames (SMRF) with and without Self-Centering Systems (SCS), the prototype is considered to be the MCEER West Coast Demonstration Hospital termed as WC70 (see Section 4.1). However, due to the limitations of dimensions and gravity capacities of the shake table, it is difficult to design a whole-frame assembly model scaled exactly from the WC70 structure. Therefore, the prototype was re-designed.

To achieve the similar seismic behavior of the WC70 frame, the re-designed prototype building is assumed to be a small outpatient building with the same structural characteristics as the WC70 frame and located at the same site (Northridge, CA). The density of gravity load in the new prototype structure is identical to that of the WC70 frame. As shown in Fig. 5-1, the prototype is a three-story SMRF building.

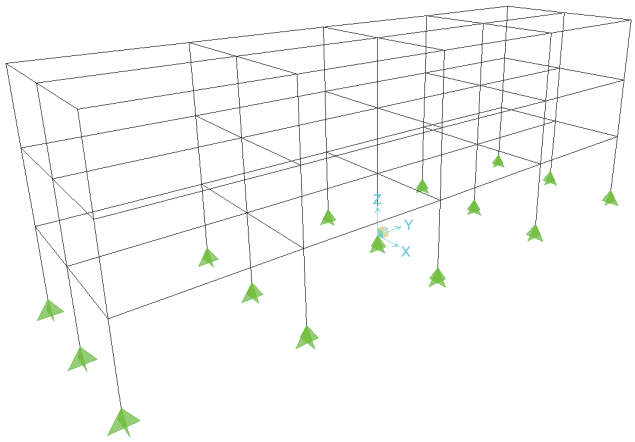

Figure 5-1 Re-Designed Prototype

The plan view of the prototype building is presented in Fig. 5-2. The surrounding Moment Resisting Frames (MRF) are represented by bold lines, which supply the lateral resistance and part of the gravity load, and the inside gravity frames are represented by simple lines, which only provide the gravity support but no lateral resistance.

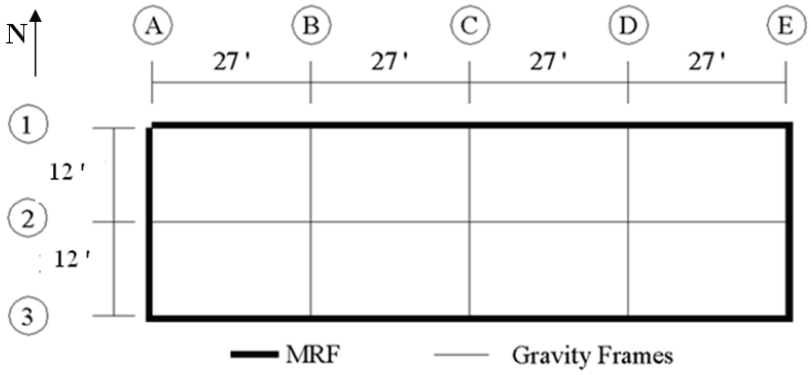

Figure 5-2 Plan View of Prototype Building

The re-designed prototype building is symmetric. Therefore, the frame in line A is selected as the prototype frame in this study, which represents half of the building. To simplify the prototype design, the seismic mass of typical floors and roof is assumed to be the same as the WC70 structure (0.5194 kip-sec^2/in.) and the corresponding weight of the half structure is 601.83 kips. According to FEMA450, the occupancy importance factor I is selected as 1.5 for a hospital building type and the site class is assumed as site class D due to the insufficient detail to determine the site class in accordance with Sec. 3.5.1 of FEMA 450. Design coefficients and factors for the prototype building are shown in Table 5-1, which is from Table 4.3-1 of FEMA 450, where R is the response modification coefficient,

Table 5-1 FEMA 450 Design Coefficients and Factors for SMRF

Basic Seismic-Force-Resisting System	Detailing Reference Section	R [a]	Ω_0 [b]	C_d [c]
Special steel moment frames	AISC Seismic, Part I, Sec. 9	8	3	5½

[a] *Response modification factor*
[b] *System overstrength factor*
[c] *Deflection amplification factor*

Following the Equivalent Lateral Force Procedure in Sec. 5.2 of FEMA 450, the seismic coefficient C_S and design seismic base shear V are, respectively:

$$C_S = \frac{S_{DS}}{R/I} = \frac{1.2578}{8/1.5} = 0.2358 \tag{5-1}$$

$$V = C_S W = 0.2358 * 601.83 = 141.91 kips \tag{5-2}$$

where:

S_{DS} = the design spectra response acceleration parameter in the short period range

W = the weight of the half prototype structure

The equivalent lateral force, F_X , at any level can be determined by:

$$F_x = C_{vx} V \tag{5-3}$$

$$C_{vx} = \frac{w_x h_x^k}{\sum_{i=1}^{n} w_i h_i^k} \tag{5-4}$$

where the values for all the coefficients in Eq. (5-3) and (5-4) can be found in Section 5.2.3 of FEMA450.

Therefore, the equivalent force for the 1st, 2nd and 3rd level is 23.51 kips, 47.27 kips and 71.12 kips, respectively. The SAP 2000 computer program was used to calculate the response of the frame under those equivalent lateral forces with story drift control and structural over-strength control. The resulting beam and column sections are shown in Fig. 5-3.

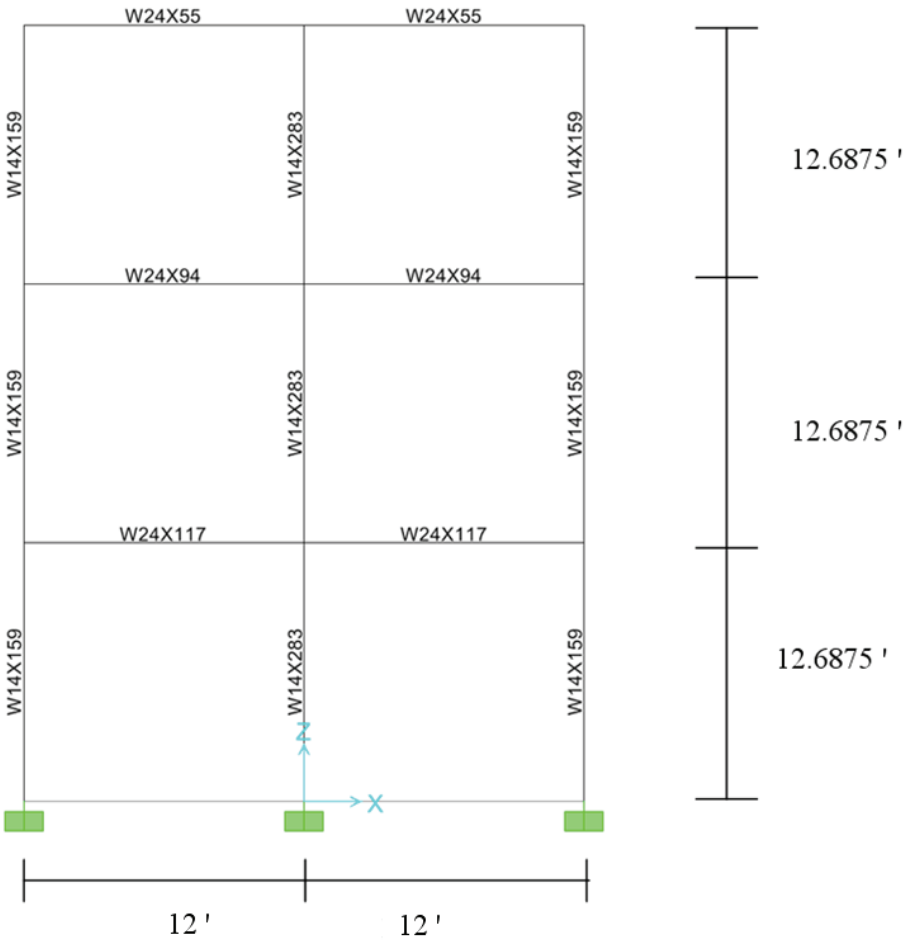

Figure 5-3 Prototype Frame

5.2 Scaling of Prototype

To experimentally investigate the seismic performance of the prototype building, the structure needs to be scaled as a model compatible with the requirements of the shake table. There are always some constraints in every shake table. The one used in this study is one of the three shake tables located in the Structural Engineering and Earthquake Simulation Laboratory (SEESL) at the University at Buffalo. The dimension of the concrete testing platform attached to this shake table is 10 ft. by 20 ft. and the acceleration limitation is ±1.15 g for a 44-kip rigid specimen. The displacement limitation is ±6 in. and the over-turning moment capacity is 333 kips-ft. Considering those limitations of the shake table as well as the gravity column frame (mass simulator), which will be presented in the next Chapter, the two fundamental scaling factors are calculated as:

$$\text{Scaling Factor of Linear Dimension: } S_l = 152.5in / 50.75in = 3 \tag{5-5}$$

$$\text{Scaling Factor of Mass: } S_M = 601.83 / 51.36 = 11.718 \tag{5-6}$$

where the scaling factor of mass is the mass ratio of prototype building to the gravity column frame.

Using the same material (structural steel) for both of the prototype and the model buildings, the scaling factor for the elastic modulus is

$$S_E = 1 \tag{5-7}$$

Therefore, the scaling factor of strain is: $S_\varepsilon = S_{\Delta l} / S_l = 1$ (5-8)

where $S_{\Delta l}$ is the scaling factor for the elongation with respect to the original length l.

All other scaling factors can be derived from scaling factors of the mass and linear dimension. From Eq. (5-7) and (5-8), the scaling factor for stress can be computed as:

$$S_\sigma = S_E S_\varepsilon = 1 \tag{5-9}$$

So, $$S_\sigma = \frac{S_{Force}}{S_{Area}} = \frac{S_M S_a}{S_{Area}} = \frac{S_M S_l S_T^{-2}}{S_l^2} = S_M S_l^{-1} S_T^{-2} = 1 \tag{5-10}$$

where S_a and S_T are the scaling factors for acceleration and time.

From Eq. (5-10), the time scaling factor can be determined as:

$$S_T = S_M^{1/2} S_l^{-1/2} \tag{5-11}$$

Therefore, from Eq (5-5) to (5-11), the following scaling factors can be defined as:

Frequency: $S_\omega = S_T^{-1} = S_M^{-1/2} S_l^{1/2}$ (5-12)

Velocity: $S_v = S_l S_T^{-1} = S_M^{-1/2} S_l^{3/2}$ (5-13)

Acceleration: $S_a = S_l S_T^{-2} = S_M^{-1} S_l^2$ (5-14)

Force: $S_F = S_M S_a = S_l^2$ (5-15)

Moment of Inertia: $S_I = S_l^4$ (5-16)

Energy: $S_{EN} = S_F S_l = S_l^3$ (5-17)

All the scaling factors along with their numerical values are presented in the Table 5-2.

Table 5-2 Scaling Factors for Shake Table Testing

		Dimension	Scale Factors	
			Artificial Mass Simulation	Value
Loading	Force	MLT^{-2}	S_l^2	9
	Pressure	$ML^{-1}T^{-2}$	1	1
	Horizontal Acceleration	LT^{-2}	$S_M^{-1}S_l^2$	0.768
	Velocity	LT^{-1}	$S_M^{-1/2}S_l^{3/2}$	1.518
	Time	T	$S_M^{1/2}S_l^{-1/2}$	1.976
Geometry	Linear dimension	L	S_l	3
	Displacement	L	S_l	3
	Elastic Section Modulus	L^3	S_l^3	27
	Moment of Inertia	L^4	S_l^4	81
	Frequency	T^{-1}	$S_M^{-1/2}S_l^{1/2}$	0.506
Material Properties	Modulus of Elasticity of Steel	-	1	1
	Stress	$ML^{-1}T^{-2}$	1	1
	Strain	-	1	1
	Poisson ratio	-	1	1
	Mass	M	S_M	11.718
	Energy	ML^2T^{-2}	S_l^3	81

Based on the scaling factors for elastic section modulus and moment of inertia in Table 5-2, the SMRF model for shake table testing is designed as shown in Fig. 5-4. The actual scaling factors in terms of the properties of the beams and the columns are shown in Table 5-3. The differences between the target and actual scaling factors are due to the limitation of structural steel products for the beam and column sections.

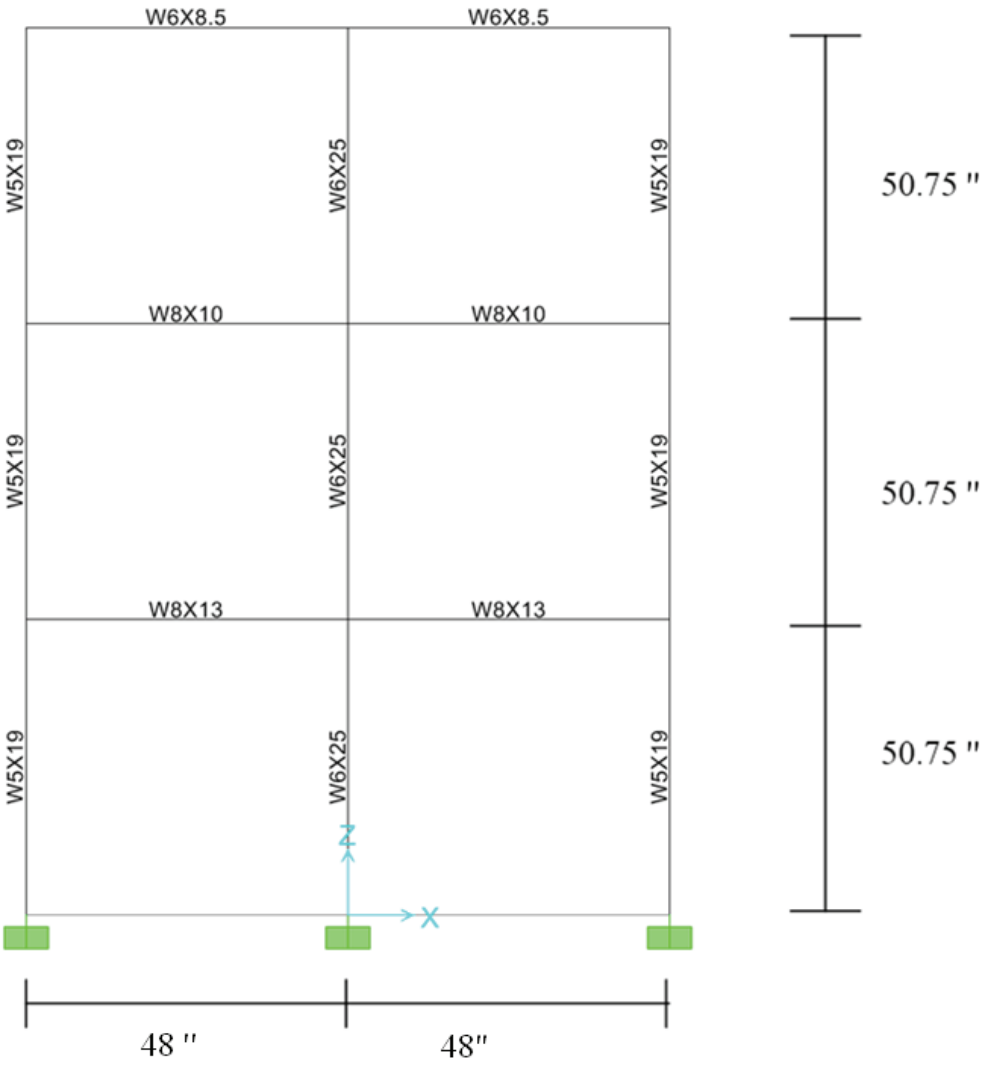

Figure 5-4 SMRF Model Configuration

Table 5-3 Actual Scaling Factors of Beams and Columns Properties

Sections			Elastic Section Modulus (S_X)		Moment of Inertia (I_X)	
			in^3	Scaling Factor (Target value 27)	in^4	Scaling Factor (Target value 81)
Beams	Prototype	w24x117	291	29.4	3540	89.4
	Model	w8x13	9.91		39.6	
	Prototype	w24x94	222	28.4	2700	87.7
	Model	w8x10	7.81		30.8	
	Prototype	w24x55	115	22.6	1360	91.9
	Model	w6x8.5	5.08		14.8	
Columns	Prototype	w14x159	254	24.9	1900	72.2
	Model	w5x19	10.2		26.3	
	Prototype	w14x283	459	27.3	3840	71.6
	Model	w6x25	16.8		53.6	

5.3 Analytical Verification of Scaling Factors

In order to verify the scaling factors obtained in the previous section, the seismic analysis of the 2D SMRF prototype and model (Fig. 5-3 and 5-4) was carried out using the SAP 2000 computer program. The seismic excitation considered was the first 3 seconds of the MCEER simulated earthquake in Scenario 1, Event 1, with a 2% probability of exceedance in 50 years. The joint information for the numerical analysis is found in Fig. 5-5.

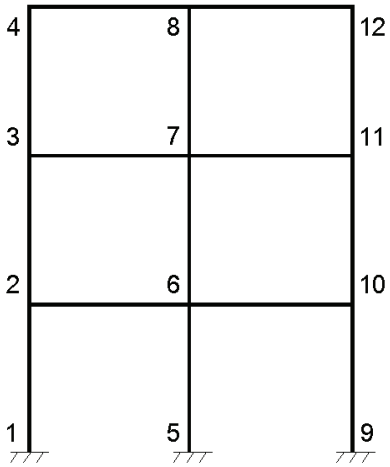

Figure 5-5 Nodal Information of Models in SAP

The displacement and acceleration responses of both the SMRF prototype and model are shown in Table 5-4. The target scaling factors for displacements and accelerations are 3 and 0.768, respectively, to which the corresponding average values calculated in Table 5-4 are approximately equal. There are small differences between the values of acceleration ratios and the target acceleration scaling factor as described in the previous section, when the sections of beams and columns in the scaled model are selected. Due to the available structural steel products, it is impossible to find the exact section with the exact scaling factor for depths and widths as well as elastic modulus and moment inertia. Finally, it leads to the difference between the target scaling factor and the ones calculated with the model implementing actual sections. However, the differences are small such that the scaling procedure can be considered to be in accordance with the simulation principles.

Table 5-4 Verification of Scaling Factors

		Relative Displacement		Scaling Factor		Absolute Acceleration		Scaling Factor
Joint*		Prototype	Model	ratio		Prototype	Model	ratio
		in	in	(S_l=3)		g	g	(Sa=0.768)
1	Max	0.000	0.000	--		0.318	0.413	0.770
1	Min	0.000	0.000	--		-0.252	-0.329	0.768
2	Max	0.548	0.177	3.096		0.352	0.501	0.702
2	Min	-0.515	-0.166	3.102		-0.448	-0.475	0.944
3	Max	1.296	0.416	3.115		0.518	0.648	0.800
3	Min	-1.054	-0.335	3.146		-0.505	-0.619	0.816
4	Max	1.840	0.601	3.062		0.460	0.653	0.704
4	Min	-1.363	-0.447	3.049		-0.612	-0.733	0.835
5	Max	0.000	0.000	--		0.318	0.413	0.770
5	Min	0.000	0.000	--		-0.252	-0.329	0.768
6	Max	0.548	0.177	3.096		0.349	0.500	0.699
6	Min	-0.514	-0.165	3.115		-0.444	-0.469	0.946
7	Max	1.294	0.415	3.118		0.515	0.644	0.799
7	Min	-1.052	-0.334	3.150		-0.501	-0.614	0.816
8	Max	1.837	0.600	3.062		0.457	0.651	0.703
8	Min	-1.361	-0.446	3.052		-0.609	-0.731	0.832
9	Max	0.000	0.000	--		0.318	0.413	0.770
9	Min	0.000	0.000	--		-0.252	-0.329	0.768
10	Max	0.548	0.177	3.096		0.352	0.501	0.702
10	Min	-0.515	-0.166	3.102		-0.448	-0.475	0.944
11	Max	1.296	0.416	3.115		0.518	0.648	0.800
11	Min	-1.054	-0.335	3.146		-0.505	-0.619	0.816
12	Max	1.840	0.601	3.062		0.460	0.653	0.704
12	Min	-1.363	-0.447	3.049		-0.612	-0.733	0.835
Average				3.096				0.792

*see Figure 5-5

5.4 Design of Self-Centering Post-Tensioned (SCPT) Frame Model

To compare the seismic performance of the SMRF and SCS, two models are considered for shake table testing: a conventional Steel Moment-Resisting Frame (SMRF) model as shown in Fig. 5-4 and a Self-Centering Post-Tensioned (SCPT) frame model in which the Post-Tensioned Energy-Dissipating (PTED) connections are implemented in the beam-column connections as discussed in Chapter IV. Those PTED connections are designed according to the procedure proposed in Section 4.4.2

5.4.1 Preliminary Design

Following the procedure of Section 4.4.2, the modal and push-over analyses of the SMRF prototype are conducted using SAP 2000. As a result of those analyses, the fundamental period and yielding strength can be determined as shown in Table 5-5 and Fig. 5-6, respectively. Therefore,

Prototype Natural Period: $T_0 = 0.581$ sec (5-18)

Prototype Effective Weight in 1st mode:

$$W_{effective} = 85.15\% W_{total} = 85.15\% * 200.61 * 3 = 512.46 kips \quad (5\text{-}19)$$

Strength Ratio: $$\eta_{prototype} = \frac{F_Y}{W_{effective}} = \frac{401.94}{512.46} = 0.78 \quad (5\text{-}20)$$

where F_Y is yielding strength of the SMRF prototype as shown in Fig. 5-6.

Table 5-5 Modal Information of SMRF Prototype

Modal Number	Period	Modal Participating Mass Ratios		
	Second	Horizontal Direction	Vertical Direction	Sum (horizontal direction)
1st Mode	0.58089	0.8515	0	85.15%
2nd Mode	0.557528	0	0.7007	85.15%
3rd Mode	0.53076	0	0	85.15%
4th Mode	0.213143	0	0.00002376	85.15%
5th Mode	0.193317	0.1208	0	97.23%

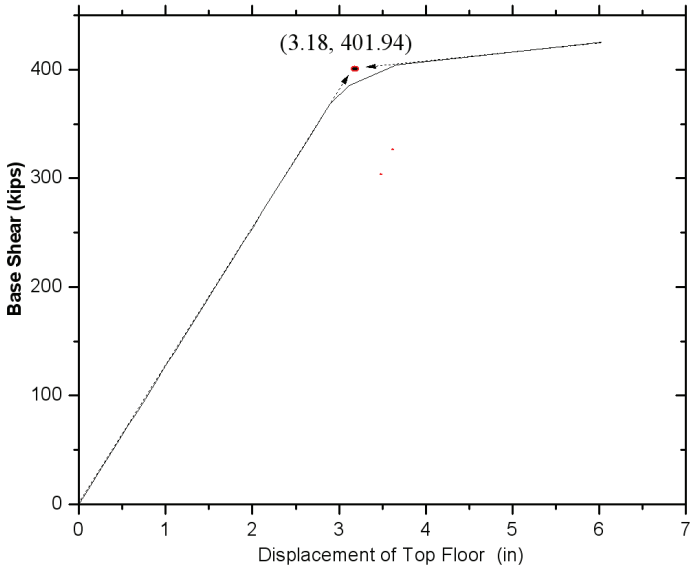

Figure 5-6 Push-Over Analysis of SMRF Prototype

Considering that the prototype building is a hospital, there are more acceleration-sensitive non-structural components than displacement- or velocity-sensitive ones. Therefore, the Relative Performance Index (RPI, see Chapter III) is concentrated on 70% acceleration response and 30% displacement response when the controlling parameters of SCS are selected. As shown in Fig. 5-7, the dash circle represents the desirable RPI. According to the page B13 and B14 in appendix B, Eq. (5-14) and (5-16), the controlling parameters are

determined by interpolation, as seen in table 5-6, because the strength ratio of original SMRF in page B13 and B14 is 0.5 and 1, respectively, while the strength ratio of the SMRF prototype is 0.78.

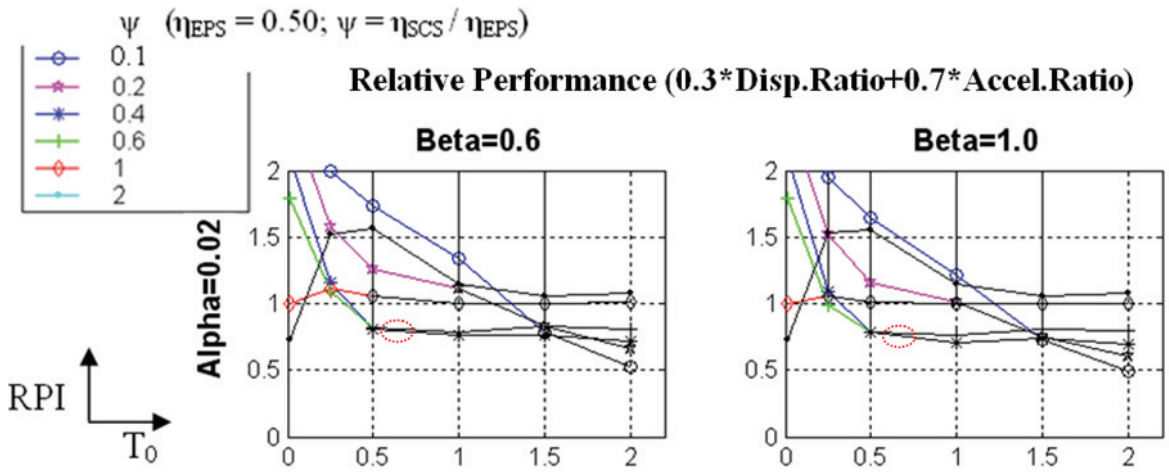

Figure 5-7 Relative Performance Index (RPI, part of page B13 in Appendix B)

Table 5-6 Design Parameters of SCPT Frame

α	β	$\psi = \eta_{SCPT} / \eta_{prototype}$
0.03	0.8	0.5

Based on the selected SCS parameters and the practical design procedure, the preliminary design of the SCPT frame model are presented in Table 5-7, in which the real controlling parameters (α, β and ψ) are calculated based on the selected SCPT parameters (i.e. initial PT force, area of PT strands and ED bars, and thickness of R-plate) in order to be compared with the desirable SCS parameters. The maximum stresses in the R-plates and the beam flanges are also listed whereas the yielding stresses of these two parts are 100 ksi and 50 ksi, respectively, such that the beams remain elastic under seismic loading.

Table 5-7 Preliminary Design of SCPT Frame Model

	1st floor	2nd floor	3rd floor
Beam Section	w8x13	w8x10	w6x8.5
Initial force in PT bars (kips)	37.06	29.9	27.48
Area of PT strands (in^2)	0.57	0.42	0.24
Area of ED (2_EDbar) (in^2)	0.15	0.12	0.11
Thickness of R plate (in)	0.268	0.205	0.126
α	0.051	0.046	0.026
β	0.798	0.799	0.799
$\psi = \eta_{SCPT}/ \eta_{prototype}$	0.5	0.502	0.502
Max Stress of R plate (ksi)	81.26	75.07	72.82
Max Stress of Flange (ksi)	48.8	48.81	49.58

5.4.2 Final Design

The intermediate design is neglected since the beams of the two spans at the same level in the SCPT model are identical. In the final design, according to the results of the preliminary design and the products supplied by DYWIDAG Systems International (DSI), the real sections of Post-Tensioned (PT) strands and Energy-Dissipating (ED) bars are selected based on the procedure proposed in Section 4.4.2.3. The final design results are shown in Table 5-8. The cross sectional area of 0.6 and 0.5 inch PT strands are 0.217 and 0.153 in^2, respectively. The yield and ultimate stress of PT strands are 243 and 270 ksi, respectively. The original

diameter of #6 ED bars used in this model is 0.86 in while it was machined to 5/16 and 9/32 inch for the 1st and 2nd/3rd floors as shown in Table 5-8 and the yield stress of ED bars is 75 ksi. The steel of Reinforcing Plate (R-Plate) implemented in this model is ASTM A514 with a 100 ksi yield stress. The controlling parameters (α, β and ψ), as calculated from the selected PT strands and ED bars, are slightly different than the desirable ones, which does not lead to much influence on the relative performance of SCPT frame model as compared to the SMRF model. The maximum stress in the beam flanges is reduced slightly such that the beam stresses remain much lower than those in the preliminary design, in which they are close to the yielding stress.

Table 5-8 Final Design of SCPT Frame Model

	1st floor	2nd floor	3rd floor
Beam Section	w8x13	w8x10	w6x8.5
Initial force in PT bars (kips)	37	30	27
Area of PT strands (in^2)	2@0.6in. (0.434)	2@0.6in. (0.434)	2@0.5in. (0.306)
Area of ED (2_EDbar) (in^2)	#6 2ǿ5/16 in. (0.153 in^2)	#6 2ǿ9/32 in. (0.124 in^2)	#6 2ǿ9/32 in. (0.124 in^2)
Thickness of R plate (in)	5/16	1/4	3/16
α	0.047	0.053	0.034
β	0.820	0.829	0.877
$\psi = \eta_{SCPT}/\eta_{SMRF}$	0.48	0.48	0.51
Max Stress of R plate (ksi)	78.59	77.13	75.66
Max Stress of Flange (ksi)	41.24	46.08	43.30

CHAPTER 6
EXPERIMENTAL PROCEDURES

To experimentally investigate the seismic performance of the Steel Moment Resisting Frame (SMRF) and Self-Centering Post-Tensioned (SCPT) frame designed in Chapter V, a shake table testing program was conducted. This chapter describes the experimental procedures used in this testing program.

First, the scope of the testing program is discussed in terms of the two models, the floor mass simulator and the shake table used in the tests. Thereafter, based on the numerical predictions of the seismic performance of the designed SCPT frame, the ground motion used in the shake table tests is selected. Finally, the test protocol and instrumentations are presented.

6.1 Scope of Testing

To compare the seismic performance of the SMRF and SCPT frame, two different frame models were used in the shake table testing program. An existing floor mass simulator was implemented to provide the scaled mass added to the frame models. This floor mass simulator supported only the gravity loading used to simulate the mass of the models but did not contribute any lateral stiffness or strength to the test specimen. Also, the characteristics of the shake table system are detailed.

6.1.1 Description of Frame Models

Two frame models (SMRF and SCPT frame) were considered in the shake table testing program. These frame models were designed in Chapter V. More details on these two models are presented in this section.

6.1.1.1 Steel Moment Resisting Frame (SMRF) Model

As shown in Fig. 6-1 and Table 6-1, the SMRF model is a 2-bay, 3-story frame, made of ASTM A572 Grade 50 steel. The prototype of the SMRF model is a hospital building constructed in the 1970s incorporating fully welded beam-to-column connections (beam flanges and webs welded to the column flanges). Similar welded connections were used in the SMRF model in order to simulate the similar performance of the prototype building. The

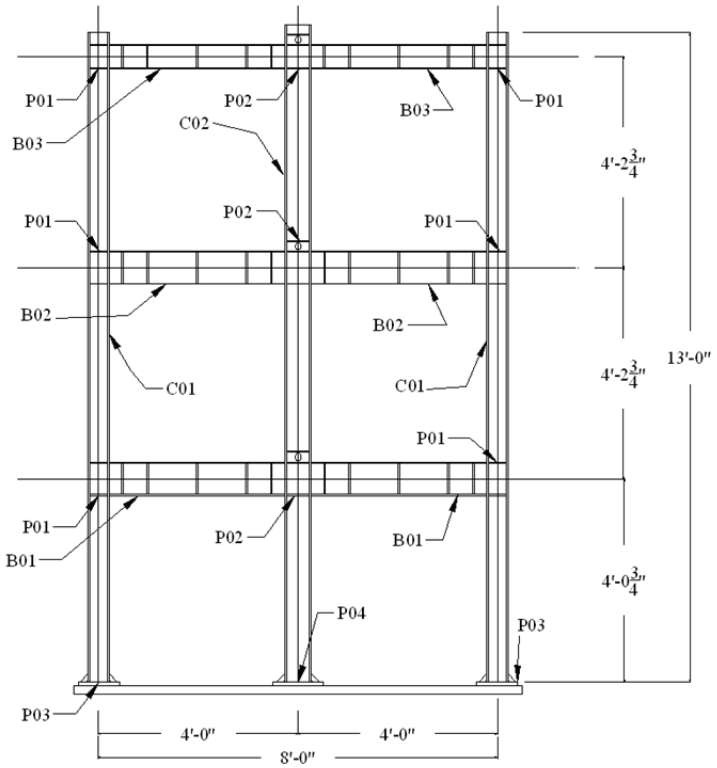

Figure 6-1 SMRF model

Table 6-1 Part Description for SMRF model

Part Code	Part Description	QTY
C01	Exterior Column, 13-ft length W5x16	2
C02	Interior Column, 13-ft 2-in length W6x25	1
B01	Beam in 1st floor, 3ft 6 1/4 in W8x13	2
B02	Beam in 2nd floor, 3ft 6 1/4 in W8x10	2
B03	Beam in 3rd floor, 3ft 6 1/4 in W6x8.5	2
P01	3/8 in thick Continuity Plate 4 9/32 x 2 3/8 in	24
P02	3/8 in thick Continuity Plate 5 15/32 x 2 7/8 in	12
P03	1 in thick Exterior Base Plate 12 x 9 3/4	2
P04	1 in thick Interior Base Plate 12 x 12	1

two exterior columns (i.e. part code C01 in Table 6-1) were designed as w5x19 in Chapter V. However, a w5x16 section was used in the model since the w5x19 was not available from local manufacturers. Although the w5x16 section is slightly lighter than the w5x19 section, both the moment of inertia and the elastic section modulus are similar, which did not affect significantly the fundamental period and yielding strength of the model. As shown in Fig 6-2, the base columns were welded to stiffened base plates. These steel base plates were then bolted on the shake table. Therefore, a fixed-base connection was assumed for the model.

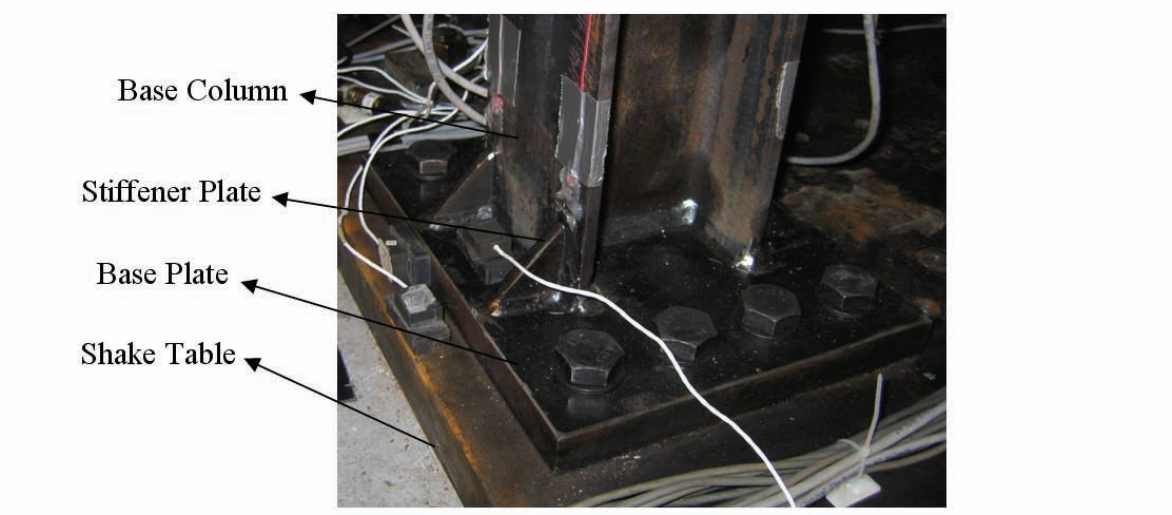

Figure 6-2 Base Column Connection of SMRF Model

As seen in Fig. 6-3, continuity plates were welded to the columns to reinforce the panel zone and stiffener plates were welded to the beams to prevent local buckling in accordance with the requirements of the Load & Resistance Factor Design (LRFD 3rd edition, 2001). All the construction drawings for the SMRF model are included in Appendix C.

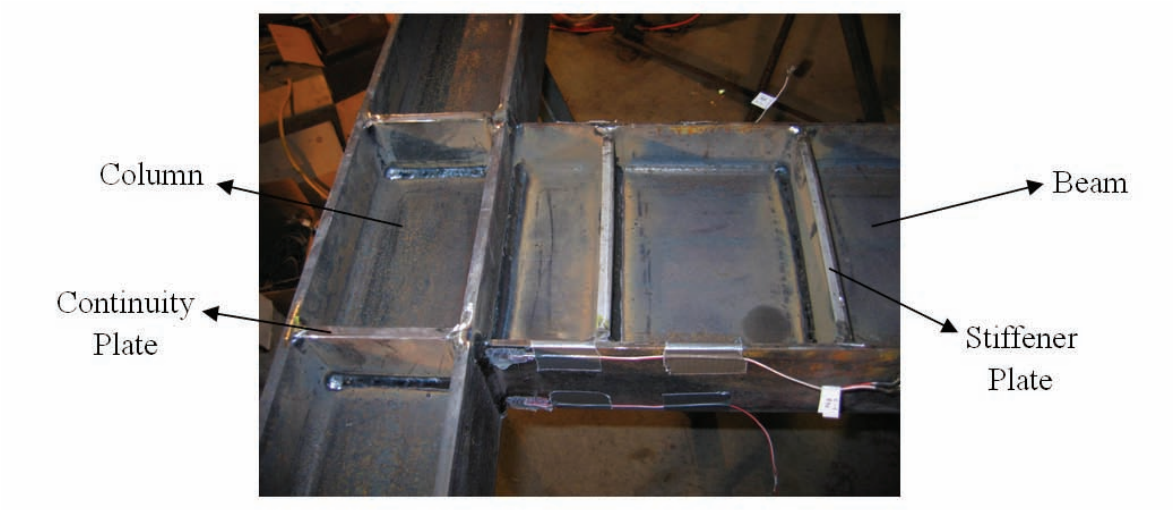

Figure 6-3 Beam-Column Connection in SMRF Mode

6.1.1.2 Self-Centering Post-Tensioned (SCPT) Frame Model

A photograph of the SCPT frame model is shown in Fig. 6-4. This model incorporated the same beam and column sections as those used in the SMRF model. However, no welding is introduced between the beams and columns. Instead, Post-Tensioned (PT) strands were installed along the beam to provide a "clamping" force for the beam-column connections. The PT strands also provided a re-centering capability to the structural system under earthquakes. As shown in Fig. 6-5, two PT strands were used for each level along with Energy Dissipating (ED) bars. Four ED bars were welded to each beam-column connection. Each ED bar is connected to a threaded mechanic connector (i.e. coupler), which is welded to the beam flange and continuity plate in the adjacent column. The ED bars were designed to yield in tension and compression in order to absorb energy during seismic shaking.

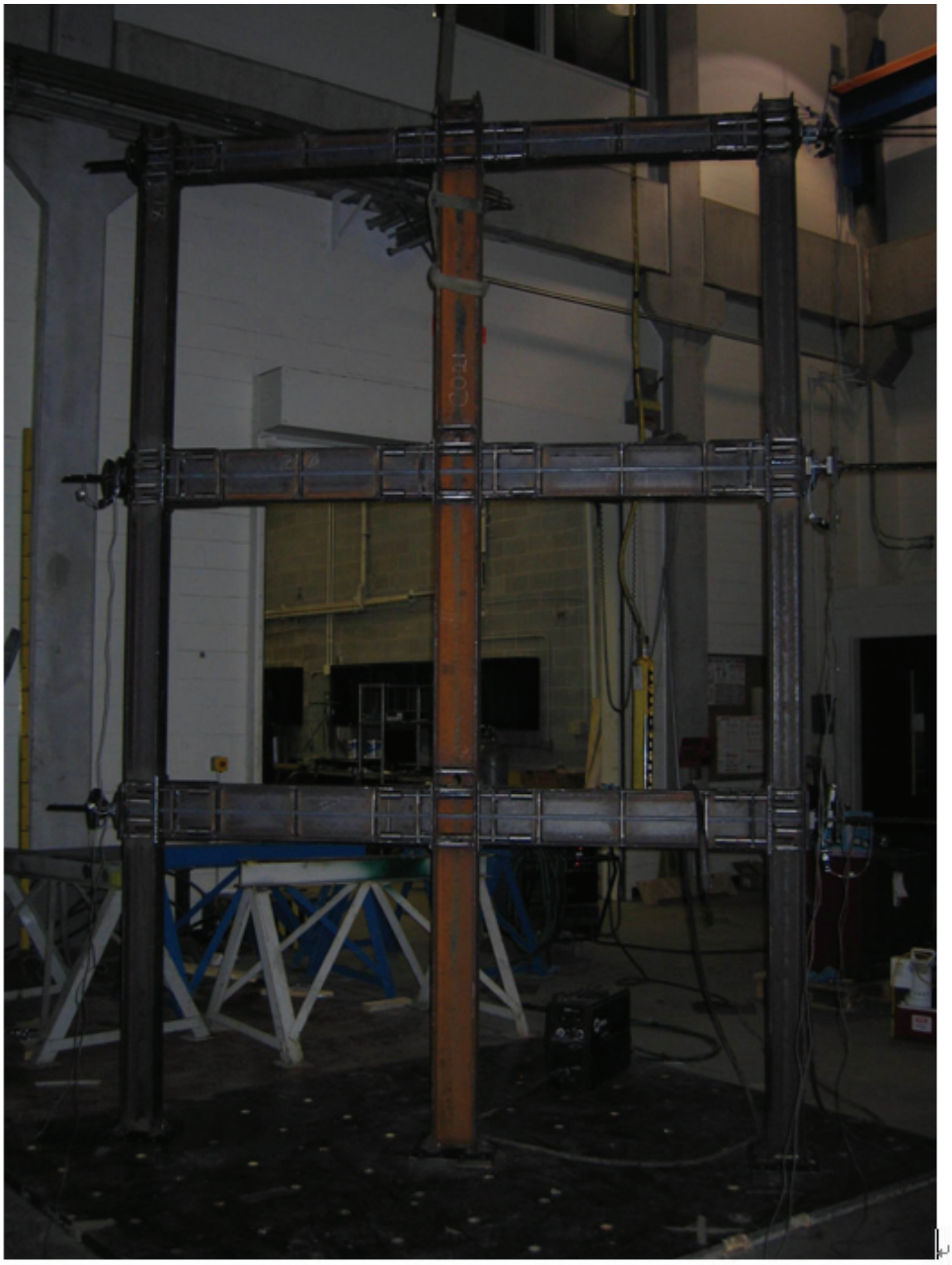

Figure 6-4 SCPT Frame Model

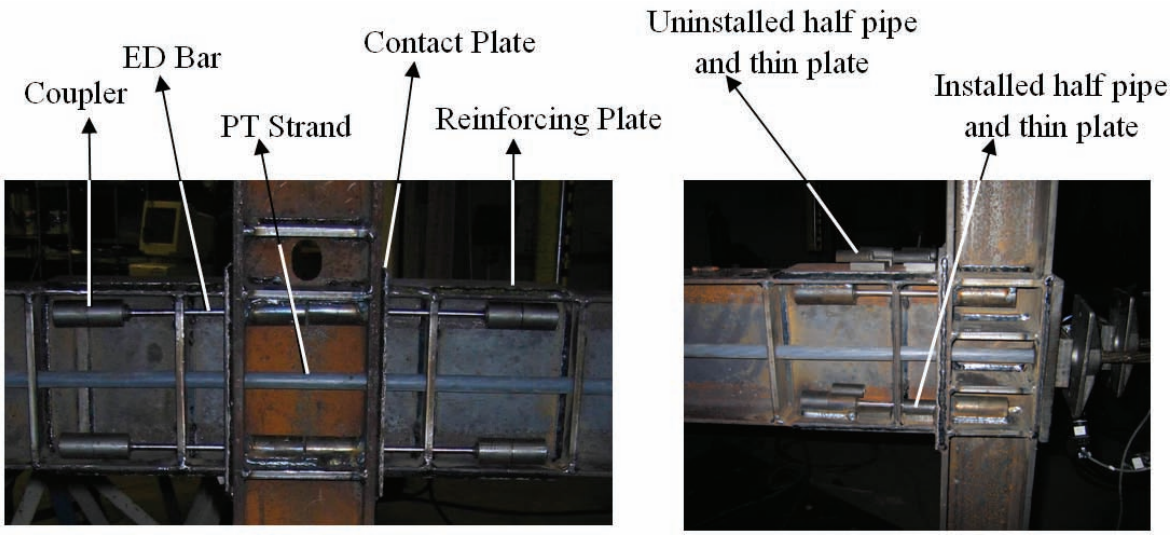

(a) (b)

Figure 6-5 Beam-Column Connections in the SCPT Frame1 Model
(a) Central Connection in the 1st level (b) Right Exterior Connection in the 1st level

To prevent buckling in compression of the ED bars, thin plates and half pipes (see DWG ED103 in Appendix D) were welded to the beam flanges surrounding the ED bars as shown in Fig. 6-5(b). The PT strands, ED bars and couplers were donated by the DYWIDAG-System International (DSI). To prevent the beam from yielding, reinforcing plates, made of ASTM A514 steel with a 100ksi yielding strength, were welded to the beam flanges. Due to the large expected compressive stress in the beam-column connections when a gap opened, contact plates (also made of ASTM A514) were welded to the column flanges to avoid local yielding. The holes in the central column, as seen in Fig. 6-5 (a), are used to connect the two mass floors. The order of assembling the SCPT frame model is to prestress the PT strands at first and then to weld the ED bars. All the construction drawings for the SCPT frame model are included in Appendix D.

6.1.2 Floor Mass Simulator

The Floor Mass Simulator (FMS) was designed in an earlier research (Kusumastuti 2005) and has been utilized for several seismic projects in SEESL. As shown in Fig. 6-6 (a), the main purpose of the FMS is to simulate the floor mass of the prototype structure. The FMS is composed of two adjacent frames supporting six steel plates, each weighting about 8.5 kips. As seen in Fig. 6-6 (b) and (c), due to the rocking support design, the FMS performs as a pin-based structure in the shaking direction providing no lateral stiffness. The bracing

(a)

(b)

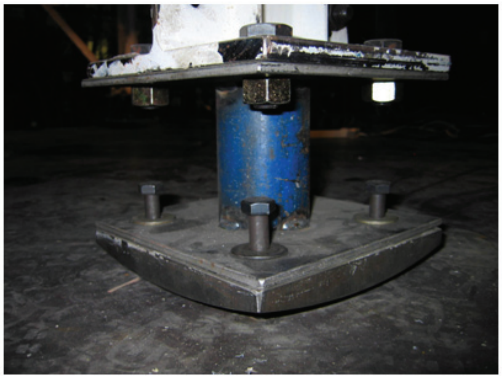

(c)

Figure 6-6 Floor Mass Simulator (a) FMS installed with SCPT Frame Model (b) Rocking Support at the top of the column (c) Rocking Support at the base of the column

system resists the deformations in the transverse direction. Each frame model (SMRF and SCPT frame) was installed between two frames of the FMS and was connected to the FMS by circular steel bars through the central column at each level, as shown in Fig. 6-7 (a). Connecting the frame model only through its central column allows the axial deformation of the beams of the frame model. Axial elongation of the beams must not be prevented for the SCPT frame in order for the gap openings to occur freely. Through the connections shown in Fig. 6-7 (b), the FMS prevents the out-of-plane deformations of the frame model and the torsion deformations of its beams.

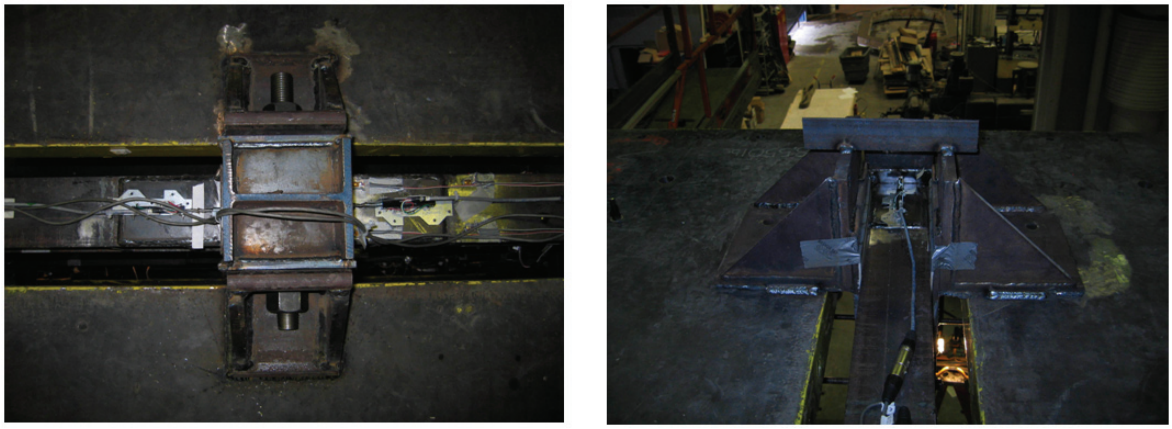

(a) (b)

Figure 6-7 Connections between FMS and Frame Model
(a) Connection of the floor mass (b) Transverse support

6.1.3 Shaking Table System

The shaking table system used in this experimental investigation is a 5-degree-of-freedom system located in the Structural Engineering and Earthquake Simulation Laboratory (SEESL) at University at Buffalo, as shown in Fig. 6-8. The 12 ft. by 12 ft. shaking table is usually covered by a reinforced concrete testing platform with plan dimensions of 10ft. by 20ft.,

which extends its testing area. The payload of the shaking table is 110 kips without the concrete platform and 85 kips with it. In this experimental study, only the longitudinal (horizontal) movement of the shake table was utilized. The shake table limitations for displacement, velocity and acceleration in this direction are ±6 in., 30 in./sec and 1.15g, respectively, at a payload of 44 kips.

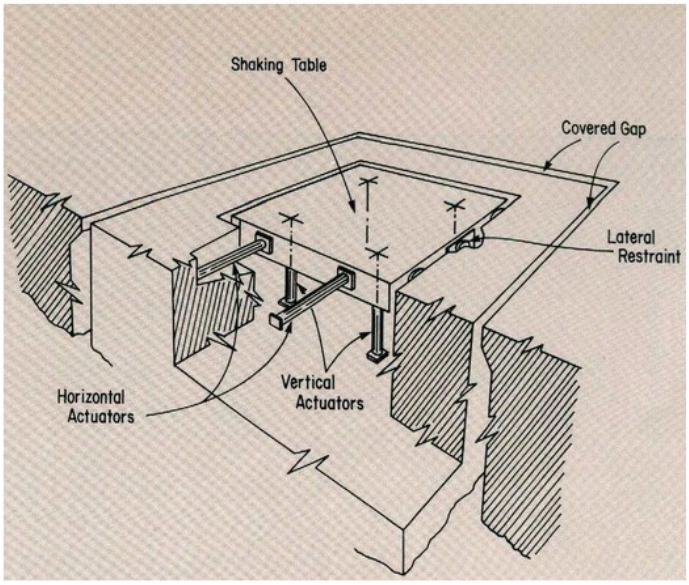

Figure 6-8 Perspective View of Shaking Table and Foundation
(From http://Nees.Buffalo.edu)

6.2 Selection of Ground Motions

Since the prototype structure was designed for a life safety performance in Chapter V, the ground motion used in the shaking table testing was selected among an ensemble of 25 synthetic MCEER earthquake records with a 10% probability of exceedance in 50 years (see the Section 3.2.1). A numerical seismic analysis was conducted to evaluate the seismic

performance of the SCPT frame model under this ensemble of scaled 25 records in order to select the ground motion to be used in the testing program within the limitations of the shake table. For this purpose, the maximum inter-story drift, maximum displacement of the top floor and maximum acceleration in each floor for each of these input motion were calculated and are shown in Figs. 6-9 to 6-15. In these figures, the Earthquake No. Label represents each of the 25 earthquake records. The values between mean plus one positive and one negative standard deviation (top and bottom horizontal lines in Figs. 6-9 to 6-15) are considered to be statistically representative responses and thus, these earthquake records causing those responses are candidates as the excitation for the seismic testing. Considering the displacements and accelerations limitations of the shaking table, the Earthquake No. 7 (Event 7 of Scenario 1) was selected as the input ground motion for the seismic tests. According to the scaling factors in Table 5-2 in Chapter V, the amplitude of this selected ground motion is divided by 0.768 and its duration is divided by 1.976.

Note (for Figs. 6-9 to 6-15): The three horizontal lines in each figure represents the standard deviations and mean of the bar values. The horizontal axis in regard to Earthquake No. means the different earthquake records: No. 1 to 12 for the Event 1 to 12 of Scenario 1; No. 13 to 20 for the Event 1 to 8 of Scenario 2; No. 21 to 23 for the Event 1 to 3 of Scenario 3; No. 24 to 25 for the Event 1 to 2 of Scenario 4 in the ensemble of 25 synthetic MCEER earthquake records with 10% probability of exceedance in 50 years.

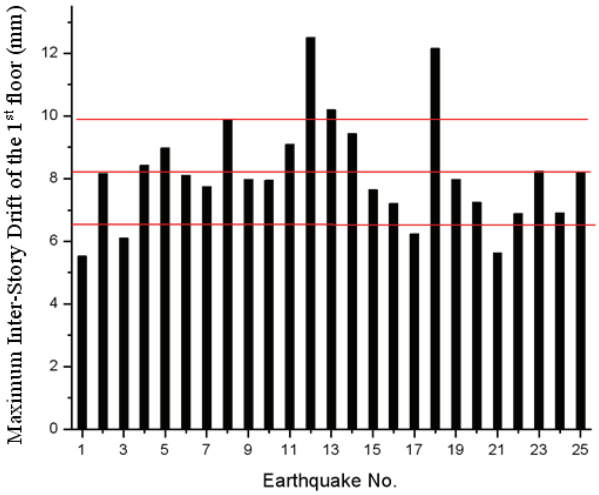

Figure 6-9 Maximum Inter-story Drift in the 1st level

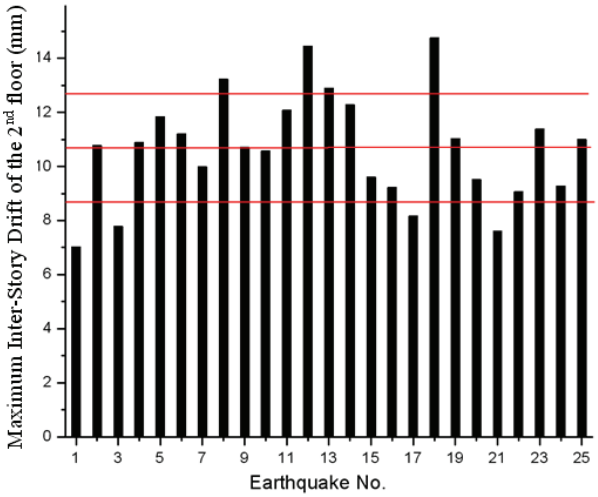

Figure 6-10 Maximum Inter-story Drift in the 2nd level

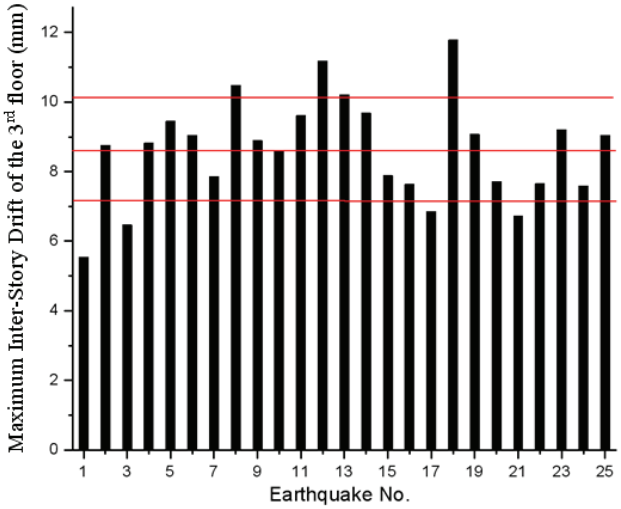

Figure 6-11 Maximum Inter-story Drift in the 3rd level

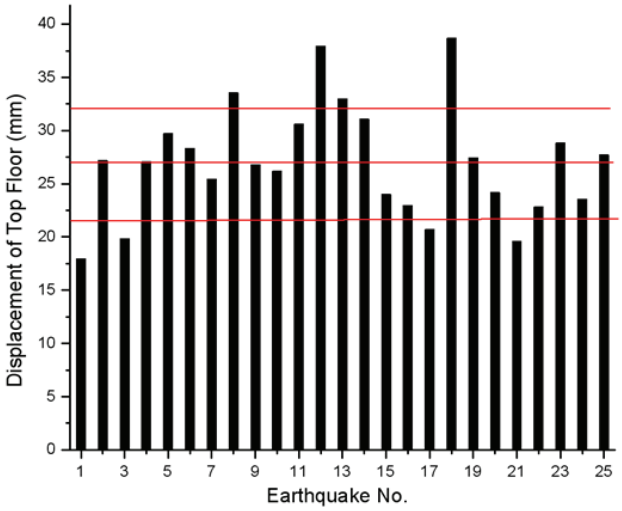

Figure 6-12 Maximum Displacement of Top Floor

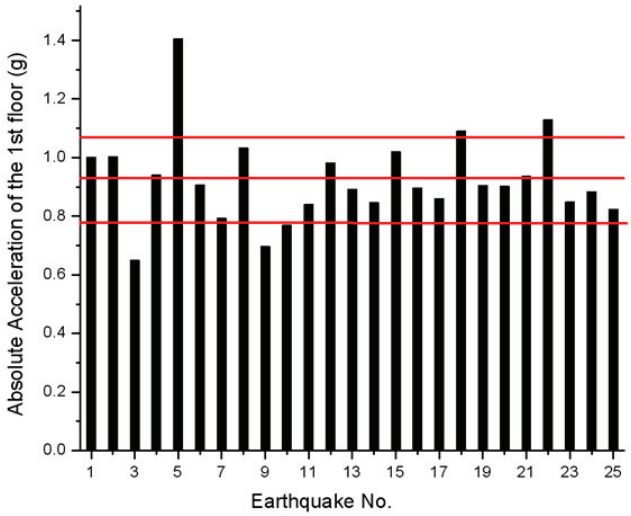

Figure 6-13 Maximum Acceleration in the 1st level

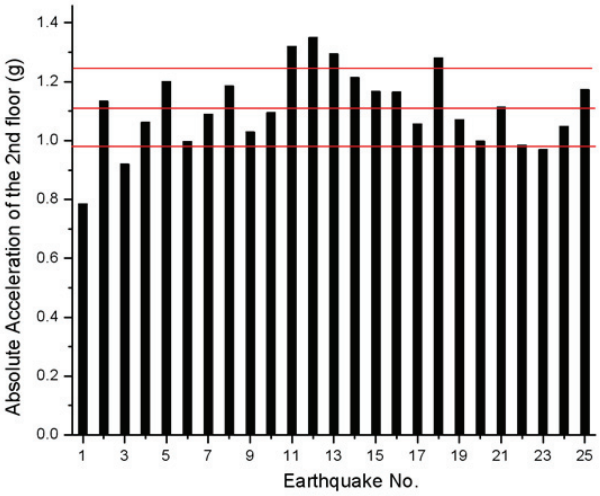

Figure 6-14 Maximum Acceleration in the 2nd level

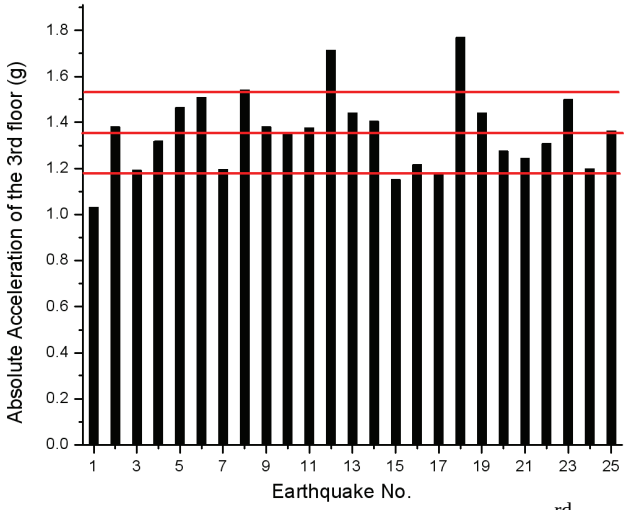

Figure 6-15 Maximum Acceleration in the 3rd level

As shown in Fig. 6-16, the Peak Ground Acceleration (PGA) of the selected ground motion is 0.68g, which is below the acceleration limit of 1.15g of the shake table. Therefore, the maximum possible amplitude of the acceleration input is 150%.

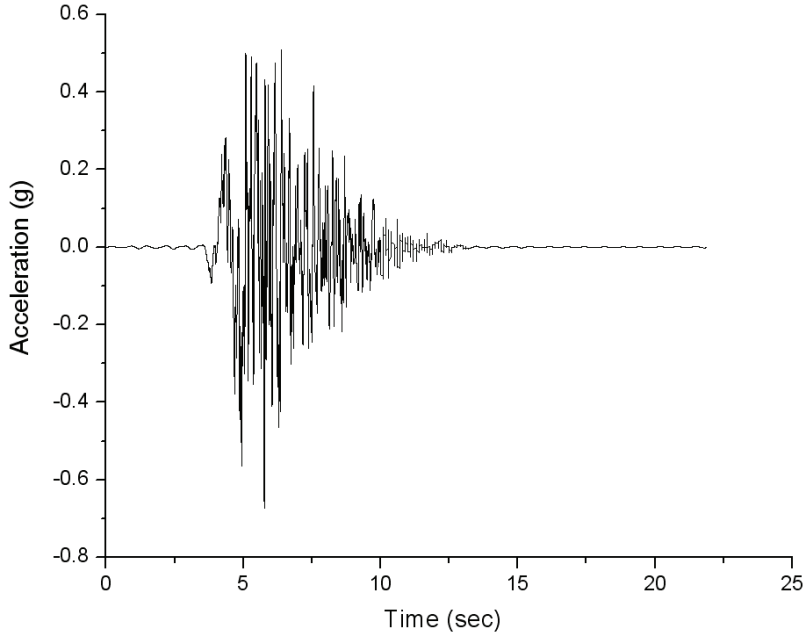

Figure 6-16 Selected Ground Motion

(Scaled MCEER ground motion for event 7 of Scenario 1 with 10% probability of exceedance in 50 years)

6.3 Test Protocols

Two series of shake table tests were conducted for both the Steel Moment Resisting Frame (SMRF) and Self-Centering Post-Tensioned (SCPT) frame model. In the first series, the selected ground motion shown in Fig. 6-16 was used. In the second series, the direction of the ground motion was reversed (polarity). These two series were conducted in order to observe maximum gap opening under positive and negative moments at each beam-column joint of the SCPT frame. Different amplitudes of the selected ground motion were used during the tests. The amplitude of the input excitation was expressed as a percentage of the full-scale record shown in Fig. 6-15 and varied from 25% to 150%. Low level white noise tests were also conducted after each seismic test and used to monitor the changes in dynamic

characteristic of the test frames such as their natural frequencies and mode shapes. This white noise excitation has 0.05g amplitude and a wide frequency band (0.5 - 50Hz). Pull-Back tests were also conducted to double check the system information.

The test protocols for both the SCPT and SMRF models are shown in Table 6-2 and 6-3, respectively. Due to some malfunction of the test equipment such as the failure of the video capture and miscalibration of the instrumentation, some tests were repeated. Some beams of the SCPT frame model slid down vertically along the face of the columns in the large amplitude seismic tests during gap openings, which was not expected. Therefore, small round bars were welded to the columns under the beam flanges to provide a vertical support and then the tests were repeated (Tests no. 42 to 78 in Table 6-2). To better limit the vertical movement of the beams, round bars were also installed on the top of the beams and the same tests were repeated again (Tests no. 79 to 108 in Table 6-2). Therefore, tests of No. 1 to 41 are named as the 1st test phase, No. 42 to 78 as the 2nd phase and No. 79 to 108 as the 3rd phase in the SCPT model. Theoretically, the friction between the beams and columns in the SCPT frame model should have been sufficient to resist the shear and prevent the vertical movement. However, it is believed that due to the fact that the ends of the beams were not manufactured perfectly flat, and then grinded, the friction coefficient was lower and the area of contact surface was reduced. Therefore, in the large amplitude seismic tests (e.g. 150% amplitude), the beams moved vertically. Presumably, this movement could have been prevented by sand blasting the contact surfaces between the beams and columns. The notes included in Table 6-2 and 6-3 are predictions from the numerical results, where the term

"elastic range" means the beams and columns remain elastic and the term "gap" refers to the possible gap between beams and columns in the SCPT model.

Table 6-2 Test Protocol for the SCPT Frame Model

Test No.	Test Label	Excitation	Direction	PGA		Note
				g	%	
1	PWN1	White Noise	N/A	0.05	N/A	System Identification
2	PWN1A	White Noise	N/A	0.05	N/A	System Identification
3	PE1	S1E7*	Positive	0.17	25	Elastic Range
4	PWN2	White Noise	N/A	0.05	N/A	System Identification
5	PWN1B	White Noise	N/A	0.10	N/A	System Identification
6	PWN1C	White Noise	N/A	0.15	N/A	System Identification
7	PE1A	S1E7	Positive	0.17	25	Elastic Range
8	PWN1D	White Noise	N/A	0.05	N/A	System Identification
9	PE1B	S1E7	Positive	0.17	25	Elastic Range
10	PD1	Sinusoidal Wave	N/A	N/A	N/A	System Identification
11	PWN2A	White Noise	N/A	0.05	N/A	System Identification
12	PE2	S1E7	Positive	0.34	50	Elastic Range
13	PWN3	White Noise	N/A	0.05	N/A	System Identification
14	PE3	S1E7	Positive	0.48	70	Gap begins opening
15	PWN4	White Noise	N/A	0.05	N/A	System Identification
16	PER1	S1E7	Negative	0.17	25	Elastic Range

Table 6-2 Test Protocol for the SCPT Frame Model (continued)

Test No.	Test Label	Excitation	Direction	PGA		Note
				g	%	
17	PER2	S1E7	Negative	0.34	50	Elastic Range
18	PER3	S1E7	Negative	0.48	70	Gap begins opening
19	PWN4A	White Noise	N/A	0.05	N/A	System Identification
20	PE4	S1E7	Positive	0.58	85	Most Gaps Opening
21	PWN5	White Noise	N/A	0.05	N/A	System Identification
22	PER4	S1E7	Negative	0.58	85	Most Gaps Opening
23	PWN5A	White Noise	N/A	0.05	N/A	System Identification
24	PE5	S1E7	Positive	0.68	100	Most Gaps Opening
25	PWN6	White Noise	N/A	0.05	N/A	System Identification
26	PE5A	S1E7	Positive	0.68	100	Most Gaps Opening
27	PWN6A	White Noise	N/A	0.05	N/A	System Identification
28	PER5	S1E7	Negative	0.68	100	Most Gaps Opening
29	PWN6B	White Noise	N/A	0.05	N/A	System Identification
30	PE6	S1E7	Positive	0.85	125	Most Gaps Opening
31	PWN7	White Noise	N/A	0.05	N/A	System Identification
32	PWN7A	White Noise	N/A	0.05	N/A	System Identification
33	PE6A	S1E7	Positive	0.85	125	Most Gaps Opening
34	PWN7B	White Noise	N/A	0.05	N/A	System Identification
35	PER6	S1E7	Negative	0.85	125	Most Gaps Opening

Table 6-2 Test Protocol for the SCPT Frame Model (continued)

Test No.	Test Label	Excitation	Direction	PGA		Note
				g	%	
36	PWN7C	White Noise	N/A	0.05	N/A	System Identification
37	PE7	S1E7	Positive	1.02	150	Most Gaps Opening
38	PE7A	S1E7	Positive	1.02	150	Most Gaps Opening
39	PWN8	White Noise	N/A	0.05	N/A	System Identification
40	PER7	S1E7	Negative	1.02	150	Most Gaps Opening
41	PWN8A	White Noise	N/A	0.05	N/A	System Identification
Round bars were installed under the beam flanges after Test no. 41.						
42	PWN9	White Noise	N/A	0.05	N/A	System Identification
43	PE8	S1E7	Positive	0.17	25	Elastic Range
44	PWN10	White Noise	N/A	0.05	N/A	System Identification
45	PER8	S1E7	Negative	0.17	25	Elastic Range
46	PWN11	White Noise	N/A	0.05	N/A	System Identification
47	PE9	S1E7	Positive	0.34	50	Elastic Range
48	PWN12	White Noise	N/A	0.05	N/A	System Identification
49	PER9	S1E7	Negative	0.34	50	Elastic Range
50	PWN13	White Noise	N/A	0.05	N/A	System Identification
51	PE10	S1E7	Positive	0.48	70	Gap begins opening
52	PWN14	White Noise	N/A	0.05	N/A	System Identification
53	PER10	S1E7	Negative	0.48	70	Gap begins opening

Table 6-2 Test Protocol for the SCPT Frame Model (continued)

Test No.	Test Label	Excitation	Direction	PGA		Note
				g	%	
54	PWN15	White Noise	N/A	0.05	N/A	System Identification
55	PE11	S1E7	Positive	0.58	85	Most Gaps Opening
56	PWN16	White Noise	N/A	0.05	N/A	System Identification
57	PER11	S1E7	Negative	0.58	85	Most Gaps Opening
58	PWN17	White Noise	N/A	0.05	N/A	System Identification
59	PE12	S1E7	Positive	0.68	100	Most Gaps Opening
60	PWN18	White Noise	N/A	0.05	N/A	System Identification
61	PER12	S1E7	Negative	0.68	100	Most Gaps Opening
62	PWN19	White Noise	N/A	0.05	N/A	System Identification
63	PE13	S1E7	Positive	0.85	125	Most Gaps Opening
64	PE13A	S1E7	Positive	0.85	125	Most Gaps Opening
65	PWN20	White Noise	N/A	0.05	N/A	System Identification
66	PER13	S1E7	Negative	0.85	125	Most Gaps Opening
67	PWN21	White Noise	N/A	0.05	N/A	System Identification
68	PE14	S1E7	Positive	1.02	150	Most Gaps Opening
69	PE15	S1E7	Positive	0.85	125	Most Gaps Opening
70	PWN22	White Noise	N/A	0.05	N/A	System Identification
71	PER15	S1E7	Negative	0.85	125	Most Gaps Opening
72	PWN23	White Noise	N/A	0.05	N/A	System Identification
73	PE16	S1E7	Positive	1.02	150	Most Gaps Opening

Table 6-2 Test Protocol for the SCPT Frame Model (continued)

Test No.	Test Label	Excitation	Direction	PGA		Note
				g	%	
74	PWN24	White Noise	N/A	0.05	N/A	System Identification
75	PE16A	S1E7	Positive	1.02	150	Most Gaps Opening
76	PWN25	White Noise	N/A	0.05	N/A	System Identification
77	PER16	S1E7	Negative	1.02	150	Most Gaps Opening
78	PWN26	White Noise	N/A	0.05	N/A	System Identification
Round bars were welded on the top of the beam flanges after Test no. 78.						
79	PWN27	White Noise	N/A	0.05	N/A	System Identification
80	PWN28	White Noise	N/A	0.05	N/A	System Identification
81	PE17	S1E7	Positive	0.17	25	Elastic Range
82	PWN29	White Noise	N/A	0.05	N/A	System Identification
83	PER17	S1E7	Negative	0.17	25	Elastic Range
84	PWN30	White Noise	N/A	0.05	N/A	System Identification
85	PE18	S1E7	Positive	0.34	50	Elastic Range
86	PWN31	White Noise	N/A	0.05	N/A	System Identification
87	PER18	S1E7	Negative	0.34	50	Elastic Range
88	PWN32	White Noise	N/A	0.05	N/A	System Identification
89	PE19	S1E7	Positive	0.48	70	Gap begins opening
90	PWN33	White Noise	N/A	0.05	N/A	System Identification
91	PER19	S1E7	Negative	0.48	70	Gap begins opening

Table 6-2 Test Protocol for the SCPT Frame Model (continued)

Test No.	Test Label	Excitation	Direction	PGA		Note
				g	%	
92	PWN34	White Noise	N/A	0.05	N/A	System Identification
93	PE20	S1E7	Positive	0.58	85	Most Gaps Opening
94	PWN35	White Noise	N/A	0.05	N/A	System Identification
95	PER20	S1E7	Negative	0.58	85	Most Gaps Opening
96	PWN36	White Noise	N/A	0.05	N/A	System Identification
97	PE21	S1E7	Positive	0.68	100	Most Gaps Opening
98	PWN37	White Noise	N/A	0.05	N/A	System Identification
99	PER21	S1E7	Negative	0.68	100	Most Gaps Opening
100	PWN38	White Noise	N/A	0.05	N/A	System Identification
101	PE22	S1E7	Positive	0.85	125	Most Gaps Opening
102	PWN39	White Noise	N/A	0.05	N/A	System Identification
103	PER22	S1E7	Negative	0.85	125	Most Gaps Opening
104	PWN40	White Noise	N/A	0.05	N/A	System Identification
105	PE23	S1E7	Positive	1.02	150	Most Gaps Opening
106	PWN41	White Noise	N/A	0.05	N/A	System Identification
107	PER23	S1E7	Negative	1.02	150	Most Gaps Opening
108	PWN42	White Noise	N/A	0.05	N/A	System Identification

* S1E7is the scaled MCEER simulated ground motion for event 7 at scenario 1 with 10% probability in 50 years

Note: 1st phase: Test No. 1-41; 2nd phase: Test No. 42-78; 3rd phase: Test No. 79-108

Table 6-3 Test Protocol for SMRF Model

Test No.	Test Label	Excitation	Direction	PGA		Note
				(g)	%	
1	MWN01	White Noise	N/A	0.05	N/A	System Identification
2	ME01	S1E7	Positive	0.17	25	Elastic Range
3	MWN02	White Noise	N/A	0.05	N/A	System Identification
4	MER01	S1E7	Negative	0.17	25	Elastic Range
5	MWN03	White Noise	N/A	0.05	N/A	System Identification
6	ME02	S1E7	Positive	0.34	50	Elastic Range
7	MWN04	White Noise	N/A	0.05	N/A	System Identification
8	MER02	S1E7	Negative	0.34	50	Elastic Range
9	MWN05	White Noise	N/A	0.05	N/A	System Identification
10	MER02A	S1E7	Negative	0.34	50	Elastic Range
11	MWN05A	White Noise	N/A	0.05	N/A	System Identification
12	ME02A	S1E7	Positive	0.34	50	Elastic Range
13	MWN05B	White Noise	N/A	0.05	N/A	System Identification
14	ME03	S1E7	Positive	0.48	70	Elastic Range
15	MWN06	White Noise	N/A	0.05	N/A	System Identification
16	MER03	S1E7	Negative	0.48	70	Elastic Range
17	MWN07	White Noise	N/A	0.05	N/A	System Identification
18	ME04	S1E7	Positive	0.58	85	Elastic Range
19	MWN08	White Noise	N/A	0.05	N/A	System Identification

Table 6-3 Test Protocol for SMRF Model (continued)

Test No.	Test Label	Excitation	Direction	PGA		Note
				(g)	%	
20	MER04	S1E7	Negative	0.58	85	Elastic Range
21	MWN09	White Noise	N/A	0.05	N/A	System Identification
22	ME05	S1E7	Positive	0.68	100	Elastic Range
23	MWN10	White Noise	N/A	0.05	N/A	System Identification
24	MER05	S1E7	Negative	0.68	100	Elastic Range
25	MWN11	White Noise	N/A	0.05	N/A	System Identification
26	ME06	S1E7	Positive	0.85	125	Beams Yielding
27	ME06A	S1E7	Positive	0.85	125	Beams Yielding
28	MWN12	White Noise	N/A	0.05	N/A	System Identification
29	MER06	S1E7	Negative	0.85	125	Beams Yielding
30	MWN13	White Noise	N/A	0.05	N/A	System Identification
31	ME07	S1E7	Positive	1.02	150	Beams Yielding
32	MWN14	White Noise	N/A	0.05	N/A	System Identification
33	MER07	S1E7	Negative	1.02	150	Beams Yielding
34	MWN15	White Noise	N/A	0.05	N/A	System Identification

6.4 Instrumentation

6.4.1 Instrumentation for the Self-Centering Post-Tensioned (SCPT) Frame Model

As shown in Table 6-4, a total of 126 channels of data acquisition were used to measure the global and local responses of the SCPT frame model during the shake table testing. The accelerometers were installed at each floor and base plate to measure the horizontal and vertical acceleration responses. The displacement responses at each level were captured by string potentiometers and temposonic transducers. The potentiometers were attached to the top and bottom of the beam flanges to measure the gap opening in the beam-column connections of the SCPT frame. Load cells were installed at the end of the post-tensioned strands in order to measure the changes in prestress forces. Since both models are symmetric, the strain gages were attached to the beams and columns in only one span to measure the local response of the beams and columns. As shown in Fig. 6-17, the load cells were fabricated by drilling round steel bars and installing strain gages to form a four-element Wheatstone bridge circuit. The position of all the instrumentations used on the SCPT frame model is shown in Fig. 6-18.

Figure 6-17 Load Cell

Table 6-4 Instrumentation List for SCPT Frame Model

Tag Name	Channel No.	Sensor Type	Position & Function
AC0-1	1	Accelerometer	Base Plate, Acceleration
AC1-1	2	Accelerometer	Model frame in the 1st floor, Acceleration
AC1-2	3	Accelerometer	Front Mass plate in the 1st floor, Acceleration
AC1-3	4	Accelerometer	Back Mass plate in the 1st floor, Acceleration
AC2-1	5	Accelerometer	Model frame in the 2nd floor, Acceleration
AC2-2	6	Accelerometer	Front Mass plate in the 2nd floor, Acceleration
AC2-3	7	Accelerometer	Back Mass plate in the 2nd floor, Acceleration
AC3-1	8	Accelerometer	Model frame in the 3rd floor, Acceleration
AC3-2	9	Accelerometer	Front Mass plate in the 3rd floor, Acceleration
AC3-3	10	Accelerometer	Back Mass plate in the 3rd floor, Acceleration
AC0-2	11	Accelerometer	Left end of Base Plate, Vertical Acceleration
AC0-3	12	Accelerometer	Left end of Base Concrete Boat, Vertical Acceleration
AC0-4	13	Accelerometer	Right end of Base Plate, Vertical Acceleration
AC0-5	14	Accelerometer	Right end of Base Concrete Boat, Vertical Acceleration
SP0-1	15	String Pot	Base Plate, Displacement
TE1-1	16	Temposonic	Model frame in the 1st floor, Displacement
TE1-2	17	Temposonic	Front Mass plate in the 1st floor, Displacement
TE1-3	18	Temposonic	Back Mass plate in the 1st floor, Displacement
TE2-1	19	Temposonic	Model frame in the 2nd floor, Displacement

Table 6-4 Instrumentation List for SCPT Frame Model (continued)

Tag Name	Channel No.	Sensor Type	Position & Function
TE2-2	20	Temposonic	Front Mass plate in the 2nd floor, Displacement
TE2-3	21	Temposonic	Back Mass plate in the 2nd floor, Displacement
TE3-1	22	Temposonic	Model frame in the 3rd floor, Displacement
TE3-2	23	Temposonic	Front Mass plate in the 3rd floor, Displacement
TE3-3	24	Temposonic	Back Mass plate in the 3rd floor, Displacement
PM1-1	25	Potentiometer	Left beam, 1st floor, left end, top beam flange
PM1-2	26	Potentiometer	Left beam, 1st floor, left end, bottom beam flange
PM1-3	27	Potentiometer	Left beam, 1st floor, right end, top beam flange
PM1-4	28	Potentiometer	Left beam, 1st floor, right end, bottom beam flange
PM1-5	29	Potentiometer	Right beam, 1st floor, left end, top beam flange
PM1-6	30	Potentiometer	Right beam, 1st floor, left end, bottom beam flange
PM1-7	31	Potentiometer	Right beam, 1st floor, right end, top beam flange
PM1-8	32	Potentiometer	Right beam, 1st floor, right end, bottom beam flange
PM2-1	33	Potentiometer	Left beam, 2nd floor, left end, top beam flange
PM2-2	34	Potentiometer	Left beam, 2nd floor, left end, bottom beam flange
PM2-3	35	Potentiometer	Left beam, 2nd floor, right end, top beam flange
PM2-4	36	Potentiometer	Left beam, 2nd floor, right end, bottom beam flange
PM2-5	37	Potentiometer	Right beam, 2nd floor, left end, top beam flange

Table 6-4 Instrumentation List for SCPT Frame Model (continued)

Tag Name	Channel No.	Sensor Type	Position & Function
PM2-6	38	Potentiometer	Right beam, 2nd floor, left end, bottom beam flange
PM2-7	39	Potentiometer	Right beam, 2nd floor, right end, top beam flange
PM2-8	40	Potentiometer	Right beam, 2nd floor, right end, bottom beam flange
PM3-1	41	Potentiometer	Left beam, 3rd floor, left end, top beam flange
PM3-2	42	Potentiometer	Left beam, 3rd floor, left end, bottom beam flange
PM3-3	43	Potentiometer	Left beam, 3rd floor, right end, top beam flange
PM3-4	44	Potentiometer	Left beam, 3rd floor, right end, bottom beam flange
PM3-5	45	Potentiometer	Right beam, 3rd floor, left end, top beam flange
PM3-6	46	Potentiometer	Right beam, 3rd floor, left end, bottom beam flange
PM3-7	47	Potentiometer	Right beam, 3rd floor, right end, top beam flange
PM3-8	48	Potentiometer	Right beam, 3rd floor, right end, bottom beam flange
LC1-1	49	Load Cell	Model frame, 1st floor, front side.
LC1-2	50	Load Cell	Model frame, 1st floor, back side
LC2-1	51	Load Cell	Model frame, 2nd floor, front side
LC2-2	52	Load Cell	Model frame, 2nd floor, back side
LC3-1	53	Load Cell	Model frame, 3rd floor, front side
LC3-2	54	Load Cell	Model frame, 3rd floor, back side
SGB1-1	55	Strain Gauge	Left beam, 1st floor, left end, front side, top beam flange

Table 6-4 Instrumentation List for SCPT Frame Model (continued)

Tag Name	Channel No.	Sensor Type	Position & Function
SGB1-2	56	Strain Gauge	Left beam, 1st floor, left end, back side, top beam flange
SGB1-3	57	Strain Gauge	Left beam, 1st floor, left end, front side, bottom beam flange
SGB1-4	58	Strain Gauge	Left beam, 1st floor, left end, back side, bottom beam flange
SGB1-5	59	Strain Gauge	Left beam, 1st floor, right end, front side, top beam flange
SGB1-6	60	Strain Gauge	Left beam, 1st floor, right end, back side, top beam flange
SGB1-7	61	Strain Gauge	Left beam, 1st floor, right end, front side, bottom beam flange
SGB1-8	62	Strain Gauge	Left beam, 1st floor, right end, back side, bottom beam flange
SGB1-9	63	Strain Gauge	Left beam, top beam flange, right end of left reinforcing plate, 1st floor
SGB1-10	64	Strain Gauge	Left beam, top beam flange, right end of left reinforcing plate, 1st floor
SGB1-11	65	Strain Gauge	Left beam, bottom beam flange, right end of left reinforcing plate, 1st floor
SGB1-12	66	Strain Gauge	Left beam, bottom beam flange, right end of left reinforcing plate, 1st floor
SGB1-13	67	Strain Gauge	Left beam, top beam flange, left end of right reinforcing plate, 1st floor
SGB1-14	68	Strain Gauge	Left beam, top beam flange, left end of right reinforcing plate, 1st floor
SGB1-15	69	Strain Gauge	Left beam, bottom beam flange, left end of right reinforcing plate, 1st floor
SGB1-16	70	Strain Gauge	Left beam, bottom beam flange, left end of right reinforcing plate, 1st floor
SGB2-1	71	Strain Gauge	Left beam, 2nd floor, left end, front side, top beam flange
SGB2-2	72	Strain Gauge	Left beam, 2nd floor, left end, back side, top beam flange
SGB2-3	73	Strain Gauge	Left beam, 2nd floor, left end, front side, bottom beam flange

Table 6-4 Instrumentation List for SCPT Frame Model (continued)

Tag Name	Channel No.	Sensor Type	Position & Function
SGB2-4	74	Strain Gauge	Left beam, 2nd floor, left end, back side, bottom beam flange
SGB2-5	75	Strain Gauge	Left beam, 2nd floor, right end, front side, top beam flange
SGB2-6	76	Strain Gauge	Left beam, 2nd floor, right end, back side, top beam flange
SGB2-7	77	Strain Gauge	Left beam, 2nd floor, right end, front side, bottom beam flange
SGB2-8	78	Strain Gauge	Left beam, 2nd floor, right end, back side, bottom beam flange
SGB2-9	79	Strain Gauge	Left beam, top beam flange, right end of left reinforcing plate, 2nd floor
SGB2-10	80	Strain Gauge	Left beam, top beam flange, right end of left reinforcing plate, 2nd floor
SGB2-11	81	Strain Gauge	Left beam, bottom beam flange, right end of left reinforcing plate, 2nd floor
SGB2-12	82	Strain Gauge	Left beam, bottom beam flange, right end of left reinforcing plate, 2nd floor
SGB2-13	83	Strain Gauge	Left beam, top beam flange, left end of right reinforcing plate, 2nd floor
SGB2-14	84	Strain Gauge	Left beam, top beam flange, left end of right reinforcing plate, 2nd floor
SGB2-15	85	Strain Gauge	Left beam, bottom beam flange, left end of right reinforcing plate, 2nd floor
SGB2-16	86	Strain Gauge	Left beam, bottom beam flange, left end of right reinforcing plate, 2nd floor
SGB3-1	87	Strain Gauge	Left beam, 3rd floor, left end, front side, top beam flange
SGB3-2	88	Strain Gauge	Left beam, 3rd floor, left end, back side, top beam flange
SGB3-3	89	Strain Gauge	Left beam, 3rd floor, left end, front side, bottom beam flange
SGB3-4	90	Strain Gauge	Left beam, 3rd floor, left end, back side, bottom beam flange
SGB3-5	91	Strain Gauge	Left beam, 3rd floor, right end, front side, top beam flange

Table 6-4 Instrumentation List for SCPT Frame Model (continued)

Tag Name	Channel No.	Sensor Type	Position & Function
SGB3-6	92	Strain Gauge	Left beam, 3rd floor, right end, back side, top beam flange
SGB3-7	93	Strain Gauge	Left beam, 3rd floor, right end, front side, bottom beam flange
SGB3-8	94	Strain Gauge	Left beam, 3rd floor, right end, back side, bottom beam flange
SGB3-9	95	Strain Gauge	Left beam, top beam flange, right end of left reinforcing plate, 3rd floor
SGB3-10	96	Strain Gauge	Left beam, top beam flange, right end of left reinforcing plate, 3rd floor
SGB3-11	97	Strain Gauge	Left beam, bottom beam flange, right end of left reinforcing plate, 3rd floor
SGB3-12	98	Strain Gauge	Left beam, bottom beam flange, right end of left reinforcing plate, 3rd floor
SGB3-13	99	Strain Gauge	Left beam, top beam flange, left end of right reinforcing plate, 3rd floor
SGB3-14	100	Strain Gauge	Left beam, top beam flange, left end of right reinforcing plate, 3rd floor
SGB3-15	101	Strain Gauge	Left beam, bottom beam flange, left end of right reinforcing plate, 3rd floor
SGB3-16	102	Strain Gauge	Left beam, bottom beam flange, left end of right reinforcing plate, 3rd floor
SGC0-1	103	Strain Gauge	Left base column, left flange, Strain
SGC0-2	104	Strain Gauge	Left base column, left flange, Strain
SGC0-3	105	Strain Gauge	Left base column, right flange, Strain
SGC0-4	106	Strain Gauge	Left base column, right flange, Strain
SGC0-5	107	Strain Gauge	Middle base column, left flange, Strain
SGC0-6	108	Strain Gauge	Middle base column, left flange, Strain
SGC0-7	109	Strain Gauge	Middle base column, right flange, Strain

Table 6-4 Instrumentation List for SCPT Frame Model (continued)

Tag Name	Channel No.	Sensor Type	Position & Function
SGC0-8	110	Strain Gauge	Middle base column, right flange, Strain
SGC0-9	111	Strain Gauge	Right base column, left flange, Strain
SGC0-10	112	Strain Gauge	Right base column, left flange, Strain
SGC0-11	113	Strain Gauge	Right base column, right flange, Strain
SGC0-12	114	Strain Gauge	Right base column, right flange, Strain
SGC1-1	115	Strain Gauge	Left beam-column connection, 1st floor, left lower column flange
SGC1-2	116	Strain Gauge	Left beam-column connection, 1st floor, left lower column flange
SGC1-3	117	Strain Gauge	Left beam-column connection, 1st floor, right lower column flange
SGC1-4	118	Strain Gauge	Left beam-column connection, 1st floor, right lower column flange
SGC1-5	119	Strain Gauge	Left beam-column connection, 1st floor, left upper column flange
SGC1-6	120	Strain Gauge	Left beam-column connection, 1st floor, left upper column flange
SGC1-7	121	Strain Gauge	Left beam-column connection, 1st floor, right upper column flange
SGC1-8	122	Strain Gauge	Left beam-column connection, 1st floor, right upper column flange
SGC1-9	123	Strain Gauge	Middle beam-column connection, 1st floor, left lower column flange
SGC1-10	124	Strain Gauge	Middle beam-column connection, 1st floor, left lower column flange
SGC1-11	125	Strain Gauge	Middle beam-column connection, 1st floor, right lower column flange
SGC1-12	126	Strain Gauge	Middle beam-column connection, 1st floor, right lower column flange

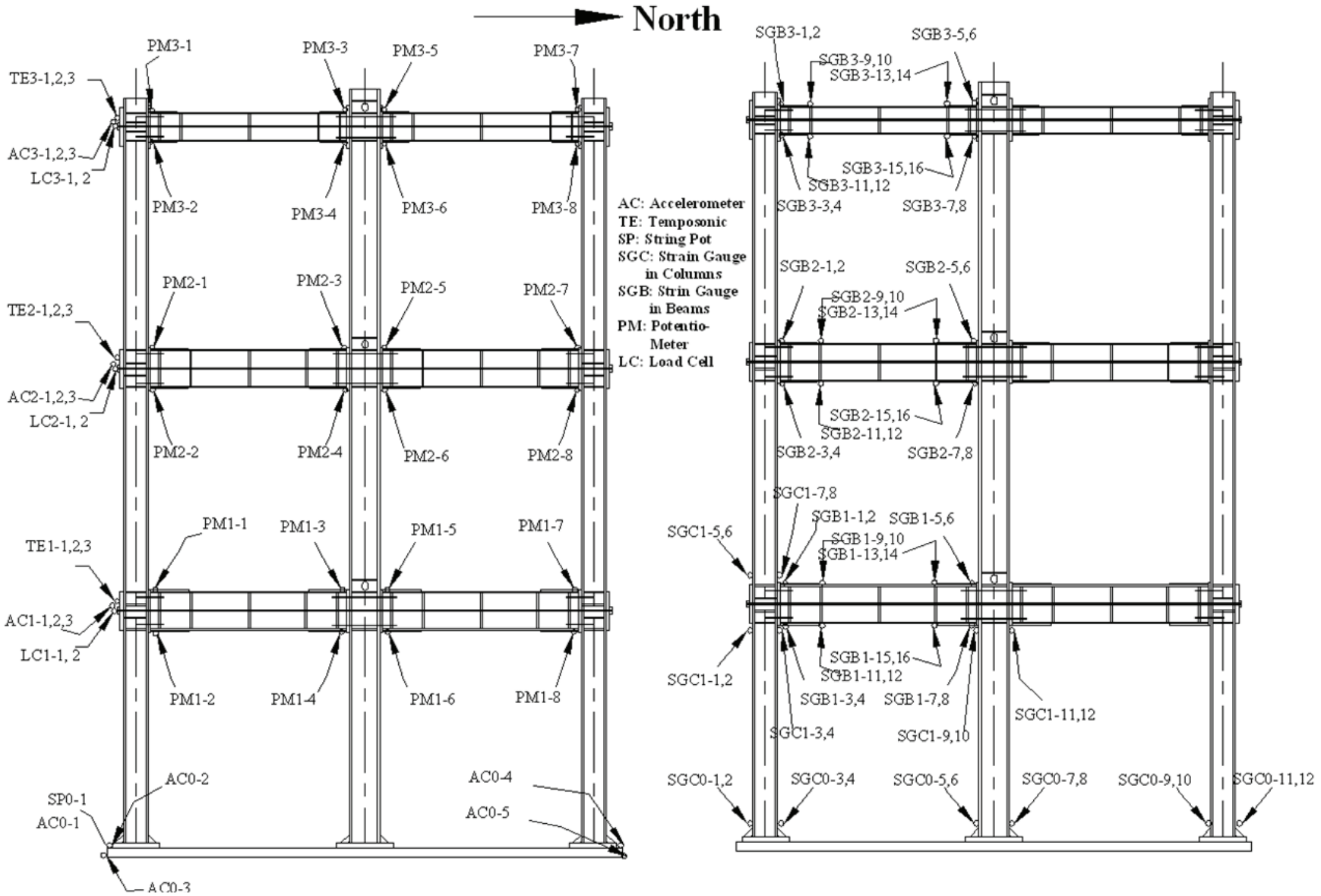

Figure 6-18 Position of Instrumentations for the SCPT Frame Model
(Tag names listed in Table 6-4)

6.4.2 Instrumentation for the Steel Moment Resisting Frame (SMRF) Model

As shown in Table 6-5 and Fig. 6-19, the instrumentation for the SMRF model was reduced compared to the one used on the SCPT model. The accelerometers, string potentiometers, temposonic transducers and strain gauges remained in the same position as in the SCPT model. The potentiometers and load cells were removed. The number of strain gages was also reduced.

Table 6-5 Instrumentation List for SMRF Model

Tag Name	Channel No.	Sensor Type	Position & Function
SGB1-1	1	Strain Gauge	Left beam, 1st floor, left end, front side, top beam flange
SGB1-2	2	Strain Gauge	Left beam, 1st floor, left end, back side, top beam flange
SGB1-3	3	Strain Gauge	Left beam, 1st floor, left end, front side, bottom beam flange
SGB1-4	4	Strain Gauge	Left beam, 1st floor, left end, back side, bottom beam flange
SGB1-5	5	Strain Gauge	Left beam, 1st floor, right end, front side, top beam flange
SGB1-6	6	Strain Gauge	Left beam, 1st floor, right end, back side, top beam flange
SGB1-7	7	Strain Gauge	Left beam, 1st floor, right end, front side, bottom beam flange
SGB1-8	8	Strain Gauge	Left beam, 1st floor, right end, back side, bottom beam flange
SGB2-1	9	Strain Gauge	Left beam, 2nd floor, left end, front side, top beam flange
SGB2-2	10	Strain Gauge	Left beam, 2nd floor, left end, back side, top beam flange
SGB2-3	11	Strain Gauge	Left beam, 2nd floor, left end, front side, bottom beam flange
SGB2-4	12	Strain Gauge	Left beam, 2nd floor, left end, back side, bottom beam flange

Table 6-5 Instrumentation List for SMRF Model (continued)

Tag Name	Channel No.	Sensor Type	Position & Function
SGB2-5	13	Strain Gauge	Left beam, 2nd floor, right end, front side, top beam flange
SGB2-6	14	Strain Gauge	Left beam, 2nd floor, right end, back side, top beam flange
SGB2-7	15	Strain Gauge	Left beam, 2nd floor, right end, front side, bottom beam flange
SGB2-8	16	Strain Gauge	Left beam, 2nd floor, right end, back side, bottom beam flange
SGB3-1	17	Strain Gauge	Left beam, 3rd floor, left end, front side, top beam flange
SGB3-2	18	Strain Gauge	Left beam, 3rd floor, left end, back side, top beam flange
SGB3-3	19	Strain Gauge	Left beam, 3rd floor, left end, front side, bottom beam flange
SGB3-4	20	Strain Gauge	Left beam, 3rd floor, left end, back side, bottom beam flange
SGB3-5	21	Strain Gauge	Left beam, 3rd floor, right end, front side, top beam flange
SGB3-6	22	Strain Gauge	Left beam, 3rd floor, right end, back side, top beam flange
SGB3-7	23	Strain Gauge	Left beam, 3rd floor, right end, front side, bottom beam flange
SGB3-8	24	Strain Gauge	Left beam, 3rd floor, right end, back side, bottom beam flange
SGC0-1	25	Strain Gauge	Left base column, left flange, Strain
SGC0-2	26	Strain Gauge	Left base column, left flange, Strain
SGC0-3	27	Strain Gauge	Left base column, right flange, Strain
SGC0-4	28	Strain Gauge	Left base column, right flange, Strain
SGC0-5	29	Strain Gauge	Middle base column, left flange, Strain
SGC0-6	30	Strain Gauge	Middle base column, left flange, Strain

Table 6-5 Instrumentation List for SMRF Model (continued)

Tag Name	Channel No.	Sensor Type	Position & Function
SGC0-7	31	Strain Gauge	Middle base column, right flange, Strain
SGC0-8	32	Strain Gauge	Middle base column, right flange, Strain
SGC0-9	33	Strain Gauge	Right base column, left flange, Strain
SGC0-10	34	Strain Gauge	Right base column, left flange, Strain
SGC0-11	35	Strain Gauge	Right base column, right flange, Strain
SGC0-12	36	Strain Gauge	Right base column, right flange, Strain
SGC1-1	37	Strain Gauge	Left beam-column connection, 1st floor, left lower column flange
SGC1-2	38	Strain Gauge	Left beam-column connection, 1st floor, left lower column flange
SGC1-3	39	Strain Gauge	Left beam-column connection, 1st floor, right lower column flange
SGC1-4	40	Strain Gauge	Left beam-column connection, 1st floor, right lower column flange
SGC1-5	41	Strain Gauge	Left beam-column connection, 1st floor, left upper column flange
SGC1-6	42	Strain Gauge	Left beam-column connection, 1st floor, left upper column flange
SGC1-7	43	Strain Gauge	Left beam-column connection, 1st floor, right upper column flange
SGC1-8	44	Strain Gauge	Left beam-column connection, 1st floor, right upper column flange
SGC1-9	45	Strain Gauge	Middle beam-column connection, 1st floor, left lower column flange
SGC1-10	46	Strain Gauge	Middle beam-column connection, 1st floor, left lower column flange
SGC1-11	47	Strain Gauge	Middle beam-column connection, 1st floor, right lower column flange
SGC1-12	48	Strain Gauge	Middle beam-column connection, 1st floor, right lower column flange

Table 6-5 Instrumentation List for SMRF Model (continued)

Tag Name	Channel No.	Sensor Type	Position & Function
SP0-1	49	String Pot	Base Plate, Displacement
TE1-1	50	Temposonic	Model frame in the 1st floor, Displacement
TE1-2	51	Temposonic	Front Mass plate in the 1st floor, Displacement
TE1-3	52	Temposonic	Back Mass plate in the 1st floor, Displacement
TE2-1	53	Temposonic	Model frame in the 2nd floor, Displacement
TE2-2	54	Temposonic	Front Mass plate in the 2nd floor, Displacement
TE2-3	55	Temposonic	Back Mass plate in the 2nd floor, Displacement
TE3-1	56	Temposonic	Model frame in the 3rd floor, Displacement
TE3-2	57	Temposonic	Front Mass plate in the 3rd floor, Displacement
TE3-3	58	Temposonic	Back Mass plate in the 3rd floor, Displacement
AC0-1	59	Accelerometer	Base Plate, Acceleration
AC1-1	60	Accelerometer	Model frame in the 1st floor, Acceleration
AC1-2	61	Accelerometer	Front Mass plate in the 1st floor, Acceleration
AC1-3	62	Accelerometer	Back Mass plate in the 1st floor, Acceleration
AC2-1	63	Accelerometer	Model frame in the 2nd floor, Acceleration
AC2-2	64	Accelerometer	Front Mass plate in the 2nd floor, Acceleration
AC2-3	65	Accelerometer	Back Mass plate in the 2nd floor, Acceleration
AC3-1	66	Accelerometer	Model frame in the 3rd floor, Acceleration

Table 6-5 Instrumentation List for SMRF Model (continued)

Tag Name	Channel No.	Sensor Type	Position & Function
AC3-2	67	Accelerometer	Front Mass plate in the 3rd floor, Acceleration
AC3-3	68	Accelerometer	Back Mass plate in the 3rd floor, Acceleration
AC0-2	69	Accelerometer	Left end of Base Plate, **Vertical** Acceleration
AC0-3	70	Accelerometer	Left end of Base Concrete Boat, **Vertical** Acceleration
AC0-4	71	Accelerometer	Right end of Base Plate, **Vertical** Acceleration
AC0-5	72	Accelerometer	Right end of Base Concrete Boat, **Vertical** Acceleration

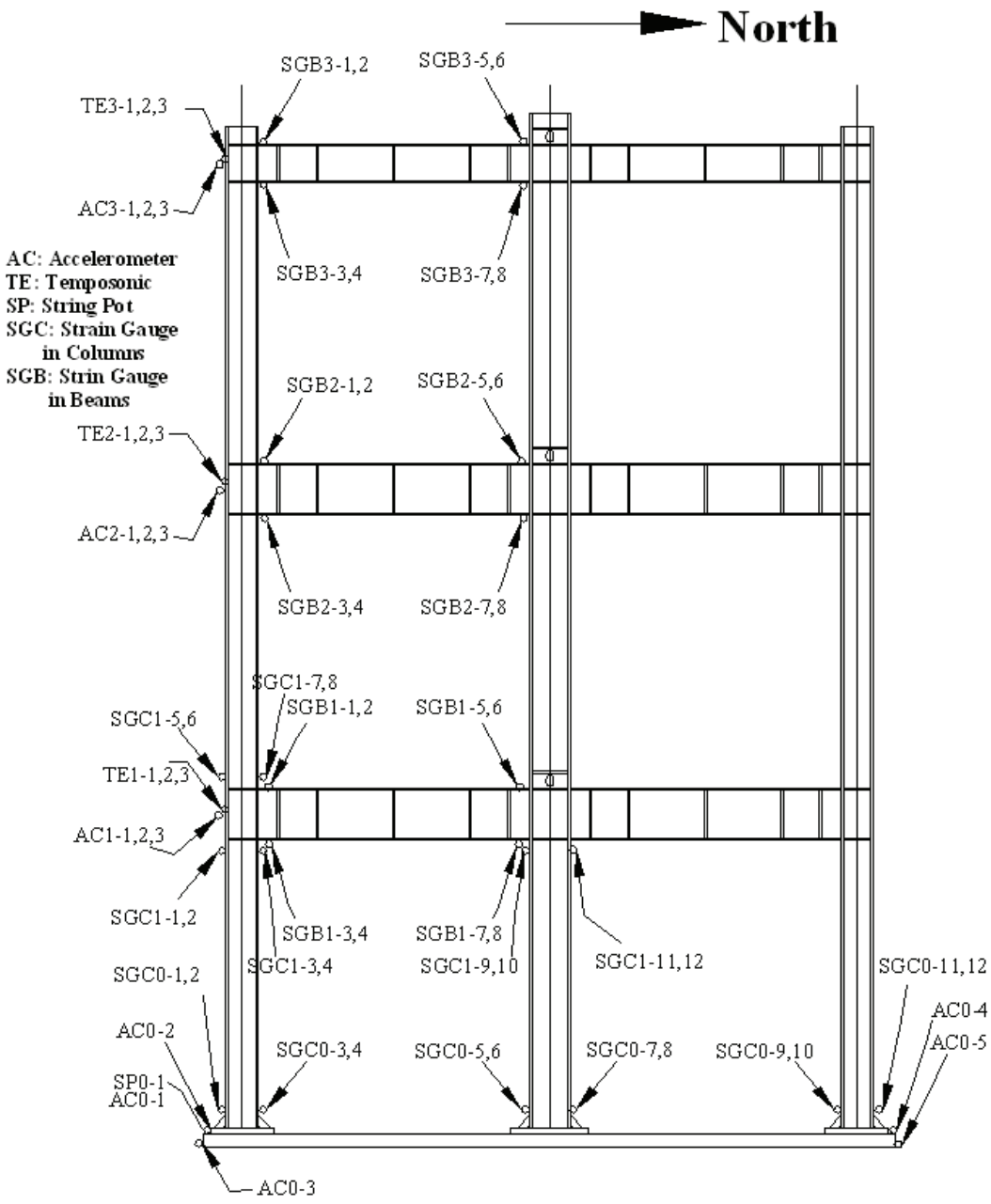

Figure 6-19 Position of Instrumentations for the SMRF Model

(Tag names listed in Table 6-5)

CHAPTER 7
EXPERIMENTAL RESULTS

This chapter discusses the experimental results of two series of seismic tests conducted according to the testing program described in Chapter VI. The Steel Moment Resisting Frame (SMRF) and Self-Centering Post-Tensioned (SCPT) frame models were used in these two series of tests under different seismic excitations. In order to identify the dynamic characteristics of those two models, white noise, snap-back and sine sweep tests were carried out and the results are compared. Then, the shake table fidelity is evaluated. Thereafter, the global response in terms of the acceleration and displacement of the model structures and the local response with respect to the individual structural components are presented. Finally, the seismic energy dissipation is evaluated.

Throughout this chapter, the experimental results are discussed by comparing the responses between the SCPT and SMRF models. This comparison is used to experimentally verify the conclusions obtained numerically in previous chapters. Note that the test nomenclature used in this chapter can be found in the test protocols presented in Section 6.3.

7.1 Identification of Dynamic Characteristics

The dynamic characteristics of a structure are considered to be the natural period/frequency, stiffness, mode shape and damping. To identify these properties for the frame models, different types of tests including white noise, snap-back and sine-sweep tests were conducted. Based on the results of those tests, the dynamic properties of the SCPT and SMRF models

are calculated. Finally, a comparison of the structural properties obtained from different tests is presented and discussed at the end of this section.

7.1.1 White Noise Tests

White noise tests were conducted before the seismic tests to identify the initial dynamic properties of the frame models and then carried out after every seismic test to verify any change of the structural characteristics. These white noise excitations had an amplitude of 0.05 g with a flat frequency band from 0.5 to 50 Hz. Two different amplitudes (0.1g and 0.15g) were also used to see if the structural properties changed with the excitation amplitude.

Using the experimental results in terms of the ground acceleration and the accelerations of the three stories of the frame models, transfer functions were calculated from the ratio of the Fourier transform amplitudes between the output (floor accelerations) and the input (ground acceleration) in the frequency domain. Based on the transfer functions, the natural frequencies of the structures in various modes were determined by the frequencies with peak magnitudes. The mode shapes were also obtained by comparing the amplitudes of the transfer functions of different floors. The directions of the various mode shape components were determined from the phase values between the different transfer functions. The well known half-power (bandwidth) method (Chopra, 2000) was used to calculate the equivalent viscous damping ratios.

The transfer functions in the frequency domain obtained from the white noise tests PWN1B (0.1g), PWN1C (0.15g), PWN1D (0.1g) and PWN2A for the SCPT model and from the white noise tests MWN01, MWN02 and MWN03 for the SMRF model, are shown in Figs. 7-1 to 7-7. Among these tests, tests PWN1D, PWN2A, MWN02 and MWN03 were conducted after a seismic test with 25% intensity (see Section 6.3). Those tests were selected to calculate the initial dynamic properties since both the SCPT and SMRF structures remained elastic without any change in terms of dynamic properties under low intensity seismic tests. Based on those transfer functions, the natural frequencies, mode shapes and damping ratios were determined as shown in Table 7-1 and 7-2.

Table 7-1 indicates that the natural frequencies of the SMRF model are identical for all three white noise tests conducted initially. As seen in Table 7-2, the natural frequencies of the SCPT model in the 1^{st} mode are slightly different across the various tests, which may be due to the different amplitude of the white noise tests. Also, the mode shapes and damping ratios, obtained from those white noise tests, are similar for all tests. Basically, those calculated properties are similar under the same type excitation (white noise). Therefore, the average values in terms of natural frequencies, mode shapes and damping ratios were determined to represent the initial dynamic characteristics of the two models as a result of the white noise tests. Further evaluation of these results will be presented in the summary of Sec. 7.1.4.

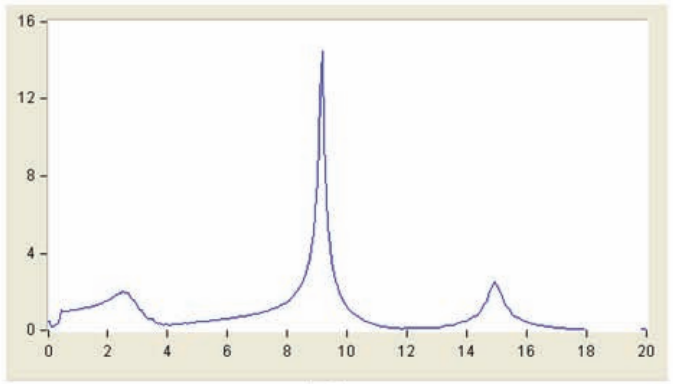

(a)

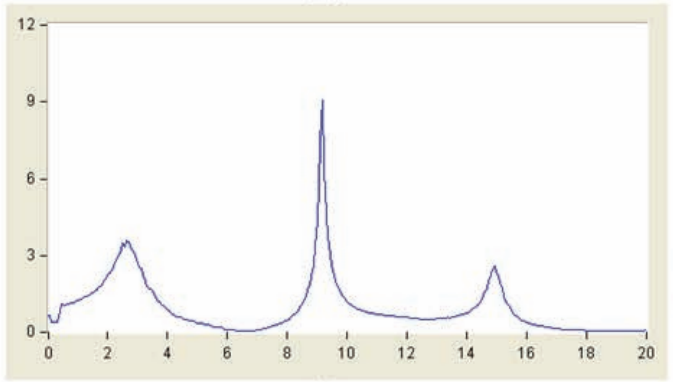

(b)

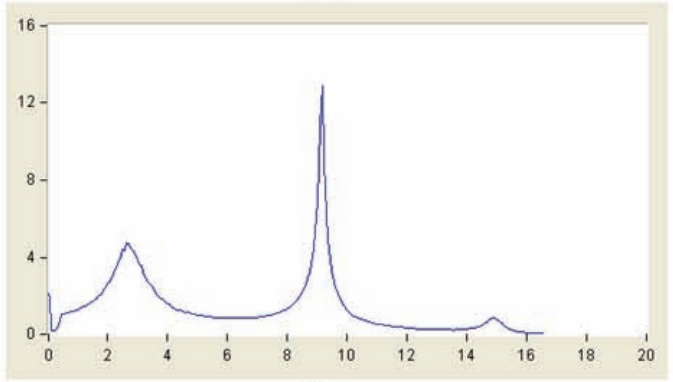

(c)

Figure 7-1 Transfer Function of SCPT model for Test PWN1B
(a) 1st floor (b) 2nd floor (3) 3rd floor

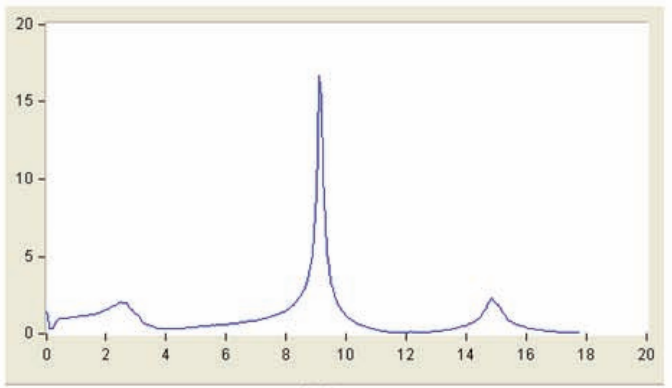

(a)

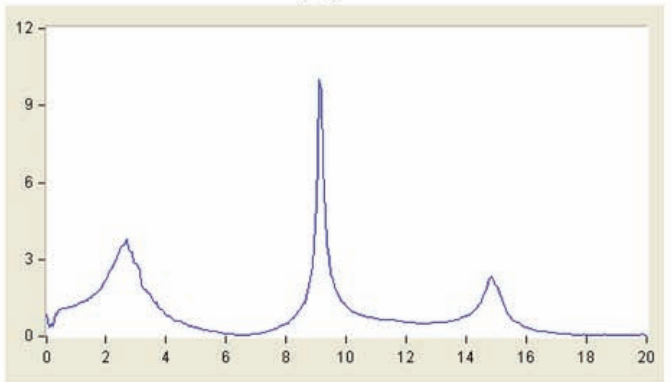

(b)

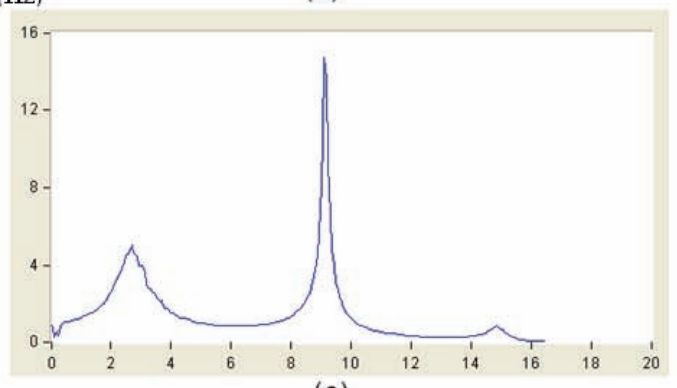

(c)

Figure 7-2 Transfer Function of SCPT model for Test PWN1C
(a) 1st floor (b) 2nd floor (3) 3rd floor

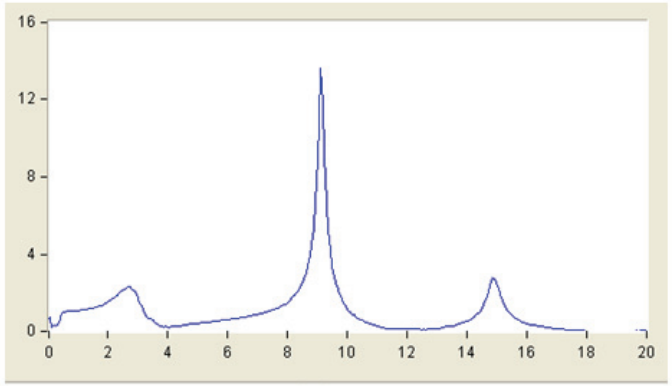

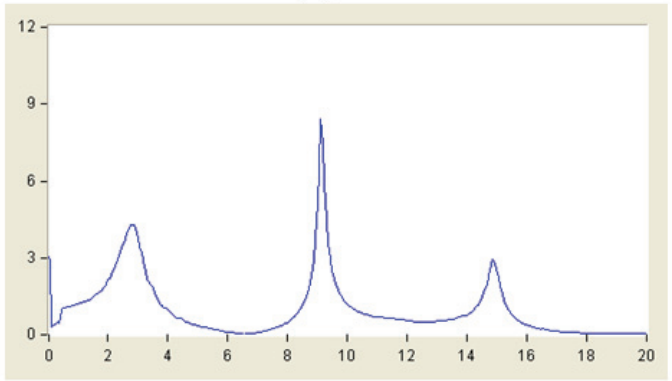

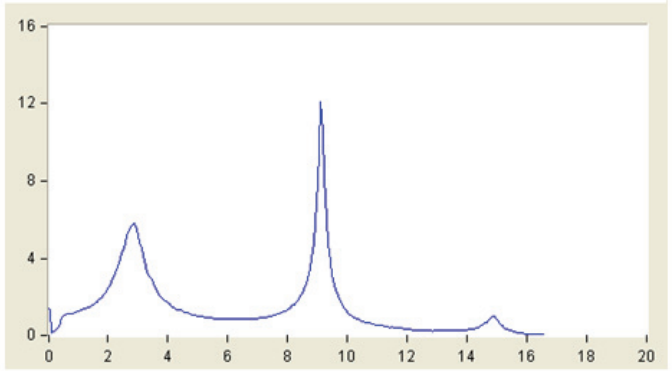

Figure 7-3 Transfer Function of SCPT model for Test PWN1D
(a) 1st floor (b) 2nd floor (3) 3rd floor

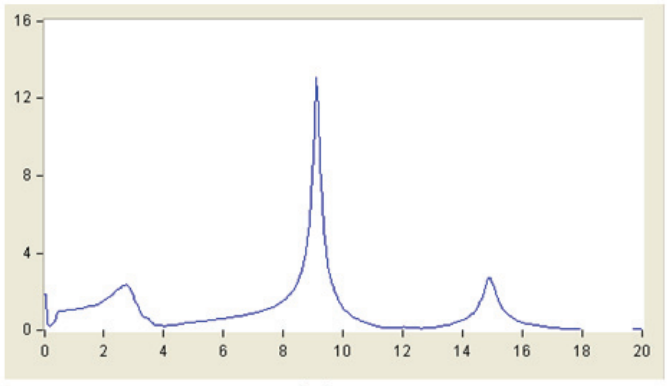

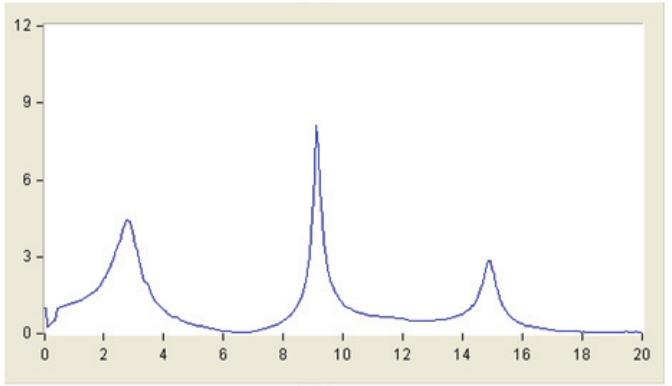

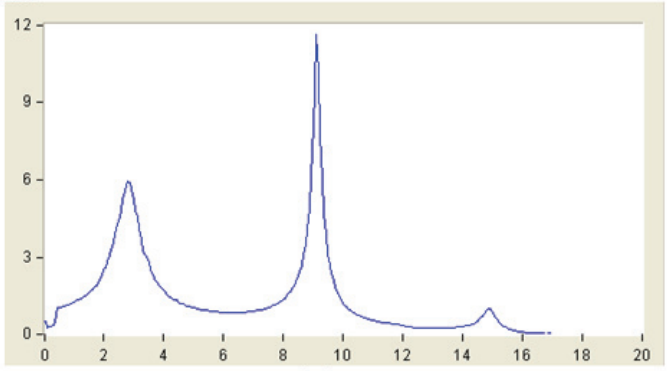

Figure 7-4 Transfer Function of SCPT model for Test PWN2A
(a) 1st floor (b) 2nd floor (3) 3rd floor

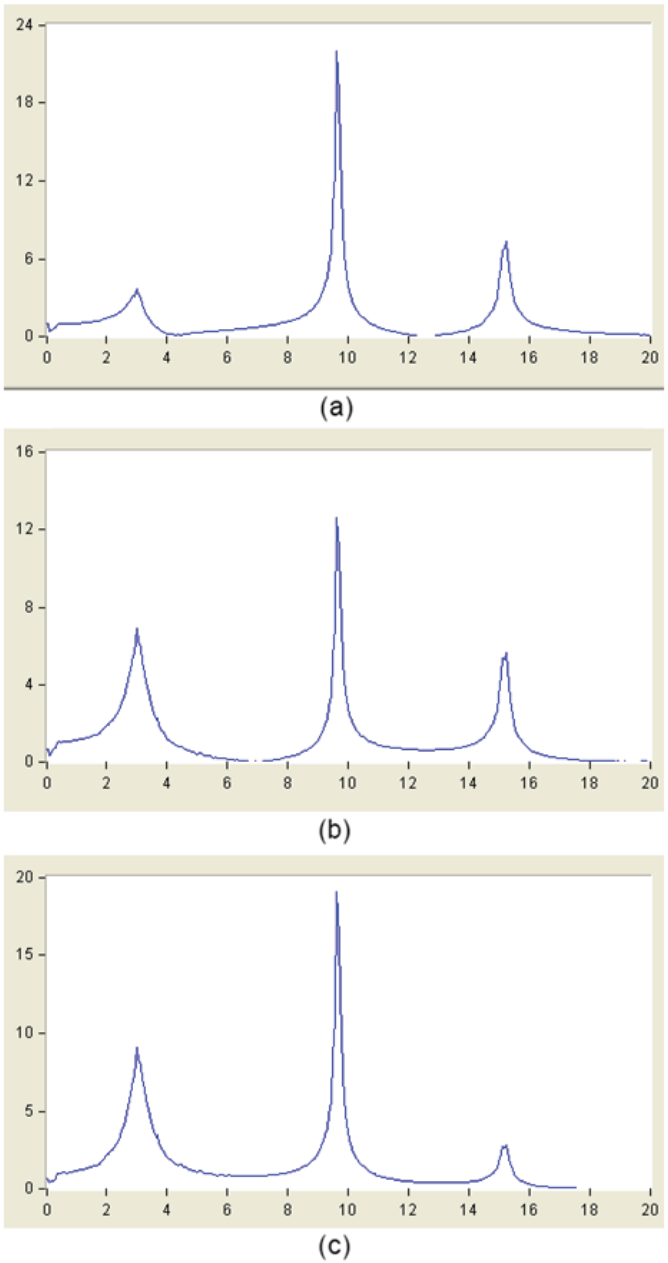

Figure 7-5 Transfer Function of SMRF model for Test MWN01
(a) 1st floor (b) 2nd floor (3) 3rd floor

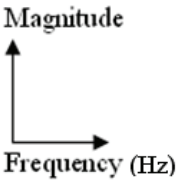

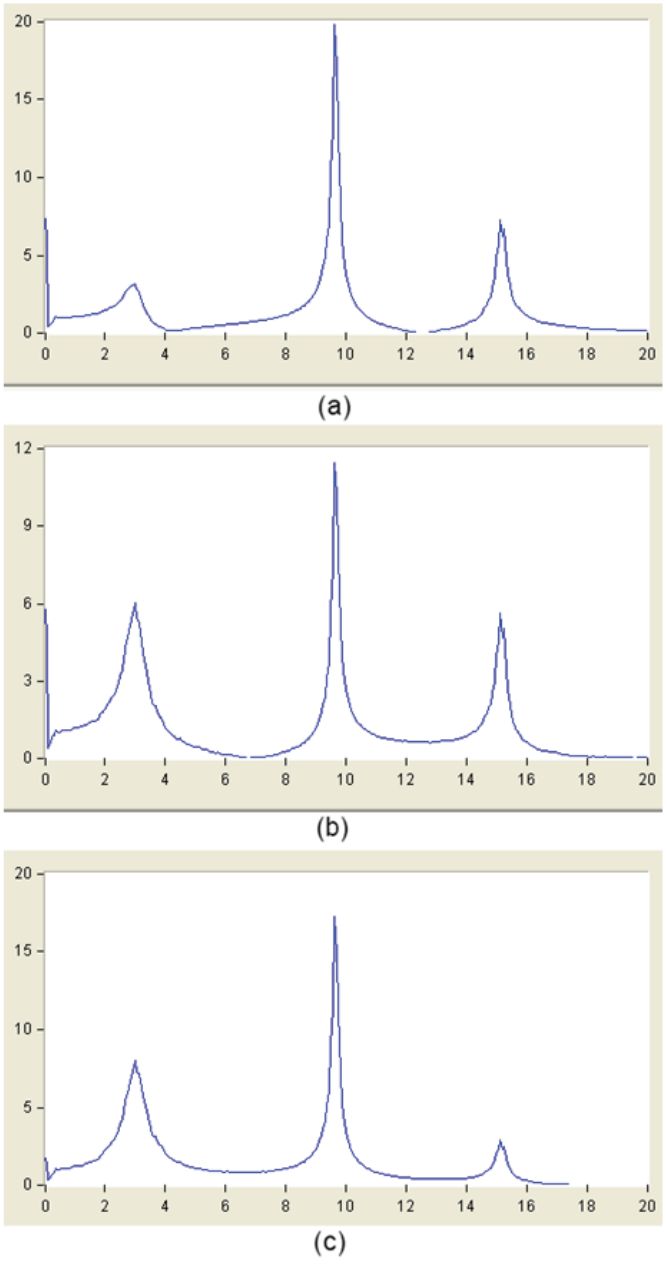

Figure 7-6 Transfer Function of SMRF model for Test MWN02
(a) 1st floor (b) 2nd floor (3) 3rd floor

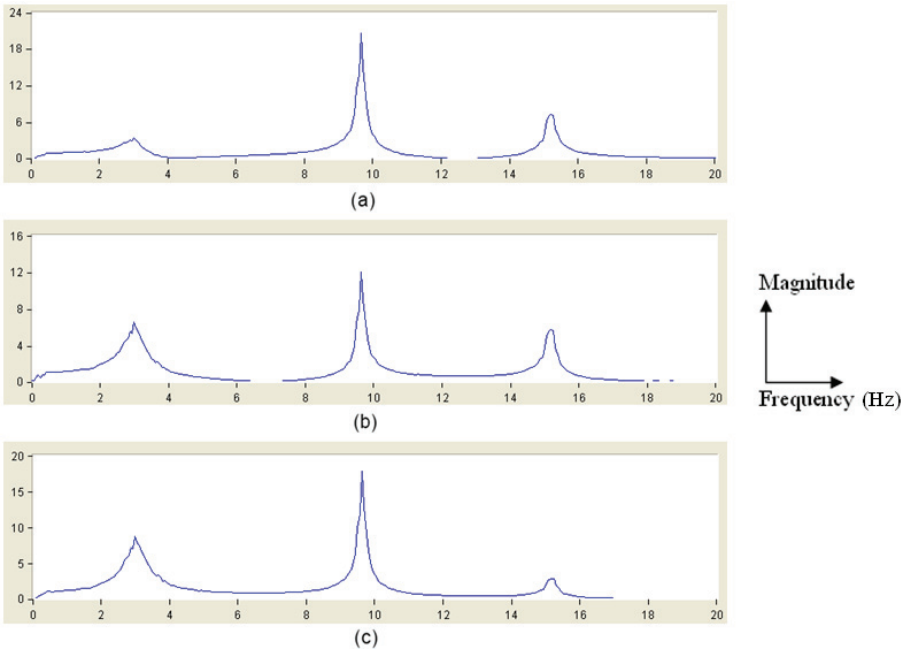

Figure 7-7 Transfer Function of SMRF model for Test MWN03
(a) 1st floor (b) 2nd floor (3) 3rd floor

Table 7-1 Dynamic Properties of the SMRF model obtained from initial white noise tests

Test No.	Mode	Frequency (Hz)	Mode Shape Φ			Damping Ratio ξ (%)
			1st floor	2nd floor	3rd floor	
MWN01	1st	3.000	0.405	0.756	1.000	14.8
	2nd	9.625	1.000	0.573	-0.870	2.4
	3rd	15.250	1.000	-0.769	0.385	1.8
MWN02	1st	3.000	0.398	0.751	1.000	16.8
	2nd	9.625	1.000	0.576	-0.868	2.6
	3rd	15.125	1.000	-0.774	0.400	1.9
MWN03	1st	3.000	0.399	0.754	1.000	15.4
	2nd	9.625	1.000	0.582	-0.861	2.6
	3rd	15.188	1.000	-0.785	0.389	1.9
Average	1st	3	0.401	0.754	1	15.7
	2nd	9.625	1	0.577	-0.866	2.5
	3rd	15.188	1	-0.776	0.391	1.9

Table 7-2 Dynamic Properties of the SCPT model obtained from initial white noise tests

Test No.	Mode	Frequency (Hz)	Mode Shape Φ			Damping Ratio ξ (%)
			1st floor	2nd floor	3rd floor	
PWN1B	1st	2.625	0.424	0.762	1	16.9
	2nd	9.188	1	0.628	-0.892	0.9
	3rd	14.938	-0.974	1	-0.353	1.5
PWN1C	1st	2.688	0.401	0.752	1	15.6
	2nd	9.125	1	0.598	-0.884	1.0
	3rd	14.875	-0.98	1	-0.363	1.7
PWN1D	1st	2.875	0.373	0.742	1	13.7
	2nd	9.125	1	0.617	-0.89	1.2
	3rd	14.875	-0.951	1	-0.354	1.3
PWN2A	1st	2.813	0.389	0.753	1	13.4
	2nd	9.125	1	0.621	-0.893	1.3
	3rd	14.875	-0.943	1	-0.354	1.1
Average	1st	2.75	0.397	0.752	1	14.9
	2nd	9.141	1	0.616	-0.89	1.1
	3rd	14.891	-0.962	1	-0.356	1.4

According to the theory of linear structural dynamics, the stiffness matrix and damping matrix of the frame models can be calculated with the obtained natural frequencies, mode shapes and damping ratios. The stiffness matrix, K, is defined by:

$$K = M\Phi_n \Omega \Phi_n^T M \tag{7.1}$$

where:

M : Mass matrix. For these two modes with lumped mass in each floor, the mass matrix is diagonal matrix ([45.21, 45.14, 44.81]) lb-sec^2/in.

Φ_n : Mass normalized mode shape matrix. $\Phi_n^T M \Phi_n = I$, where I is the unit matrix.

Ω : Diagonal natural frequency matrix [ω_1^2 , ω_2^2 , … ω_i^2 ..., ω_n^2].

ω_i : Circular natural frequency of the i-th mode (rad/sec)

The damping matrix, C, is defined as follows:

$$C = M\Phi_n \zeta \Phi_n^T M \tag{7.2}$$

where:

ζ : Diagonal matrix [$2\xi_1\omega_1$, $2\xi_2\omega_2$, … $2\xi_i\omega_i$ …, $2\xi_n\omega_n$].

ξ_i : Damping ratio of the i-th mode.

By using Eq. (7.1) and (7.2) as well as the results indicated in Table 7-1 and 7-2, the stiffness matrix and damping matrix of the two model structures were calculated as shown in Table 7-3.

Table 7-3 Stiffness and Damping Matrices of the SCPT and SMRF models

	Stiffness Matrix K (kips/in)	Damping Matrix C (lb-sec/in)
SCPT Model	$\begin{bmatrix} 248.9 & -140.8 & 7.9 \\ -140.8 & 223.0 & -99.6 \\ 7.9 & -99.6 & 85.4 \end{bmatrix}$	$\begin{bmatrix} 101.3 & 1.2 & 49.8 \\ 1.2 & 144.2 & 66.4 \\ 49.8 & 66.4 & 161.2 \end{bmatrix}$
SMRF Model	$\begin{bmatrix} 316.1 & -133.3 & 26.4 \\ -133.3 & 172.7 & -103.0 \\ 26.4 & -103.0 & 103.1 \end{bmatrix}$	$\begin{bmatrix} 184.4 & 12.4 & 41.6 \\ 12.4 & 166.2 & 55.5 \\ 41.6 & 55.5 & 215.4 \end{bmatrix}$

Comparisons of the transfer functions for most of the white noise tests conducted between seismic tests of increasing intensities are shown in Figs. 7-8 to 7-10. The percentage (i.e. intensity of seismic tests) indicated next to the test label indicates that the white noise test was carried out after that seismic test with that normalized intensity.

From these figures, it can be seen that both frame models maintained similar natural frequencies in each mode after all seismic tests, which indicates that no significant yielding occurred during the seismic tests. Major inelastic deformation (yielding) of the structural components would have damaged the structure and caused the large residual drifts or stresses which would decreases the natural frequencies. The natural frequencies for those tests are also listed in Table 7-4 and 7-5.

For the SCPT model, as shown in Table 7-4, it should be noted that in the 1st phase of seismic tests (earthquake excitations with 25% to 150% intensity before PWN9), the natural frequencies increased after the 25%-intensity seismic test and decreased after the 70%-intensity test. It is believed that the reason for the first increase is that the contact surface of the beam to the column in the SCPT model was not machined perfectly flat such that not all the area of the beam end was in contact with the column flange. Therefore, after the 25%-intensity seismic test, that contact area may have increased leading to a higher stiffness of the total structure.

The decrease of natural frequency after the 70% seismic test indicates that some gap openings occurred at the interface of some beam-to-column connections, which is consistent

with the numerical predictions obtained in Chapter VI. Although from a theoretical perspective, the natural frequencies should not change in the SCPT structure when only the Energy-Dissipating (ED) bars yield, the changes in the experimental natural frequencies remain relatively small, which can be considered to be in accordance with the theory. Note also that the natural frequencies are higher after tests PWN9 (2^{nd} Phase) and PWN28 (3^{rd} Phase) compared to those after tests PWN8 and PWN24, which is attributed to the installation of support bars on the bottom and top of the beams to prevent the unexpected vertical movement of the beams observed during the seismic tests (see Section 7.3).

For the SMRF model, as shown in Table 7-5, the natural frequency in the 1^{st} mode remains constant until the 100%-intensity seismic test. After the 125%-intensity seismic test, the natural frequency of 1^{st} mode is decreased, which indicates that the beams and/or columns yielded. Note that this decrease is very small, which suggests that the ductility of the yielding is low and do not make severe damage on the structure. The natural frequencies of the 2^{nd} and 3^{rd} modes were also reduced, which may be related to the yielding. No further explanations are given to the change of the higher-mode natural frequencies.

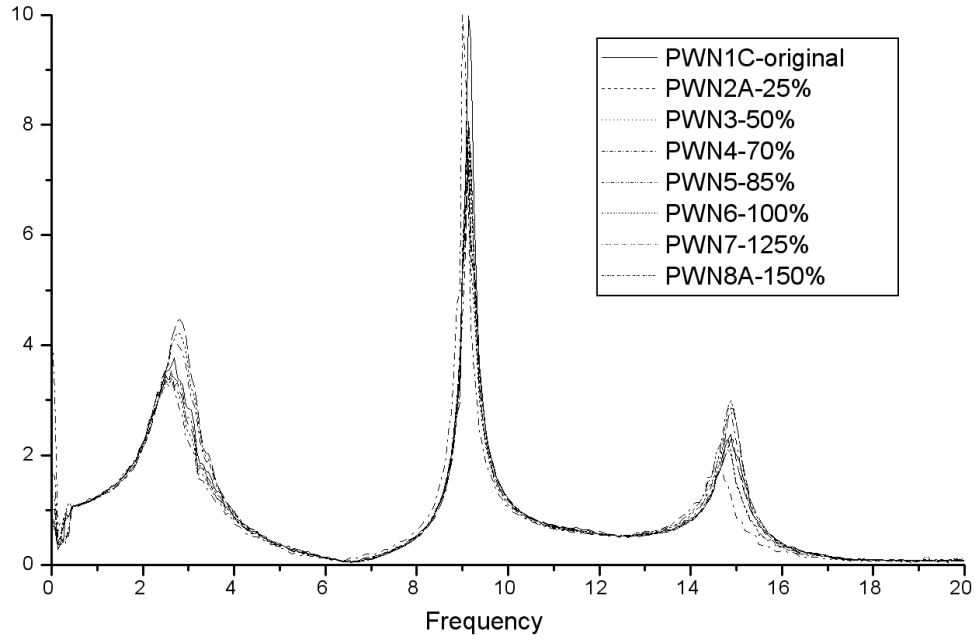

Figure 7-8 Transfer Functions for White Noise Tests, SCPT Model

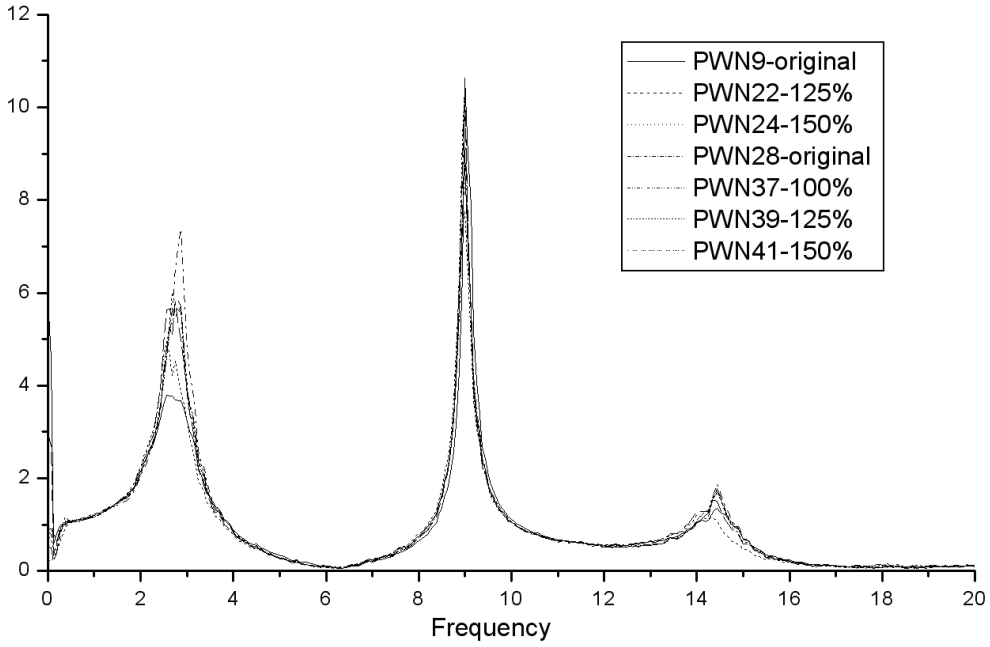

Figure 7-9 Transfer Functions for White Noise Tests, SCPT Model

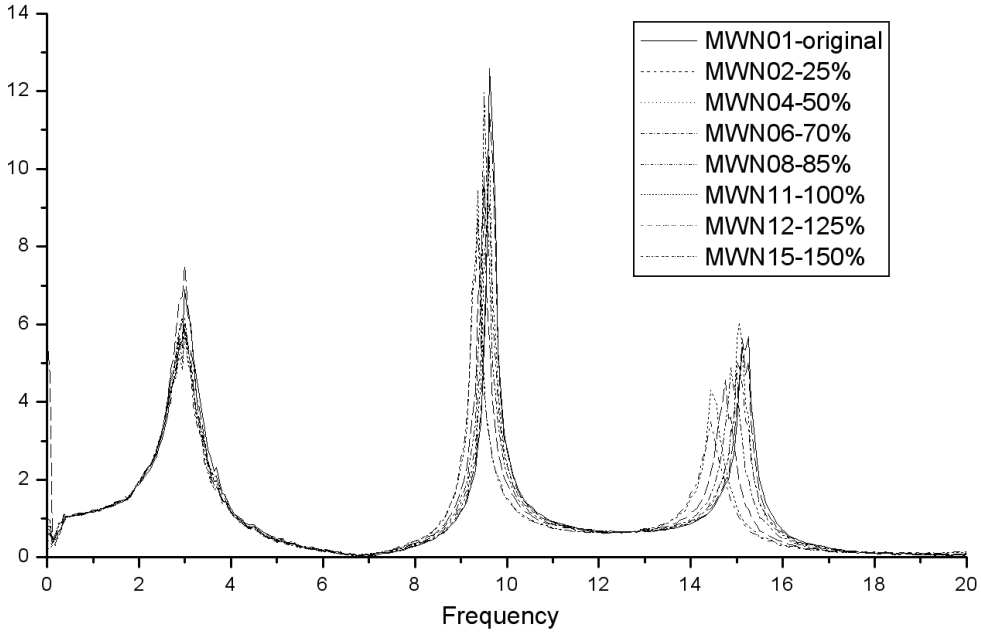

Figure 7-10 Transfer Functions for White Noise Tests, SMRF Model

Table 7-4 Natural Frequencies of the SCPT Model obtained from all white noise tests

	Natural Frequencies (Hz)							
Test number	PWN1C	PWN2A	PWN3	PWN4	PWN5	PWN6	PWN7	PWN8
1st mode	2.688	2.813	2.813	2.75	2.688	2.625	2.625	2.625
2nd mode	9.125	9.125	9.125	9.125	9.125	9.125	9.125	9
3rd mode	14.875	14.875	14.875	14.813	14.813	14.875	14.75	14.56
Test number	PWN9	PWN22	PWN24	PWN28	PWN37	PWN39	PWN41	
1st mode	2.75	2.75	2.563	2.875	2.875	2.813	2.688	
2nd mode	9	9	9	9	9	9	9	
3rd mode	14.438	14.438	14	14.438	14.438	14.438	14.438	

Table 7-5 Natural Frequencies of the SMRF Model obtained from all white noise tests

	Natural Frequencies (Hz)							
Test number	MWN01	MWN02	MWN04	MWN06	MWN08	MWN11	MWN12	MWN15
1st mode	3.000	3.000	3.000	3.000	3.000	3.000	2.938	2.938
2nd mode	9.625	9.625	9.625	9.500	9.500	9.500	9.375	9.375
3rd mode	15.250	15.125	15.063	15.000	14.875	14.750	14.438	14.438

7.1.2 Snap-Back Tests

A snap-back test consists in pulling the structure with a relatively low force or to a certain displacement and then quickly releasing it to induce free vibrations. For the two frame models (SCPT & SMRF), snap-back tests were conducted by pulling the structures with a 400~500 lb. force in order to determine their dynamic properties from the recorded acceleration and displacement responses.

By using the same procedure used in the white noise tests, the dynamic characteristics of the two models were calculated through the transfer functions as shown in Fig. 7-11 and 7-12. The calculated results of these dynamic properties will be summarized in Section7.1.4.

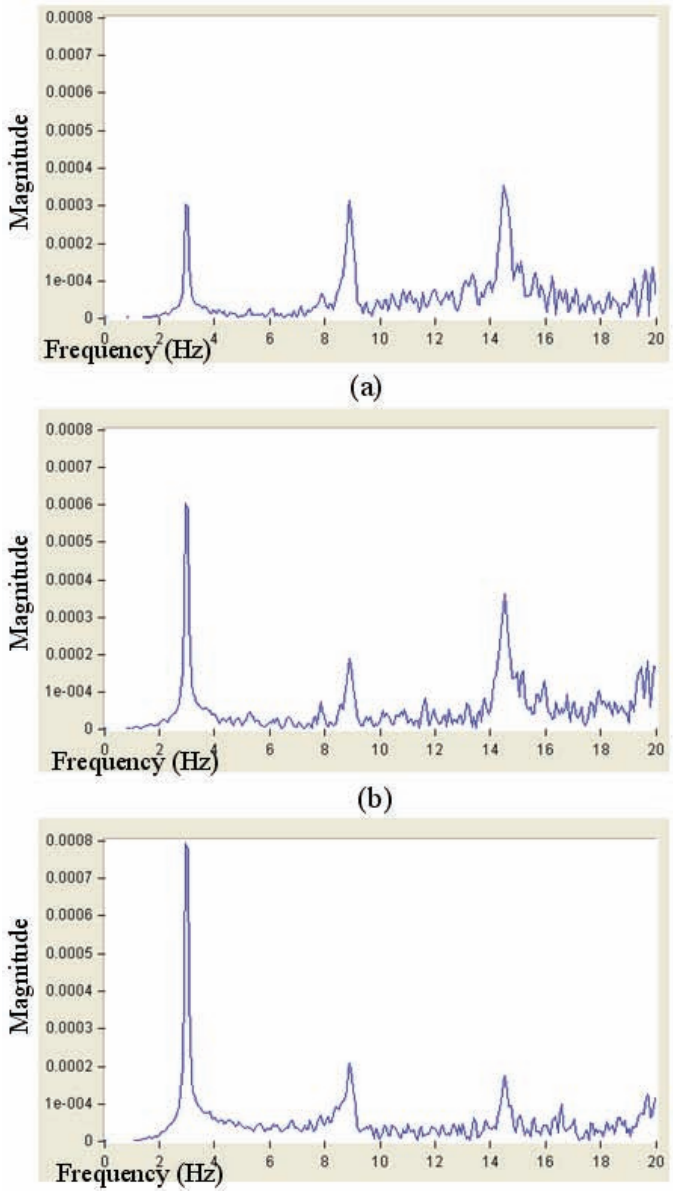

Figure 7-11 Transfer Function of the SCPT model for Snap-Back Test
(a) 1st floor (b) 2nd floor (3) 3rd floor

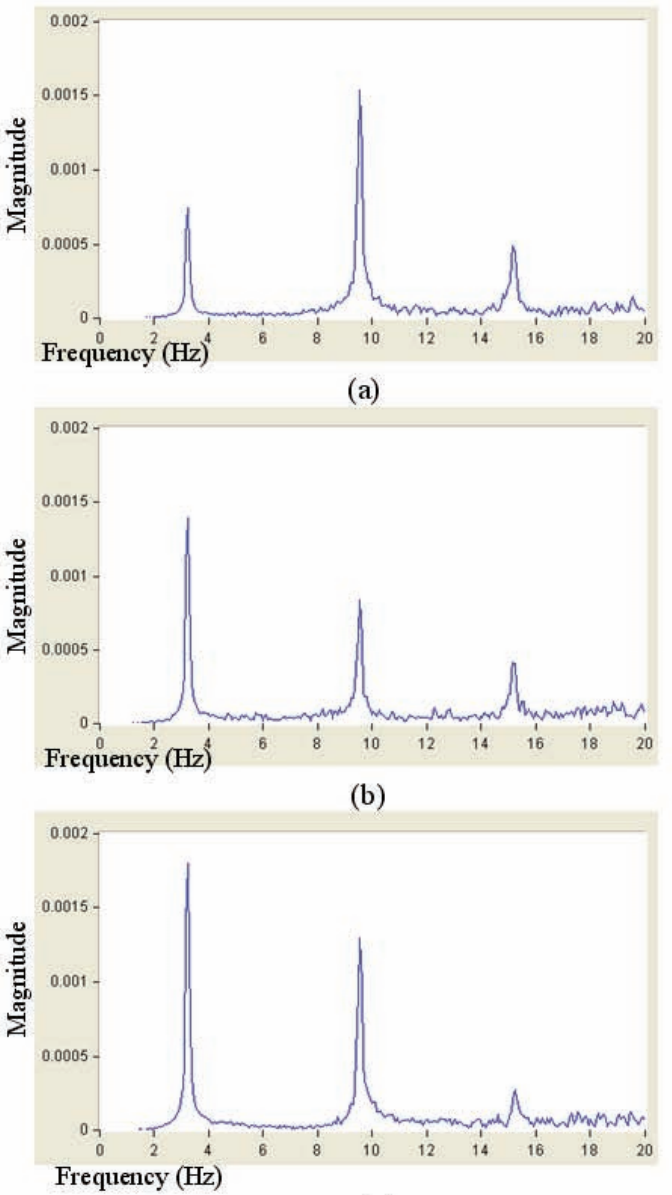

Figure 7-12 Transfer Function of the SMRF model for Snap-Back Test
(a) 1st floor (b) 2nd floor (3) 3rd floor

For the damping ratios, except using the half-bandwidth method, another well-known logarithmic decrement decay method (Chopra, 2000) was used. As shown in Fig. 7-13, based on this method, the damping ratio, ξ, can be estimated as follows:

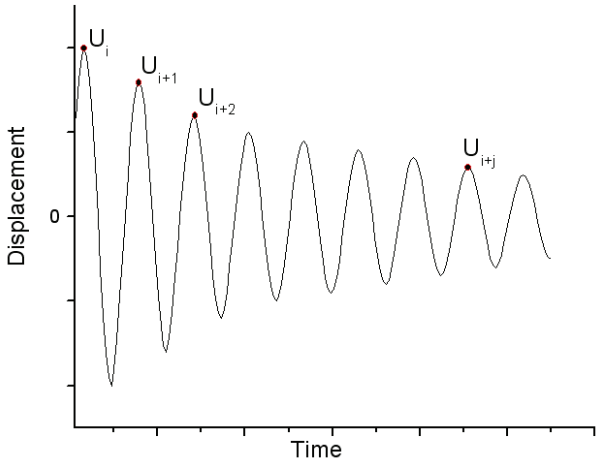

Figure 7-13 Displacement time history of a freely vibration system

$$\xi = \frac{1}{2\pi j} \ln \frac{U_i}{U_{i+j}} \qquad (7.3)$$

where, U_i and U_{i+j} are the displacement amplitudes at the i-th and (i+j)-th cycles; and j is the number of cycles after the i-th cycle.

The displacement time histories of the model structures were notch-filtered around the natural frequencies of the first 3 modes such that only the contribution of a given modal natural frequency remained in the displacement time histories. The selected notch-filtering band is determined by the range of a full peak of the transfer function at a given modal frequency (e.g. as shown in Fig. 7-11, the range 2.6 ~ 3.6 Hz is selected for the 1st modal natural frequency 2.973Hz of SCPT modal obtained from the snap-back test as listed in Table 7-6). Figure 7-14 and 7-15 show the displacement responses notch-filtered by the modal frequency for two model structures. By using these filtered displacement time histories, the damping ratios can be estimated by Eq. (7.3). The results of damping ratios calculated from the above method will be also presented in Section 7.1.4.

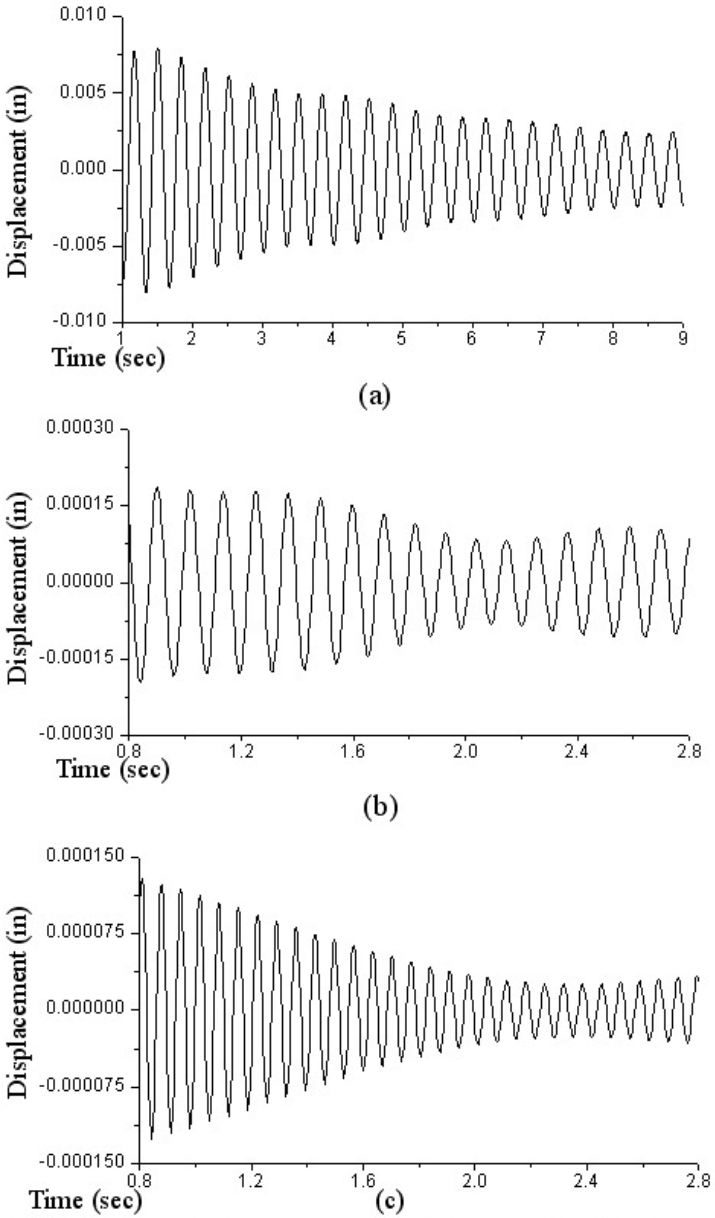

Figure 7-14 Displacement Time History of SCPT Model notch-filtered around the modal frequency of (a) 1st mode (b) 2nd mode (c) 3rd mode

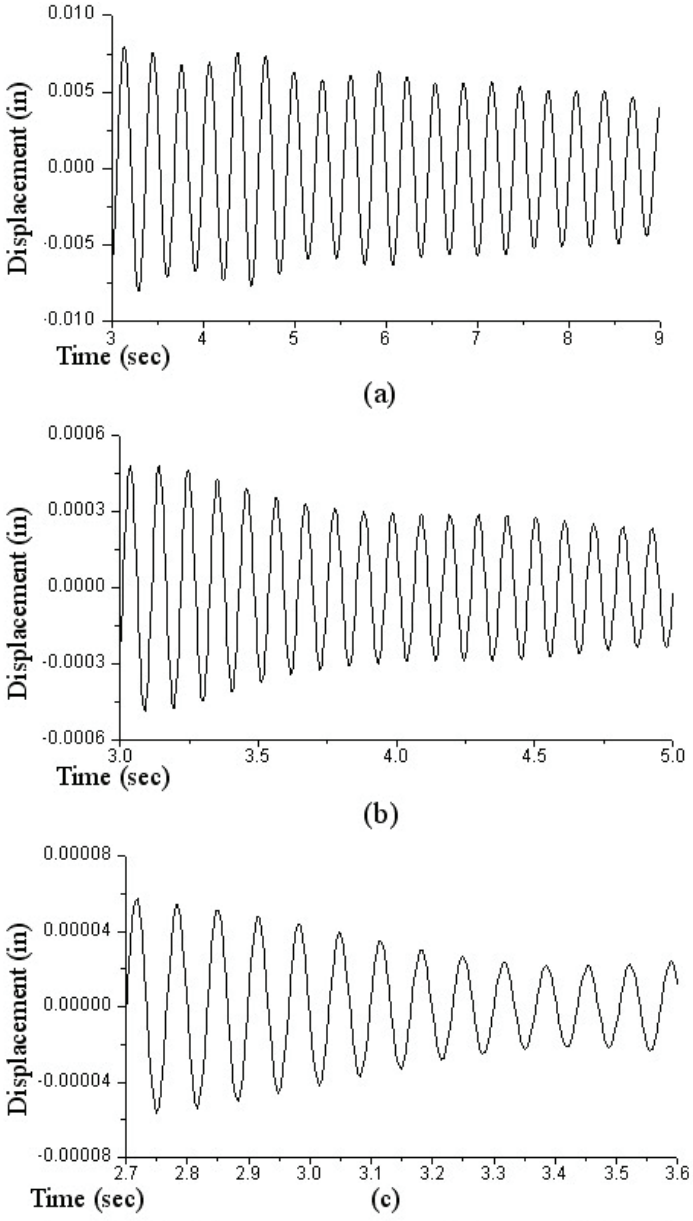

Figure 7-15 Displacement Time History of SMRF Model notch-filtered around the modal frequency of (a) 1st mode (b) 2nd mode (c) 3rd mode

7.1.3 Sine-Sweep Test

A sine-sweep test is a dynamic test using a sequence of sinusoidal vibrations as input motion to the shake table. The advantage of a sine-sweep test is that a resonance response occurs when the varying frequency of the sinusoidal signal is close to the natural frequency of the model structure, which leads to a clear peak amplitude in the transfer function. Therefore, the dynamic properties can be easily identified. The disadvantage of this test method is also due to this resonance response, which may damage the model structures. In order to avoid the inelastic deformation of the SMRF model, which would make unrecoverable damage to the structure components, the sine-sweep test was carried out only for the SCPT model.

As shown in Fig. 7-16, the sinusoidal signal used for the sine-sweep test has 5~30 Hz frequency contents and 0.17g acceleration amplitude with a 25 second duration. The transfer functions calculated from the acceleration responses in the frequency domain are shown in Fig. 7-17. The dynamic properties were calculated through the same method used for the white noise tests. All the results are shown in the summary of Section 7.1.4.

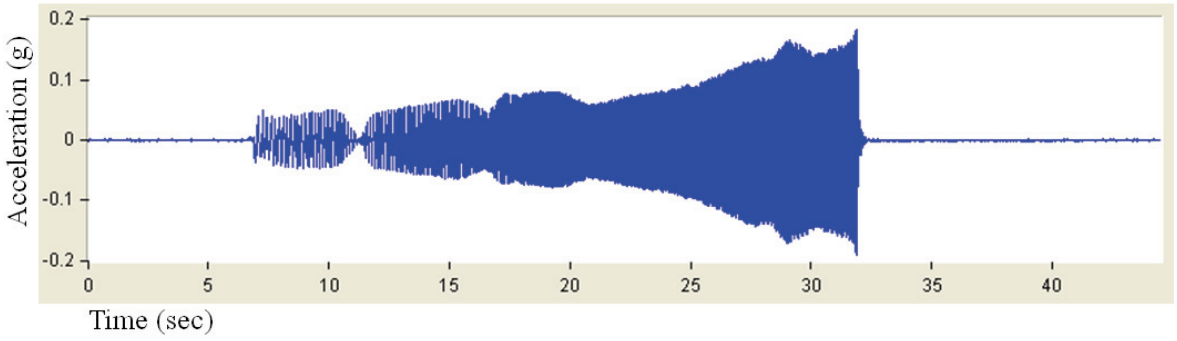

Figure 7-16 Sine-Sweep Excitation used for the SCPT model

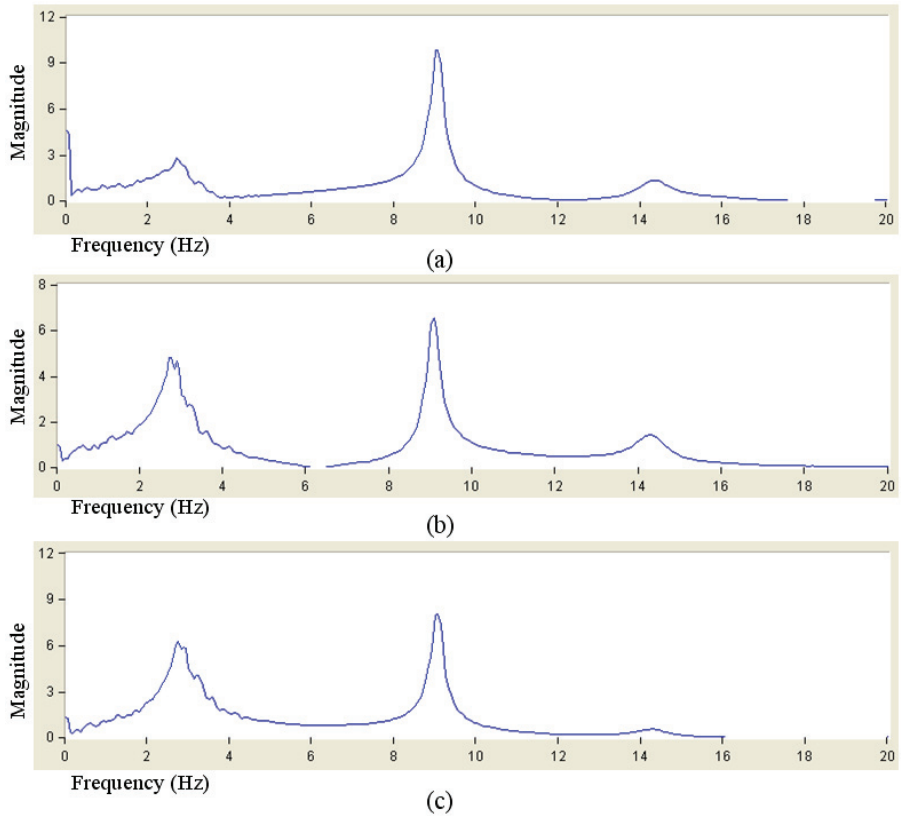

Figure 7-17 Transfer Functions in the SCPT model from the Sine Sweep Test
(a) 1st floor (b) 2nd floor (3) 3rd floor

7.1.4 Summary of Identification Tests

To identify the dynamic properties of the SCPT and SMRF model structures, white noise, snap-back and sine-sweep tests were conducted. The dynamic characteristics of the two frame models were calculated based on the transfer functions according to the theory of linear structural dynamics. The results of the identification tests are summarized in Table 7-6 and 7-7, in which the natural frequencies and mode shapes from the white noise tests are average values calculated from Table 7-1 and 7-2. For the snap-back tests, two methods

(half-bandwidth and logarithmic decrement decay methods) were used to calculate the damping ratios.

By comparing the natural frequencies shown in Table 7-6 and 7-7, it is noted that the 1st modal natural frequency obtained from the snap-back tests is always slightly higher than those calculated from the white noise and sine-sweep tests for both of two models. The reason for this difference is that for the white noise and sine-sweep tests, the shake table was activated while for the snap-back tests, the shake table was held still and the model structure was pull-released to obtain its free vibration response. Therefore, an additional flexibility was added to the model structure due to the movement of the shake table considering that the shake table was supported by four oil-hydraulic columns (i.e. vertical actuators). Although the stiffness of those supporting columns was very high compared to the low-amplitude white noise and sine-sweep excitations, the structures seems to be slightly "softened" by this effect, leading to the observed reduction of the natural frequency. By comparing the natural frequencies in corresponding tests between the SCPT and SMRF models, the results are always lower for the SCPT model. The reason for this difference is that the beam ends clamped to the column by the Post-Tensioned (PT) strands in the SCPT model were not perfectly flat, thereby reducing the stiffness of the beam-column joints compared to the fully welded beam-column connections in the SMRF model. It is believed that this imperfection of the beam ends led to the slight reduction of the natural frequency for the whole structure. Considering the small difference in natural frequencies between the two models, it should

pointed out that it is consistent with the theoretical assumption that the natural frequencies remains unchanged after redesigning a SMRF using SCPT connections.

As shown in Tables 7-6 and 7-7, the mode shapes calculated from the different identification tests are similar for both SCPT and SMRF models. By comparing the mode shapes of the two models, the 1st and 2nd modes are essentially identical, while a small difference occurs for the 3rd mode. Considering that the seismic response is mainly governed by the lower modes, it can be concluded that both the SCPT and SMRF model structures have similar seismic behavior (i.e. no yielding) in the elastic phase, which is also in accordance with the theory. The stiffness matrix was calculated based on the modal natural frequencies and mass normalized mode shapes. Therefore, the differences among those stiffness matrices are due to the corresponding differences in frequencies and mode shapes.

By comparing the damping ratios in Tables 7-6 and 7-7, it can be observed that the 1st modal damping ratios calculated from the white noise and sine-sweep tests are much higher than the ones obtained from the snap-back tests for both models. Considering that the damping ratio for steel structures is generally considered to be 2%~3% of critical (Chopra, 2000), the 14.9% and 8.6% damping ratio values listed in the tables appear to be very high even for the SCPT model. This overestimation of the 1st modal damping can be attributed to the accuracy of the calculated transfer functions. By using the half-bandwidth method, as shown in Fig. 7-18(a), the damping ratio can be estimated as $(f_4-f_3)/2f_k$ for the results (i.e. dash line) calculated from the acceleration response in the experimental tests. However, in that figure, when the peak value m_2 is lower than the real peak m_1 due to the lower frequency resolution

of the transfer function, the real damping ratio (i.e. $(f_2-f_1)/2f_k$ in solid line) is increased to the calculated one (i.e. $(f_4-f_3)/2f_k$), which is called the missing-peak effect. Another reason for the over-estimation of the damping ratio, as shown in Fig. 7-18 (b), is called the "fatty" effect. When the calculated transfer function is fatter than the real one, the real damping ratio (i.e. $(f_2-f_1)/2f_k$) is estimated to be a higher value (i.e. $(f_4-f_3)/2f_k$). The reason for the fatty effect is that when the shake table was moving along with the above model structures in the white noise and sine-sweep tests, the response represented by the transfer function was not

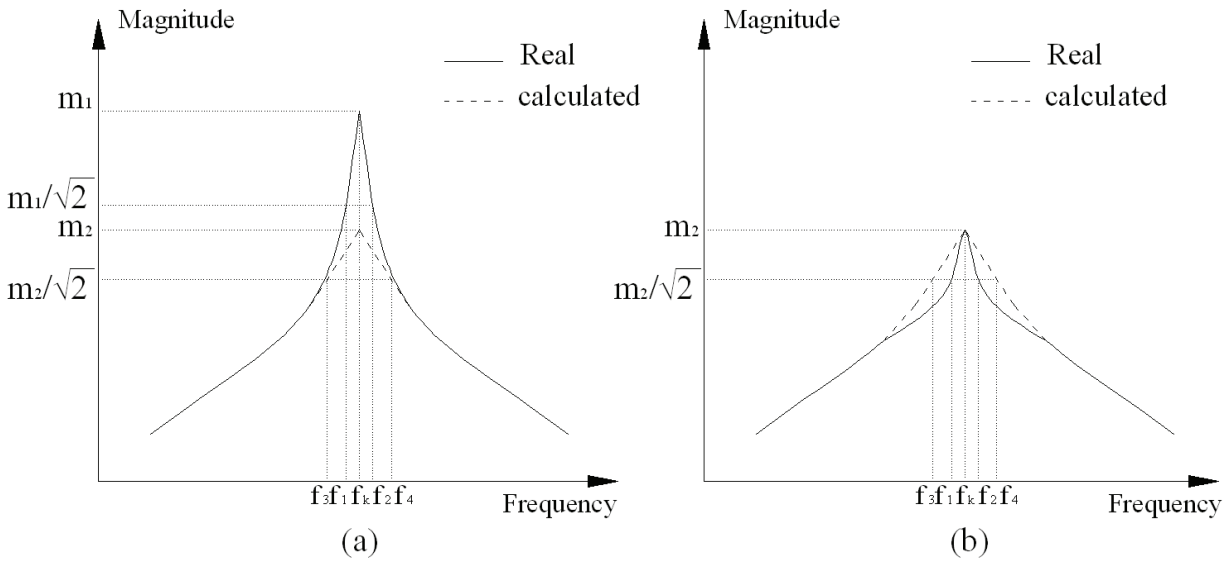

Figure 7-18 Transfer Function for Estimating Damping Ratio
(a) missing-peak effect (b) fatty effect

only from the structure itself but also from the movement of the shake table. In another words, the damping ratio is related not only to the structure but also to the foundation, which can be considered as the soil-foundation interaction. However, in the snap-back test the shake table was not moving, so the damping ratios estimated by the transfer functions through the half-bandwidth method are similar to those estimated by the free vibration

response through the logarithmic decrement decay method. Therefore, the damping ratios estimated from the snap-back tests were closer to the real ones of the model structures. Also, the differences in damping matrices are directly due to the differences in modal damping ratios and mode shapes.

Table 7-6 Dynamic Properties of the SCPT model from identification tests

Dynamic Properties	White Noise Test	Snap-Back Test		Sine-Sweep Test
Frequencies (Hz)	$\begin{bmatrix} 2.750 \\ 9.141 \\ 14.891 \end{bmatrix}$	$\begin{bmatrix} 2.973 \\ 8.919 \\ 14.534 \end{bmatrix}$		$\begin{bmatrix} 2.750 \\ 9.063 \\ 14.313 \end{bmatrix}$
Mode Shapes	$\begin{bmatrix} 0.397 & 1 & -0.962 \\ 0.752 & 0.616 & 1 \\ 1 & -0.89 & -0.356 \end{bmatrix}$	$\begin{bmatrix} 0.384 & 1 & -0.975 \\ 0.762 & 0.604 & 1 \\ 1 & -0.671 & -0.482 \end{bmatrix}$		$\begin{bmatrix} 0.444 & 1 & -0.952 \\ 0.766 & 0.666 & 1 \\ 1 & -0.82 & -0.417 \end{bmatrix}$
Modal Damping Ratios ξ (%)	$\begin{bmatrix} 14.9 \\ 1.1 \\ 1.4 \end{bmatrix}$	Half-Bandwidth $\begin{bmatrix} 2.4 \\ 1.3 \\ 1.2 \end{bmatrix}$	Decay $\begin{bmatrix} 1.0 \\ 1.3 \\ 1.2 \end{bmatrix}$	$\begin{bmatrix} 8.6 \\ 1.6 \\ 2.5 \end{bmatrix}$
Stiffness Matrix (kips/in)	$\begin{bmatrix} 248.9 & -140.7 & 7.9 \\ -140.7 & 223 & -99.6 \\ 7.9 & -99.6 & 85.4 \end{bmatrix}$	$\begin{bmatrix} 244.2 & -118.4 & 31.9 \\ -118.4 & 206.3 & -107.1 \\ 31.9 & -107.1 & 83.2 \end{bmatrix}$		$\begin{bmatrix} 230.5 & -118.5 & 16.1 \\ -118.5 & 210.7 & -104.4 \\ 16.1 & -104.4 & 83.5 \end{bmatrix}$
Damping Matrix (lb-sec/in)	$\begin{bmatrix} 101.3 & 1.2 & 49.8 \\ 1.2 & 144.2 & 66.4 \\ 49.8 & 66.4 & 161.2 \end{bmatrix}$	$\begin{bmatrix} 83.1 & -15.4 & 6.0 \\ -15.4 & 72.2 & -18.5 \\ 6.0 & -18.5 & 49.6 \end{bmatrix}$		$\begin{bmatrix} 142.7 & -41.3 & 40.1 \\ -41.3 & 159.1 & -4.1 \\ 40.1 & -4.1 & 116.9 \end{bmatrix}$

Table 7-7 Dynamic Properties of the SMRF model from identification tests

Dynamic Properties	White Noise Test	Snap-Back Test	
Frequencies (Hz)	$\begin{bmatrix} 3 \\ 9.625 \\ 15.188 \end{bmatrix}$	$\begin{bmatrix} 3.25 \\ 9.563 \\ 15.188 \end{bmatrix}$	
Mode Shapes	$\begin{bmatrix} 0.401 & 1 & 1 \\ 0.754 & 0.577 & -0.776 \\ 1 & -0.866 & 0.391 \end{bmatrix}$	$\begin{bmatrix} 0.413 & 1 & 1 \\ 0.77 & 0.545 & -0.847 \\ 1 & -0.847 & 0.554 \end{bmatrix}$	
Modal Damping Ratios ξ (%)	$\begin{bmatrix} 15.7 \\ 2.5 \\ 1.9 \end{bmatrix}$	Half-Bandwidth	Decay
		$\begin{bmatrix} 2.1 \\ 0.8 \\ 0.6 \end{bmatrix}$	$\begin{bmatrix} 0.7 \\ 0.8 \\ 1.3 \end{bmatrix}$
Stiffness Matrix (kips/in)	$\begin{bmatrix} 361.1 & -133.3 & 26.4 \\ -133.3 & 172.7 & -103 \\ 26.4 & -103 & 103.1 \end{bmatrix}$	$\begin{bmatrix} 286.9 & -124.7 & 48 \\ -124.7 & 176.2 & -123.6 \\ 48 & -123.6 & 129.3 \end{bmatrix}$	
Damping Matrix (lb-sec/in)	$\begin{bmatrix} 184.4 & 12.4 & 41.6 \\ 12.4 & 166.2 & 55.5 \\ 41.6 & 55.5 & 215.4 \end{bmatrix}$	$\begin{bmatrix} 51 & -2.9 & 4.9 \\ -2.9 & 37.8 & -4.9 \\ 4.9 & -4.9 & 44.7 \end{bmatrix}$	

7.2 Shake Table Fidelity

In seismic tests, the earthquake excitation is simulated by the vibration of the shake table. Therefore, the accurate reproduction of the earthquake excitation is a key performance characteristic for a shake table system.

As shown in Figs. 7-19 and 7-20, the shake table fidelity was evaluated by comparing the reference (desired) and feedback (achieved) acceleration response spectra for 50% and 125%-intensity earthquake motions, respectively. The 50%-PGA ground motion is representative of lower-intensity input while the 125% PGA ground motion is representative of higher-intensity motions, and those two tests were conducted for the SCPT model. For the lower-intensity ground motion, the spectrum obtained from the feedback ground acceleration matched well the spectrum calculated from the reference acceleration, which suggests that the shake table reproduced the lower-intensity earthquake motions with high accuracy. For the higher-intensity ground motion, the feedback spectrum matched well the reference spectrum in the lower frequency range but had some deviation in the high frequency range. Considering that the natural frequency of the 1st mode in both of the two models is lower than 3.5 Hz, it can be concluded that the shake table reproduced the earthquake excitation effectively and accurately in the natural frequency range of the test structures. The deviation between the reference and feedback spectrum in the higher frequency range can be explained by the fact that when the ground motion input reached near the displacement limit of the shake table, a visible rotation of the shake table was observed especially in the highest-intensity (i.e. 150%) excitation. This rotation effect distorted slightly the feedback spectra in the high frequency range.

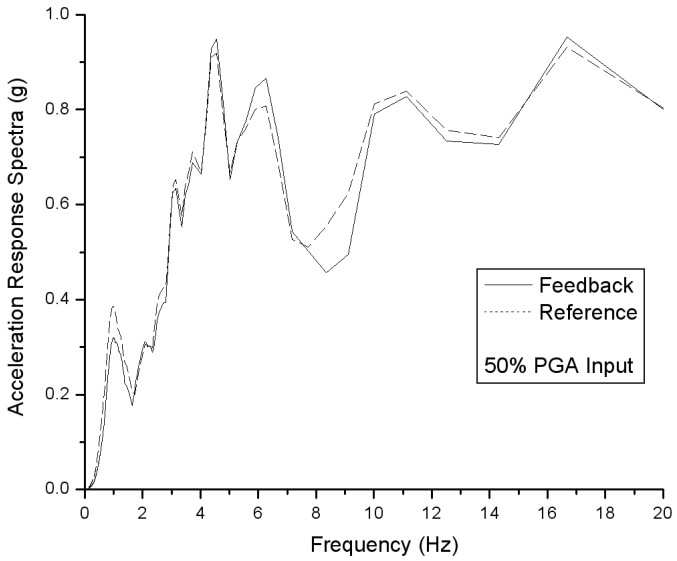

Figure 7-19 Acceleration Spectra for 50%-intensity Earthquake Excitation

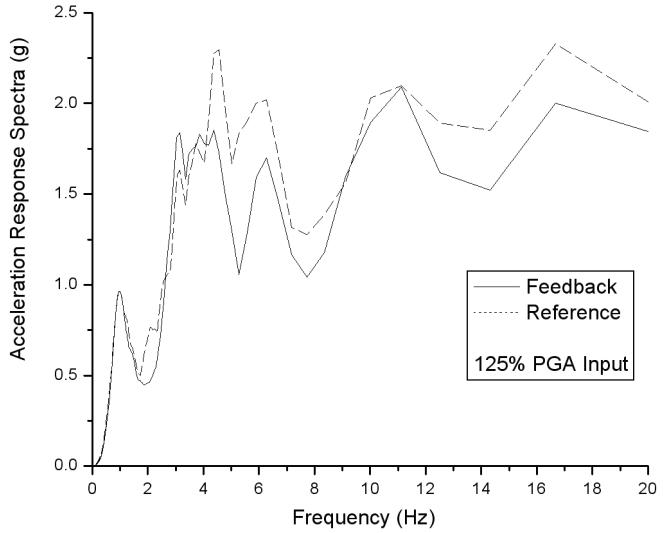

Figure 7-20 Acceleration Spectra for 125%-intensity Earthquake Excitation

7.3 Global Response

In this section, the general behavior of both test specimens is discussed. Thereafter, the acceleration and displacement response for the SCPT and SMRF models are presented. The results are discussed by comparing peak displacement and acceleration values using bar

charts. The hysteresis properties are finally discussed. Note that 3 different phases of seismic tests were performed on the SCPT model structure. Each phase included 7 different intensity ground motions from 25% to 150% intensity. Each intensity earthquake excitation was conducted twice; one time in the positive direction and a second time in the negative direction. Details about the testing sequence can be found in the test protocol shown in Section 6.3.

7.3.1 General Specimen Behavior

The seismic tests were conducted on the SMRF and SCPT frame models under the earthquake excitations from 25% to 150% intensity. During those seismic tests, no significant inelastic deformations of the 3 stories were observed. Also, no local buckling or visible local yielding deformations of critical sections in beam-to-column joints were found. These observations are consistent with the results summarized in Section 7.1.4 and verify that both frame specimens exhibited good seismic behaviors as expected.

Under the 150%-intensity earthquake excitation, a visible rotation of the shake table was observed for both SMRF and SCPT models. This rotation may be due to the displacement limit of the shake table and also be due to the limit of axial support capacity of the vertical actuators under the shake table. As discussed in previous sections, this rotation may lead to undesirable impact on the seismic performance of the two models since no such ground rotation effects were considered in the models used for the prediction analysis.

7.3.2 Absolute Acceleration Response

As reported by Kircher (2003), the damage to nonstructural components led to 50% of the $18.5 billion total loss during the 1994 Northridge earthquake. Recall that the prototype building of the SCPT model was designed as a steel frame hospital, which would have many acceleration-sensitive nonstructural components. Therefore, it is very important to reduce the acceleration response in order to decrease the damage of the acceleration-sensitive nonstructural components and the corresponding economic loss after seismic hazards such as the 1994 Northridge earthquake.

The floor acceleration time histories of the SCPT and SMRF models for all the seismic tests are shown in Appendix E. The peak floor acceleration responses of two models for different-intensity ground motions are shown in Figs. 7-21 to 23 for positive direction excitations and in Figs. 7-24 to 7-25 for negative direction inputs. In those bar charts, the peak accelerations of the SCPT model are always lower than those of the SMRF model. For the low-intensity (25%-100%) ground motions, the acceleration in the SCPT model is reduced by up to 37% compared to that in the SMRF model, while this reduction reaches up to 41.8% after the 100%-intensity excitations. The large reduction in the acceleration response demonstrates the excellent seismic performance of the SCPT structure and also validates the design procedure focused mainly on acceleration issue since the design Relative Performance Index (RPI) had a 70% weighting factor on the acceleration response (see Section 5.4).

From the results shown in Figs. 7-21 to 7-26, it is also observed that, for the SCPT model, the acceleration response for the 2nd and 3rd phase excitations is increased compared to that of the 1st phase excitations. The reason for this increase in acceleration is that after the 1st

phase 25%~150% intensity earthquakes, most of the Energy-Dissipating (ED) bars yielded which may reduce the capability of energy dissipation in ED bars since for the post-yielding ED bars with the residual deformation, the yielding force can be increased slightly due to the strain hardening effect although this effect might be very slight. Also, the additional vertically supporting bars installed on the top and bottom of the beams ends stiffened the structure which may lead to a decrease of the natural period of the structure. Those two effects lead to the higher acceleration response in the 2nd or 3rd phase excitations. Although the acceleration responses are increased in the 2nd and 3rd phase tests in the SCPT model, they are still lower than those in the SMRF model. Even after one or two 150%-intensity earthquake attacks, the seismic performance of the SCPT model without repairing its structural components is still better than the SMRF model without any earthquake attack history from the point of view of acceleration response.

The trend in acceleration responses observed above is slightly different for the 150%-intensity tests is. The acceleration responses for this highest intensity test in the 2nd and 3rd phase of the SCPT model and in the SMRF model are similar to the corresponding peak accelerations in the 125%-intensity tests. This is because only the 150%-intensity test in the 1st phase excitations of the SCPT model reached the real 150% amplitude of the ground motions while other 150%-intensity tests such as 150% in the 2nd or 3rd phase of the SCPT model and 150% in the SMRF model were not excited to the real 150% amplitude due to the limitation of the shake table. This conclusion was reached by comparing the actural amplitudes of input ground motions for those 150%-intensity tests.

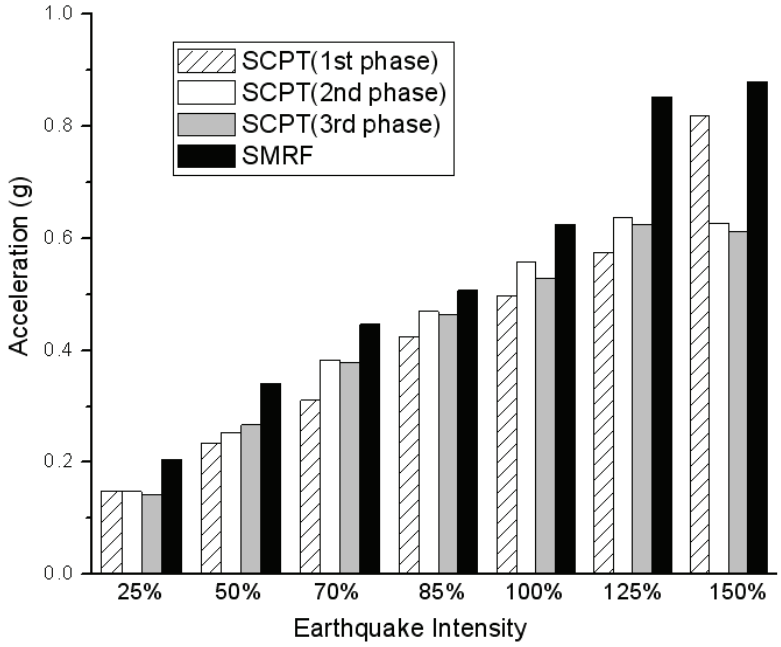

Figure 7-21 Peak Acceleration Response of the 1st floor for the SCPT and SMRF Models in Positive Direction Seismic Tests

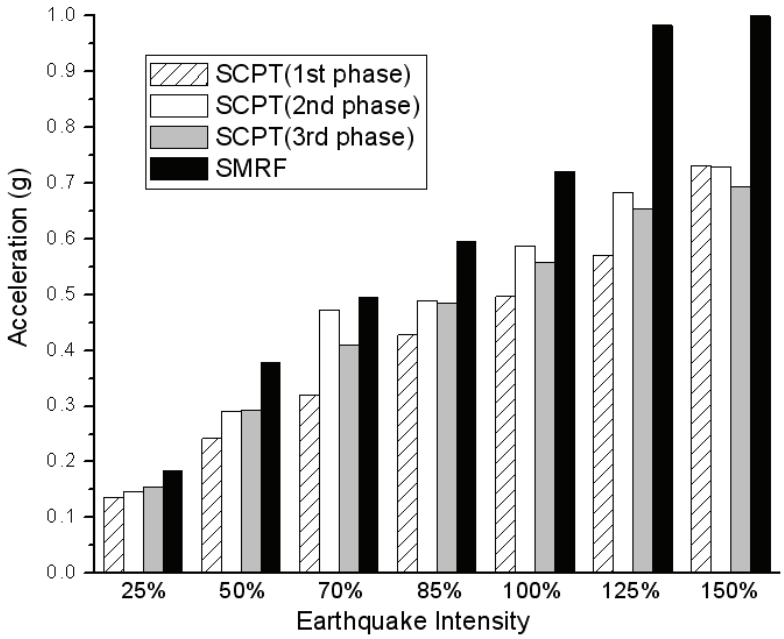

Figure 7-22 Peak Acceleration Response of the 2nd floor for the SCPT and SMRF Models in Positive Direction Seismic Tests

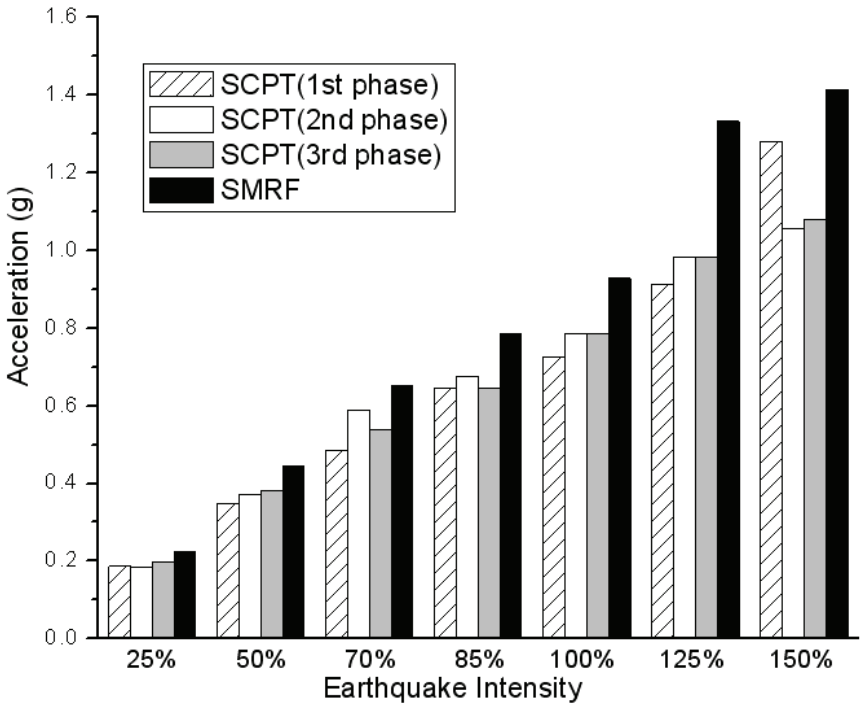

Figure 7-23 Peak Acceleration Response of the 3rd floor for the SCPT and SMRF Models in Positive Direction Seismic Tests

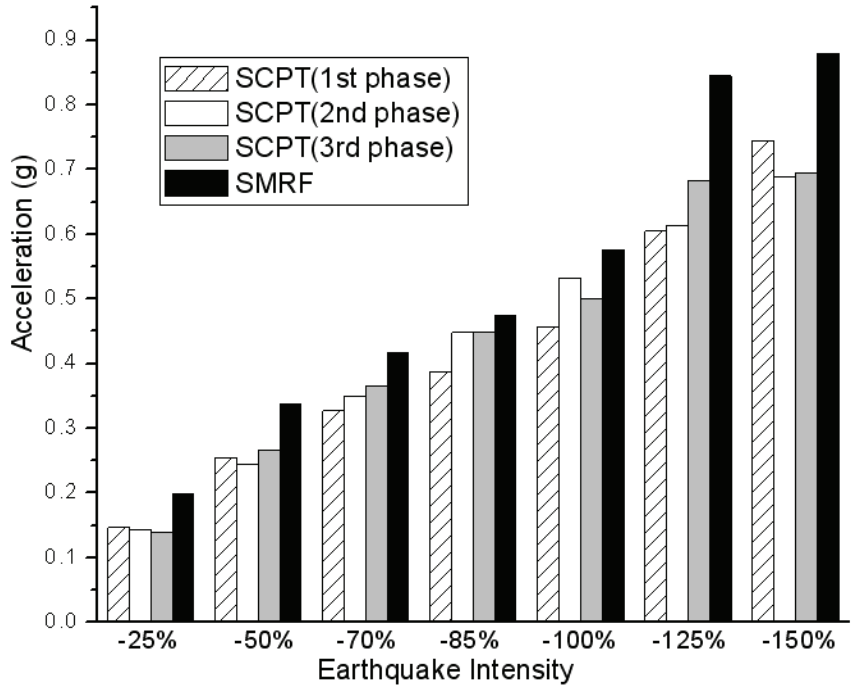

Figure 7-24 Peak Acceleration Response of the 1st floor for the SCPT and SMRF Models in Negative Direction Seismic Tests

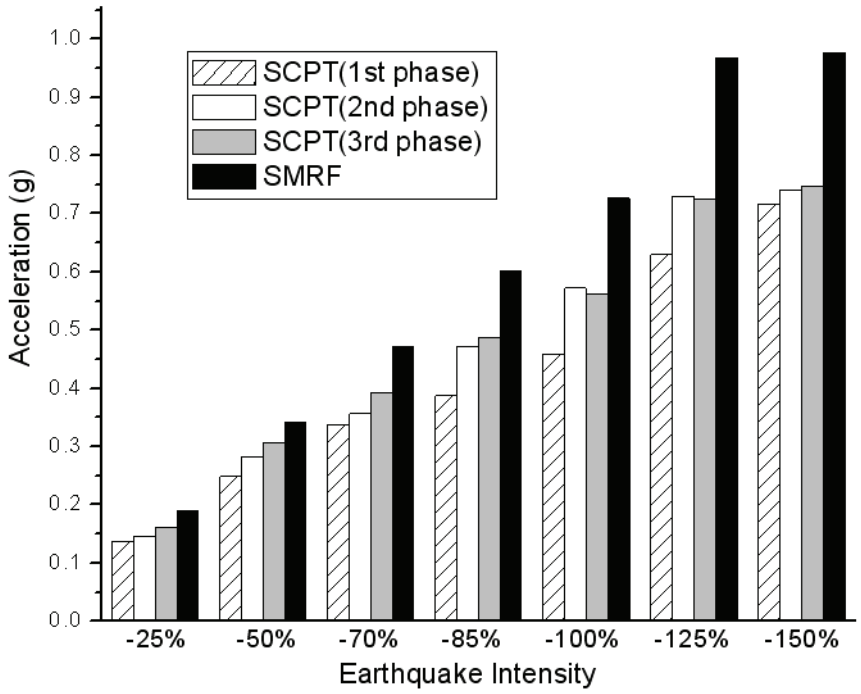

Figure 7-25 Peak Acceleration Response of the 2nd floor for the SCPT and SMRF Models in Negative Direction Seismic Tests

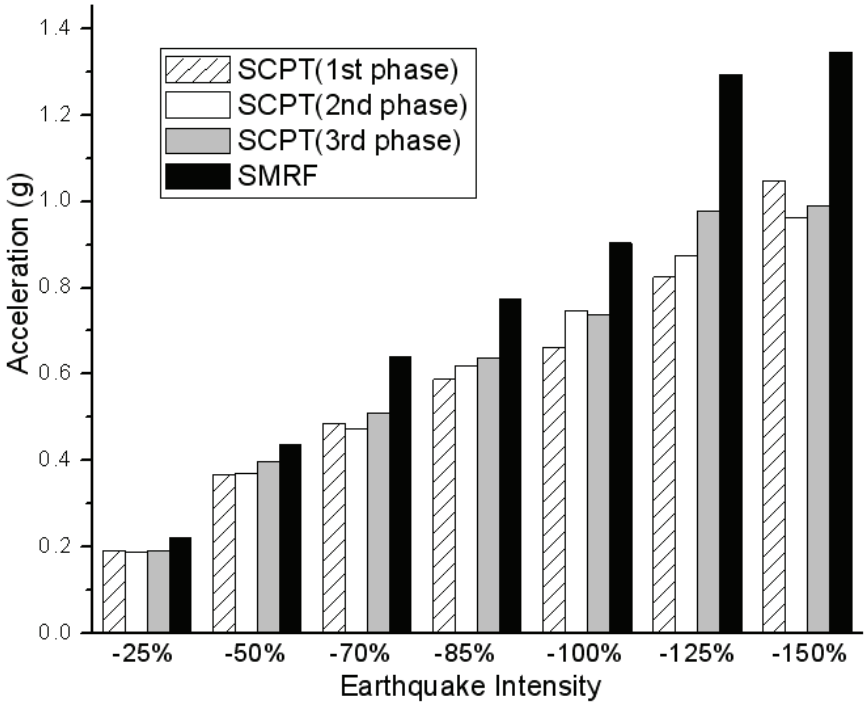

Figure 7-26 Peak Acceleration Response of the 3rd floor for the SCPT and SMRF Models in Negative Direction Seismic Tests

7.3.3 Inter-Story Drift Response

In this section, the displacement response of the two model frames is presented by comparing their inter-story drifts. The inter-story drift time histories for both models are presented in Appendix F. For comparison purpose, bar charts are used again to compare maximum inter-story drifts, as shown in Figs. 7-27 to 7-29 for positive-direction ground motions and in Figs. 7-30 to 7-32 for negative-direction excitations.

In these figures, it can be seen that the maximum inter-story drifts of the two model structures for the 100%-intensity ground motions are lower than 1%. Considering the excitation with 10% probability of exceedance in 50 years, the corresponding performance level is immediate occupancy with 0.7% maximum inter-story drift according to FEMA 356, while the next level is life safety with 2.5% maximum inter-story drift. Therefore, the performance of both of two frame models can be considered to be in accordance with the immediate occupancy level since the 1% drift is very close to 0.7% and far away from the 2.5%, and no yielding occurred in the beams or columns (see Section 7.4.1).

As indicated in those maximum inter-story drift figures, the drift values of the SCPT models are similar or slightly higher compared to those in the SMRF models in the corresponding intensity seismic tests. Therefore, it can be pointed out that the results are consistent with the design procedure since the RPI (see Section 5.4) had a 30% weighting factor for displacement response and more efforts were made to reduce the acceleration response. Another argument can be made that although the drift response in the SCPT model is

slightly higher than that in the SMRF model, the seismic performance of the SCPT structure is still better since no yielding occurred in the beams or columns while beams and columns yielded in the SMRF model.

It can be also observed from the results shown in Figs 7-27 to 7-32 that the maximum inter-story drifts of the SCPT model for the 2nd or 3rd phase excitations are higher than those in the 1st phase tests. This trend is similar to that observed for the acceleration response. As explained in Section 7.3.2, the reason is also that the capacity of energy dissipation was reduced for the post-yielding ED bars after the 1st phase tests. Again, for the 150%-intensity excitations, the trend (e.g. the highest value in the 150%-intensity test is the response from the 1st phase test as shown in Fig. 7-28) is different than the above discussions from other lower-intensity earthquakes, which is due to the insufficient input ground motion by the limit of the shake table as explained in Section. 7.3.2.

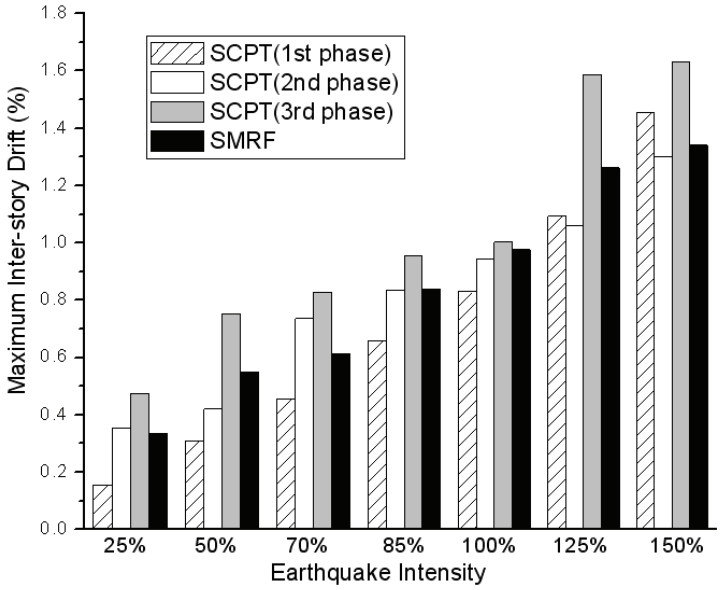

Figure 7-27 Maximum Inter-story Drift of the 1st floor for the SCPT and SMRF Models in Positive Direction Seismic Tests

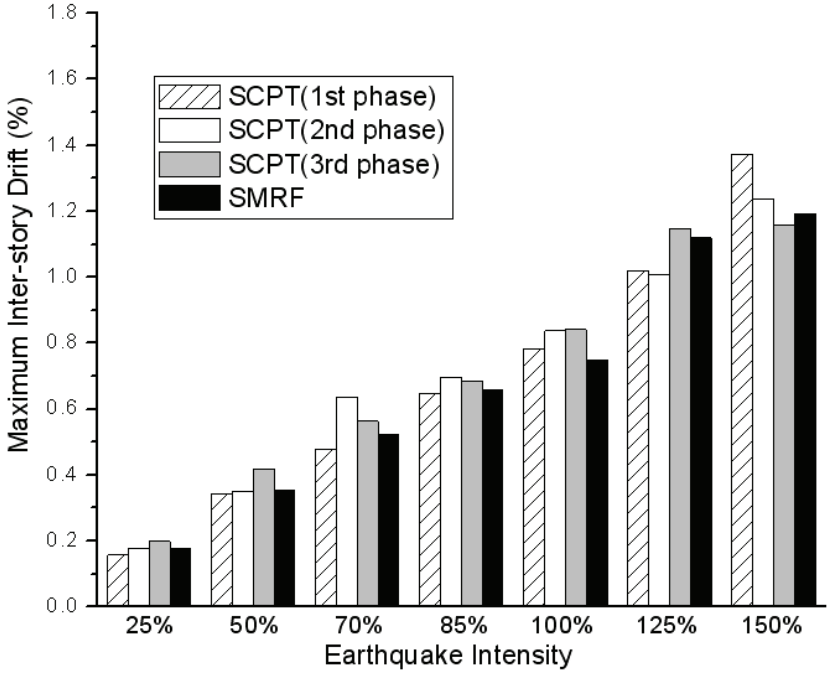

Figure 7-28 Maximum Inter-story Drift of the 2nd floor for the SCPT and SMRF Models in Positive Direction Seismic Tests

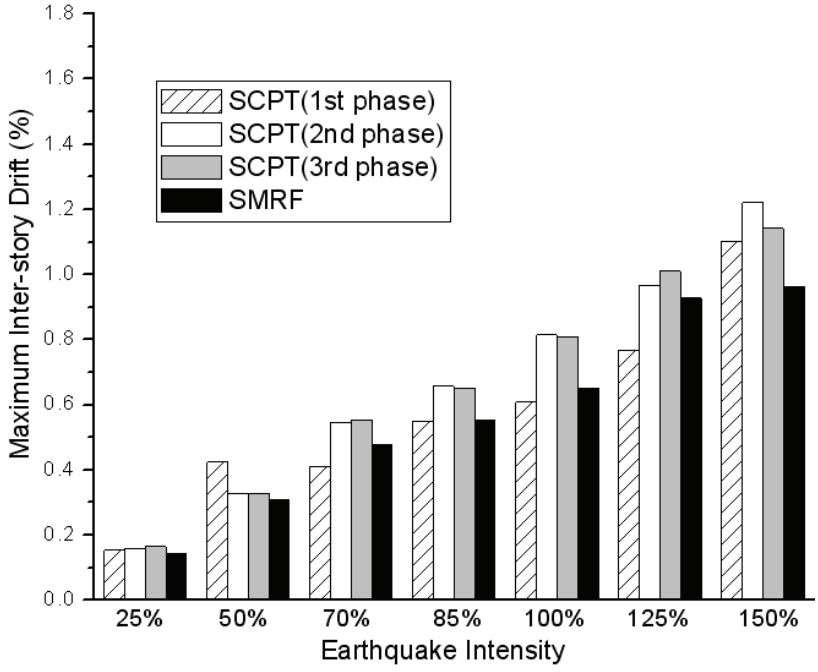

Figure 7-29 Maximum Inter-story Drift of the 3rd floor for the SCPT and SMRF Models in Positive Direction Seismic Tests

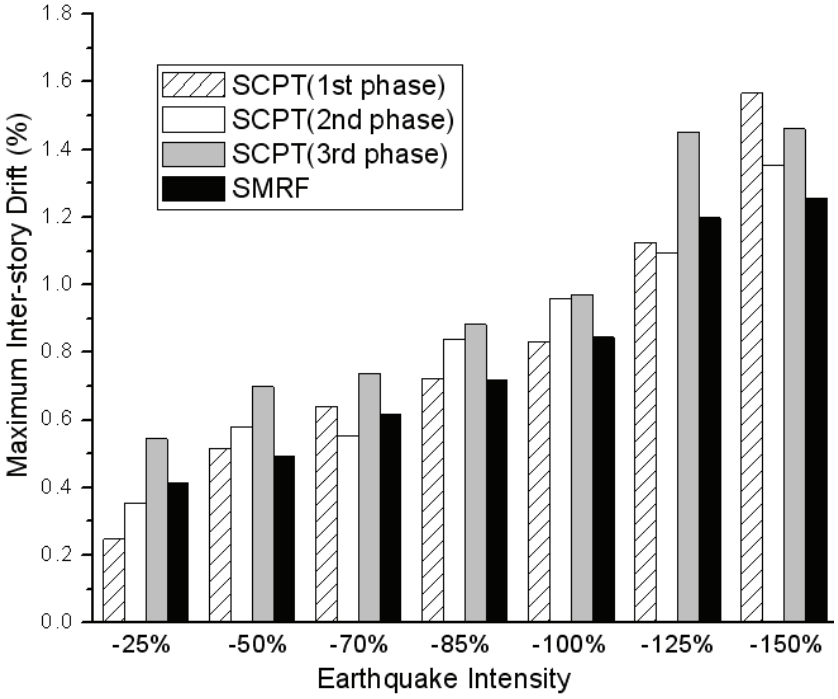

Figure 7-30 Maximum Inter-story Drift of the 1st floor for the SCPT and SMRF Models in Negative Direction Seismic Tests

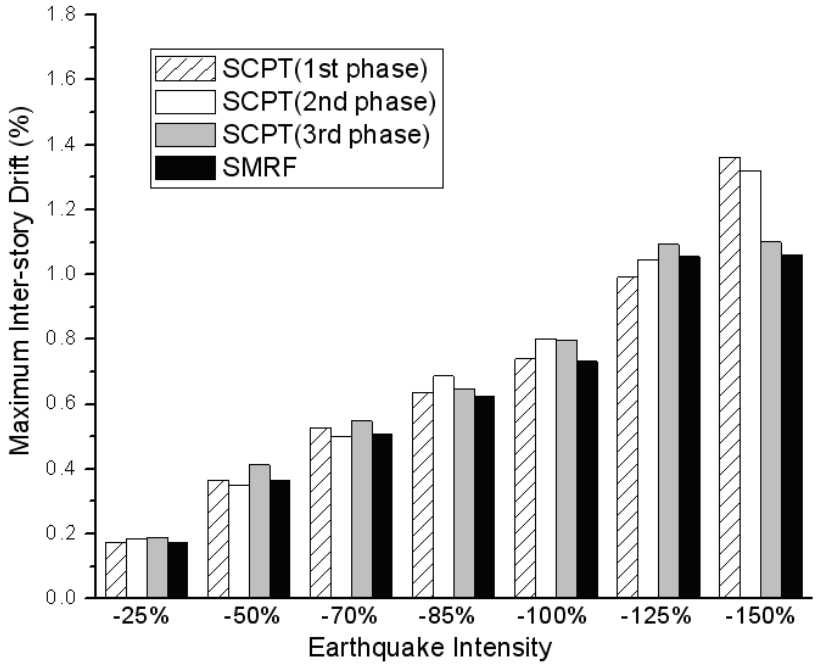

Figure 7-31 Maximum Inter-story Drift of the 2nd floor for the SCPT and SMRF Models in Negative Direction Seismic Tests

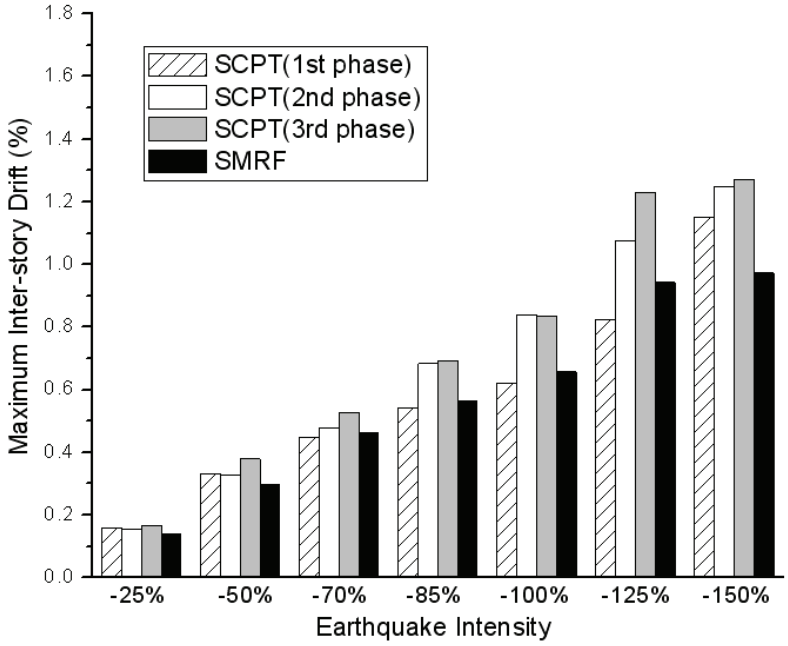

Figure 7-32 Maximum Inter-story Drift of the 3rd floor for the SCPT and SMRF Models in Negative Direction Seismic Tests

7.3.4 Hysteresis Properties

The hysteretic relationship between the base shear and top floor relative displacement for both the SCPT and SMRF models under the positive 125% intensity seismic excitation are shown in Figs. 7-33, 7-34 and 7-35, respectively, since the ground input was insufficient for the 150% intensity earthquake as mentioned earlier. In these figures, the bold slope lines represent the generalized stiffness for the 1st mode, in which K_1 is the generalized stiffness for the 1st mode of the SCPT model and is calculated based on the 1st mode shape Φ_1 and stiffness matrix K (i.e. $K_1=\Phi_1^T * K * \Phi_1$) obtained from White Noise Tests listed in Table 7-6 (see Section 7.1.4) while K_2 is that of the SMRF model based on the same calculation

method using the structural properties obtained from White Noise Tests as shown in Table 7-7 (see Section 7.1.4). From these figures, it is observed that the initial stiffness of the SCPT model is similar to the K_1 while the initial stiffness of the SMRF model is lower than K_2 but closer to K_1. These results suggest that the initial stiffness of both models is similar, which is in accordance with the theory (i.e. using SCPT connections have less influence on the initial stiffness of the SMRF structures). Also, it indicates that the responses are mainly contributed from the 1st mode response of the structures. The deviation between the initial stiffness of the SMRF model and K_2 is due to the accuracy of the transfer functions, which are used to calculate the modal frequencies and mode shapes in order to obtain stiffness matrix as discussed in Section 7.1. Since the base shear was calculated as the summation of the inertia forces in the three floors, the damping response is included in these hysteretic loops. Also, it is believed that the rotation effect of the shake table and hysteresis properties of vertical supporting actuators (see Section 8.2) made some influence on these hysteretic loops. Therefore, those issues discussed are the reasons that the hysteretic loops obtained experimentally have a little difference with the ideal theoretical ones. It is seen that the loop area in Fig. 7-33 for the SCPT model is larger than that in Fig. 7-34, which is due to the vertical movement of the beams in the 1st phase tests while this movement was limited by the additional bars installed on the top and bottom of the beam flanges in the 3rd phase tests. It is also found that the maximum base shear of the SCPT model in both the 1st and 3rd phase +125% intensity seismic tests is lower than that of the SMRF model, which indicates that the SCPT model exhibited better seismic performance than that of the SMRF model. The hysteresis energy issues will be discussed in Section 7.5.

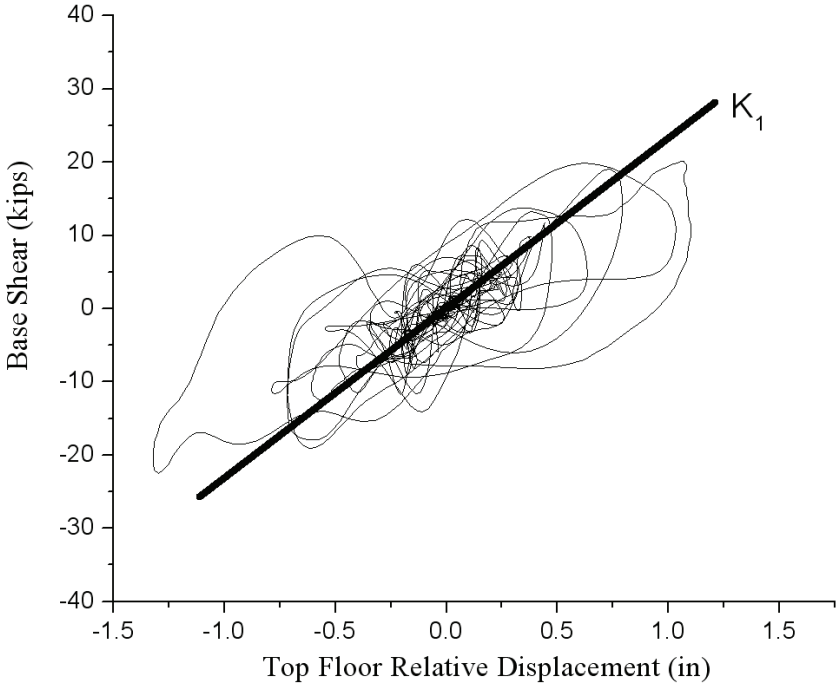

Figure 7-33 Hysteresis for the SCPT Model in test PE6A (1st phase, +125% intensity)

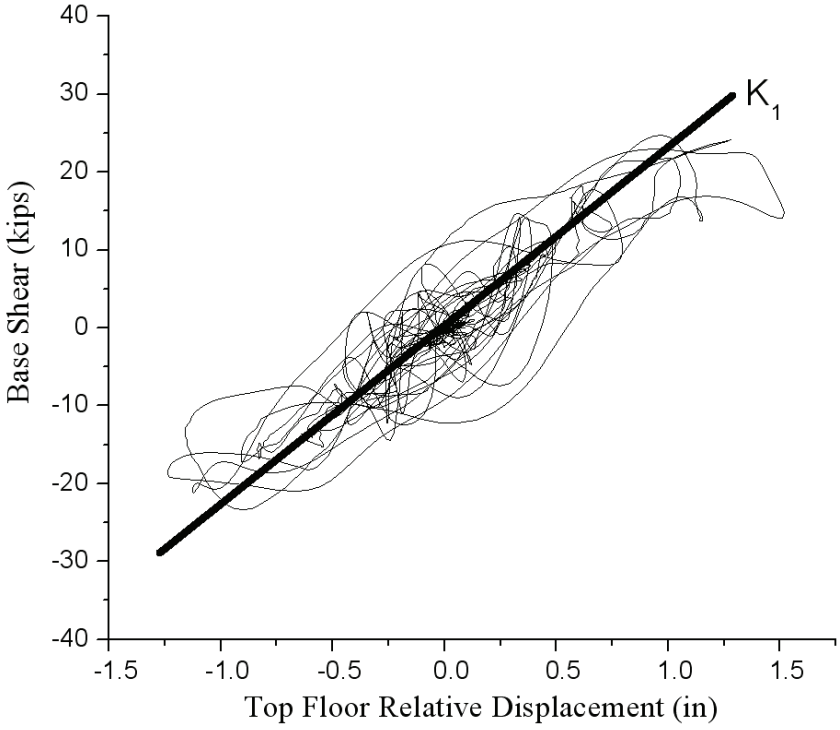

Figure 7-34 Hysteresis for the SCPT Model in test PE22 (3rd phase, +125% intensity)

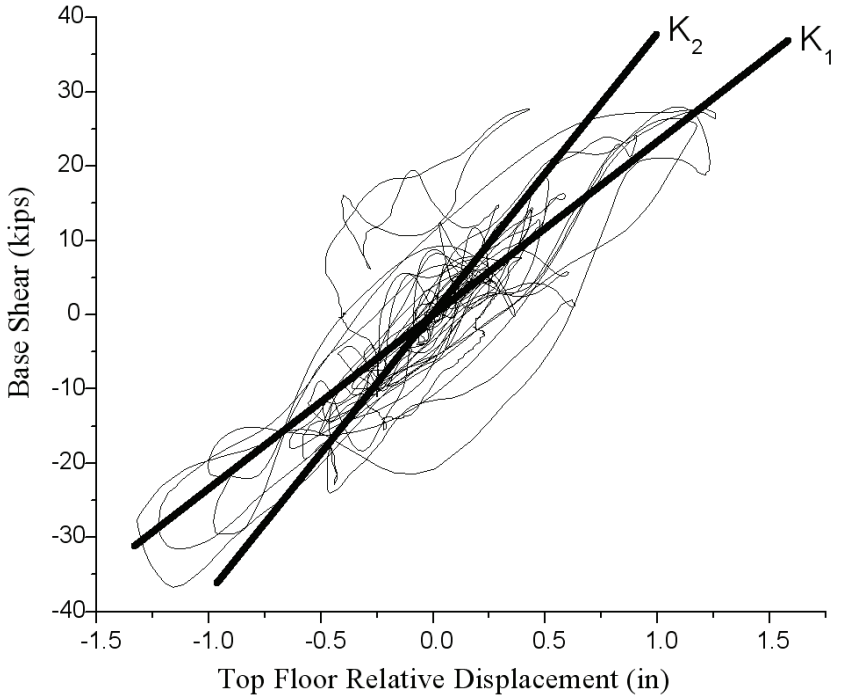

Figure 7-35 Hysteresis for the SMRF Model in test ME06A (+125% intensity)

7.4 Local Response

It is very important to evaluate the seismic performance of the individual structural components since the local response presents an index of the damage level and repair cost to the structures after seismic hazards. In this section, the seismic performance of beams and columns as well as the Energy-Dissipating (ED) bars and Post-Tensioned (PT) strands are discussed.

7.4.1 Beams and Columns

To investigate the seismic performance of the beams and columns, strain gages were installed at critical sections of the beam-column joints as shown in Section 6.4. According to

the mechanics of material, for structural steel, the strain is the direct index to evaluate if a cross section has yielded. The corresponding moment can be calculated based on the strain and section property. Therefore, the direct index, strain, is used as the only criteria for performance evaluation.

The yielding strain of the steel with 50ksi yielding strength used for the beams and columns in the SCPT and SMRF models was $1724x10^{-6}$ with the corresponding elastic modulus 29000ksi. If the strain on the exterior surface of the beam or column flanges exceeds the yielding strain, the beam or column can be considered to begin yielding. Through checking the strain time histories in different seismic tests, it was found that no yielding occurred in the beams or columns of the two models for the seismic tests with 25% to 100% intensity, which demonstrates that the seismic performance of the SMRF structure satisfied the design purpose that the structure would remain in the elastic range under the immediate occupancy earthquake level.

From the approximate 50 strain gages installed in each of two model structures, one strain gage was selected for representing each beam in the 1^{st}, 2^{nd} and 3^{rd} floor and each column in the base. The tag names of the selected strain gages were SGB1-3, SGB2-3, SGB3-4, SGC0-2 and SGC0-7 (see Section 6.4). The strain time histories of those strain gages for the 125% and 150% intensity seismic tests are presented in Appendix G, since no yielding occurred in 25%~100% intensity tests. The maximum strain obtained from those time histories were plotted in bar charts, as shown in Figs. 7-36 to 7-41. The dash line in these figures represents the yielding strain.

As seen in Fig. 7-36 and 7-37, the strains in the beams of the 1st and 2nd floor of the SMRF model exceed the yield limit, while no yielding occurs in those same beams of the SCPT model. As expected, the ED bars yielded instead of the beams as a result of the gap opening in the beam-column joints. These results demonstrate that under the high intensity (125% and 150%) earthquake hazards, the SCPT structure performed better since no damage occurred to the main structural components. The cost associated with repair of the main structural components is much more than the cost of replacing the ED bars. As shown in Fig. 7-38, although no yielding occurred in the 3rd floor beams for both models, the strains in the SCPT model is still much lower than those in the SMRF model. This result indicates that that the beams of the SMRF model would yield under higher (>150%) earthquakes.

As shown in Fig. 7-39 and 7-40, the base columns of the SMRF model yielded slightly, while still no yielding occurred in the SCPT structure, which is in accordance with the conclusion based on the performance of the beams. For the weak-beam-strong-column design philosophy of the SMRF building, the columns should not begin yielding before most of the beams yields. However, the two exterior columns were reduced from a w5x19 to w5x16 section due to the material availability, which decrease the yielding strength of the columns. Also, the beams in the 1st and 2nd floor of the SMRF model had yielded. Considering these two facts, the slight yielding of the columns can be acceptable based on the weak-beam-strong-column approach. Again, as explained in previous sections, the results shown in these figures for the 150%-intensity earthquakes are similar to those for

125%-intensity excitations due to the limit of the shake table leading to the insufficient amplitude of ground motions.

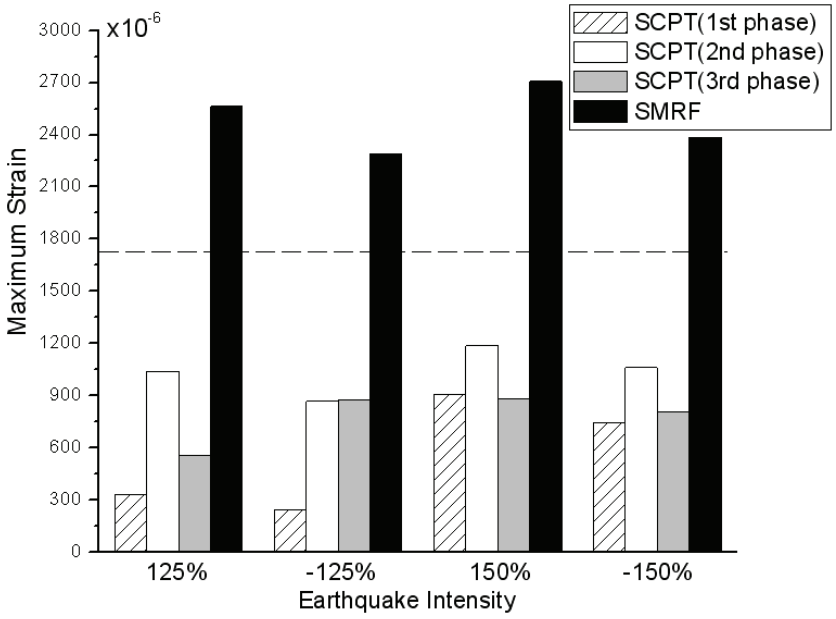

Figure 7-36 Maximum Strains of the beam of the 1st floor for the SCPT and SMRF Models

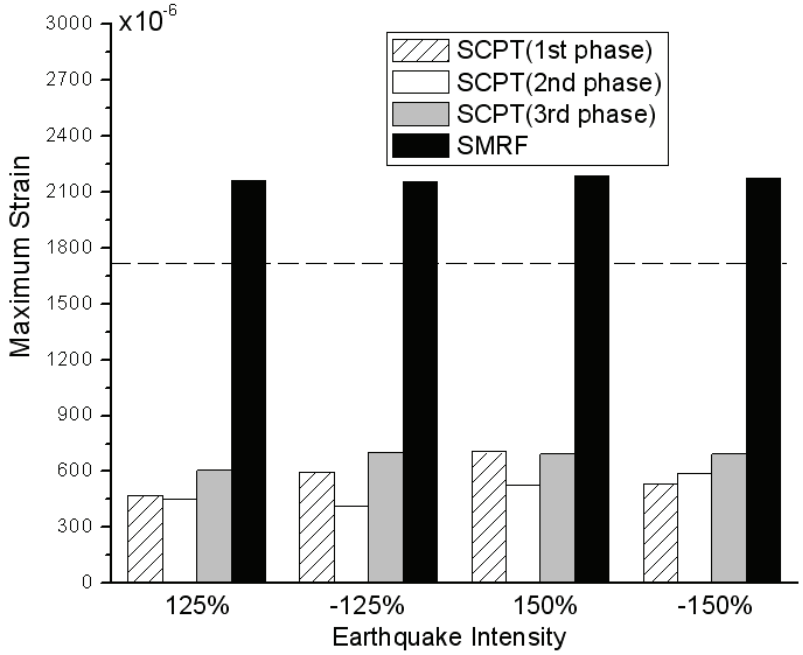

Figure 7-37 Maximum Strains of the beam of the 2nd floor for the SCPT and SMRF Models

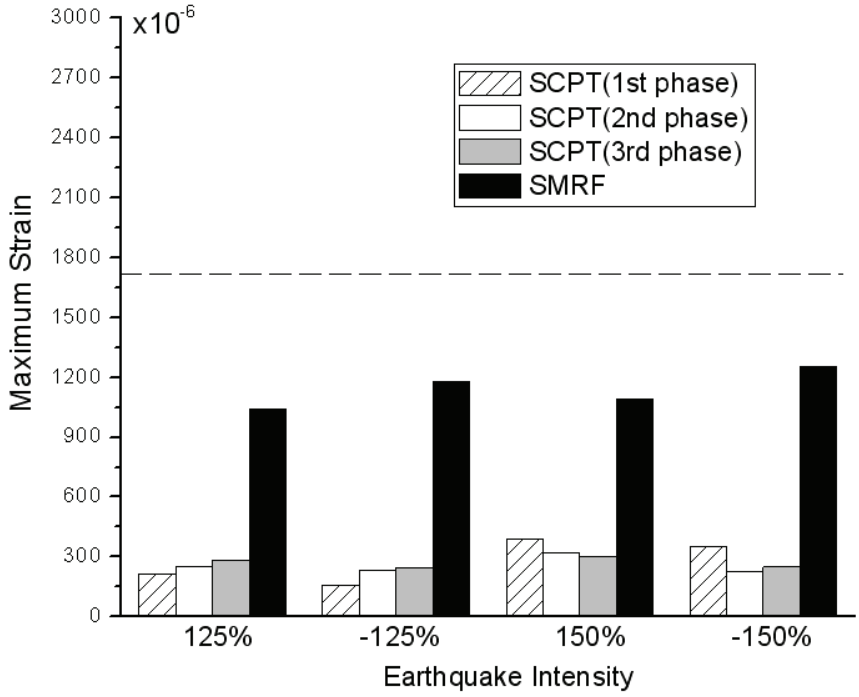

Figure 7-38 Maximum Strains of the beam of the 3rd floor for the SCPT and SMRF Models

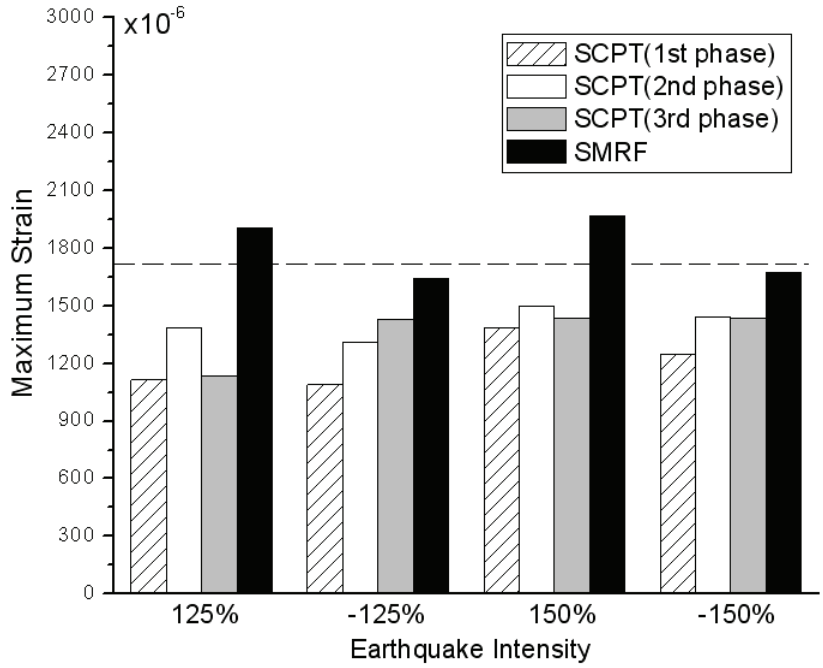

Figure 7-39 Maximum Strains of the exterior column of the base connection for the SCPT and SMRF Models

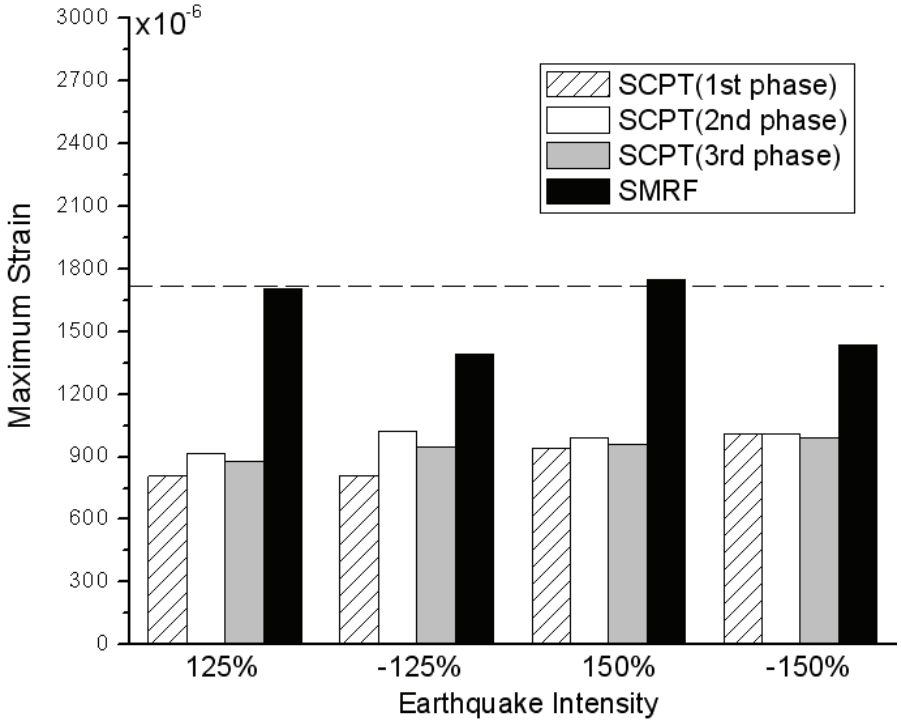

Figure 7-40 Maximum Strains of the center column of the base connection for the SCPT and SMRF Models

7.4.2 Energy Dissipating (ED) Bars

ED bars were used to dissipate energy in the SCPT model as a result of gap opening. The deformation of the ED bars was proportional to the gap opening. In order to measure the gap opening, potentiometers were installed on the top and bottom of the beam flange in each beam-column joint. However, due to unknown circuit problem of the conditioner, which was used to transfer the signal from the potentiometers to the data recording system, the results for the 3rd floor were unavailable. For the 1st and 2nd floor, the deformation of the ED bars is 82% of the gap-opening obtained from the potentiometer since the potentiometer measured the gap-opening on the outside of the beam flange, while the ED bars were welded on the inside of the beam flange. The gap opening angles were calculated as the ratio of the gap-

opening obtained from potentiometers to the depth of the beam. Two potentiometers (PM1-2 and PM2-6) are selected to represent the gap-opening for the 1st and 2nd floor, respectively. Because no yielding occurred in the ED bars for the 25%~100% intensity seismic tests, only the maximum gap-openings for the 125% and 150%-intensity seismic tests with positive and negative directions are shown in Fig. 7-41 and 7-42. The dash line (0.0015 rad) included in these figures represents the gap opening causing first yield of the ED bars. The gap-opening of the 2nd floor for 150% intensity in the 3rd phase was unavailable due to the invalid data reading.

In these figures, it can be observed that almost all of the ED bars yielded under the 125% or 150% intensity earthquakes and the largest ductility (0.0039 rad) reached a value of 2.5, which demonstrates the good capability of inelastic deformation and energy dissipation. It is also noted that the gap opening in the 2nd and 3rd phase is larger than that in the 1st phase for the same intensity earthquake. Vertical supports were installed for the 2nd and 3rd phases which may have limited the rotation of the beam ends. Therefore, the explanation of this phenomenon is that the vertical support stiffened the structure, which led to the higher response compared to those in the SCPT frame without vertical supports. This higher response caused also an increase in the deformations of the ED bars. Such higher response was also observed for the accelerations and inter-story drifts, which is in accordance with this explanation.

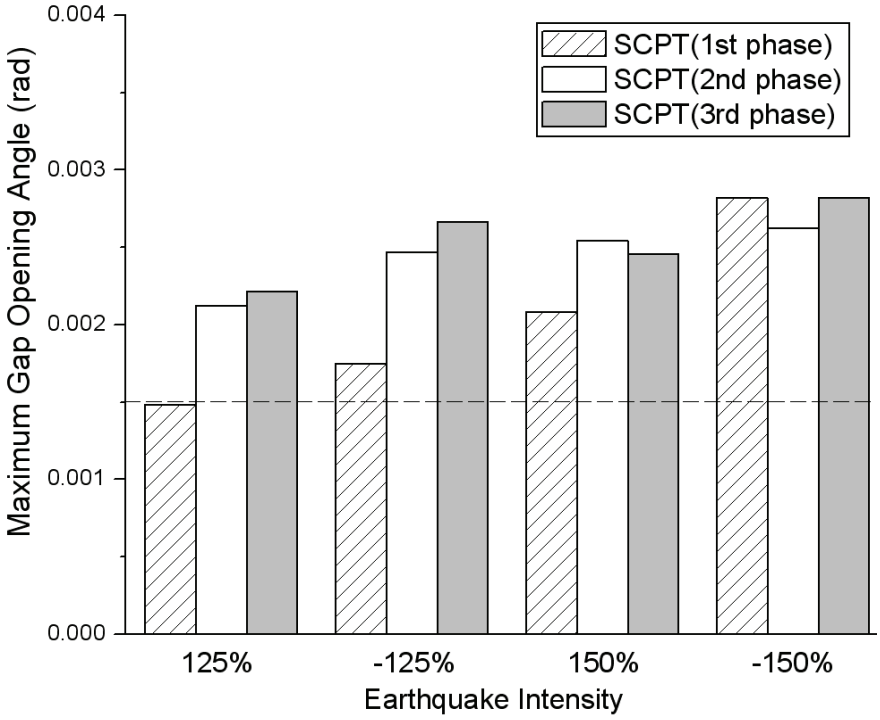

Figure 7-41 Gap Opening of the beam-column joint in 1st floor for the SCPT Model

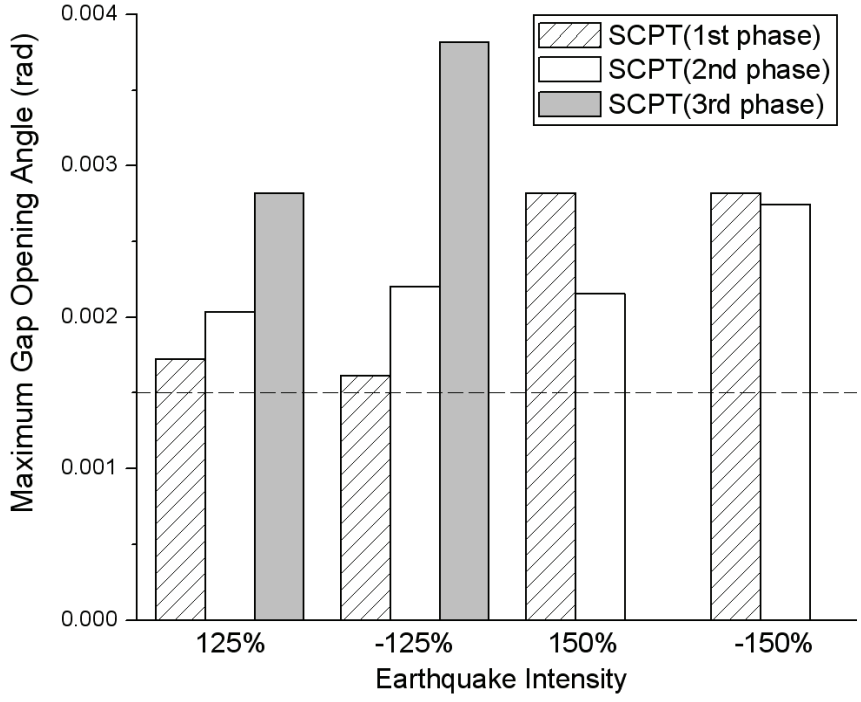

Figure 7-42 Gap Opening of the beam-column joint in 2nd floor for the SCPT Model

7.4.3 Post-Tensioned (PT) Strands

The PT strands were used to provide the re-centering force in the SCPT model. Maintaining the stress in the PT strands in the elastic range during the seismic tests is a guarantee for the good ability of re-centering.

The deformation in the PT strands was calculated using approximately 50% of the measured gap-opening since the PT strands were on the center of the beam section. The relations between the force and deformation of the PT strands during the high-intensity (125% and 150%) level seismic tests are shown in Figs. 7-43 to 7-54, where the force is the summation of the forces in the two PT strands at the same floor. The negative deformation means the gap opening transfers from the top of the beam to the bottom of the beam while the PT strands is elongated for both directions of gap opening. Note that results for the 3rd floor are not shown due to the unavailable data of the gap opening for that floor.

As shown in Fig. 7-54, the maximum force in two PT strands in the 1st floor during the seismic tests is about 42 kips. For the 2nd and 3rd floor, this maximum force is 33.7 kips and 27.6 kips, respectively. The yielding force for two PT strands are 105.4 kips in the 1st and 2nd floor and 74.4 kips in the 3rd floor. Therefore, the PT strands were in the elastic range during those high-intensity seismic tests, which satisfies the design purpose and proves the sufficient ability of PT strands to provide the re-centering force.

The ideal relation between PT force and axial deformation should be like a “V” shape since the PT strands remained in the elastic range. It is observed, however, in Figs. 7-43 to 7-54

that some hysteretic loops occur and the stiffness (the slope) for positive and negative directions are slightly different. It is believed that the potentiometers could not precisely measure the gap opening due to the vertical movement of the beams in 1st or 2nd phase. Therefore, the axial deformations calculated from the gap opening were not accurate in such condition. The relations become more symmetric in the 3rd phase compared to those in the previous phase tests, since the vertical movement of the beam was limited or eliminated by the vertical supports.

In these figures, it can be found that the maximum force in the 3rd phase tests is higher than that in the 1st phase tests (e.g. 40.3 kips in +125% of 1st phase at PE6A test vs. 41 kips in +125% of 3rd phase at PE22 test). This result indicates a higher axial deformation of the PT strands and is consistent with the results obtained fro the gap-openings in previous section (i.e. increasing gap-opening from 1st phase to 3rd phase tests).

Regarding the prestress loss in the PT strands after the seismic tests, no clear loss is observed. The prestress force of the 1st floor changed from 38.6 kips in test PE6A (+125% in 1st phase) to 38.2 kips in test no. PER23 (-150% in 3rd phase), which represents a 1% loss. Considering that the model structure was subjected to 3 phase of 150%-intensity earthquake attacks, this 1% loss is negligible. This result demonstrates again the good seismic performance of the PT strands during the seismic tests.

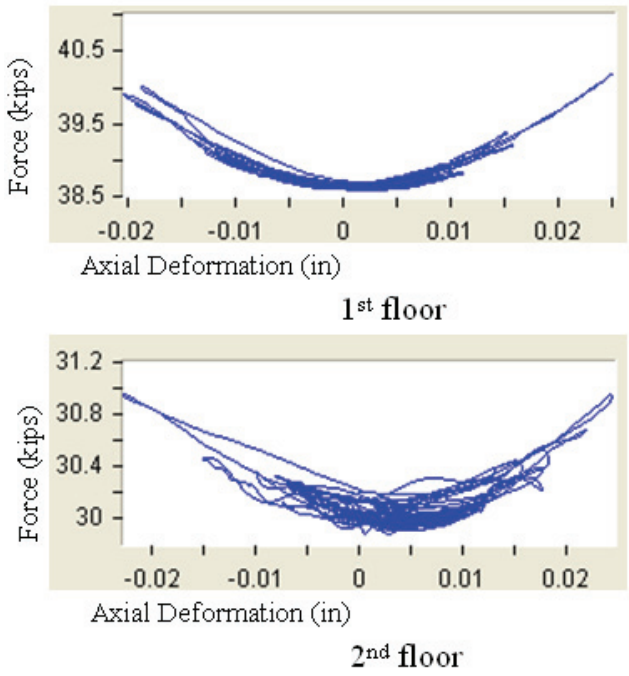

Figure 7-43 Force vs. Defomation of PT Strands For Test PE6A (+125%)

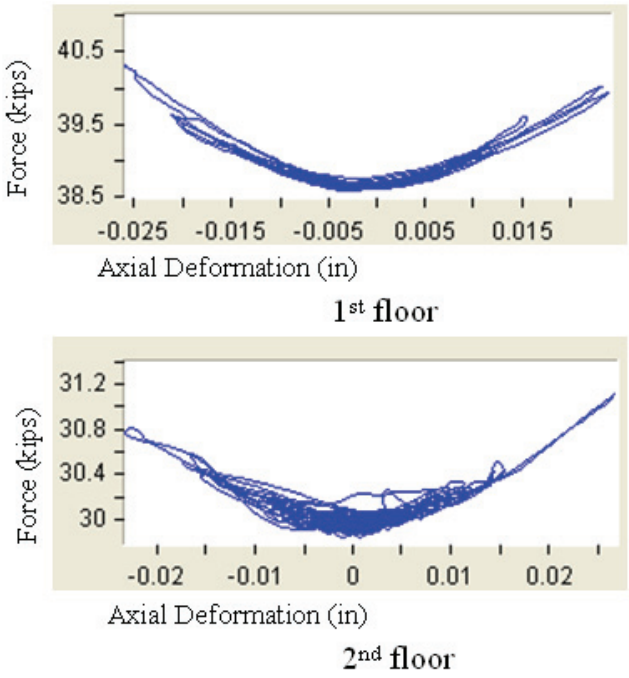

Figure 7-44 Force vs. Defomation of PT Strands For Test PER6 (-125%)

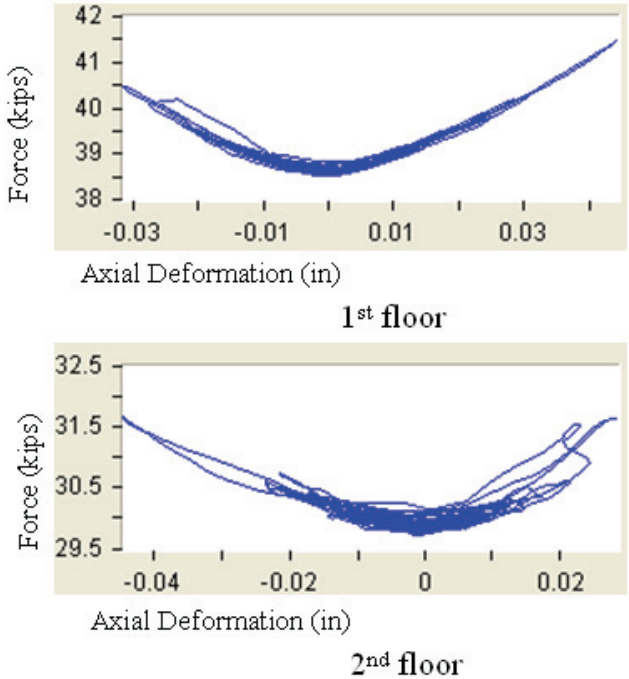

Figure 7-45 Force vs. Defomation of PT Strands For Test PE7A (+150%)

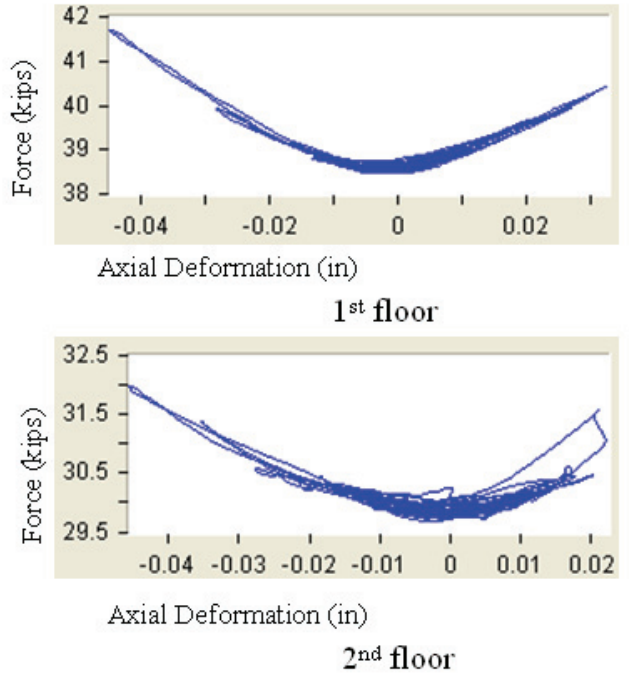

Figure 7-46 Force vs. Defomation of PT Strands For Test PER7 (-150%)

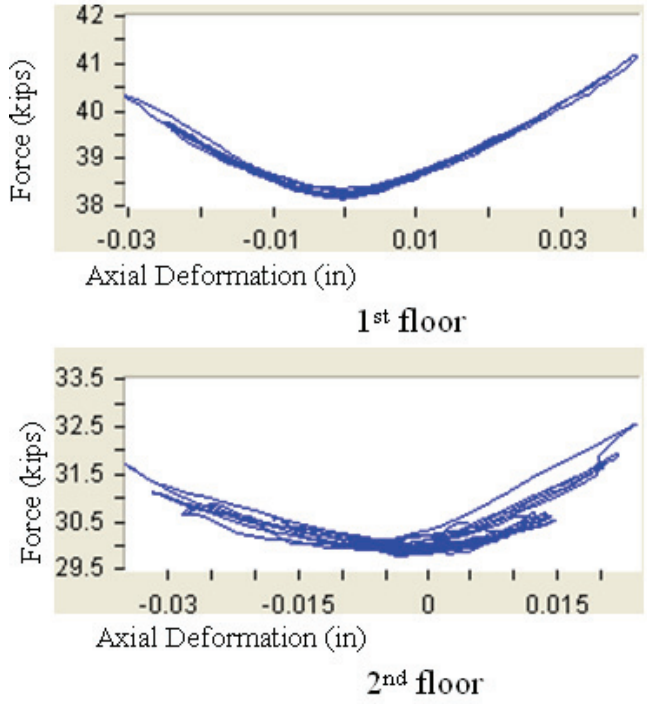

Figure 7-47 Force vs. Deformation of PT Strands For Test PE15 (+125%)

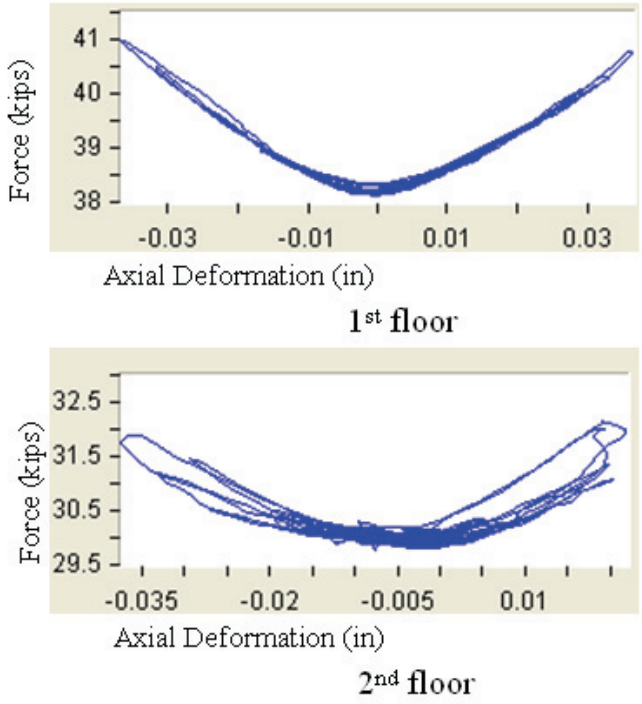

Figure 7-48 Force vs. Deformation of PT Strands For Test PER15 (-125%)

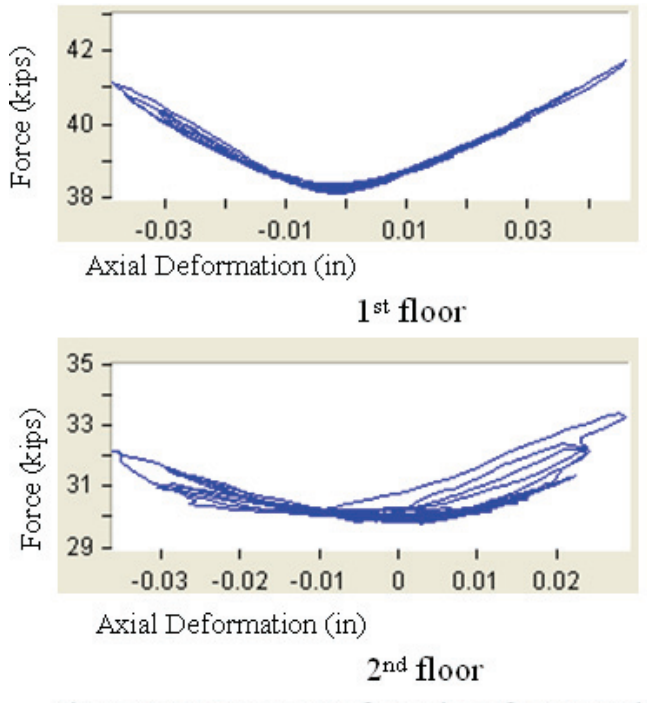

Figure 7-49 Force vs. Deformation of PT Strands For Test PE16 (+150%)

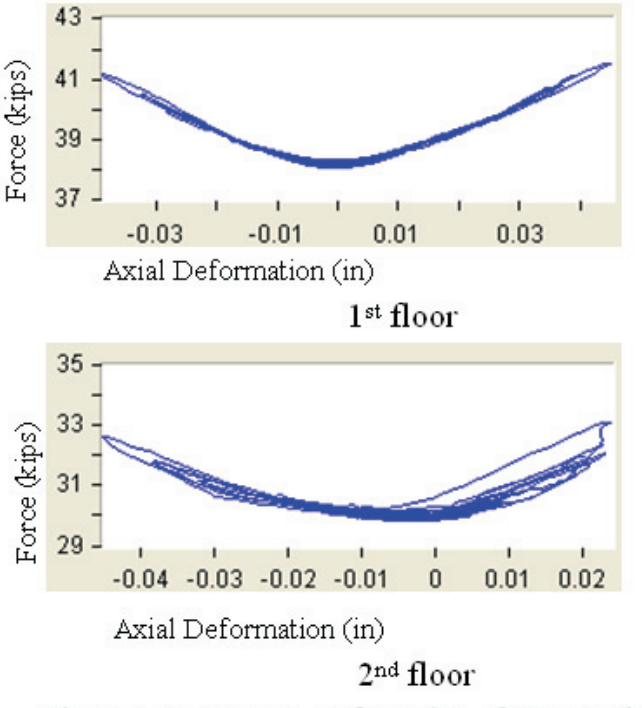

Figure 7-50 Force vs. Deformation of PT Strands For Test PER16 (-150%)

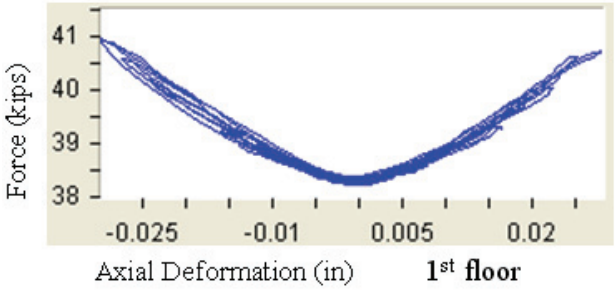

Figure 7-51 Force vs. Deformation of PT Strands For Test PE22 (+125%)

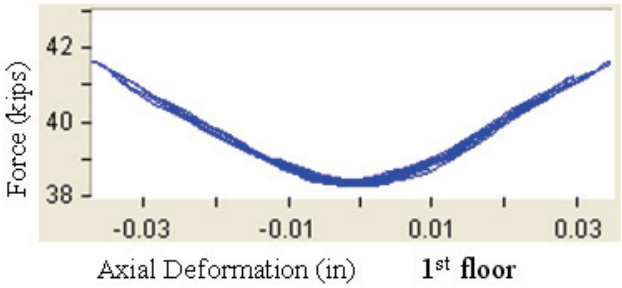

Figure 7-52 Force vs. Deformation of PT Strands For Test PER22 (-125%)

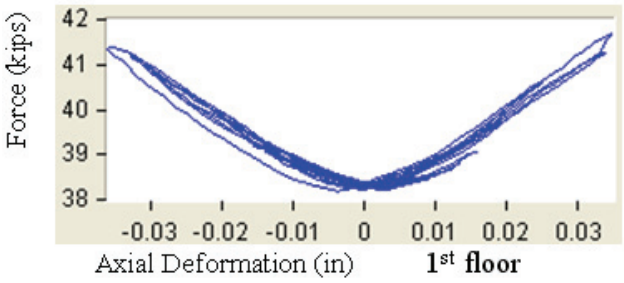

Figure 7-53 Force vs. Deformation of PT Strands For Test PE23 (+150%)

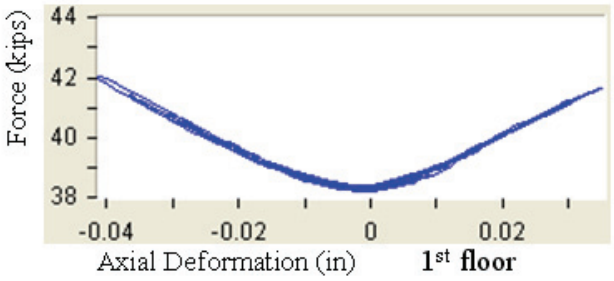

Figure 7-54 Force vs. Deformation of PT Strands For Test PER23 (-150%)

7.4.4 Shear Transfer Issues

Under the large intensity earthquake excitations (e.g. 125% or 150% intensity), vertical movements of the beam ends in the SCPT model were observed through the video cameras installed on the 1st floor. These vertical movements of the beam were unexpected since the calculation of the initial model to predict the experimental results indicated that the shear transferred from the beam to column could be resisted by the friction between the beam and column interfaces. Those unexpected vertical movements were the result of insufficient friction. The reduction of this friction is believed to be due to the fact that the contact surface between the beam and column were not sand blasted. This result indicates that the sand blasting of the contact interface or, alternatively, the inclusion of vertical supports such as

shear tab connections may be necessary for SCPT connections. As shown in Fig. 7-55, a slotted shear tab can accommodate the horizontal movement of bolts to avoid the limit to the gap opening. Also, as discussed in Section 6.3, during the experimental tests, the vertical bars were installed on the top and bottom of beam ends in order to limit this vertical movement. After installing the vertical bars, the vertical movement of beams was eliminated and the gap openings in the beam-to-column joints still occurred, which demonstrates that the vertical bars were effective and made little impact on the gap opening.

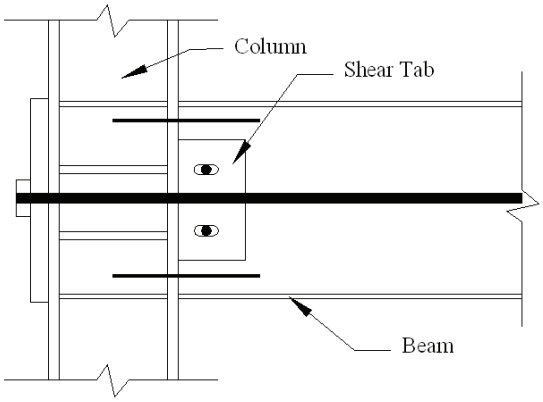

Figure 7-55 Beam-to-Column Connection in SCPT Structures

7.5 Energy Evaluation

The energy dissipation capacity is an important index to represent the seismic performance of a structure during earthquakes. Therefore, the energy evaluation for the SCPT and SMRF models is presented in this section. According to the theory of structural dynamics, the energy balance equation is given by:

$$E_K + E_D + E_F = E_I \tag{7.4}$$

where:

E_K : Kinetic Energy
E_D : Viscous Damped Energy
E_F : Hysteretic Energy (Elastic and Plastic)
E_I : Input Energy

Based on Eq(7.1), the absolute energy equation for the multi-story building subjected to an earthquake excitation was derived as follows (Uang and Bertero, 1990):

$$\frac{1}{2}[\dot{v}_a]^T M[\dot{v}_a] + \int [\dot{v}_r]^T C d[v_r] + \int [f_s]^T d[v_r] = \int (\sum_{i=1}^{N} m_i \ddot{v}_{ai}) dv_g \qquad (7.5)$$

Where:

$[\dot{v}_a]$: Absolute velocity vector
M : Diagonal mass matrix
$[\dot{v}_r]$: Relative velocity vector
C : Damping matrix
d : Derivative Sign
$[v_r]$: Relative displacement vector
$[f_s]$: Restoring force vector
m_i : Lumped mass of the i-th floor
$\ddot{v}_{ai}$: Absolute acceleration at the i-th floor
v_g : Ground displacement

In Eq. (7.5), the kinetic energy, viscous damped energy and the input energy can be directly calculated by the obtained experimental results while the hysteretic energy may be calculated as the result of $E_I - E_K - E_D$. The velocity time histories, used to calculated the kinetic and viscous damped energy, are obtained by derivatives of the corresponding floor displacement time histories measured by temposonic transducers. The damping matrix used in this calculation for the two models were obtained from the snap-back tests with 2.4% and 2.1% damping ratio of the 1st mode for the SCPT and SMRF models, respectively, as shown

in Table 7-6 and 7-7. The energy distribution time history during the 125%-intensity test for the two models is shown on Fig. 7-56 and 7-57, respectively. The label “hysteretic energy – story i” means the hysteretic energy absorbed by the whole structure due to the input energy generated by the motion of the i-the floor mass. The hysteretic energy includes the recoverable and unrecoverable strain energy. At the end of the excitation, it represents only the unrecoverable energy as a result of inelastic deformations of the structures. Comparing these two figures, it is found that the peak kinetic energy in the SMRF model is larger than that in the SCPT model, which suggests that the velocity response of SCPT is lower. The reduction of velocity response can decrease the lost to the velocity-sensitive nonstructural components during earthquakes.

The final energy distribution is presented in the table 7-8. The conventional engineering idea is that the higher energy dissipation the better seismic performance while as shown in this table, it is found that the total hysteretic energy of the SCPT model is lower than that of the SMRF model. However, the seismic performance of SCPT model is better than the SMRF model as shown in the previous sections from global and local responses. The reason is that although lower hysteretic energy is dissipated by the SCPT model compared to the energy dissipated by the SMRF model, the input energy flowing into the SCPT model is also reduced. It should be pointed out that the hysteretic energy absorbed in the SMRF model was due to the inelastic deformation of the beams and columns, which cause damage to the structural components. For the SCPT model, the ED bars played a sacrificial role without any damage to the beams and columns. Again, from the point of view of energy and repair

cost, it demonstrates the better seismic performance of the SCPT structure compared to the SMRF structure.

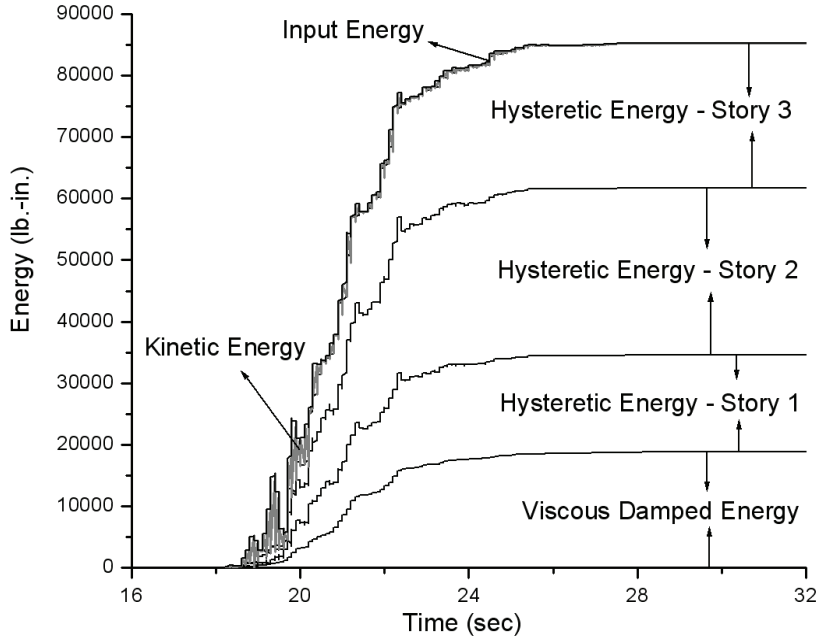

Figure 7-56 Energy Time History of the SCPT Model for Test PE6A (+125% in 1st phase)

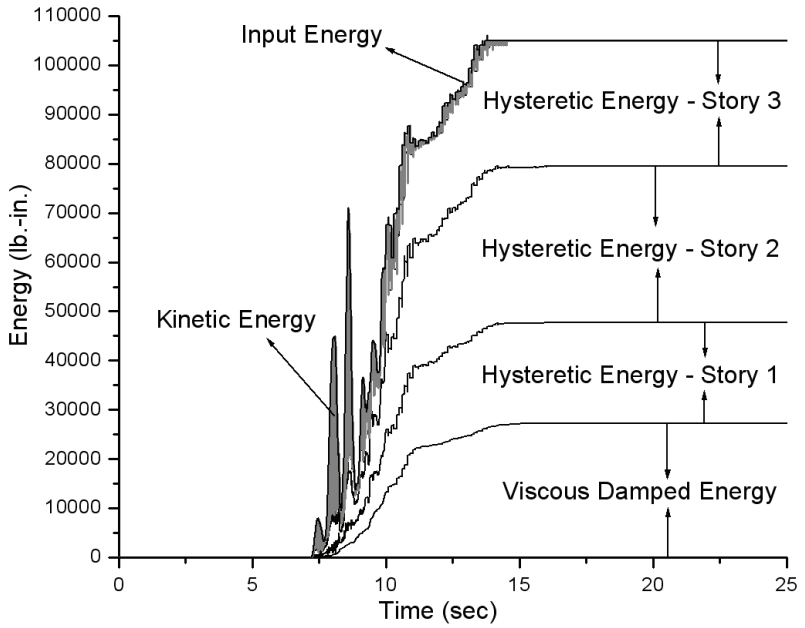

Figure 7-57 Energy Time History of the SMRF Model for Test ME06A (+125%)

Table 7-8 Energy Distribution (lb-in)

	Test No.	Input Energy	Viscous Damped Energy	Hysteretic Energy			
				1st floor	2nd floor	3rd floor	total
SCPT Model	PE6A	85155	18757	15798	27148	23452	66398
SMRF Model	ME06A	105008	27323	20404	31674	25607	77685

CHAPTER 8
COMPARISON BETWEEN NUMERICAL AND EXPERIMENTAL RESULTS

Since differences between numerical predictions and experimental results exist in almost all studies, comparisons need to be done to evaluate the performances of the numerical in predicting the experimental results. This chapter presents the comparison between numerical and experimental results for both the SMRF and SCPT models. First, two initial numerical models, one of the SMRF and the other of the SCPT structure, are developed for the prediction of the experimental results obtained from the shake table tests. These two numerical models are then calibrated based on the structural properties measured during the shake table tests. Finally, a comparison between the results obtained from the initial numerical models, calibrated numerical models and experimental testing is discussed.

The purpose of this chapter is to identify the main factors that made an impact on the seismic performance of the test models during the shake table testing and evaluate the reliability of the numerical and experimental results by comparing them. Although the numerical model can almost never be totally identical as the real structures, efforts are made to take those influencing factors as much as possible into account in the numerical models in order to reduce the difference between the numerical predictions and experimental results.

8.1 Initial Numerical Models

For the purpose of predicting the seismic response of the test specimens, two different 2D numerical models were developed in the general purpose finite element software RUAUMOKO (Carr 2004).

As shown in Fig. 8-1, the SMRF structure is simulated by a 2D frame consisting of beam and column finite elements. Also in that figure, nodal numbers and element numbers (digits

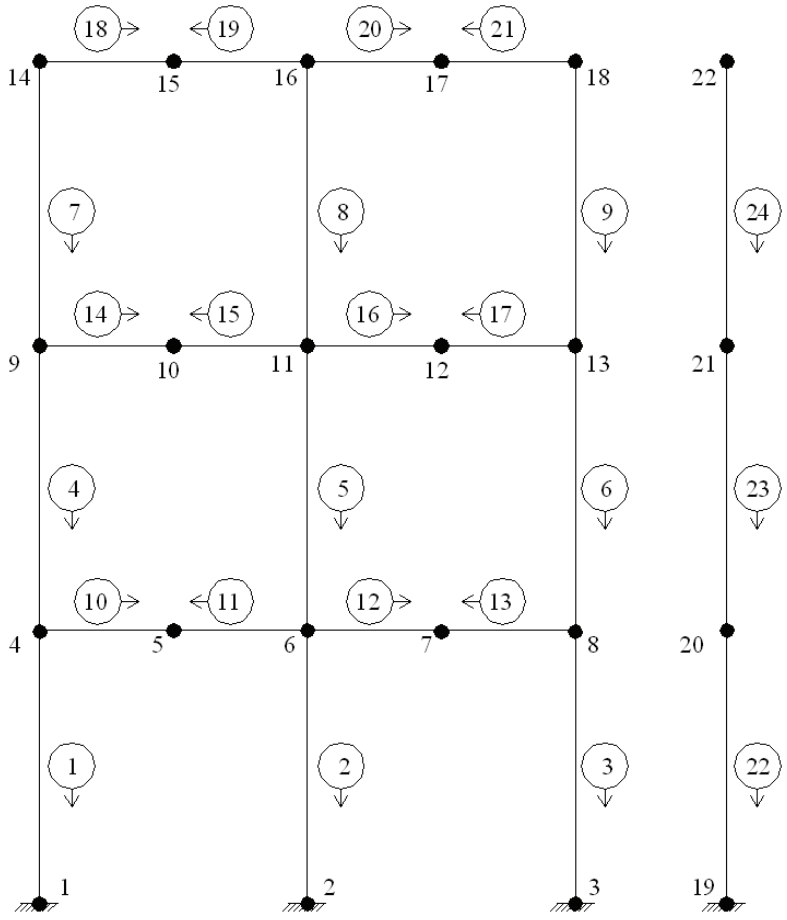

Figure 8-1 Initial Numerical Model of SMRF

with circle) are indicated and the arrow on the circle represents the local direction of each element. The dark points represent the location of the nodes. The super-spring elements on the right hand side (elements 22, 23 and 24) represent the Floor Mass Simulator (FMS) used in the tests. These super-spring elements provided only vertical support without any lateral resistance. The base connections were assumed to be fixed and the floor masses were assumed to be lumped in the central nodes (6, 11 and 16). A Rayleigh type damping model with the first and second modal damping ratios of 2% of critical was considered.

The initial numerical SCPT model is shown in Fig. 8-2. This model incorporated detailed SCPT beam-to-column connections, which can be found in Fig. 4-21(b) (See Section 4.5). The PT strands implemented in each floor are represented by one spring element with two end nodes on the exterior columns (e.g. node 4 and 8 for 1st floor). The ED bars (e.g. ED element between node 25 and 27) are located in the top and bottom of the beams and are connected to the beams by rigid bars (e.g. rigid bar element between nodes 27 and 24) since the beam finite element is a line without height in this 2D model. The multi-spring element (e.g. element between nodes 4 and 23) was used for gap elements of the beam-to-column joints. These contact elements had no tension stiffness and the compression stiffness was calculated based on the beam sections. The configurations of the lumped mass and gravity column frame are identical to those in the SMRF model.

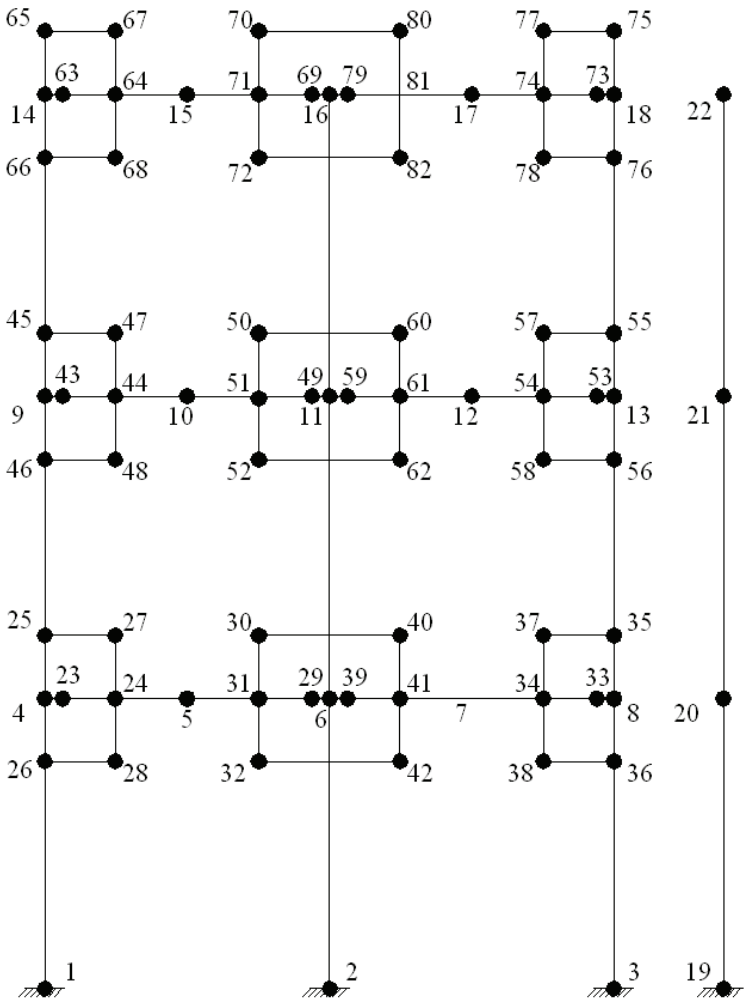

Figure 8-2 Initial Numerical Model of SCPT

8.2 Calibrated Numerical Models

By comparing the structural properties obtained from the initial models against the results of the system identification tests, it was found that the measured natural frequencies were lower than that predicted by the initial numerical models (see Section 8.3). Therefore, the numerical models should be calibrated to account for various factors influencing the

experimental results. Since the rotation of the shake table was observed during the seismic tests, the initial models were calibrated mainly for this effect.

As shown in Fig. 6-8 (see Section 6.1), the shake table was supported by four vertical actuators (Actuator Z1, Z2, Z3 and Z4). During the seismic tests, the displacement and force feedbacks of those actuators were recorded. Figure 8-3 shows the relation between the vertical displacement and the force of actuator Z1 under the ME07 excitation (+150% intensity seismic test for the SMRF model). The axial stiffness of actuator, $K_{actuator}$, can be estimated as the slope in the figure:

$$K_{actuator} = \frac{(61.6-(-30))}{(-0.25-0.174)} = 216 kips/in \tag{8.1}$$

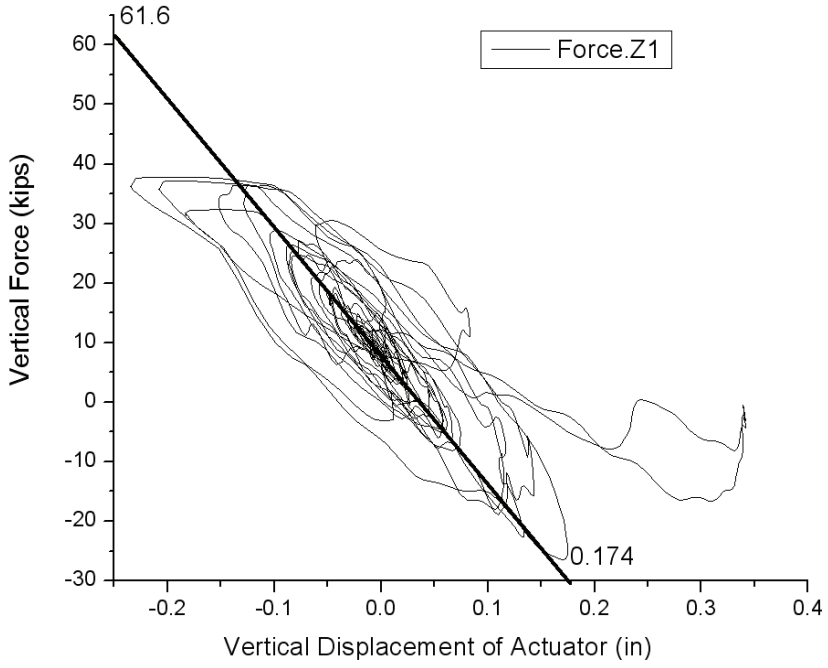

Figure 8-3 Force vs. Displacement of the vertical actuator Z1

Based on Eq. (8.1) and assuming that all four actuators have the identical stiffness, the equivalent rotational stiffness of the shake table, $K_{rotation}$, can be determined as follows:

$$K_{rotation} = 2K_{actuator}D_{actuator}\left(\frac{D_{actuator}}{2}\right) = 2\times 216\times 100.5\times\left(\frac{100.5}{2}\right) = 2.182\times 10^{6} kips - in/rad \quad (8.3)$$

where $D_{actuator}$ is the distance between the two vertical actuators in the shaking direction.

To simply simulate this rotational stiffness of the shake table, a rotational spring finite element was added to the initial models, as shown in Fig. 8-4. The nodes 1, 2, 3 and 19 in the figure are the base nodes as shown in Fig. 8-1. These nodes are connected by rigid beam elements (e.g. elements between node 1 and 2) to simulate the stiff structure of the shake table. The new rotational element between nodes 2 and 23 was assumed to be rigid in the vertical and horizontal directions, while the stiffness obtained in Eq. (8.3) was used as rotational stiffness.

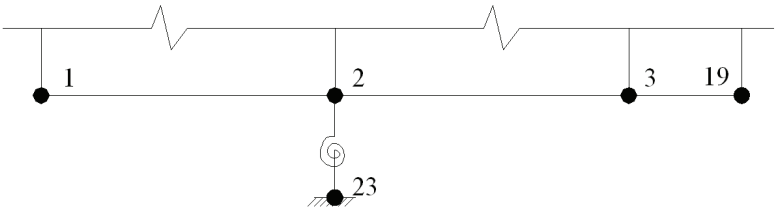

Figure 8-4 Rotational Element in the Numerical Calibrated Model

Both the SMRF and SCPT calibrated numerical models incorporated this rotational element. The calibrated numerical SCPT model was further simplified to a frame with ideal Self-Centering (SC) connections. The reason for this simplification is that in the initial numerical

SCPT model the Post-Tensioned (PT) force was added in the PT spring which was resisted by the axial resistance of the beams and the shear of columns especially in the first floor since the base is fixed, while in the experimental tests the PT strands were tensioned before the installation to the shake table and at that time the base is free. Due to the above reason, the initial PT force would be reduced if the SCPT connections in the initial model were used. Therefore, the simplified ideal SCPT model was used in the calibrated numerical model so that the self-centering property of this model was more similar to that of the experiment model. This ideal SCPT frame had the same node distribution as the SMRF model indicated in Fig. 8-1, but the beam ends connected to the columns incorporated a flag-shape hysteresis moment-curvature relation. The controlling parameters (α, β and ψ) of this flag shape hysteresis relation were determined by the corresponding values shown in Table 5-8 (see Section 5.4)

8.3 Comparison of Results

In this section, the results obtained from the initial and calibrated numerical models under 25% and 125% intensity seismic excitations are compared to those obtained from the experimental testing for the SMRF and SCPT models. The seismic response of the model structures under 25% and 125% intensity excitations can be seen as representatives of elastic and inelastic responses, respectively. Since the numerical models were simplified (e.g. no actual geometry for the beams or columns, only a line to represent the beam finite elements in the numerical models), the local responses such as strains or gap-openings are neglected

in this comparison. Only the modal natural frequencies and the global responses such as accelerations and displacements are compared.

Table 8-1 and 8-2 compares the modal frequencies obtained from the numerical models with those obtained experimentally. In these two tables, it can be seen that the modal natural frequencies of the initial numerical models are always higher than those measured experimentally for both the SMRF and SCPT structures. However, the modal natural frequencies of the calibrated numerical models are closer to those obtained experimentally. These results indicate that the rotation of the shake table reduced the stiffness of the whole structures leading to a reduction of the modal natural frequencies. It is also noted that the natural frequencies of the higher modes (2^{nd} and 3^{rd} modes) are not sensitive to the rotation effect.

Table 8-1 Modal Natural Frequencies of the SMRF Model Obtained from Numerical and Experimental Results

	Modal Natural Frequencies (Hz)			
	Numerical Model		Experimental Model	
Mode	Original	Calibrated	White Noise Test	Snap-Back test
1st	3.44	2.96	3	3.25
2nd	10.35	10.35	9.625	9.563
3rd	17.77	17.7	15.188	15.188

Table 8-2 Modal Natural Frequencies of the SCPT Model Obtained from Numerical and Experimental Results

	Modal Natural Frequencies (Hz)				
	Numerical Model		Experimental Model		
Mode	Original	Calibrated	White Noise test	Snap-Back test	Sine Sweep test
1st	3.6	2.96	2.75	2.973	2.75
2nd	10.57	10.35	9.141	8.919	9.063
3rd	18.61	17.7	14.891	14.534	14.313

The mode shapes calculated from the initial and calibrated numerical models are shown in Table 8-3. From this table, it is observed that the mode shapes of the calibrated model are similar to the ones of the original model, which indicates that rotation effect of the shake table has little influence on the mode shapes. By comparing those mode shapes with the ones obtained from the experimental testing (see Table 7-6 and 7-7 in Sec. 7.1.4), it can be observed that the mode shapes obtained numerically and experimentally have similar trends, while the observed deviations among them suggests that the numerical models are still different with the experimental models, which will be further discussed in Sec. 8.4.

Table 8-3 Mode Shapes Obtained from the Initial and Calibrated Numerical Models

	Original Model	Calibrated Model
Mode Shape of SMRF Model	$\begin{bmatrix} 0.29 & 1 & -1 \\ 0.69 & 0.82 & 0.89 \\ 1 & -0.87 & -0.32 \end{bmatrix}$	$\begin{bmatrix} 0.30 & 1 & -1 \\ 0.68 & 0.82 & 0.90 \\ 1 & -0.87 & -0.31 \end{bmatrix}$
Mode Shape of SCPT Model	$\begin{bmatrix} 0.29 & 1 & -1 \\ 0.67 & 0.86 & 0.86 \\ 1 & -0.88 & -0.30 \end{bmatrix}$	$\begin{bmatrix} 0.30 & 1 & -1 \\ 0.68 & 0.82 & 0.90 \\ 1 & -0.87 & -0.31 \end{bmatrix}$

The comparisons of displacements (inter-story drift) and accelerations between the numerical and experimental models of the SMRF structure are shown in Figs. 8-5 and 8-6. It can be observed that the displacement and acceleration responses predicted by the calibrated numerical models are much closer to those obtained experimentally. This observation verifies that the rotation effect of the shake table is one of the key factors influencing the experiment results since the main difference between the initial and calibrated numerical models is the addition of a rotational spring as discussed earlier. It is also noted that the experiment results show higher inter-story drifts and lower accelerations for the high intensity excitations (+125% intensity excitation) than those of the initial and calibrated models. This result suggests that the test specimens achieved a better seismic performance than that predicted by the numerical analyses from a point of view of larger ductility and lower accelerations. Therefore, the results from the numerical analyses can be considered conservative.

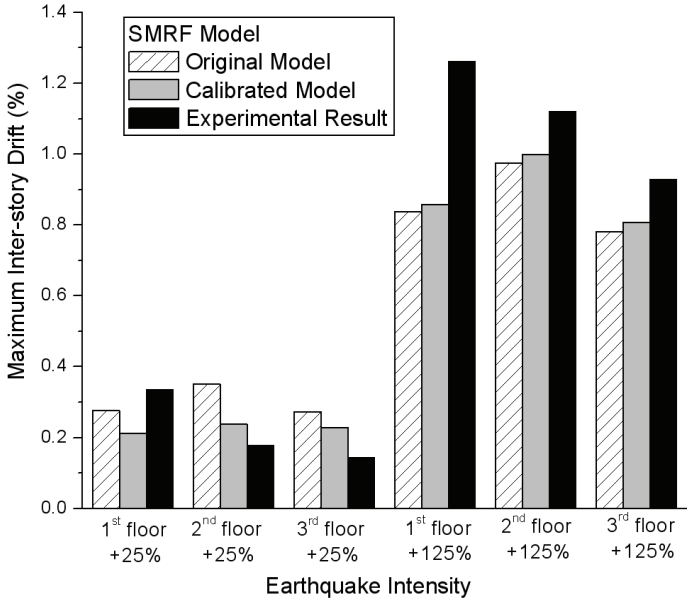

Figure 8-5 Maximum Inter-story Drifts for the SMRF Model

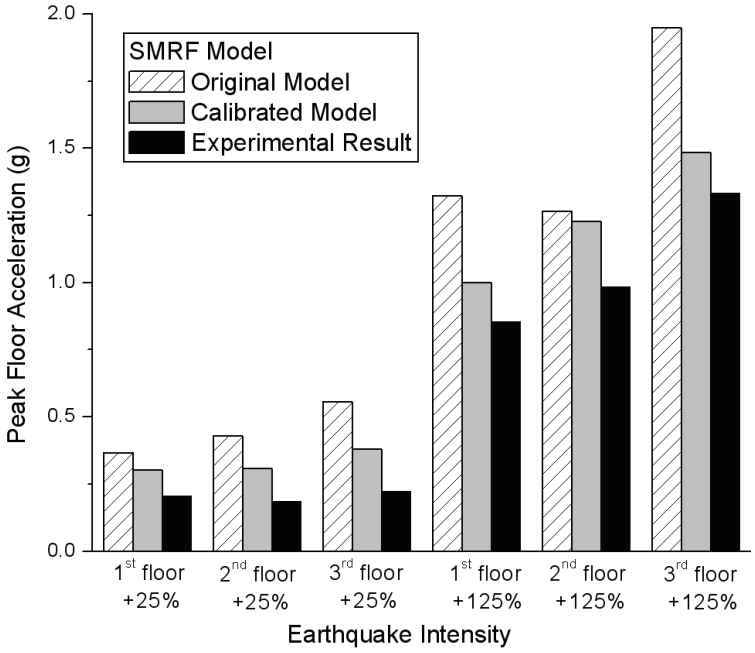

Figure 8-6 Peak Floor Accelerations for the SMRF Model

Figures 8-7 and 8-8 show a comparison of the maximum inter-story drifts and accelerations predicted by the two numerical models with those obtained experimentally for the SCPT structure. Similar to the SMRF structure, the predictions of the calibrated numerical model of the SCPT structure are in better agreement with the experimental results than that of the initial numerical model. It is observed that inter-story drifts predicted by the calibrated model are larger than those of the initial model and experimental results. However, this deviation is as low as about 0.1% of the story height (about 1mm) for the 2nd and 3rd floors under the 25%-intensity seismic excitation. It is also observed in Fig. 8-8 that a relatively large deviation of the accelerations exists between the calibrated numerical model and the experimental results for higher (+125%) intensity seismic testing. This difference may be due to the vertical movement of the beams of the SCPT structure, which lowered the

stiffness after gap-opening and resulted in lower acceleration responses compared to those predicted by the numerical analysis.

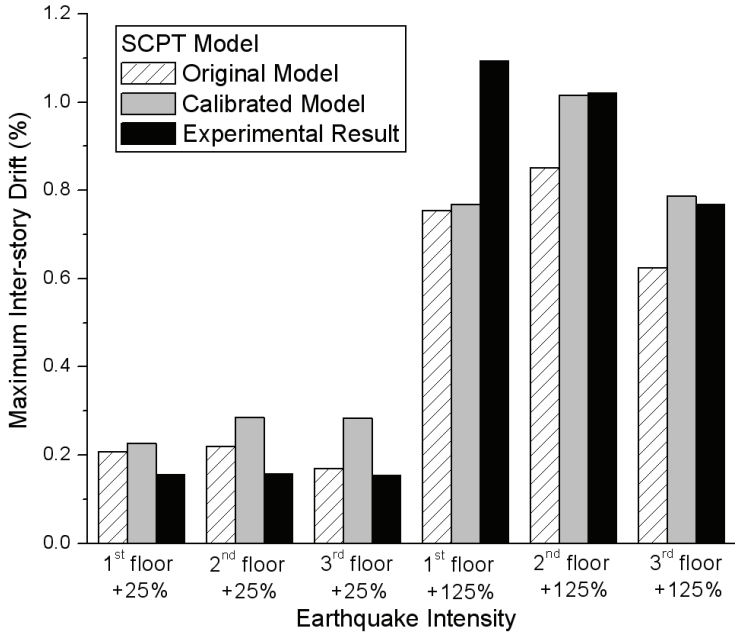

Figure 8-7 Maximum Inter-story Drift of the SCPT Model

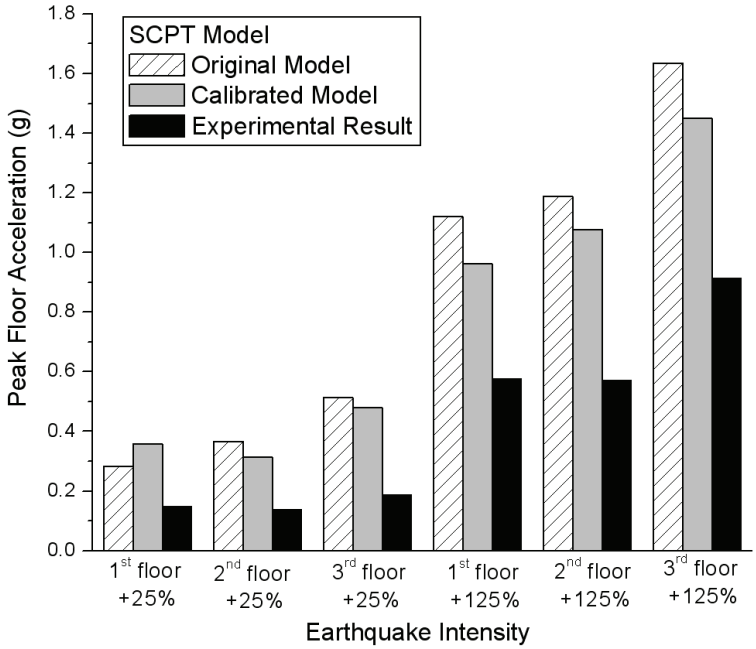

Figure 8-8 Peak Floor Acceleration of the SCPT Model

8.4 Summary

As discussed in the previous sections, by considering the effect of the shake table rotational stiffness, the calibrated numerical models for both SMRF and SCPT structures achieved better correlation with the experimental results than the initial models of the same structures. By comparing the responses between the numerical and experimental results, it can be concluded that the predictions of the numerical analysis were more conservative than the actual experimental results.

However, differences between the calibrated numerical model and experimental model still exist. The numerical models are 2D models while the real structures in testing are 3D ones. The slight out-of-plane torsion may have some influence on the response, which can not be simulated in the 2D numerical models. Another issue is that, as shown in Fig. 8-4 (see Section 8.2), the earthquake excitation arises from shaking of the ground (i.e. node 23) in the calibrated numerical models, while the real situation in the seismic testing is through the shaking of the table (i.e. node 1, 2 and 3). As shown in Fig. 8-3 (see Section 8-2), the vertical actuator supporting the shake table exhibited a force-displacement hysteresis loop under seismic excitations. This nonlinear behavior was not simulated by the simple rotational spring added to the calibrated numerical models due to the difficulty to define the property of this irregular hysteresis loop. Therefore, to better match the experimental results, the numerical models need to be refined further to completely reflect the behavior of the test structures.

Although the above differences occurred, both the numerical predictions and experimental results confirmed that the Self-Centering Post-Tensioned (SCPT) frame structure achieved better acceleration response and similar displacement response compared to the Steel Moment Resisting Frame (SMRF) structure under seismic excitations. From this point of view, it is believed that the shake table testing reproduce the same trends predicted by the numerical analysis.

CHAPTER 9
CONCLUSIONS

In this report, numerical and experimental studies of the seismic performance of Self-Centering Post-Tensioned (SCPT) steel frames were conducted. The results were presented mainly in two parts: an analytical study from Chapter I to Chapter IV and an experimental study from Chapter V to Chapter VIII. In this final chapter, the conclusions drawn from these two parts are reviewed and the suggestions for the future studies are discussed.

9.1 Summary and Conclusions from Numerical Studies

In the numerical studies, the seismic performances of Single-Degree-of-Freedom (SDOF) Self-Centering Systems (SCS) and Elasto-Plastic Systems (EPS) were first investigated through nonlinear dynamic analyses. A Relative Performance Index (RPI) was developed to evaluate the performance of SCS in reducing both relative displacements and absolute accelerations in structures under earthquake hazards. Based on this RPI, a parametric analysis was conducted to evaluate the influence of the various hysteretic parameters of SCS on the seismic response of SDOF. The results of this parametric study are included in appendices A and B. Thereafter, numerical models were developed to evaluate the seismic performance of the MCEER Demonstration Hospital building re-designed with SCPT connections. A practical re-design procedure for SCPT connections was proposed. Based on the results of these analyses, the following conclusions can be made:

(i) The comparison of seismic performance of SDOF SCS and EPS, excited by two ensembles of 25 MCEER ground motions having 2% and 10% probabilities of exceedance in 50 years for Southern California, demonstrated that at least one SDOF SCS with optimum hysteretic parameters (α, β, η and ψ) can be found to exhibit better seismic responses than a corresponding SDOF EPS. This conclusion suggests that similar SCS parameters can be found in more complex Multi-Degree-of-Freedom (MODF) systems.

(ii) The results of pushover analyses, seismic analyses and fragility analyses on the MCEER Demonstration Hospital indicated that the seismic performance of SMRF redesigned with ideal SCS exceeded that of original SMRF. Furthermore, these results also validated the feasibility of using the RPI as a guide for the design of SCS MDOF systems.

(iii) Further numerical seismic study on SMRF systems re-designed with SCPT connections showed that the seismic performance of the SCPT steel frame exceeds not only that of original SMRF but also that of the model redesigned with ideal SCS. This seismic analysis also validated the pratical re-design procedure of SCPT frame buildings.

(iv) After re-design of the MCEER Demonstration Hospital incorporating the SCPT connections, the seismic results indicated that some base columns yields in severe

earthquakes, such as some of the MCEER ground motions with 2% probability of exceedance in 50 years. Therefore, the base columns should be considered to be re-designed with SCS or to be reinforced.

(v) The reductions of the seismic responses of SMRF re-designed with SCS also reduce the recovery cost after earthquakes. The materials of SCPT connections are readily available steel products, which can be replaced with relative lower cost compared to the replacement of the structural components such as beams or columns after seismic hazards.

(vi) The residual drift of structures re-designed with SCS is largely reduced or eliminated and no permanent inelastic deformation associated with the main structural components occurs, which save a lot of cost to return the conventional SMRF structure to its original position and repair the damage of the beams or columns in the SMRF structure after earthquakes.

(vii) The SCPT frame structure can be designed for different purposes according to the requirements of buildings such as more concern on reducing acceleration responses for buildings with more acceleration-sensitive components or decreasing displacement responses for structures with more displacement-sensitive components. The weighting factor, RPI, can be used for guiding the design of structures with different seismic index sensitive components.

9.2 Summary and Conclusions from Experimental Studies

To experimentally validate the seismic performance of SCPT and SMRF structures, two 1/3 scale frames (i.e. SCPT and SMRF) were designed and tested under a selected MCEER ground motion on a shake table at the University at Buffalo. (The shop drawings of these two models are shown in Appendix C and D.) The initial dynamic properties of two models were determined based on identification tests including white noise, snap-back and sine-sweep tests. The global seismic responses such as peak accelerations and displacements, and the local responses from beams, columns, Post-Tensioned (PT) strands and Energy-Dissipating (ED) bars were presented and compared for the SCPT and SMRF structures. (The acceleration, displacement and strain time histories under seismic excitations are shown in Appendix E, F and G.) Also, the energy distribution in the two models during the seismic tests was evaluated. Finally, the predictions of initial and calibrated numerical models were compared to the experimental results. Based on those comparisons, the following conclusions can be drawn:

(i) The comparisons of the seismic performance between the SCPT and SMRF models demonstrated that the SCPT model performed better than SMRF model under the selected MCEER simulated ground motion.

(ii) The good seismic behavior of two models under severe seismic excitations (125% and 150% intensity earthquakes) satisfied the design objectives.

(iii) The reduction in acceleration response and similar displacement response of the SCPT model, compared to those in the SMRF model, validated the design procedure focused mainly on acceleration issue since the Relative Performance Index (RPI) used in the design of the SCPT connections had a 70% weighting factor on the acceleration response and 30% for the displacement response.

(iv) From the local experimental responses, the PT strands and ED bars exhibited good abilities to provide recentering force and to dissipate energy.

(v) Unexpected vertical movements of the beam ends in the SCPT model was observed under the severe seismic excitations, which suggested that the beam ending surfaces connected to the columns should be sand blasted to increase the friction or additional shear tabs should be installed to the beam-to-column joints to supply more shear resistance.

(vi) The better seismic performance of the SCPT model in the 1st, 2nd and 3rd phases of testing indicated that after two time severe earthquake attacks, the SCPT structure still exhibited better behavior than that of SMRF under the 1st time earthquake hazard.

(vii) The strain responses indicated that after severe earthquakes, the beams of the SMRF structure were damaged by yielding while only the ED bars yielded in the SCPT model without any damage to the beams. These results verified that it

would cost much more to repair the beams of the SMRF structure compared to the SCPT building.

(viii) The energy analysis suggested that although the energy dissipated by the SCPT model was less than that absorbed by the SMRF model, the total energy flowing to the SCPT model was still less than that traveling to the SMRF model. This phenomenon may be associated with the better seismic performance of the SCPT model. The different hysteresis energy distribution (i.e. in yielding beams of SMRF model and in yielding ED bars of SCPT model), again demonstrated the lower repair cost for the SCPT model.

(ix) The same trends (i.e. the SCPT model exhibited better seismic performance) were obtained from the initial numerical predictions, calibrated numerical models and experimental models. The results of the calibrated numerical models were closer to the experimental results compared to the initial numerical prediction, which verified the impact of the rotation effect of the shake table.

9.3 Suggestions for Future Studies

Since there is lack of research on implementing this new type of SCPT structures to the practical buildings, more efforts should be made to investigate the real applications and resolve the practical problems.

The practical re-design procedure of the SCPT steel frame proposed in this report is slightly complicated, therefore, it need to be further investigated to obtain more practical and simpler design equations without iterations to achieve the optimal and feasible SCPT parameters. Other research efforts on SCS may focus on the application of SCS in the base columns or other column connections in order to prevent the possible yielding of those base columns during severe earthquakes.

The limit to the gap opening of the beam-to-column joints in the SCPT structures due to the floor slab should be considered in the further study, since this limit may leads to the increase of compression in the beams and even yielding of the beams before the design gap opening angles.

The full scale shake table test of SCPT frame may be conducted to obtain more practical performance during earthquakes although it requires much larger shake table to support the structure.

Further research may be conducted to compare the seismic performance of SCPT frames with that of the frames incorporating other passive control methods such as base isolation systems, tuned mass dampers and viscous dampers, although the cost for other passive control methods is apparently higher than that of SCPT frames.

To predict the experimental results more precisely, 3D models should be developed to account for the details of beam-to-column joints and other components such as floor slabs

and gravity support frames. Also, the influence due to the shake table such as rotations and hysteresis properties of vertical supporting actuators should be further investigated in order to achieve much more accurate results compared to the real responses from the practical buildings during earthquakes.

CHAPTER 10
REFERENCES

Ajrab, J. J., Pekcan, G., and Mander, J. B., 2004. “Rocking Wall-Frame Structures with Supplemental Tendon Systems”, ASCE Journal of Structural Engineering, Vol. 130, No. 6, 895-903.

Aiken, I. D., Nims, D. K., and Kelly, J. M., 1992. “Comparative Study of Four Passive Energy dissipation Systems”. Bulletin of the New Zealand National society for Earthquake Engineering, 25(3), 175-192

Aiken, I. D., Nims, D. K., Whittaker, A. S., and Kelly, J. M., 1993. “Testing of Passive Energy Dissipating Systems”. Earthquake Spectra, Vol. 9, No. 3.

Bruneau, M., Uang, C. M. and Whittaker, A., 1998. Ductile Design of Steel Structures, McGraw-Hill, New York, NY.

Carr, A. J., 2004. RUAUMOKO-2D, Department of Civil Engineering, University of Canterbury, New Zealand.

Chopra, A. K., 2000. Dynamics of Structures (second edition), Prentice Hall, Upper Saddle River, New Jersey.

Christopoulos, C., Filiatrault, A., and Folz, B., 2002a. “Seismic Response of Self-Centering Hysteretic SDOF Systems”, Earthquake engineering and structural dynamics, Vol. 31, Wiley, New York, 1131–1150.

Christopoulos, C., Filiatrault, A., Uang, C. M., and Folz, B., 2002b. "Posttensioned Energy Dissipating Connections for Moment-Resisting Steel Frames”, Journal of Structural Engineering, Vol. 128, No. 9, 1111–1120.

Christopoulos, C., Filiatrault, A., and Uang, C. M., 2002c. "Self-Centering Post-Tensioned Energy Dissipating (PTED) Steel Frames for Seismic Regions”, Report No. SSRP-2002/06, Department of Structural Engineering, University of California, San Diego.

Collins, J. H. and Filiatrault, A., 2003. “Application of Post-Tensioned Energy Dissipating (PTED) Connections in steel Moment-Resisting Frames”, Report No. SSRP-2003/05, Department of Structural Engineering, University of California, San Diego.

Cormack, L. G., 1988. “The Design and Construction of the Major Bridges on the Mangaweka Rail Deviation”, Transaction of the Institute of Professional Engineers of New Zealand, 15, 16-23.

Engelhardt, M. D. and Husain, A. S., 1993. “Cyclic-Loading Performance of Welded Flange-Bolted web Connections”, Journal of Structural Engineering, v119, n12, December 1993.

FEMA 356, 2000. “Prestandard and Commentary for the Seismic Rehabilitation of Buildings”, Federal Emergency Management Agency, November, 2000.

Filiatrault, A., Tremblay, R., and Kar, R., 2000. “Performance Evaluation of Friction Spring Seismic Damper”, Journal of Structural Engineering, 491-499, April, 2000.

Garlock, M. M., Ricles, J. M., and Sause, R., 2005. "Experimental Studies of Full-Scale Posttensioned Steel Connections", Journal of Structural Engineering, Vol. 131, No. 3, 438-448.

Garlock, M. M., Sause R. and Ricles, J. M., 2007. "Behavior and Design of Posttensioned Steel Frame Systems", Journal of Structural Engineering, Vol. 133, No. 3, 389-399.

Gross, J. L., Engelhardt, M. D., Uang, C. M., Kasai, K., and Iwankiw, N. R., 1999. “Modification of Existing Welded Steel Moment Frame Connections for Seismic Resistance”, Design Guide No. 12, American Institute of Steel Construction, Chicago, IL.

Holden, T., Restrepo, J. and Mander, J. B., 2003, “Seismic Performance of Precast Reinforced and Prestressed Concrete Walls”, ASCE Journal of Structural Engineering, Vol. 129, No. 3, 286-296

Kircher, C. A., 2003. “It Makes Dollars and Sense to Improve Nonstructural System Performance”, Proc. ATC 29-2 Seminar on seismic Design, Performance, and Retrofit of Nonstructural Components in Critical Facilities, Newport Beach, California, October 23-24, 2003.

Newmark, N. M., 1959. “A Method of Computation for Sttrcutrual Dynamics”, Journal of the Engineering Mechanics Division, ASCE, 85, 1959, pp.67-94.

Kurama, Y. C., Pessiki, S., Sause, R., Lu, L. W., and El-Sheikh, M., 1996. "Analytical Modeling and Lateral Load Behavior of Unbonded Post-Tensioned Precast Concrete Walls", Research Report No. EQ-96-02, Department of Civil and Environmental Engineering, Lehigh University, Bethlehem, PA, Nov. 1996.

Kurama, Y. C., Sause, R., Pessiki, S., Lu, L. W., and El-Sheikh, M., 1997. "Seismic Design and Response Evaluation of Unbonded Post-Tensioned Precast Concrete Walls", Research Report No. EQ-97-01, Department of Civil and Environmental Engineering, Lehigh University, Bethlehem, PA, Nov. 1997.

Kurama, Y. C., Pessiki, S., Sause, R., and Lu, L.W., 1999. "Seismic Behavior and Design of Unbonded Post-Tensioned Precast Concrete Walls," PCI Journal, Vol. 44, No. 3, May-June, pp. 72-89, 1999.

Kurama, Y. C., and Shen, Q., 2004. "Posttensioned Hybrid Coupled Walls under Lateral Loads", ASCE Journal of Structural Engineering, Vol. 130, No. 2, 297-309

Kusumastuti, D., 2005. "A Versatile Experimentation Model for Study of Structures near Collapse: Applications to Seismic Evaluation of Irregular Structures", Ph.D. dissertation, Department of Civil, Structural and Environmental Engineering, University at Buffalo, NY

LRFD 3rd Edition, 2001. "Manual of Steel Construction, Load and Resistance Factor Design, Third Edition", American Institute of Steel Construction, Inc.

MacRae, G. and Priestley, M. J. N., 1994. "Precast Post-tensioned Ungrouted Concrete Beam-Column Subassemblage Tests", Report No. SSRP-94/10, University of California at San Diego, La Jolla, CA.

Mander, J. B. and Cheng, C. T., 1997. "Seismic Resistance of Bridge Piers Based on Damage Avoidance Design", Technical Report NCEER-97-0014, National Center for Earthquake Engineering Research, Buffalo, NY

Mavroeidis, G. and Papageorgiou, A.S., (2003), "A Mathematical Representation of Near-Fault Ground Motions", Bull. Seism. Soc. Am., 93, 1099-1131.

Nims, D. K., Richter, P. J., and Bachman, R. E., 1993. "The Use of Energy Dissipating Restraint for Seismic Hazard Mitigation", Earthquake Spectra, Vol. 9, No. 3, pp. 467-489.

Pampanin, S., Priestley, M. J. N., and Sritharan, S., 2000. "PRESSS Phase: The Five-Story Precast Test Building Vol. 3-4 Frame Direction Response", Report No. SSRP-2000/08, University of California at San Diego, La Jolla, CA.

Perez, F. J., 2004. "Large Scale Lateral Load Tests of Unbonded Post-Tensioned Precast Concrete Walls with Vertical Joint Connectors", Ph.D. dissertation, Department of Civil and Environmental Engineering, Lehigh University, Bethlehem, PA, May 2004.

Popov, E. P., Bertero, V. V., and Chandramouli, S. 1975. "Hysteretic Behavior of Steel Columns", Earthquake Engineering Research Center Report, UCB/EERC-75-11, University of California, Berkeley.

Popov, E. P. and Bertero, V. V. 1973. "Cyclic Loading of Steel Beams and Connections", Journal of Structural Division, ASCE, v99 nST6, June, 1973

Popov, E. P. and Pinkney, R. B. 1969. "Cyclic Yield Reversal in Steel Building Connections", Journal of the Structural Division, ASCE, v95 nST3, March 1969.

Priestley, M. J. N. and Tao, J. R., 1993. "Seismic Response of Precast Concrete Frames With Partially Debonded Tendons", PCI Journal, Vol. 38, No. 1, pp. 58-67.
Priestley, M. J. N., Sritharan, S., Conley, J. R., and Pampanin, S., 1999. "Preliminary Results and Conclusions From the PRESSS Five-Story Precast Concrete Test Building. PCI Journal, Vol. 44, No.6, pp. 42-47.

Restrepo, J. I., 2002. “New Generation of Earthquake Resisting Systems”, Proceedings, the first FIB Congress, Federation International du Beton, Paper E-268, Osaka, Japan.

Ricles, J. M., Sause, R., Garlock, M., and Zhao, C., 2001. “Posttensioned seismic-resistant connections for steel frames.” Journal of Structural Engineering, Vol. 127, No. 2, 113–121.

Ricles, J. M., Sause, R., Peng, S. W., and Lu, L. W., 2002. “Experimental evaluation of earthquake resistant posttensioned steel connections.” Journal of Structural Engineering, Vol. 128, No. 7, 850–859.

Rojas, P., Ricles, J. M., and Sause, R., 2005. "Seismic Performance of Post-tensioned Steel Moment Resisting Frames With Friction Devices", Journal of Structural Engineering, Vol. 131, No. 4, 529-540.

SAC, 1995. “Steel Moment Frame Connection”, Advisory No. 3, Report No. SAC 95-01, Sacramento, CA.

Stanton, J. F., Stone, W. C., and Cheok, G. S., 1997. “A Hybrid Reinforced Precast Frame for Seismic Regions”, PCI Journal, Vol. 42, No. 2, pp. 20-32.

Stanton, J. F. and Nakaki, S. D., 2002. “Design Guidelines for Precast Concrete Structural Systems”, PRESS Report No. 01/03-09.

Shen, Q., and Kurama, Y. C., 2002. “Nonlinear Behavior of Posttensioned Hybrid Coupled Wall Subassemblages”, ASCE Journal of Structural Engineering, Vol. 128, No. 10, 1290-1300

Tremblay, R., Timler, P., Bruneau, M. and Filiatrault, A., 1995. “Performance of Steel Structures during the January 17, 1994, Northridge Earthquake”. Canadian Journal of Civil Engineering. Vol. 22, No. 2: 338-360.

Wanitkorkul, A. and Filiatrault, A., 2005. “Simulation of Strong Ground Motions for Seismic Fragility Evaluation of Nonstructural Components in Hospital”, Technical Report: MCEER-05-2005, Multidisciplinary Center for Earthquake Engineering Research, University at Buffalo, NY.

Whittaker, A. S., Krumme, R., and Hayes, J. R. Jr., 1995. “Structural Control of Building response Using Shape-Memory Alloys”, Report No. TR 95/22, National Technical Information Service, VA.

Witting, P. R. and Cozzarelli, F. A., 1992. “Shape Memory Structural Dampers: Material Properties, Design and Seismic Testing”, Report NCEER-92-0013, National Center for Earthquake Engineering Research, Buffalo, NY

Yang, T. Y. and Whittaker, A., 2002. “MCEER Demonstration Hospitals”, Department of Civil, Structural and Environmental Engineering, University at Buffalo. (available online at http://civil.eng.buffalo.edu/hospital/)

Appendix A Relative Performance Index (RPI) under MCEER ground motions having a 2% probability of exceedance in 50 years in California, U.S.

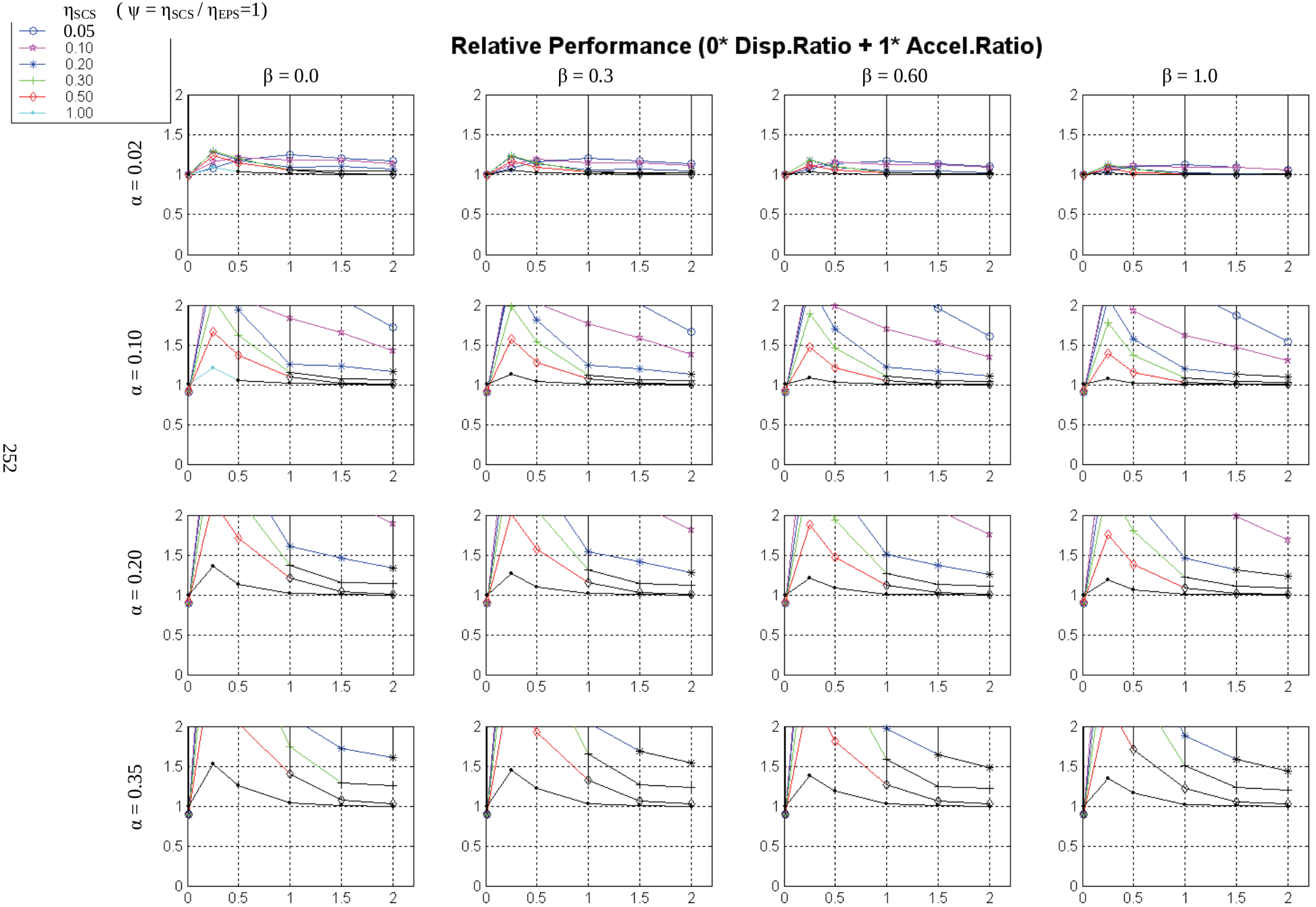
ηSCS (ψ = ηSCS / ηEPS=1)
0.05
0.10
0.20
0.30
0.50
1.00
Relative Performance (0* Disp.Ratio + 1* Accel.Ratio)
β = 0.0
β = 0.3
β = 0.60
β = 1.0
α = 0.02
α = 0.10
α = 0.20
α = 0.35

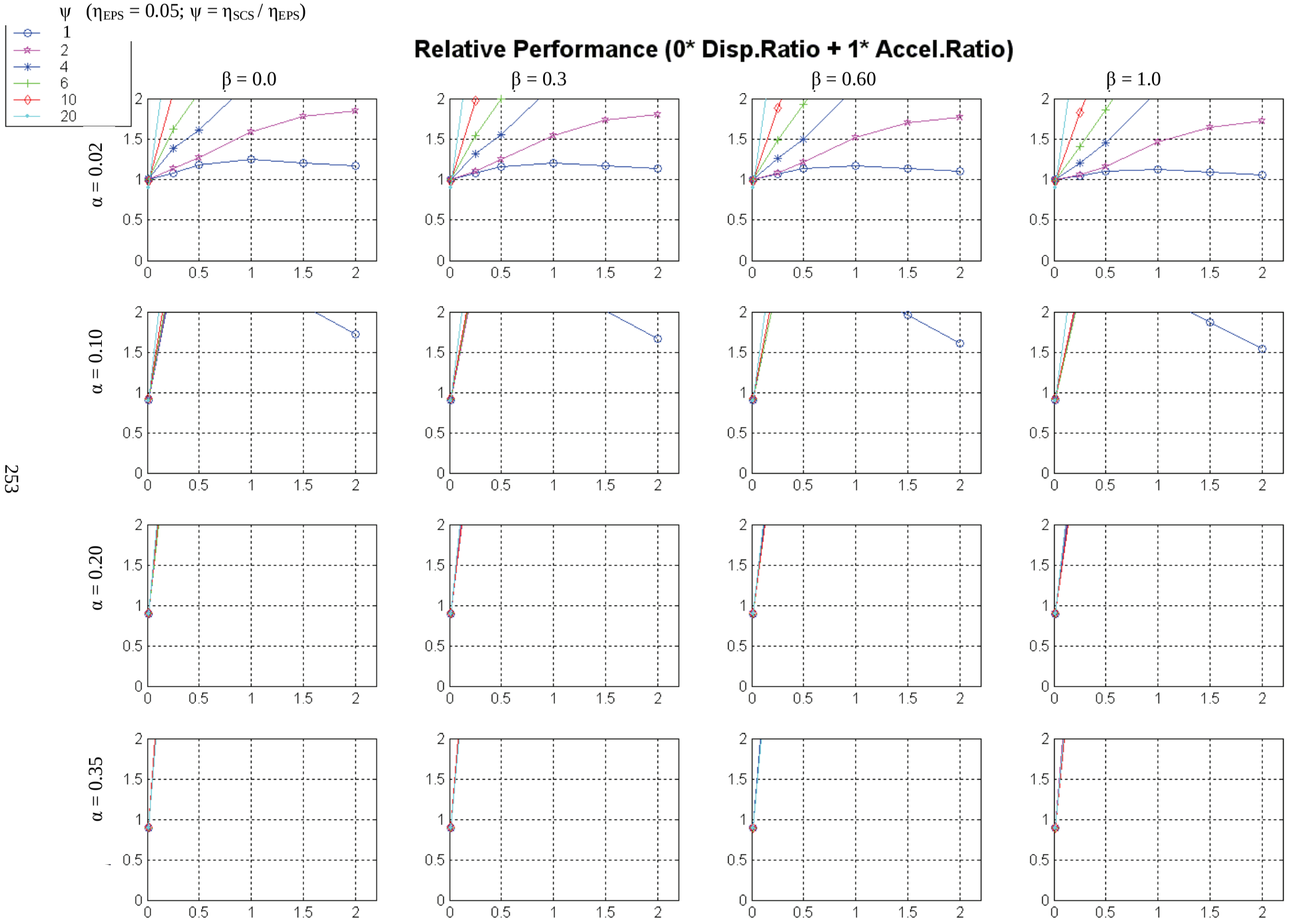
ψ (ηEPS = 0.05; ψ = ηSCS / ηEPS)
1
2
4
6
10
20
Relative Performance (0* Disp.Ratio + 1* Accel.Ratio)
β = 0.0
β = 0.3
β = 0.60
β = 1.0
α = 0.02
α = 0.10
α = 0.20
α = 0.35

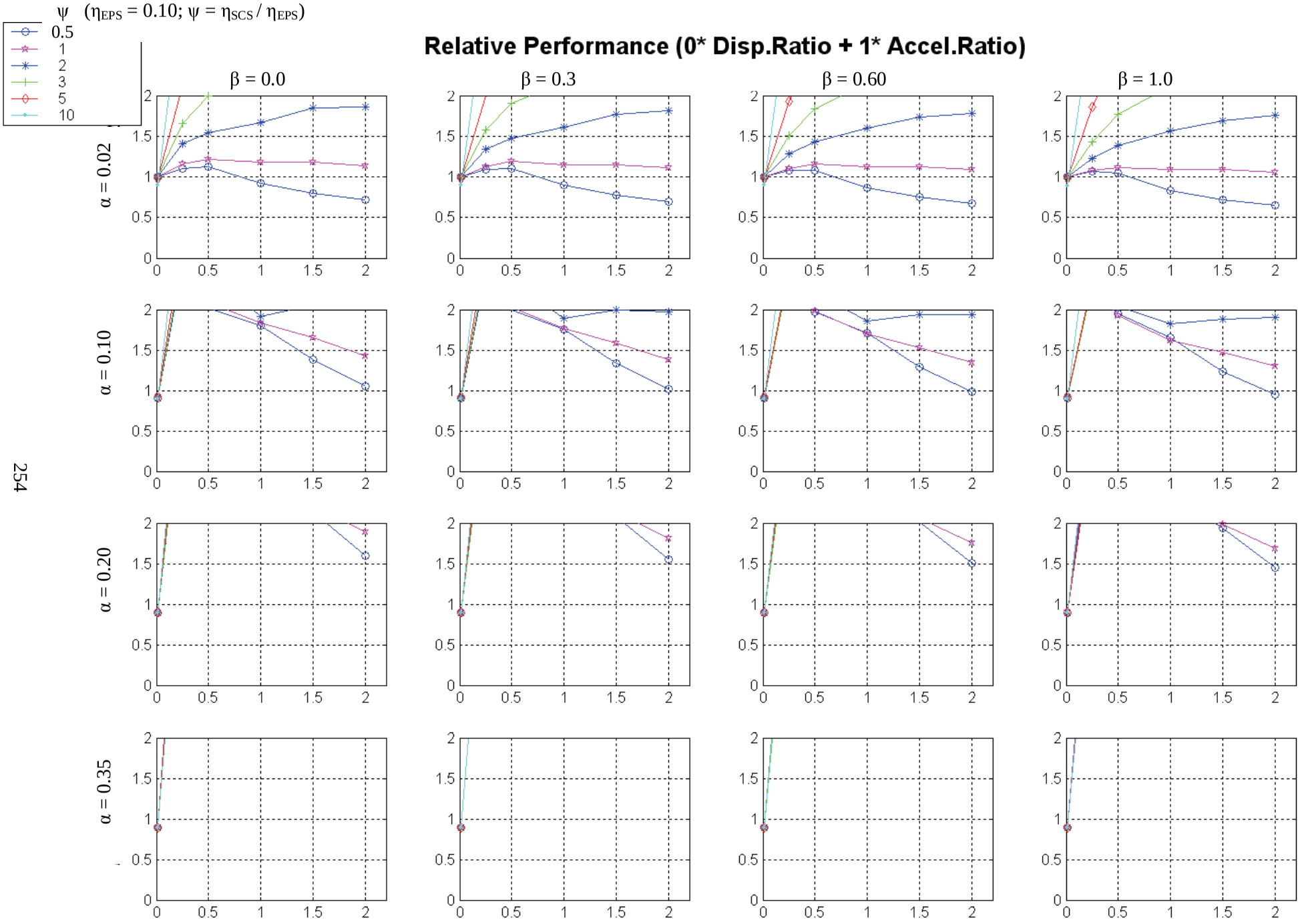
ψ (ηEPS = 0.10; ψ = ηSCS / ηEPS)
0.5
1
2
3
5
10
Relative Performance (0* Disp.Ratio + 1* Accel.Ratio)
β = 0.0
β = 0.3
β = 0.60
β = 1.0
α = 0.02
α = 0.10
α = 0.20
α = 0.35

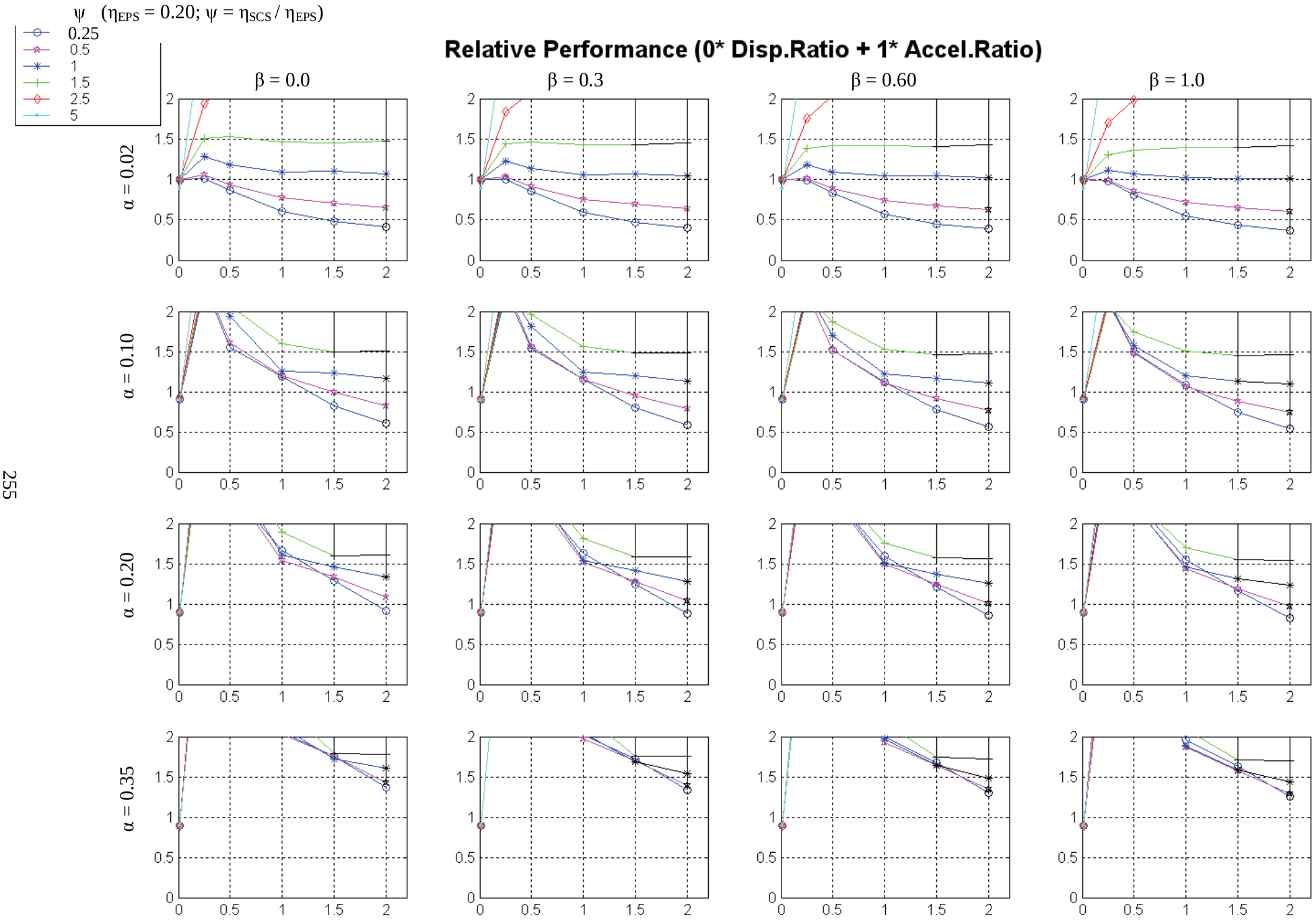
ψ (ηEPS = 0.20; ψ = ηSCS / ηEPS)
0.25
0.5
1
1.5
2.5
5
Relative Performance (0* Disp.Ratio + 1* Accel.Ratio)
β = 0.0
β = 0.3
β = 0.60
β = 1.0
α = 0.02
α = 0.10
α = 0.20
α = 0.35

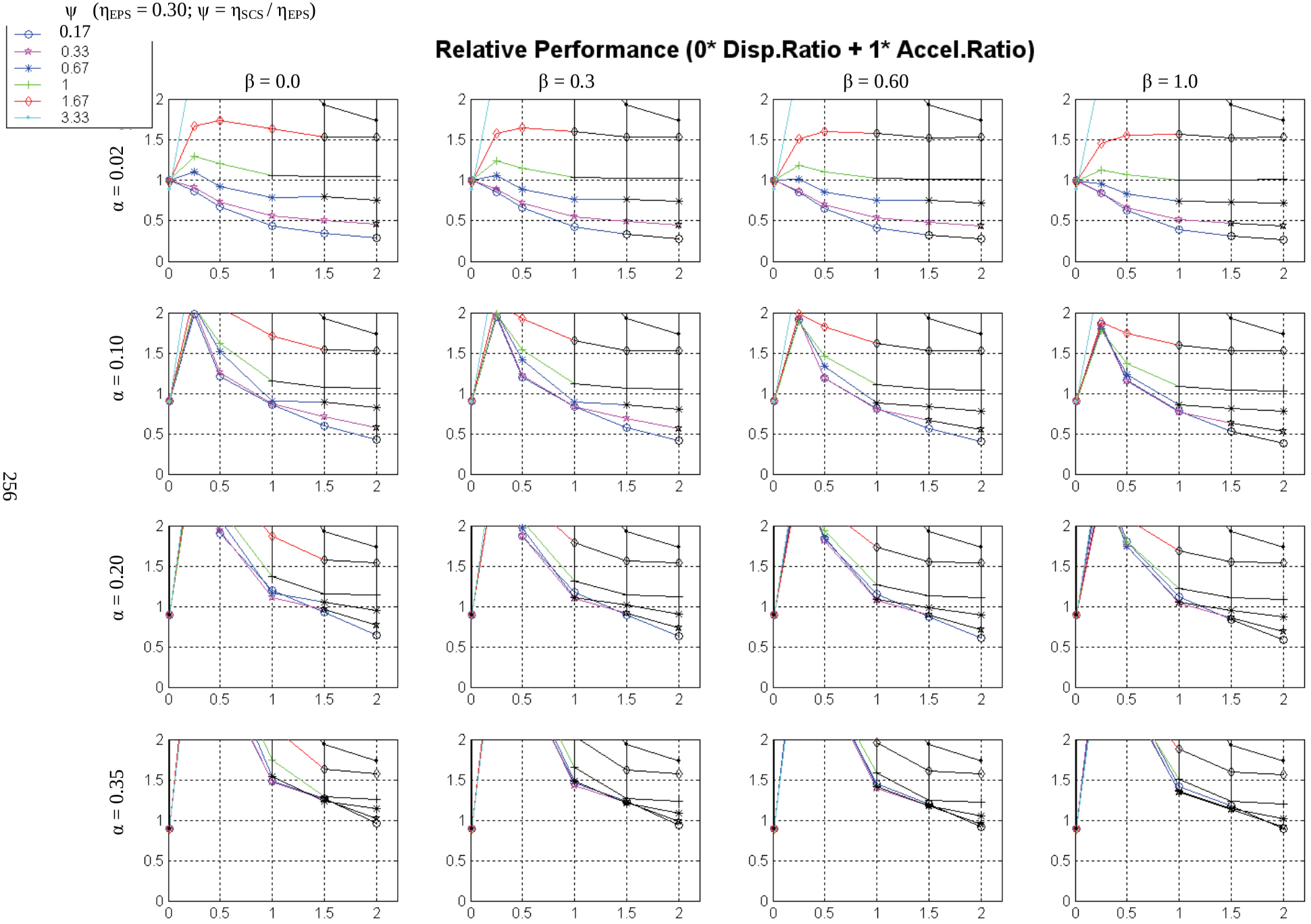
ψ (ηEPS = 0.30; ψ = ηSCS / ηEPS)
0.17
0.33
0.67
1
1.67
3.33
Relative Performance (0* Disp.Ratio + 1* Accel.Ratio)
β = 0.0
β = 0.3
β = 0.60
β = 1.0
α = 0.02
α = 0.10
α = 0.20
α = 0.35

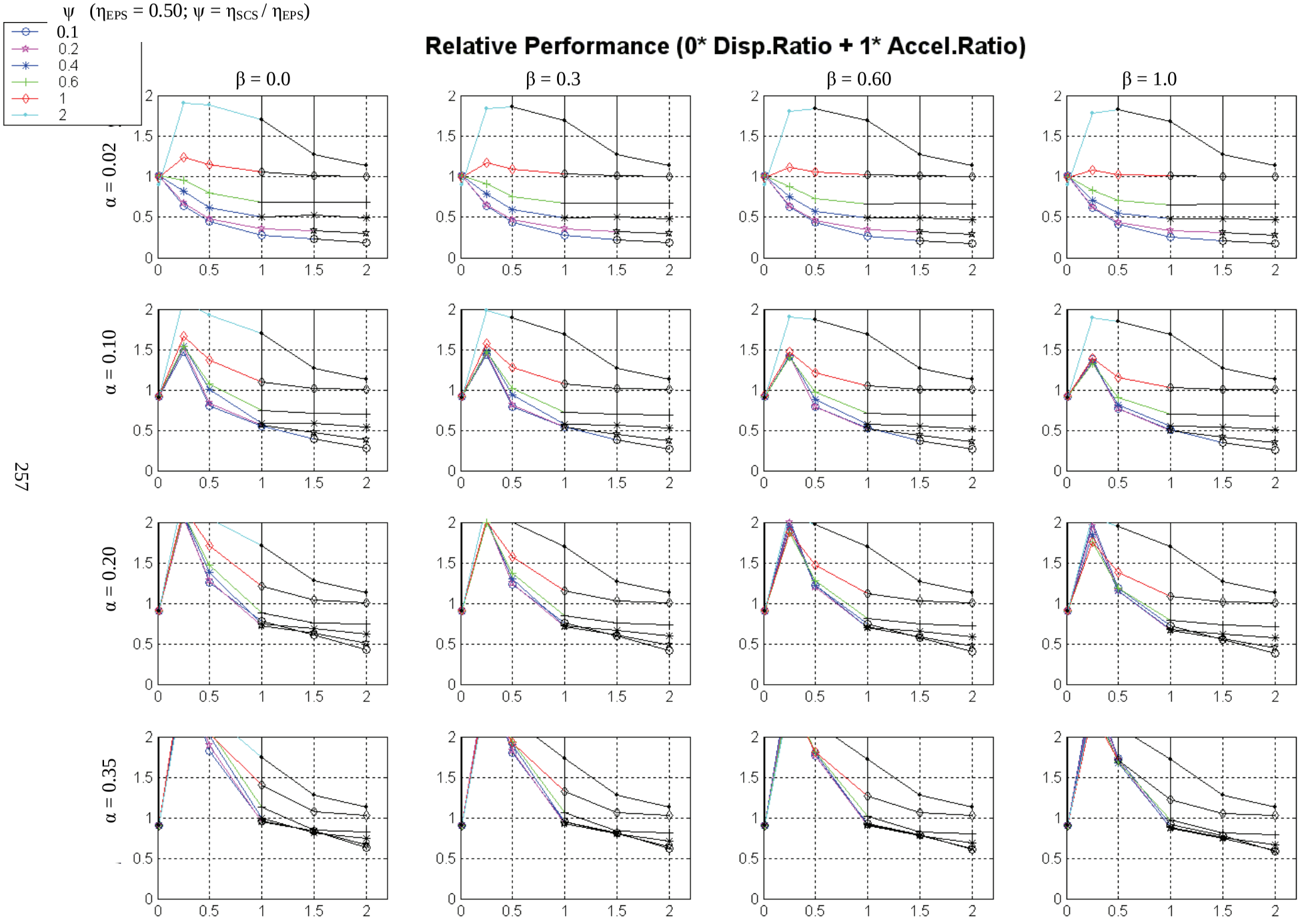
ψ (ηEPS = 0.50; ψ = ηSCS / ηEPS)
0.1
0.2
0.4
0.6
1
2
Relative Performance (0* Disp.Ratio + 1* Accel.Ratio)
β = 0.0
β = 0.3
β = 0.60
β = 1.0
α = 0.02
α = 0.10
α = 0.20
α = 0.35

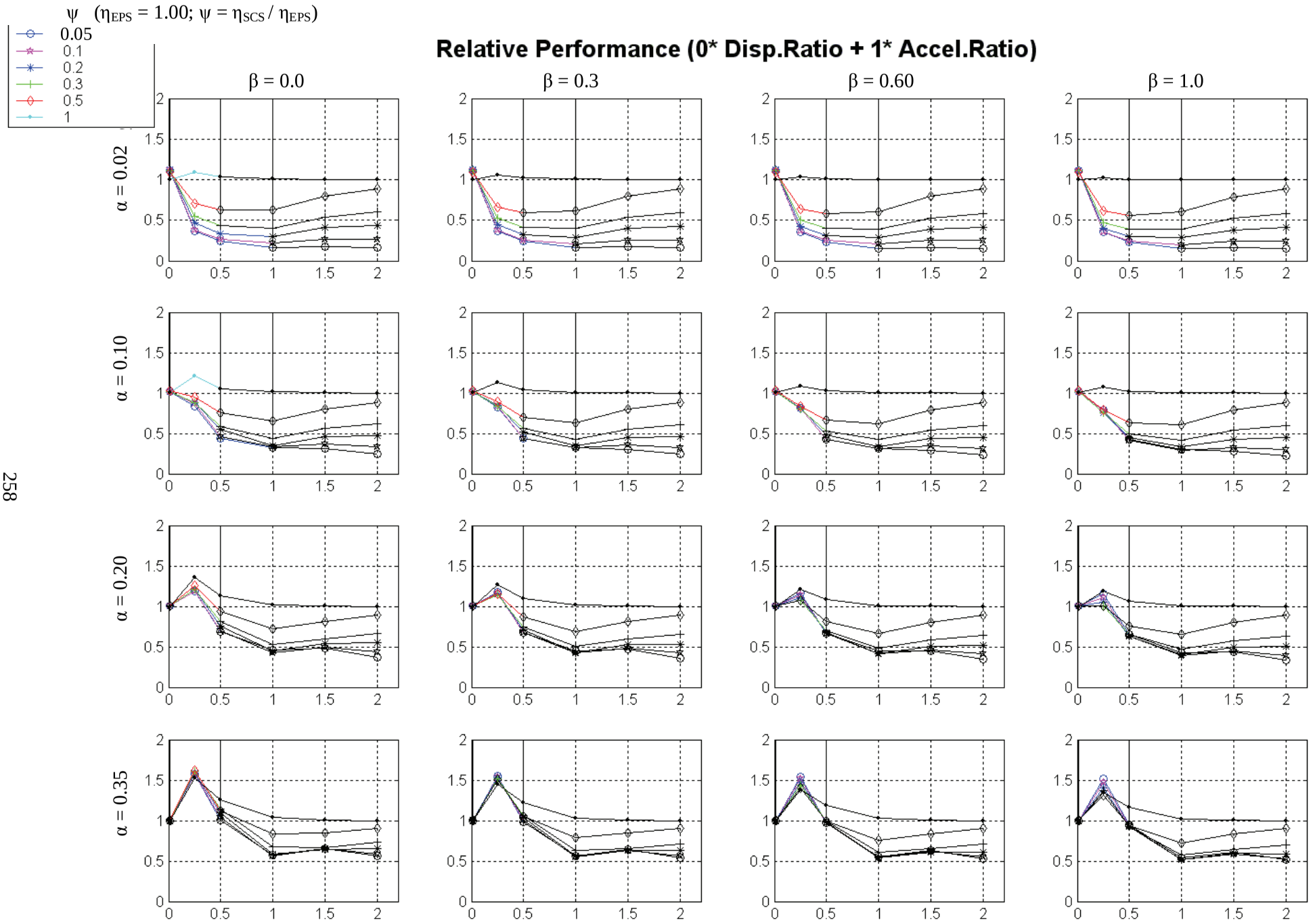
ψ (ηEPS = 1.00; ψ = ηSCS / ηEPS)
0.05
0.1
0.2
0.3
0.5
1
Relative Performance (0* Disp.Ratio + 1* Accel.Ratio)
β = 0.0
β = 0.3
β = 0.60
β = 1.0
α = 0.02
α = 0.10
α = 0.20
α = 0.35

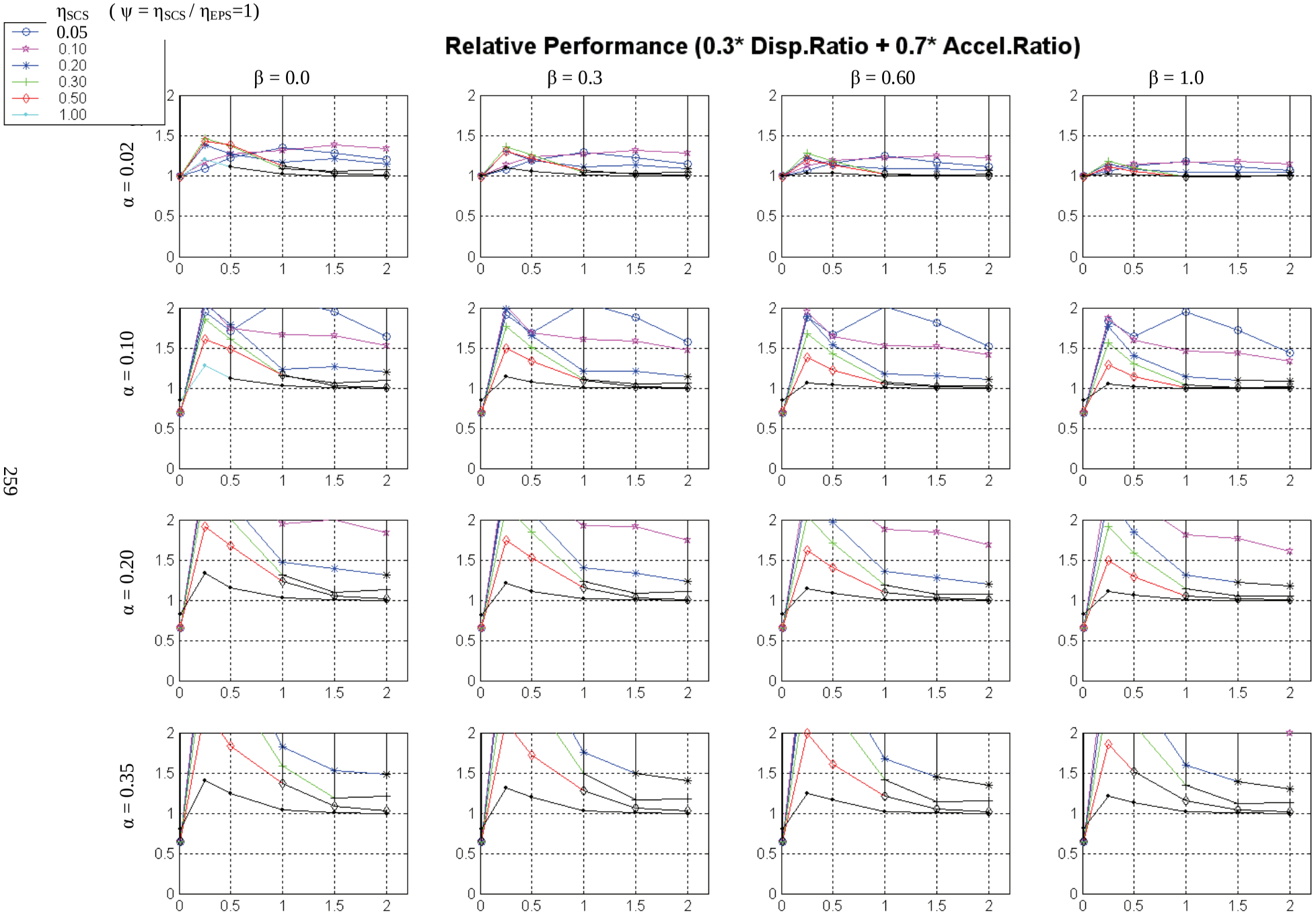
ηSCS (ψ = ηSCS / ηEPS=1)
0.05
0.10
0.20
0.30
0.50
1.00
Relative Performance (0.3* Disp.Ratio + 0.7* Accel.Ratio)
β = 0.0
β = 0.3
β = 0.60
β = 1.0
α = 0.02
α = 0.10
α = 0.20
α = 0.35

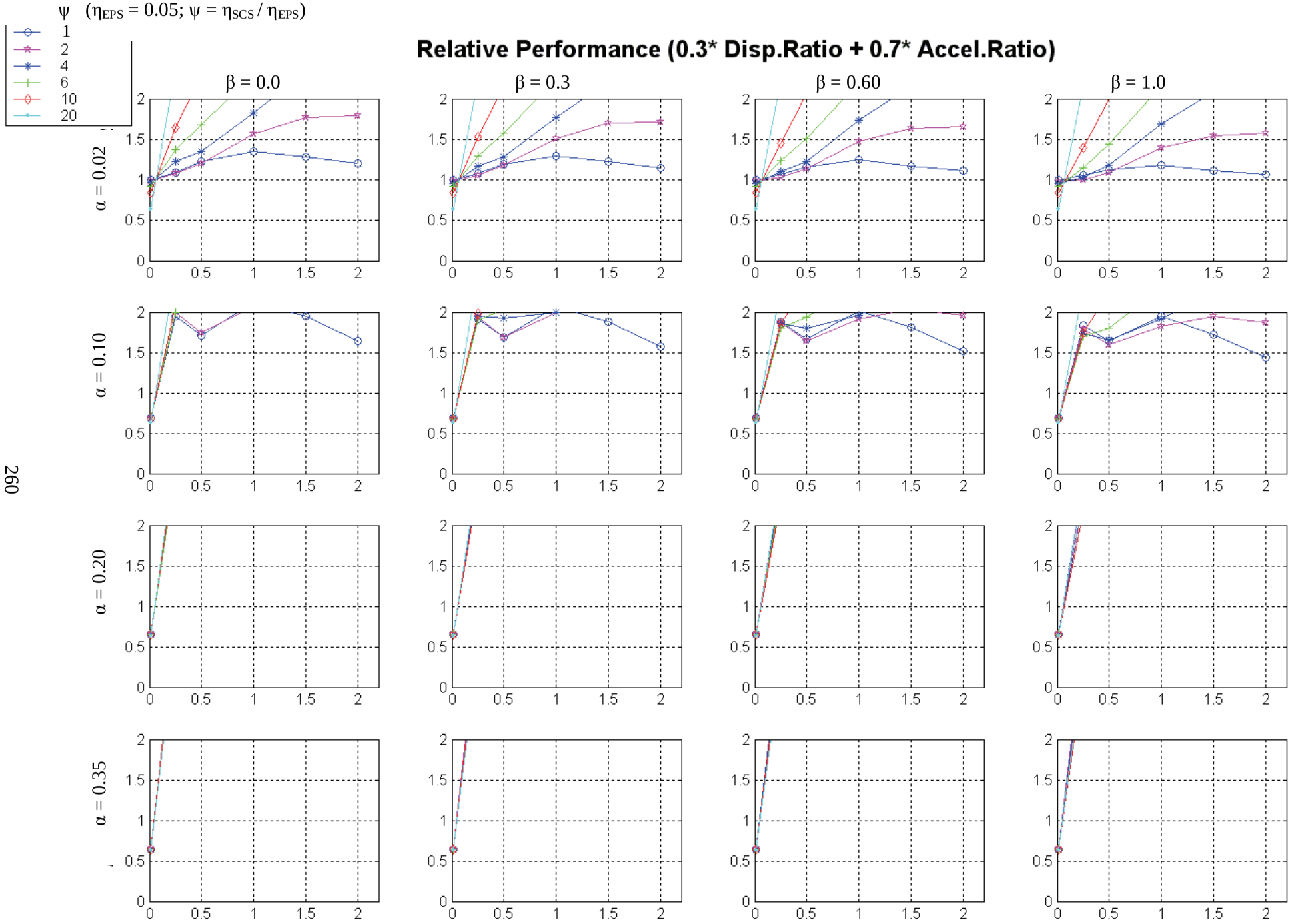
ψ (ηEPS = 0.05; ψ = ηSCS / ηEPS)
1
2
4
6
10
20
Relative Performance (0.3* Disp.Ratio + 0.7* Accel.Ratio)
β = 0.0
β = 0.3
β = 0.60
β = 1.0
α = 0.02
α = 0.10
α = 0.20
α = 0.35

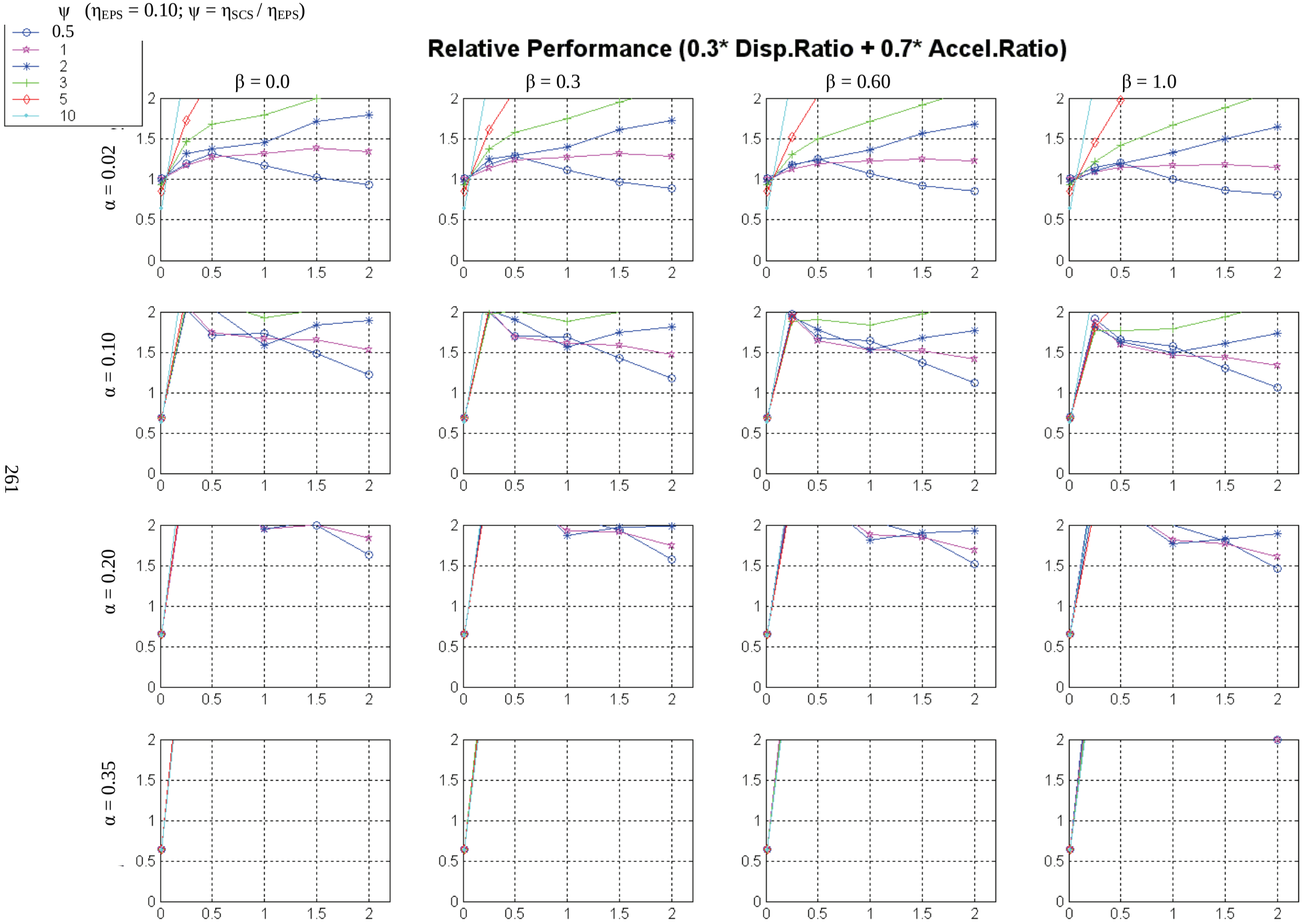
ψ (ηEPS = 0.10; ψ = ηSCS / ηEPS)
0.5
1
2
3
5
10
Relative Performance (0.3* Disp.Ratio + 0.7* Accel.Ratio)
β = 0.0
β = 0.3
β = 0.60
β = 1.0
α = 0.02
α = 0.10
α = 0.20
α = 0.35

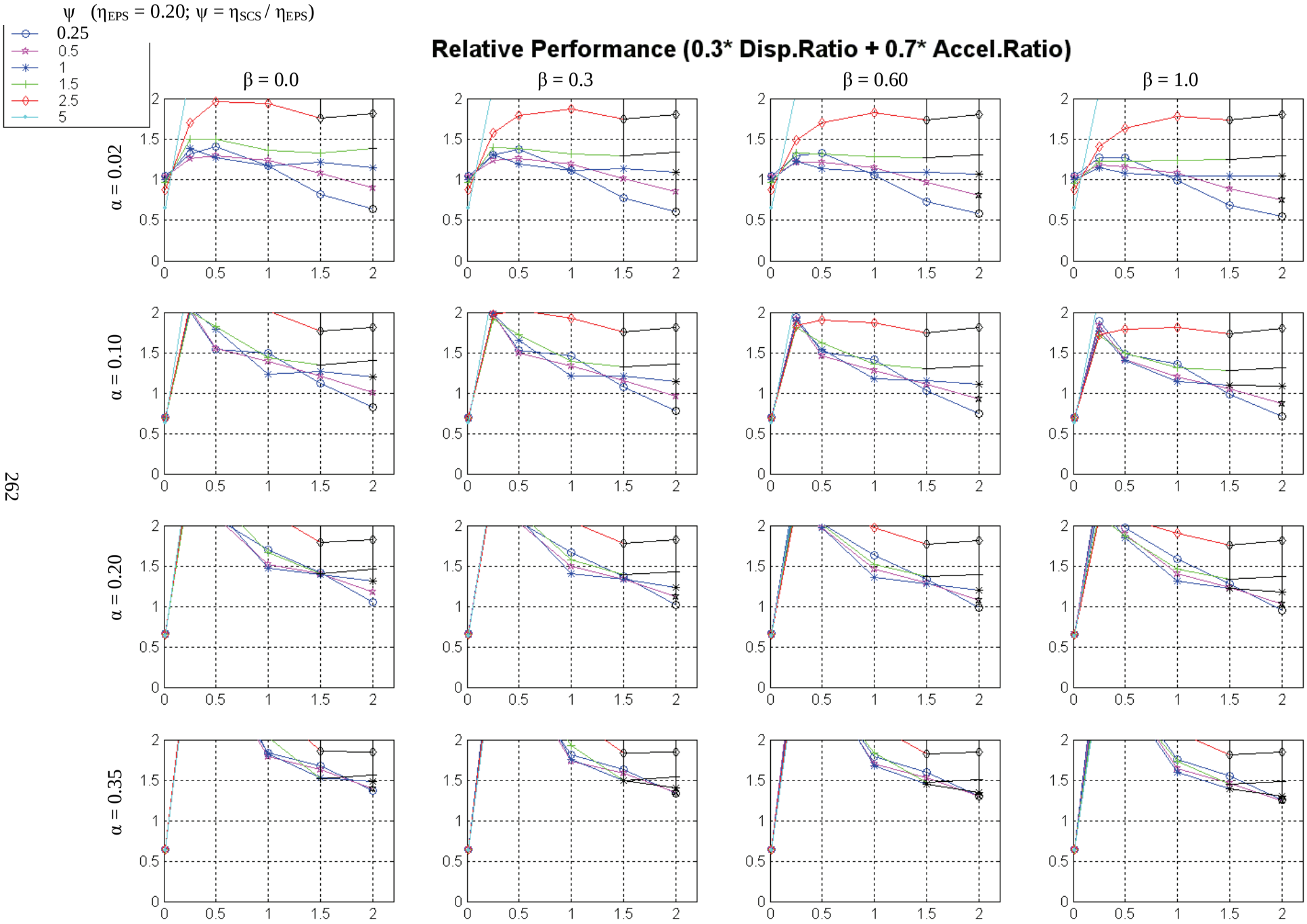
ψ (ηEPS = 0.20; ψ = ηSCS / ηEPS)
0.25
0.5
1
1.5
2.5
5
Relative Performance (0.3* Disp.Ratio + 0.7* Accel.Ratio)
β = 0.0
β = 0.3
β = 0.60
β = 1.0
α = 0.02
α = 0.10
α = 0.20
α = 0.35

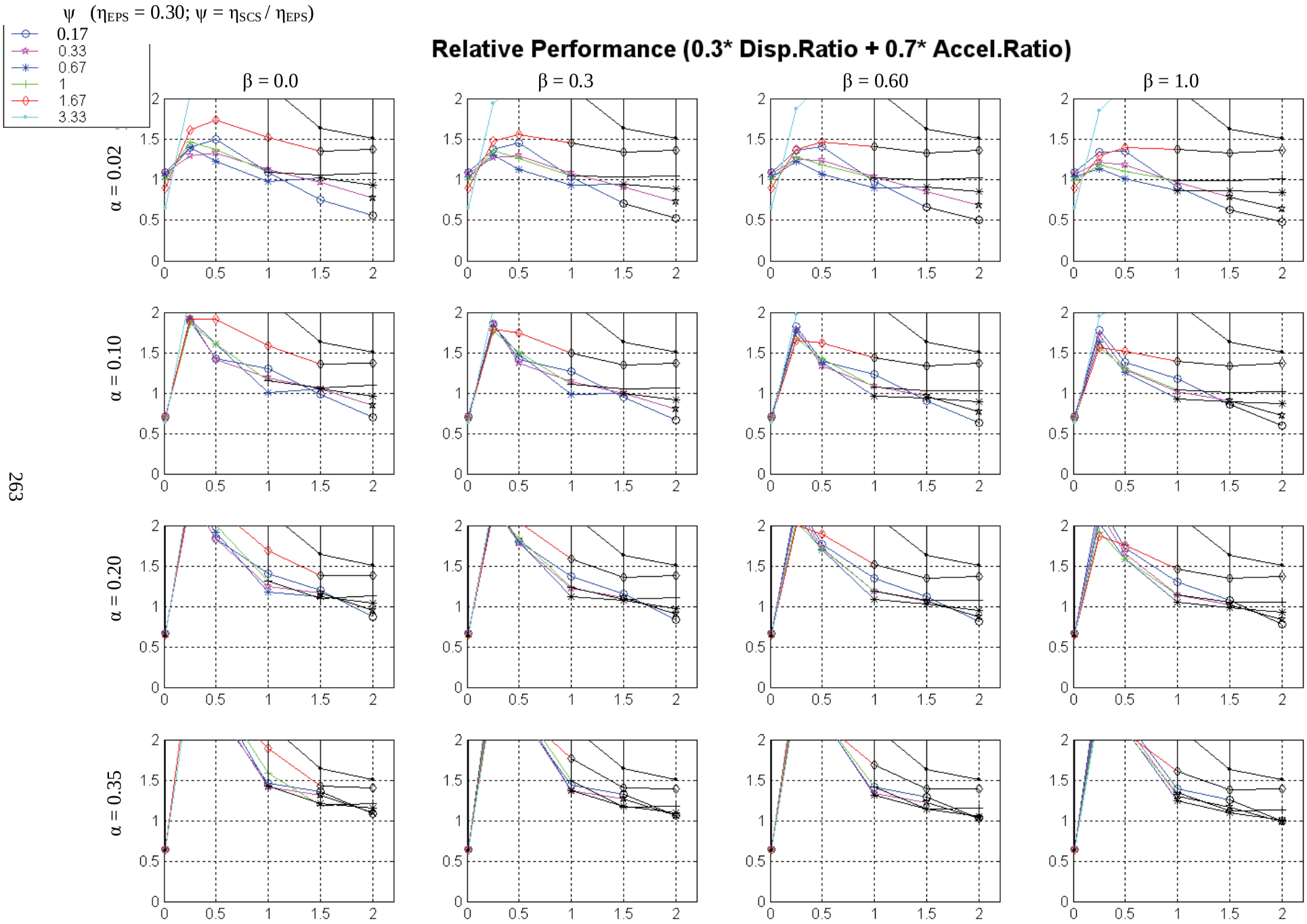
ψ (ηEPS = 0.30; ψ = ηSCS / ηEPS)
0.17
0.33
0.67
1
1.67
3.33
Relative Performance (0.3* Disp.Ratio + 0.7* Accel.Ratio)
β = 0.0
β = 0.3
β = 0.60
β = 1.0
α = 0.02
α = 0.10
α = 0.20
α = 0.35

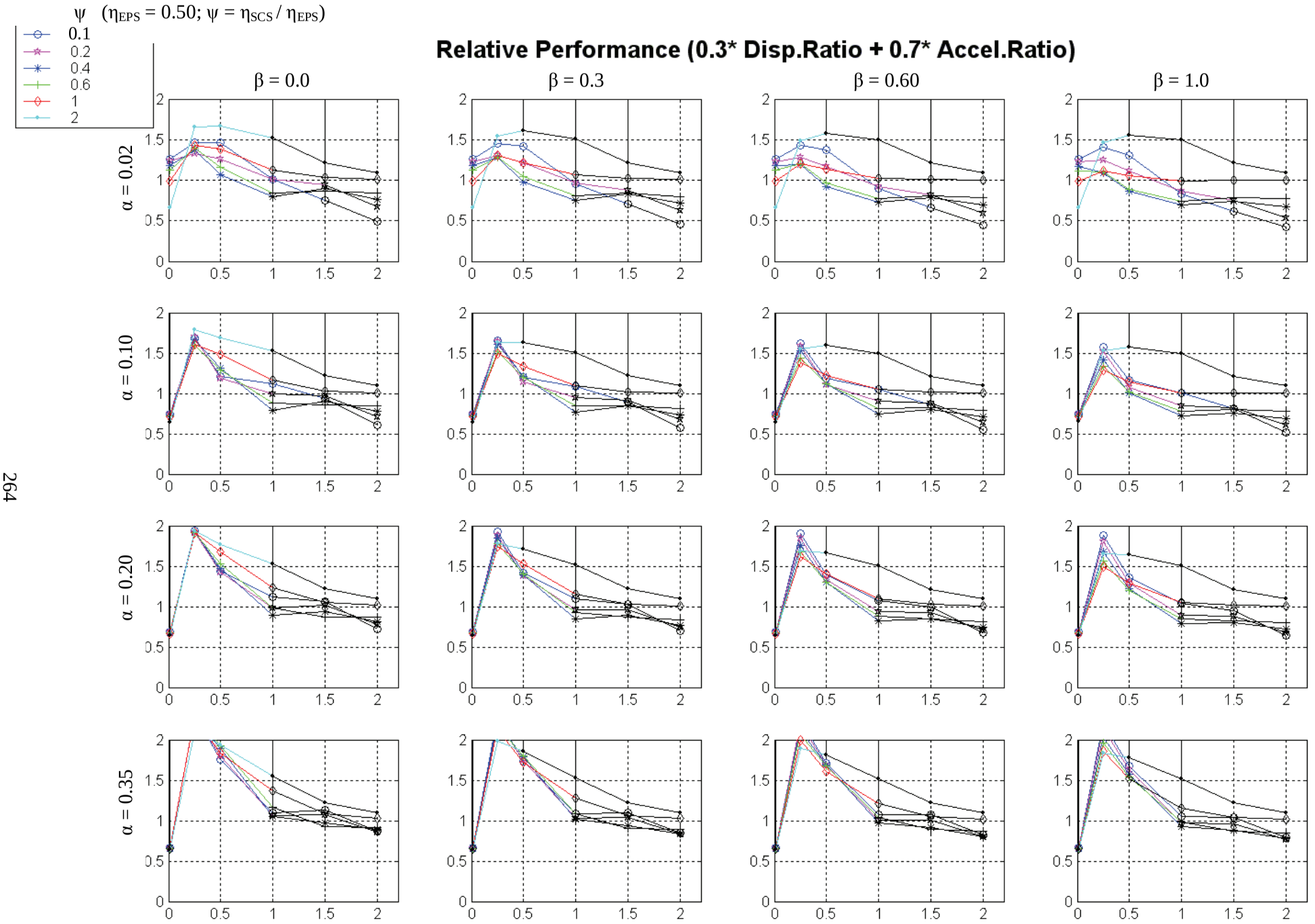
ψ (ηEPS = 0.50; ψ = ηSCS / ηEPS)
0.1
0.2
0.4
0.6
1
2
Relative Performance (0.3* Disp.Ratio + 0.7* Accel.Ratio)
β = 0.0
β = 0.3
β = 0.60
β = 1.0
α = 0.02
α = 0.10
α = 0.20
α = 0.35

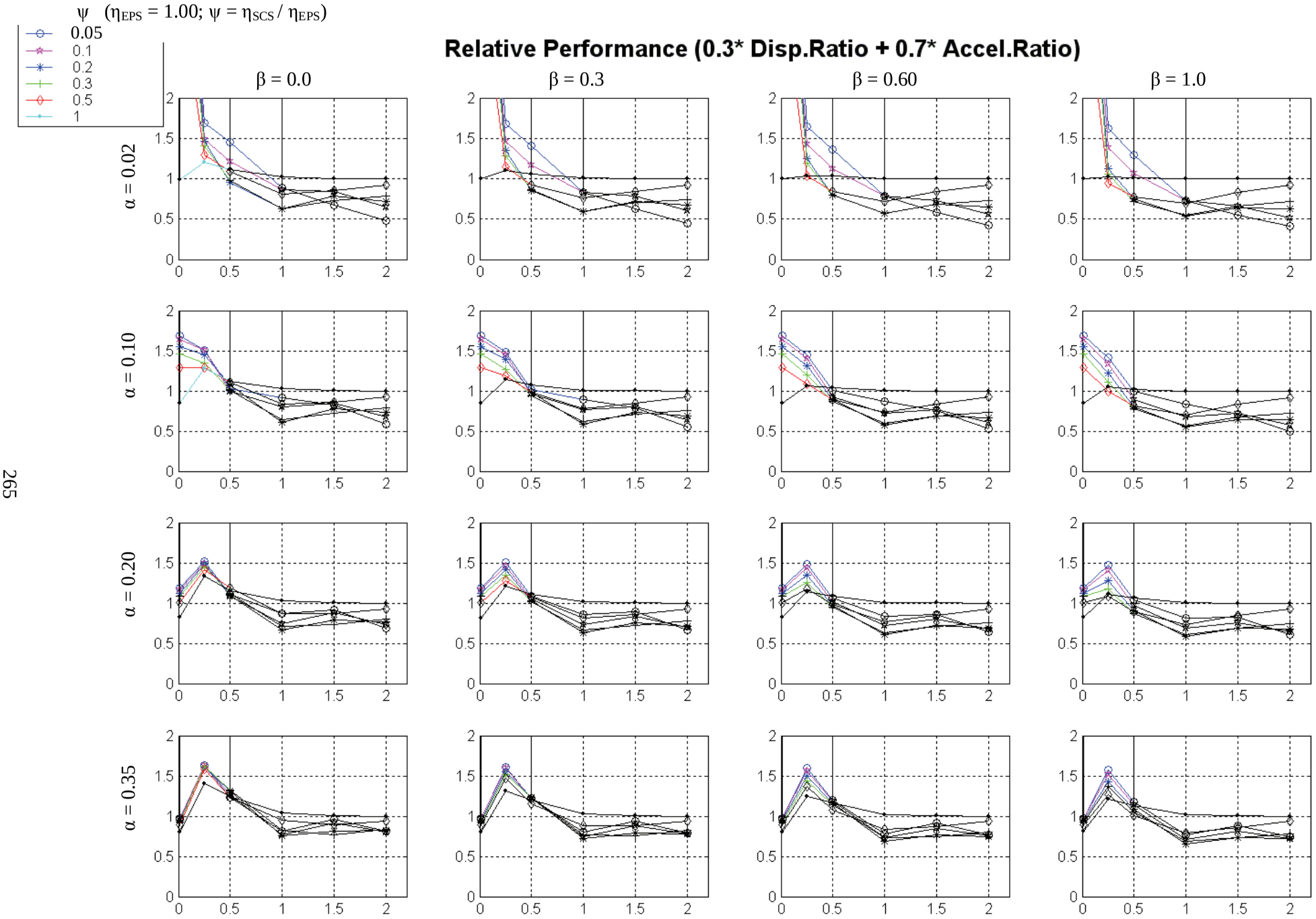
ψ (ηEPS = 1.00; ψ = ηSCS / ηEPS)
0.05
0.1
0.2
0.3
0.5
1
Relative Performance (0.3* Disp.Ratio + 0.7* Accel.Ratio)
β = 0.0
β = 0.3
β = 0.60
β = 1.0
α = 0.02
α = 0.10
α = 0.20
α = 0.35

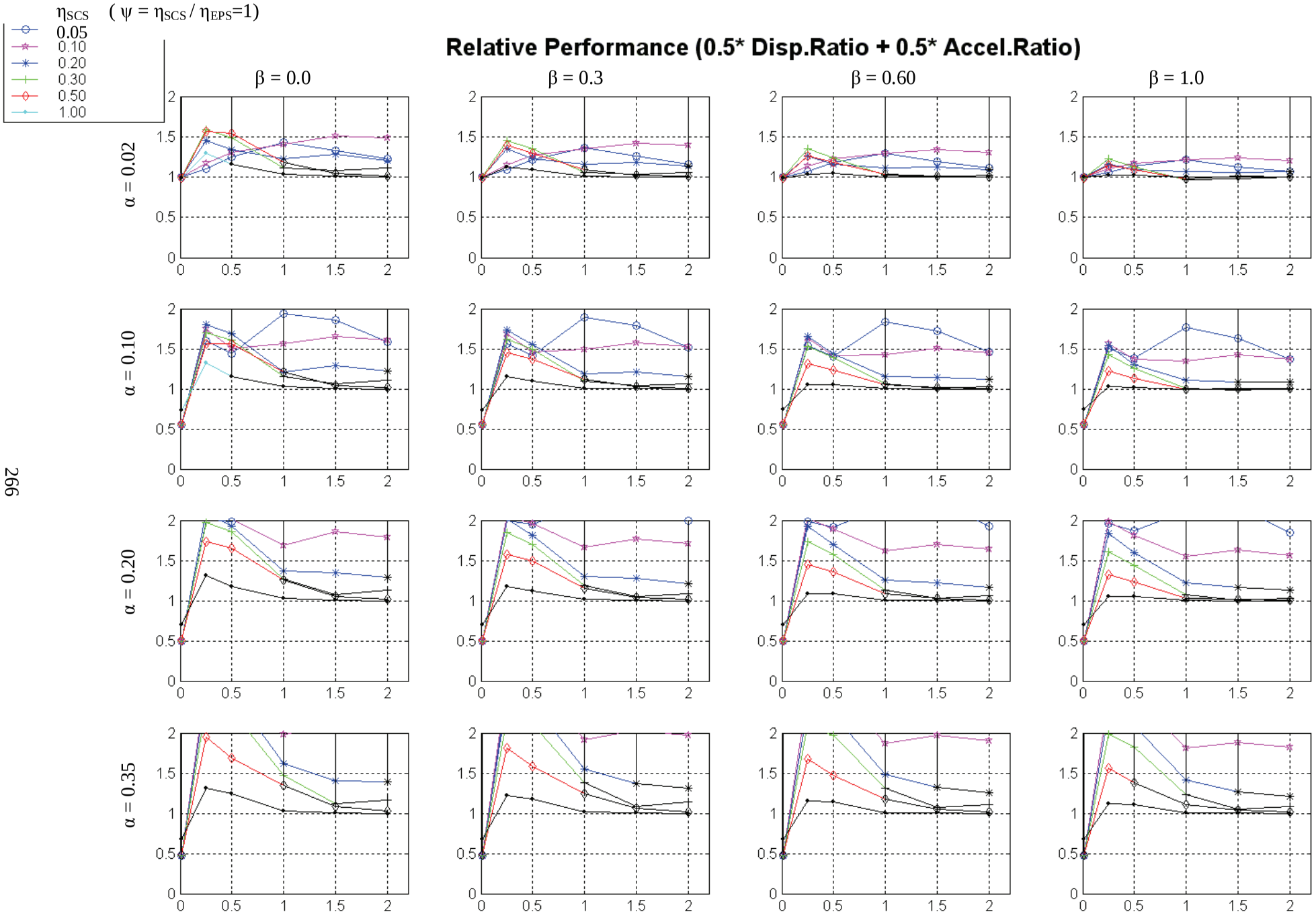
ηSCS (ψ = ηSCS / ηEPS=1)
0.05
0.10
0.20
0.30
0.50
1.00
Relative Performance (0.5* Disp.Ratio + 0.5* Accel.Ratio)
β = 0.0
β = 0.3
β = 0.60
β = 1.0
α = 0.02
α = 0.10
α = 0.20
α = 0.35

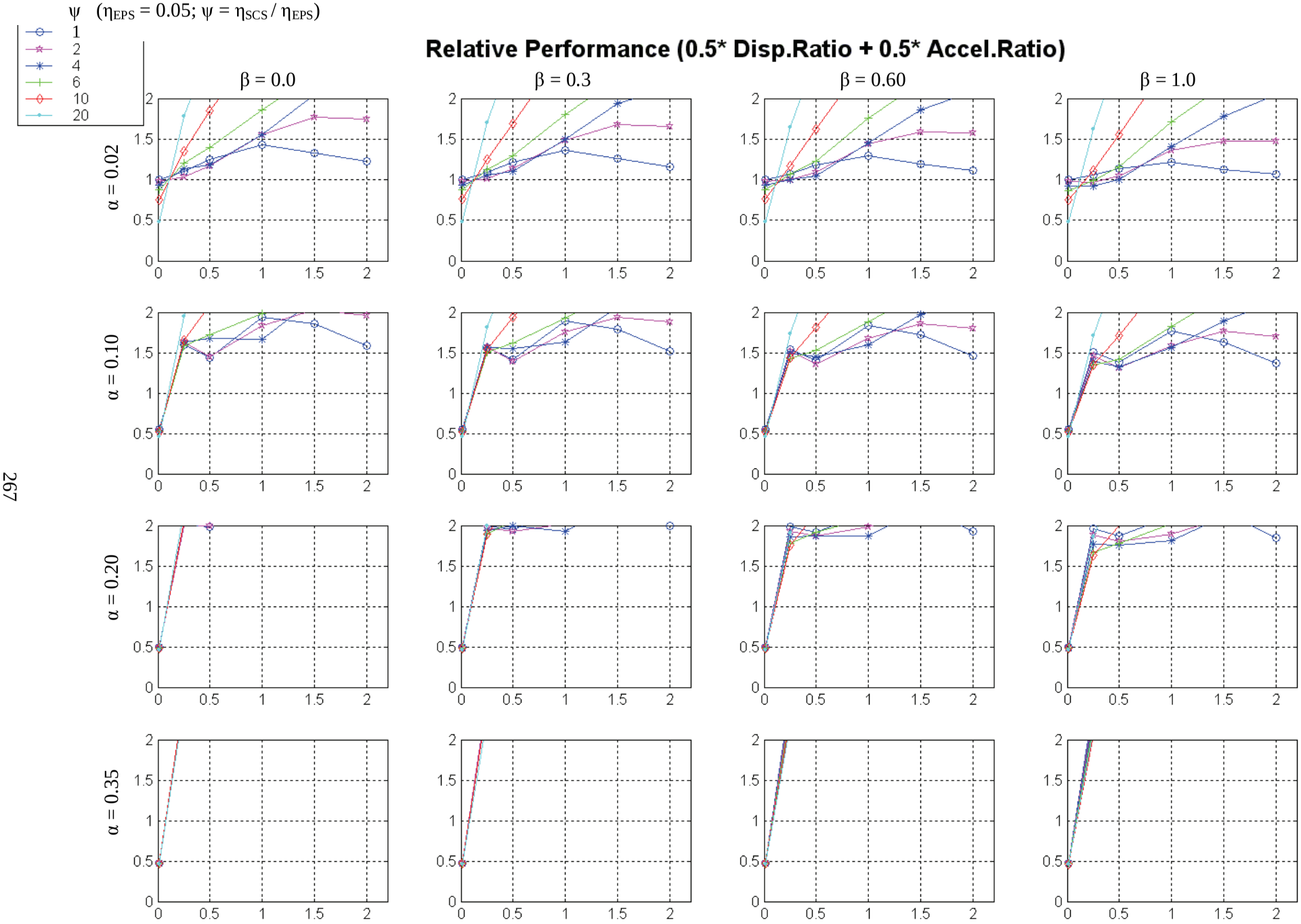
ψ (ηEPS = 0.05; ψ = ηSCS / ηEPS)
1
2
4
6
10
20
Relative Performance (0.5* Disp.Ratio + 0.5* Accel.Ratio)
β = 0.0
β = 0.3
β = 0.60
β = 1.0
α = 0.02
α = 0.10
α = 0.20
α = 0.35

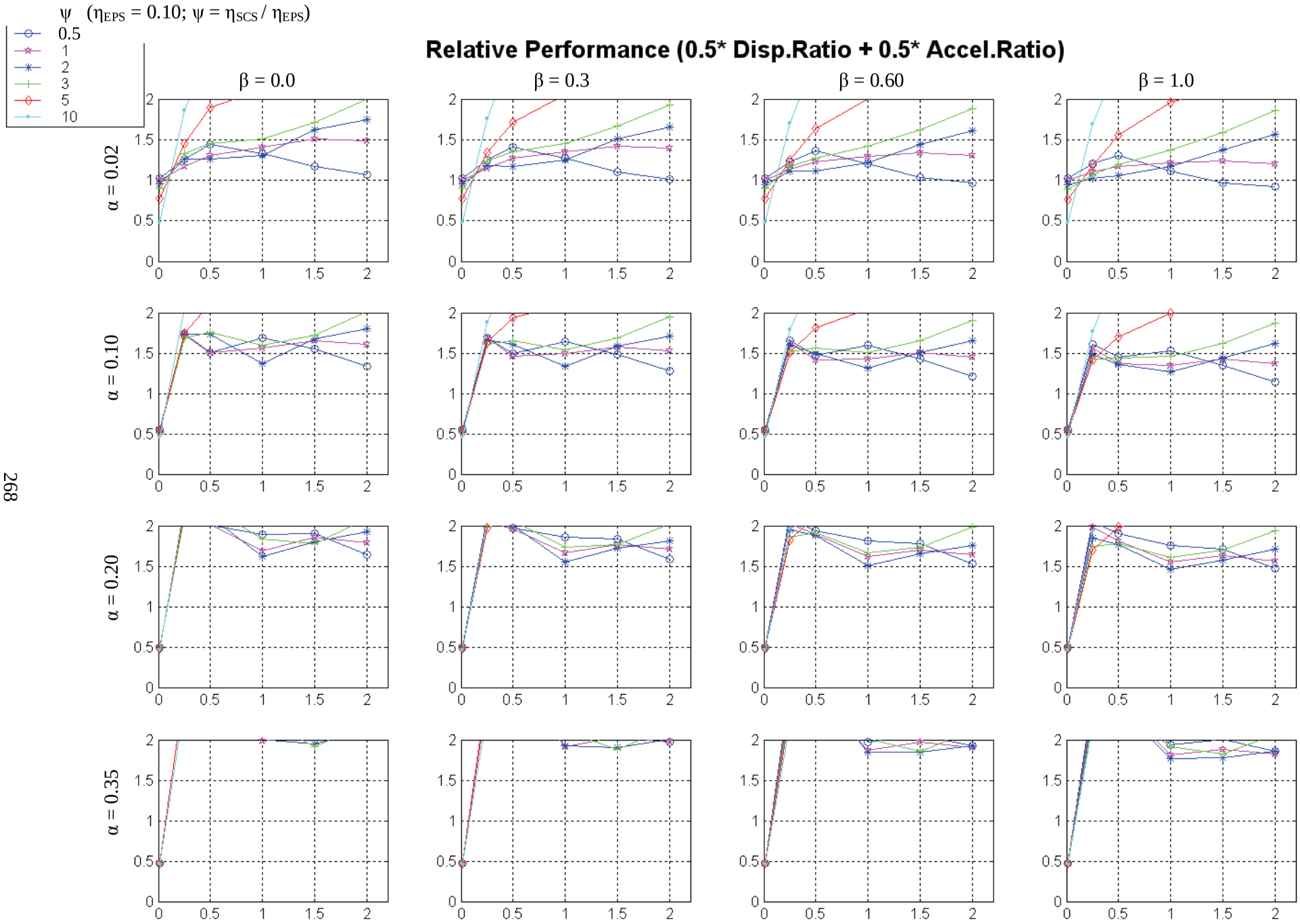
ψ (ηEPS = 0.10; ψ = ηSCS / ηEPS)
0.5
1
2
3
5
10
Relative Performance (0.5* Disp.Ratio + 0.5* Accel.Ratio)
β = 0.0
β = 0.3
β = 0.60
β = 1.0
α = 0.02
α = 0.10
α = 0.20
α = 0.35

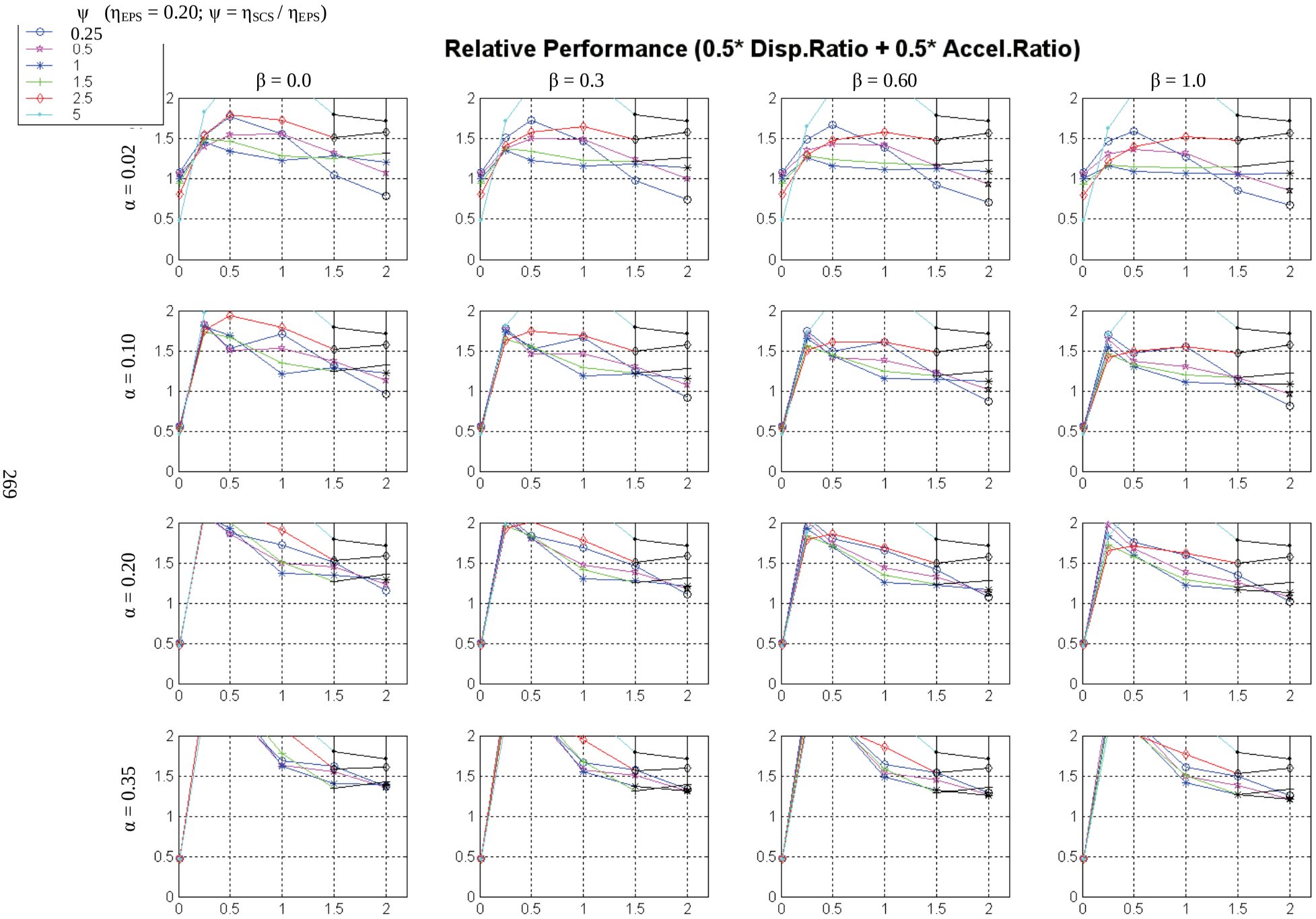
ψ (ηEPS = 0.20; ψ = ηSCS / ηEPS)
0.25
0.5
1
1.5
2.5
5
Relative Performance (0.5* Disp.Ratio + 0.5* Accel.Ratio)
β = 0.0
β = 0.3
β = 0.60
β = 1.0
α = 0.02
α = 0.10
α = 0.20
α = 0.35

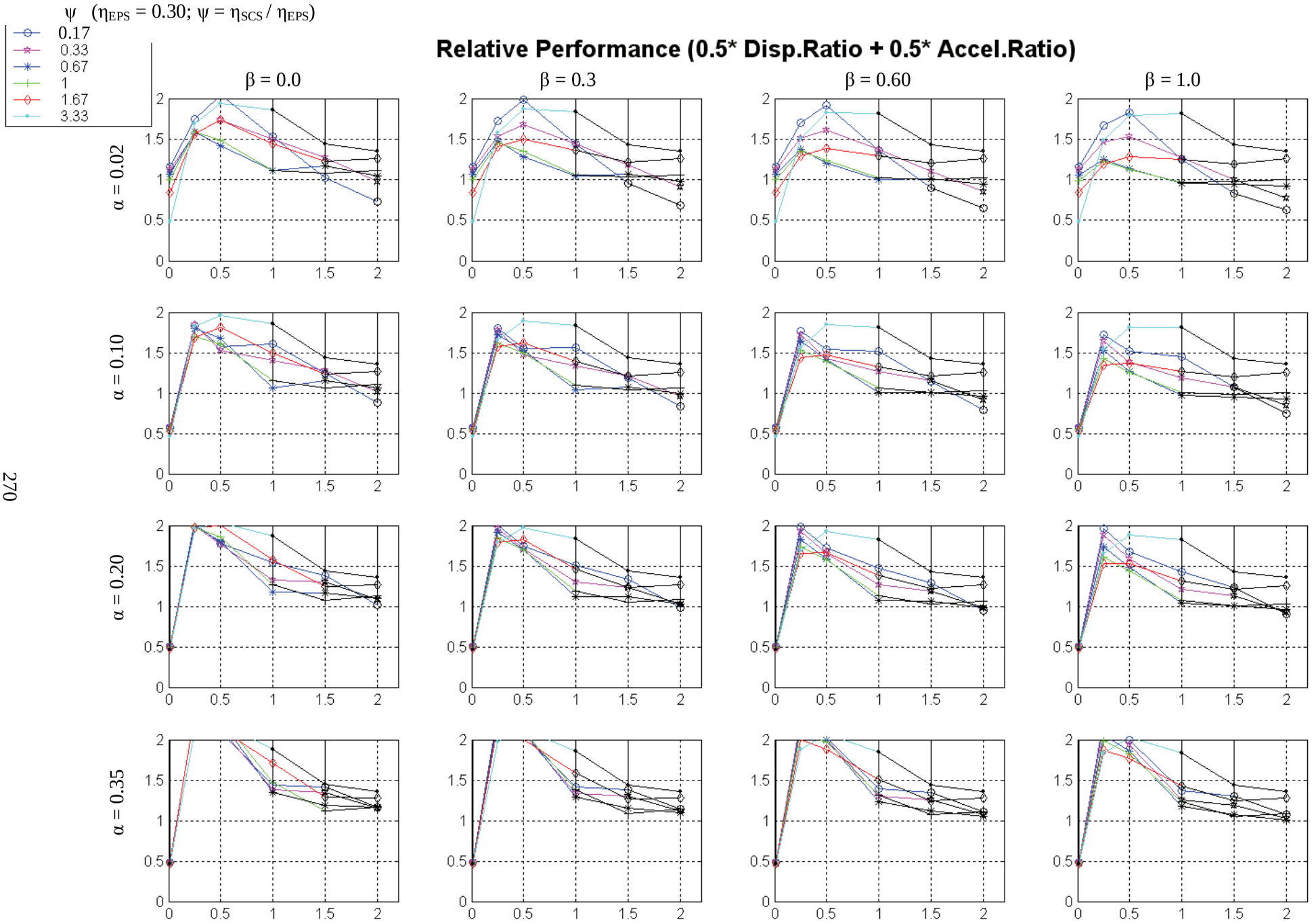
ψ (ηEPS = 0.30; ψ = ηSCS / ηEPS)
0.17
0.33
0.67
1
1.67
3.33
Relative Performance (0.5* Disp.Ratio + 0.5* Accel.Ratio)
β = 0.0
β = 0.3
β = 0.60
β = 1.0
α = 0.02
α = 0.10
α = 0.20
α = 0.35

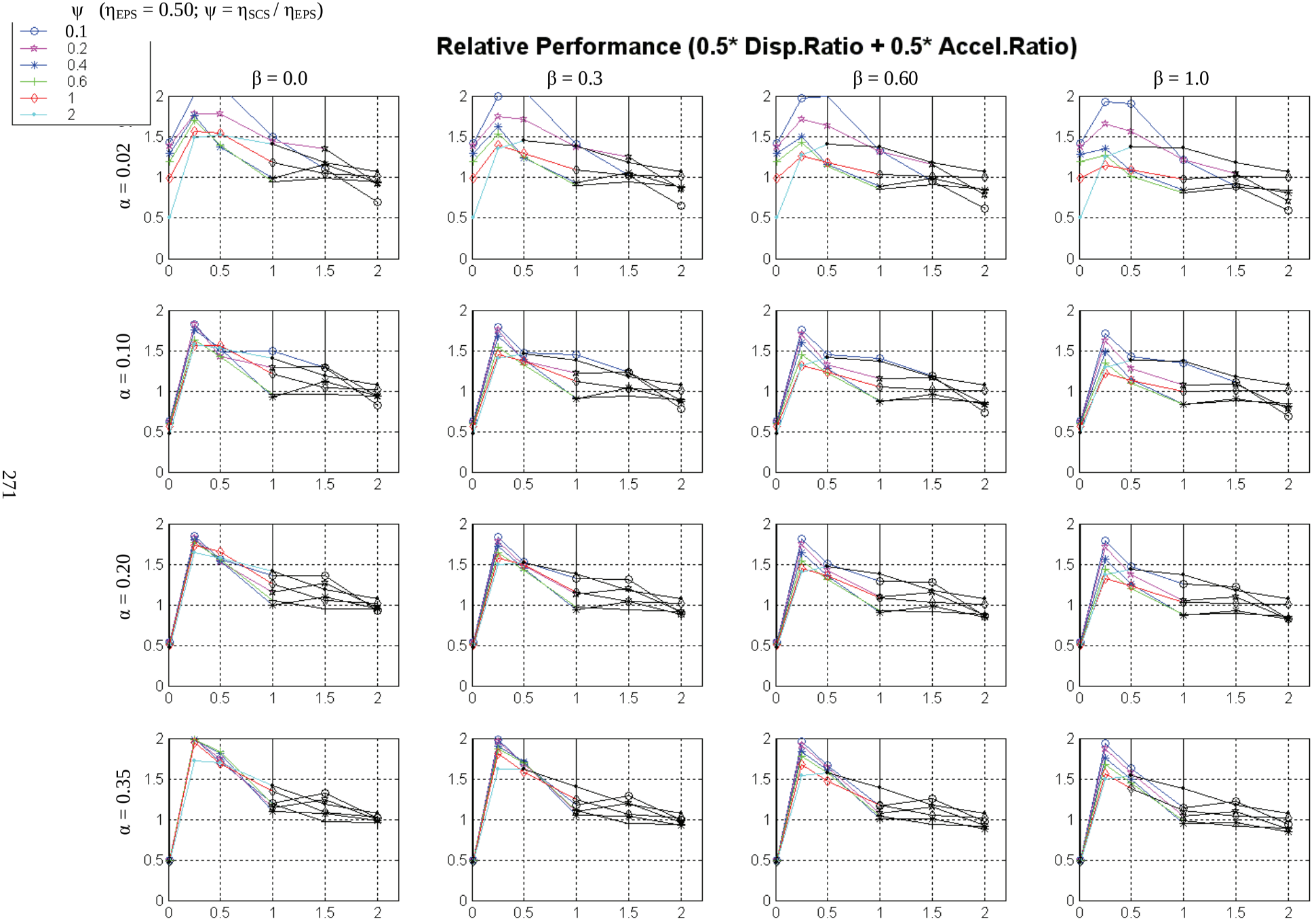
ψ (ηEPS = 0.50; ψ = ηSCS / ηEPS)
0.1
0.2
0.4
0.6
1
2
Relative Performance (0.5* Disp.Ratio + 0.5* Accel.Ratio)
β = 0.0
β = 0.3
β = 0.60
β = 1.0
α = 0.02
α = 0.10
α = 0.20
α = 0.35

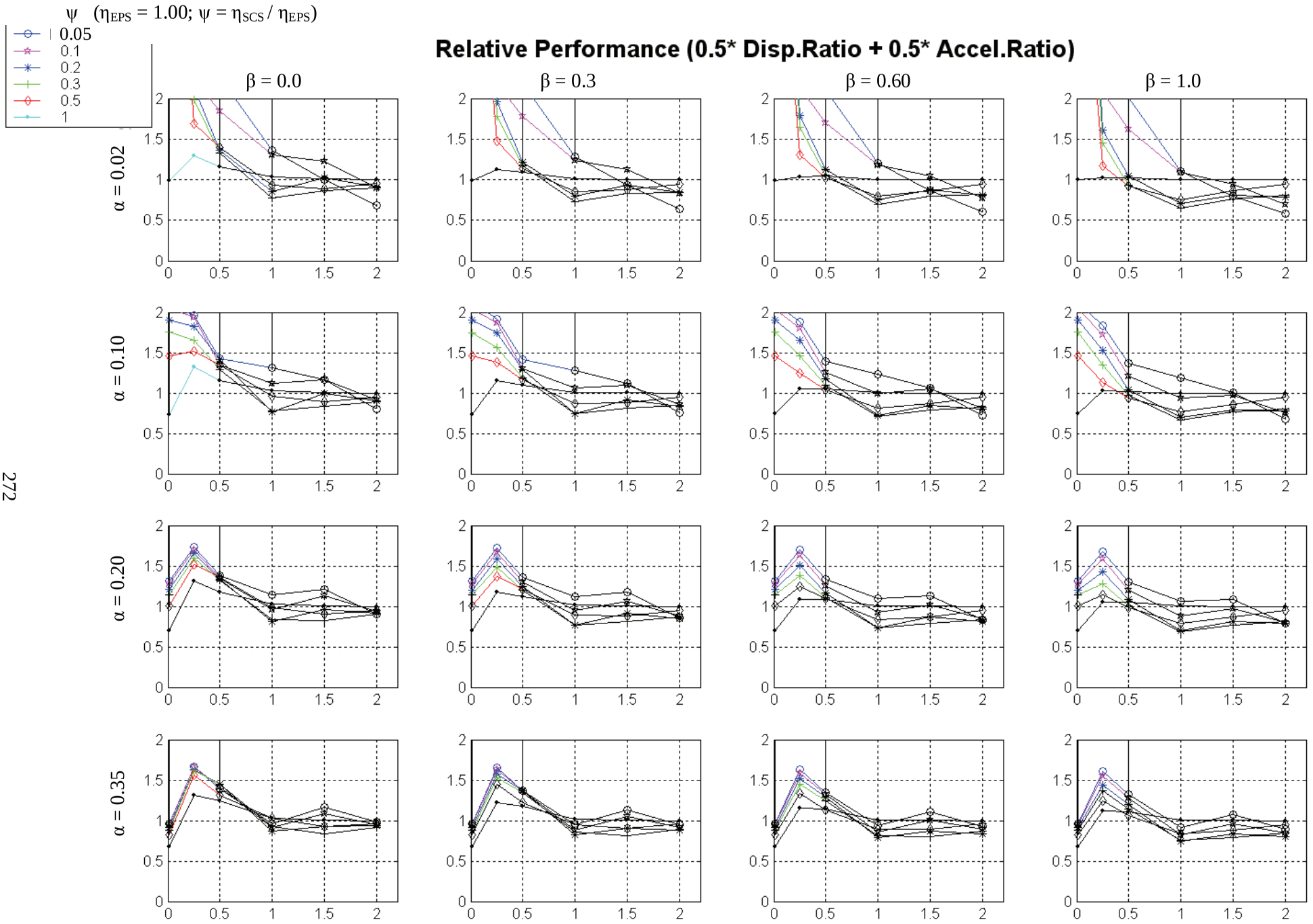
ψ (ηEPS = 1.00; ψ = ηSCS / ηEPS)
0.05
0.1
0.2
0.3
0.5
1
Relative Performance (0.5* Disp.Ratio + 0.5* Accel.Ratio)
β = 0.0
β = 0.3
β = 0.60
β = 1.0
α = 0.02
α = 0.10
α = 0.20
α = 0.35

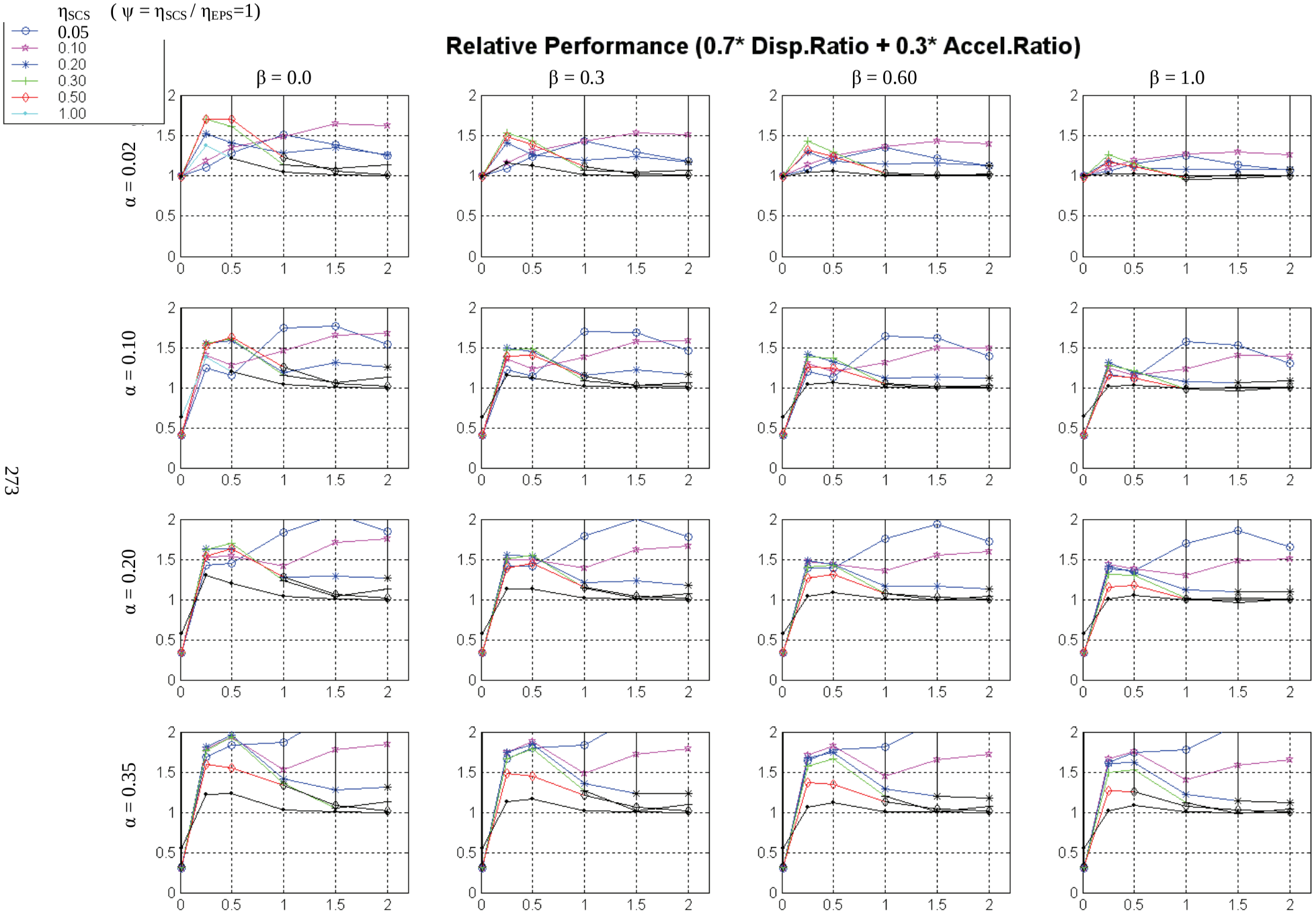
ηSCS (ψ = ηSCS / ηEPS=1)
0.05
0.10
0.20
0.30
0.50
1.00
Relative Performance (0.7* Disp.Ratio + 0.3* Accel.Ratio)
β = 0.0
β = 0.3
β = 0.60
β = 1.0
α = 0.02
α = 0.10
α = 0.20
α = 0.35

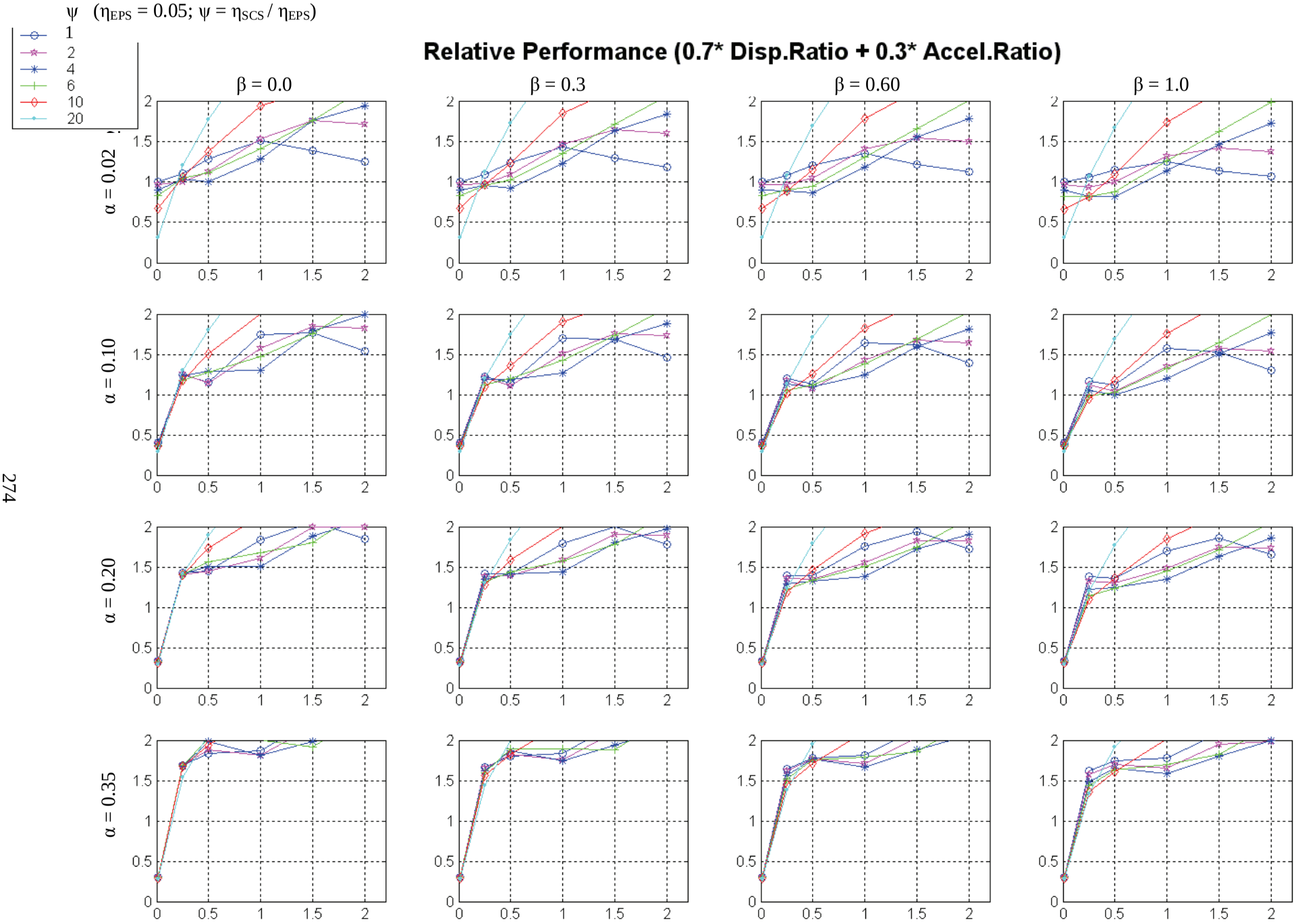
ψ (ηEPS = 0.05; ψ = ηSCS / ηEPS)
1
2
4
6
10
20
Relative Performance (0.7* Disp.Ratio + 0.3* Accel.Ratio)
β = 0.0
β = 0.3
β = 0.60
β = 1.0
α = 0.02
α = 0.10
α = 0.20
α = 0.35

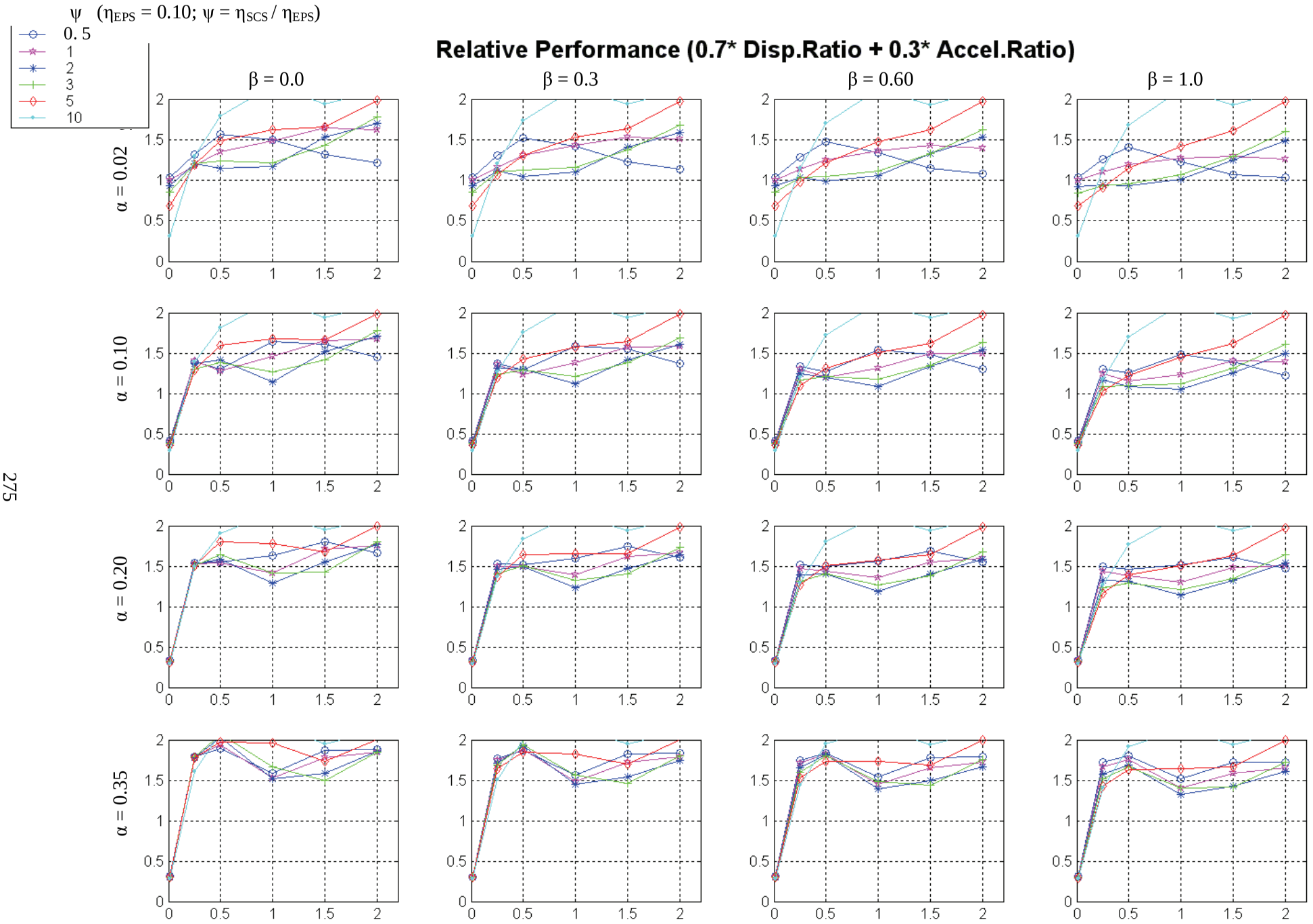
ψ (ηEPS = 0.10; ψ = ηSCS / ηEPS)
0. 5
1
2
3
5
10
Relative Performance (0.7* Disp.Ratio + 0.3* Accel.Ratio)
β = 0.0
β = 0.3
β = 0.60
β = 1.0
α = 0.02
α = 0.10
α = 0.20
α = 0.35

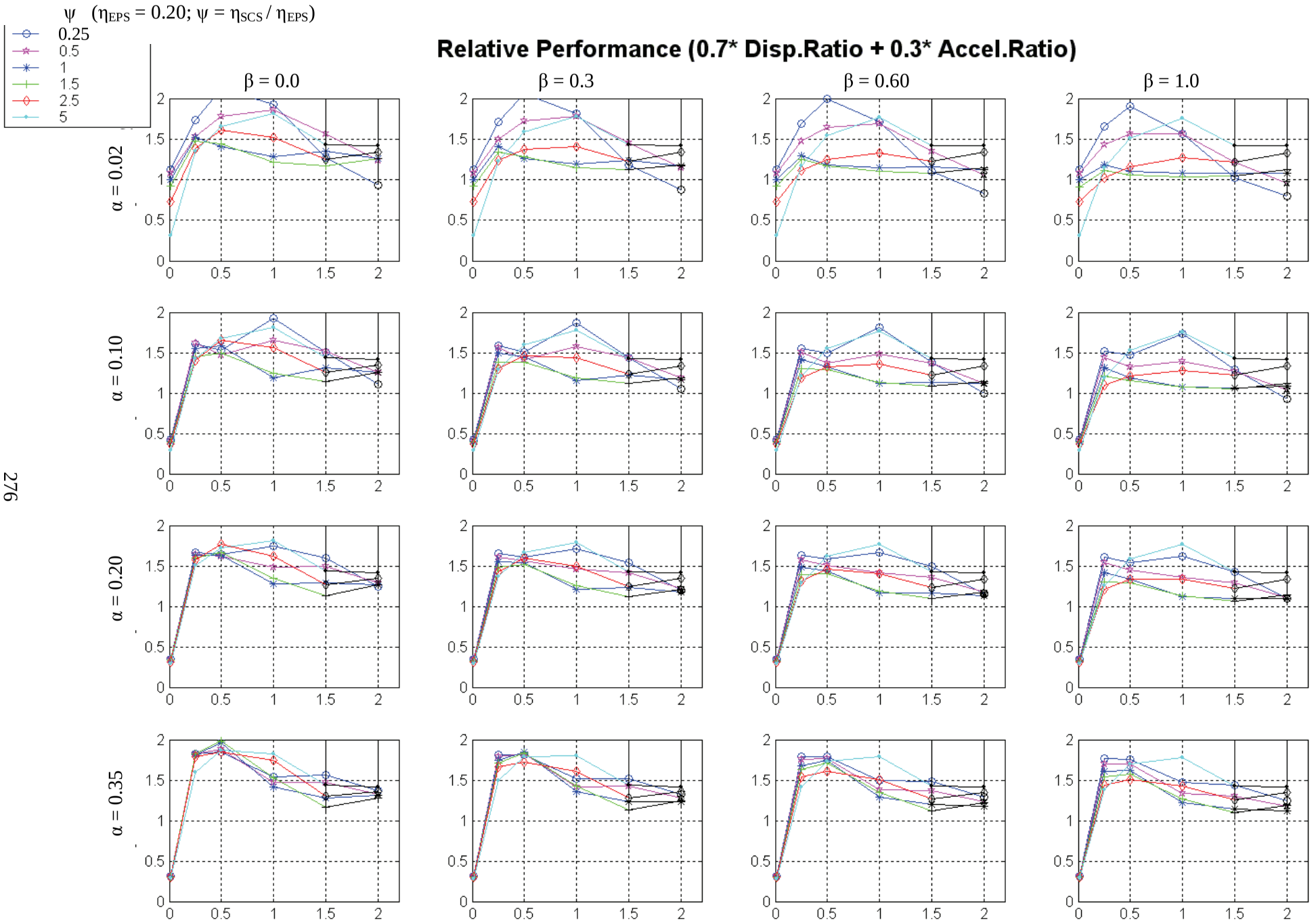
ψ (ηEPS = 0.20; ψ = ηSCS / ηEPS)
0.25
0.5
1
1.5
2.5
5
Relative Performance (0.7* Disp.Ratio + 0.3* Accel.Ratio)
β = 0.0
β = 0.3
β = 0.60
β = 1.0
α = 0.02
α = 0.10
α = 0.20
α = 0.35

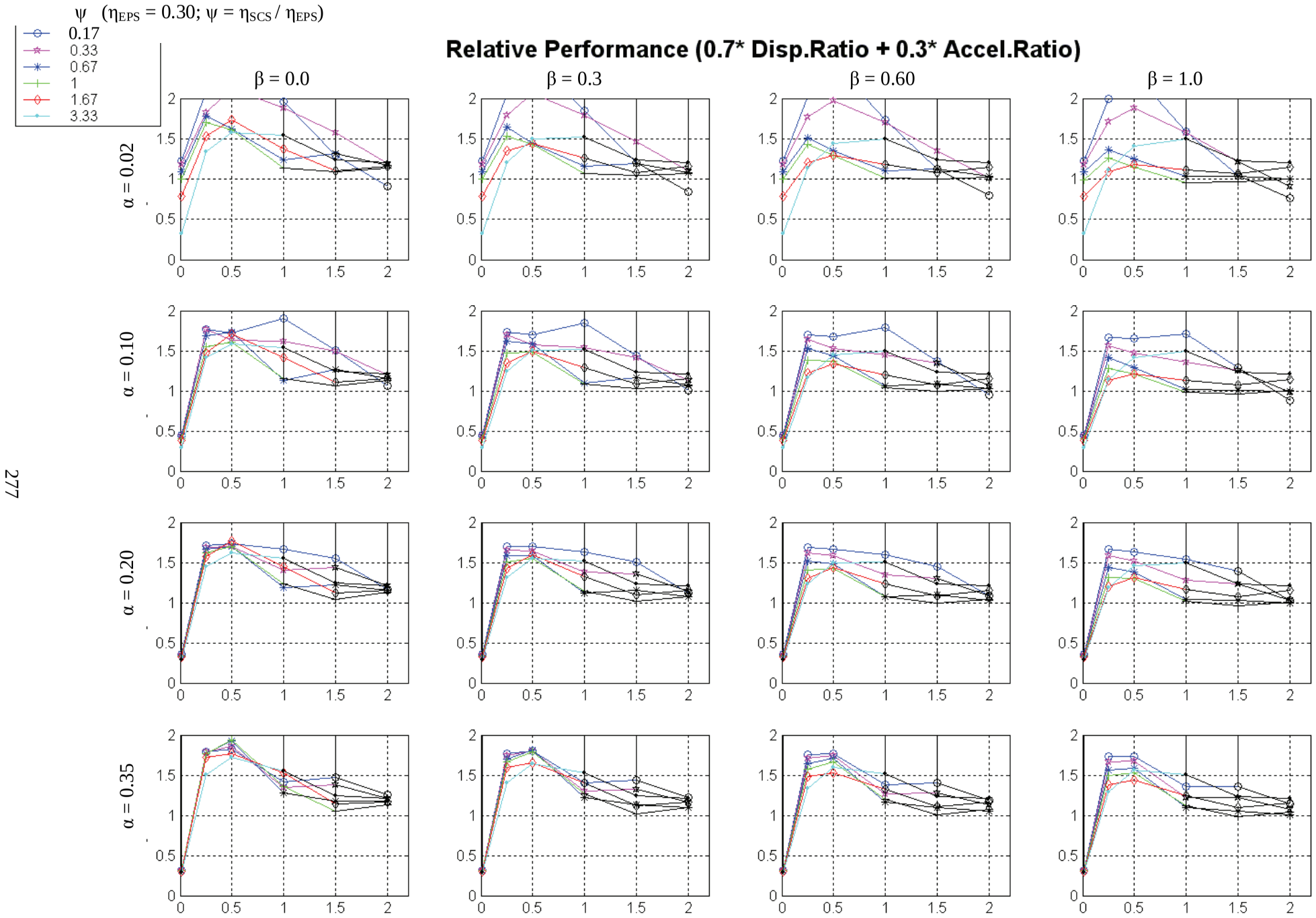
ψ (ηEPS = 0.30; ψ = ηSCS / ηEPS)
0.17
0.33
0.67
1
1.67
3.33
Relative Performance (0.7* Disp.Ratio + 0.3* Accel.Ratio)
β = 0.0
β = 0.3
β = 0.60
β = 1.0
α = 0.02
α = 0.10
α = 0.20
α = 0.35

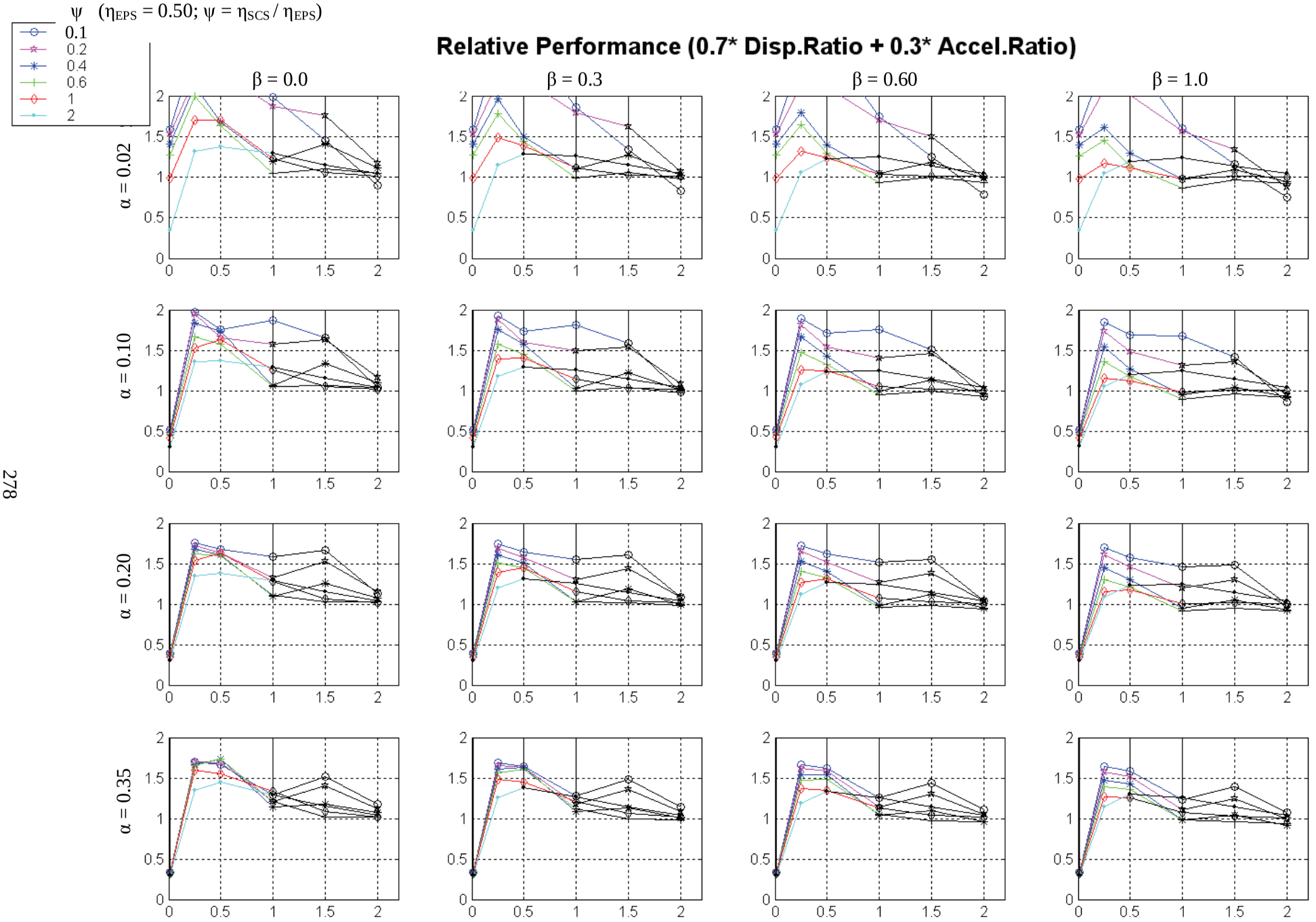
ψ (ηEPS = 0.50; ψ = ηSCS / ηEPS)
0.1
0.2
0.4
0.6
1
2
Relative Performance (0.7* Disp.Ratio + 0.3* Accel.Ratio)
β = 0.0
β = 0.3
β = 0.60
β = 1.0
α = 0.02
α = 0.10
α = 0.20
α = 0.35

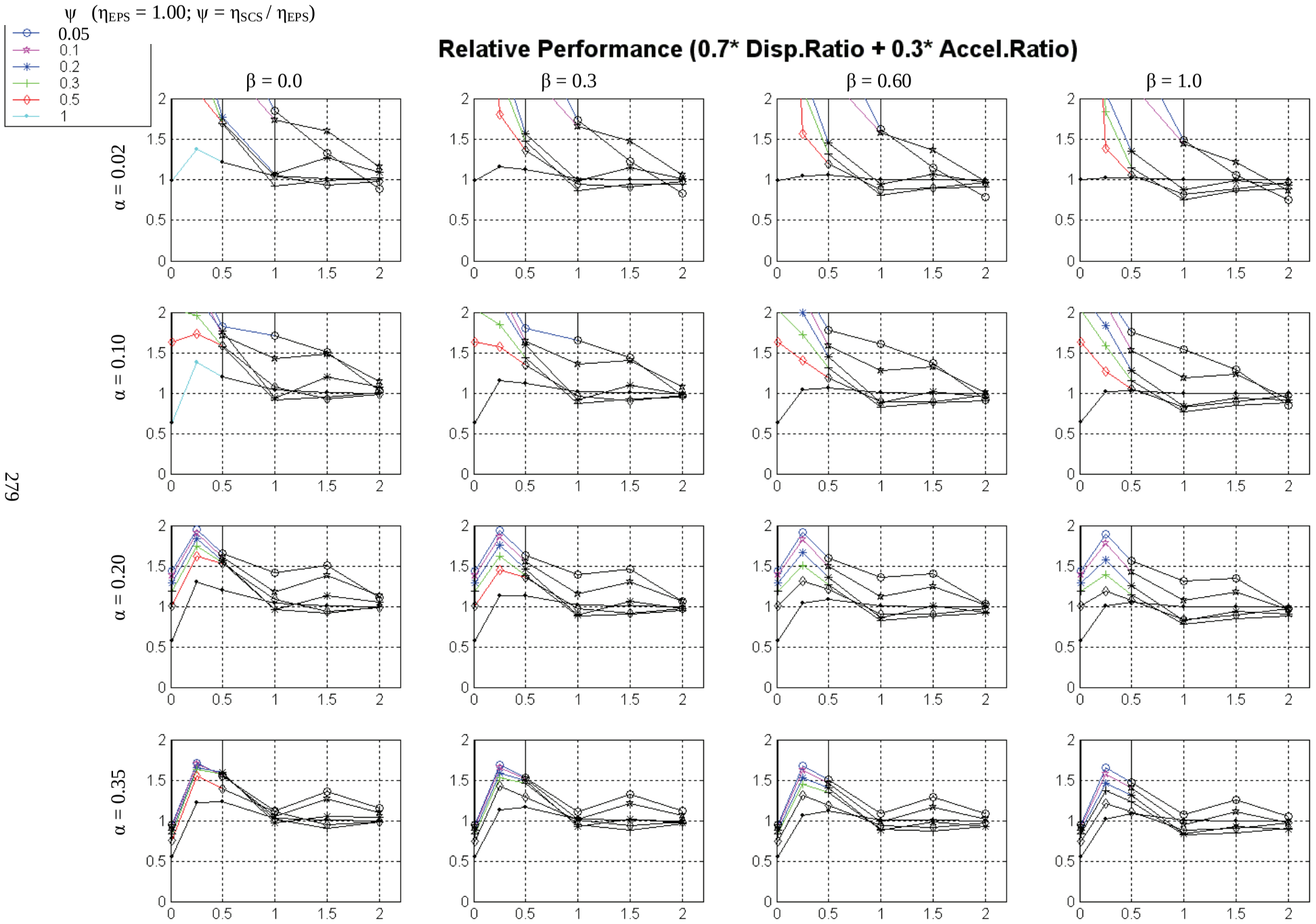
ψ (ηEPS = 1.00; ψ = ηSCS / ηEPS)
0.05
0.1
0.2
0.3
0.5
1
Relative Performance (0.7* Disp.Ratio + 0.3* Accel.Ratio)
β = 0.0
β = 0.3
β = 0.60
β = 1.0
α = 0.02
α = 0.10
α = 0.20
α = 0.35

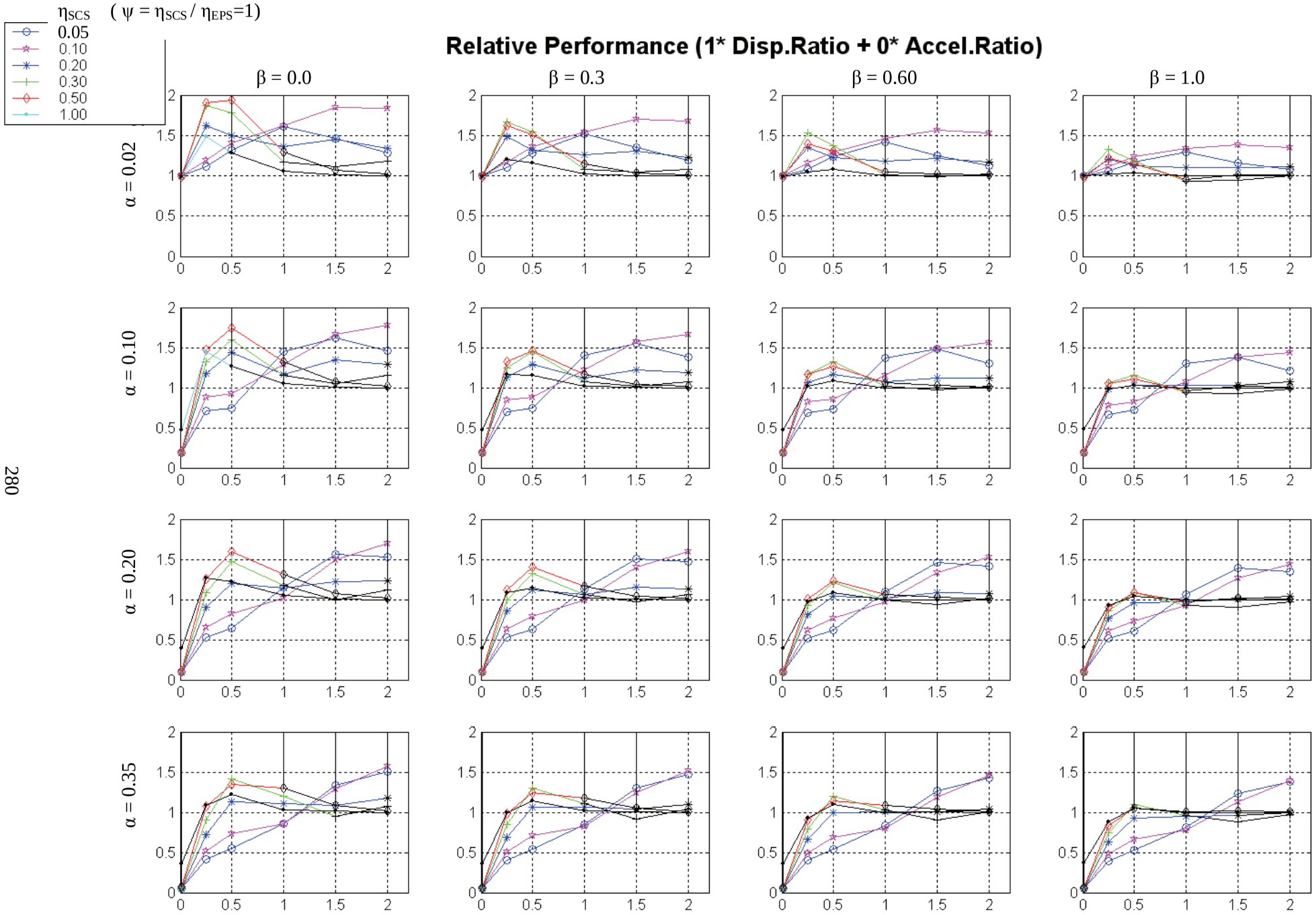
ηSCS (ψ = ηSCS / ηEPS=1)
0.05
0.10
0.20
0.30
0.50
1.00
Relative Performance (1* Disp.Ratio + 0* Accel.Ratio)
β = 0.0
β = 0.3
β = 0.60
β = 1.0
α = 0.02
α = 0.10
α = 0.20
α = 0.35

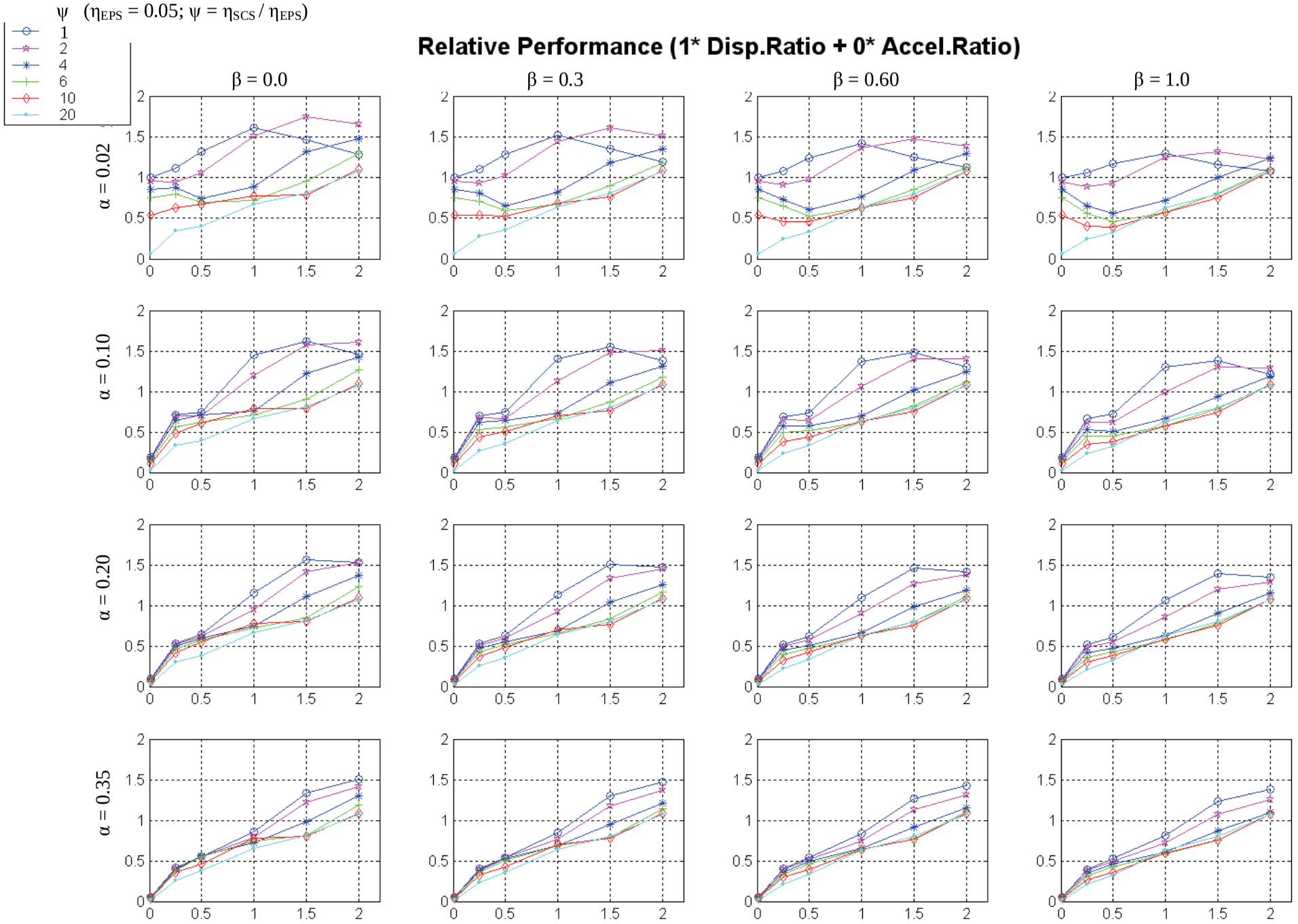
ψ (ηEPS = 0.05; ψ = ηSCS / ηEPS)
1
2
4
6
10
20
Relative Performance (1* Disp.Ratio + 0* Accel.Ratio)
β = 0.0
β = 0.3
β = 0.60
β = 1.0
α = 0.02
α = 0.10
α = 0.20
α = 0.35

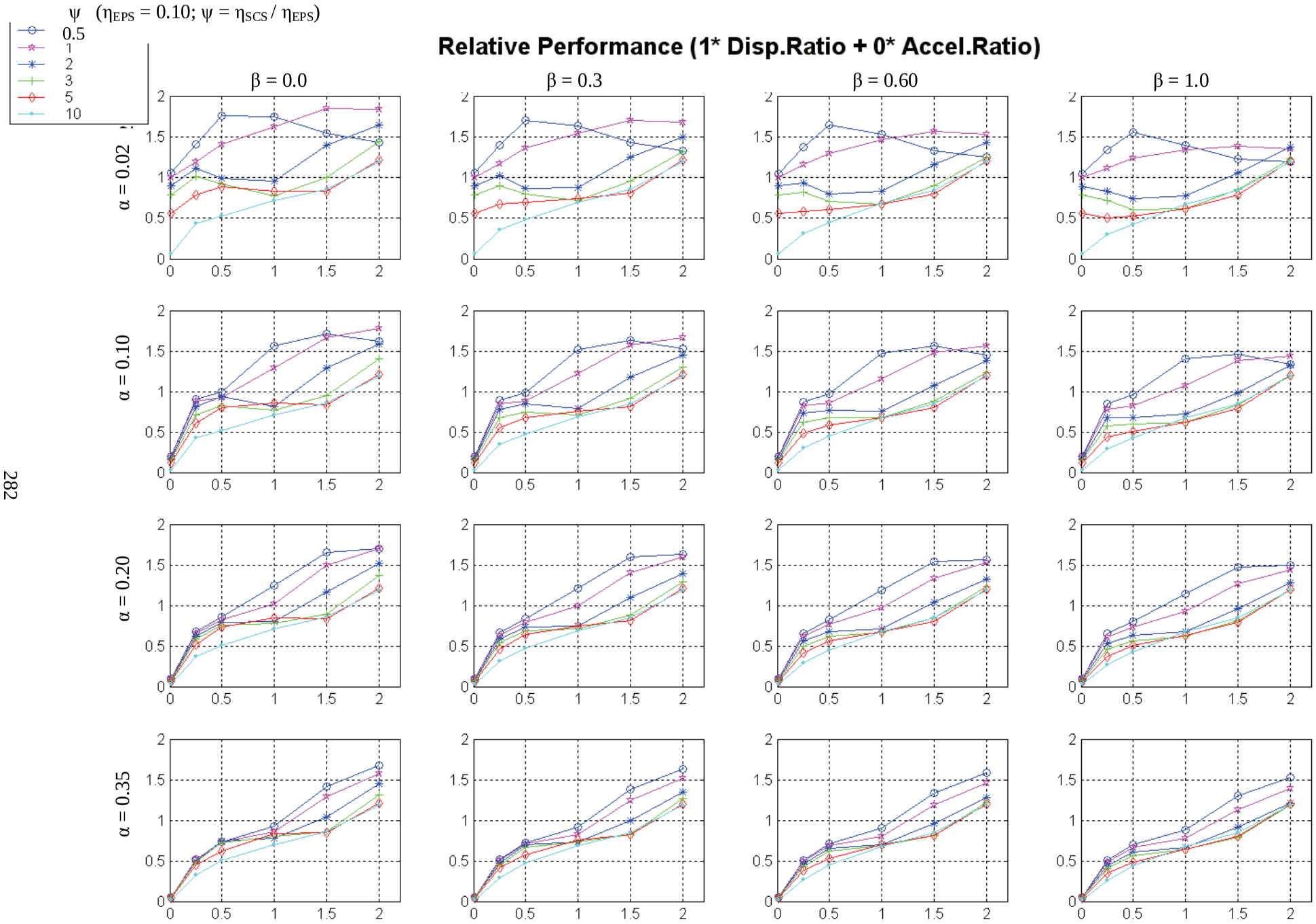
ψ (ηEPS = 0.10; ψ = ηSCS / ηEPS)
0.5
1
2
3
5
10
Relative Performance (1* Disp.Ratio + 0* Accel.Ratio)
β = 0.0
β = 0.3
β = 0.60
β = 1.0
α = 0.02
α = 0.10
α = 0.20
α = 0.35

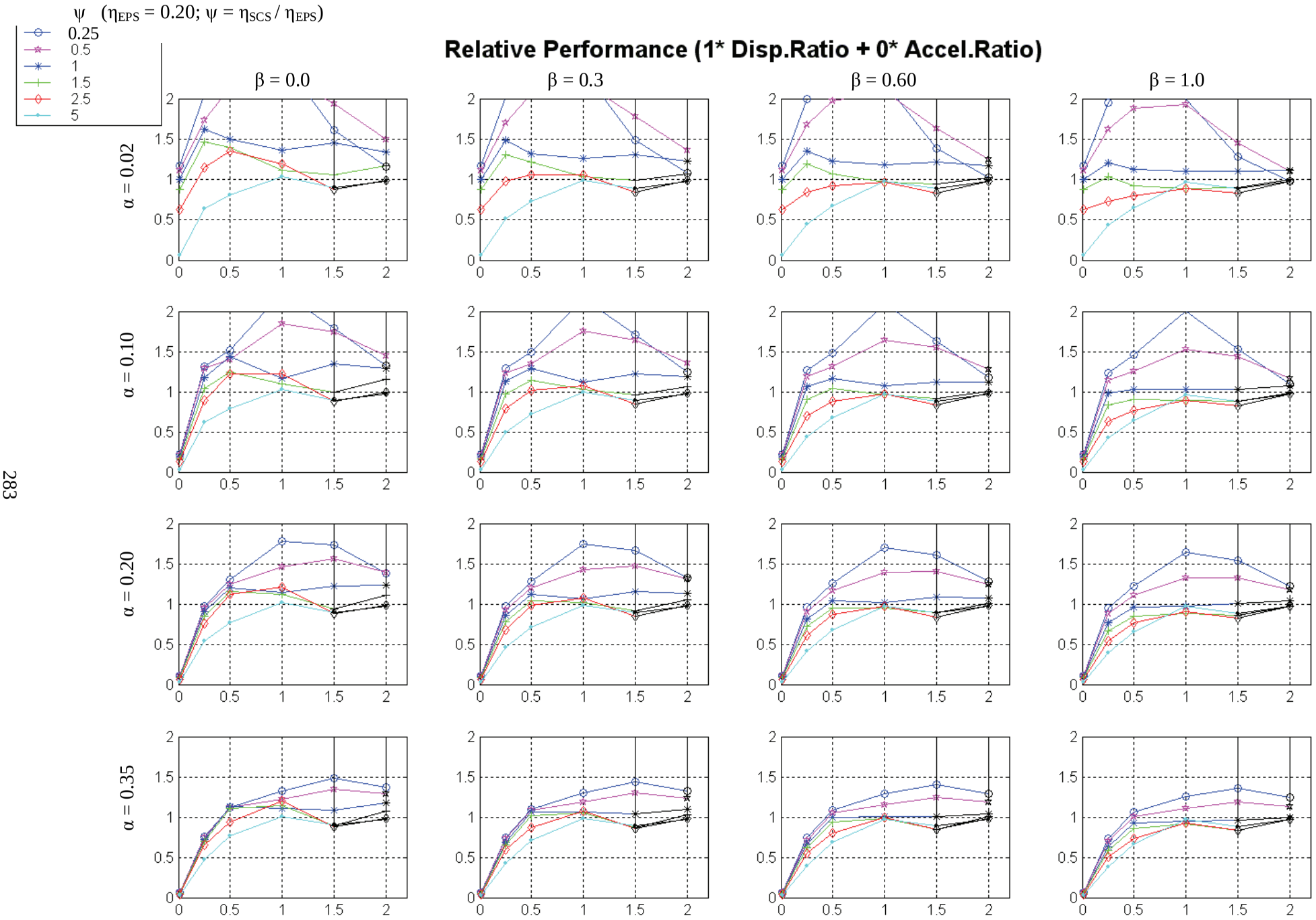
ψ (ηEPS = 0.20; ψ = ηSCS / ηEPS)
0.25
0.5
1
1.5
2.5
5
Relative Performance (1* Disp.Ratio + 0* Accel.Ratio)
β = 0.0
β = 0.3
β = 0.60
β = 1.0
α = 0.02
α = 0.10
α = 0.20
α = 0.35

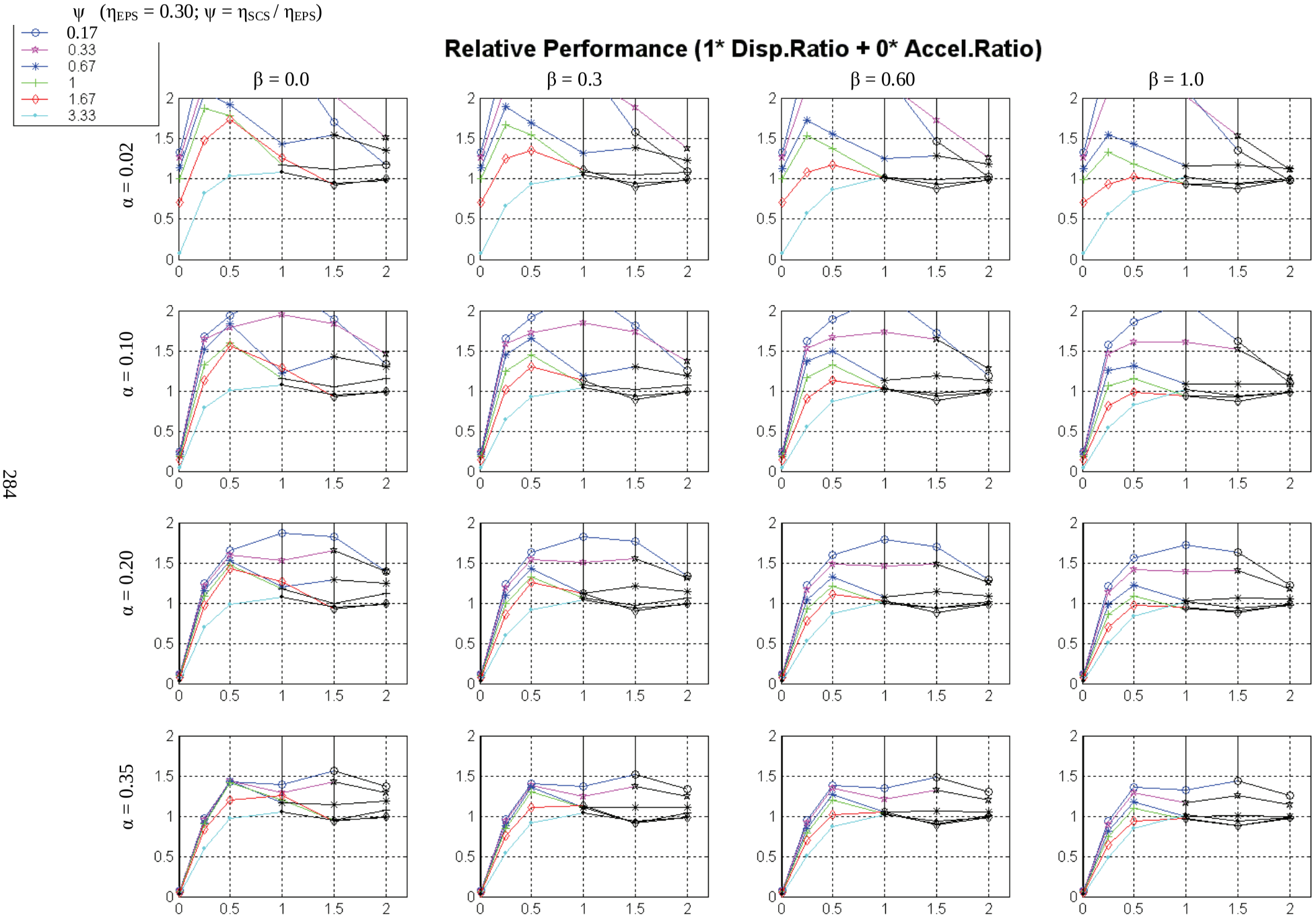
ψ (ηEPS = 0.30; ψ = ηSCS / ηEPS)
0.17
0.33
0.67
1
1.67
3.33
Relative Performance (1* Disp.Ratio + 0* Accel.Ratio)
β = 0.0
β = 0.3
β = 0.60
β = 1.0
α = 0.02
α = 0.10
α = 0.20
α = 0.35

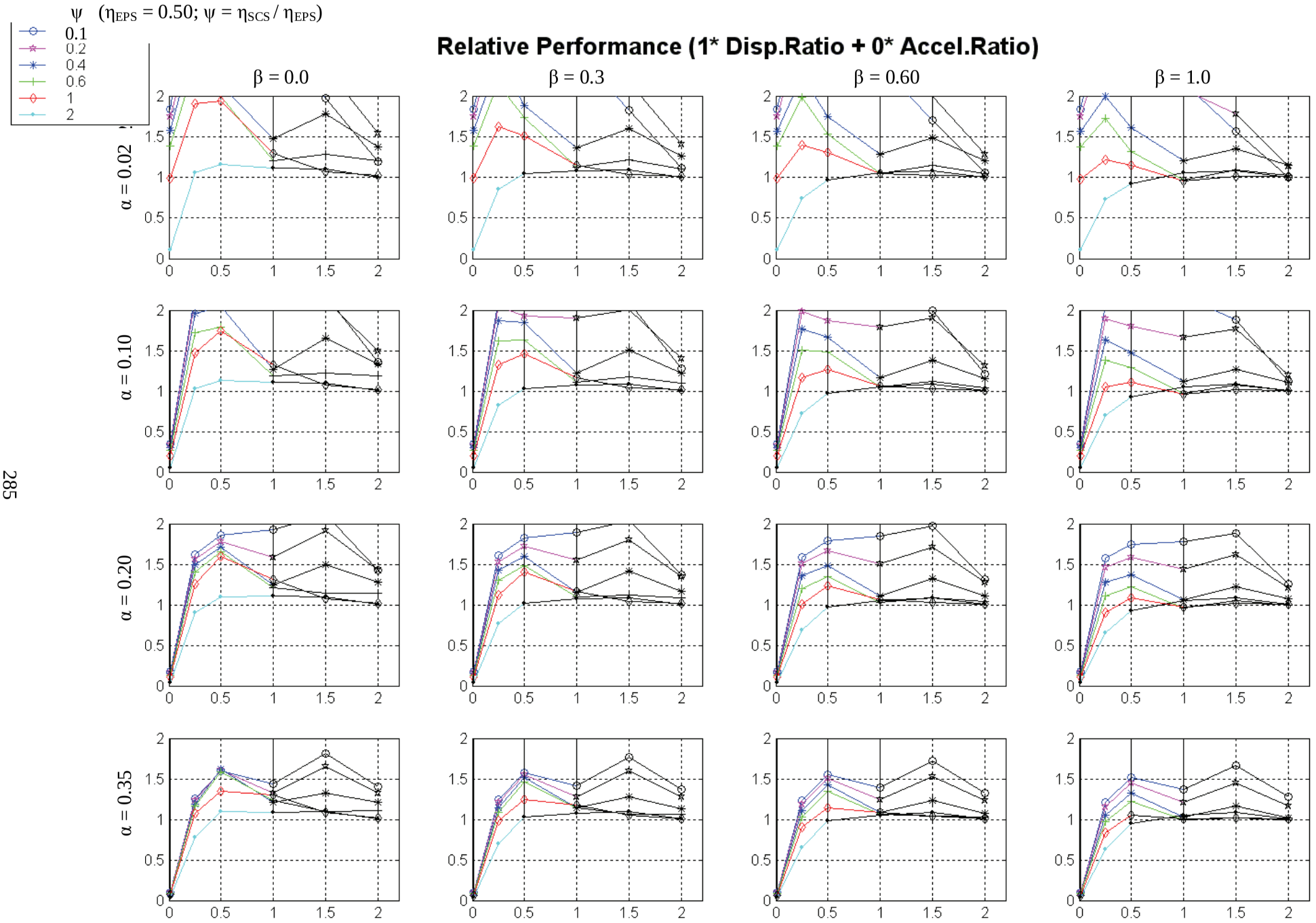
ψ (ηEPS = 0.50; ψ = ηSCS / ηEPS)
0.1
0.2
0.4
0.6
1
2
Relative Performance (1* Disp.Ratio + 0* Accel.Ratio)
β = 0.0
β = 0.3
β = 0.60
β = 1.0
α = 0.02
α = 0.10
α = 0.20
α = 0.35

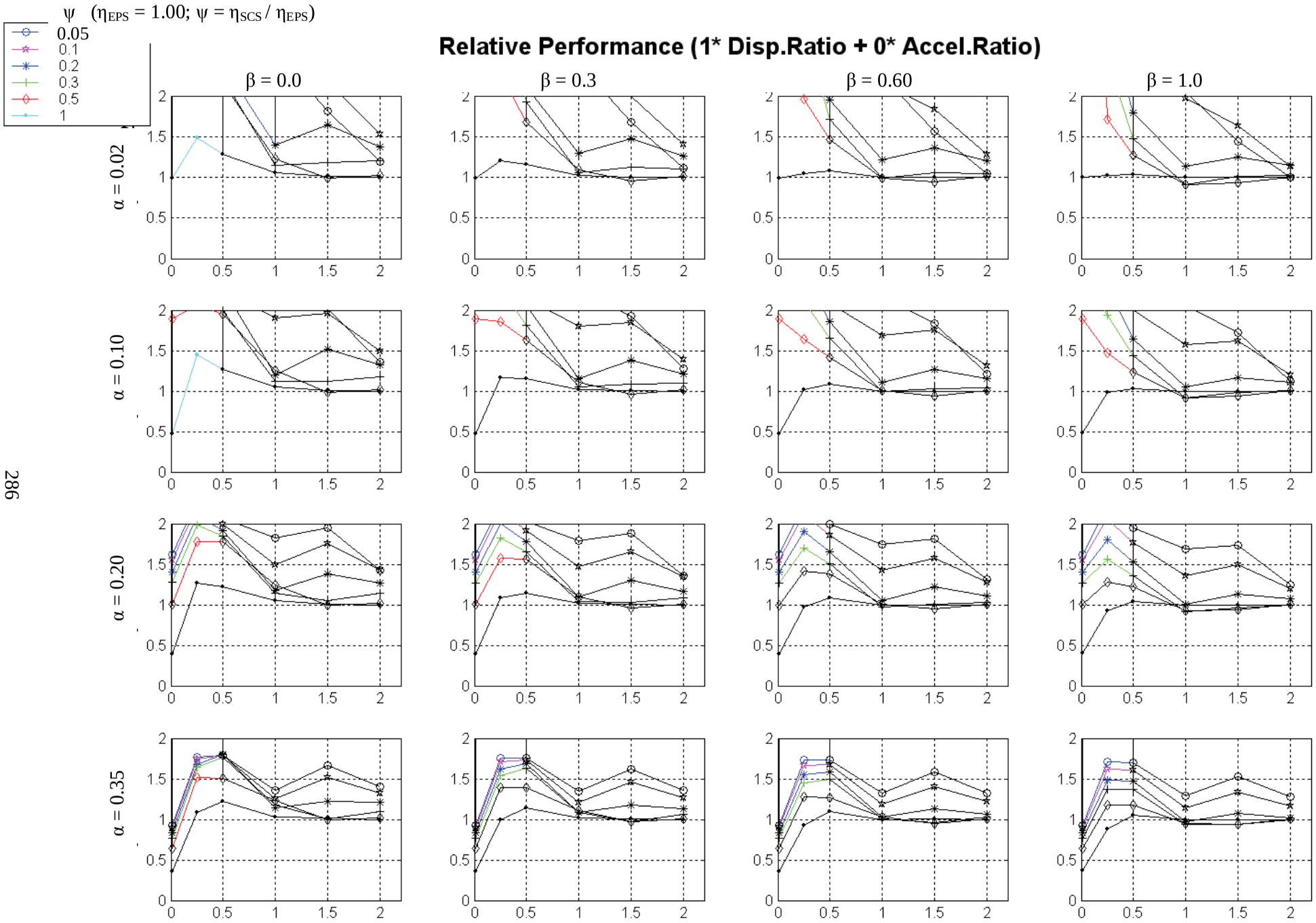
ψ (ηEPS = 1.00; ψ = ηSCS / ηEPS)
0.05
0.1
0.2
0.3
0.5
1
Relative Performance (1* Disp.Ratio + 0* Accel.Ratio)
β = 0.0
β = 0.3
β = 0.60
β = 1.0
α = 0.02
α = 0.10
α = 0.20
α = 0.35

Appendix B Relative Performance Index (RPI) under MCEER ground motions having a 10% probability of exceedance in 50 years in California, U.S.

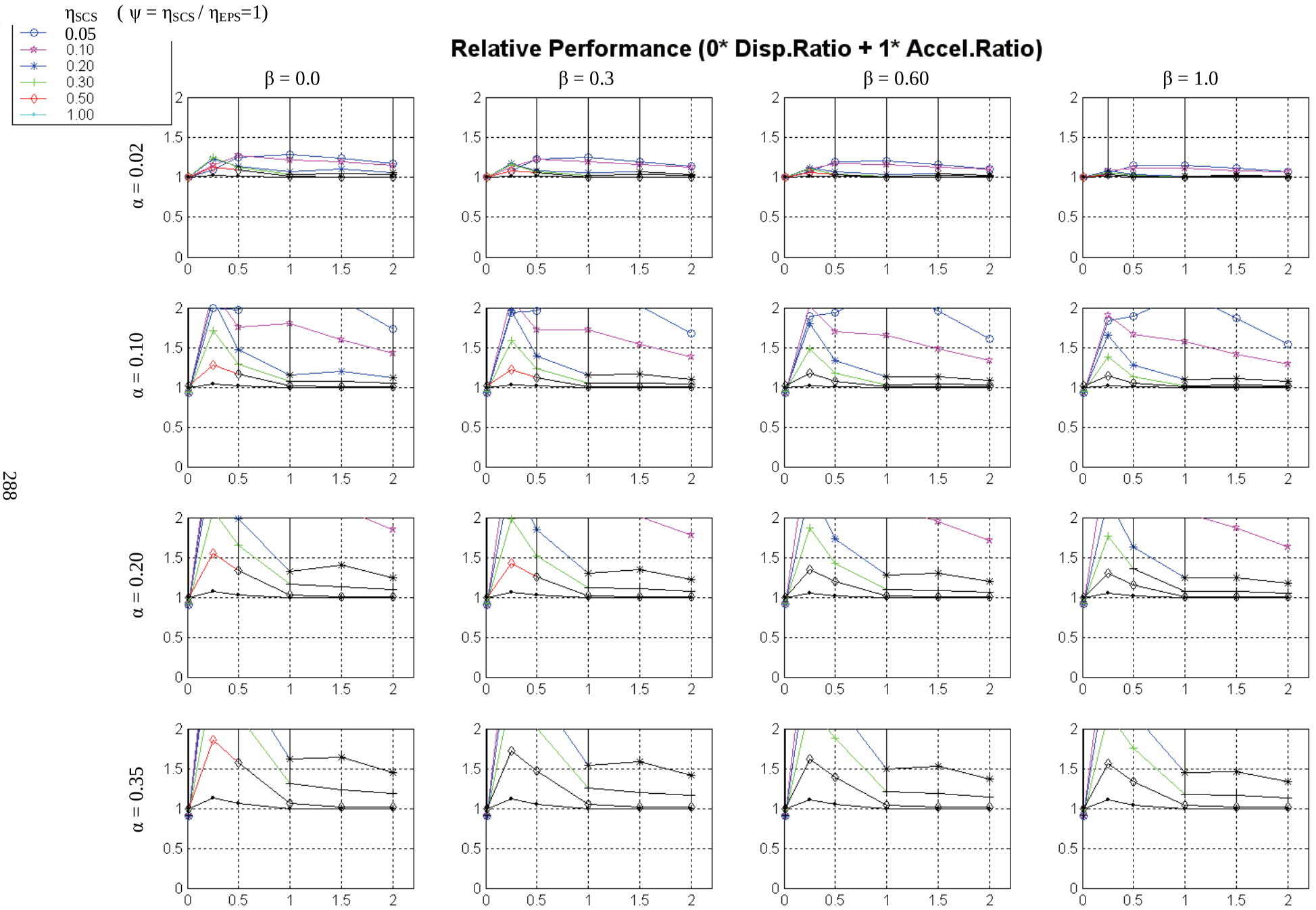
ηSCS (ψ = ηSCS / ηEPS=1)
0.05
0.10
0.20
0.30
0.50
1.00
Relative Performance (0* Disp.Ratio + 1* Accel.Ratio)
β = 0.0
β = 0.3
β = 0.60
β = 1.0
α = 0.02
α = 0.10
α = 0.20
α = 0.35

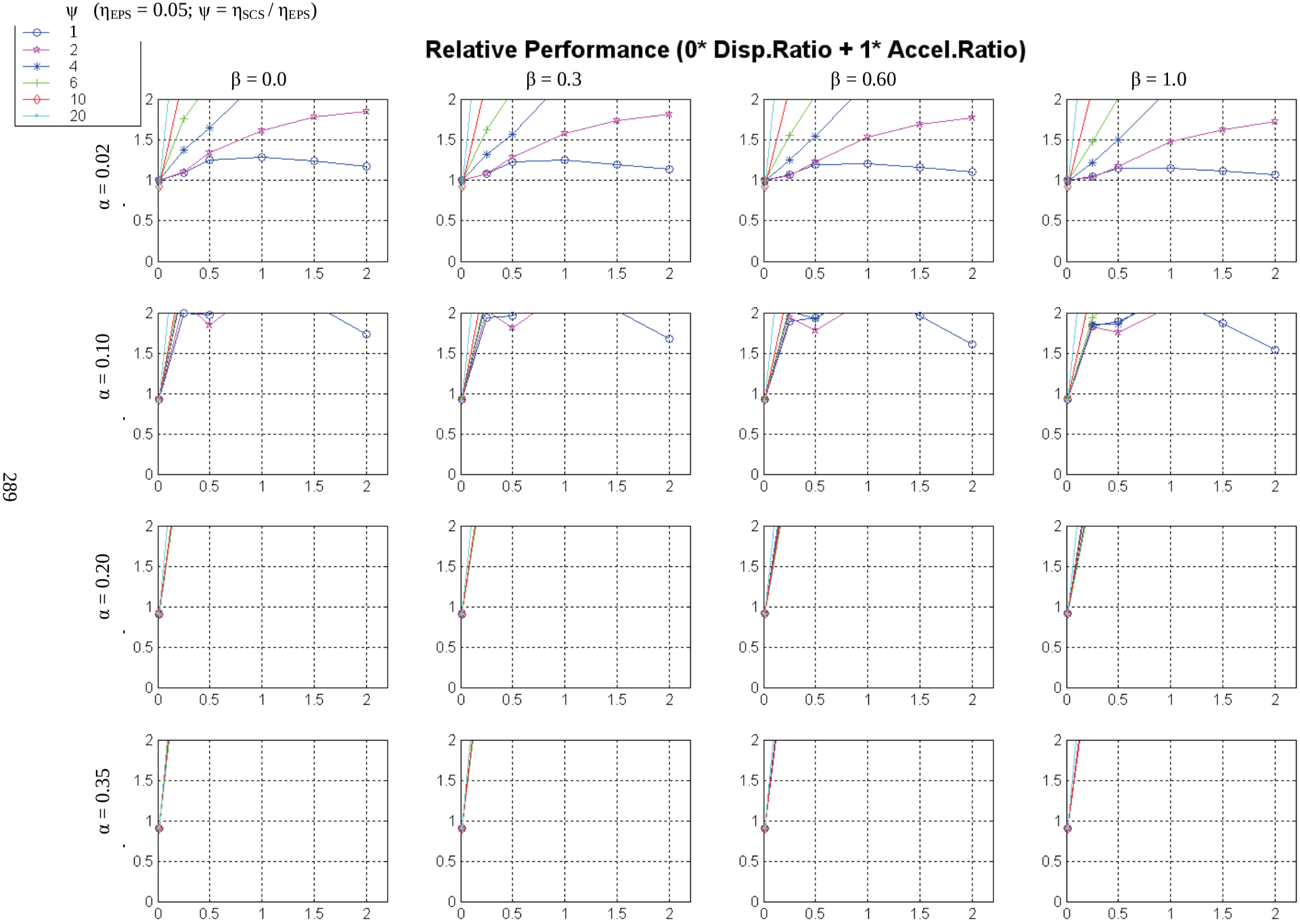
ψ (ηEPS = 0.05; ψ = ηSCS / ηEPS)
1
2
4
6
10
20
Relative Performance (0* Disp.Ratio + 1* Accel.Ratio)
β = 0.0
β = 0.3
β = 0.60
β = 1.0
α = 0.02
α = 0.10
α = 0.20
α = 0.35

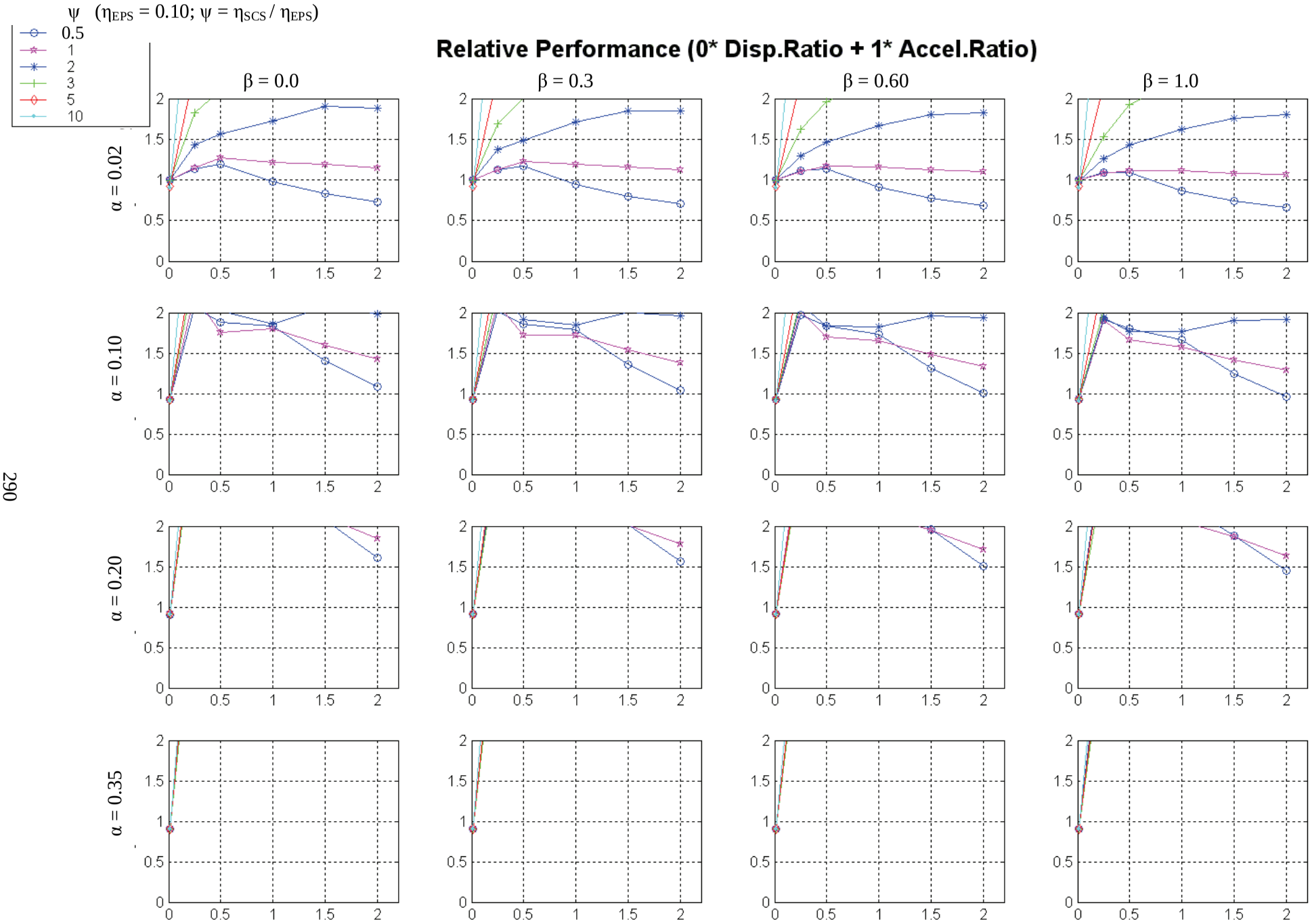
ψ (ηEPS = 0.10; ψ = ηSCS / ηEPS)
0.5
1
2
3
5
10
Relative Performance (0* Disp.Ratio + 1* Accel.Ratio)
β = 0.0
β = 0.3
β = 0.60
β = 1.0
α = 0.02
α = 0.10
α = 0.20
α = 0.35

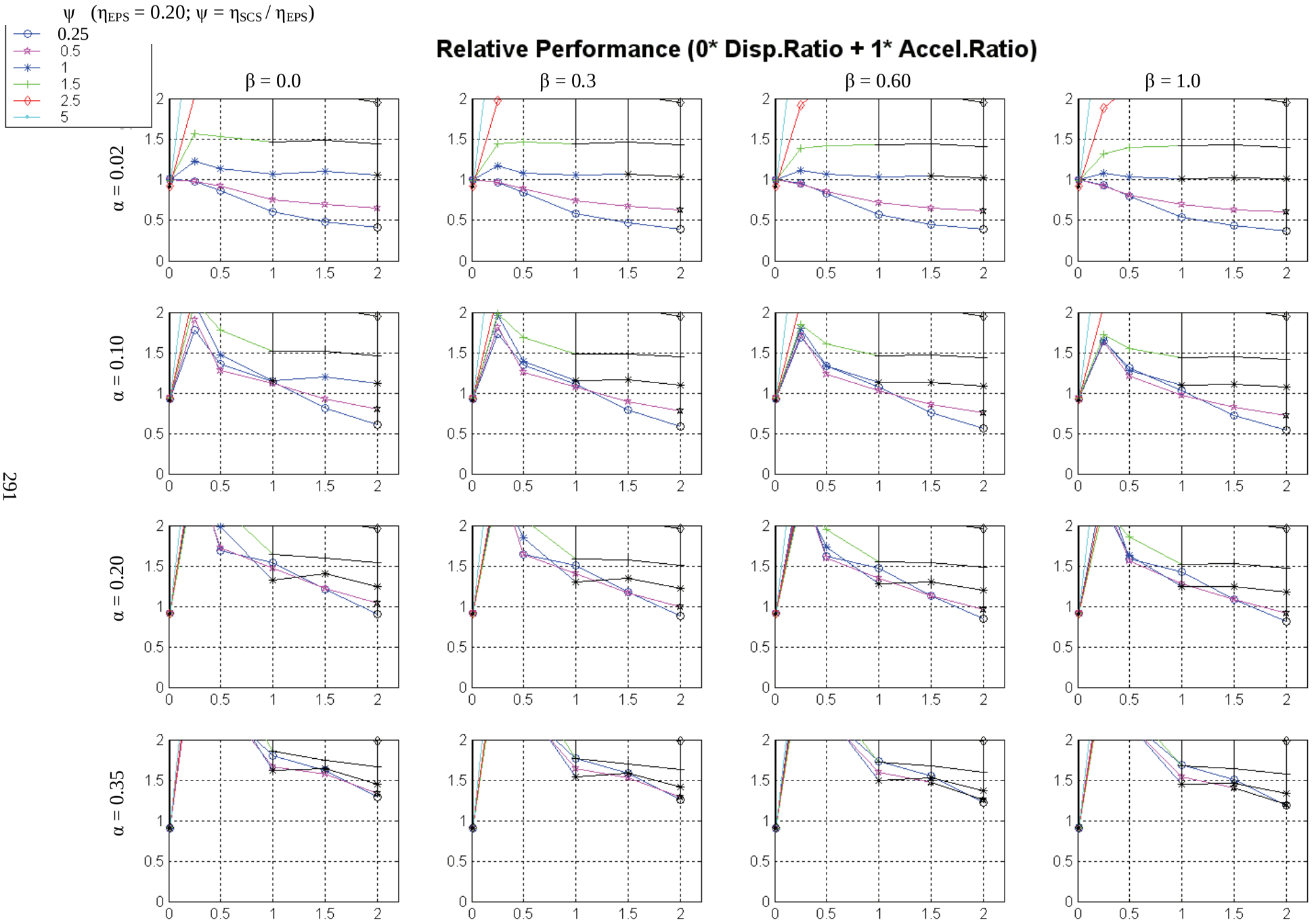
ψ (ηEPS = 0.20; ψ = ηSCS / ηEPS)
0.25
0.5
1
1.5
2.5
5
Relative Performance (0* Disp.Ratio + 1* Accel.Ratio)
β = 0.0
β = 0.3
β = 0.60
β = 1.0
α = 0.02
α = 0.10
α = 0.20
α = 0.35

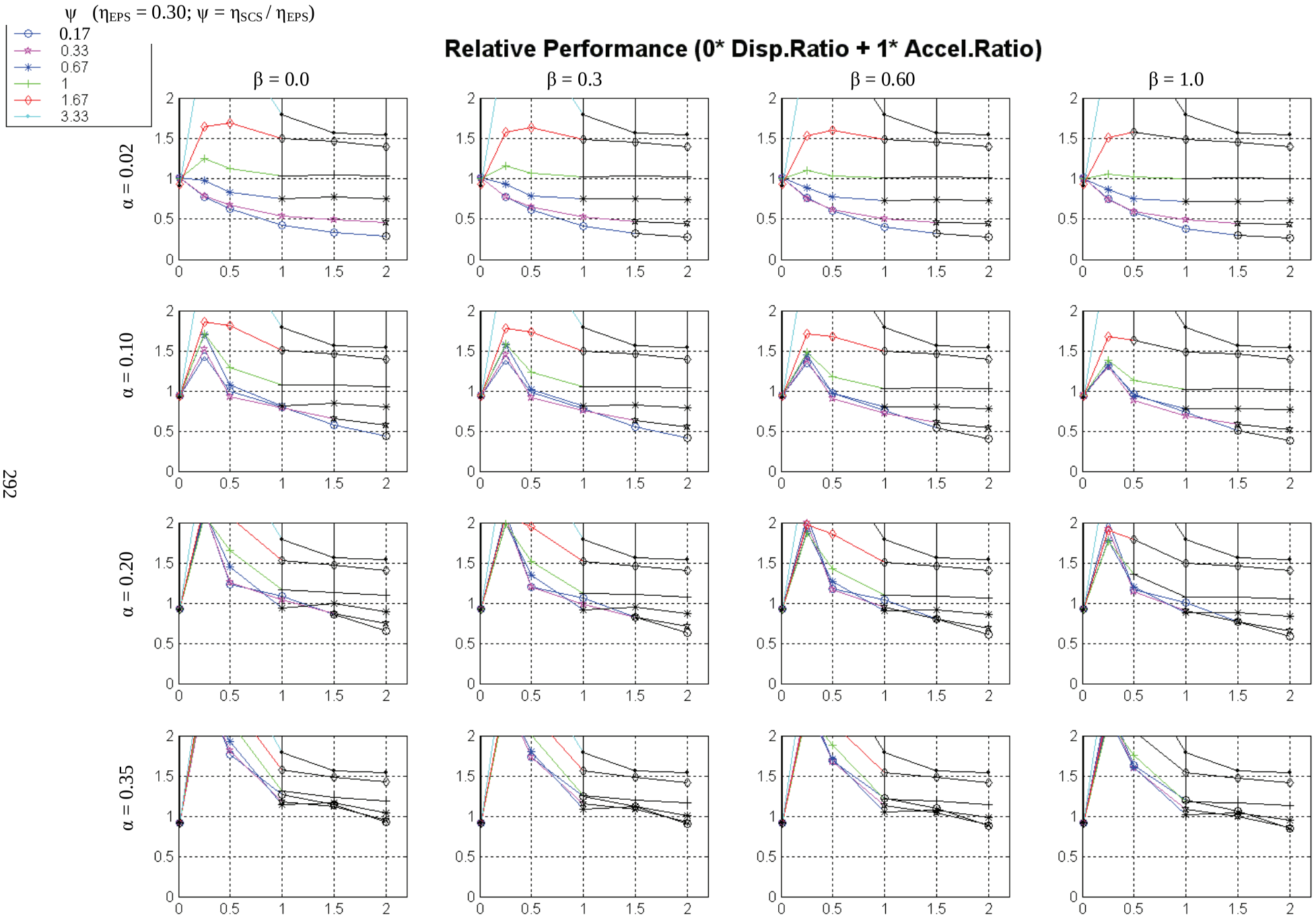
ψ (ηEPS = 0.30; ψ = ηSCS / ηEPS)
0.17
0.33
0.67
1
1.67
3.33
Relative Performance (0* Disp.Ratio + 1* Accel.Ratio)
β = 0.0
β = 0.3
β = 0.60
β = 1.0
α = 0.02
α = 0.10
α = 0.20
α = 0.35

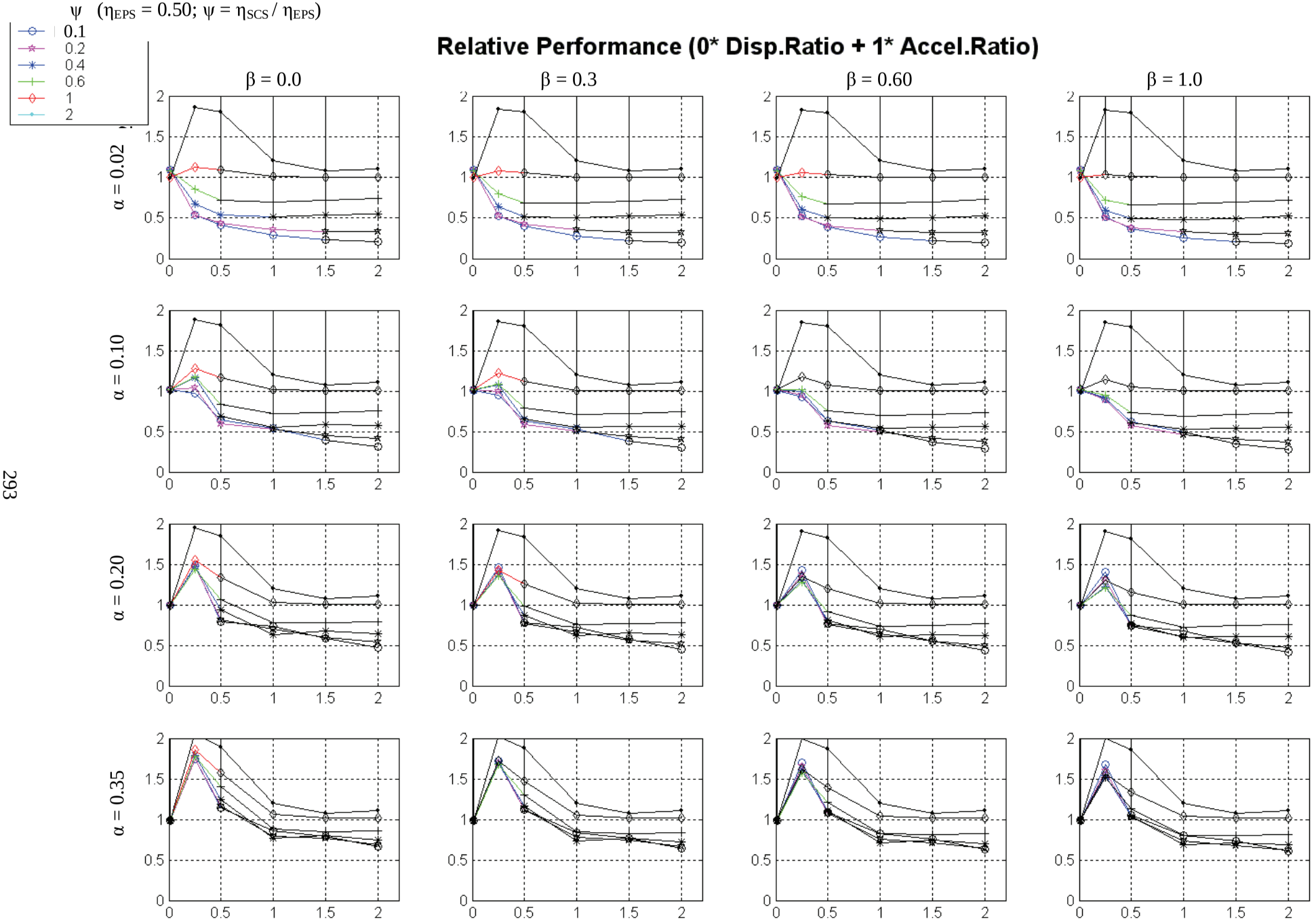
ψ (ηEPS = 0.50; ψ = ηSCS / ηEPS)
0.1
0.2
0.4
0.6
1
2
Relative Performance (0* Disp.Ratio + 1* Accel.Ratio)
β = 0.0
β = 0.3
β = 0.60
β = 1.0
α = 0.02
α = 0.10
α = 0.20
α = 0.35

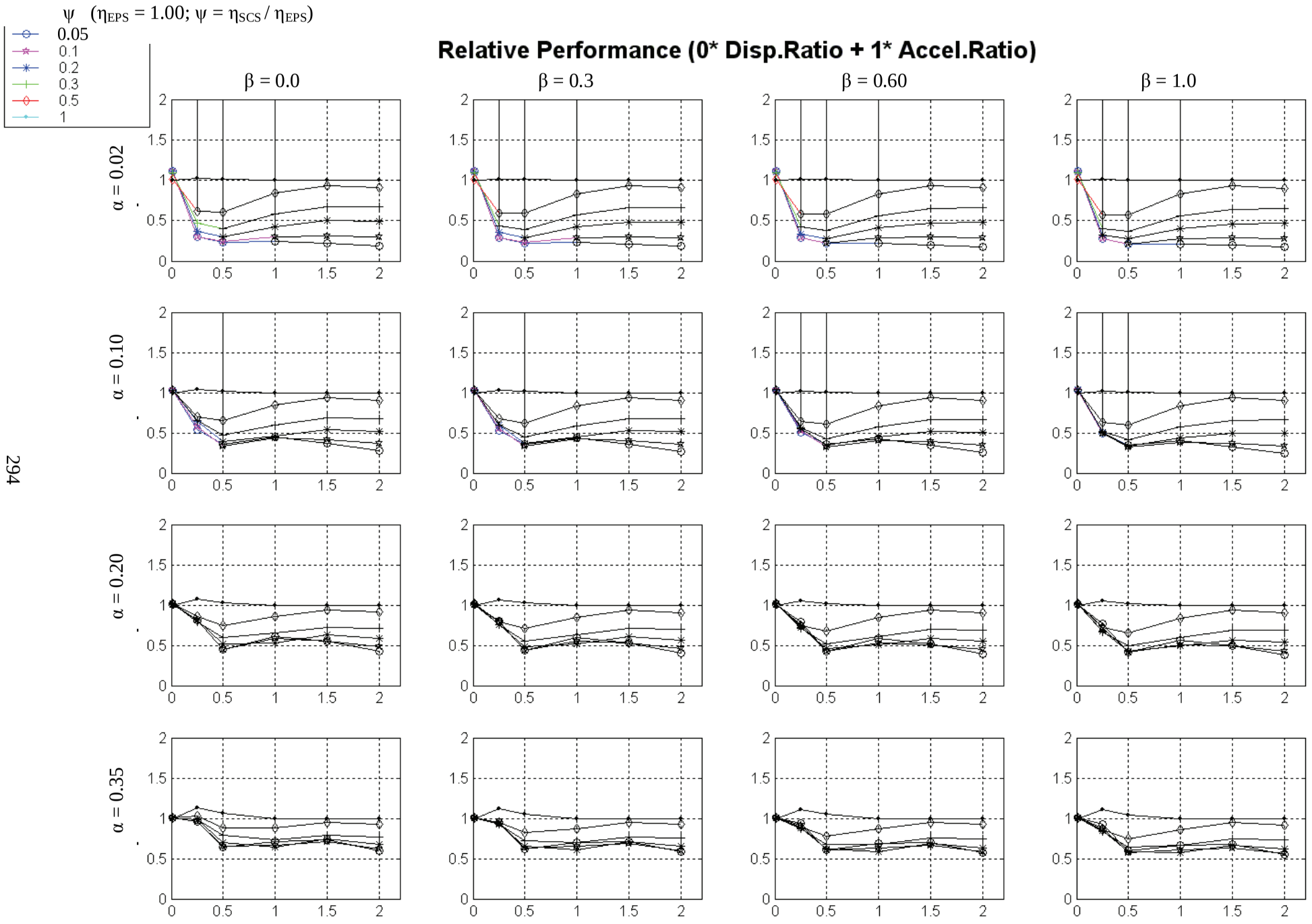
ψ (ηEPS = 1.00; ψ = ηSCS / ηEPS)
0.05
0.1
0.2
0.3
0.5
1
Relative Performance (0* Disp.Ratio + 1* Accel.Ratio)
β = 0.0
β = 0.3
β = 0.60
β = 1.0
α = 0.02
α = 0.10
α = 0.20
α = 0.35

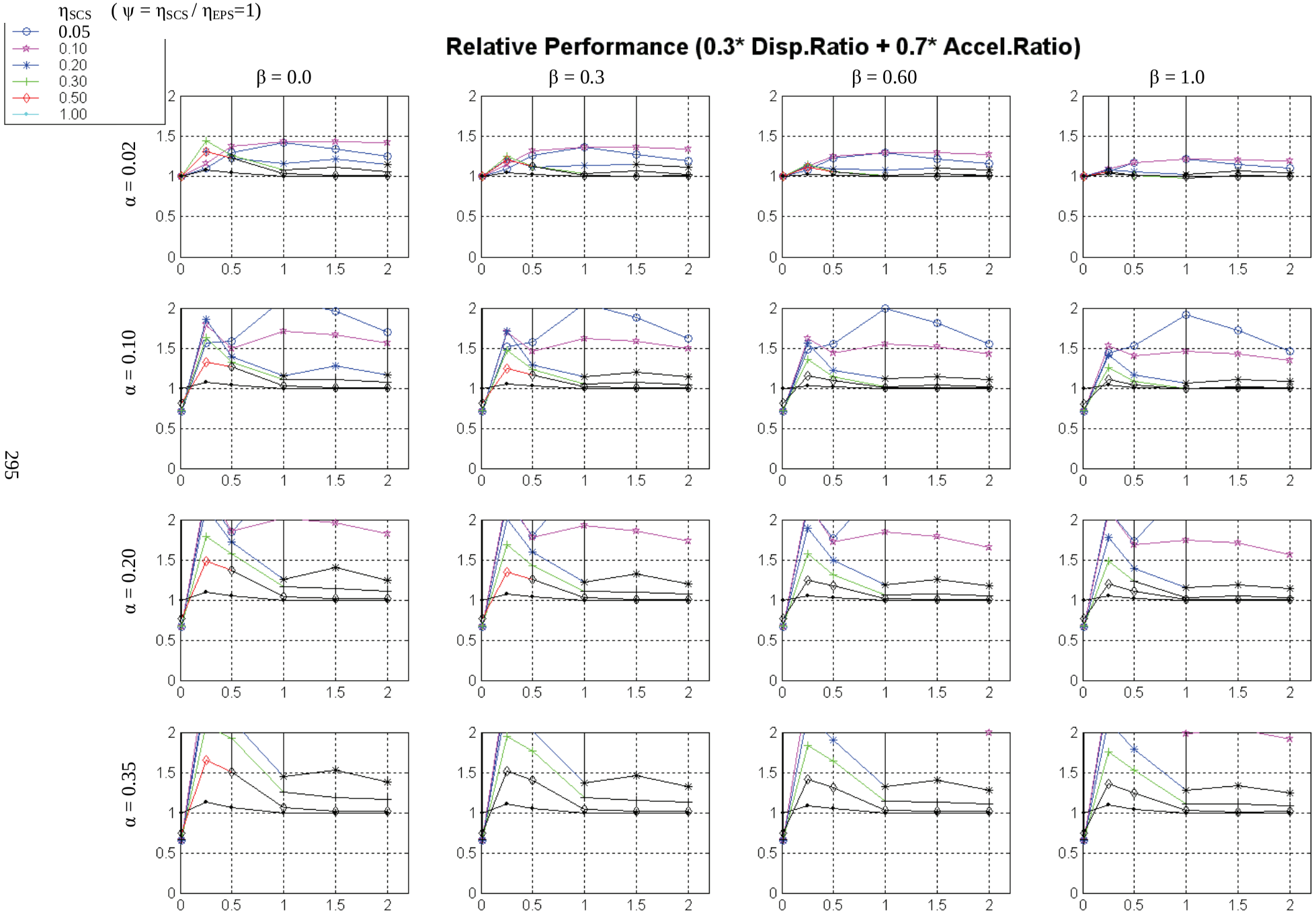
ηSCS (ψ = ηSCS / ηEPS=1)
0.05
0.10
0.20
0.30
0.50
1.00
Relative Performance (0.3* Disp.Ratio + 0.7* Accel.Ratio)
β = 0.0
β = 0.3
β = 0.60
β = 1.0
α = 0.02
α = 0.10
α = 0.20
α = 0.35

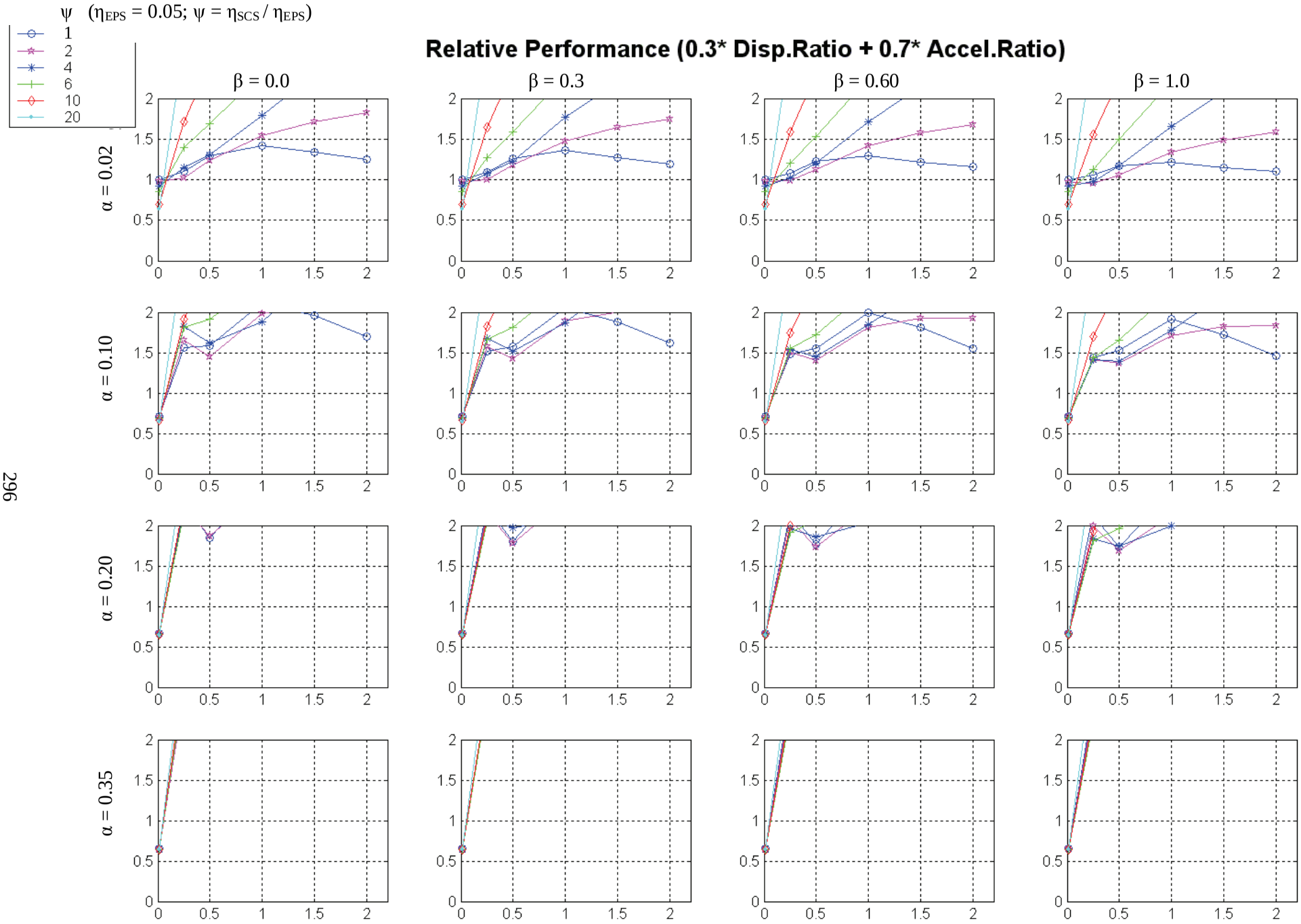
ψ (ηEPS = 0.05; ψ = ηSCS / ηEPS)
1
2
4
6
10
20
Relative Performance (0.3* Disp.Ratio + 0.7* Accel.Ratio)
β = 0.0
β = 0.3
β = 0.60
β = 1.0
α = 0.02
α = 0.10
α = 0.20
α = 0.35

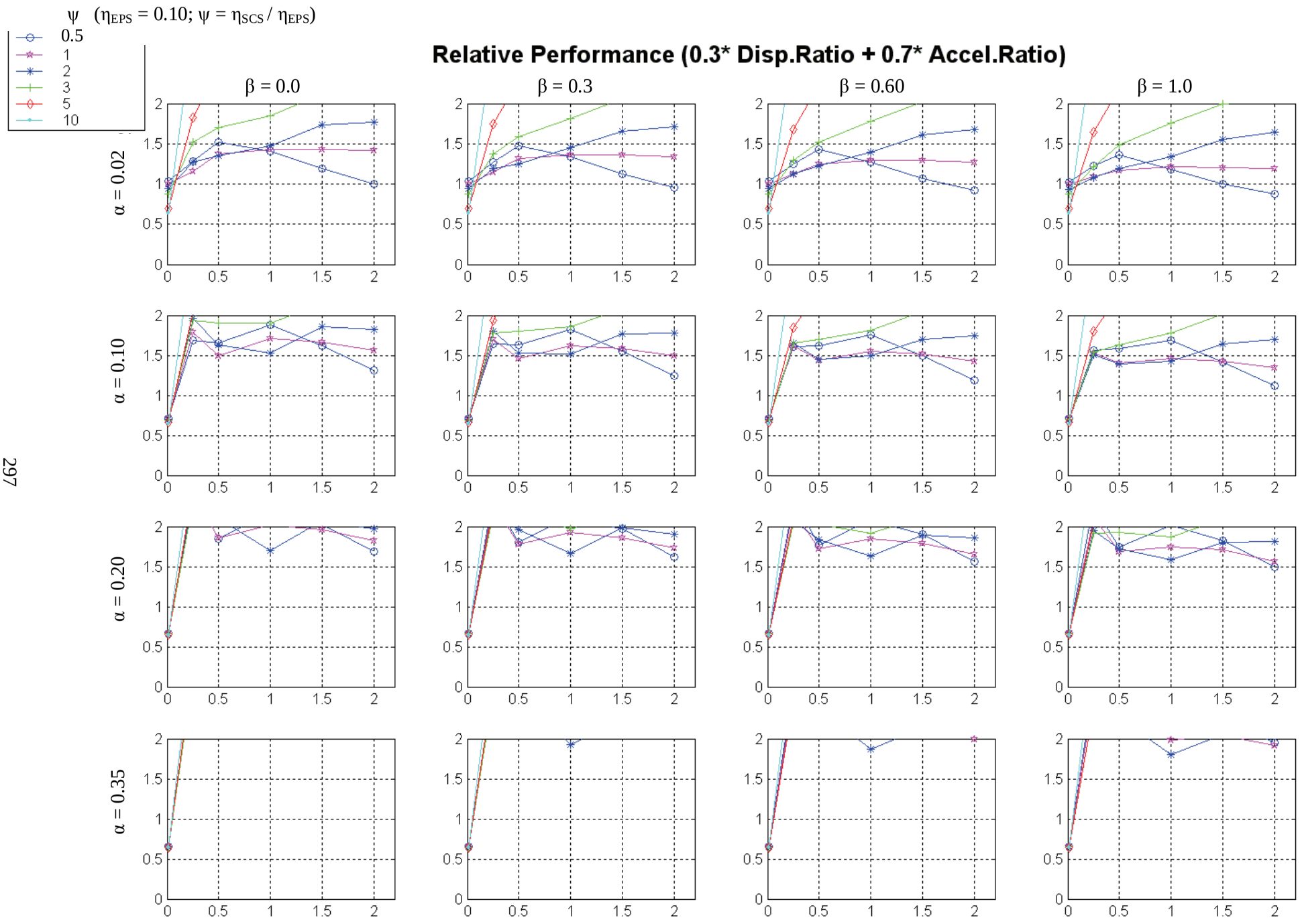
ψ (ηEPS = 0.10; ψ = ηSCS / ηEPS)
0.5
1
2
3
5
10
Relative Performance (0.3* Disp.Ratio + 0.7* Accel.Ratio)
β = 0.0
β = 0.3
β = 0.60
β = 1.0
α = 0.02
α = 0.10
α = 0.20
α = 0.35

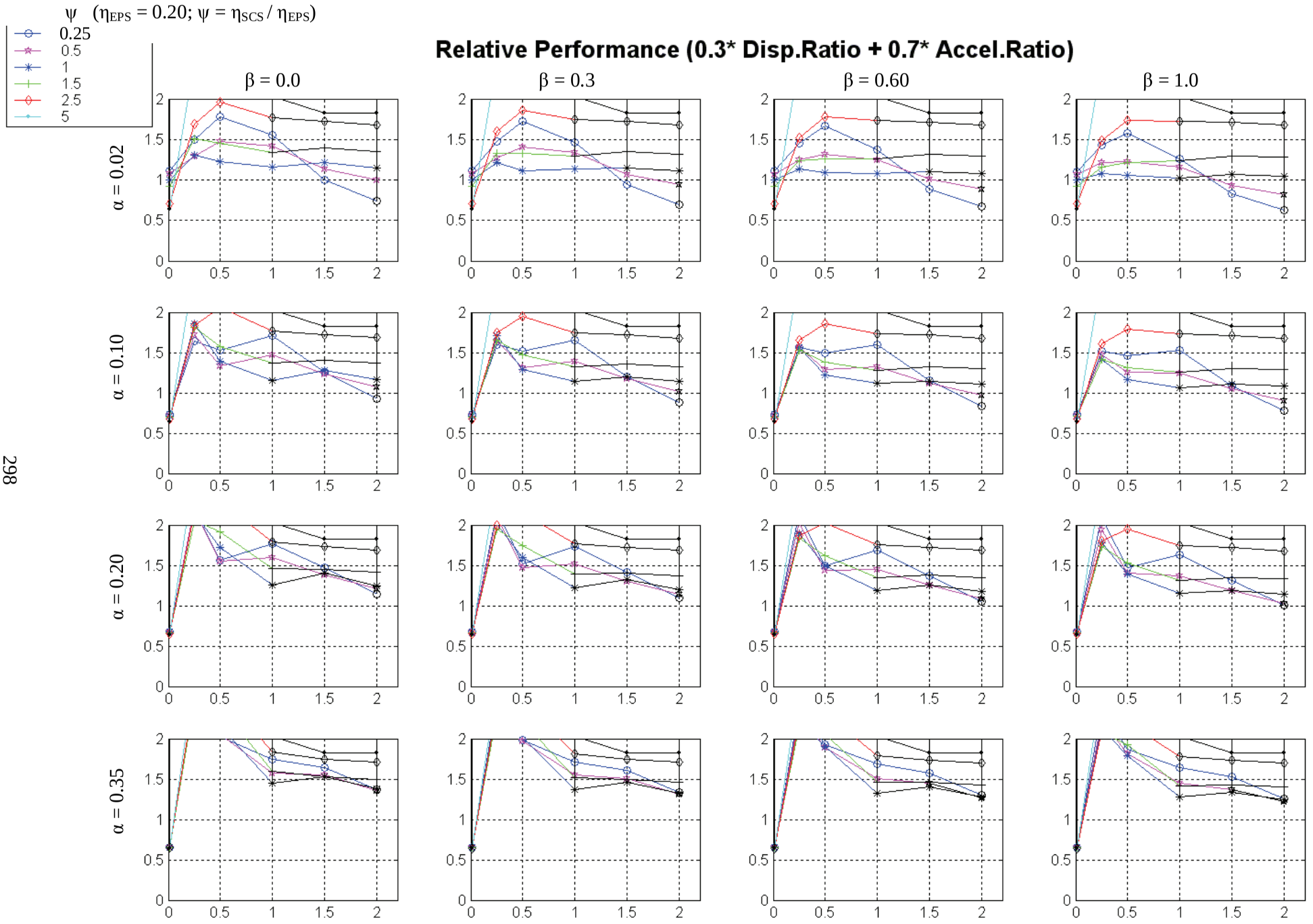
ψ (ηEPS = 0.20; ψ = ηSCS / ηEPS)
0.25
0.5
1
1.5
2.5
5
Relative Performance (0.3* Disp.Ratio + 0.7* Accel.Ratio)
β = 0.0
β = 0.3
β = 0.60
β = 1.0
α = 0.02
α = 0.10
α = 0.20
α = 0.35

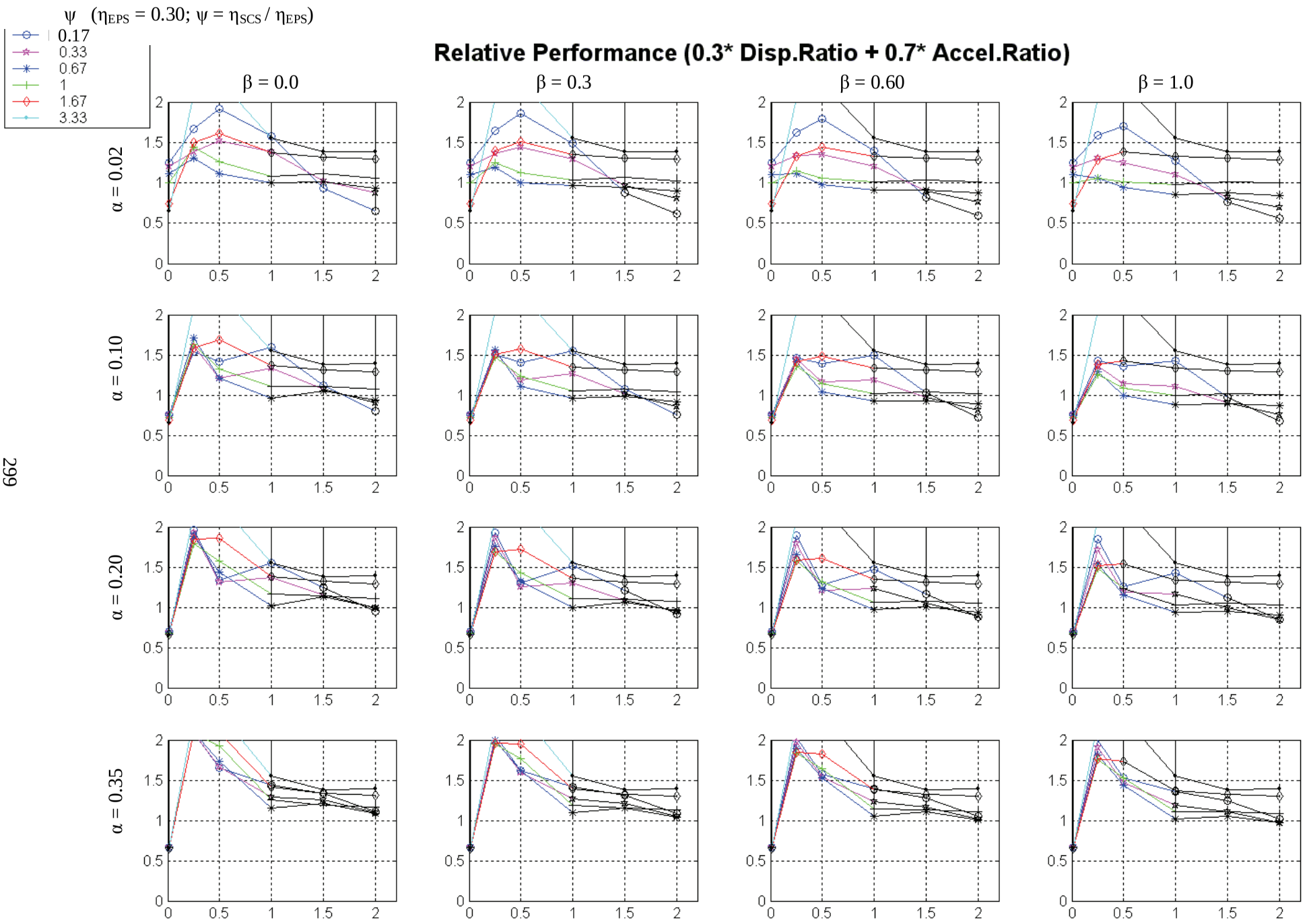
ψ (ηEPS = 0.30; ψ = ηSCS / ηEPS)
0.17
0.33
0.67
1
1.67
3.33
Relative Performance (0.3* Disp.Ratio + 0.7* Accel.Ratio)
β = 0.0
β = 0.3
β = 0.60
β = 1.0
α = 0.02
α = 0.10
α = 0.20
α = 0.35

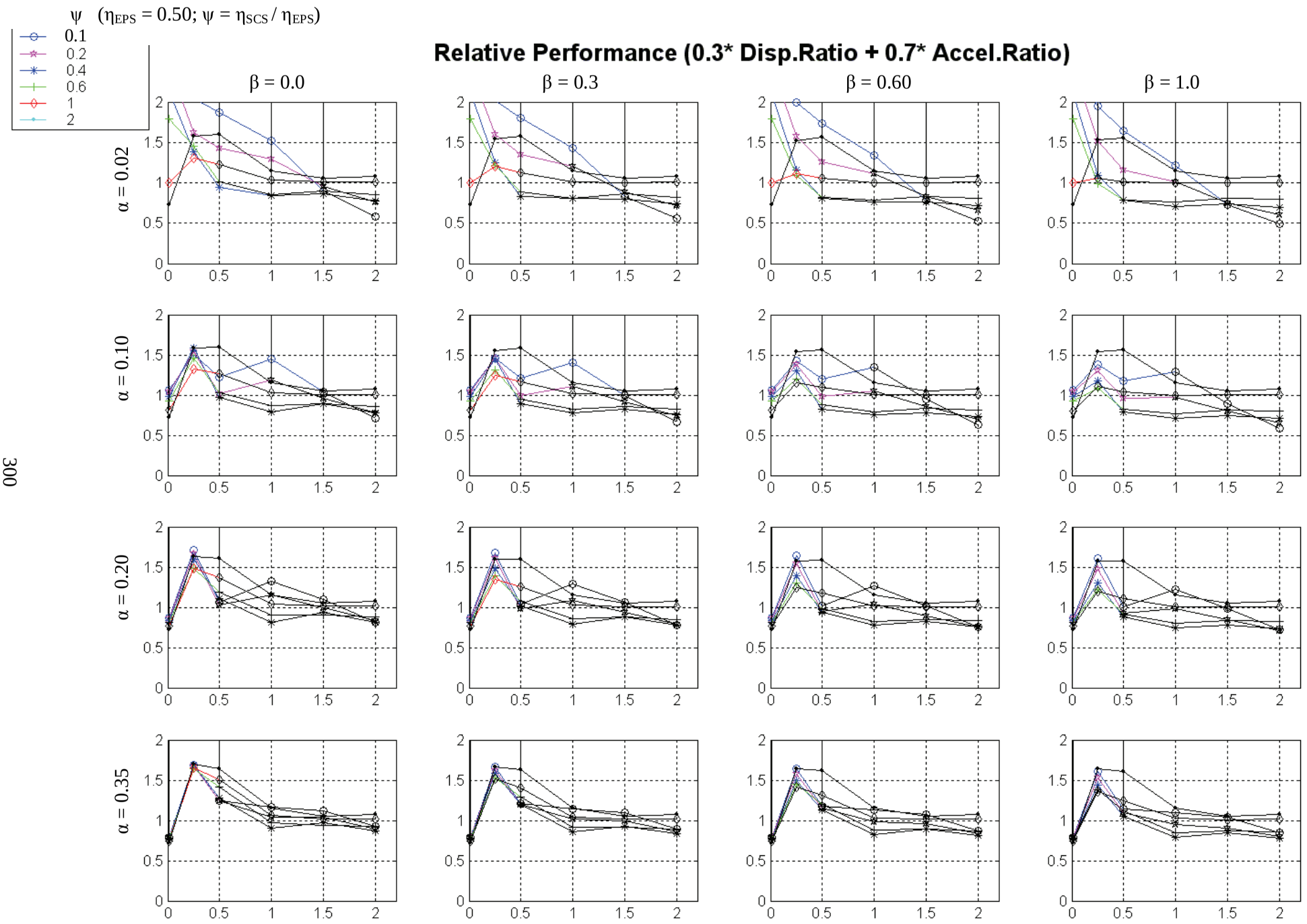
ψ (ηEPS = 0.50; ψ = ηSCS / ηEPS)
0.1
0.2
0.4
0.6
1
2
Relative Performance (0.3* Disp.Ratio + 0.7* Accel.Ratio)
β = 0.0
β = 0.3
β = 0.60
β = 1.0
α = 0.02
α = 0.10
α = 0.20
α = 0.35
0
0.5
1
1.5
2

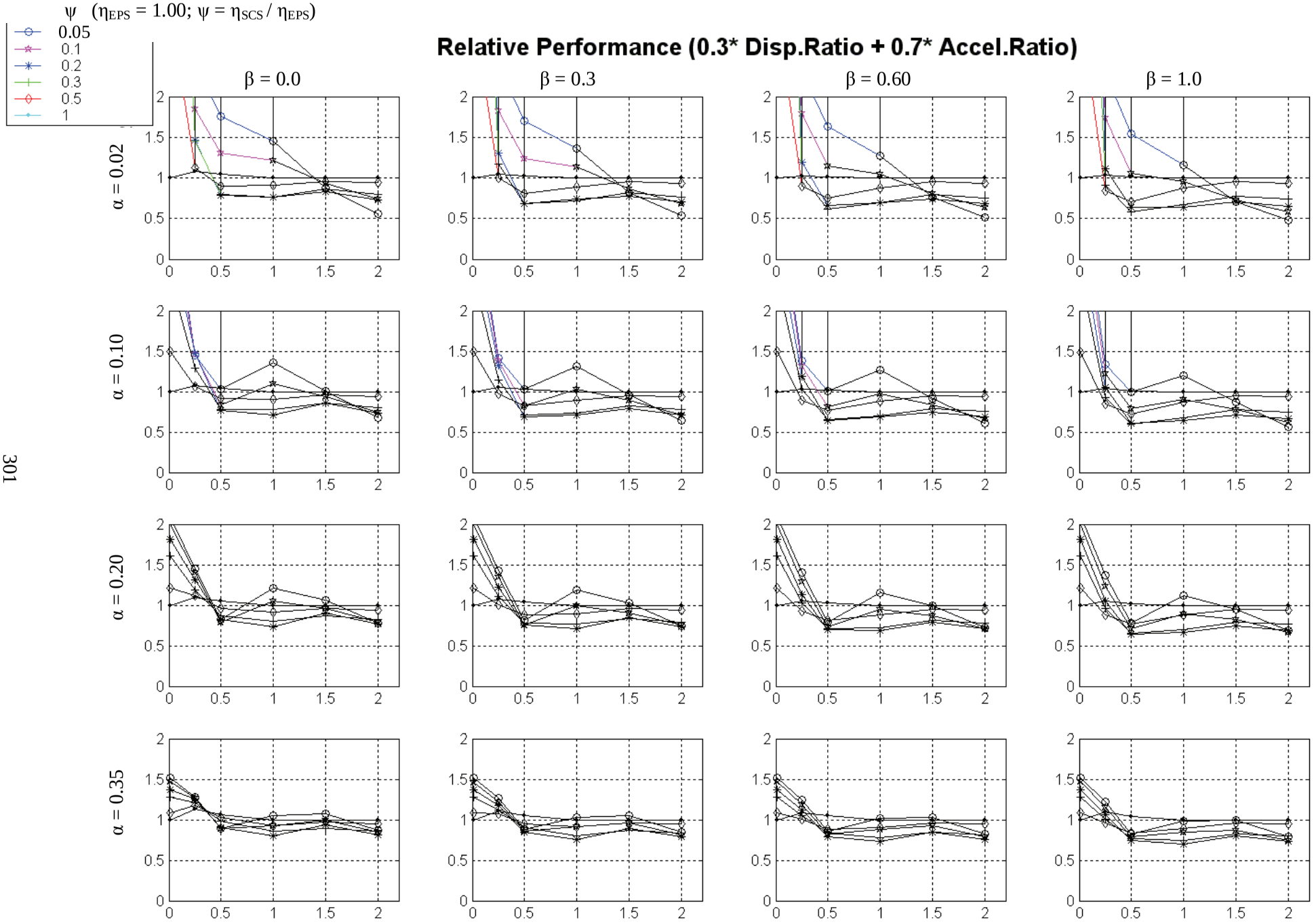
ψ (ηEPS = 1.00; ψ = ηSCS / ηEPS)
0.05
0.1
0.2
0.3
0.5
1
Relative Performance (0.3* Disp.Ratio + 0.7* Accel.Ratio)
β = 0.0
β = 0.3
β = 0.60
β = 1.0
α = 0.02
α = 0.10
α = 0.20
α = 0.35

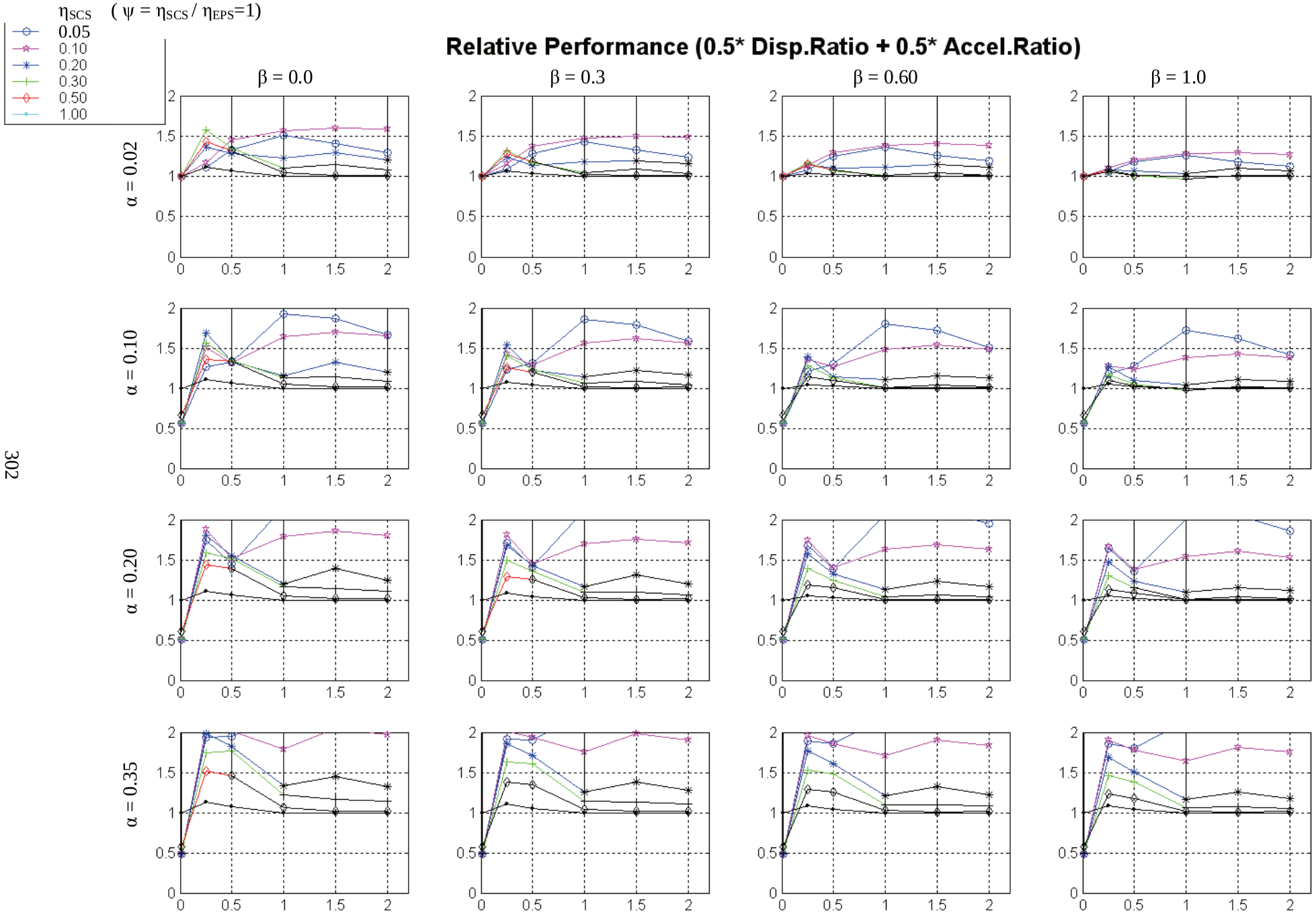
ηSCS (ψ = ηSCS / ηEPS=1)
0.05
0.10
0.20
0.30
0.50
1.00
Relative Performance (0.5* Disp.Ratio + 0.5* Accel.Ratio)
β = 0.0
β = 0.3
β = 0.60
β = 1.0
α = 0.02
α = 0.10
α = 0.20
α = 0.35

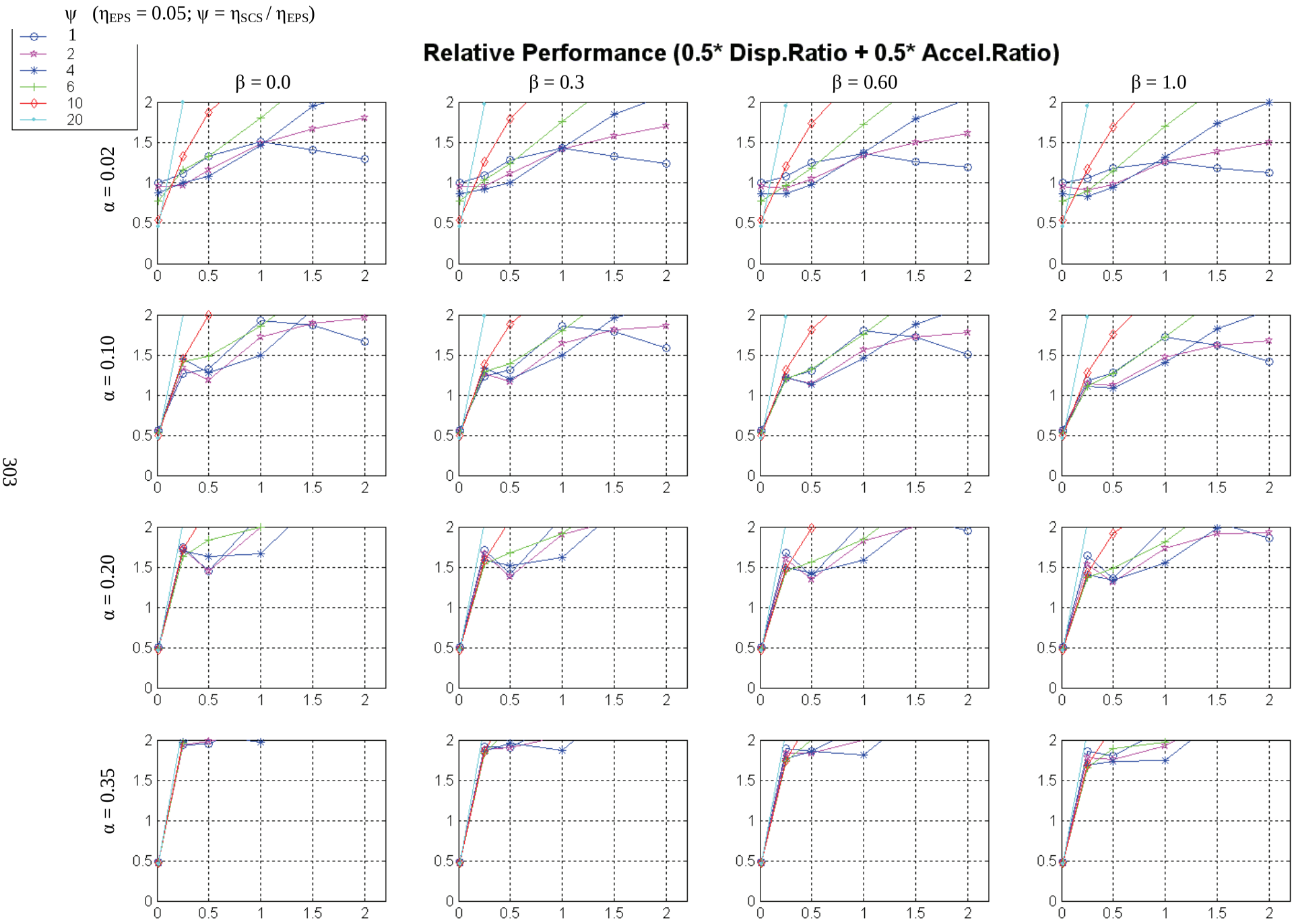
ψ (ηEPS = 0.05; ψ = ηSCS / ηEPS)
1
2
4
6
10
20
Relative Performance (0.5* Disp.Ratio + 0.5* Accel.Ratio)
β = 0.0
β = 0.3
β = 0.60
β = 1.0
α = 0.02
α = 0.10
α = 0.20
α = 0.35

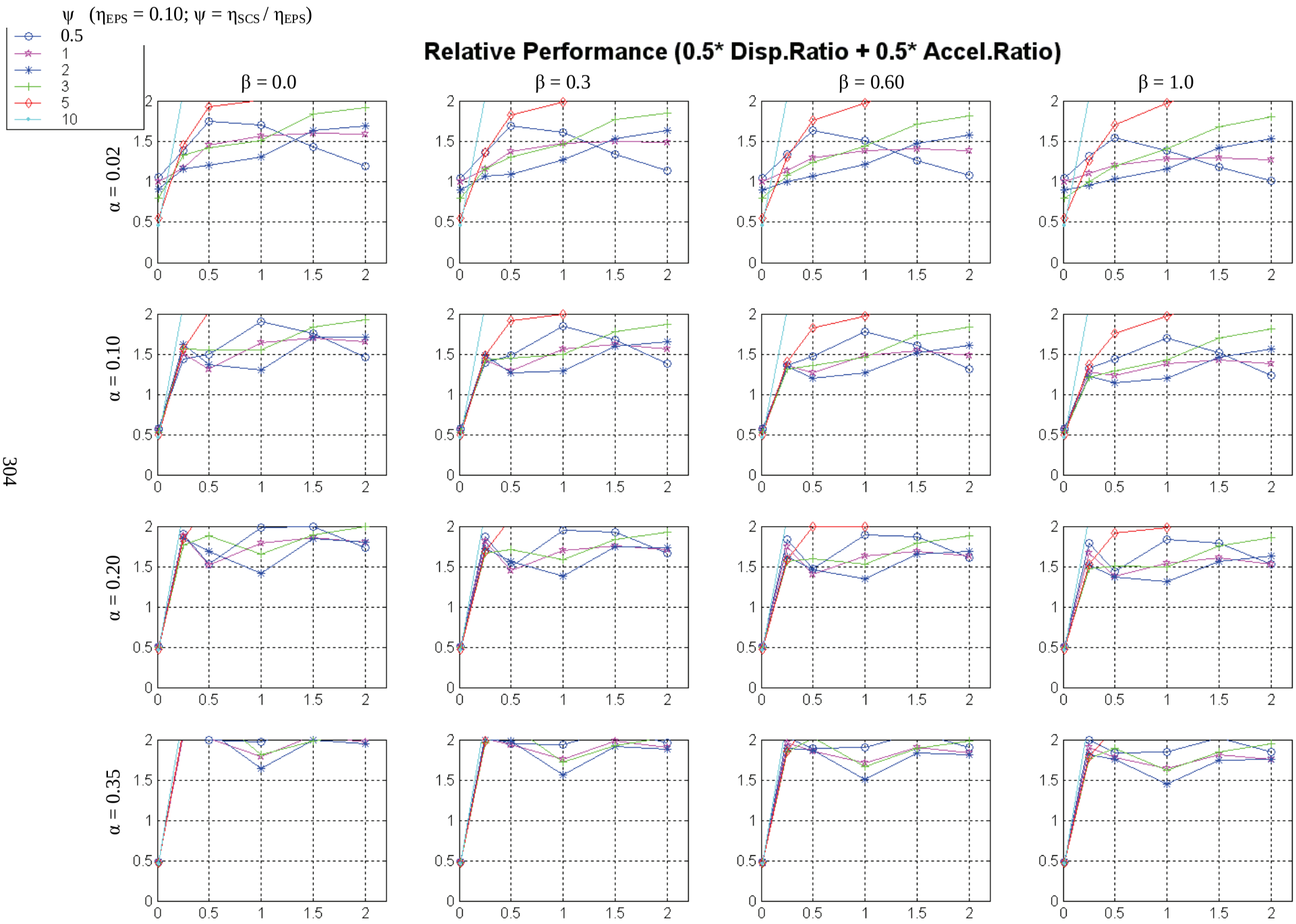
ψ (ηEPS = 0.10; ψ = ηSCS / ηEPS)
0.5
1
2
3
5
10
Relative Performance (0.5* Disp.Ratio + 0.5* Accel.Ratio)
β = 0.0
β = 0.3
β = 0.60
β = 1.0
α = 0.02
α = 0.10
α = 0.20
α = 0.35

Relative Performance (0.5* Disp.Ratio + 0.5* Accel.Ratio)
β = 0.0
β = 0.3
β = 0.60
β = 1.0
α = 0.02
α = 0.10
α = 0.20
α = 0.35
ψ (ηEPS = 0.20; ψ = ηSCS / ηEPS)
0.25
0.5
1
1.5
2.5
5

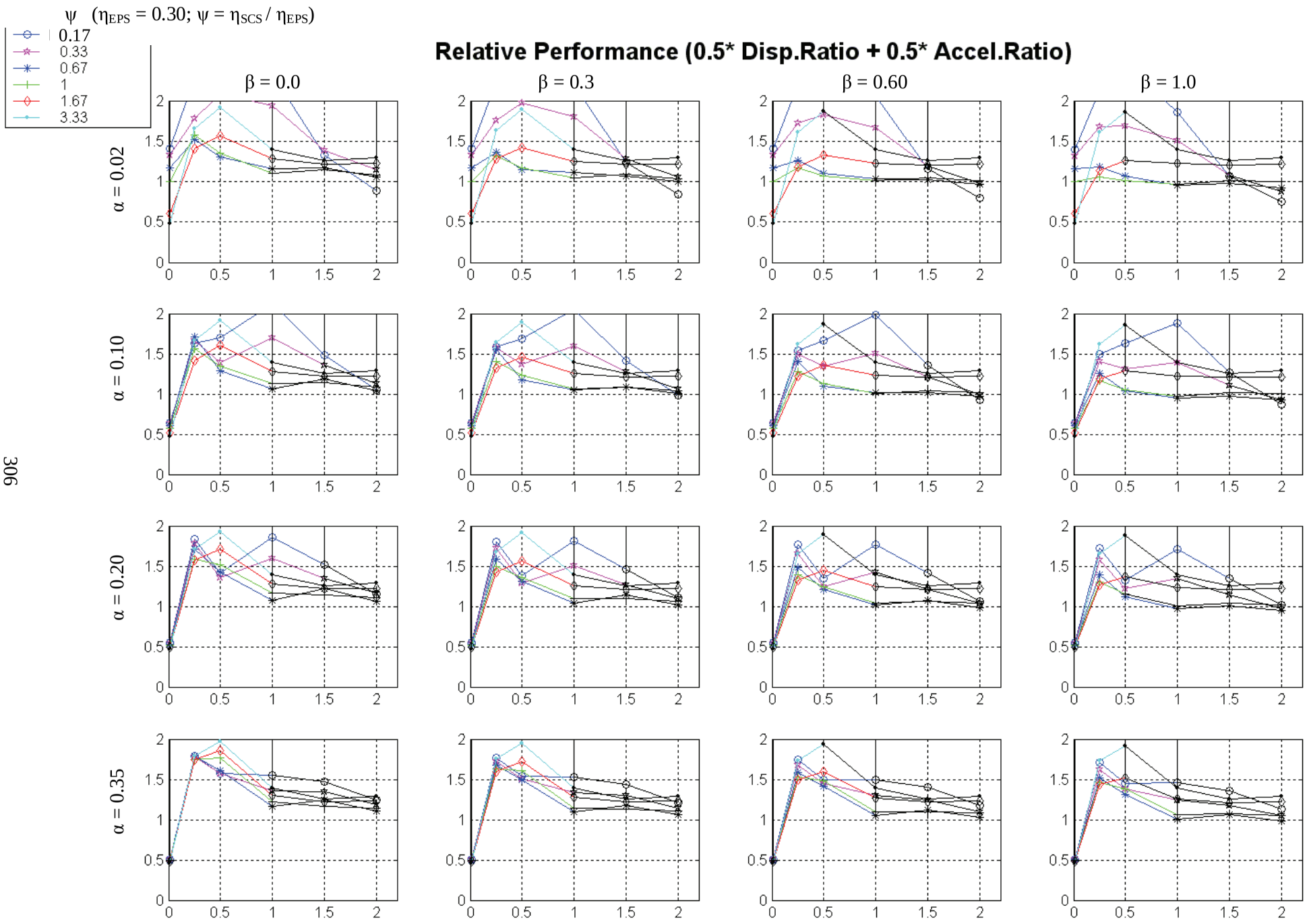
ψ (ηEPS = 0.30; ψ = ηSCS / ηEPS)
0.17
0.33
0.67
1
1.67
3.33
Relative Performance (0.5* Disp.Ratio + 0.5* Accel.Ratio)
β = 0.0
β = 0.3
β = 0.60
β = 1.0
α = 0.02
α = 0.10
α = 0.20
α = 0.35

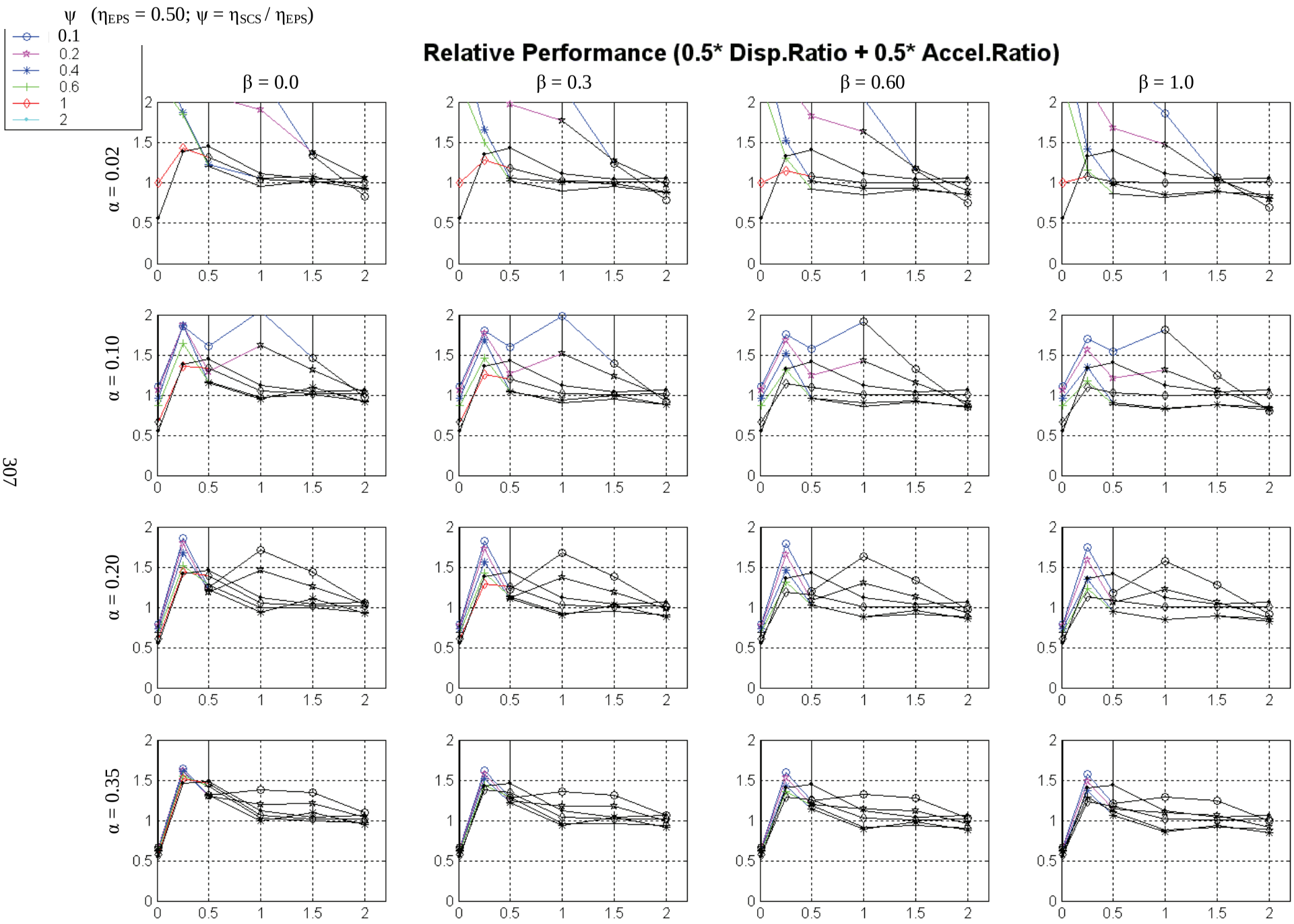
ψ (ηEPS = 0.50; ψ = ηSCS / ηEPS)
0.1
0.2
0.4
0.6
1
2
Relative Performance (0.5* Disp.Ratio + 0.5* Accel.Ratio)
β = 0.0
β = 0.3
β = 0.60
β = 1.0
α = 0.02
α = 0.10
α = 0.20
α = 0.35

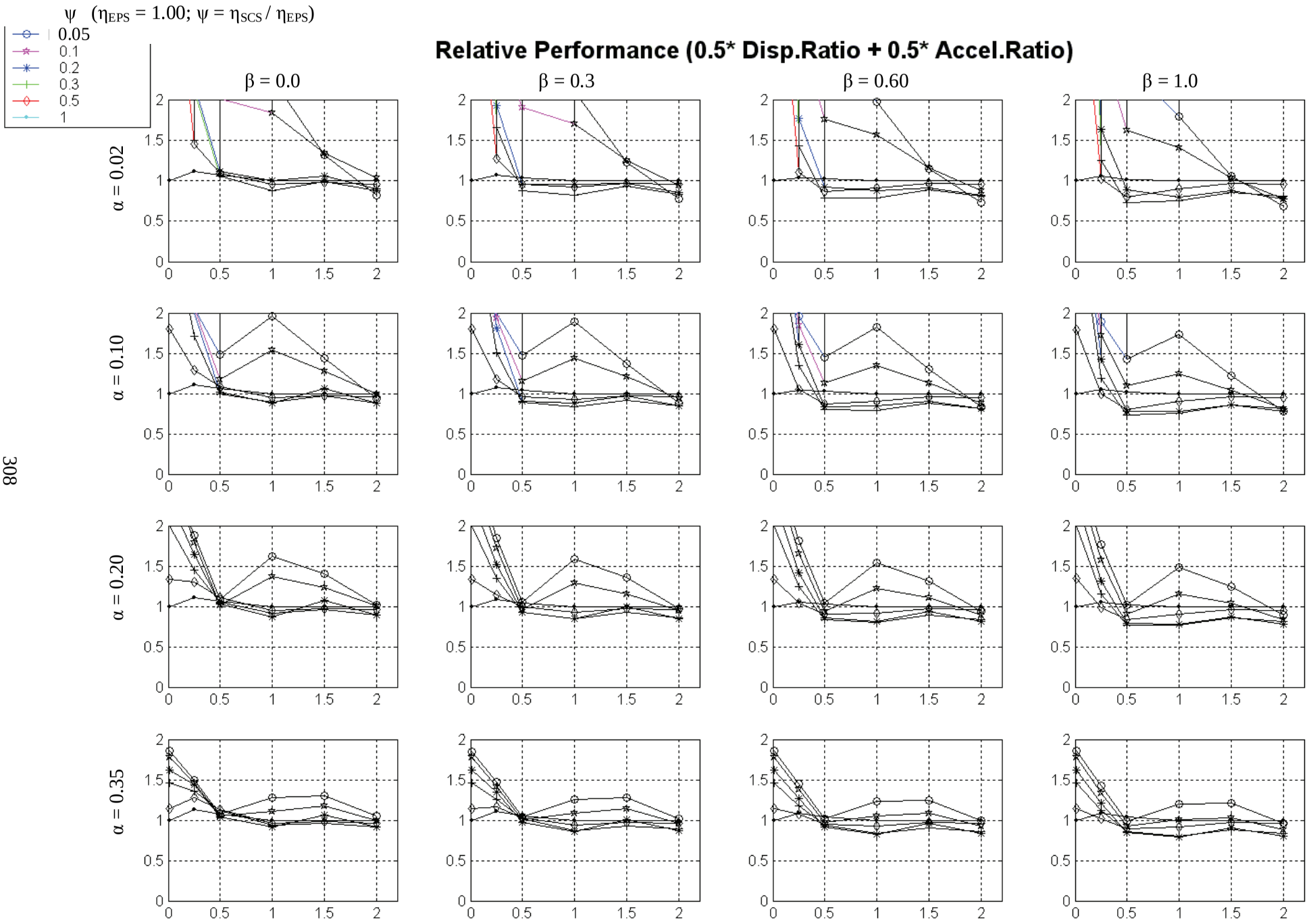
ψ (ηEPS = 1.00; ψ = ηSCS / ηEPS)
0.05
0.1
0.2
0.3
0.5
1
Relative Performance (0.5* Disp.Ratio + 0.5* Accel.Ratio)
β = 0.0
β = 0.3
β = 0.60
β = 1.0
α = 0.02
α = 0.10
α = 0.20
α = 0.35

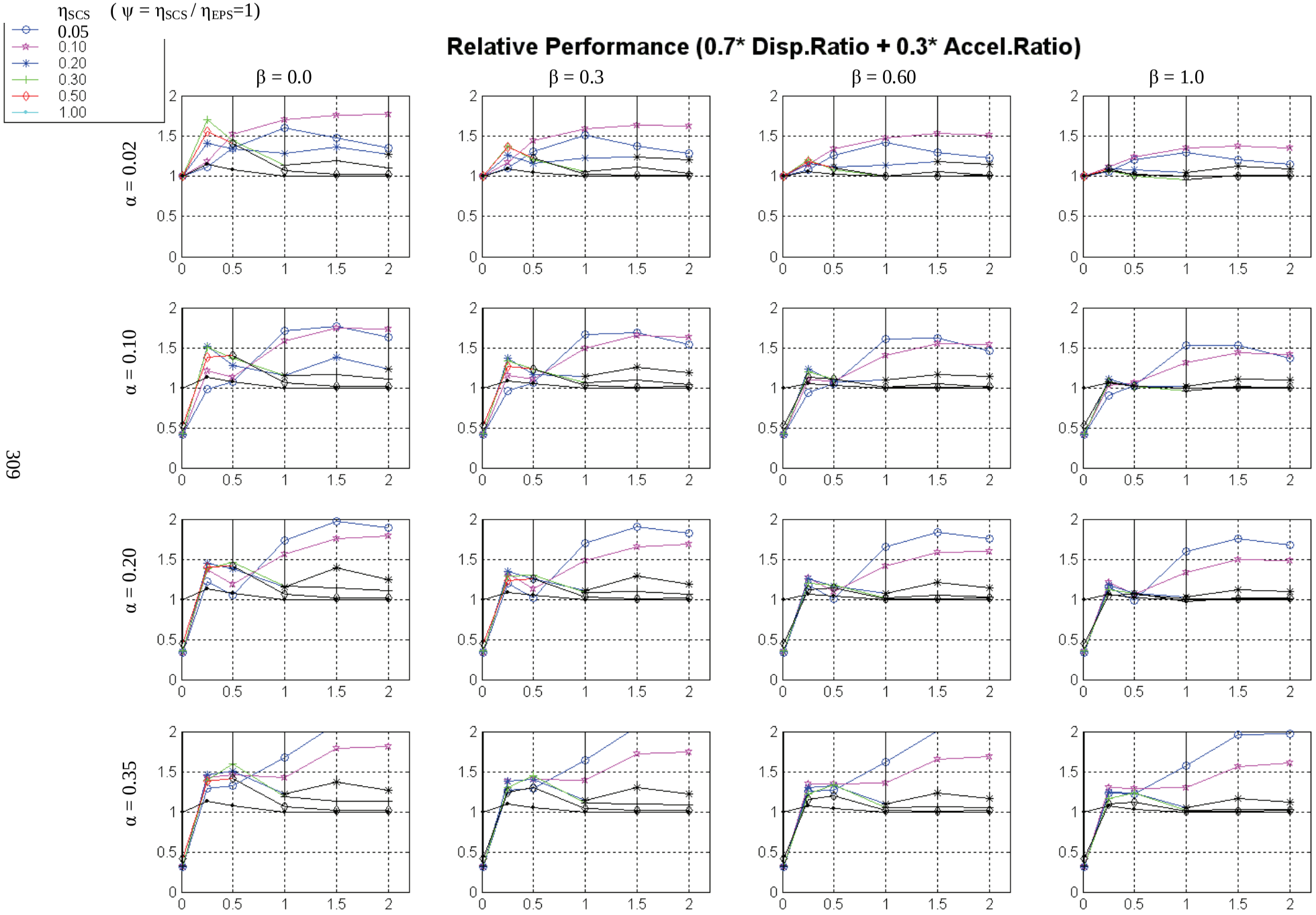
ηSCS (ψ = ηSCS / ηEPS=1)
0.05
0.10
0.20
0.30
0.50
1.00
Relative Performance (0.7* Disp.Ratio + 0.3* Accel.Ratio)
β = 0.0
β = 0.3
β = 0.60
β = 1.0
α = 0.02
α = 0.10
α = 0.20
α = 0.35

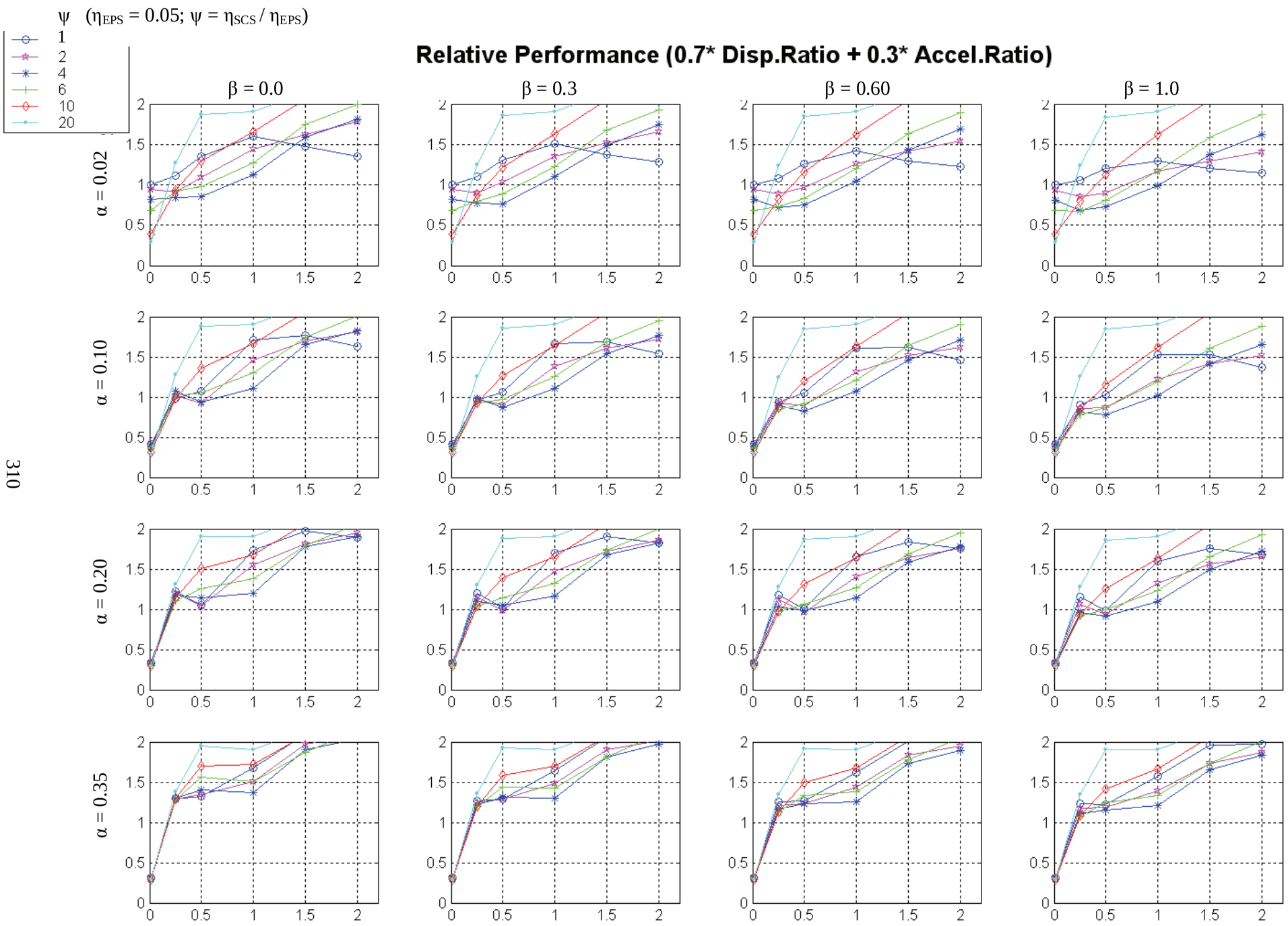
ψ (ηEPS = 0.05; ψ = ηSCS / ηEPS)
1
2
4
6
10
20
Relative Performance (0.7* Disp.Ratio + 0.3* Accel.Ratio)
β = 0.0
β = 0.3
β = 0.60
β = 1.0
α = 0.02
α = 0.10
α = 0.20
α = 0.35
0
0.5
1
1.5
2

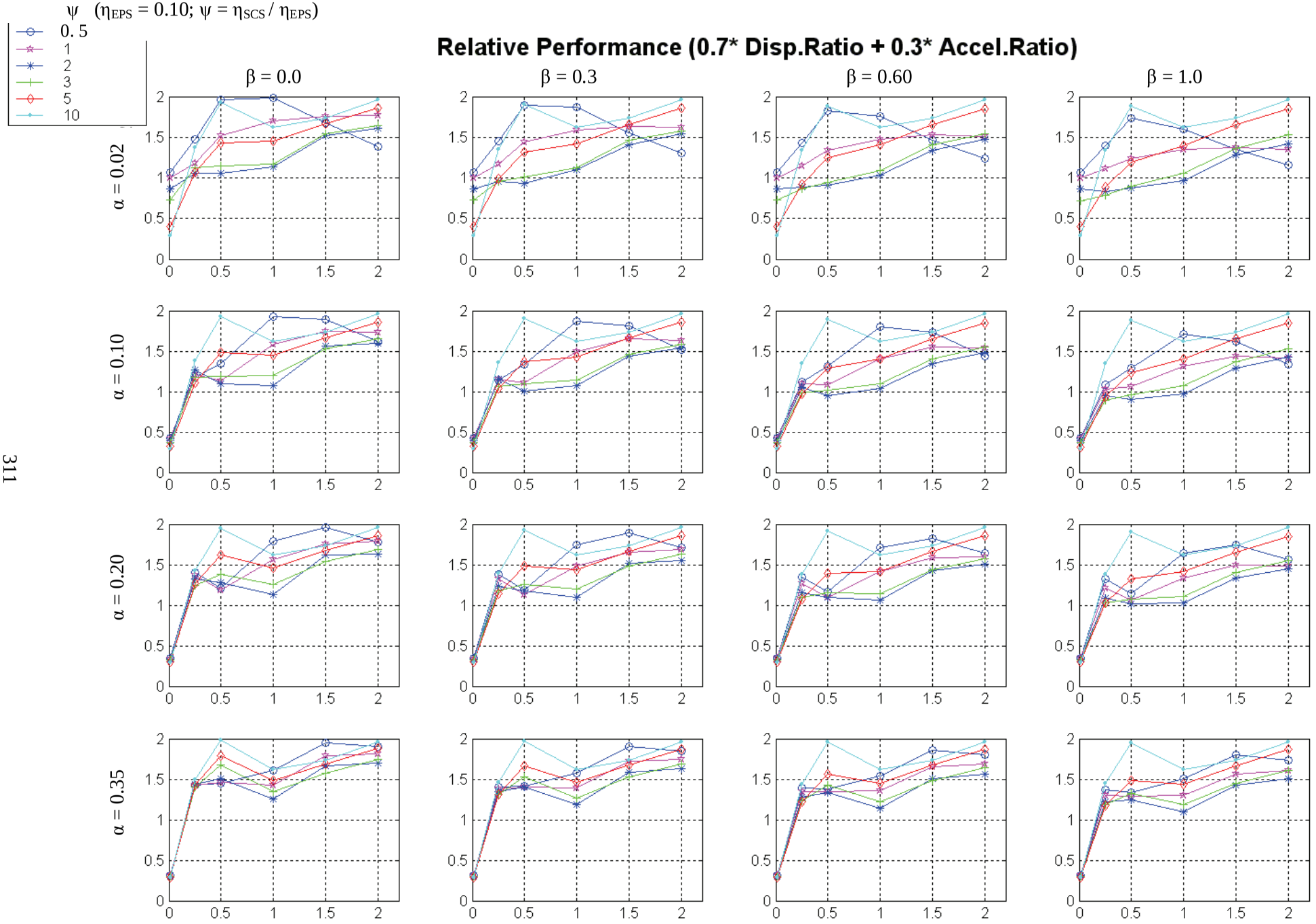
ψ (ηEPS = 0.10; ψ = ηSCS / ηEPS)
0. 5
1
2
3
5
10
Relative Performance (0.7* Disp.Ratio + 0.3* Accel.Ratio)
β = 0.0
β = 0.3
β = 0.60
β = 1.0
α = 0.02
α = 0.10
α = 0.20
α = 0.35

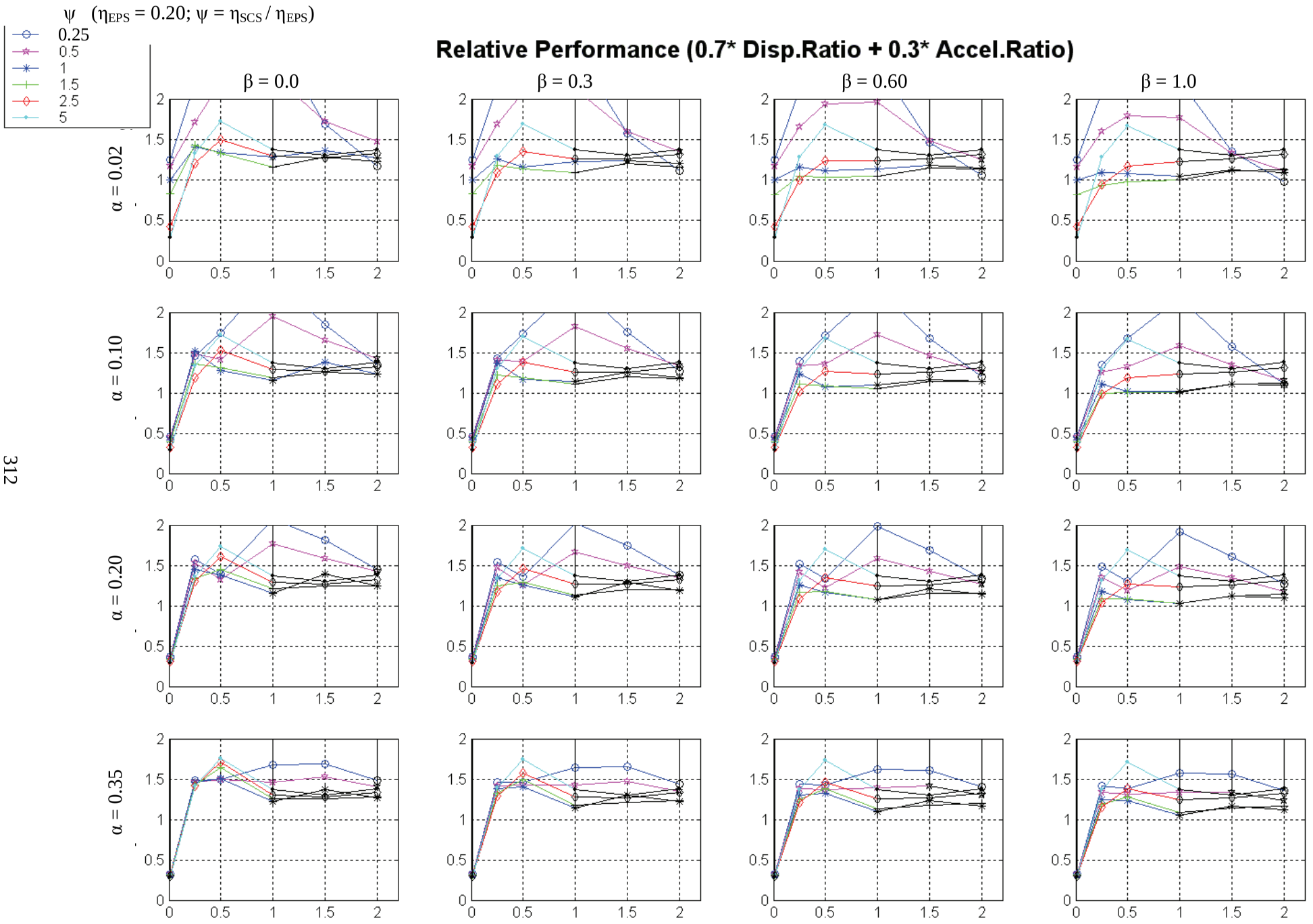
ψ (ηEPS = 0.20; ψ = ηSCS / ηEPS)
0.25
0.5
1
1.5
2.5
5
Relative Performance (0.7* Disp.Ratio + 0.3* Accel.Ratio)
β = 0.0
β = 0.3
β = 0.60
β = 1.0
α = 0.02
α = 0.10
α = 0.20
α = 0.35

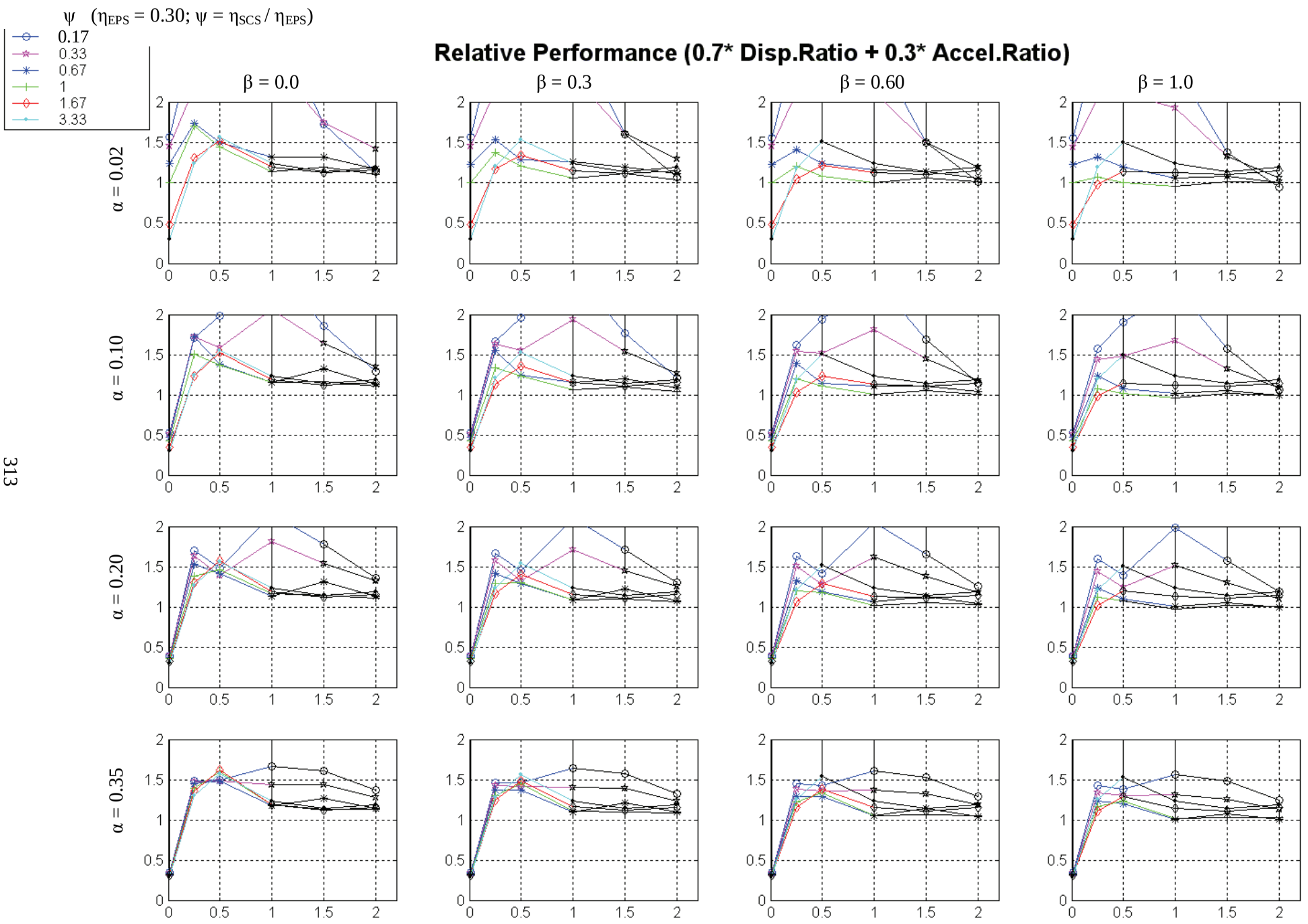
ψ (ηEPS = 0.30; ψ = ηSCS / ηEPS)
0.17
0.33
0.67
1
1.67
3.33
Relative Performance (0.7* Disp.Ratio + 0.3* Accel.Ratio)
β = 0.0
β = 0.3
β = 0.60
β = 1.0
α = 0.02
α = 0.10
α = 0.20
α = 0.35

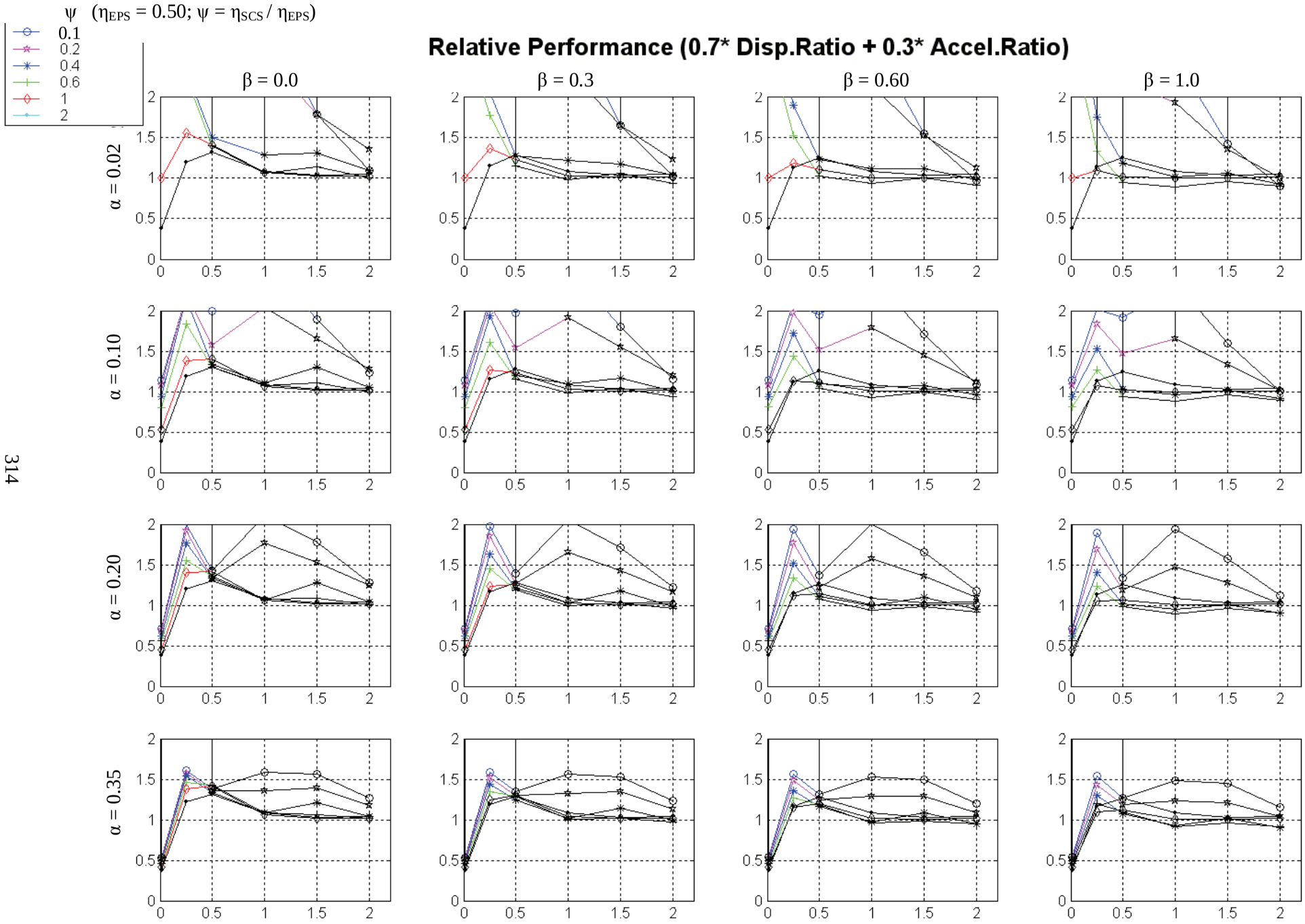
ψ (ηEPS = 0.50; ψ = ηSCS / ηEPS)
0.1
0.2
0.4
0.6
1
2
Relative Performance (0.7* Disp.Ratio + 0.3* Accel.Ratio)
β = 0.0
β = 0.3
β = 0.60
β = 1.0
α = 0.02
α = 0.10
α = 0.20
α = 0.35

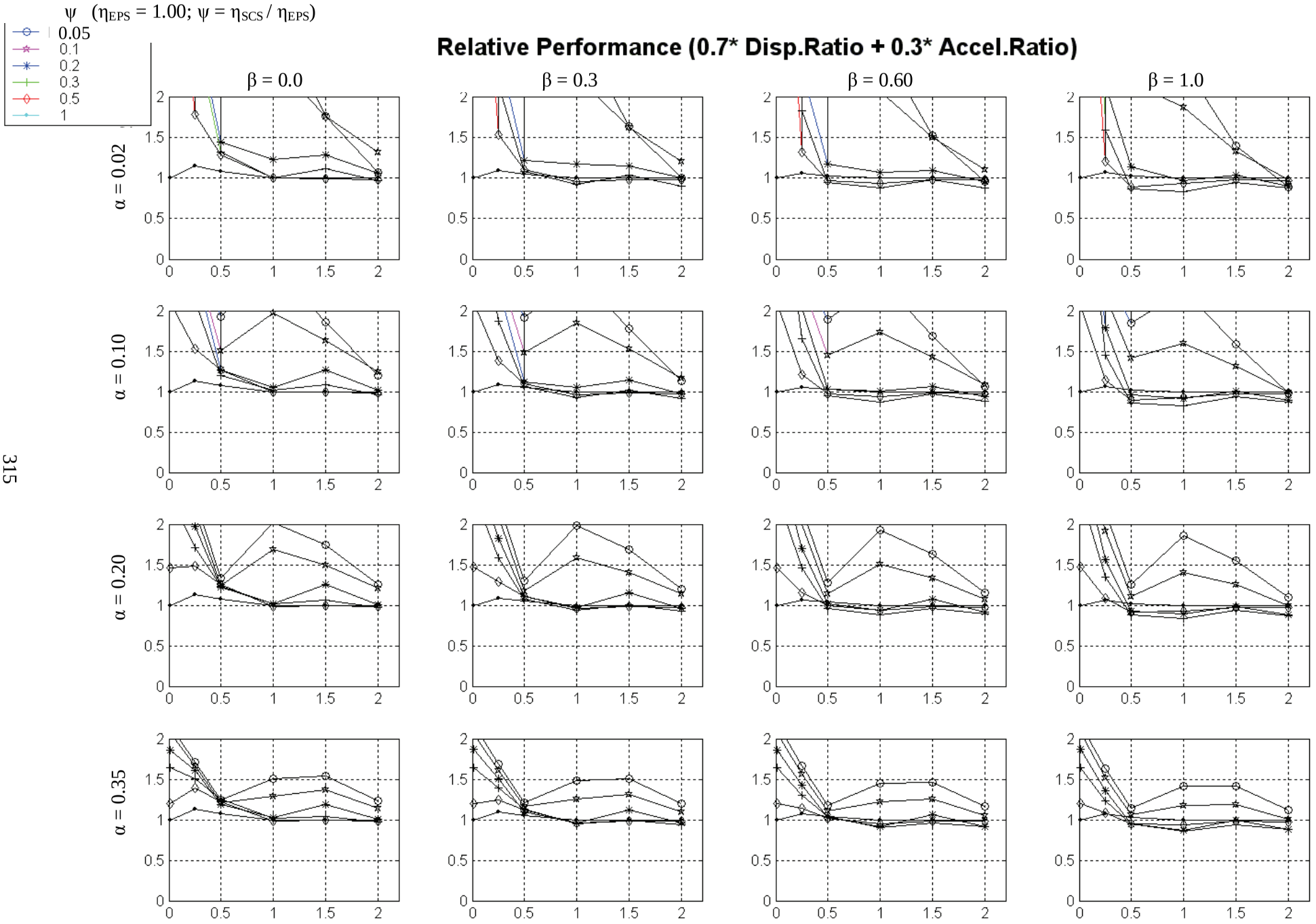
ψ (ηEPS = 1.00; ψ = ηSCS / ηEPS)
0.05
0.1
0.2
0.3
0.5
1
Relative Performance (0.7* Disp.Ratio + 0.3* Accel.Ratio)
β = 0.0
β = 0.3
β = 0.60
β = 1.0
α = 0.02
α = 0.10
α = 0.20
α = 0.35

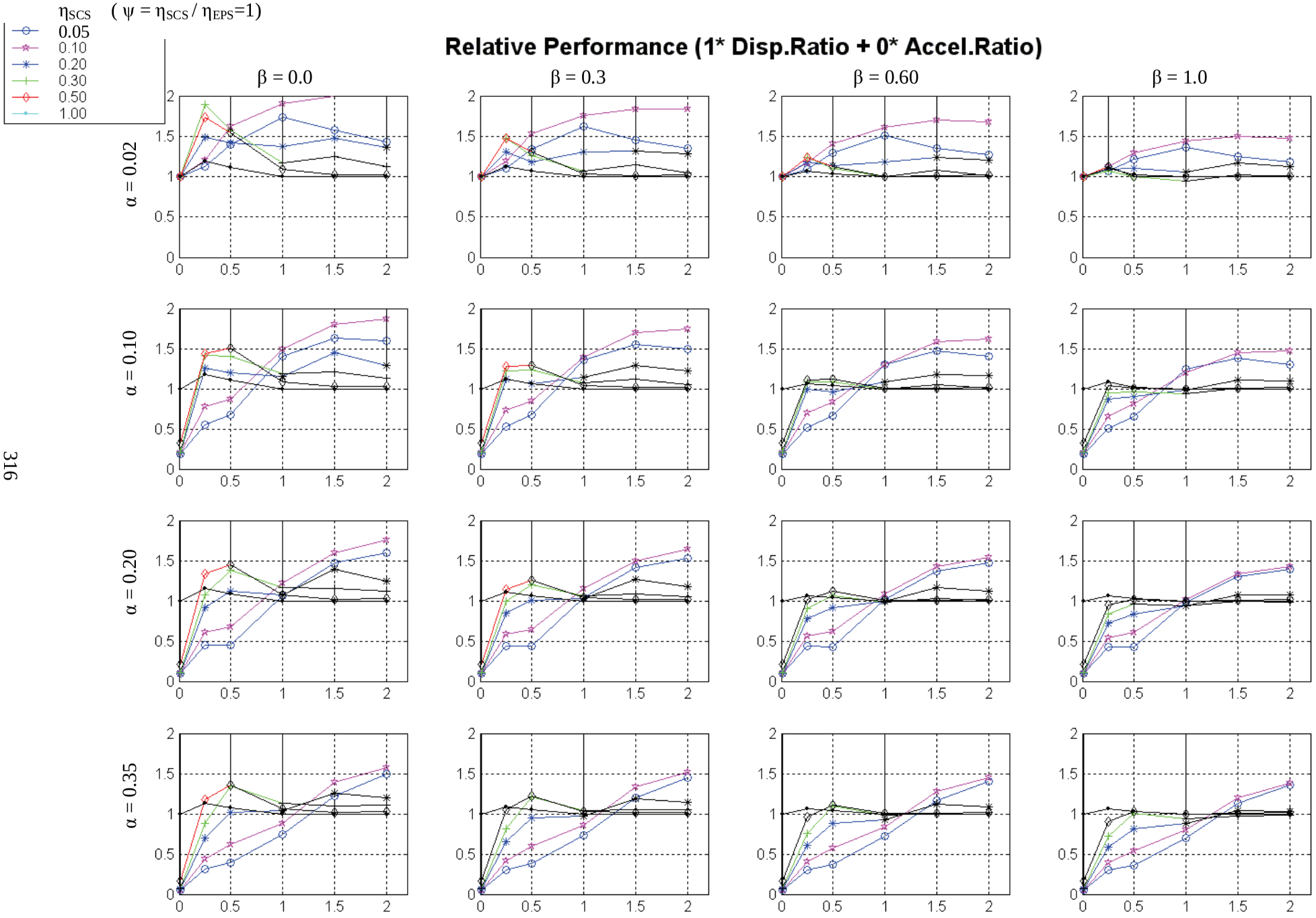
ηSCS (ψ = ηSCS / ηEPS=1)
0.05
0.10
0.20
0.30
0.50
1.00
Relative Performance (1* Disp.Ratio + 0* Accel.Ratio)
β = 0.0
β = 0.3
β = 0.60
β = 1.0
α = 0.02
α = 0.10
α = 0.20
α = 0.35

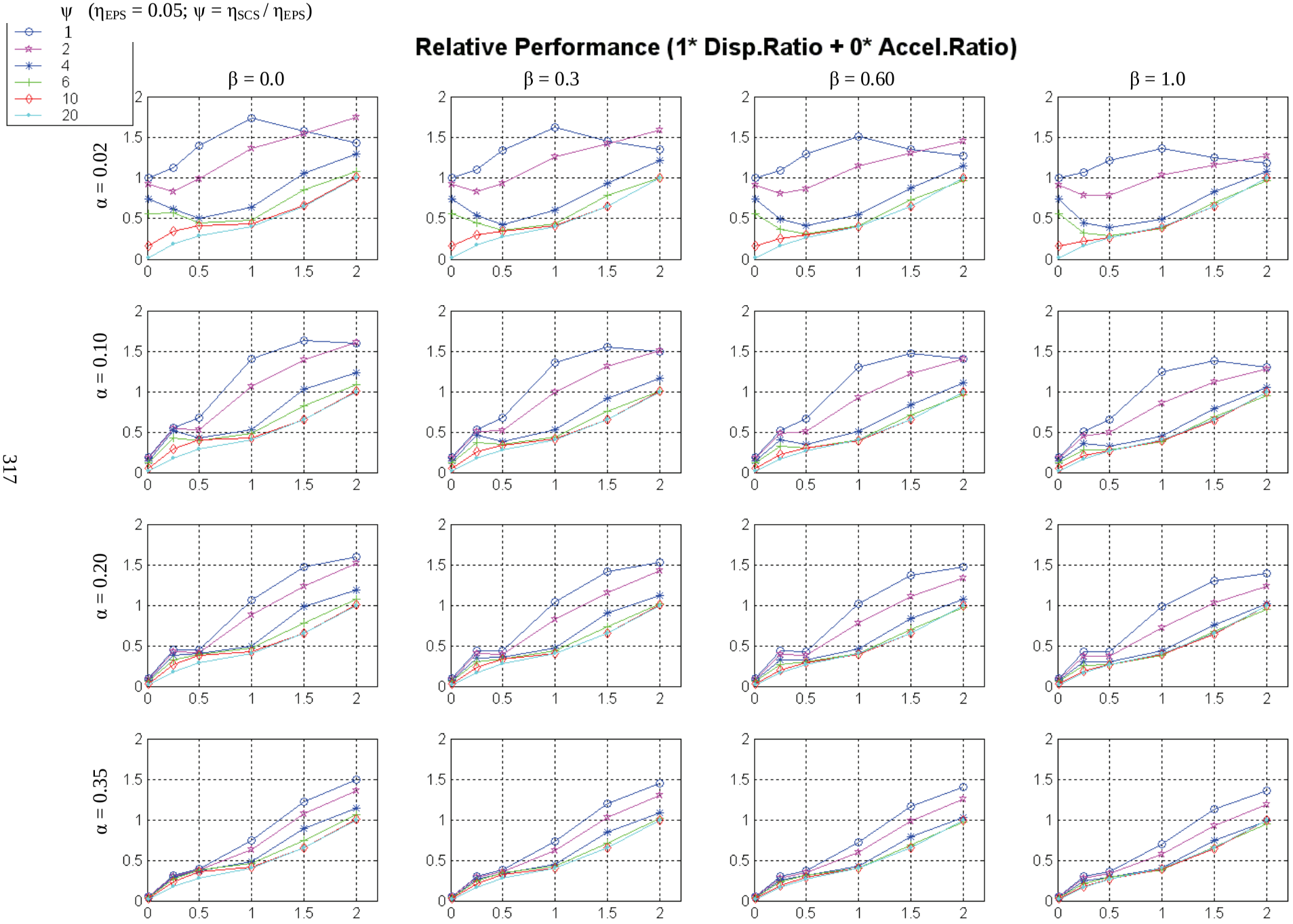
ψ (ηEPS = 0.05; ψ = ηSCS / ηEPS)
1
2
4
6
10
20
Relative Performance (1* Disp.Ratio + 0* Accel.Ratio)
β = 0.0
β = 0.3
β = 0.60
β = 1.0
α = 0.02
α = 0.10
α = 0.20
α = 0.35

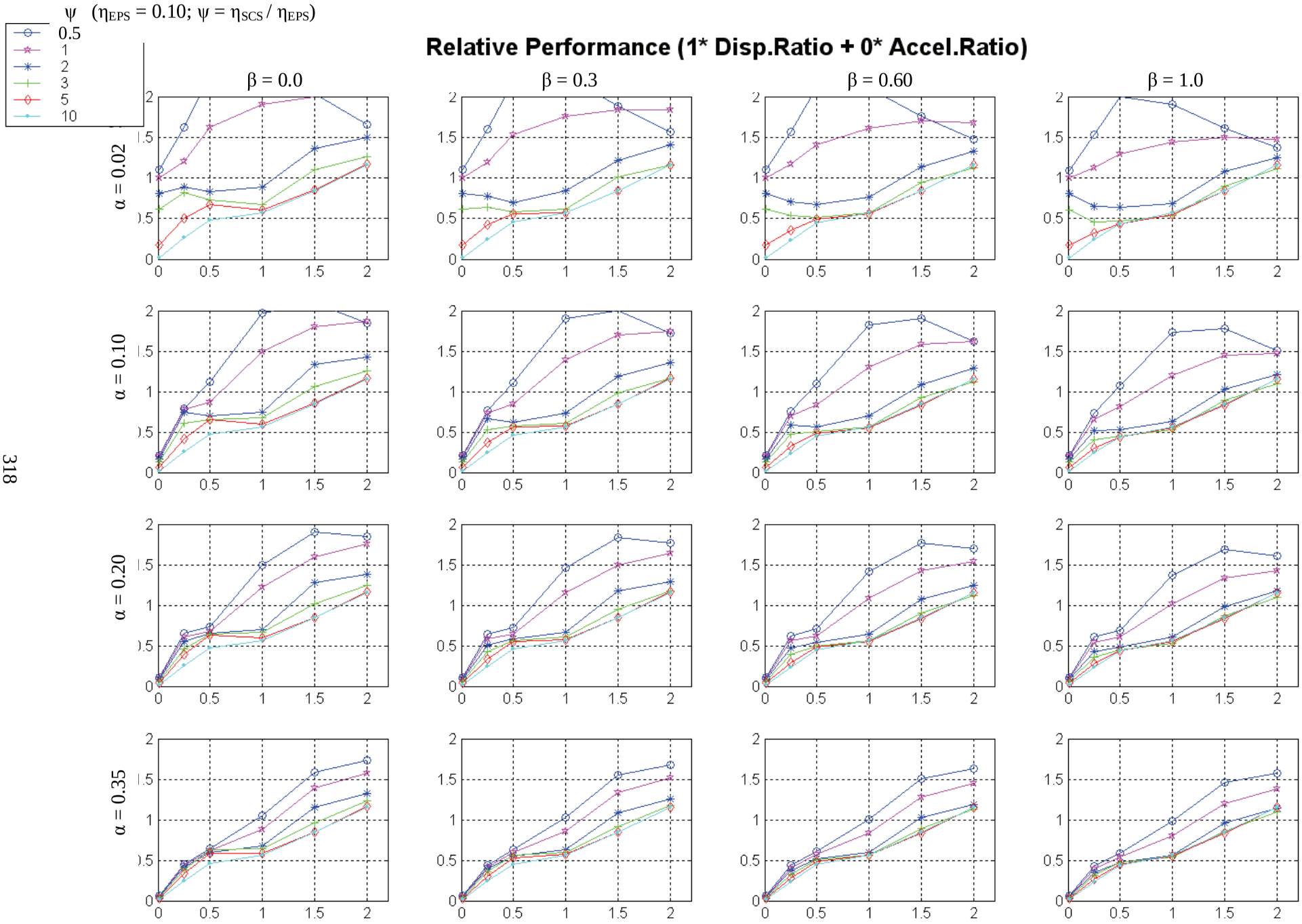
ψ (ηEPS = 0.10; ψ = ηSCS / ηEPS)
0.5
1
2
3
5
10
Relative Performance (1* Disp.Ratio + 0* Accel.Ratio)
β = 0.0
β = 0.3
β = 0.60
β = 1.0
α = 0.02
α = 0.10
α = 0.20
α = 0.35

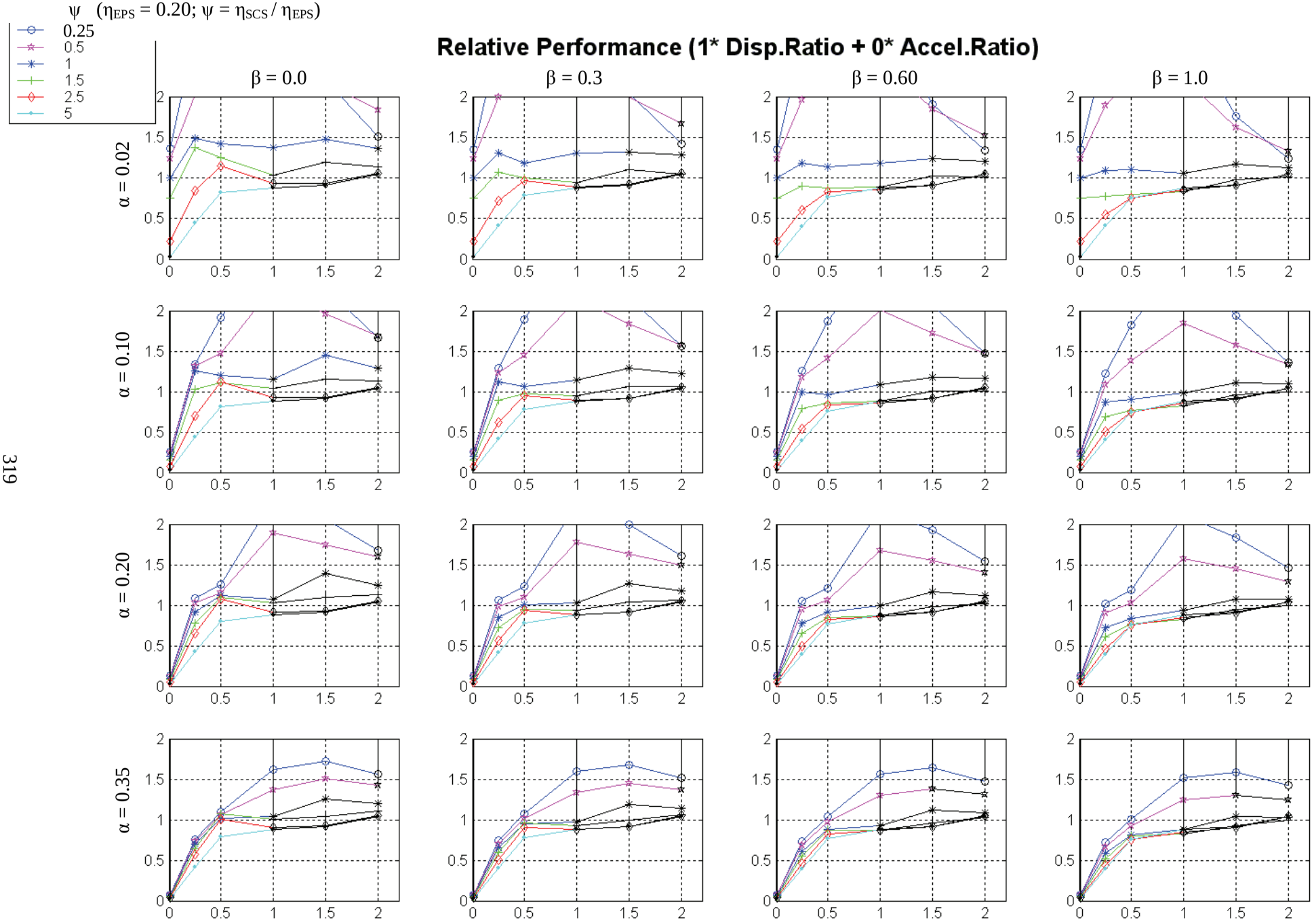
ψ (ηEPS = 0.20; ψ = ηSCS / ηEPS)
0.25
0.5
1
1.5
2.5
5
Relative Performance (1* Disp.Ratio + 0* Accel.Ratio)
β = 0.0
β = 0.3
β = 0.60
β = 1.0
α = 0.02
α = 0.10
α = 0.20
α = 0.35

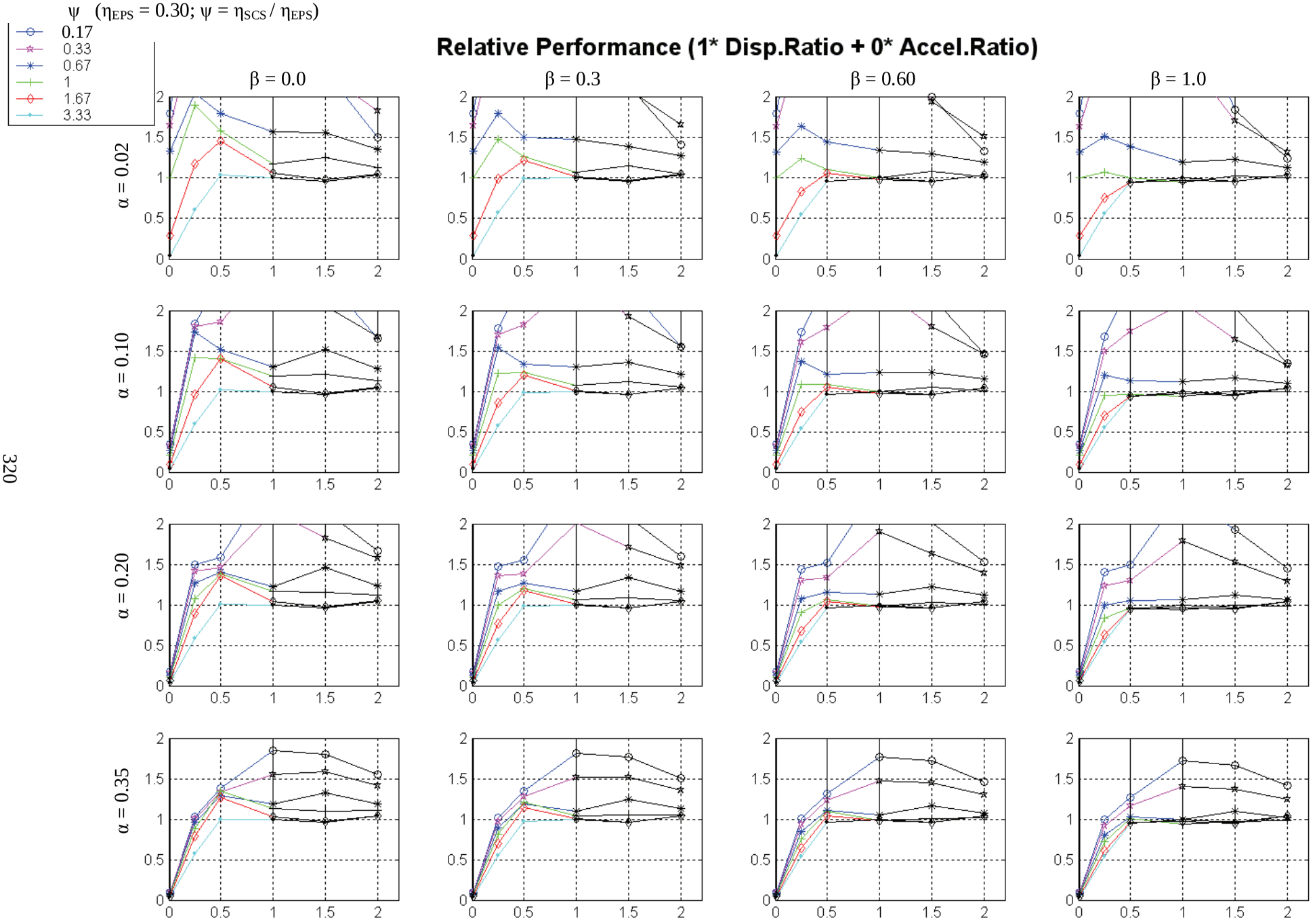
ψ (ηEPS = 0.30; ψ = ηSCS / ηEPS)
0.17
0.33
0.67
1
1.67
3.33
Relative Performance (1* Disp.Ratio + 0* Accel.Ratio)
β = 0.0
β = 0.3
β = 0.60
β = 1.0
α = 0.02
α = 0.10
α = 0.20
α = 0.35

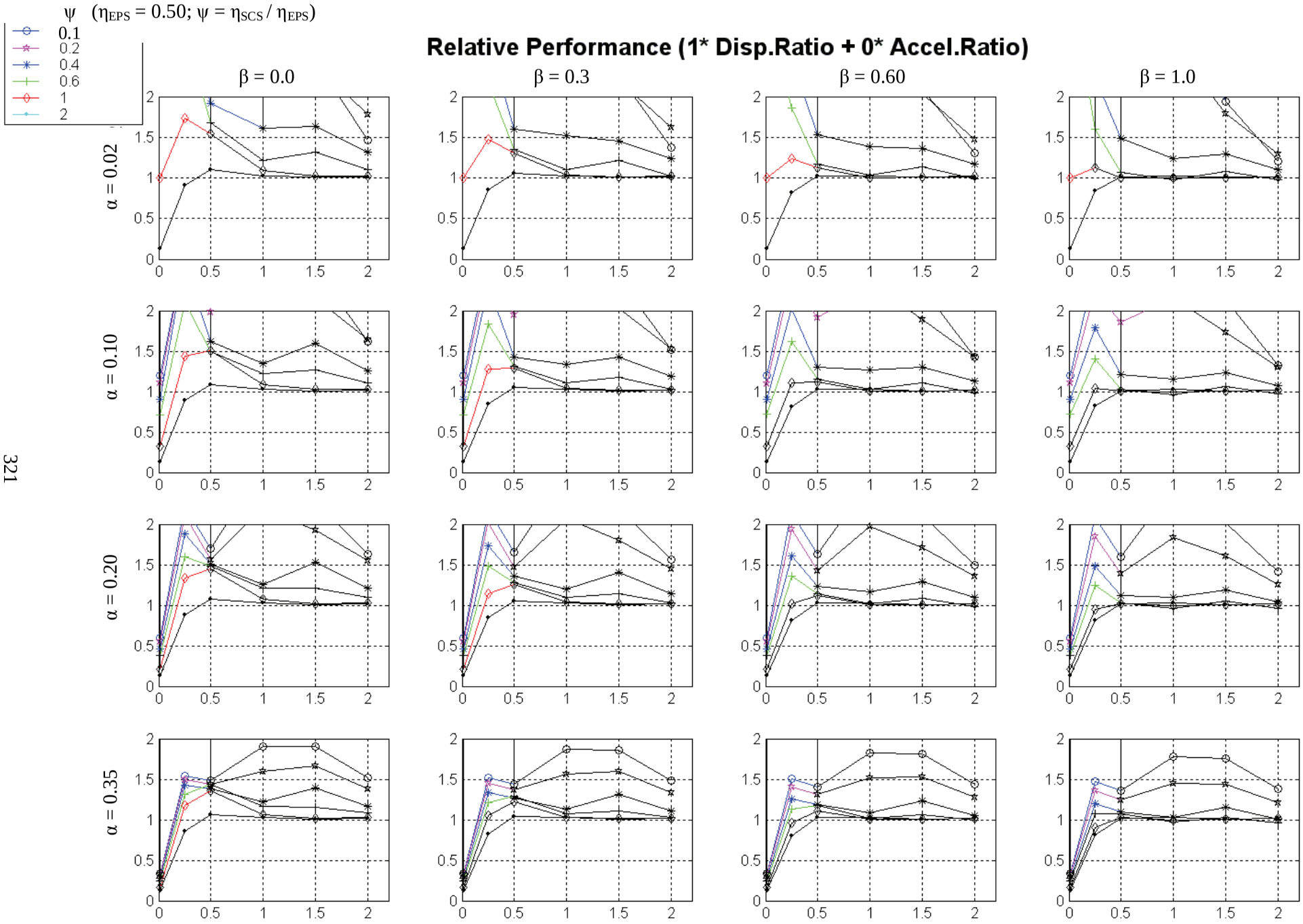
ψ (ηEPS = 0.50; ψ = ηSCS / ηEPS)
0.1
0.2
0.4
0.6
1
2
Relative Performance (1* Disp.Ratio + 0* Accel.Ratio)
β = 0.0
β = 0.3
β = 0.60
β = 1.0
α = 0.02
α = 0.10
α = 0.20
α = 0.35

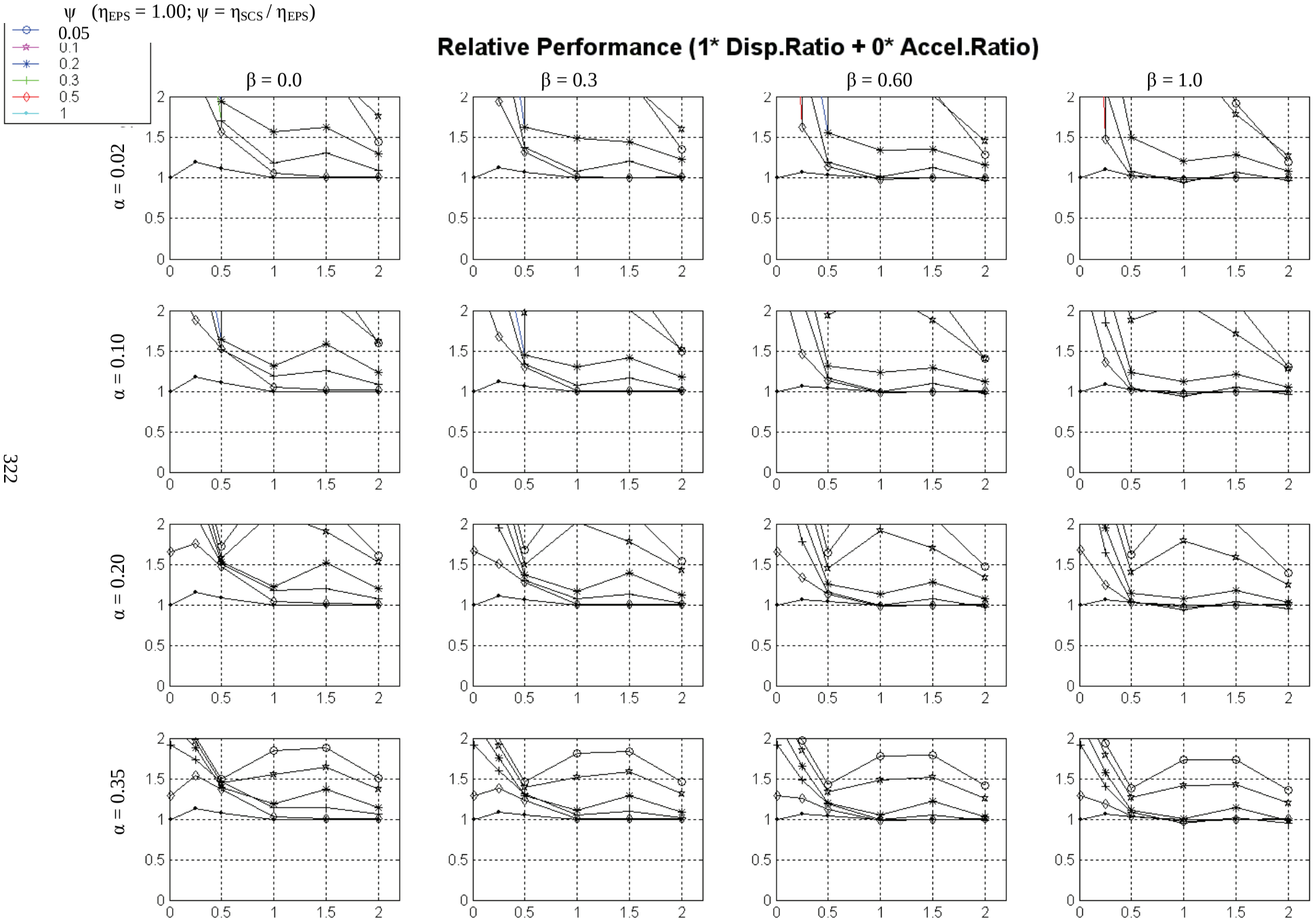
ψ (ηEPS = 1.00; ψ = ηSCS / ηEPS)
0.05
0.1
0.2
0.3
0.5
1
Relative Performance (1* Disp.Ratio + 0* Accel.Ratio)
β = 0.0
β = 0.3
β = 0.60
β = 1.0
α = 0.02
α = 0.10
α = 0.20
α = 0.35

Appendix C Model of Steel Moment Resisting Frame for Shake Table Testing

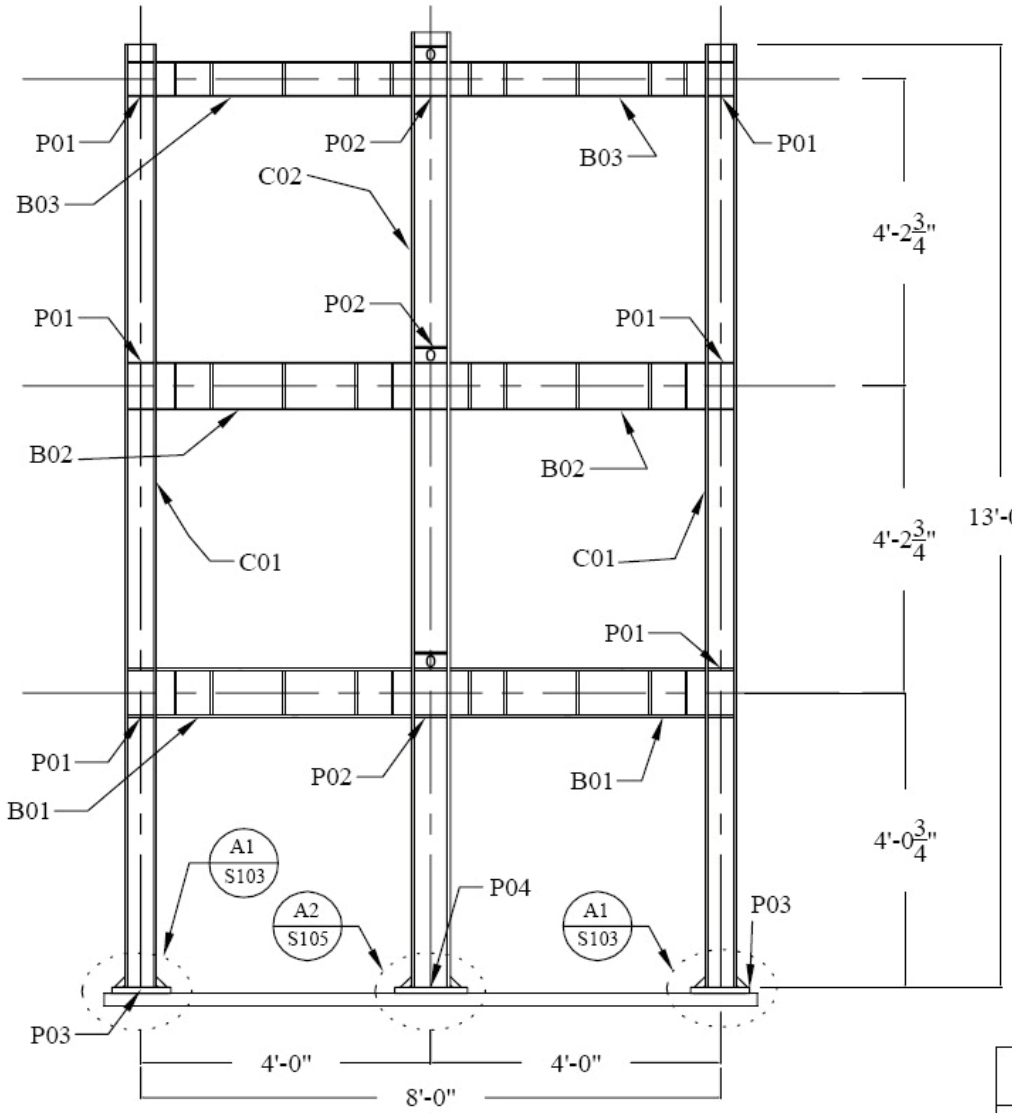

General Note:

1.All steels are ASTM A572 Grade 50 unless specified.

2.All weld material shall be E70 Electrode unless specified.

Part Code	Part Description	QTY
C01	Exterior Column, 13-ft length W5x19	2
C02	Interior Column, 13-ft 2-in length W6x25	1
B01	Beam in 1st floor, 3ft 6 1/4 in W8x13	2
B02	Beam in 2nd floor, 3ft 6 1/4 in W8x10	2
B03	Beam in 3rd floor, 3ft 6 1/4 in W6x8.5	2
P01	3/8 in thick Continuity Plate 4 9/32 x 2 3/8 in	24
P02	3/8 in thick Continuity Plate 5 15/32 x 2 7/8 in	12
P03	1 in thick Exterior Base Plate 12 x 9 3/4	2
P04	1 in thick Interior Base Plate 12 x 12	1

University at Buffalo			DWG. NO. S101
PROJECT: Shake Table Test	CONTENT: SMRF Model		
BY: DONG WANG	DATE: 9/25/06	REV. NO. 1	SCALE:

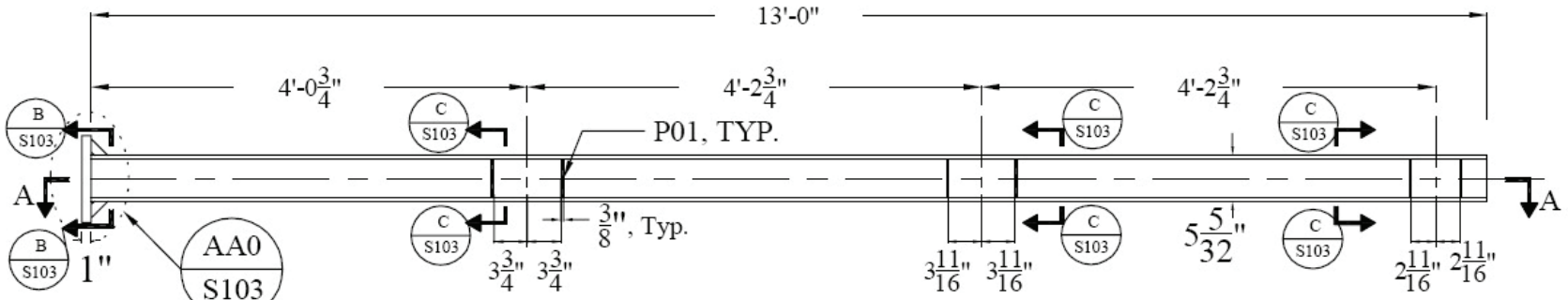

C01 W5x19 Exterior Column (DWG S101 C01)

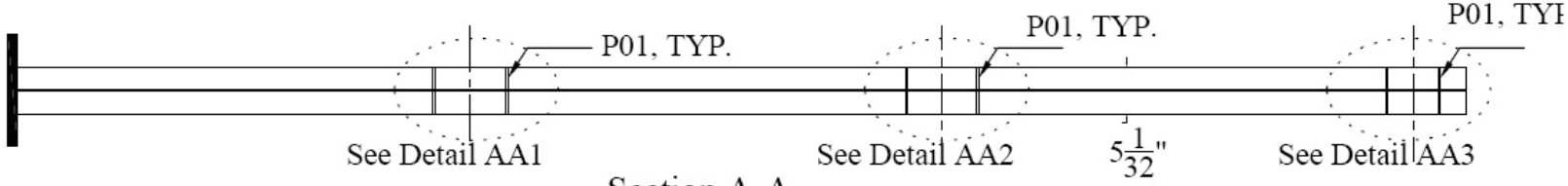

Section A-A

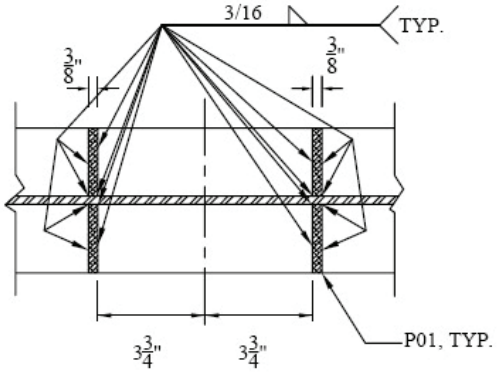

Detail AA1

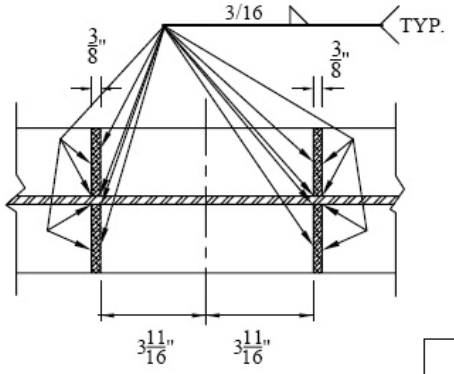

Detail AA2

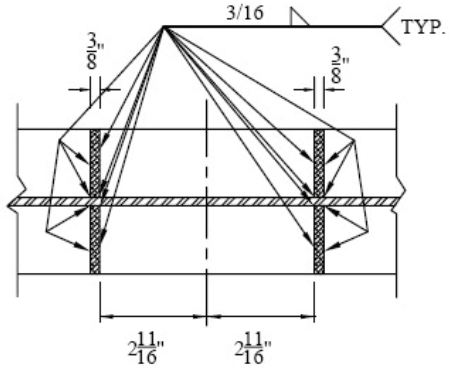

Detail AA3

University at Buffalo			DWG. NO. S102
PROJECT: Shake Table Test	CONTENT: C01 W5x19 Exterior Column		
BY: DONG WANG	DATE: 9/25/06	REV. NO. 1	SCALE:

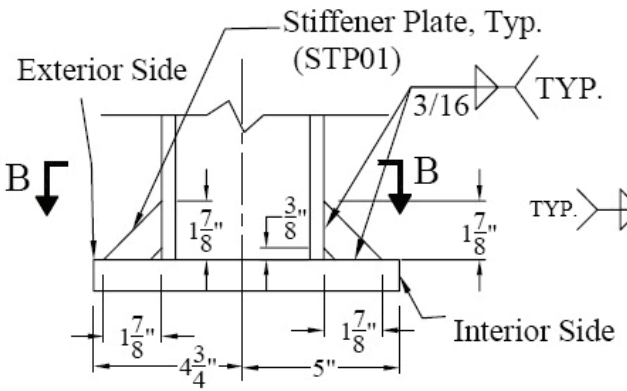

Detail AA0 in DWG S102
(Exterior Column w5x19 base connection with stiffener plates)

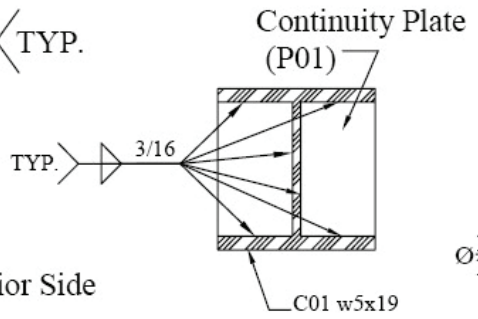

DWG S102 Section C-C

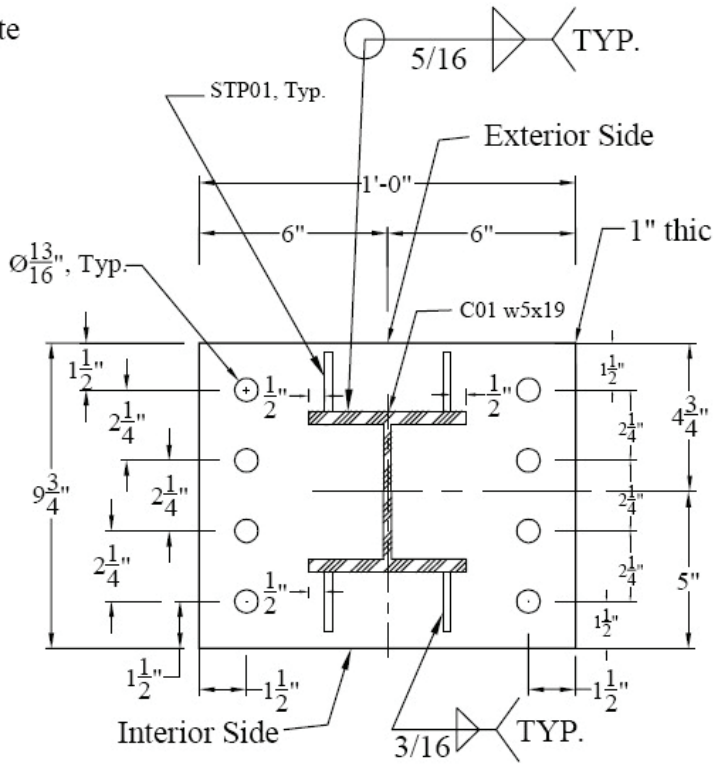

Section B-B Base Connection
(DWG S102 Section B-B,
DWG S101 Detail A1)

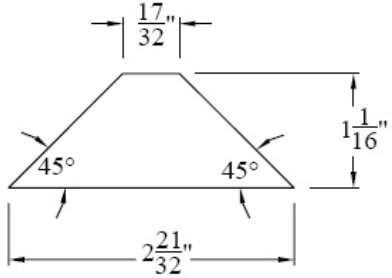

Plate Thk. = 3/8"

STP01 Stiffener Plate
(Total 12 pc. Each base-column connetion has 4 pc.)

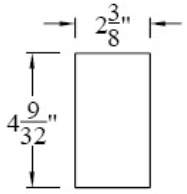

Plate Thk. = 3/8"

P01 Continuity Plate
(DWG S101 & S102 P01)

University at Buffalo			DWG. NO. S103
PROJECT: Shake Table Test	CONTENT: Detail AA0, Section B-B and C-C in DWG S102		
BY: DONG WANG	DATE: 10/29/06	REV. NO. 1	SCALE:

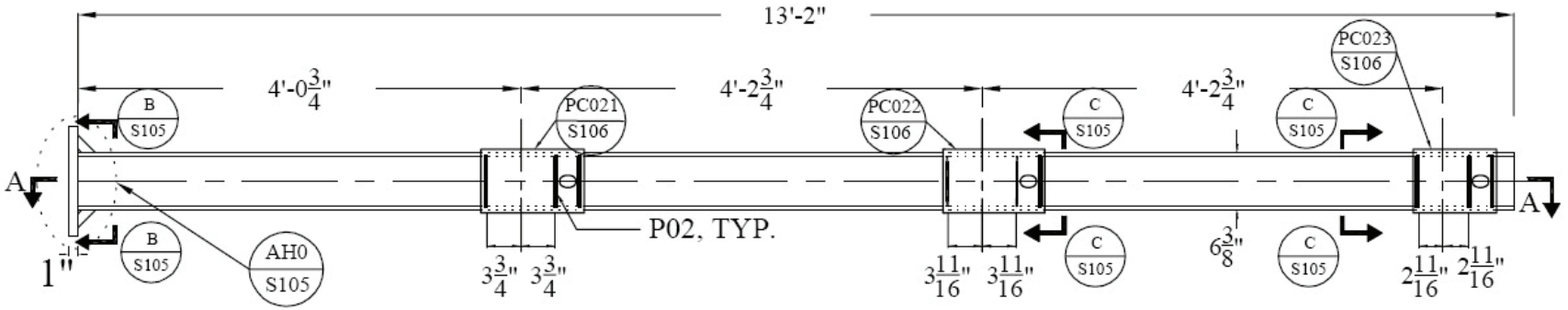

C02 W6x25 Interior Column (DWG S101 C02)

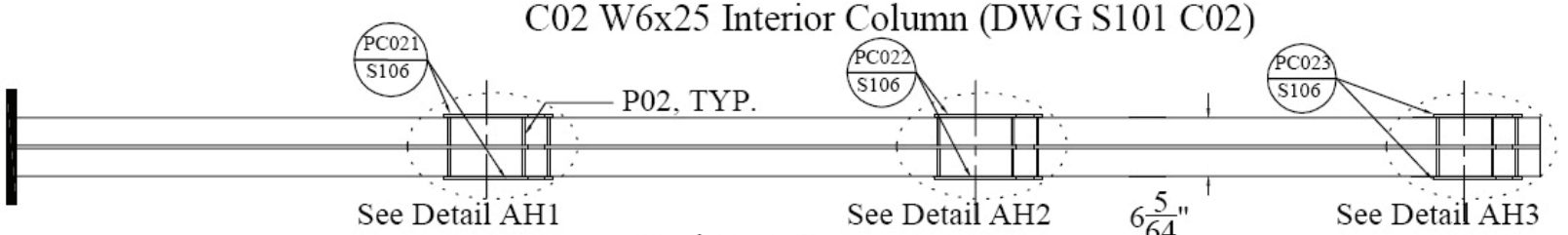

Section A-A

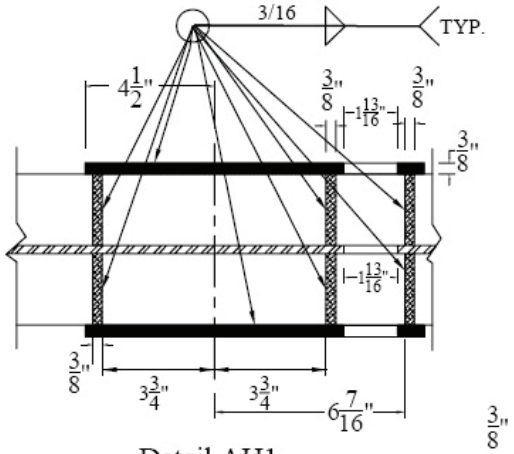

Detail AH1

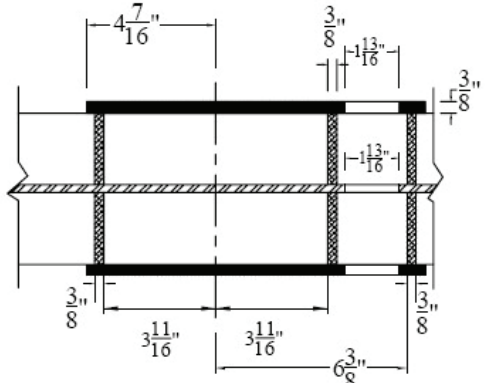

Detail AH2
(All weldings are identical to Detail AH1)

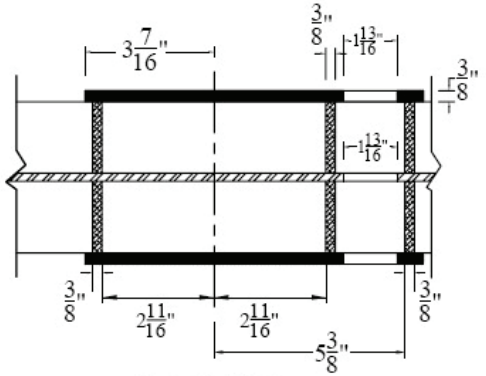

Detail AH3
(All weldings are identical to Detail AH1)

University at Buffalo			DWG. NO. S104
PROJECT: Shake Table Test	CONTENT: C02 W6x25 Interior Column		
BY: DONG WANG	DATE: 10/29/06	REV. NO. 1	SCALE:

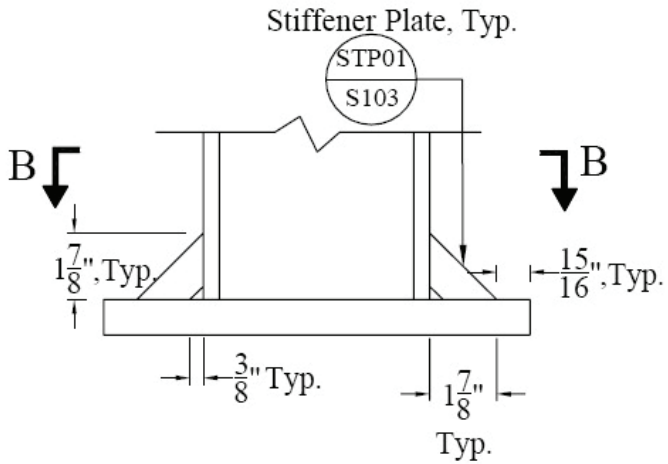

Detail AH0 in DWG S104
(Interior Column w6x25 base connection with stiffener plates)

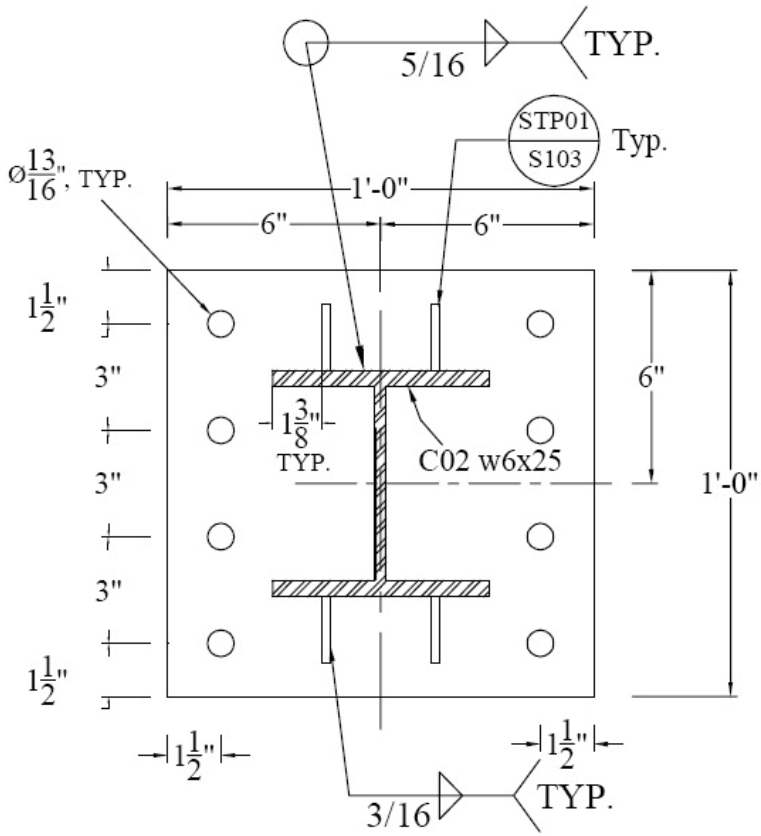

Section B-B Base Plate
(DWG S104 Section B-B,
DWG S101 Detail A2)

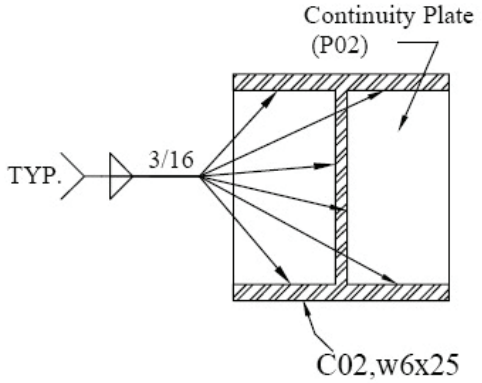

DWG S104 Section C-C

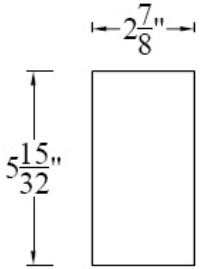

Plate Thk. = 3/8"

P02 Continuity Plate
(DWG S101 & S104 P02)

University at Buffalo			DWG. NO. S105
PROJECT: Shake Table Test	CONTENT: Detail AH0, Section B-B and C-C in DWG S104		
BY: DONG WANG	DATE: 10/29/06	REV. NO. 1	SCALE:

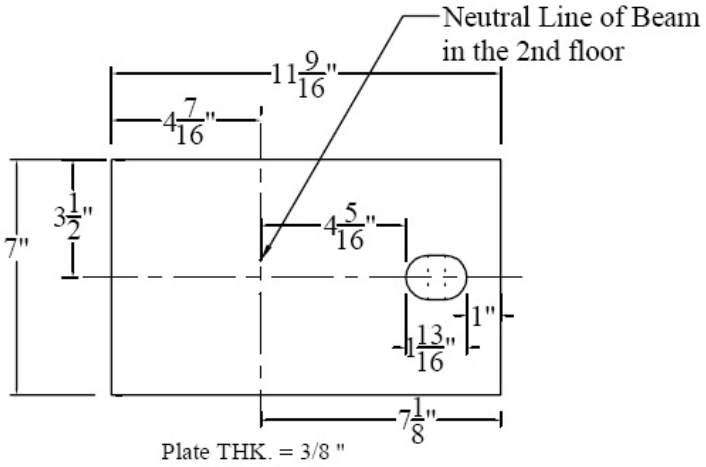

Plate THK. = 3/8 "

PC022 Web Reinforcing Plate (2pc)
(DWG S104 PC022)

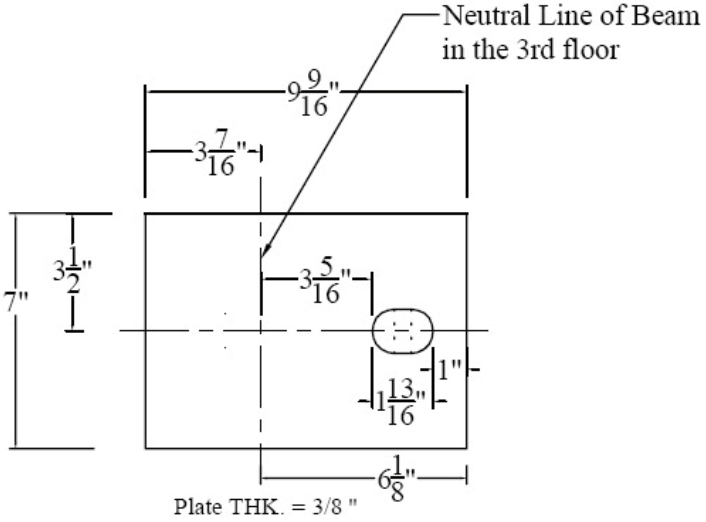

Plate THK. = 3/8 "

PC023 Web Reinforcing Plate (2pc)
(DWG S104 PC023)

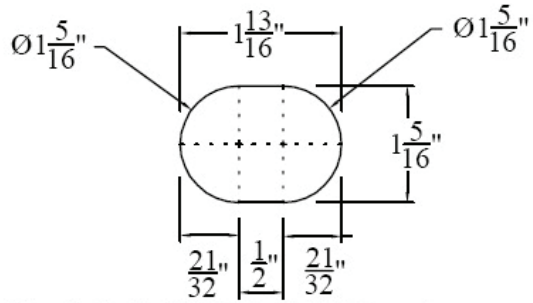

The hole in PC021, PC022 and PC023.

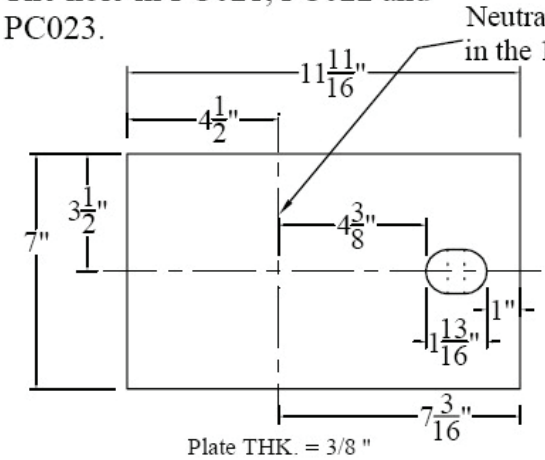

Plate THK. = 3/8 "

PC021 Web Reinforcing Plate (2pc)
(DWG S104 PC021.)

Note:The corresponding part of column (C02) web should be machined with the same holes as shown in these plates.

University at Buffalo			DWG. NO. S106
PROJECT: Shake Table Test	CONTENT: Plate PC021, PC022 and PC023 in DWG S104.		
BY: DONG WANG	DATE: 9/25/06	REV. NO. 1	SCALE:

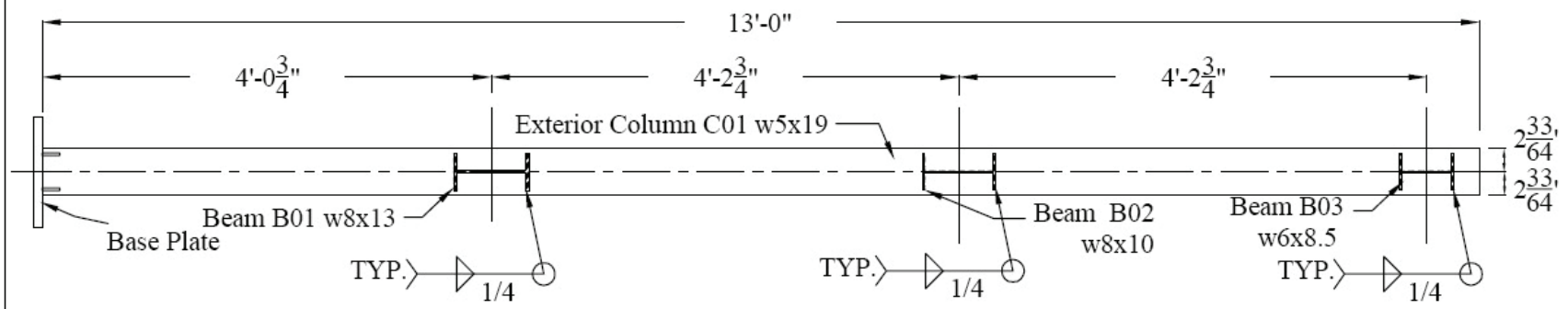

Exterior Beam-Column Connetions

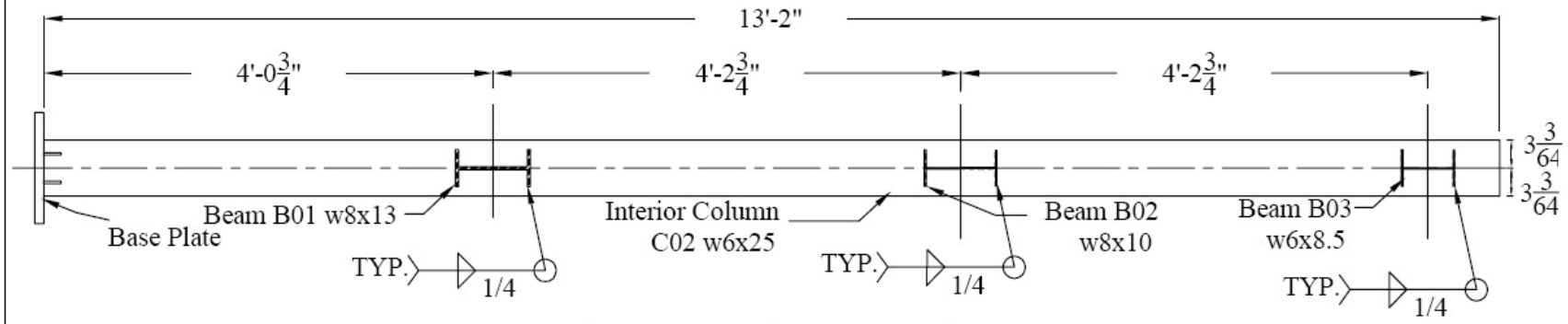

Interior Beam-Column Connetions

University at Buffalo			DWG. NO. S107
PROJECT: Shake Table Test	CONTENT: Beam-Column Connections		
BY: DONG WANG	DATE: 10/29/06	REV. NO. 2	SCALE:

Beams

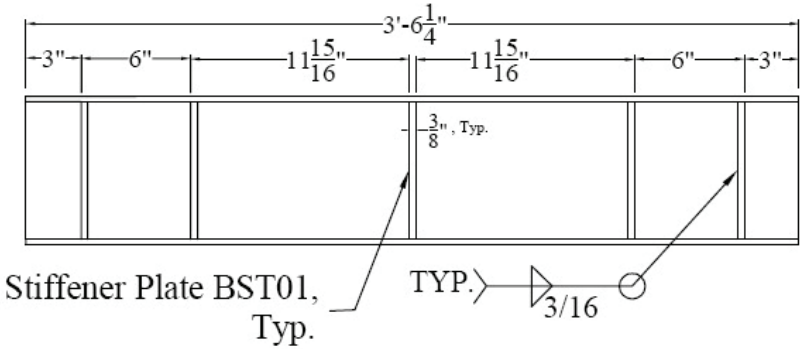

DWG S101 B01 w8x13 (2pc)

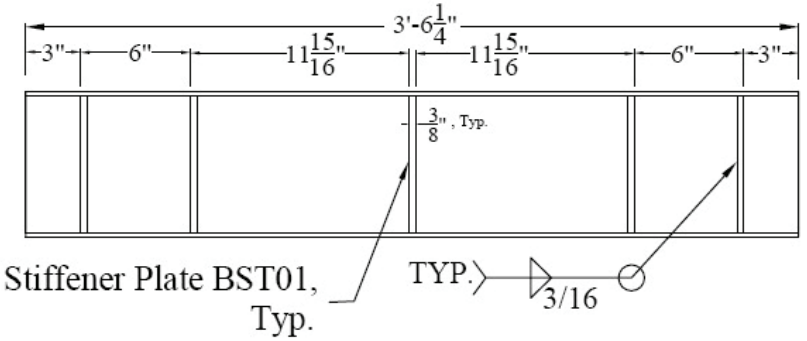

DWG S101 B02 w8x10 (2pc)

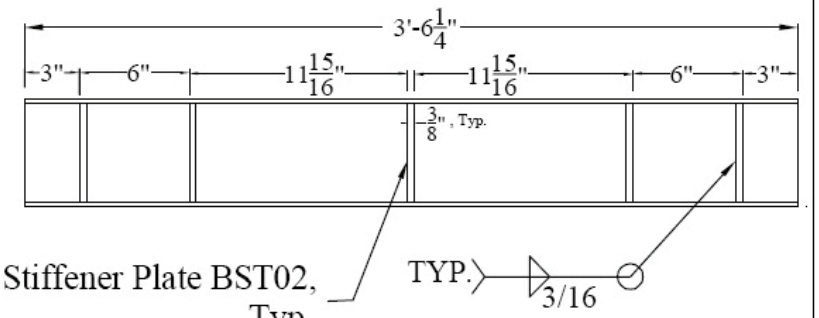

DWG S101 B03 w6x8.5 (2 pc)

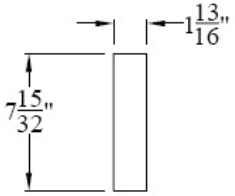

3/8" Thk.
Stiffener Plate BST01
(Total 40 pc, all are welded to the beams in the 1st and 2nd floor.)

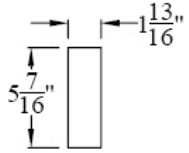

3/8" Thk.
Stiffener Plate BST02
(Total 20 pc, all are welded to the beams in the 3rd floor.)

University at Buffalo			DWG. NO. S108
PROJECT: Shake Table Test	CONTENT: Beams		
BY: DONG WANG	DATE: 10/29/06	REV. NO. 1	SCALE:

Appendix D Model of Self-Centering Post-Tensioned Frame for Shake Table Testing

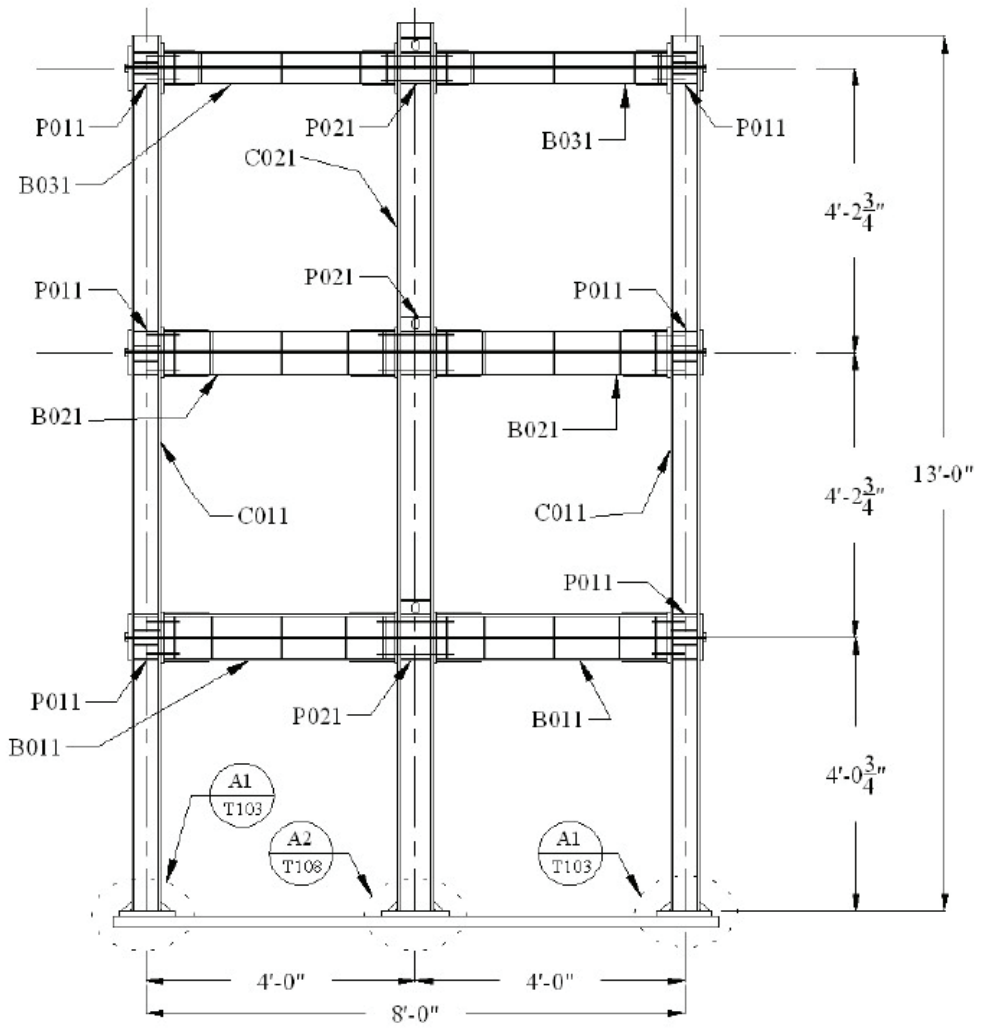

PTED FRAME MODEL

General Note:

1. **All steels are ASTM A572 Grade 50 unless specified.**
2. **All weld material shall be E70 Electrode unless specified.**
3. **Do not weld beams to columns in this SCPT model**

Part Code	Part Description	QTY
C011	Exterior Column, 13-ft length W5x19	2
C021	Interior Column, 13ft 2in length W6x25	1
B011	Beam in 1st floor, 3ft 5 1/2 in W8x13	2
B021	Beam in 2nd floor, 3ft 5 1/2 in W8x10	2
B031	Beam in 3rd floor, 3ft 5 1/2 in W6x8.5	2
P011	3/8 in. thick Continuity Plate 4 9/32 x 2 3/8 in.	48
P021	3/8 in. thick Continuity Plate 5 15/32 x 2 7/8 in.	18

University at Buffalo			DWG. NO.
PROJECT: Shake Table Test	CONTENT: **PTED FRAME MODEL**		T101
BY: **Dong Wang**	REV. NO.: 1	Date: 9/25/2006	SCALE

Please note that plate CR1, CR2 and CR3 are in the exterior side of the column and plates CT1, CT2 and CT3 are in the interior side of the column.

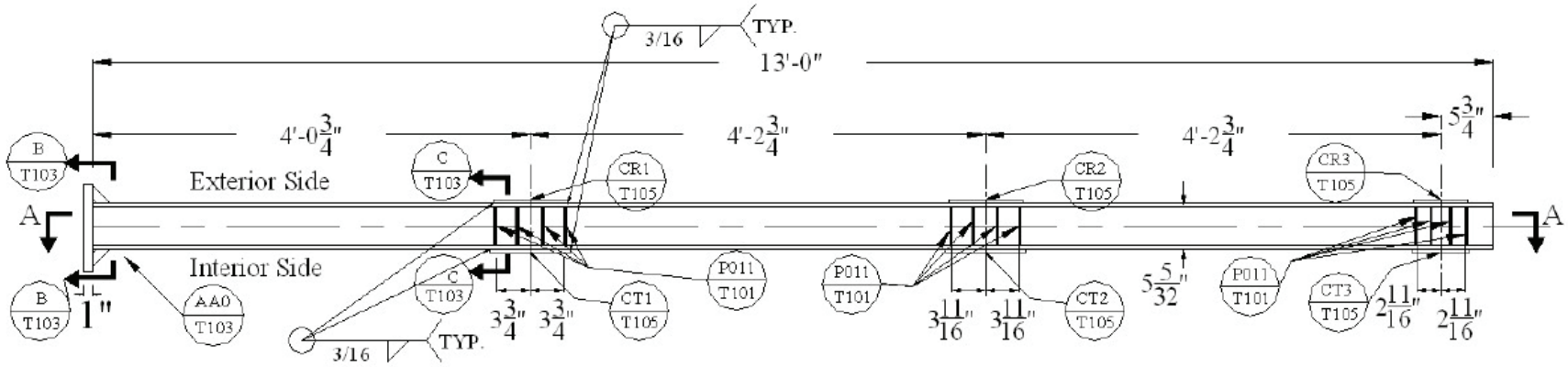

C011 W5x19 Eterior Column (DWG T101 C011)

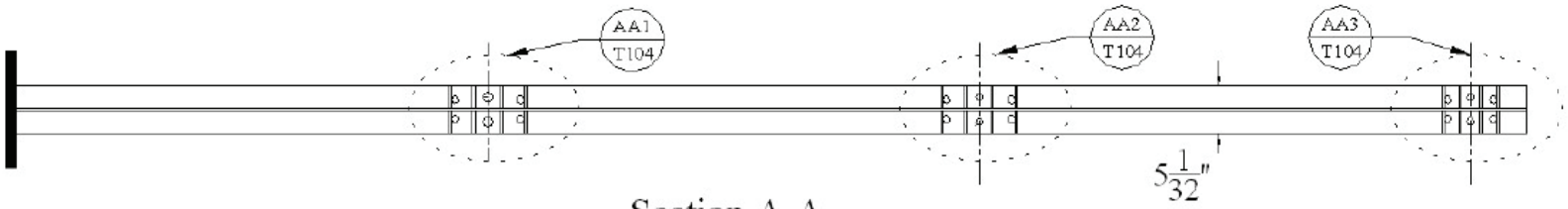

Section A-A

University at Buffalo			DWG. NO.
PROJECT Shake Table Test	CONTENT **C011 W5x19 Exterior Column**		T102
BY: **Dong Wang**	REV. NO. 1	Date 9/25/2006	SCALE

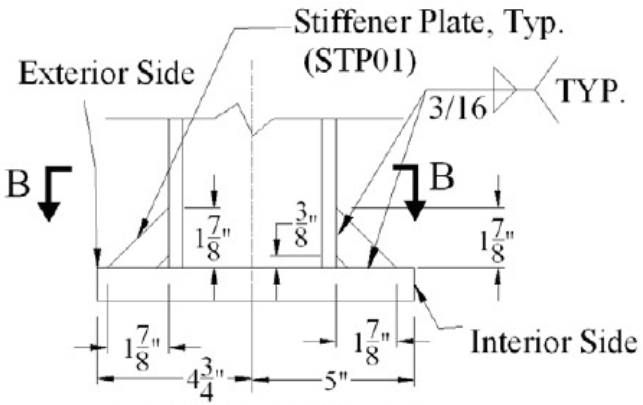

Detail AA0 in DWG T102
(Exterior Column w5x19 base connection with stiffener plates)

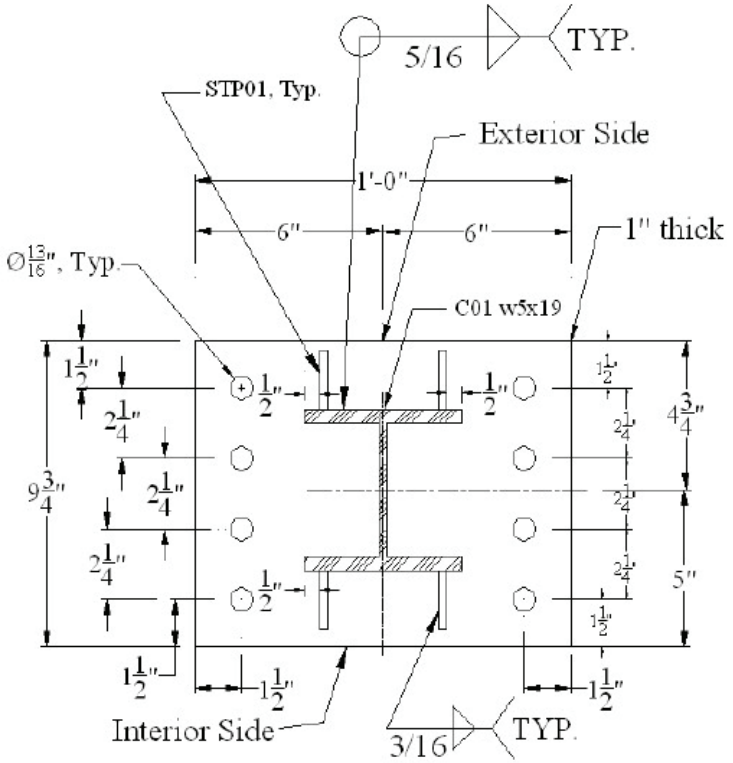

Section B-B Base Connection
(DWG T102 Section B-B,
DWG T101 Detail A1)

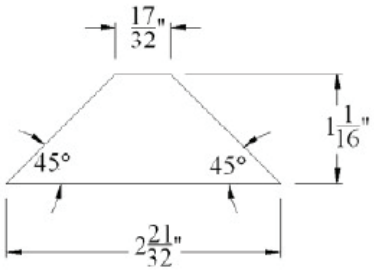

Plate Thk. = 3/8"

STP01 Stiffener Plate
(Total 12 pc. Each base-column connetion has 4 pc.)

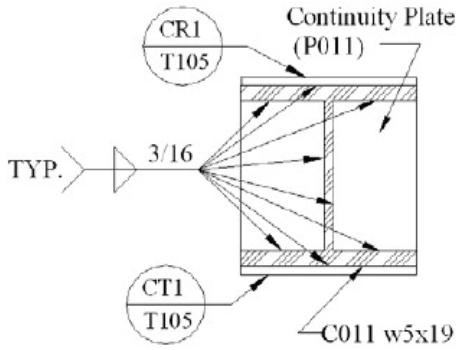

DWG T102 Section C-C

University at Buffalo			DWG. NO.
PROJECT Shake Table Test	CONTENT **Section B-B,C-C in DWG T102**		T103
BY: **Dong Wang**	REV. NO. 1	Date 10/29/2006	SCALE

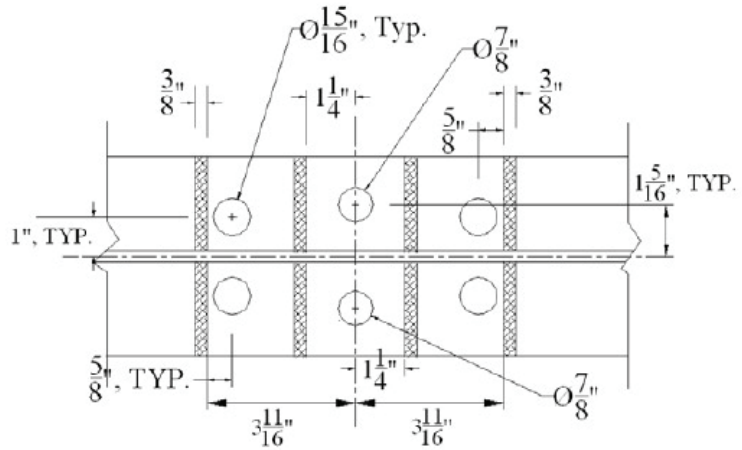

DWG T102 Detail AA2
(All welds are identical to those of Detail AA1.)

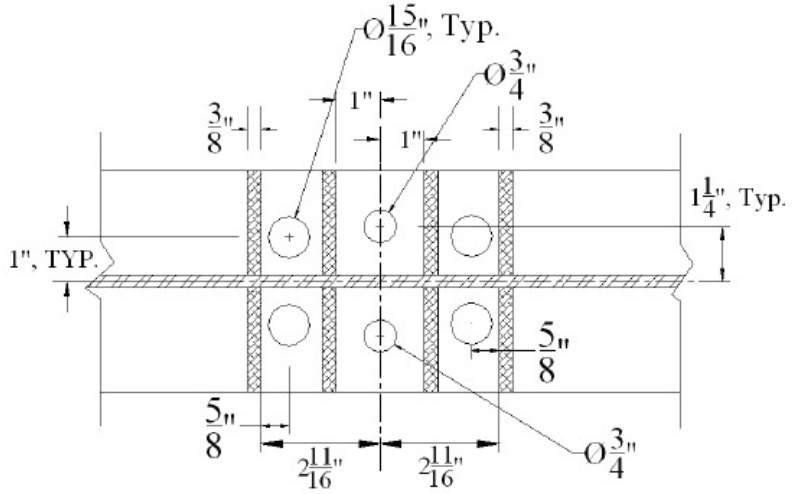

DWG T102 Detail AA3
(All welds are identical to those of Detail AA1.)

Note: Do not weld the area near between the continuity plates (shade parts) and holes.

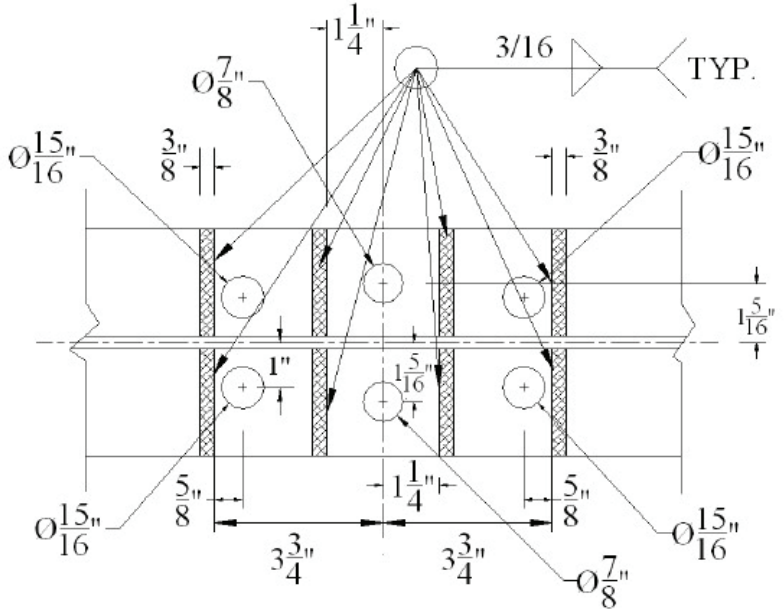

DWG T102 Detail AA1

University at Buffalo			DWG. NO.
PROJECT Shake Table Test	CONTENT **Details AA1-3 in DWG T102**		T104
BY: **Dong Wang**	REV. NO. 1	Date 9/25/2006	SCALE

Note: All materials in this figure are made from ASTM A514 with Fy=100kis.

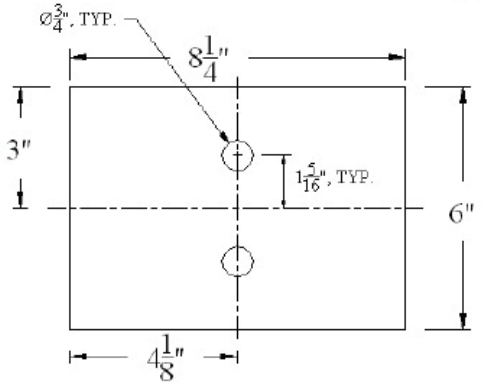

Plate Thk.=1/2"

CR1 Reinforcing Plate (2pc)

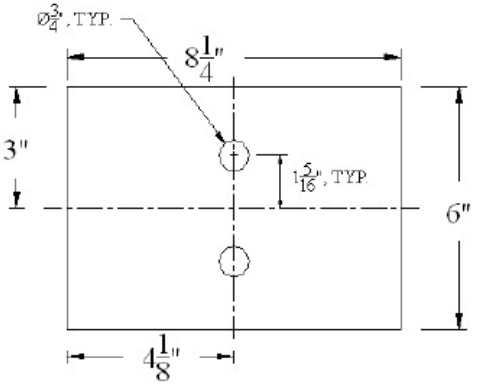

Plate Thk.=1/2"

CR2 Reinforcing Plate (2pc)

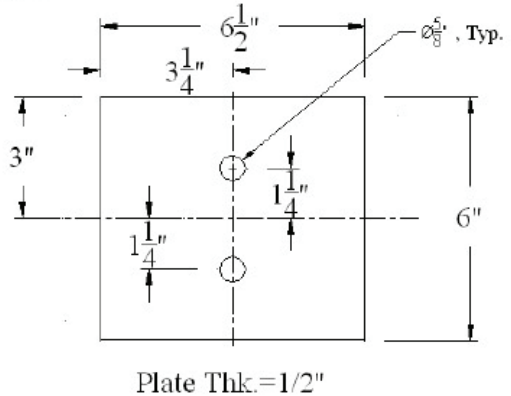

Plate Thk.=1/2"

CR3 Reinforcing Plate (2pc)

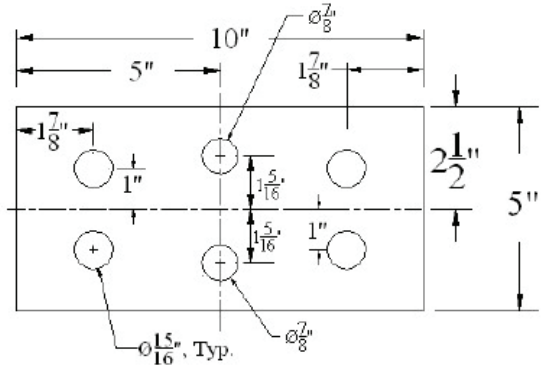

Plate Thk.=3/8"

CT1 Contact Plate (4pc)

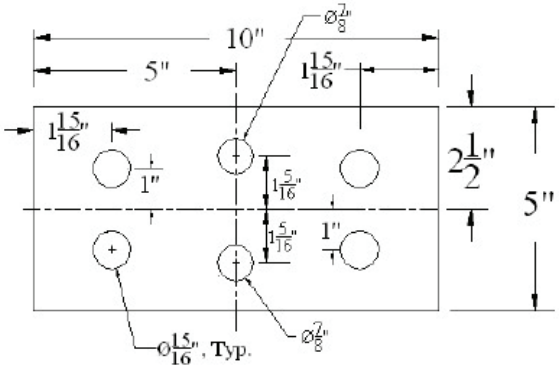

Plate Thk.=3/8"

CT2 Contact Plate (4pc)

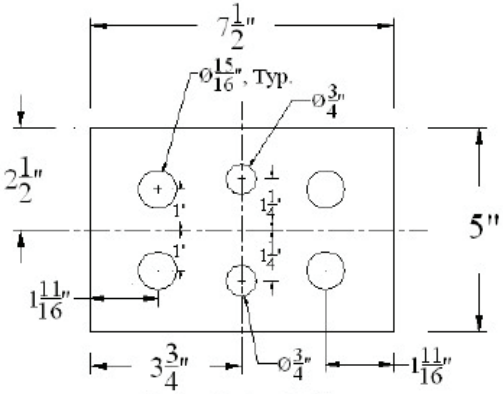

Plate Thk.=3/8"

CT3 Contact Plate (4pc)

Note: The corresponding part of columns (C011 & C021) flanges should be machined with the same holes as shown in these plates.

University at Buffalo			DWG. NO.
PROJECT Shake Table Test	CONTENT **Plates in DWG T102**		T105
BY: **Dong Wang**	REV. NO. 1	Date 10/11/2006	SCALE

Note: As shown in the figure of C021 interior column, the contact plate CT1, CT2 and CT3 are between the end of beam and column flange and welded (3/16'' welding) by 4 sides to the flange of the column. The contact plates are perpendicular to the web reinforcing plates (PC021, 022 and 023).

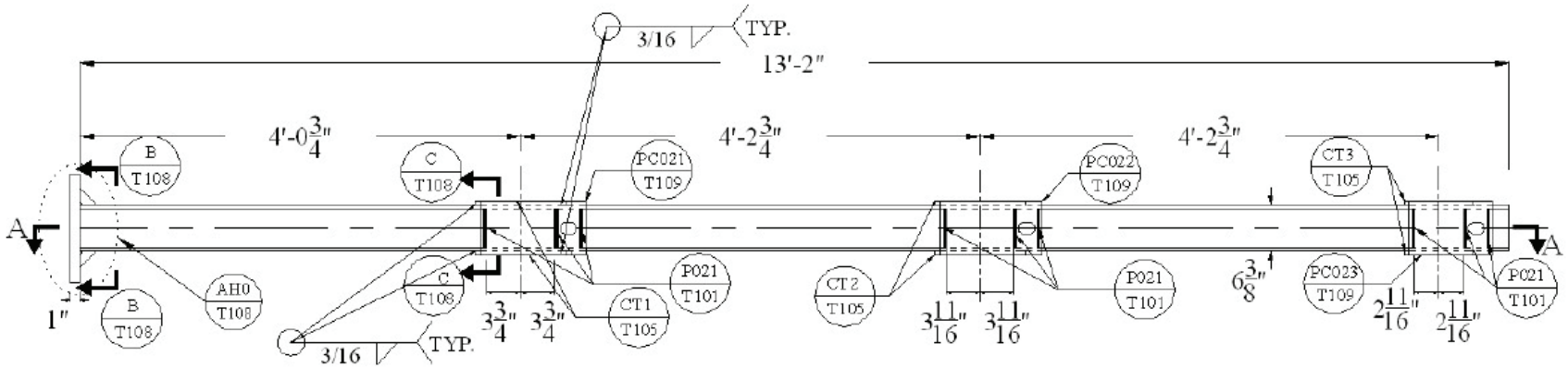

C021 W6x25 Interior Column (DWG T101 C021)

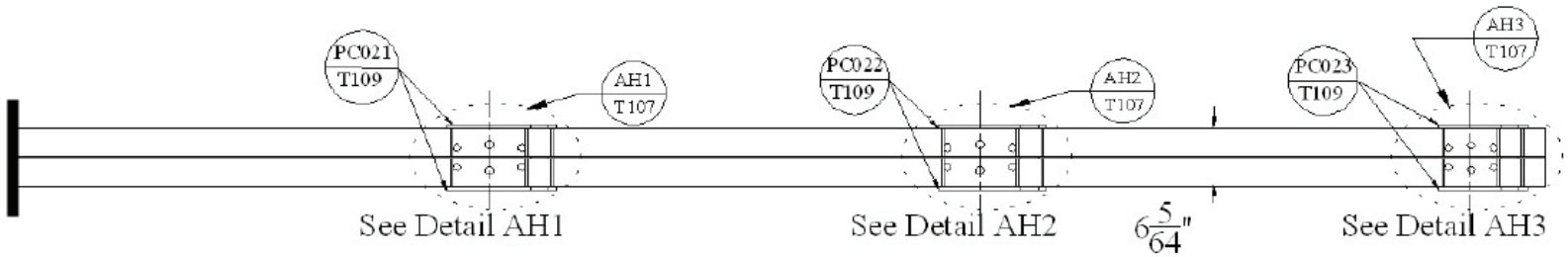

Section A-A

University at Buffalo			DWG. NO.
PROJECT Shake Table Test	CONTENT **C021 Interior Column w6x25**		T106
BY: **Dong Wang**	REV. NO. 2	Date 9/5/2006	SCALE

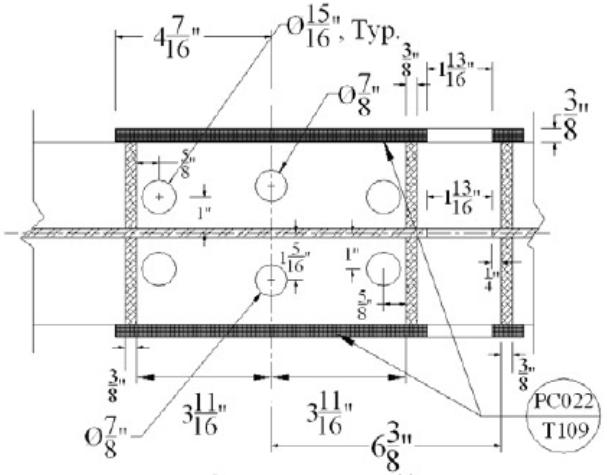

DWG T106 Detail AH2
(All weldings are identical to Detail AH1)

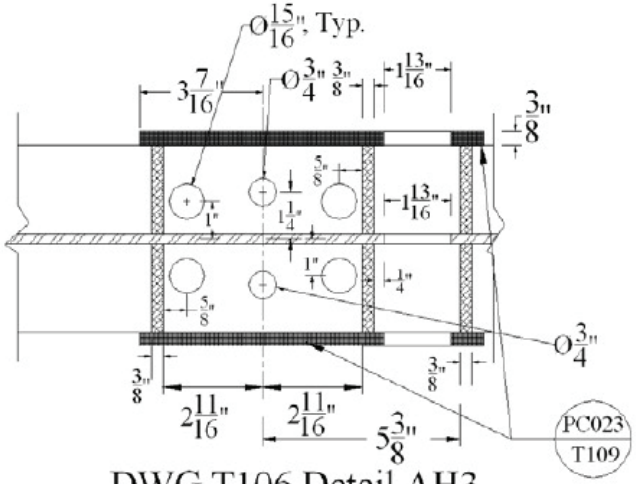

DWG T106 Detail AH3
(All weldings are identical to Detail AH1)

Note: Do not weld the area near between the continuity plates (shade parts) and holes.

Do not weld the plates PC021, PC022 and PC023, just manufacture these plates as shown in DWG 109.

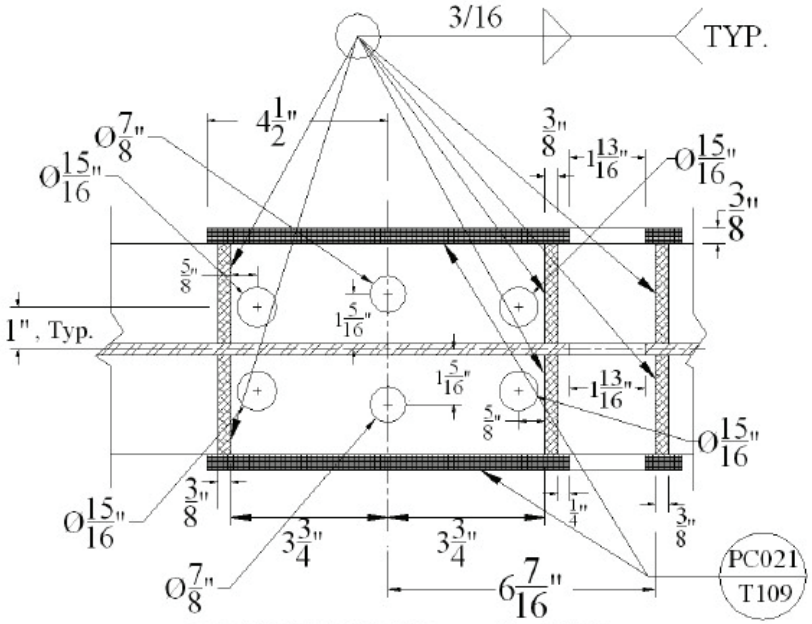

DWG T106 Detail AH1

University at Buffalo			DWG. NO.
PROJECT Shake Table Test	CONTENT **Details AH1,2, 3 in DWG T106**		T107
BY: **Dong Wang**	REV. NO. 1	Date 10/29/2006	SCALE

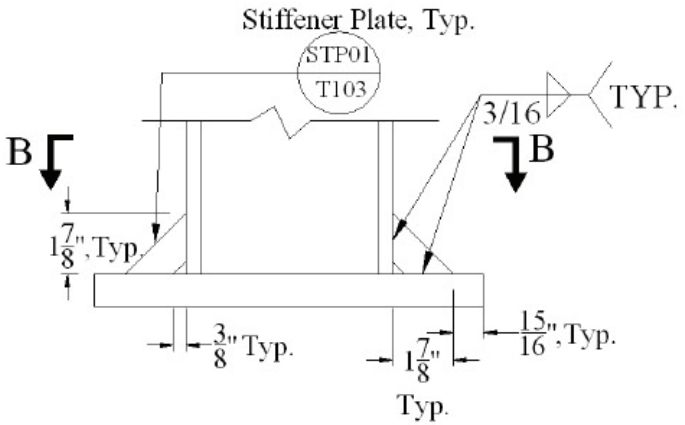

Detail AH0 in DWG T106
(Interior Column w6x25 base
connection with stiffener plates)

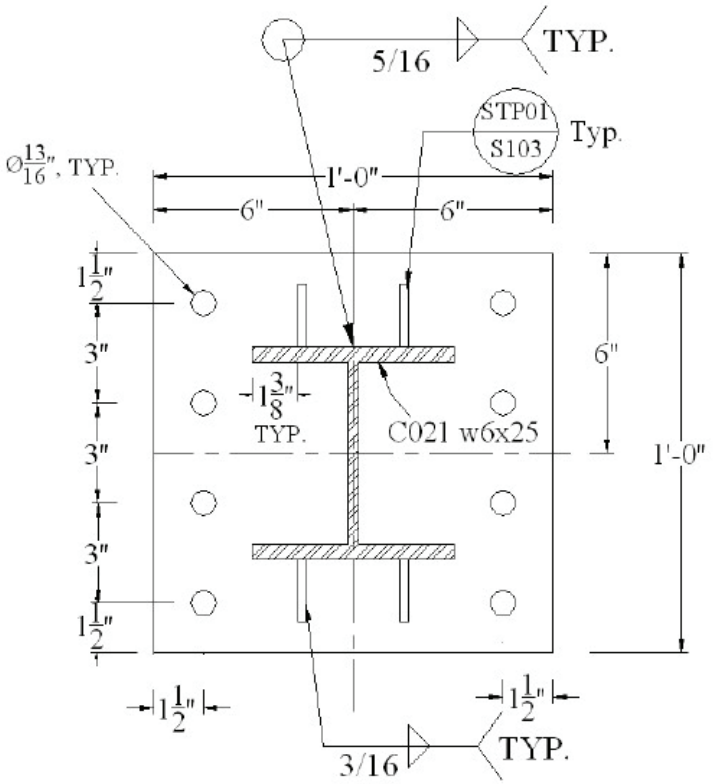

Section B-B Base Connection
(DWG T106 section B-B,
DWG T101 Detail A2)

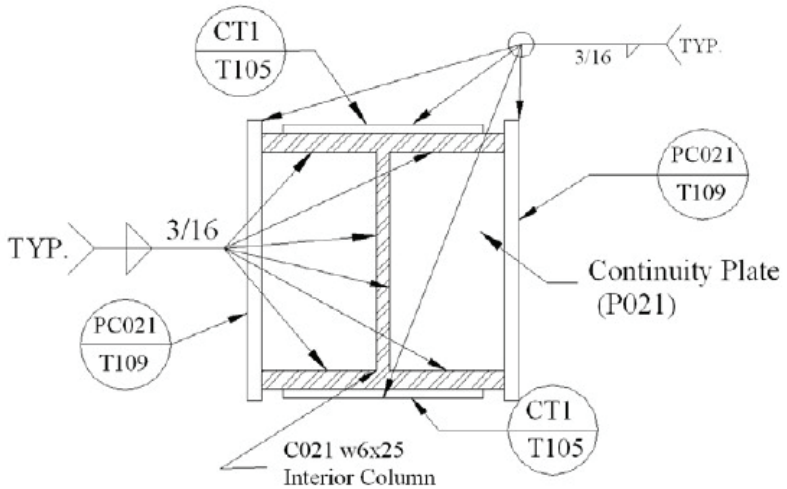

DWG T106 Section C-C

University at Buffalo			DWG. NO.
PROJECT Shake Table Test	CONTENT **Section B-B,C-C in DWG T106**		T108
BY: **Dong Wang**	REV. NO. 2	Date 10/29/2006	SCALE

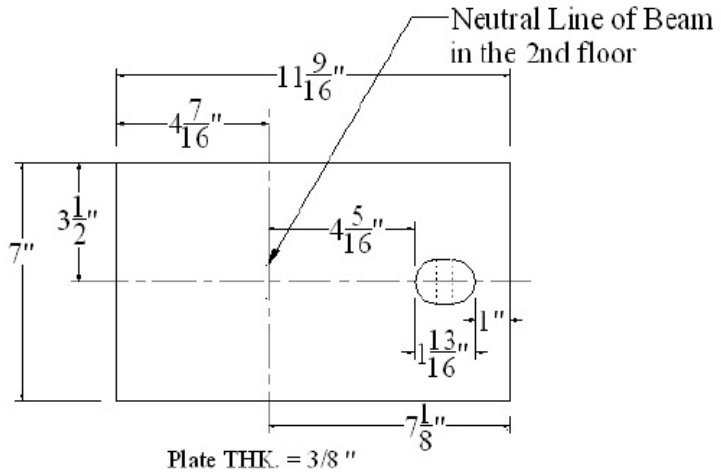

DWG T106 PC022 Web Reinforcing Plate (2pc.)

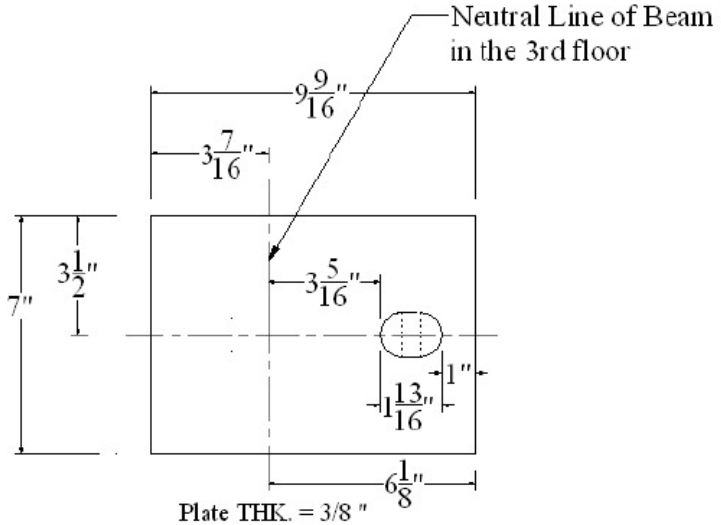

DWG T106 PC023 Web Reinforcing Plate (2pc.)

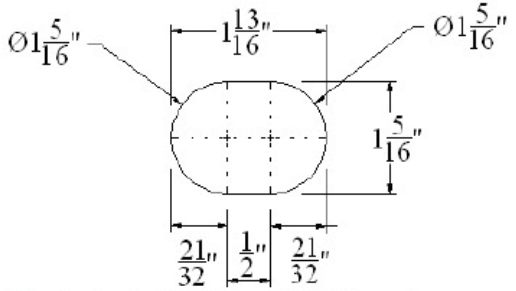

The hole in PC021, PC022 and PC023.

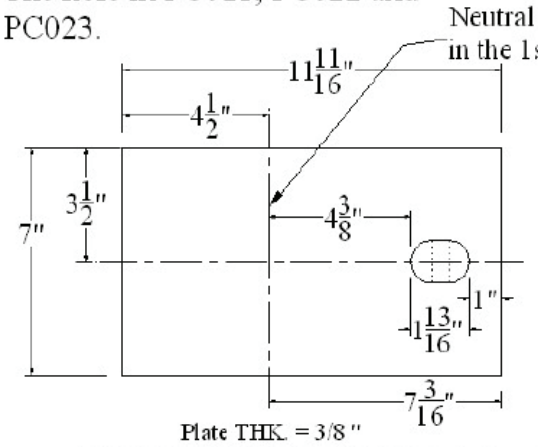

DWG T106 PC021 Web Reinforcing Plate (2pc.)

Note:The corresponding part of column (C021) web should be machined with the same holes as shown in these plates.

University at Buffalo			DWG. NO.
PROJECT Shake Table Test	CONTENT **Web Reinforcing Plates**		T109
BY: **Dong Wang**	REV. NO. 1	Date 9/25/2006	SCALE

Beams

Note: For the Reinforcing Plates (R-plates, A514, Fy =100ksi) on the top of beam flanges, only 3-side welding around plates is necessary and do not weld these plates on the 4th side at the both ends of

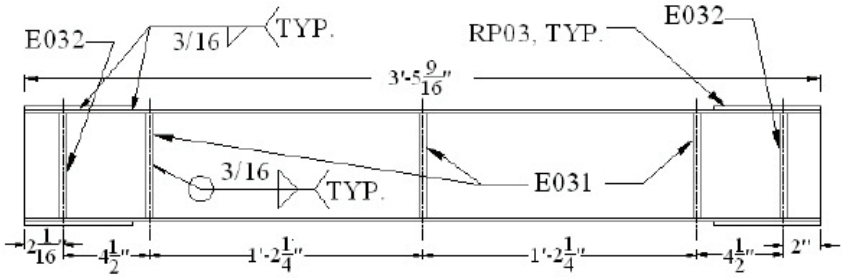

DWG T101 B031 w6x8.5 (2 pc)

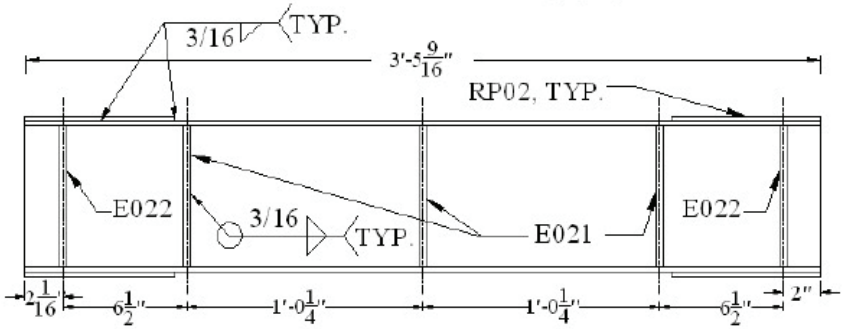

DWG T101 B021 w8x10 (2pc)

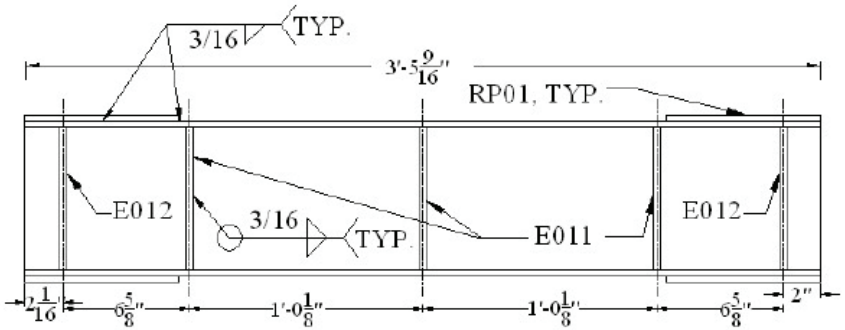

DWG T101 B011 w8x13 (2pc)

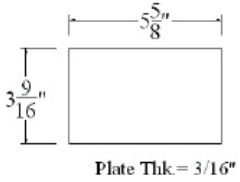

Plate Thk.= 3/16"

RP03 R-Plate (8pc.)

Note: RP03 Plates use ASTM A514 with 100 ksi.

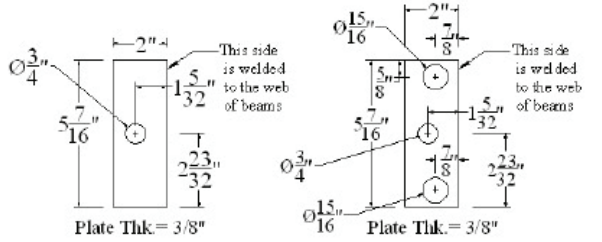

Plate Thk.= 3/8"

E031 Stiffener Plate (12pc.)

Plate Thk.= 3/8"

E032 Stiffener Plate (8pc.)

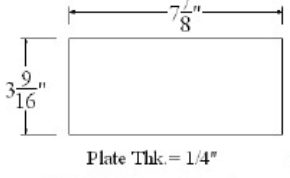

Plate Thk.= 1/4"

RP02 R-Plate (8pc.)

Note: RP02 Plates use ASTM A514 with 100 ksi.

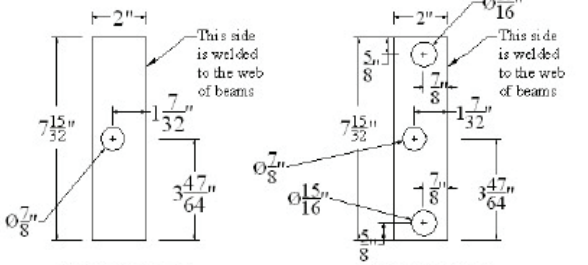

Plate Thk.= 3/8"

E021 Stiffener Plate (8pc.)

Plate Thk.= 3/8"

E022 Stiffener Plate (8pc.)

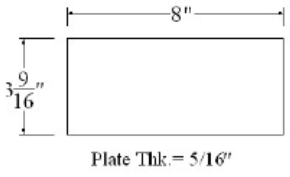

Plate Thk.= 5/16"

RP01 R-Plate (8pc.)

Note: RP01 Plates use ASTM A514 with 100 ksi.

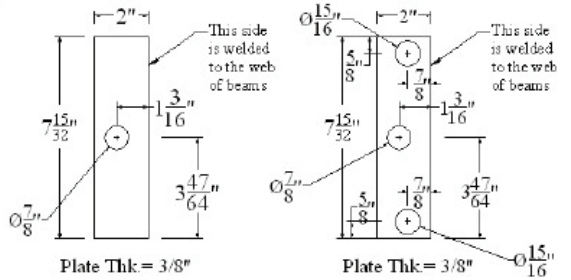

Plate Thk.= 3/8"

E011 Stiffener Plate (8pc.)

Plate Thk.= 3/8"

E012 Stiffener Plate (8pc.)

University at Buffalo			DWG. NO.
PROJECT Shake Table Test	CONTENT **Beams**		T110
BY: **Dong Wang**	REV. NO. 1	Date 11/07/2006	SCALE

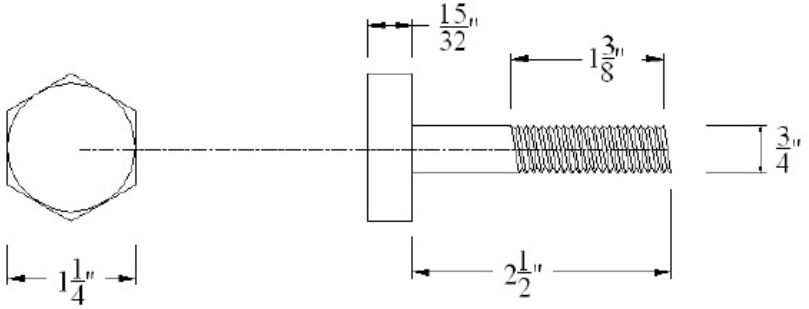

Headed Anchor Bolts (ASTM A325 Ø$\frac{3}{4}$, total 24 pc.)

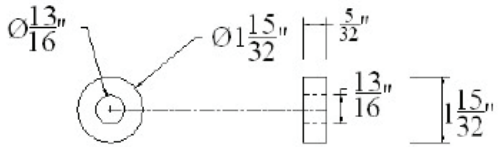

Washer for Headed Anchor Bolts (total 24 pc.)

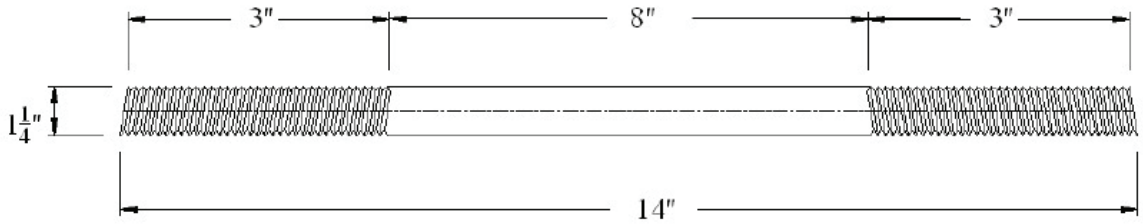

Threaded Rods(ASTM A325 Ø$1\frac{1}{4}$, total 3 pc.
and corresponding ASTM A563 nuts, 6pc.)

University at Buffalo			DWG. NO.
PROJECT Shake Table Test	CONTENT **Anchor Bolts and Rods**		T111
BY: **Dong Wang**	REV. NO. 1	Date 9/25/2006	SCALE

Whole View

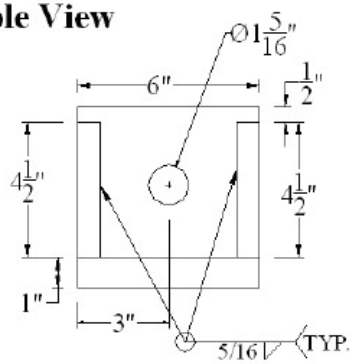

Elevation View

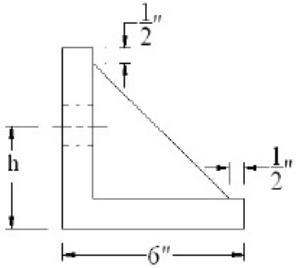

Side View
(See Part Dimension for h)

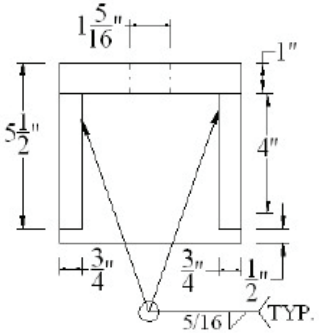

Plan View

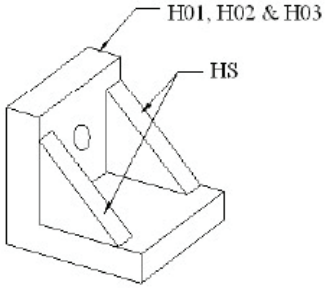

3-D View

Part Dimension

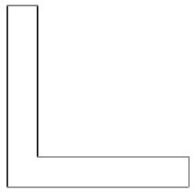

Part	h
H01	3 17/32"
H02	3 15/32"
H03	2 15/32"

6" long Angles L6x6x1
Part H01(2pc.), H02(2pc.), H03(2pc.)
total 6pc.

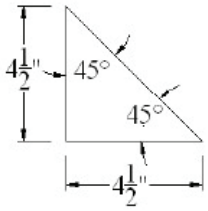

3/4" Thick Plate
Part HS (12pc.)

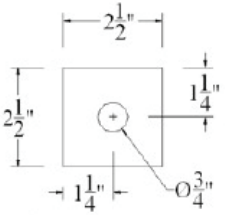

3/4" Thickness Plate

Washers for PT strands in the 1st and 2nd floor
Total 12 pieces
(ASTM A514 with Fy=100 ksi)

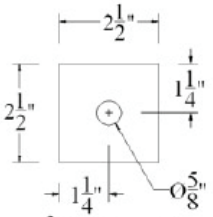

3/4" Thickness Plate

Washers for PT strands in the 3rd floor
Total 6 pieces
(ASTM A514 with Fy=100 ksi)

University at Buffalo			DWG. NO.
PROJECT Shake Table Test	CONTENT **Connections between Mass Floors and Frame**		T112
BY: **Dong Wang**	REV. NO. 1	Date 10/11/2006	SCALE

Load Cell

6 pieces of **Extra Strong** Steel Pipe (Fy = 50ksi)
Nominal Diameter: $\mathbf{1^1/_4}$"
Outside Diameter: 1.66"
Inside Diameter: 1.278"
Wall Thickness: 0.191"
Area: 0.881 in^2
Total 13.5" of steel pipe

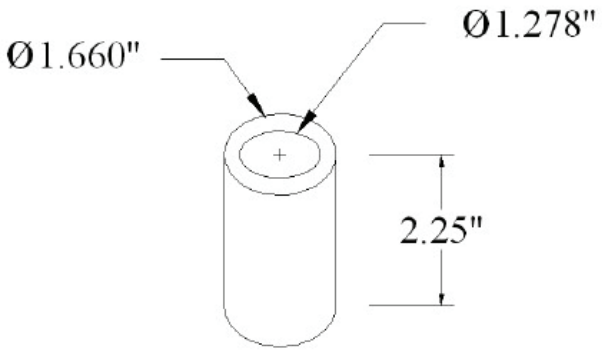

University at Buffalo			DWG. NO.
PROJECT Shake Table Test	CONTENT **Load Cell**		T113
BY: **Dong Wang**	REV. NO. 1	Date 11/1/2006	SCALE

Materials: $\frac{3}{4}$" thread bars with maximum diameter 0.86"

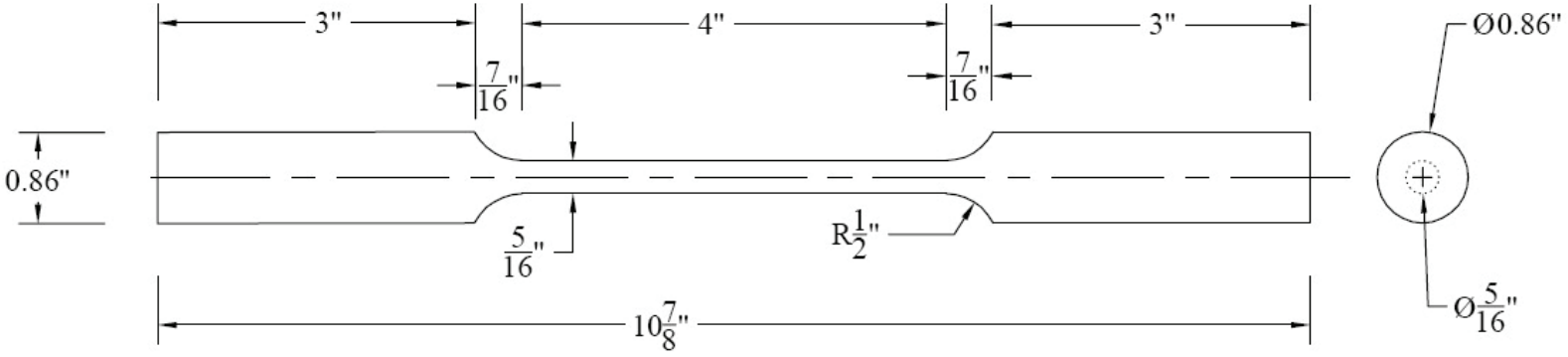

ED Bars in 1st floor (total 16 pc)

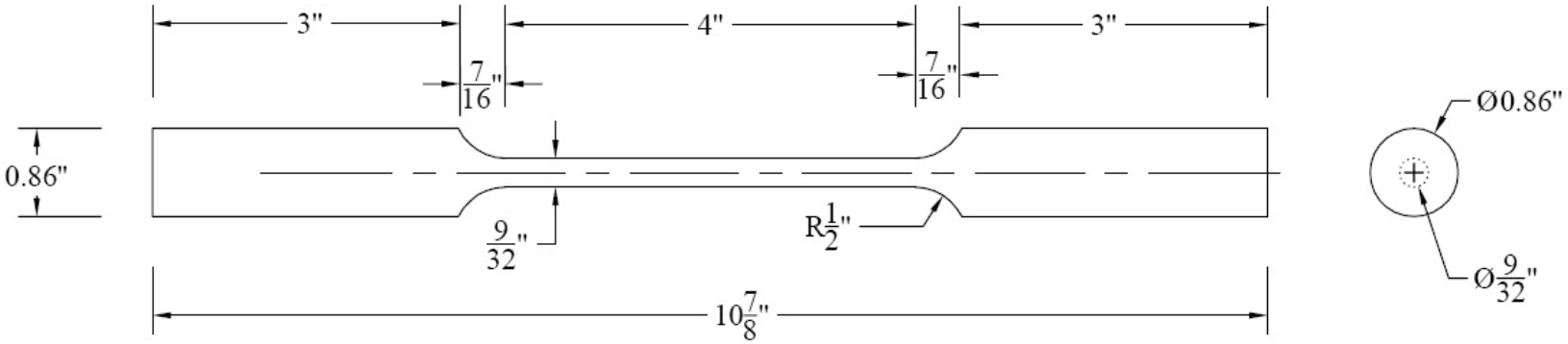

ED Bars in 2nd floor (total 16 pc)

University at Buffalo			DWG. NO. ED101
PROJECT: Shake Table Test	CONTENT: ED Bars in 1st & 2nd floor		
BY: DONG WANG	DATE: 11/14/06	REV. NO. 1	SCALE:

Materials: $\frac{3}{4}$" thread bars with maximum diameter 0.86"

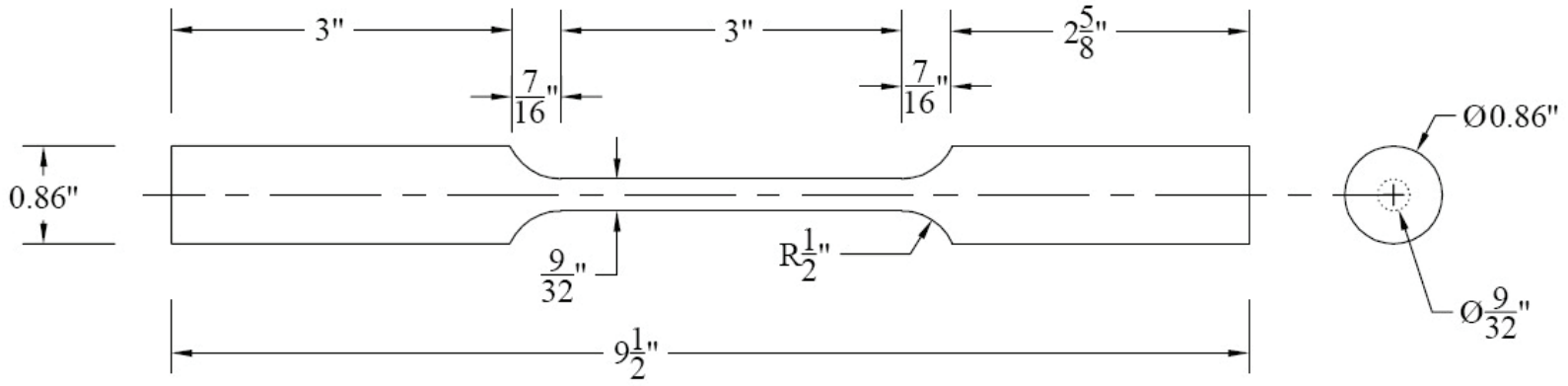

ED Bars in the 3rd floor
(total 16 pc)

University at Buffalo			DWG. NO. ED102
PROJECT: Shake Table Test	CONTENT: ED Bars in 3rd floor		
BY: DONG WANG	DATE: 11/14/06	REV. NO. 1	SCALE:

Material: 16-ft Extra Strong Pipe with Nominal Diameter $\frac{1}{2}$" (from lab)
12" x 16" Plate with $\frac{3}{8}$ " thickness

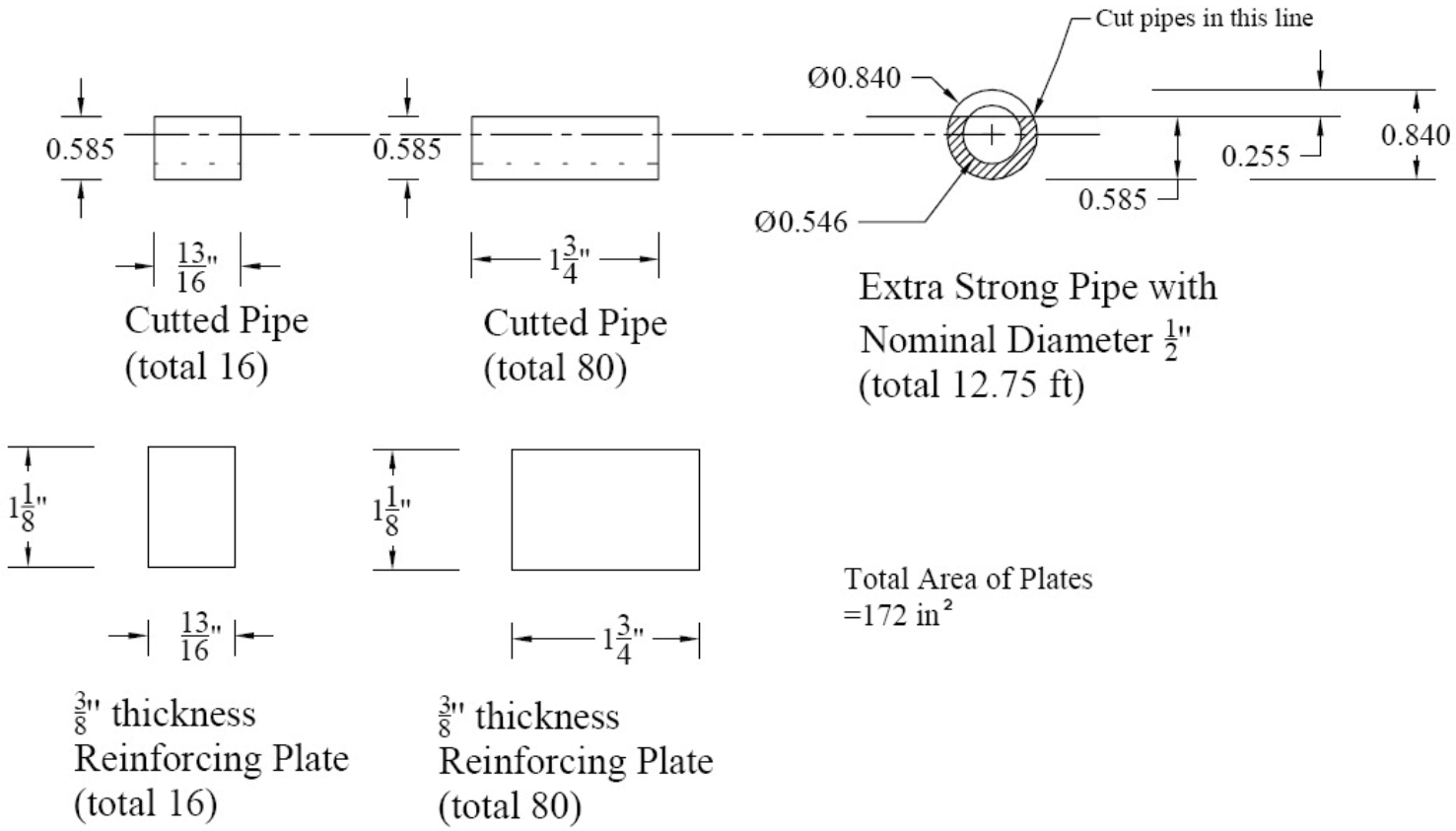

University at Buffalo			DWG. NO. ED103
PROJECT: Shake Table Test	CONTENT: Reinforcing Plates		
BY: DONG WANG	DATE: 11/12/06	REV. NO. 1	SCALE:

Appendix E Absolute Acceleration Time History of the SCPT and SMRF Models for Seismic Tests

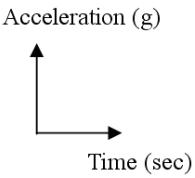

SCPT 1st floor 2nd floor 3rd floor

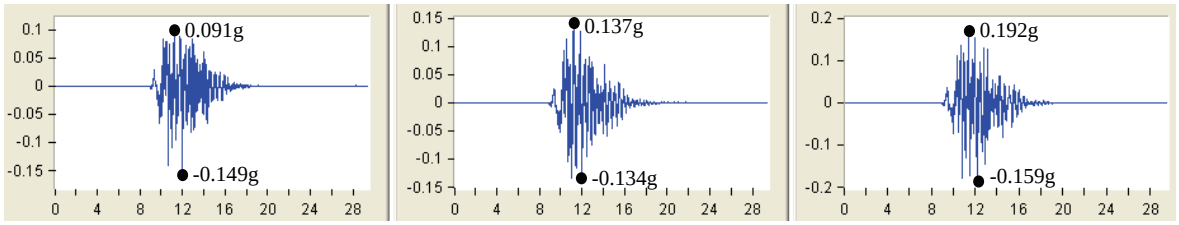

Acceleration Time History of Test PE1B

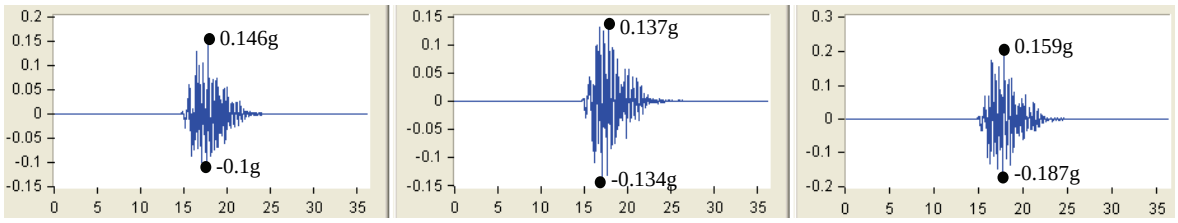

Acceleration Time History of Test PER1

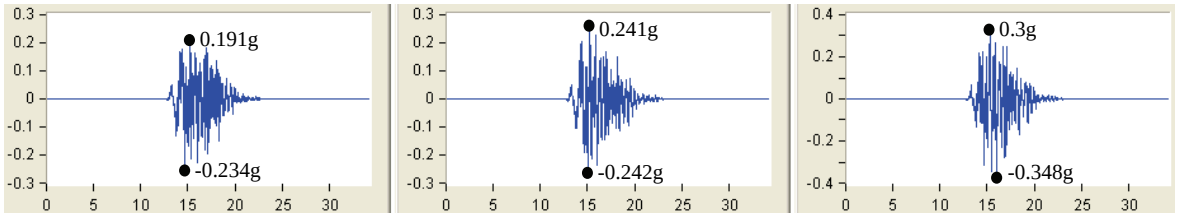

Acceleration Time History of Test PE2

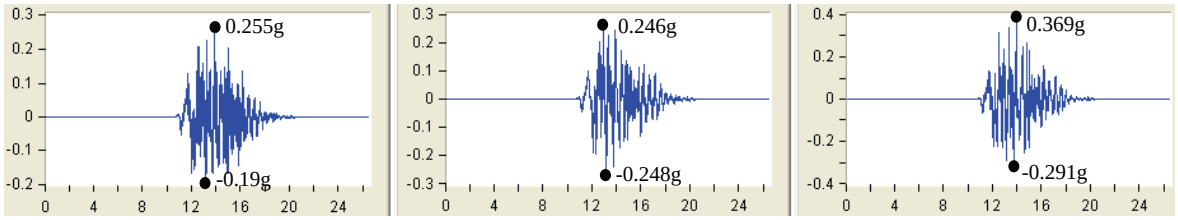

Acceleration Time History of Test PER2

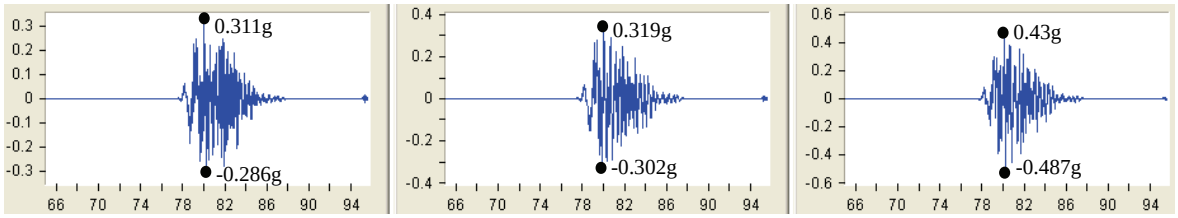

Acceleration Time History of Test PE3

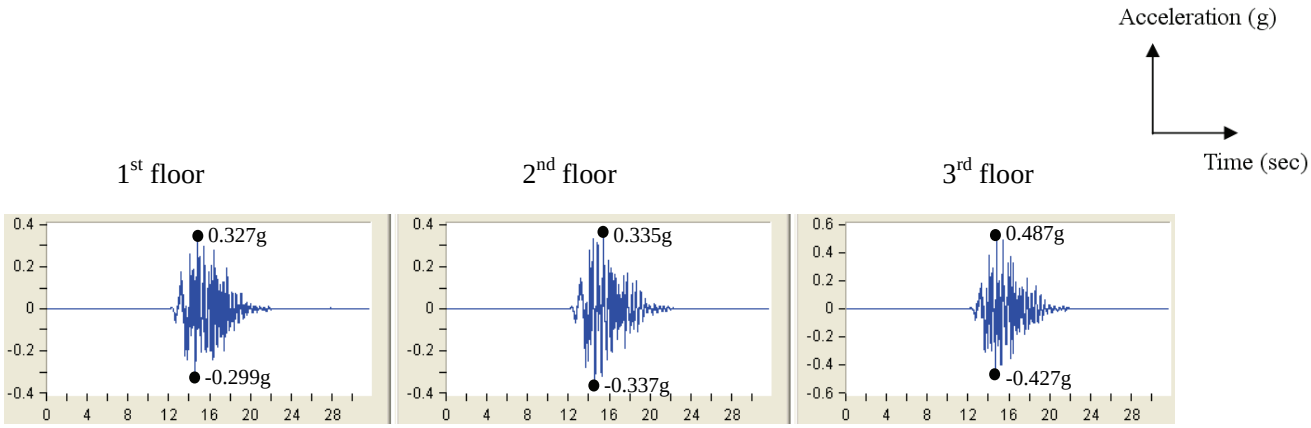

Acceleration Time History of Test PER3

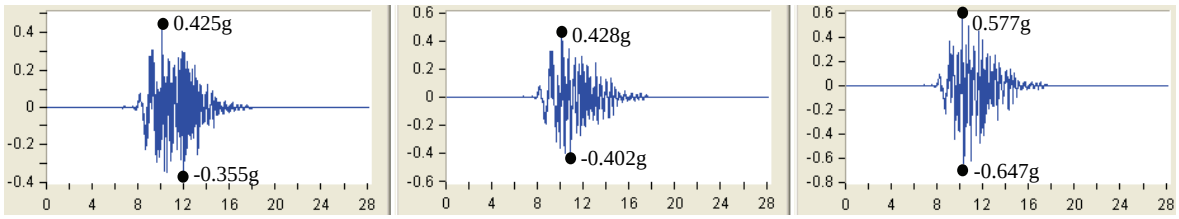

Acceleration Time History of Test PE4

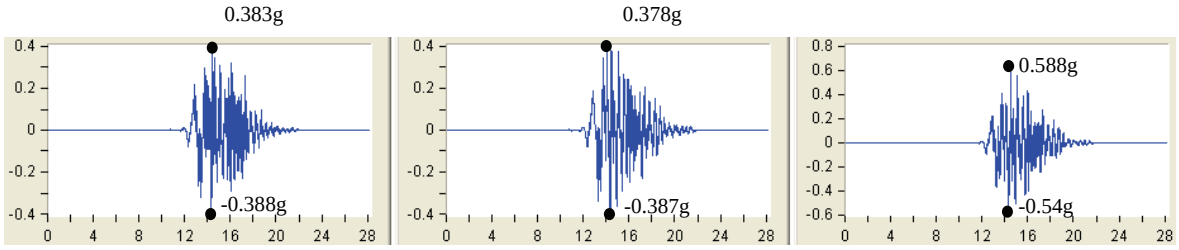

Acceleration Time History of Test PER4

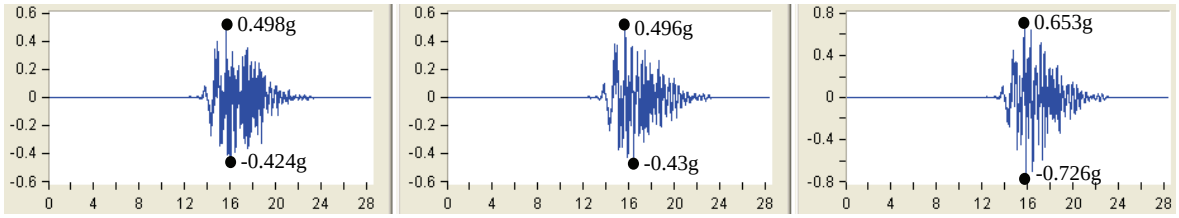

Acceleration Time History of Test PE5A

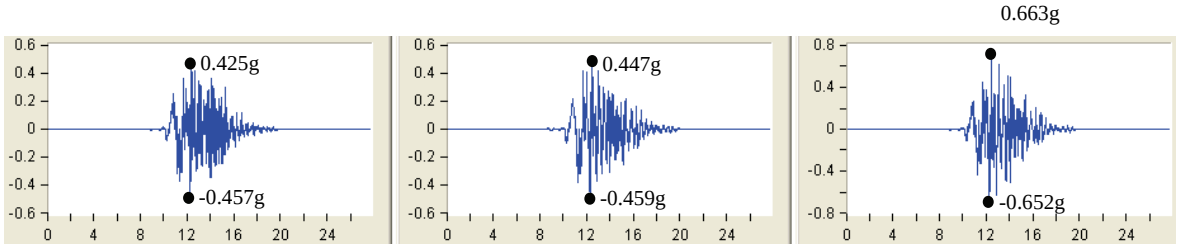

Acceleration Time History of Test PER5

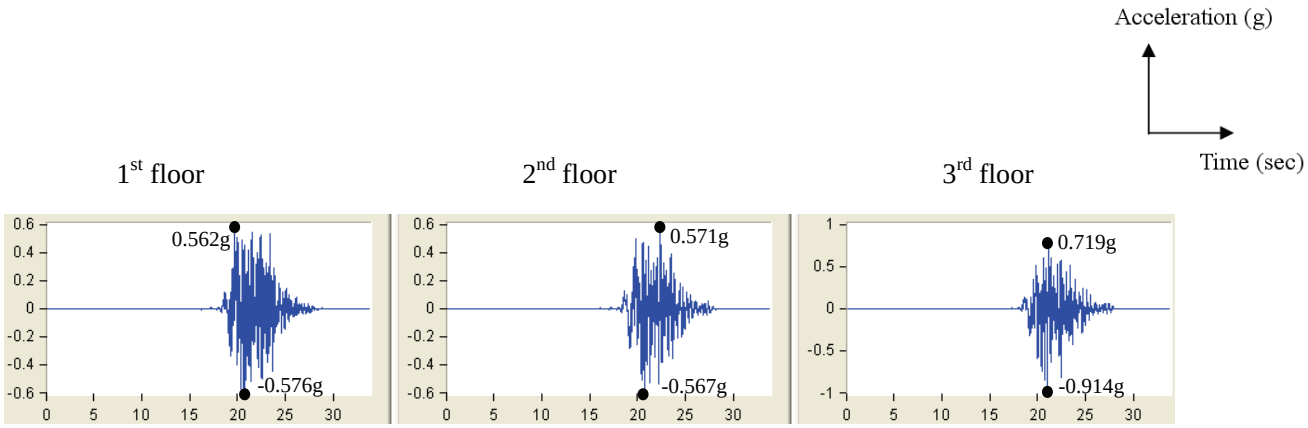

Acceleration Time History of Test PE6A

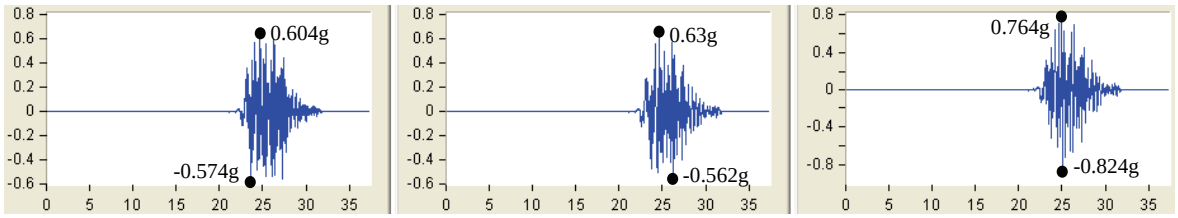

Acceleration Time History of Test PER6

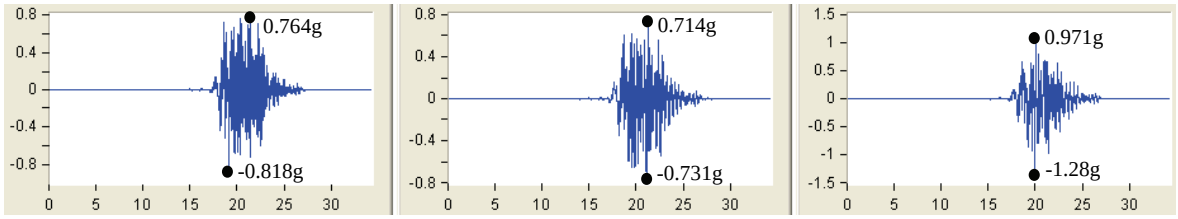

Acceleration Time History of Test PE7A

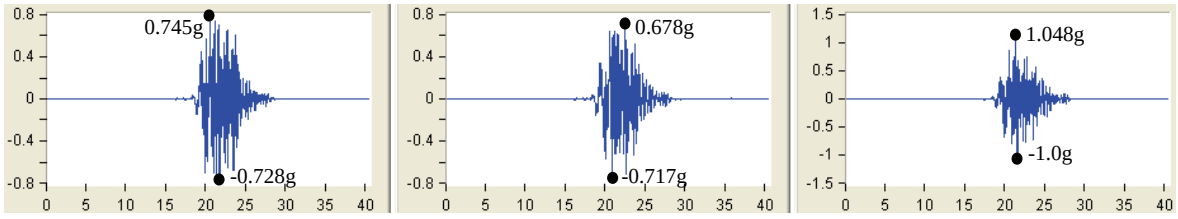

Acceleration Time History of Test PER7

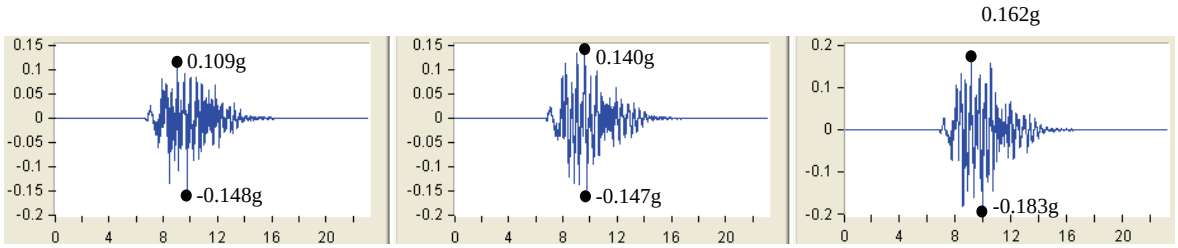

Acceleration Time History of Test PE8

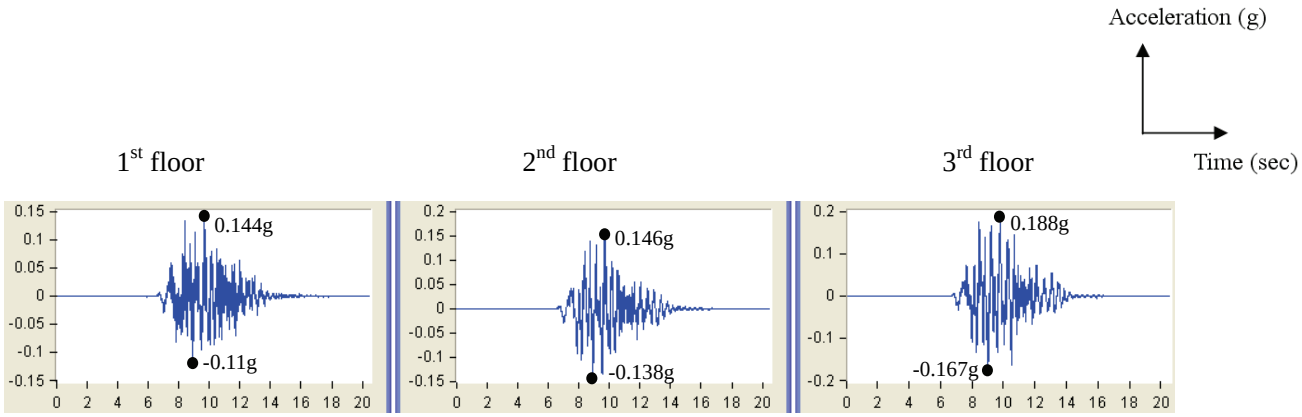

Acceleration Time History of Test PER8

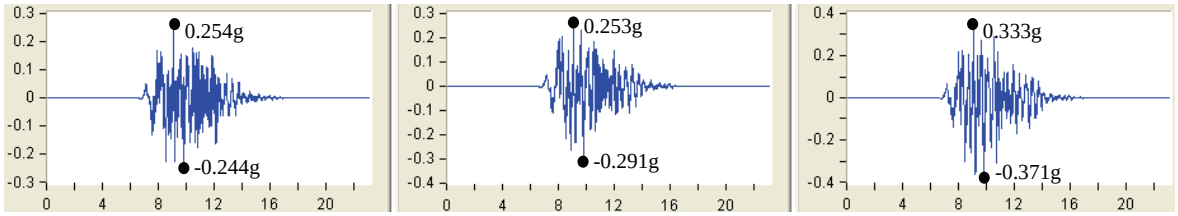

Acceleration Time History of Test PE9

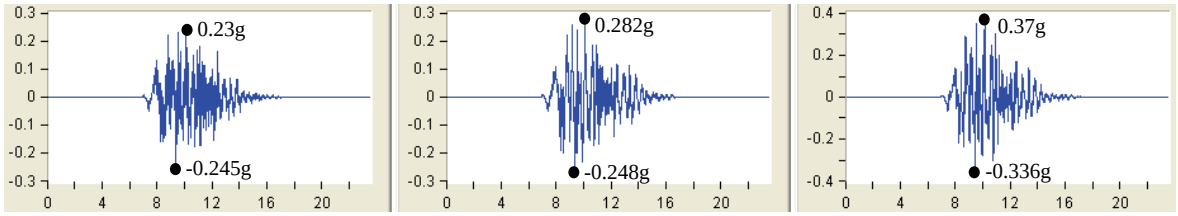

Acceleration Time History of Test PER9

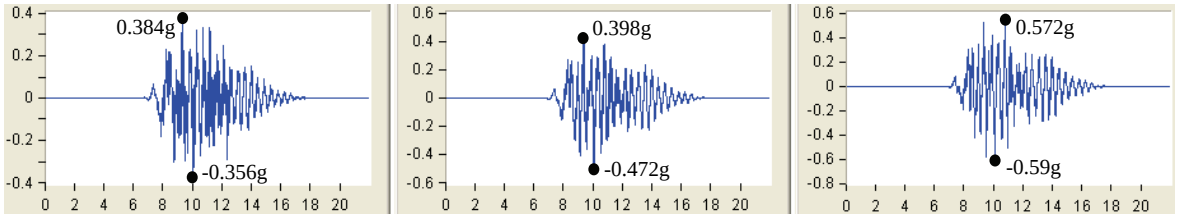

Acceleration Time History of Test PE10

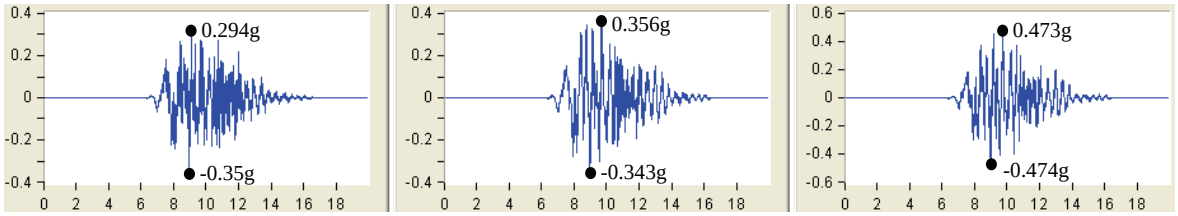

Acceleration Time History of Test PER10

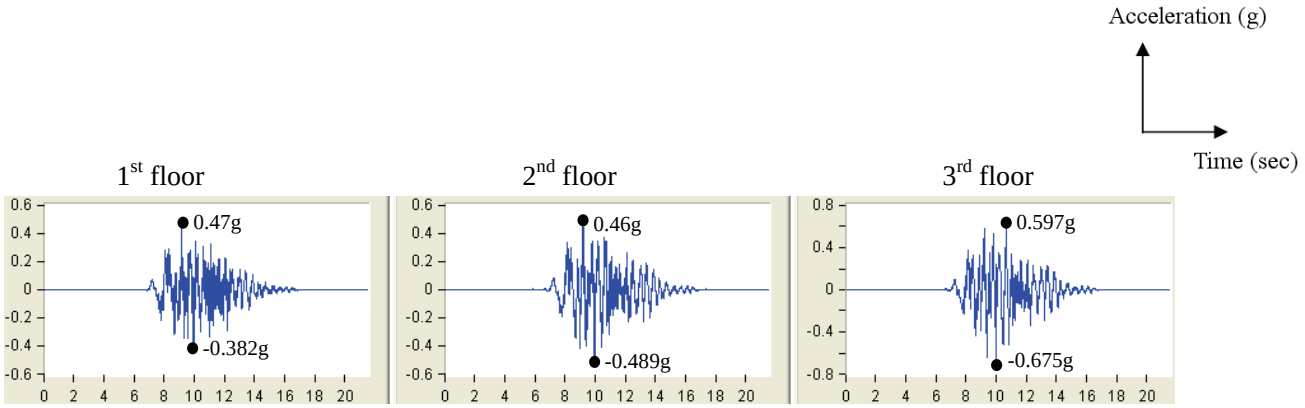

Acceleration Time History of Test PE11

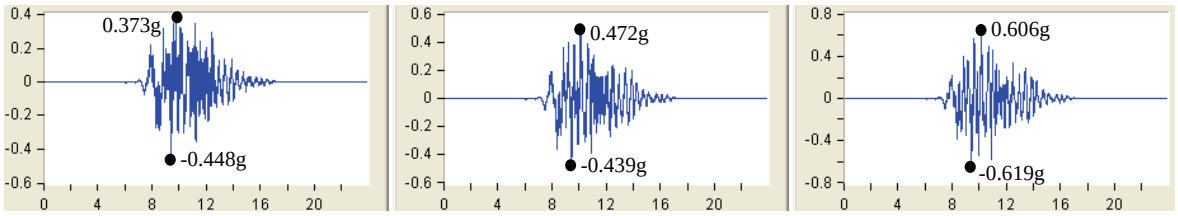

Acceleration Time History of Test PER11

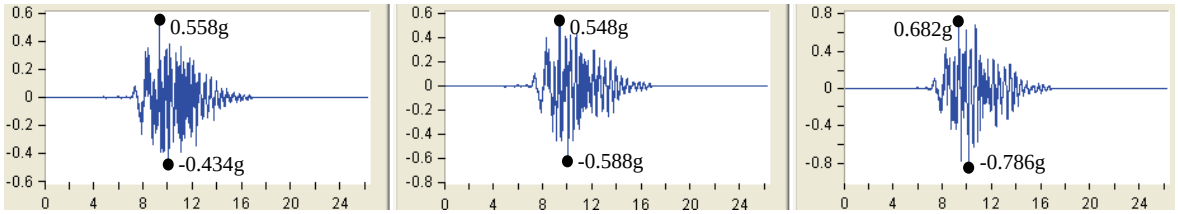

Acceleration Time History of Test PE12

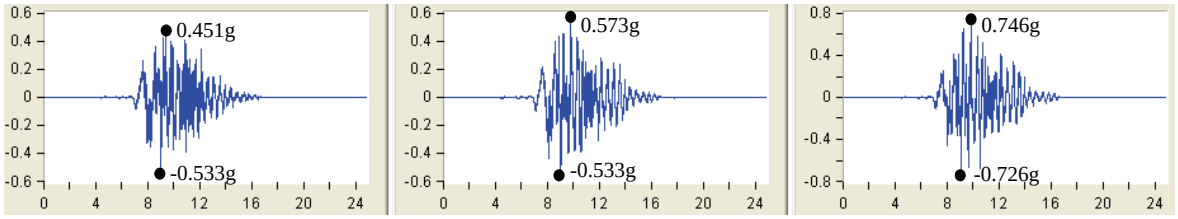

Acceleration Time History of Test PER12

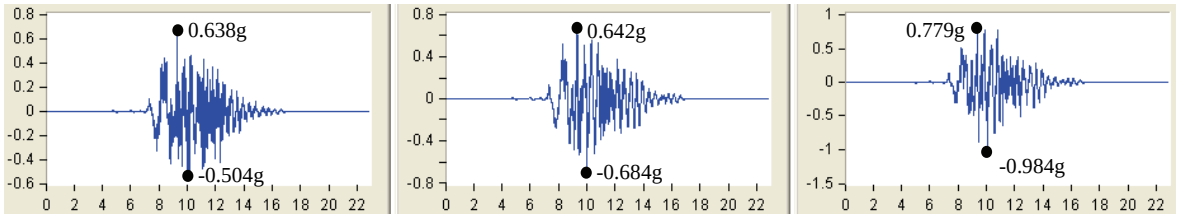

Acceleration Time History of Test PE15

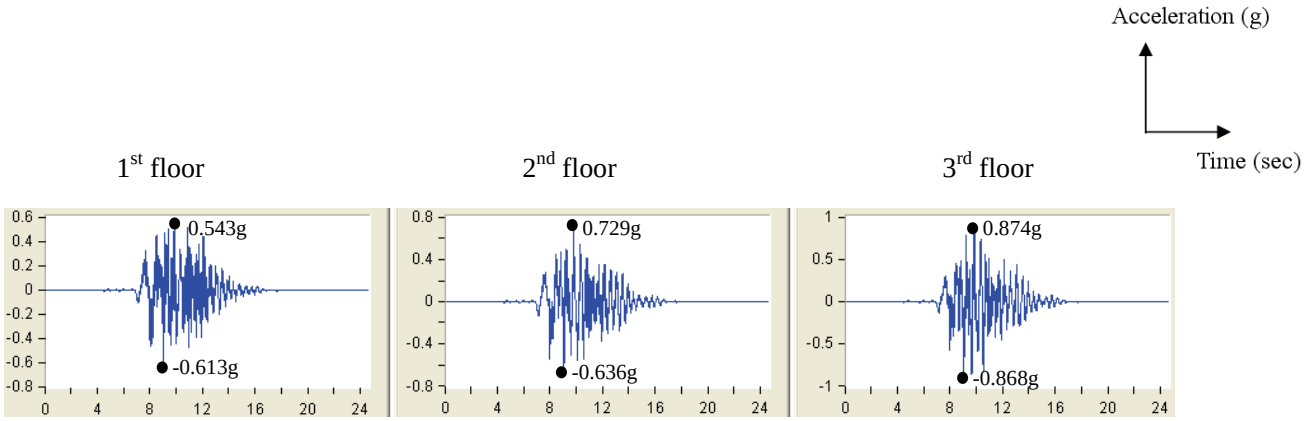

Acceleration Time History of Test PER15

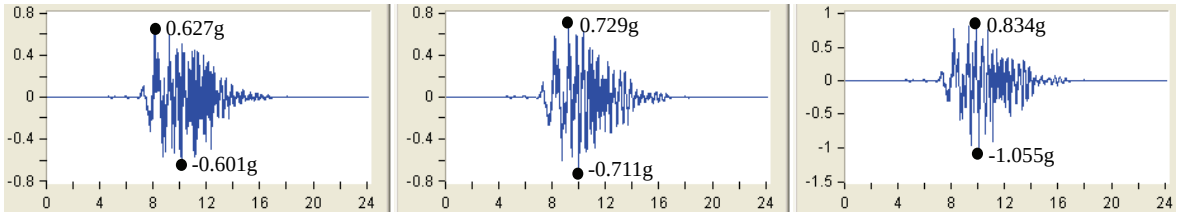

Acceleration Time History of Test PE16

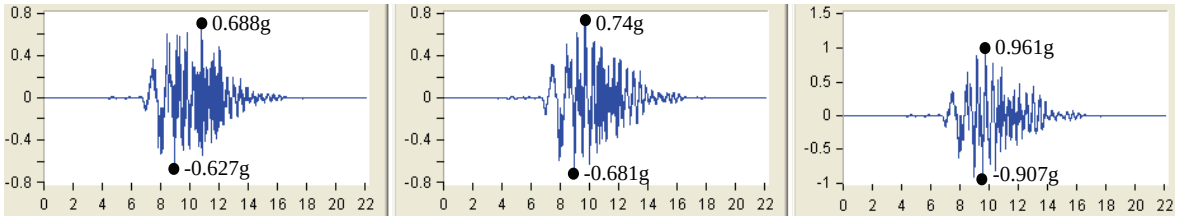

Acceleration Time History of Test PER16

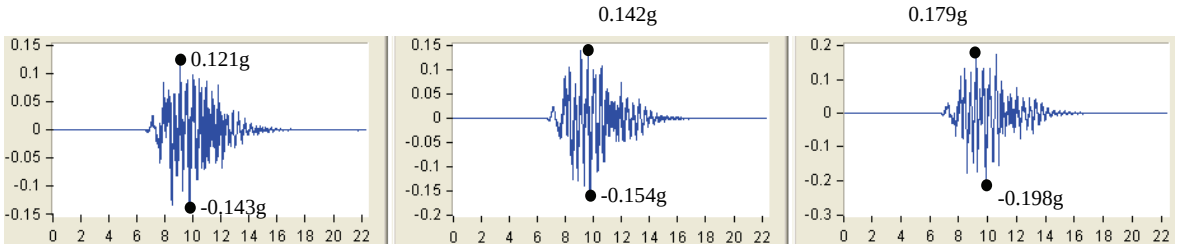

Acceleration Time History of Test PE17

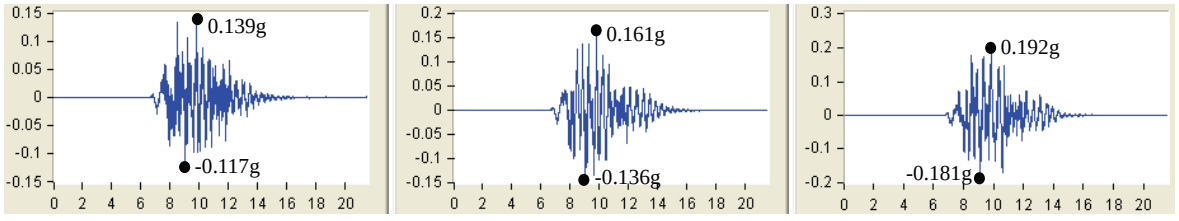

Acceleration Time History of Test PER17

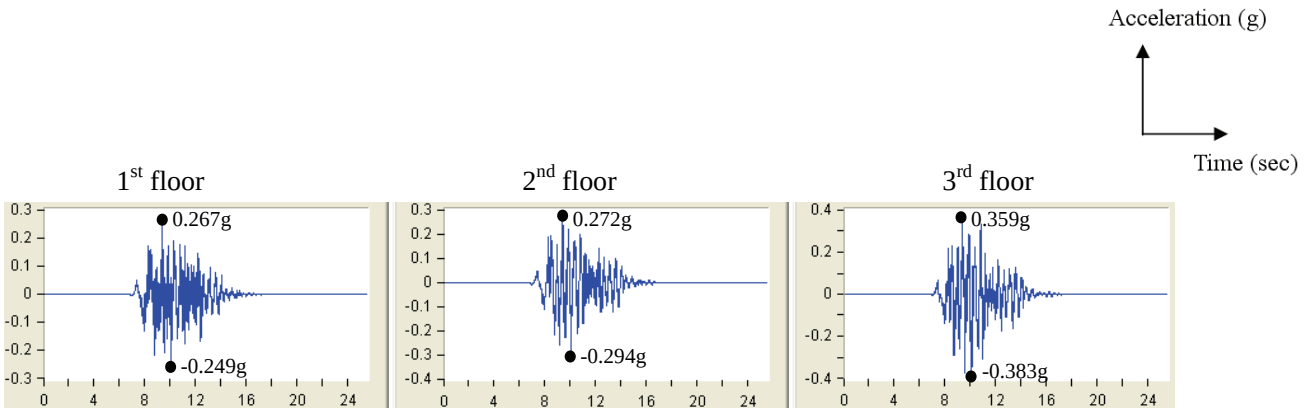

Acceleration Time History of Test PE18

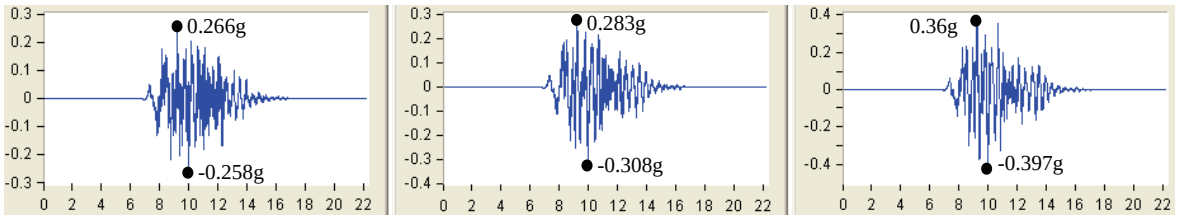

Acceleration Time History of Test PER18

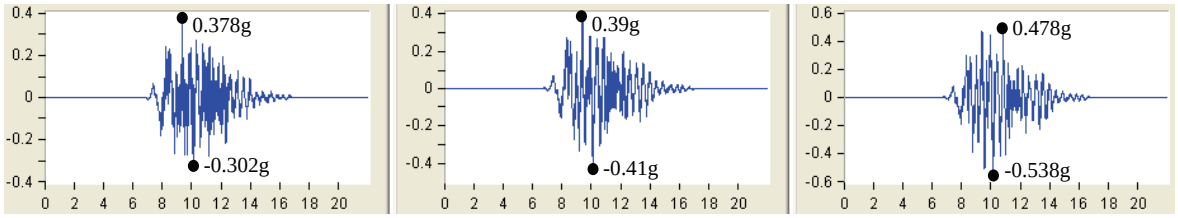

Acceleration Time History of Test PE19

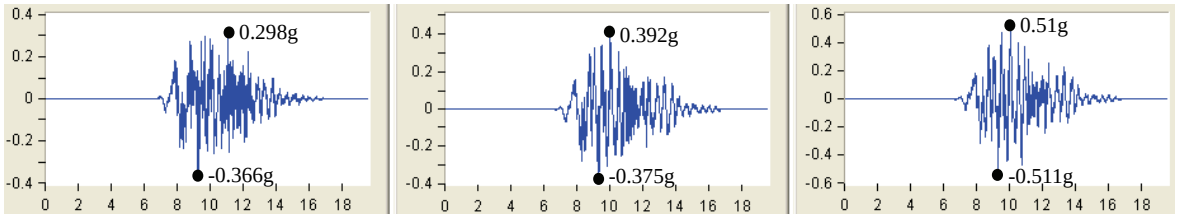

Acceleration Time History of Test PER19

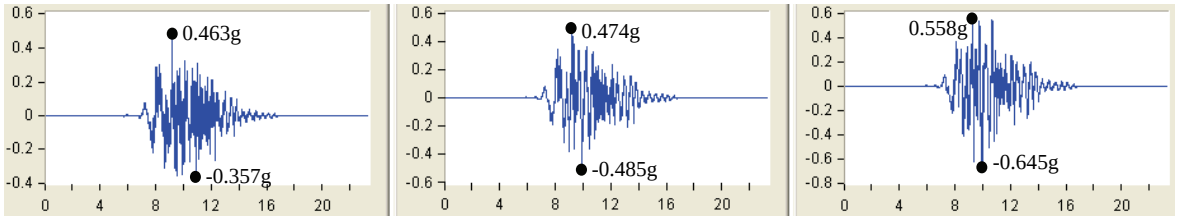

Acceleration Time History of Test PE20

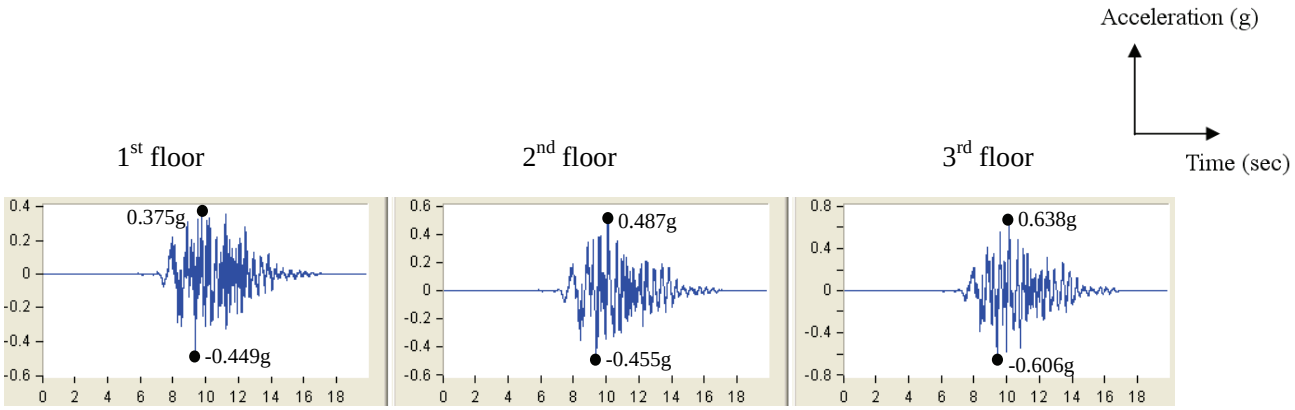

Acceleration Time History of Test PER20

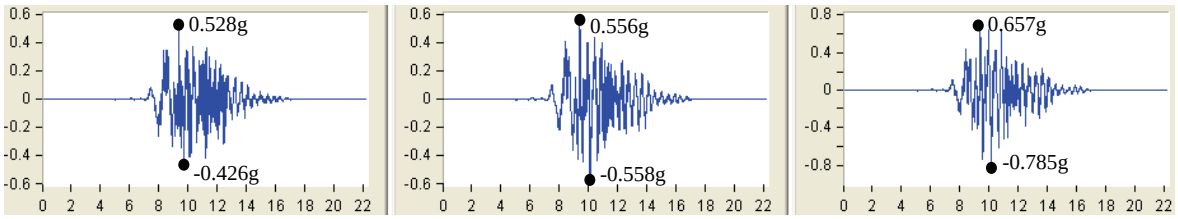

Acceleration Time History of Test PE21

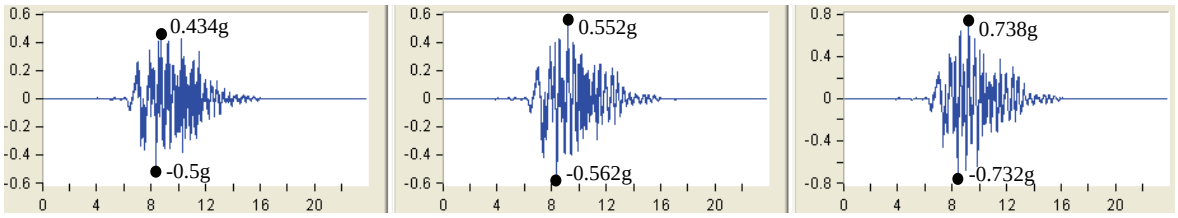

Acceleration Time History of Test PER21

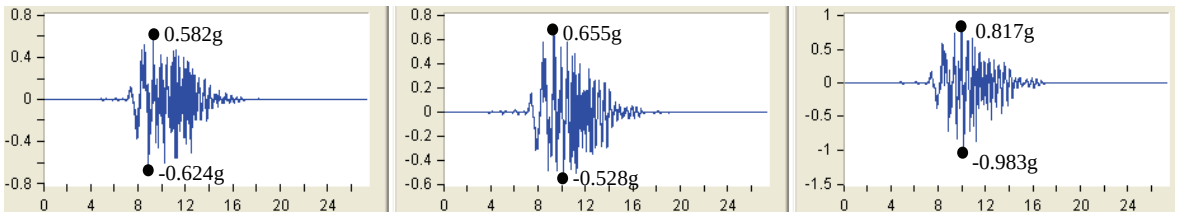

Acceleration Time History of Test PE22

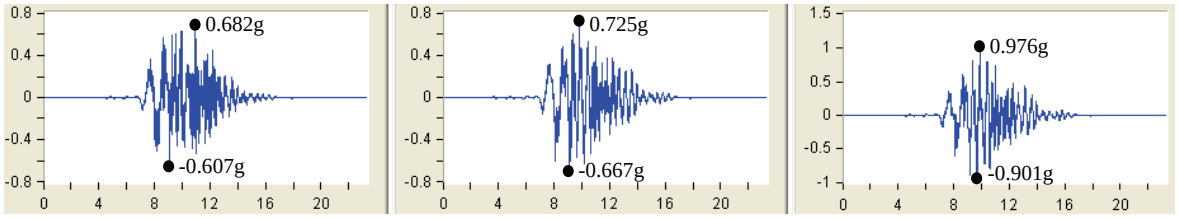

Acceleration Time History of Test PER22

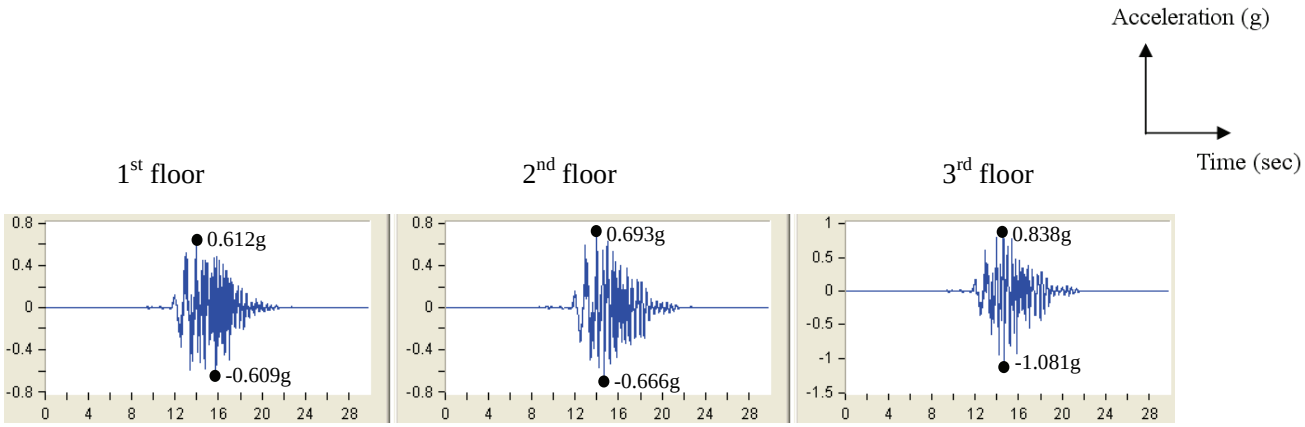

Acceleration Time History of Test PE23

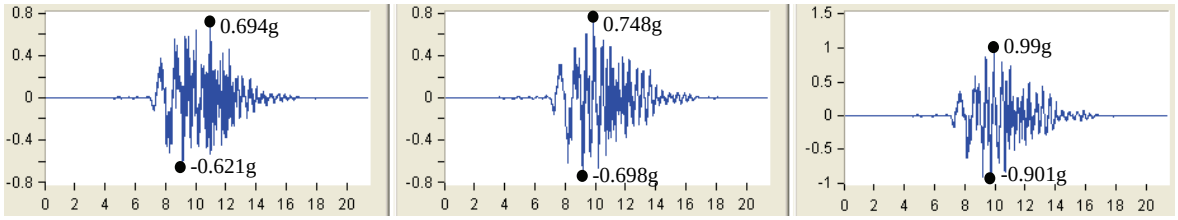

Acceleration Time History of Test PER23

SMRF

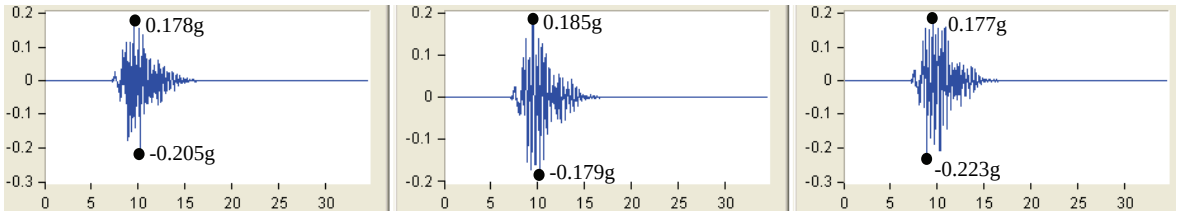

Acceleration Time History of Test ME01

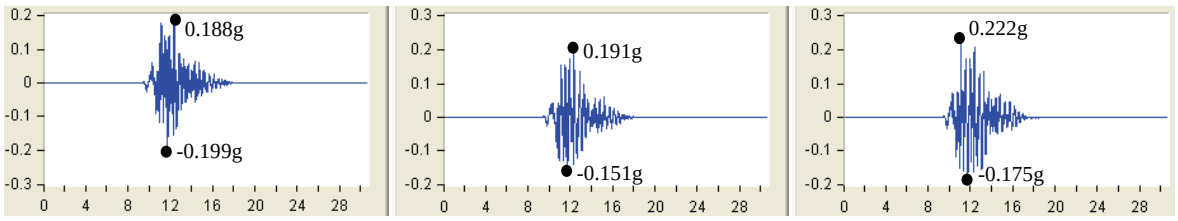

Acceleration Time History of Test MER01

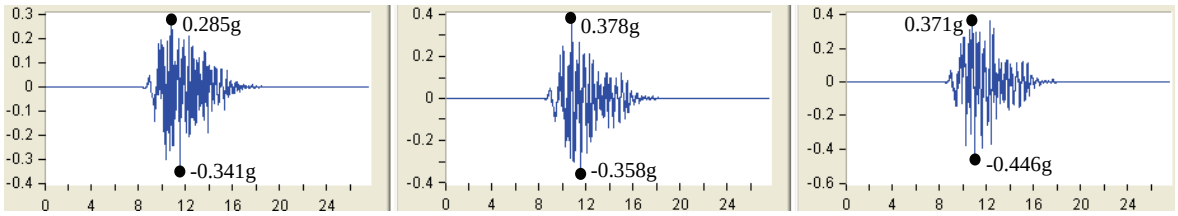

Acceleration Time History of Test ME02

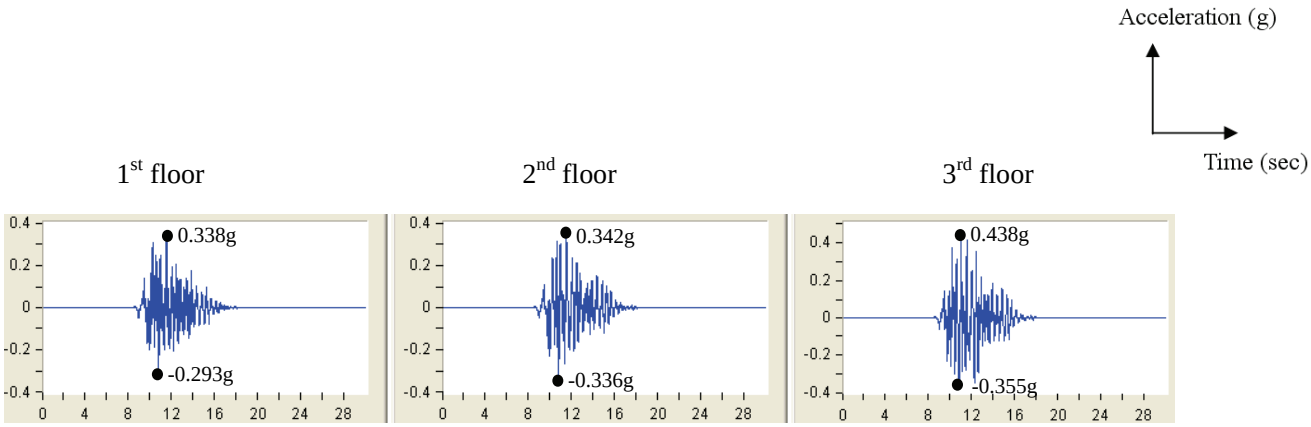

Acceleration Time History of Test MER02A

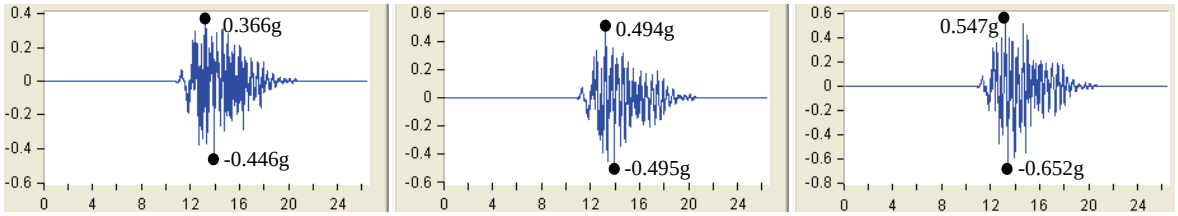

Acceleration Time History of Test ME03

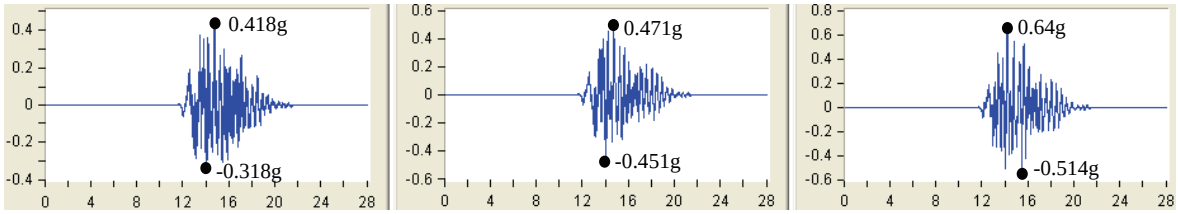

Acceleration Time History of Test MER03

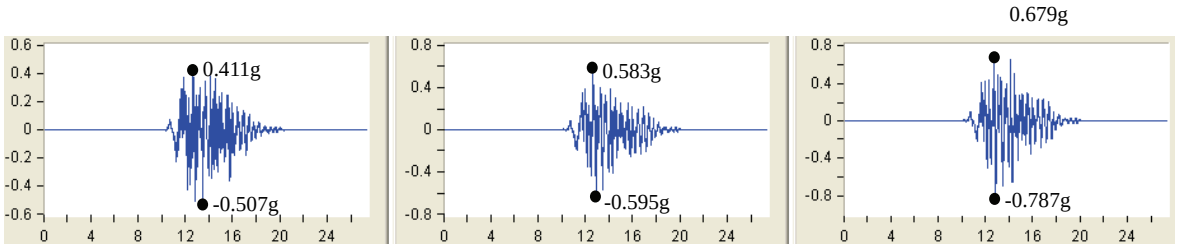

Acceleration Time History of Test ME04

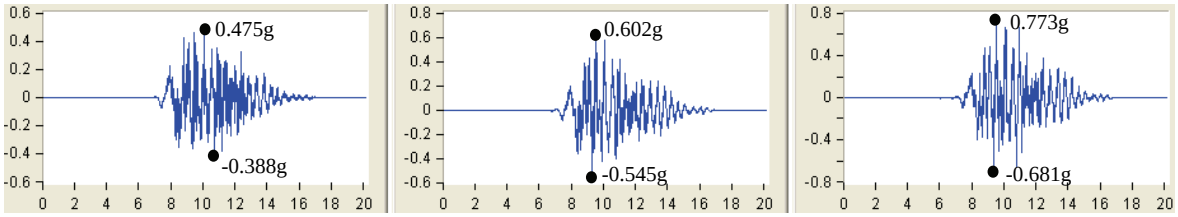

Acceleration Time History of Test MER04

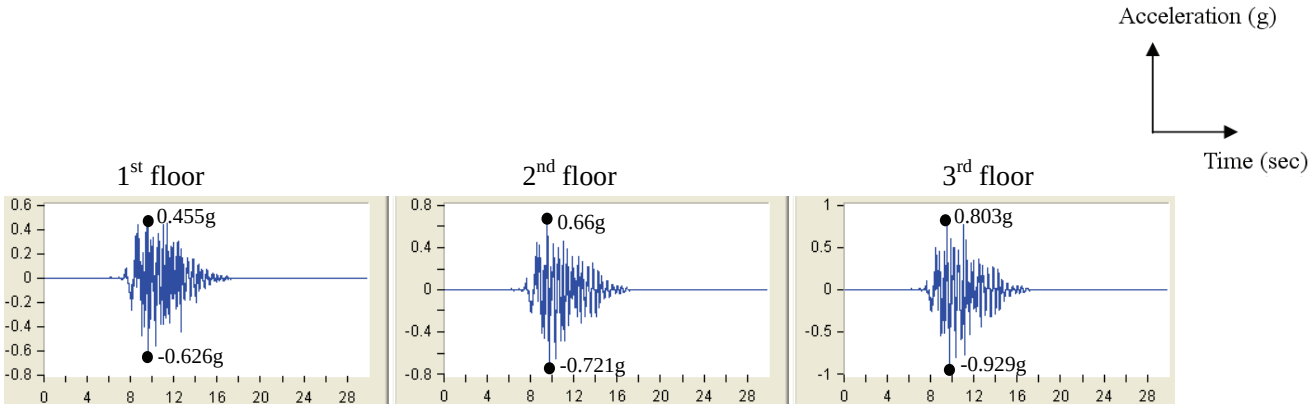

Acceleration Time History of Test ME05

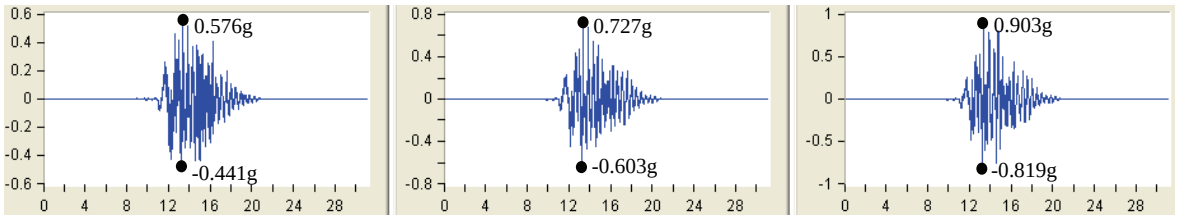

Acceleration Time History of Test MER05

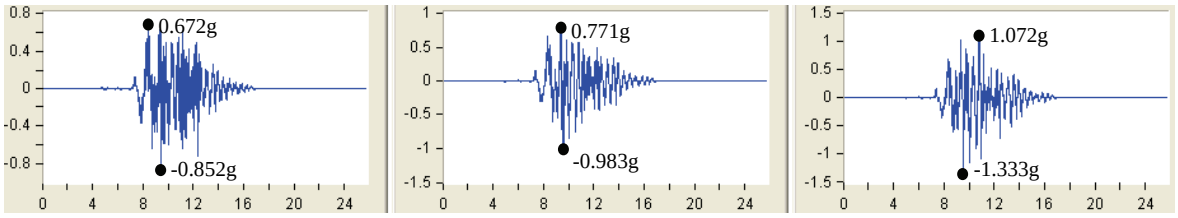

Acceleration Time History of Test ME06A

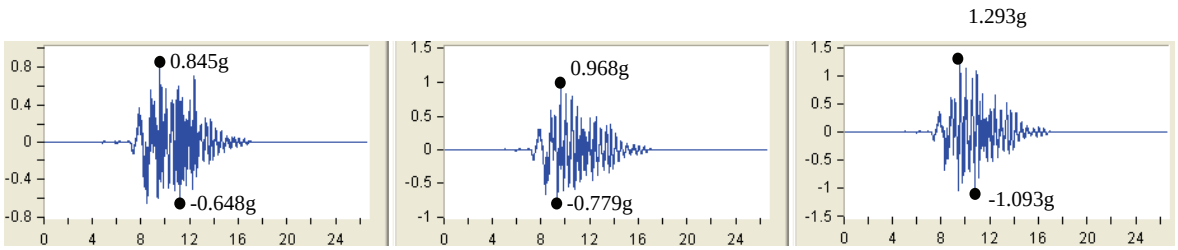

Acceleration Time History of Test MER06

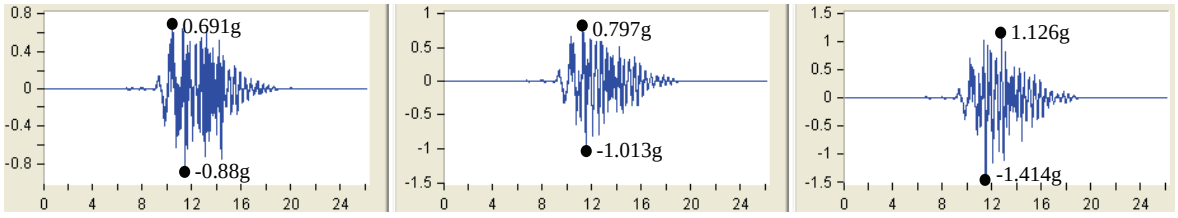

Acceleration Time History of Test ME07

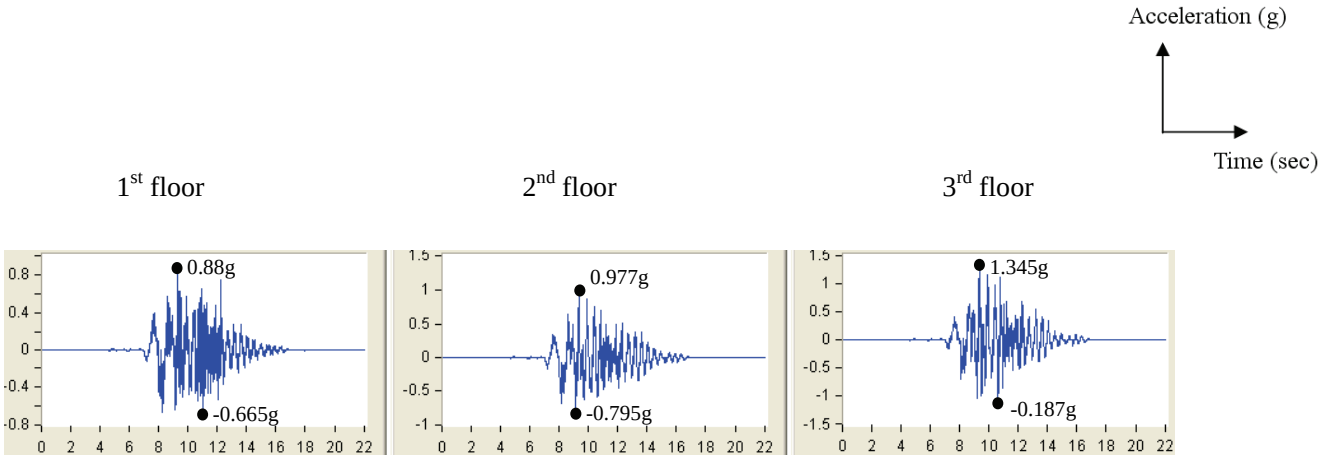

Acceleration Time History of Test MER07

Appendix F Inter-Story Drift Time History of the SCPT and SMRF Models for Seismic Tests

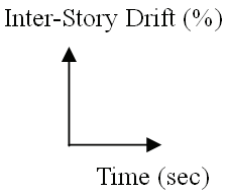

SCPT 1st floor 2nd floor 3rd floor

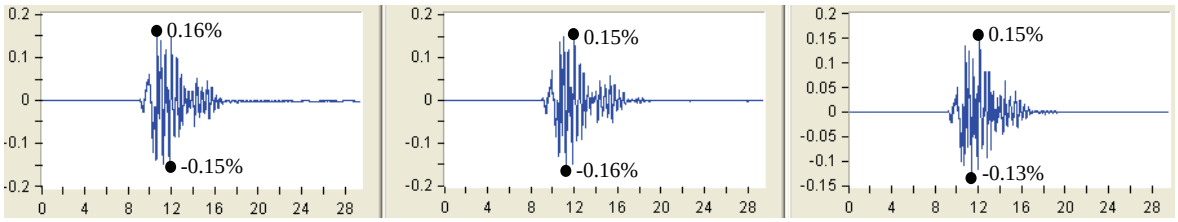

Inter-story Drift Time History of Test PE1B

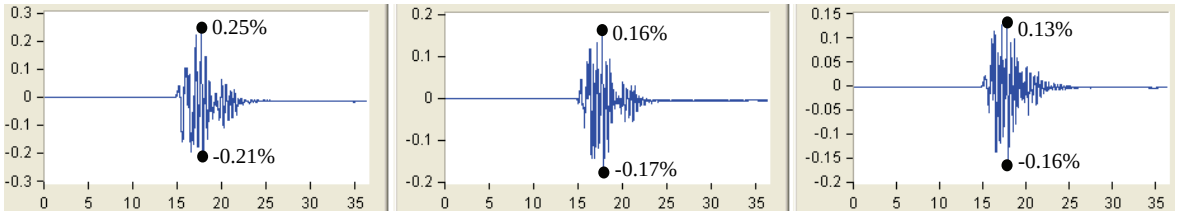

Inter-story Drift Time History of Test PER1

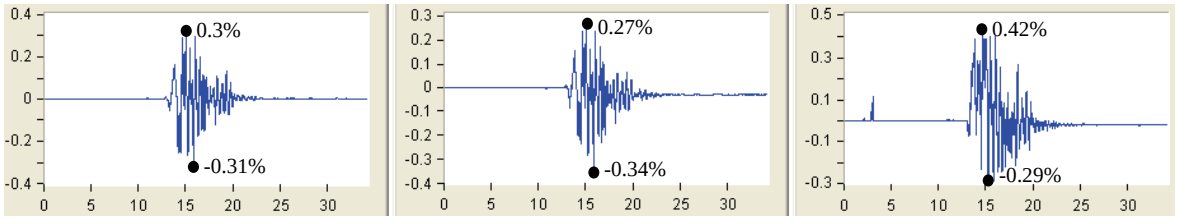

Inter-story Drift Time History of Test PE2

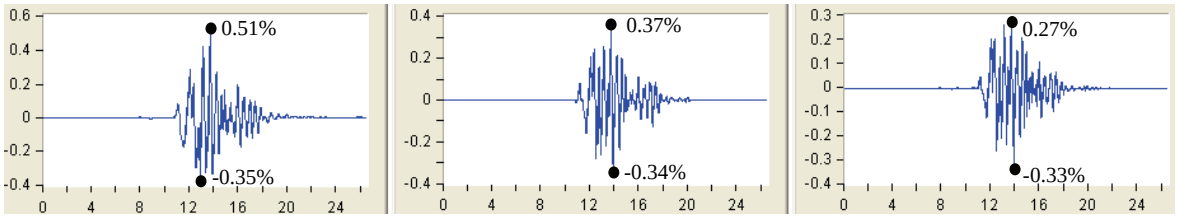

Inter-story Drift Time History of Test PER2

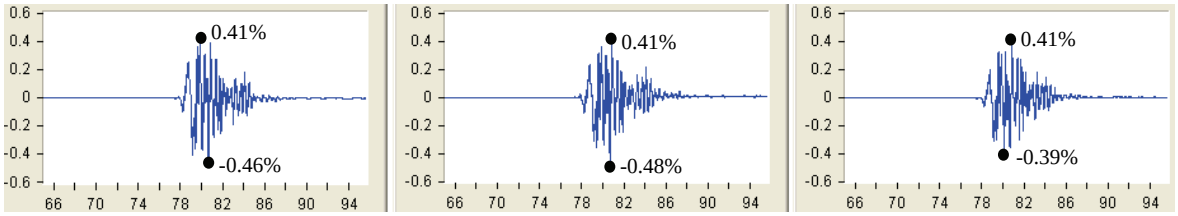

Inter-story Drift Time History of Test PE3

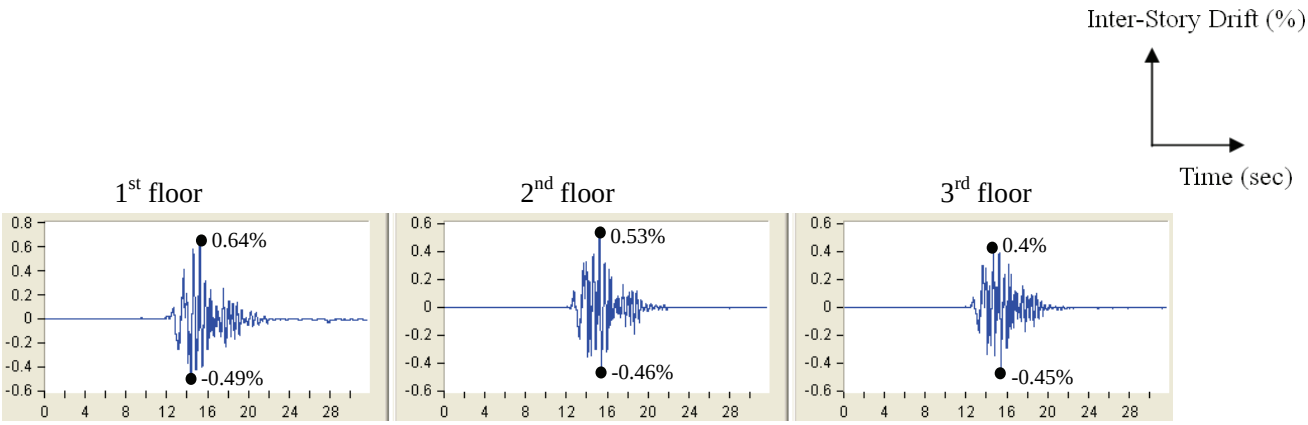

Inter-story Drift Time History of Test PER3

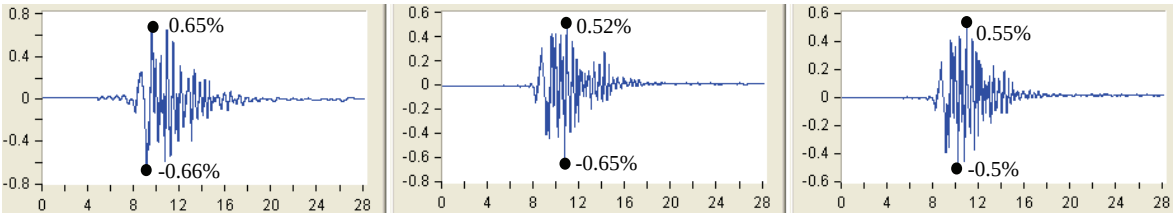

Inter-story Drift Time History of Test PE4

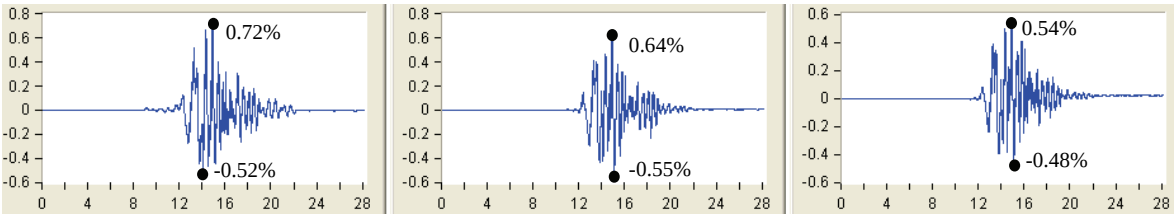

Inter-story Drift Time History of Test PER4

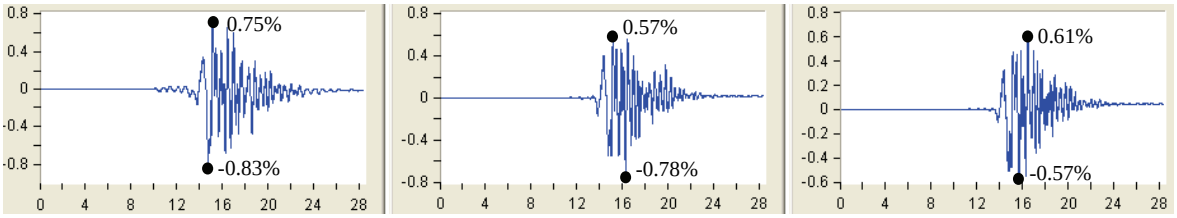

Inter-story Drift Time History of Test PE5A

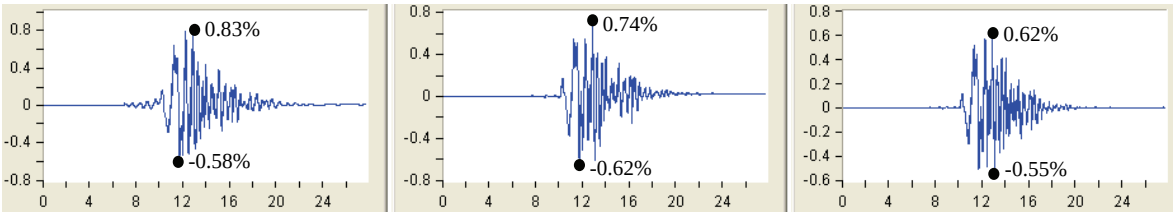

Inter-story Drift Time History of Test PER5

Inter-Story Drift (%)

Time (sec)

1st floor 2nd floor 3rd floor

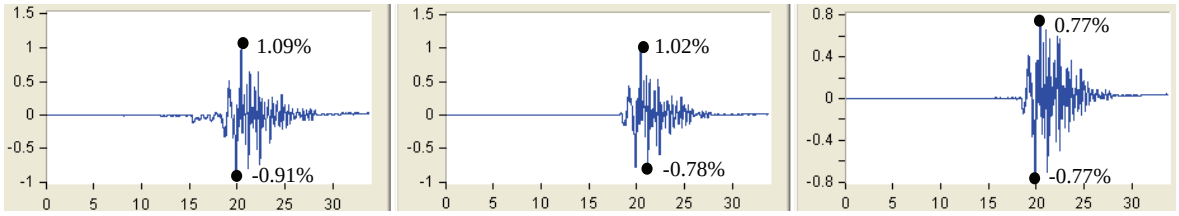

Inter-story Drift Time History of Test PE6A

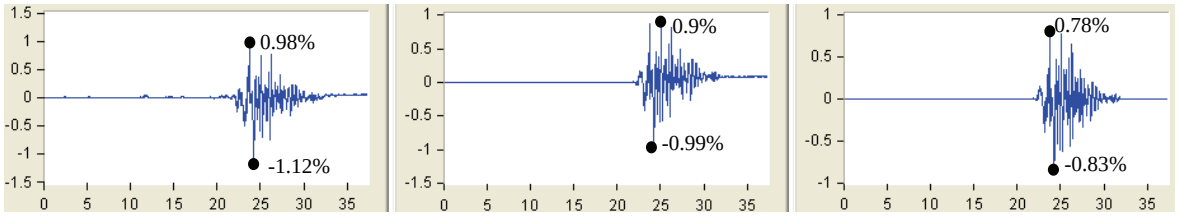

Inter-story Drift Time History of Test PER6

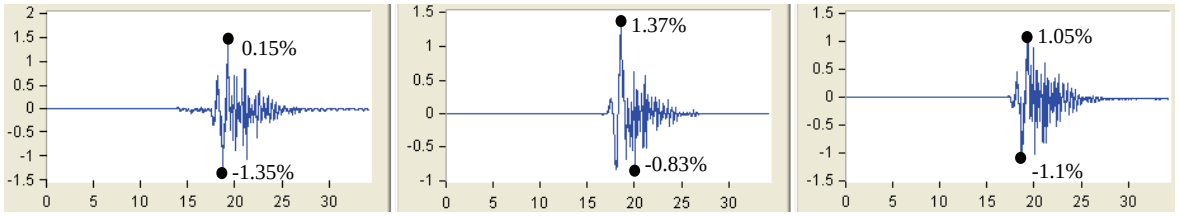

Inter-story Drift Time History of Test PE7A

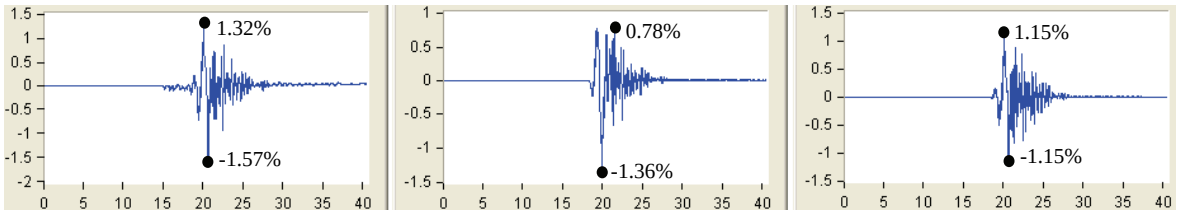

Inter-story Drift Time History of Test PER7

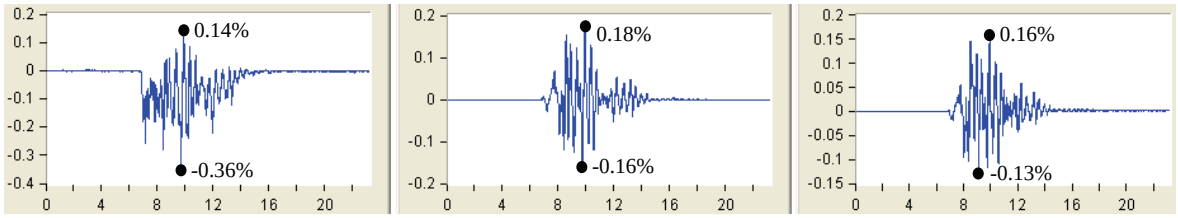

Inter-story Drift Time History of Test PE8

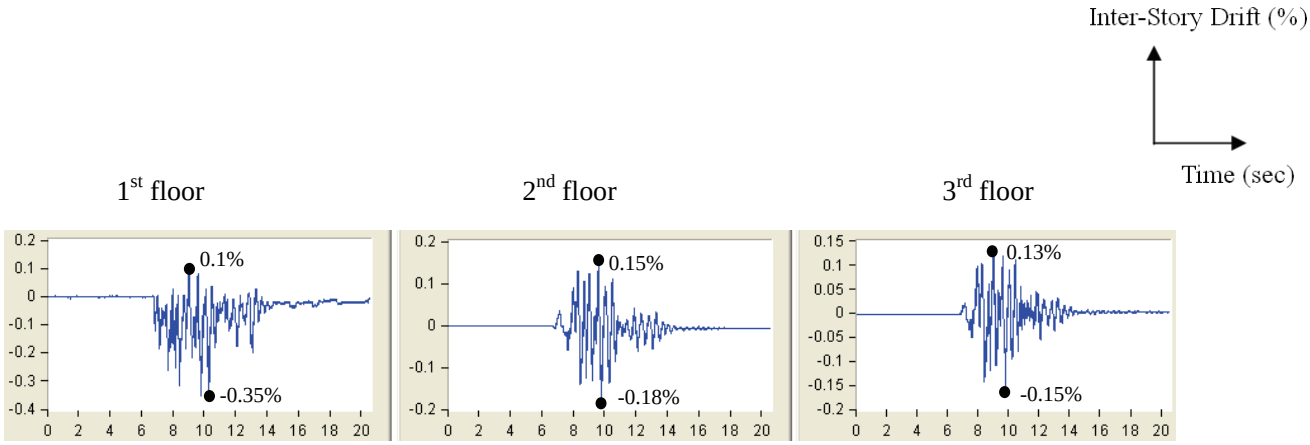

Inter-story Drift Time History of Test PER8

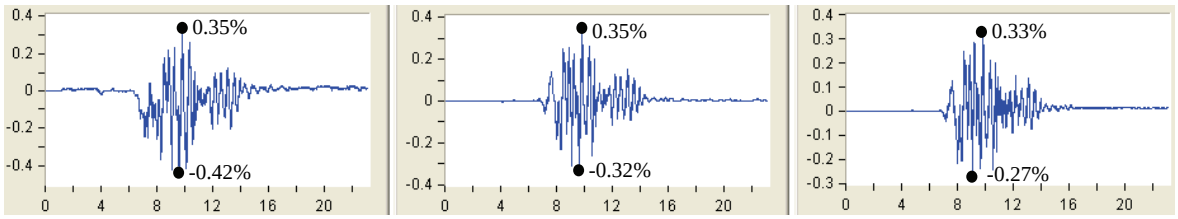

Inter-story Drift Time History of Test PE9

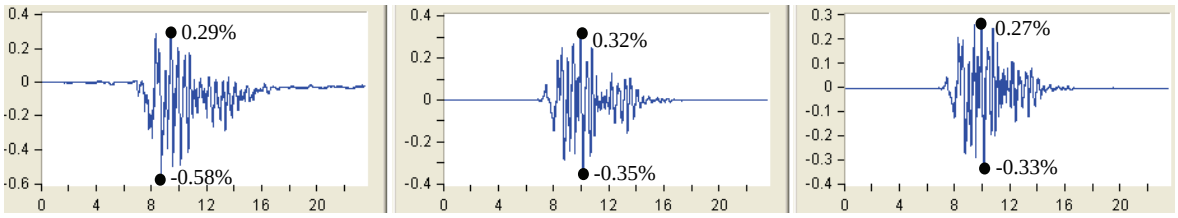

Inter-story Drift Time History of Test PER9

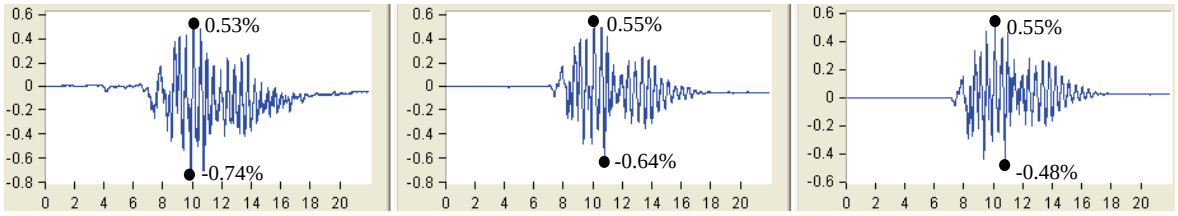

Inter-story Drift Time History of Test PE10

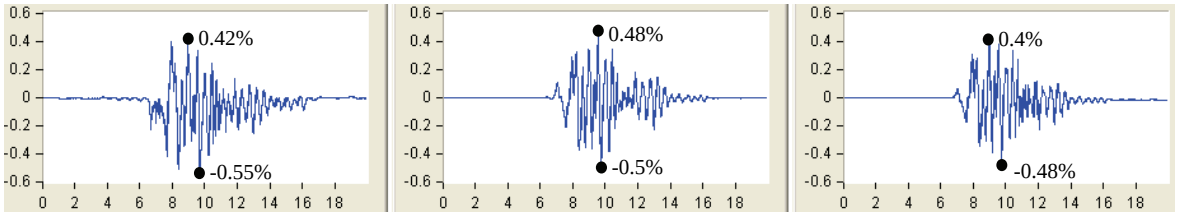

Inter-story Drift Time History of Test PER10

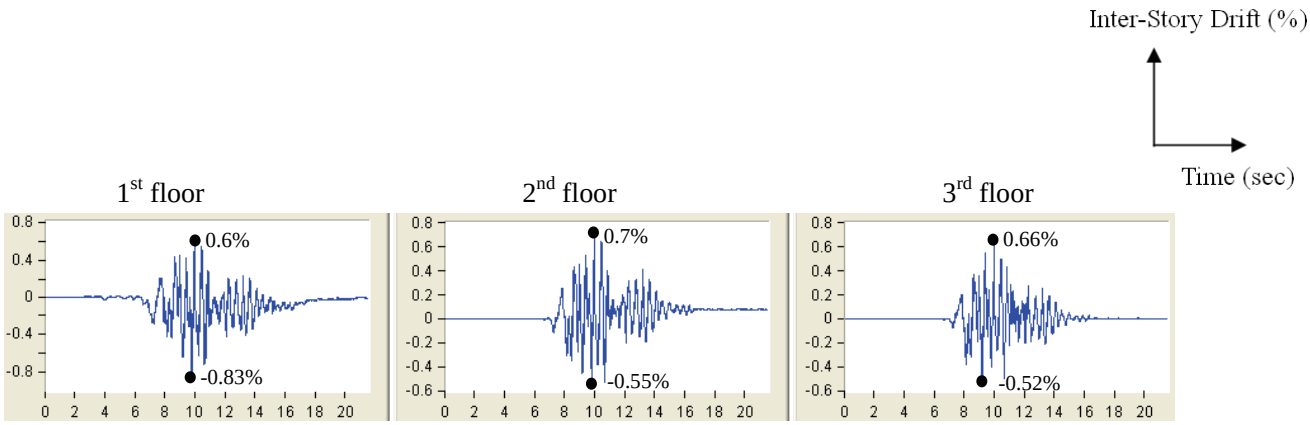

Inter-story Drift Time History of Test PE11

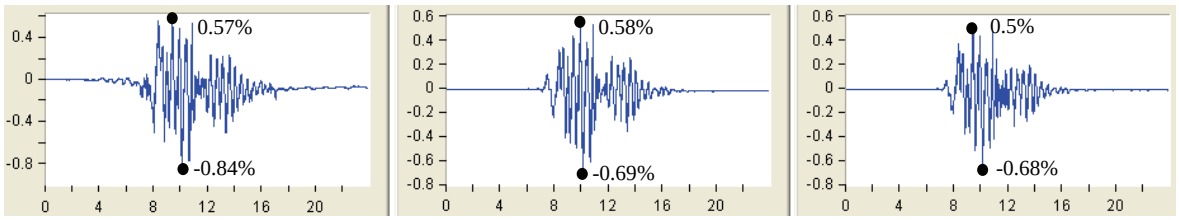

Inter-story Drift Time History of Test PER11

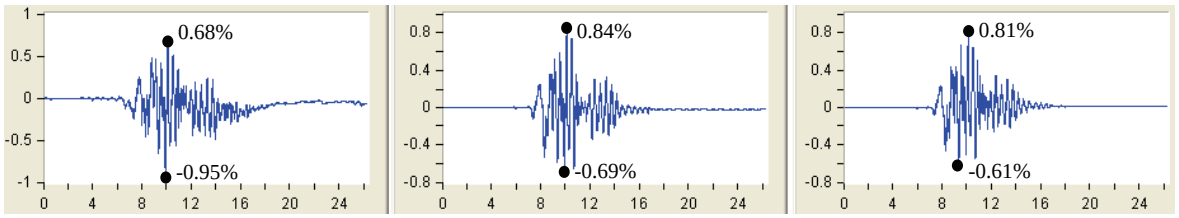

Inter-story Drift Time History of Test PE12

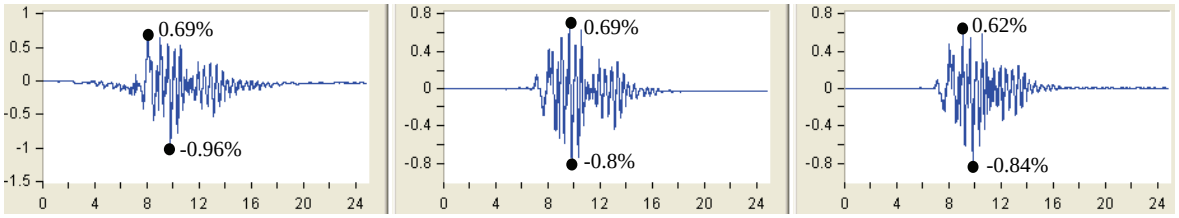

Inter-story Drift Time History of Test PER12

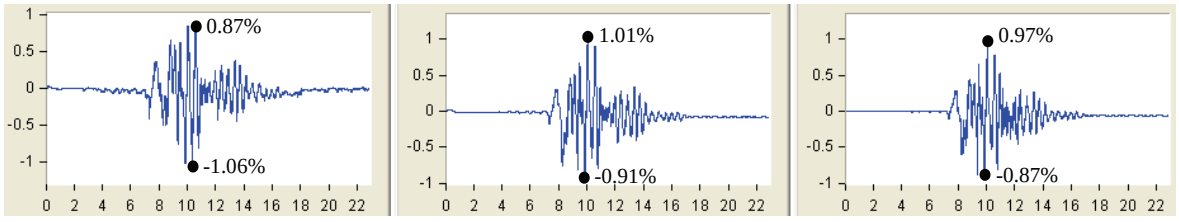

Inter-story Drift Time History of Test PE15

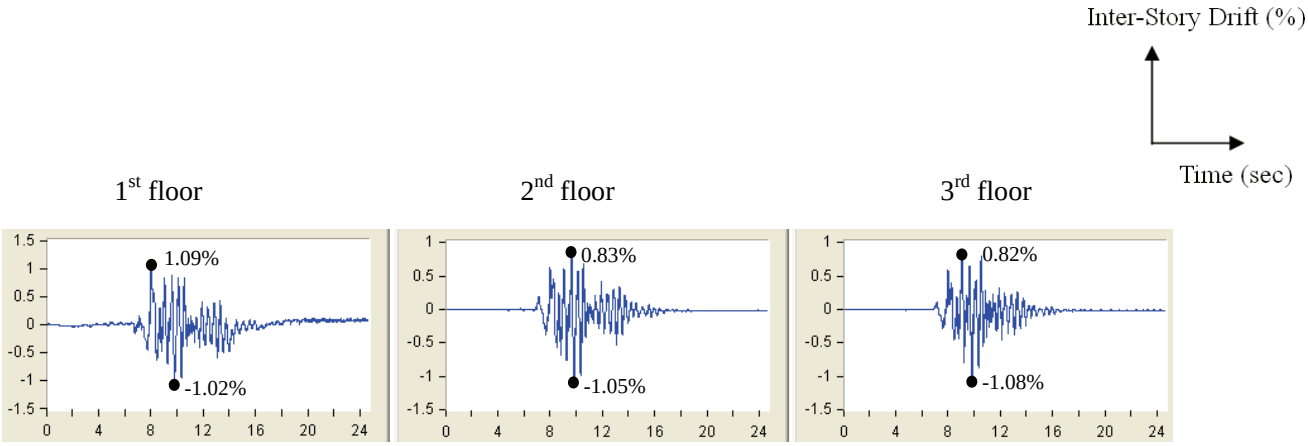

Inter-story Drift Time History of Test PER15

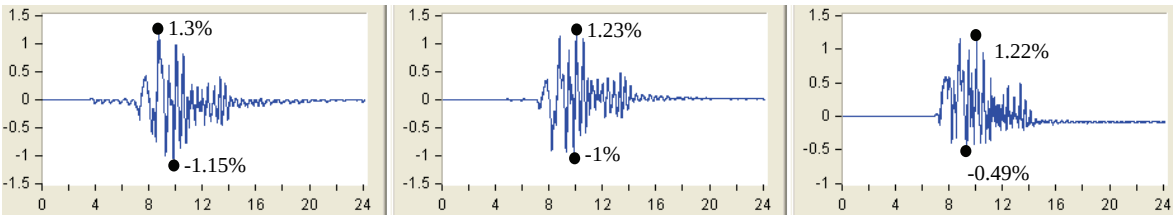

Inter-story Drift Time History of Test PE16

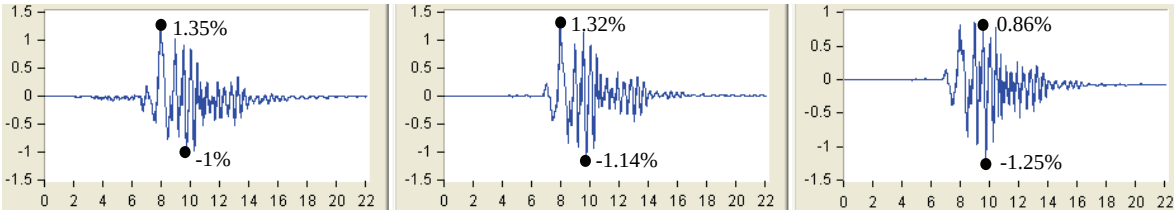

Inter-story Drift Time History of Test PER16

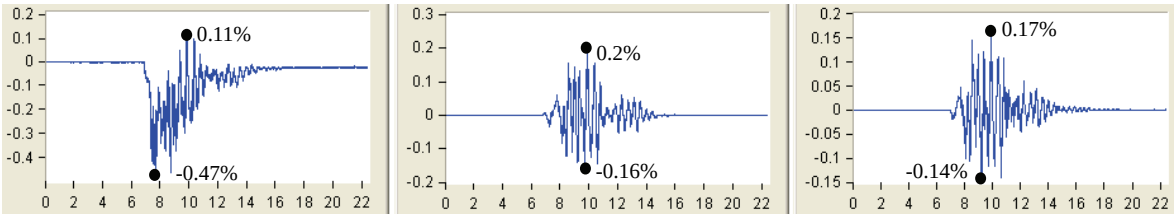

Inter-story Drift Time History of Test PE17

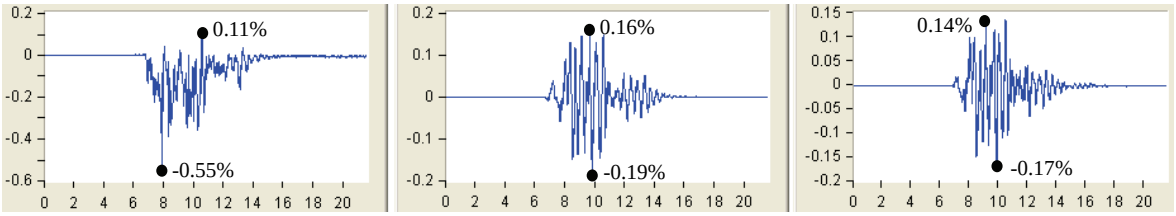

Inter-story Drift Time History of Test PER17

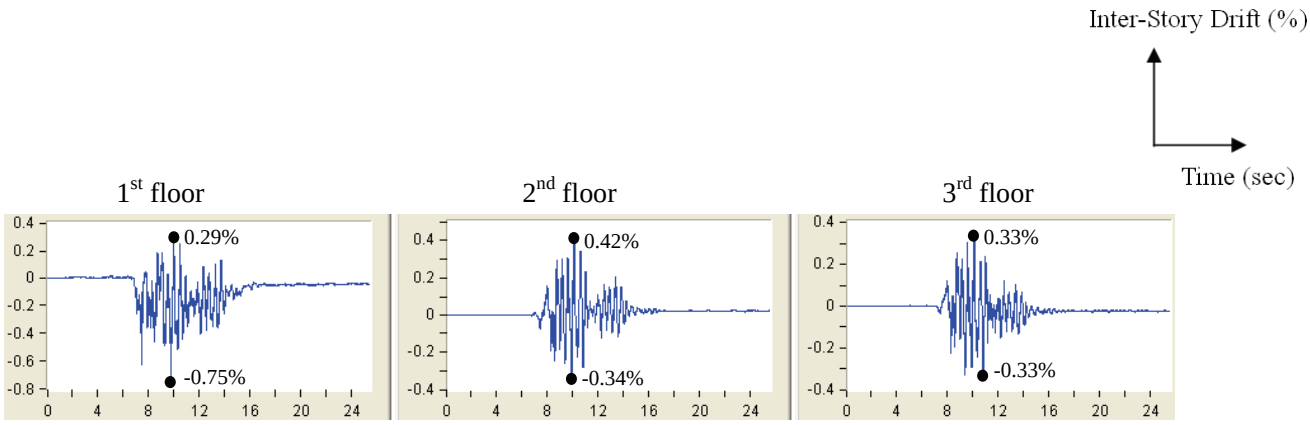

Inter-story Drift Time History of Test PE18

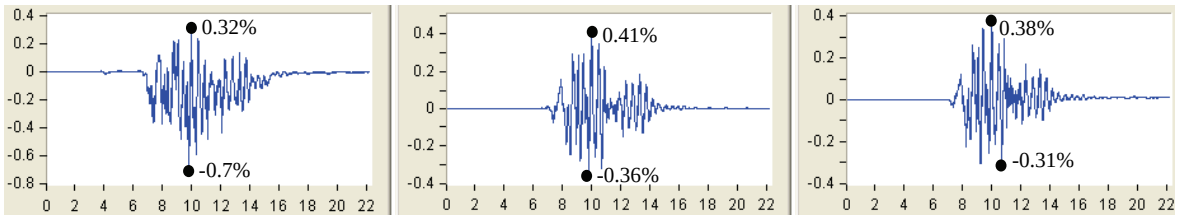

Inter-story Drift Time History of Test PER18

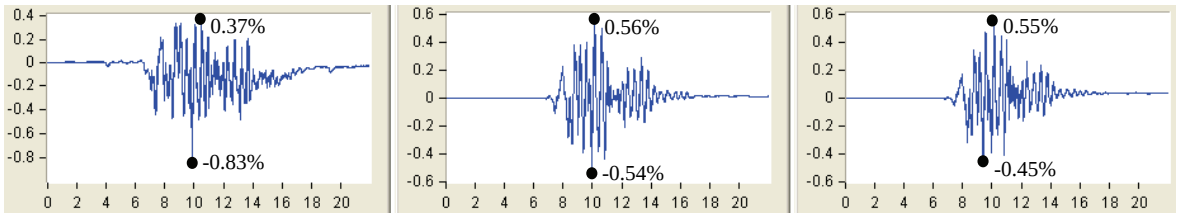

Inter-story Drift Time History of Test PE19

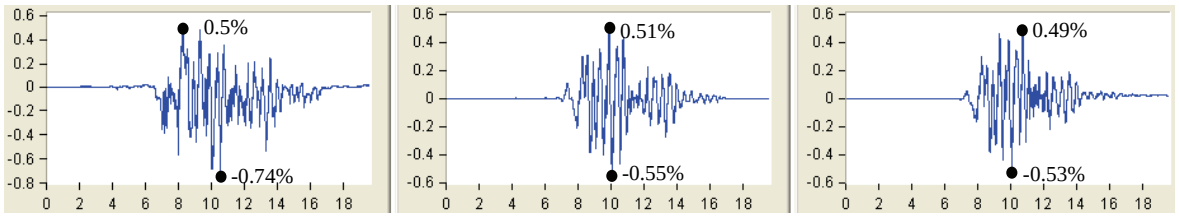

Inter-story Drift Time History of Test PER19

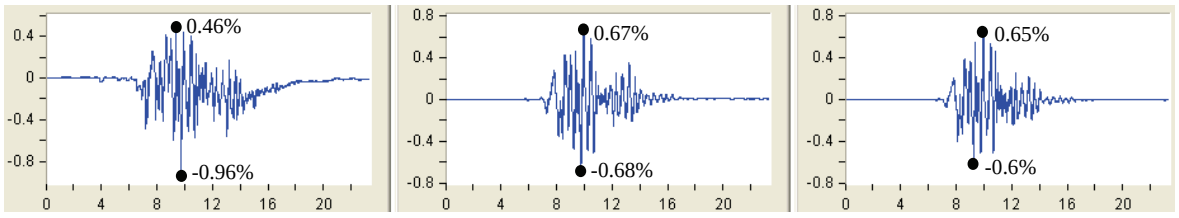

Inter-story Drift Time History of Test PE20

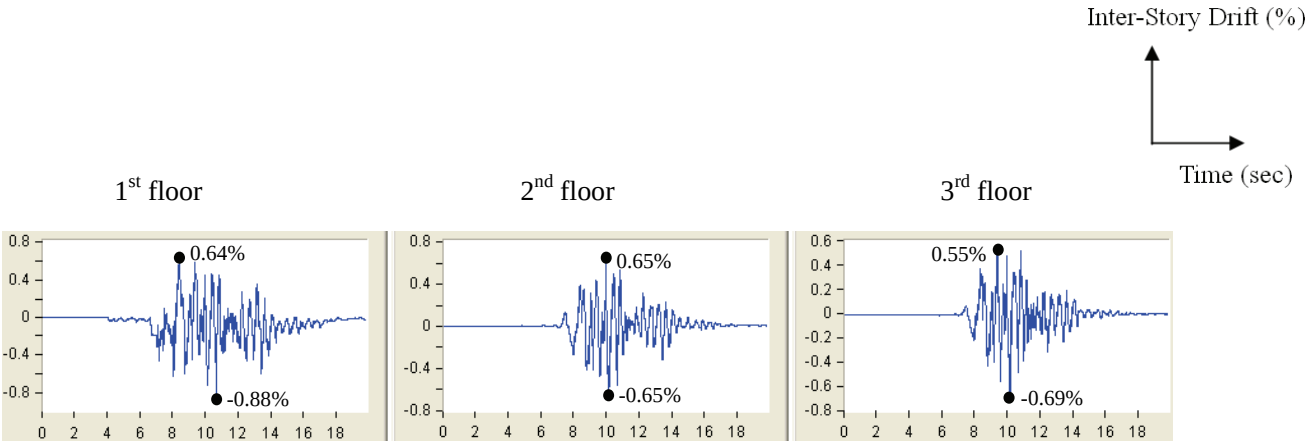

Inter-story Drift Time History of Test PER20

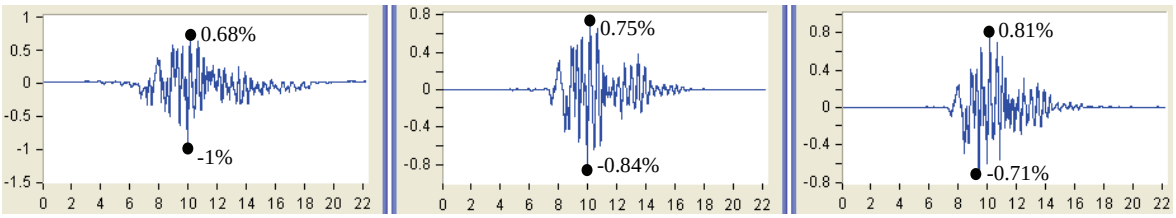

Inter-story Drift Time History of Test PE21

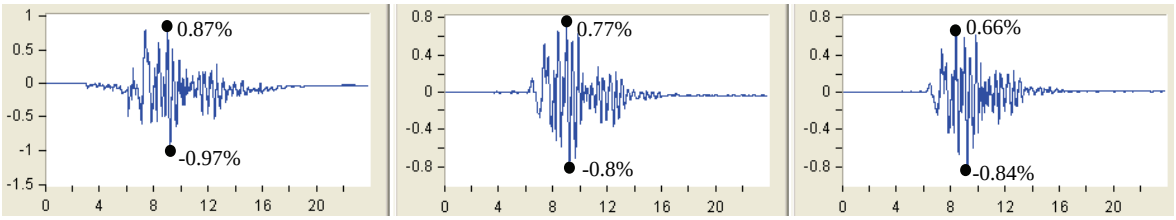

Inter-story Drift Time History of Test PER21

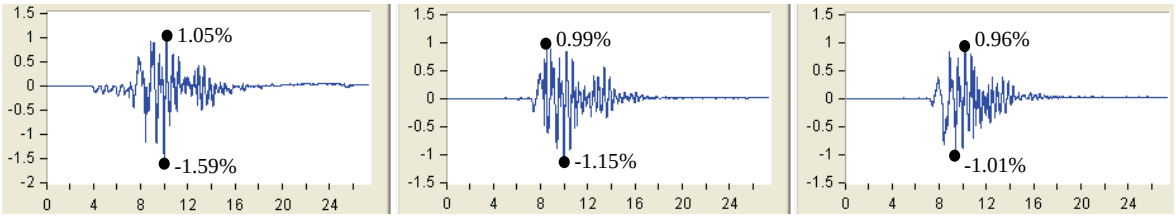

Inter-story Drift Time History of Test PE22

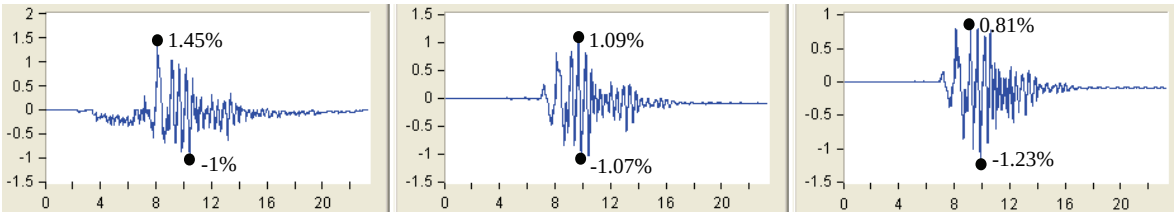

Inter-story Drift Time History of Test PER22

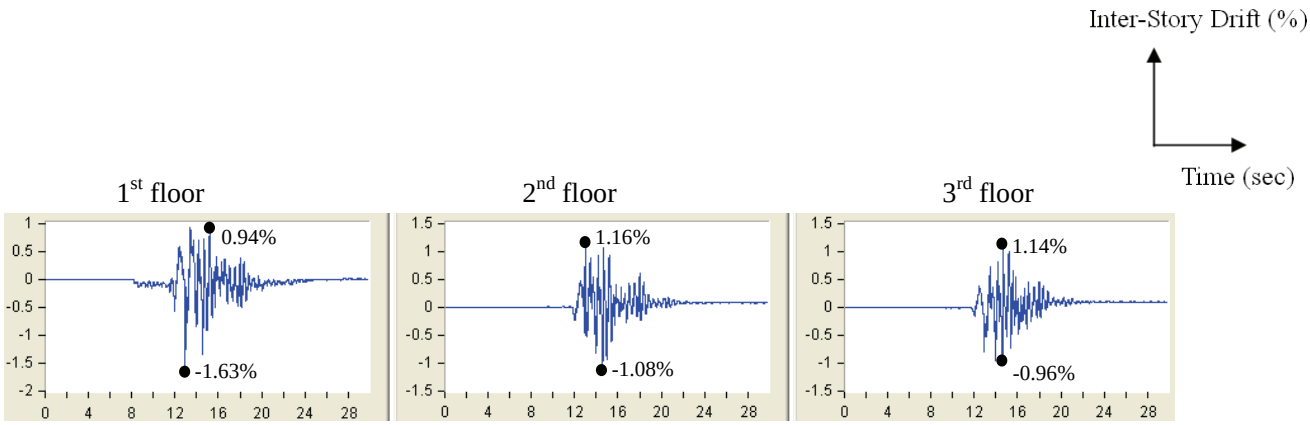

Inter-story Drift Time History of Test PE23

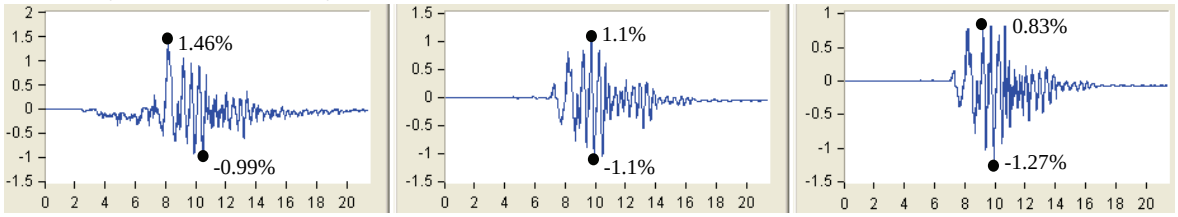

Inter-story Drift Time History of Test PER23

SMRF

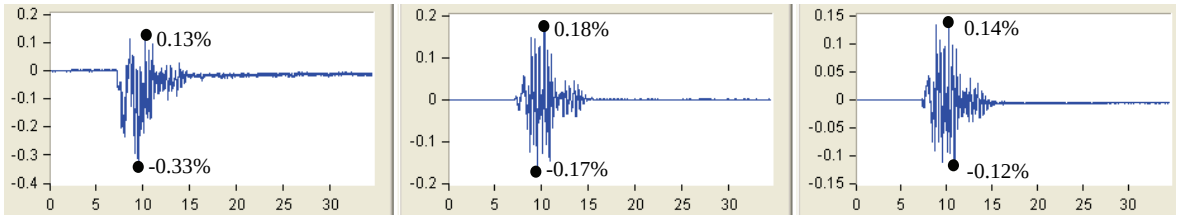

Inter-story Drift Time History of Test ME01

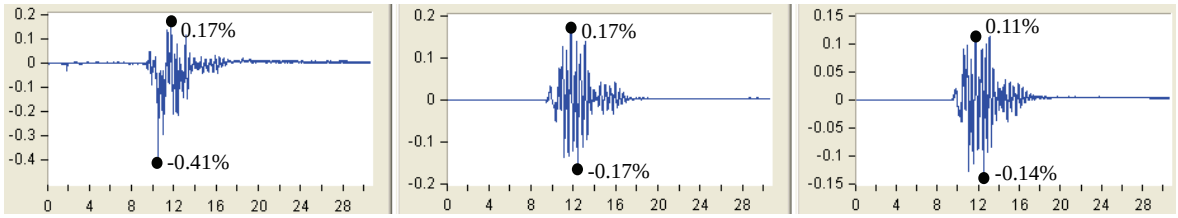

Inter-story Drift Time History of Test MER01

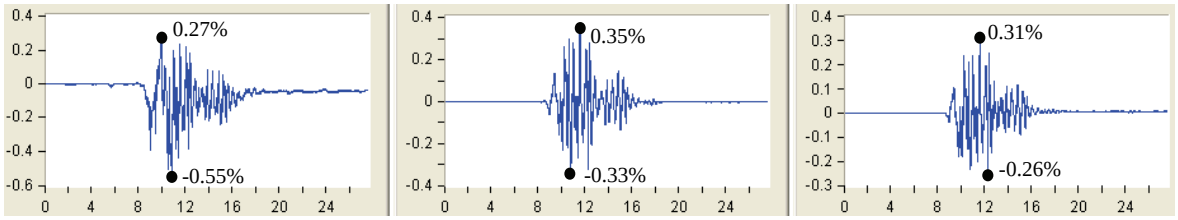

Inter-story Drift Time History of Test ME02

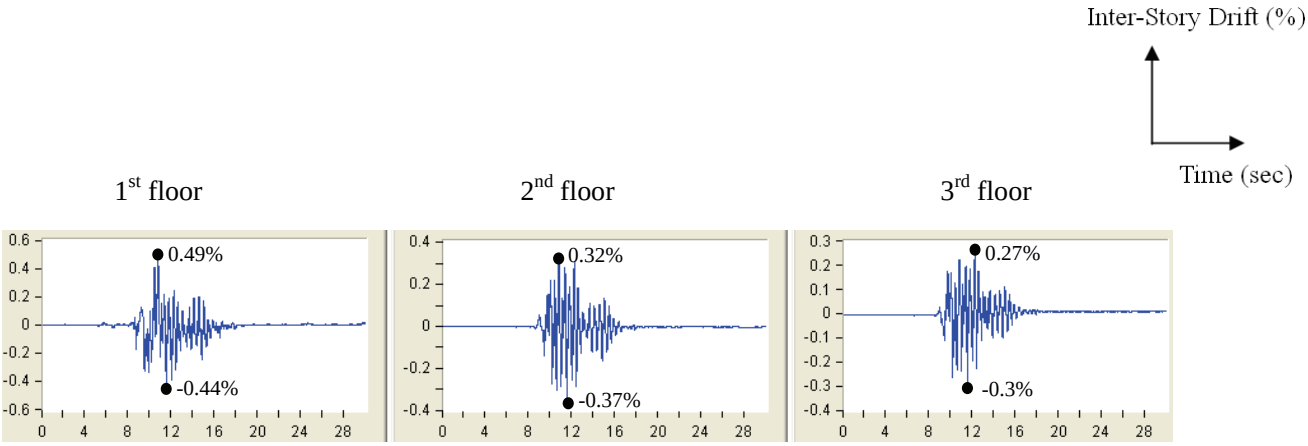

Inter-story Drift Time History of Test MER02A

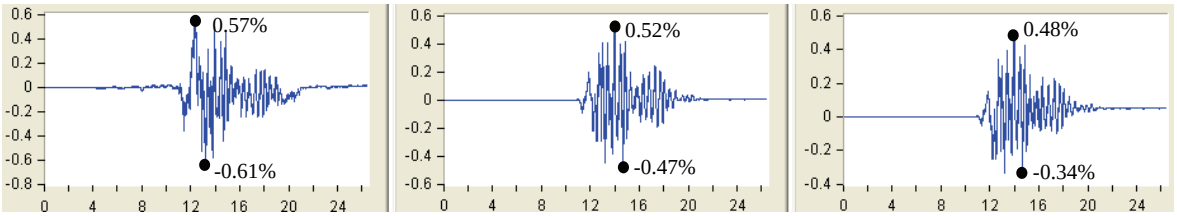

Inter-story Drift Time History of Test ME03

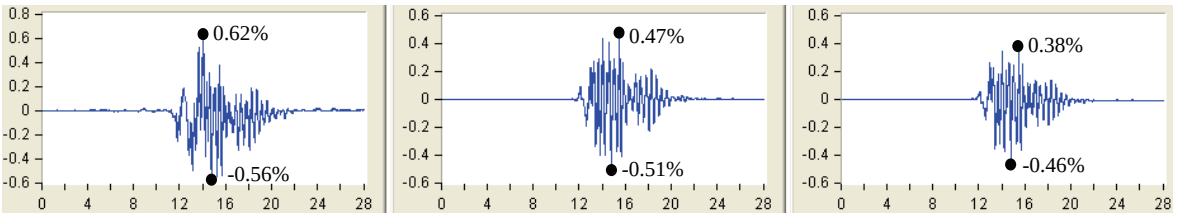

Inter-story Drift Time History of Test MER03

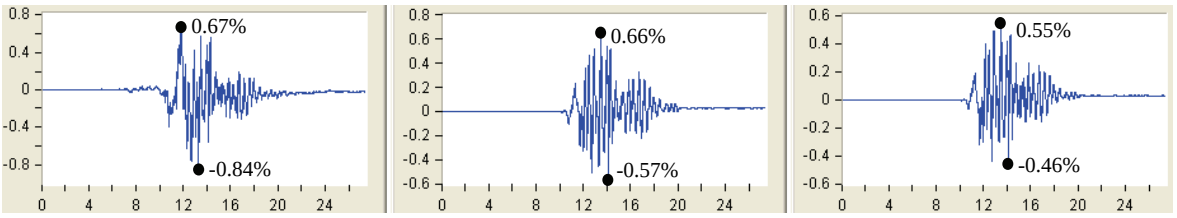

Inter-story Drift Time History of Test ME04

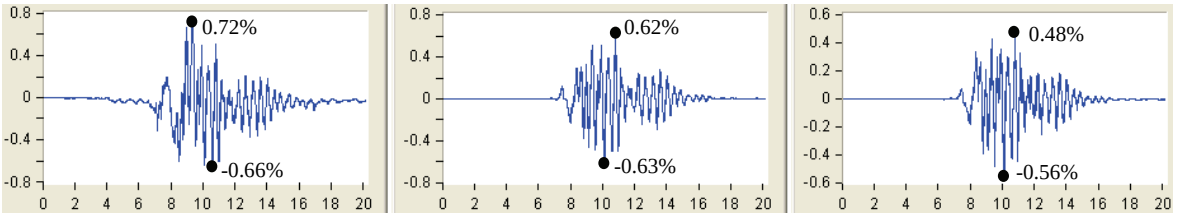

Inter-story Drift Time History of Test MER04

Inter-Story Drift (%)

Time (sec)

1st floor 2nd floor 3rd floor

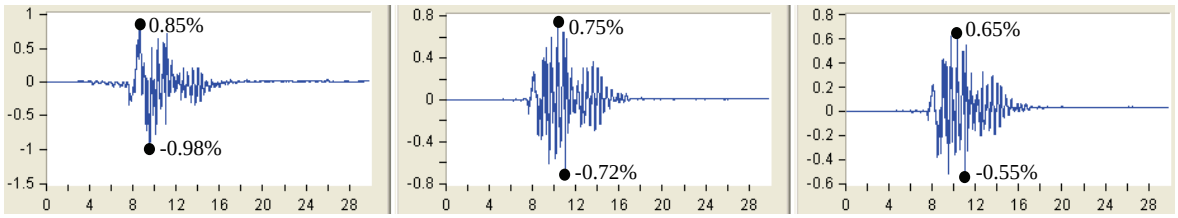

Inter-story Drift Time History of Test ME05

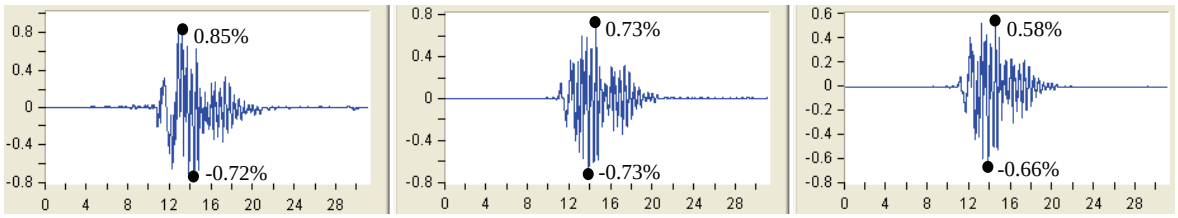

Inter-story Drift Time History of Test MER05

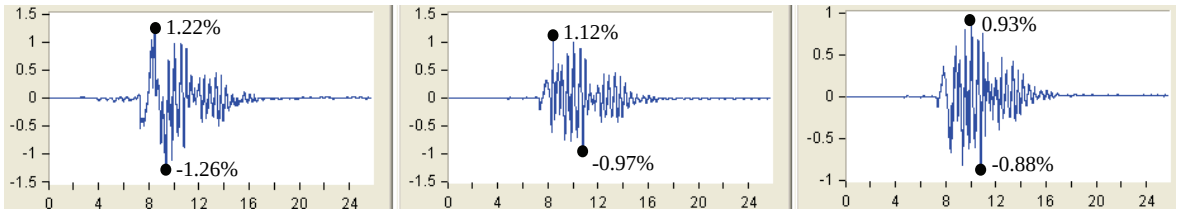

Inter-story Drift Time History of Test ME06A

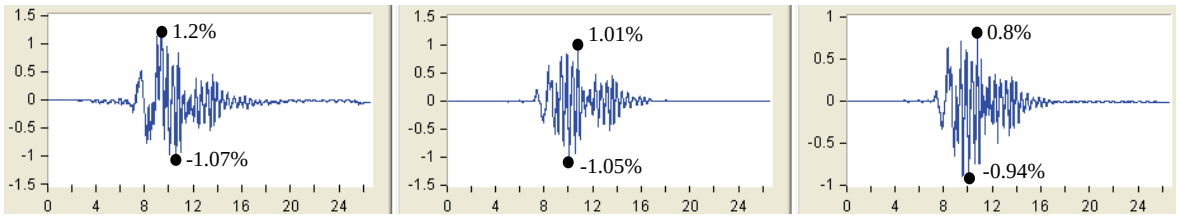

Inter-story Drift Time History of Test MER06

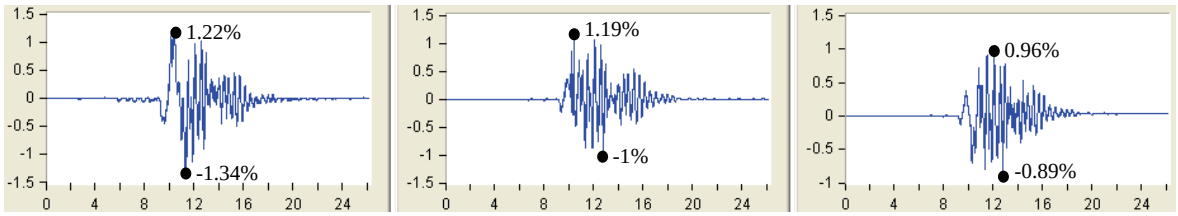

Inter-story Drift Time History of Test ME07

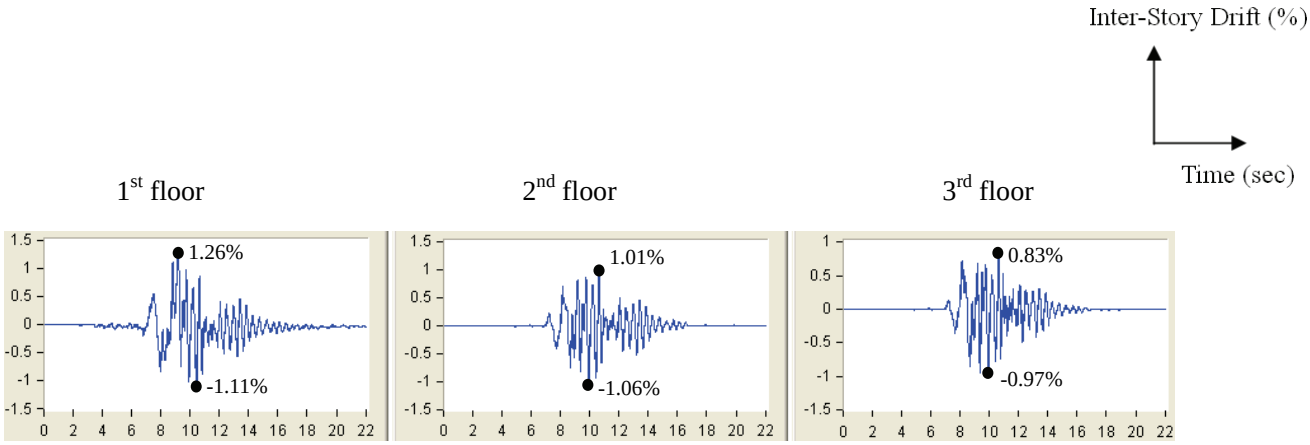

Inter-story Drift Time History of Test MER07

Appendix G Strain Time History of the SCPT and SMRF Models for 125% and 150%-Intesity Seismic Tests

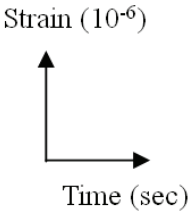

Note: In the following figures, the unit of strain is 10^{-6}.

SCPT

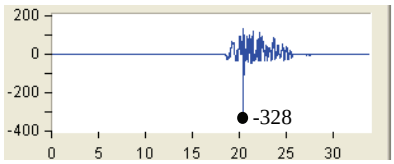

Beam in 1st floor

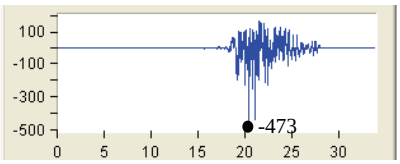

Beam in 2nd floor

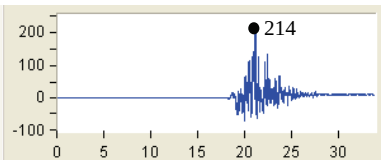

Beam in 3rd floor

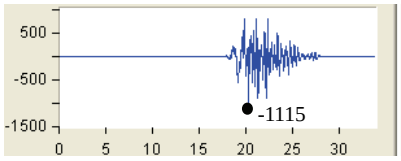

Left Exterior Base Column

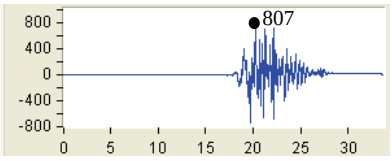

Center Base Column

Strains Time History for Test PE6A (125%)

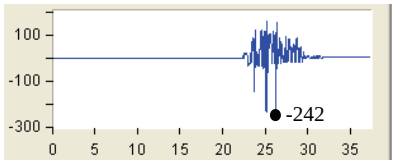

Beam in 1st floor

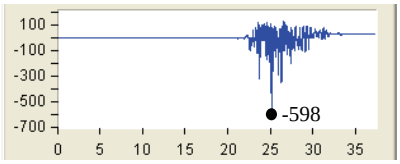

Beam in 2nd floor

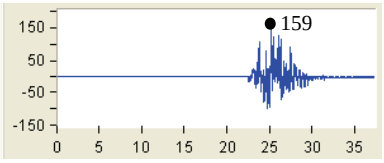

Beam in 3rd floor

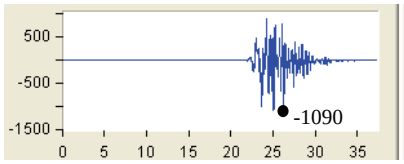

Left Exterior Base Column

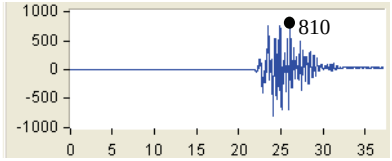

Center Base Column

Strains Time History for Test PER6 (-125%)

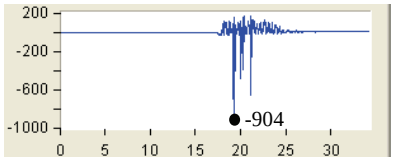

Beam in 1st floor

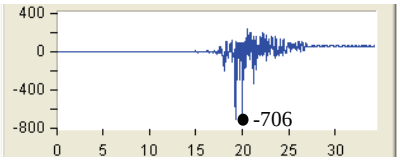

Beam in 2nd floor

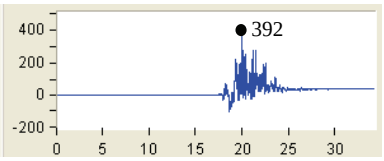

Beam in 3rd floor

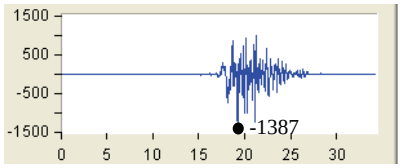

Left Exterior Base Column

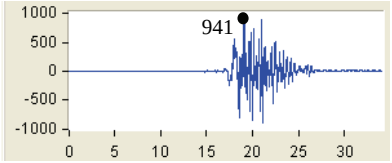

Center Base Column

Strains Time History for Test PE7A (150%)

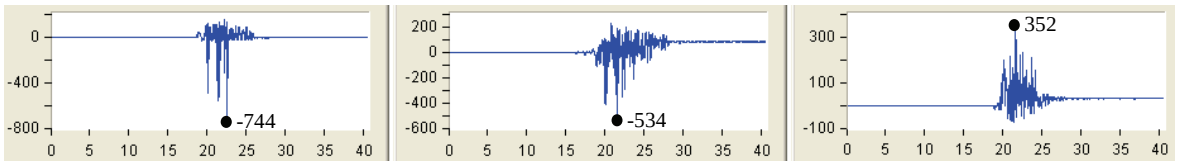

Beam in 1st floor Beam in 2nd floor Beam in 3rd floor

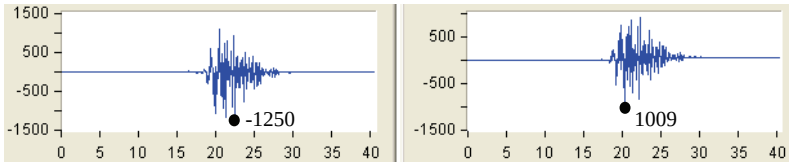

Left Exterior Base Column Center Base Column

Strains Time History for Test PER7 (-150%)

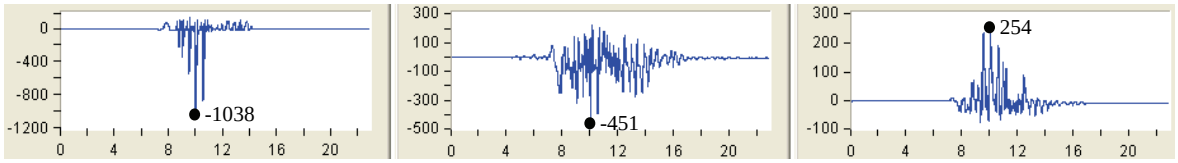

Beam in 1st floor Beam in 2nd floor Beam in 3rd floor

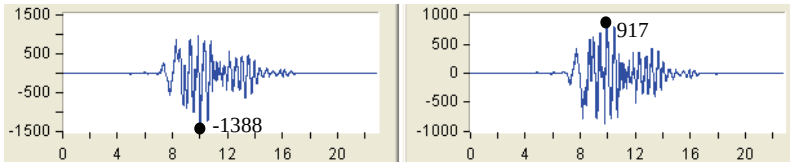

Left Exterior Base Column Center Base Column

Strains Time History for Test PE15 (125%)

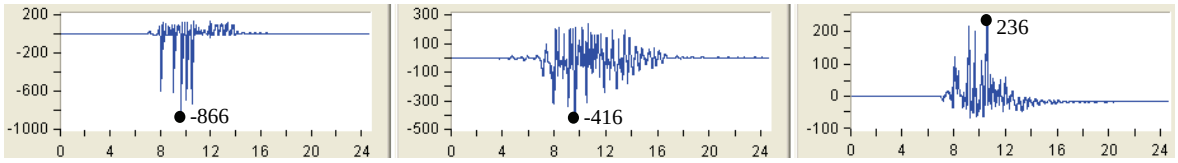

Beam in 1st floor Beam in 2nd floor Beam in 3rd floor

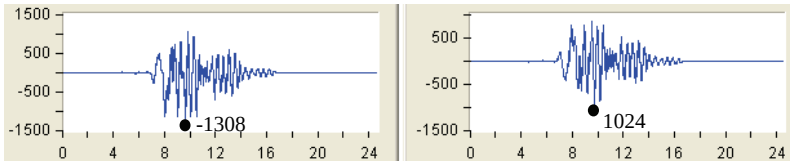

Left Exterior Base Column Center Base Column

Strains Time History for Test PER15 (-125%)

Strains Time History for Test PE16 (150%)

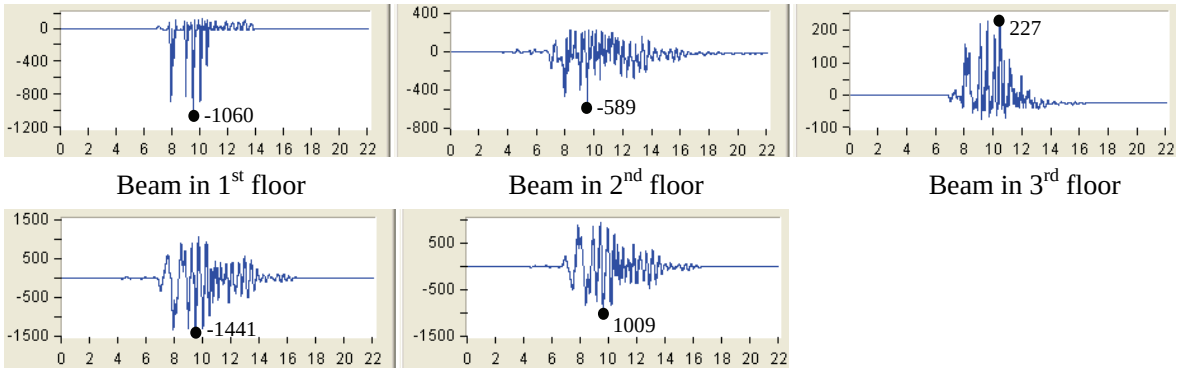

Strains Time History for Test PER16 (-150%)

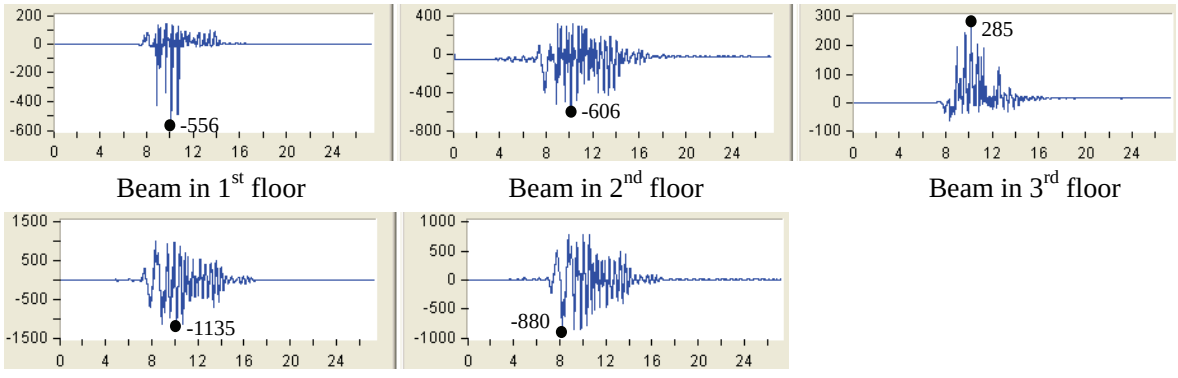

Strains Time History for Test PE22 (125%)

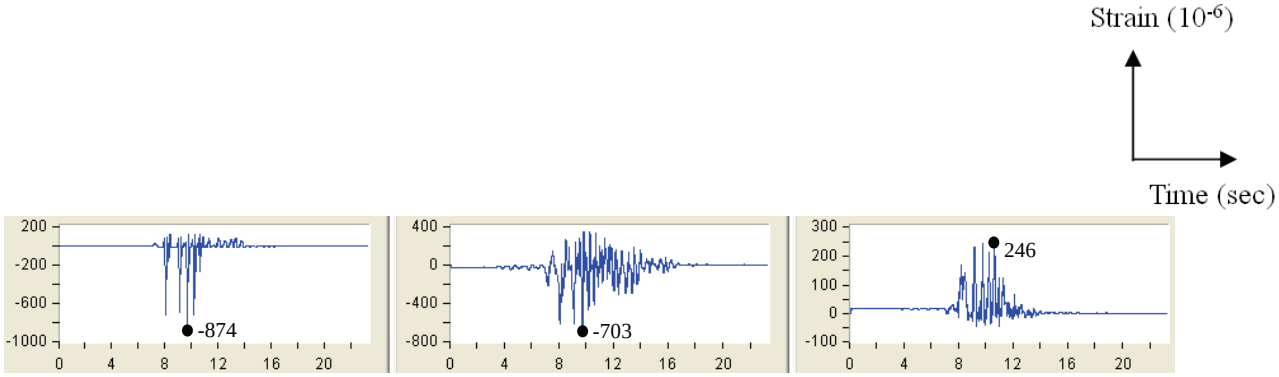

Beam in 1st floor | Beam in 2nd floor | Beam in 3rd floor

Left Exterior Base Column | Center Base Column

Strains Time History for Test PER22 (-125%)

Beam in 1st floor | Beam in 2nd floor | Beam in 3rd floor

Left Exterior Base Column | Center Base Column

Strains Time History for Test PE23 (150%)

Beam in 1st floor | Beam in 2nd floor | Beam in 3rd floor

Left Exterior Base Column | Center Base Column

Strains Time History for Test PER23 (-150%)

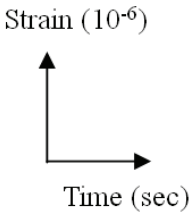

SMRF

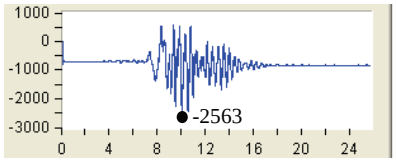

Beam in 1st floor

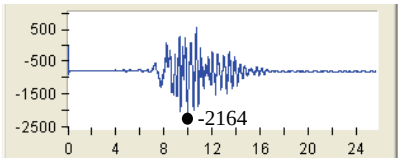

Beam in 2nd floor

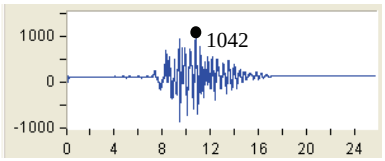

Beam in 3rd floor

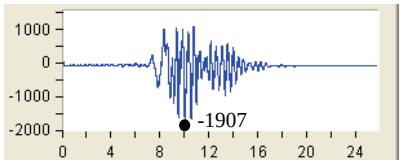

Left Exterior Base Column

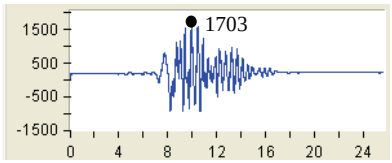

Center Base Column

Strains Time History for Test ME06A (125%)

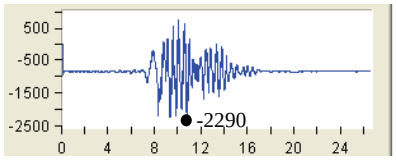

Beam in 1st floor

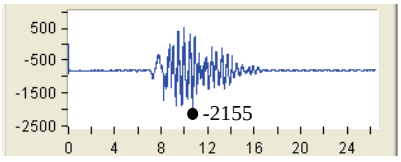

Beam in 2nd floor

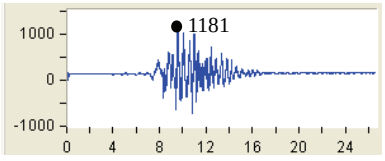

Beam in 3rd floor

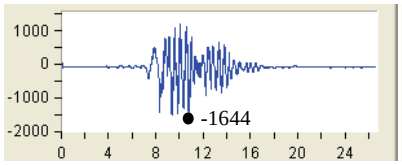

Left Exterior Base Column

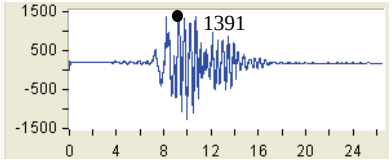

Center Base Column

Strains Time History for Test MER06 (-125%)

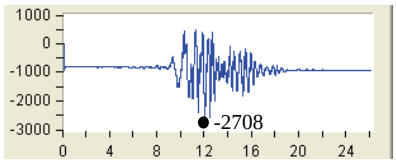

Beam in 1st floor

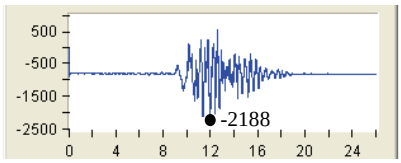

Beam in 2nd floor

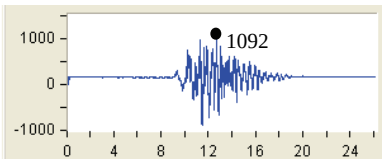

Beam in 3rd floor

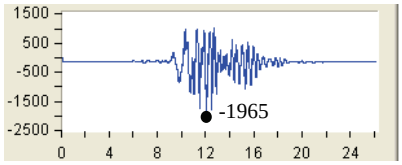

Left Exterior Base Column

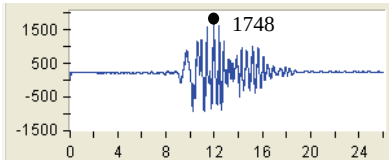

Center Base Column

Strains Time History for Test ME07 (150%)

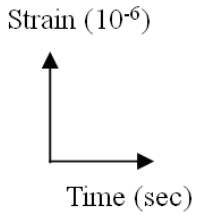

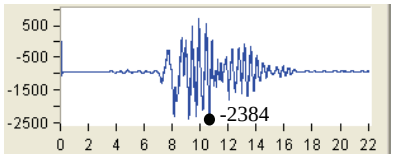

Beam in 1st floor

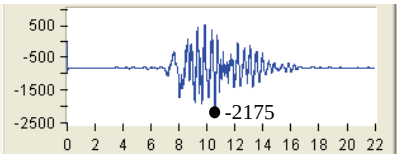

Beam in 2nd floor

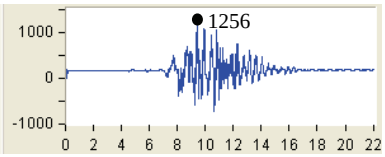

Beam in 3rd floor

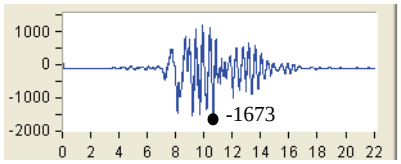

Left Exterior Base Column

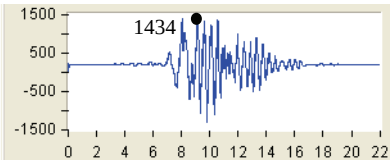

Center Base Column

Strains Time History for Test MER07 (-150%)

MCEER Technical Reports

MCEER publishes technical reports on a variety of subjects written by authors funded through MCEER. These reports are available from both MCEER Publications and the National Technical Information Service (NTIS). Requests for reports should be directed to MCEER Publications, MCEER, University at Buffalo, State University of New York, Red Jacket Quadrangle, Buffalo, New York 14261. Reports can also be requested through NTIS, 5285 Port Royal Road, Springfield, Virginia 22161. NTIS accession numbers are shown in parenthesis, if available.

NCEER-87-0001 "First-Year Program in Research, Education and Technology Transfer," 3/5/87, (PB88-134275, A04, MF-A01).

NCEER-87-0002 "Experimental Evaluation of Instantaneous Optimal Algorithms for Structural Control," by R.C. Lin, T.T. Soong and A.M. Reinhorn, 4/20/87, (PB88-134341, A04, MF-A01).

NCEER-87-0003 "Experimentation Using the Earthquake Simulation Facilities at University at Buffalo," by A.M. Reinhorn and R.L. Ketter, to be published.

NCEER-87-0004 "The System Characteristics and Performance of a Shaking Table," by J.S. Hwang, K.C. Chang and G.C. Lee, 6/1/87, (PB88-134259, A03, MF-A01). This report is available only through NTIS (see address given above).

NCEER-87-0005 "A Finite Element Formulation for Nonlinear Viscoplastic Material Using a Q Model," by O. Gyebi and G. Dasgupta, 11/2/87, (PB88-213764, A08, MF-A01).

NCEER-87-0006 "Symbolic Manipulation Program (SMP) - Algebraic Codes for Two and Three Dimensional Finite Element Formulations," by X. Lee and G. Dasgupta, 11/9/87, (PB88-218522, A05, MF-A01).

NCEER-87-0007 "Instantaneous Optimal Control Laws for Tall Buildings Under Seismic Excitations," by J.N. Yang, A. Akbarpour and P. Ghaemmaghami, 6/10/87, (PB88-134333, A06, MF-A01). This report is only available through NTIS (see address given above).

NCEER-87-0008 "IDARC: Inelastic Damage Analysis of Reinforced Concrete Frame - Shear-Wall Structures," by Y.J. Park, A.M. Reinhorn and S.K. Kunnath, 7/20/87, (PB88-134325, A09, MF-A01). This report is only available through NTIS (see address given above).

NCEER-87-0009 "Liquefaction Potential for New York State: A Preliminary Report on Sites in Manhattan and Buffalo," by M. Budhu, V. Vijayakumar, R.F. Giese and L. Baumgras, 8/31/87, (PB88-163704, A03, MF-A01). This report is available only through NTIS (see address given above).

NCEER-87-0010 "Vertical and Torsional Vibration of Foundations in Inhomogeneous Media," by A.S. Veletsos and K.W. Dotson, 6/1/87, (PB88-134291, A03, MF-A01). This report is only available through NTIS (see address given above).

NCEER-87-0011 "Seismic Probabilistic Risk Assessment and Seismic Margins Studies for Nuclear Power Plants," by Howard H.M. Hwang, 6/15/87, (PB88-134267, A03, MF-A01). This report is only available through NTIS (see address given above).

NCEER-87-0012 "Parametric Studies of Frequency Response of Secondary Systems Under Ground-Acceleration Excitations," by Y. Yong and Y.K. Lin, 6/10/87, (PB88-134309, A03, MF-A01). This report is only available through NTIS (see address given above).

NCEER-87-0013 "Frequency Response of Secondary Systems Under Seismic Excitation," by J.A. HoLung, J. Cai and Y.K. Lin, 7/31/87, (PB88-134317, A05, MF-A01). This report is only available through NTIS (see address given above).

NCEER-87-0014 "Modelling Earthquake Ground Motions in Seismically Active Regions Using Parametric Time Series Methods," by G.W. Ellis and A.S. Cakmak, 8/25/87, (PB88-134283, A08, MF-A01). This report is only available through NTIS (see address given above).

NCEER-87-0015 "Detection and Assessment of Seismic Structural Damage," by E. DiPasquale and A.S. Cakmak, 8/25/87, (PB88-163712, A05, MF-A01). This report is only available through NTIS (see address given above).

NCEER-87-0016 "Pipeline Experiment at Parkfield, California," by J. Isenberg and E. Richardson, 9/15/87, (PB88-163720, A03, MF-A01). This report is available only through NTIS (see address given above).

NCEER-87-0017 "Digital Simulation of Seismic Ground Motion," by M. Shinozuka, G. Deodatis and T. Harada, 8/31/87, (PB88-155197, A04, MF-A01). This report is available only through NTIS (see address given above).

NCEER-87-0018 "Practical Considerations for Structural Control: System Uncertainty, System Time Delay and Truncation of Small Control Forces," J.N. Yang and A. Akbarpour, 8/10/87, (PB88-163738, A08, MF-A01). This report is only available through NTIS (see address given above).

NCEER-87-0019 "Modal Analysis of Nonclassically Damped Structural Systems Using Canonical Transformation," by J.N. Yang, S. Sarkani and F.X. Long, 9/27/87, (PB88-187851, A04, MF-A01).

NCEER-87-0020 "A Nonstationary Solution in Random Vibration Theory," by J.R. Red-Horse and P.D. Spanos, 11/3/87, (PB88-163746, A03, MF-A01).

NCEER-87-0021 "Horizontal Impedances for Radially Inhomogeneous Viscoelastic Soil Layers," by A.S. Veletsos and K.W. Dotson, 10/15/87, (PB88-150859, A04, MF-A01).

NCEER-87-0022 "Seismic Damage Assessment of Reinforced Concrete Members," by Y.S. Chung, C. Meyer and M. Shinozuka, 10/9/87, (PB88-150867, A05, MF-A01). This report is available only through NTIS (see address given above).

NCEER-87-0023 "Active Structural Control in Civil Engineering," by T.T. Soong, 11/11/87, (PB88-187778, A03, MF-A01).

NCEER-87-0024 "Vertical and Torsional Impedances for Radially Inhomogeneous Viscoelastic Soil Layers," by K.W. Dotson and A.S. Veletsos, 12/87, (PB88-187786, A03, MF-A01).

NCEER-87-0025 "Proceedings from the Symposium on Seismic Hazards, Ground Motions, Soil-Liquefaction and Engineering Practice in Eastern North America," October 20-22, 1987, edited by K.H. Jacob, 12/87, (PB88-188115, A23, MF-A01). This report is available only through NTIS (see address given above).

NCEER-87-0026 "Report on the Whittier-Narrows, California, Earthquake of October 1, 1987," by J. Pantelic and A. Reinhorn, 11/87, (PB88-187752, A03, MF-A01). This report is available only through NTIS (see address given above).

NCEER-87-0027 "Design of a Modular Program for Transient Nonlinear Analysis of Large 3-D Building Structures," by S. Srivastav and J.F. Abel, 12/30/87, (PB88-187950, A05, MF-A01). This report is only available through NTIS (see address given above).

NCEER-87-0028 "Second-Year Program in Research, Education and Technology Transfer," 3/8/88, (PB88-219480, A04, MF-A01).

NCEER-88-0001 "Workshop on Seismic Computer Analysis and Design of Buildings With Interactive Graphics," by W. McGuire, J.F. Abel and C.H. Conley, 1/18/88, (PB88-187760, A03, MF-A01). This report is only available through NTIS (see address given above).

NCEER-88-0002 "Optimal Control of Nonlinear Flexible Structures," by J.N. Yang, F.X. Long and D. Wong, 1/22/88, (PB88-213772, A06, MF-A01).

NCEER-88-0003 "Substructuring Techniques in the Time Domain for Primary-Secondary Structural Systems," by G.D. Manolis and G. Juhn, 2/10/88, (PB88-213780, A04, MF-A01).

NCEER-88-0004 "Iterative Seismic Analysis of Primary-Secondary Systems," by A. Singhal, L.D. Lutes and P.D. Spanos, 2/23/88, (PB88-213798, A04, MF-A01).

NCEER-88-0005 "Stochastic Finite Element Expansion for Random Media," by P.D. Spanos and R. Ghanem, 3/14/88, (PB88-213806, A03, MF-A01).

NCEER-88-0006 "Combining Structural Optimization and Structural Control," by F.Y. Cheng and C.P. Pantelides, 1/10/88, (PB88-213814, A05, MF-A01).

NCEER-88-0007 "Seismic Performance Assessment of Code-Designed Structures," by H.H-M. Hwang, J-W. Jaw and H-J. Shau, 3/20/88, (PB88-219423, A04, MF-A01). This report is only available through NTIS (see address given above).

NCEER-88-0008 "Reliability Analysis of Code-Designed Structures Under Natural Hazards," by H.H-M. Hwang, H. Ushiba and M. Shinozuka, 2/29/88, (PB88-229471, A07, MF-A01). This report is only available through NTIS (see address given above).

NCEER-88-0009 "Seismic Fragility Analysis of Shear Wall Structures," by J-W Jaw and H.H-M. Hwang, 4/30/88, (PB89-102867, A04, MF-A01).

NCEER-88-0010 "Base Isolation of a Multi-Story Building Under a Harmonic Ground Motion - A Comparison of Performances of Various Systems," by F-G Fan, G. Ahmadi and I.G. Tadjbakhsh, 5/18/88, (PB89-122238, A06, MF-A01). This report is only available through NTIS (see address given above).

NCEER-88-0011 "Seismic Floor Response Spectra for a Combined System by Green's Functions," by F.M. Lavelle, L.A. Bergman and P.D. Spanos, 5/1/88, (PB89-102875, A03, MF-A01).

NCEER-88-0012 "A New Solution Technique for Randomly Excited Hysteretic Structures," by G.Q. Cai and Y.K. Lin, 5/16/88, (PB89-102883, A03, MF-A01).

NCEER-88-0013 "A Study of Radiation Damping and Soil-Structure Interaction Effects in the Centrifuge," by K. Weissman, supervised by J.H. Prevost, 5/24/88, (PB89-144703, A06, MF-A01).

NCEER-88-0014 "Parameter Identification and Implementation of a Kinematic Plasticity Model for Frictional Soils," by J.H. Prevost and D.V. Griffiths, to be published.

NCEER-88-0015 "Two- and Three- Dimensional Dynamic Finite Element Analyses of the Long Valley Dam," by D.V. Griffiths and J.H. Prevost, 6/17/88, (PB89-144711, A04, MF-A01).

NCEER-88-0016 "Damage Assessment of Reinforced Concrete Structures in Eastern United States," by A.M. Reinhorn, M.J. Seidel, S.K. Kunnath and Y.J. Park, 6/15/88, (PB89-122220, A04, MF-A01). This report is only available through NTIS (see address given above).

NCEER-88-0017 "Dynamic Compliance of Vertically Loaded Strip Foundations in Multilayered Viscoelastic Soils," by S. Ahmad and A.S.M. Israil, 6/17/88, (PB89-102891, A04, MF-A01).

NCEER-88-0018 "An Experimental Study of Seismic Structural Response With Added Viscoelastic Dampers," by R.C. Lin, Z. Liang, T.T. Soong and R.H. Zhang, 6/30/88, (PB89-122212, A05, MF-A01). This report is available only through NTIS (see address given above).

NCEER-88-0019 "Experimental Investigation of Primary - Secondary System Interaction," by G.D. Manolis, G. Juhn and A.M. Reinhorn, 5/27/88, (PB89-122204, A04, MF-A01).

NCEER-88-0020 "A Response Spectrum Approach For Analysis of Nonclassically Damped Structures," by J.N. Yang, S. Sarkani and F.X. Long, 4/22/88, (PB89-102909, A04, MF-A01).

NCEER-88-0021 "Seismic Interaction of Structures and Soils: Stochastic Approach," by A.S. Veletsos and A.M. Prasad, 7/21/88, (PB89-122196, A04, MF-A01). This report is only available through NTIS (see address given above).

NCEER-88-0022 "Identification of the Serviceability Limit State and Detection of Seismic Structural Damage," by E. DiPasquale and A.S. Cakmak, 6/15/88, (PB89-122188, A05, MF-A01). This report is available only through NTIS (see address given above).

NCEER-88-0023 "Multi-Hazard Risk Analysis: Case of a Simple Offshore Structure," by B.K. Bhartia and E.H. Vanmarcke, 7/21/88, (PB89-145213, A05, MF-A01).

NCEER-88-0024 "Automated Seismic Design of Reinforced Concrete Buildings," by Y.S. Chung, C. Meyer and M. Shinozuka, 7/5/88, (PB89-122170, A06, MF-A01). This report is available only through NTIS (see address given above).

NCEER-88-0025 "Experimental Study of Active Control of MDOF Structures Under Seismic Excitations," by L.L. Chung, R.C. Lin, T.T. Soong and A.M. Reinhorn, 7/10/88, (PB89-122600, A04, MF-A01).

NCEER-88-0026 "Earthquake Simulation Tests of a Low-Rise Metal Structure," by J.S. Hwang, K.C. Chang, G.C. Lee and R.L. Ketter, 8/1/88, (PB89-102917, A04, MF-A01).

NCEER-88-0027 "Systems Study of Urban Response and Reconstruction Due to Catastrophic Earthquakes," by F. Kozin and H.K. Zhou, 9/22/88, (PB90-162348, A04, MF-A01).

NCEER-88-0028 "Seismic Fragility Analysis of Plane Frame Structures," by H.H-M. Hwang and Y.K. Low, 7/31/88, (PB89-131445, A06, MF-A01).

NCEER-88-0029 "Response Analysis of Stochastic Structures," by A. Kardara, C. Bucher and M. Shinozuka, 9/22/88, (PB89-174429, A04, MF-A01).

NCEER-88-0030 "Nonnormal Accelerations Due to Yielding in a Primary Structure," by D.C.K. Chen and L.D. Lutes, 9/19/88, (PB89-131437, A04, MF-A01).

NCEER-88-0031 "Design Approaches for Soil-Structure Interaction," by A.S. Veletsos, A.M. Prasad and Y. Tang, 12/30/88, (PB89-174437, A03, MF-A01). This report is available only through NTIS (see address given above).

NCEER-88-0032 "A Re-evaluation of Design Spectra for Seismic Damage Control," by C.J. Turkstra and A.G. Tallin, 11/7/88, (PB89-145221, A05, MF-A01).

NCEER-88-0033 "The Behavior and Design of Noncontact Lap Splices Subjected to Repeated Inelastic Tensile Loading," by V.E. Sagan, P. Gergely and R.N. White, 12/8/88, (PB89-163737, A08, MF-A01).

NCEER-88-0034 "Seismic Response of Pile Foundations," by S.M. Mamoon, P.K. Banerjee and S. Ahmad, 11/1/88, (PB89-145239, A04, MF-A01).

NCEER-88-0035 "Modeling of R/C Building Structures With Flexible Floor Diaphragms (IDARC2)," by A.M. Reinhorn, S.K. Kunnath and N. Panahshahi, 9/7/88, (PB89-207153, A07, MF-A01).

NCEER-88-0036 "Solution of the Dam-Reservoir Interaction Problem Using a Combination of FEM, BEM with Particular Integrals, Modal Analysis, and Substructuring," by C-S. Tsai, G.C. Lee and R.L. Ketter, 12/31/88, (PB89-207146, A04, MF-A01).

NCEER-88-0037 "Optimal Placement of Actuators for Structural Control," by F.Y. Cheng and C.P. Pantelides, 8/15/88, (PB89-162846, A05, MF-A01).

NCEER-88-0038 "Teflon Bearings in Aseismic Base Isolation: Experimental Studies and Mathematical Modeling," by A. Mokha, M.C. Constantinou and A.M. Reinhorn, 12/5/88, (PB89-218457, A10, MF-A01). This report is available only through NTIS (see address given above).

NCEER-88-0039 "Seismic Behavior of Flat Slab High-Rise Buildings in the New York City Area," by P. Weidlinger and M. Ettouney, 10/15/88, (PB90-145681, A04, MF-A01).

NCEER-88-0040 "Evaluation of the Earthquake Resistance of Existing Buildings in New York City," by P. Weidlinger and M. Ettouney, 10/15/88, to be published.

NCEER-88-0041 "Small-Scale Modeling Techniques for Reinforced Concrete Structures Subjected to Seismic Loads," by W. Kim, A. El-Attar and R.N. White, 11/22/88, (PB89-189625, A05, MF-A01).

NCEER-88-0042 "Modeling Strong Ground Motion from Multiple Event Earthquakes," by G.W. Ellis and A.S. Cakmak, 10/15/88, (PB89-174445, A03, MF-A01).

NCEER-88-0043 "Nonstationary Models of Seismic Ground Acceleration," by M. Grigoriu, S.E. Ruiz and E. Rosenblueth, 7/15/88, (PB89-189617, A04, MF-A01).

NCEER-88-0044 "SARCF User's Guide: Seismic Analysis of Reinforced Concrete Frames," by Y.S. Chung, C. Meyer and M. Shinozuka, 11/9/88, (PB89-174452, A08, MF-A01).

NCEER-88-0045 "First Expert Panel Meeting on Disaster Research and Planning," edited by J. Pantelic and J. Stoyle, 9/15/88, (PB89-174460, A05, MF-A01).

NCEER-88-0046 "Preliminary Studies of the Effect of Degrading Infill Walls on the Nonlinear Seismic Response of Steel Frames," by C.Z. Chrysostomou, P. Gergely and J.F. Abel, 12/19/88, (PB89-208383, A05, MF-A01).

NCEER-88-0047 "Reinforced Concrete Frame Component Testing Facility - Design, Construction, Instrumentation and Operation," by S.P. Pessiki, C. Conley, T. Bond, P. Gergely and R.N. White, 12/16/88, (PB89-174478, A04, MF-A01).

NCEER-89-0001 "Effects of Protective Cushion and Soil Compliancy on the Response of Equipment Within a Seismically Excited Building," by J.A. HoLung, 2/16/89, (PB89-207179, A04, MF-A01).

NCEER-89-0002 "Statistical Evaluation of Response Modification Factors for Reinforced Concrete Structures," by H.H-M. Hwang and J-W. Jaw, 2/17/89, (PB89-207187, A05, MF-A01).

NCEER-89-0003 "Hysteretic Columns Under Random Excitation," by G-Q. Cai and Y.K. Lin, 1/9/89, (PB89-196513, A03, MF-A01).

NCEER-89-0004 "Experimental Study of `Elephant Foot Bulge' Instability of Thin-Walled Metal Tanks," by Z-H. Jia and R.L. Ketter, 2/22/89, (PB89-207195, A03, MF-A01).

NCEER-89-0005 "Experiment on Performance of Buried Pipelines Across San Andreas Fault," by J. Isenberg, E. Richardson and T.D. O'Rourke, 3/10/89, (PB89-218440, A04, MF-A01). This report is available only through NTIS (see address given above).

NCEER-89-0006 "A Knowledge-Based Approach to Structural Design of Earthquake-Resistant Buildings," by M. Subramani, P. Gergely, C.H. Conley, J.F. Abel and A.H. Zaghw, 1/15/89, (PB89-218465, A06, MF-A01).

NCEER-89-0007 "Liquefaction Hazards and Their Effects on Buried Pipelines," by T.D. O'Rourke and P.A. Lane, 2/1/89, (PB89-218481, A09, MF-A01).

NCEER-89-0008 "Fundamentals of System Identification in Structural Dynamics," by H. Imai, C-B. Yun, O. Maruyama and M. Shinozuka, 1/26/89, (PB89-207211, A04, MF-A01).

NCEER-89-0009 "Effects of the 1985 Michoacan Earthquake on Water Systems and Other Buried Lifelines in Mexico," by A.G. Ayala and M.J. O'Rourke, 3/8/89, (PB89-207229, A06, MF-A01).

NCEER-89-R010 "NCEER Bibliography of Earthquake Education Materials," by K.E.K. Ross, Second Revision, 9/1/89, (PB90-125352, A05, MF-A01). This report is replaced by NCEER-92-0018.

NCEER-89-0011 "Inelastic Three-Dimensional Response Analysis of Reinforced Concrete Building Structures (IDARC-3D), Part I - Modeling," by S.K. Kunnath and A.M. Reinhorn, 4/17/89, (PB90-114612, A07, MF-A01). This report is available only through NTIS (see address given above).

NCEER-89-0012 "Recommended Modifications to ATC-14," by C.D. Poland and J.O. Malley, 4/12/89, (PB90-108648, A15, MF-A01).

NCEER-89-0013 "Repair and Strengthening of Beam-to-Column Connections Subjected to Earthquake Loading," by M. Corazao and A.J. Durrani, 2/28/89, (PB90-109885, A06, MF-A01).

NCEER-89-0014 "Program EXKAL2 for Identification of Structural Dynamic Systems," by O. Maruyama, C-B. Yun, M. Hoshiya and M. Shinozuka, 5/19/89, (PB90-109877, A09, MF-A01).

NCEER-89-0015 "Response of Frames With Bolted Semi-Rigid Connections, Part I - Experimental Study and Analytical Predictions," by P.J. DiCorso, A.M. Reinhorn, J.R. Dickerson, J.B. Radziminski and W.L. Harper, 6/1/89, to be published.

NCEER-89-0016 "ARMA Monte Carlo Simulation in Probabilistic Structural Analysis," by P.D. Spanos and M.P. Mignolet, 7/10/89, (PB90-109893, A03, MF-A01).

NCEER-89-P017 "Preliminary Proceedings from the Conference on Disaster Preparedness - The Place of Earthquake Education in Our Schools," Edited by K.E.K. Ross, 6/23/89, (PB90-108606, A03, MF-A01).

NCEER-89-0017 "Proceedings from the Conference on Disaster Preparedness - The Place of Earthquake Education in Our Schools," Edited by K.E.K. Ross, 12/31/89, (PB90-207895, A012, MF-A02). This report is available only through NTIS (see address given above).

NCEER-89-0018 "Multidimensional Models of Hysteretic Material Behavior for Vibration Analysis of Shape Memory Energy Absorbing Devices, by E.J. Graesser and F.A. Cozzarelli, 6/7/89, (PB90-164146, A04, MF-A01).

NCEER-89-0019 "Nonlinear Dynamic Analysis of Three-Dimensional Base Isolated Structures (3D-BASIS)," by S. Nagarajaiah, A.M. Reinhorn and M.C. Constantinou, 8/3/89, (PB90-161936, A06, MF-A01). This report has been replaced by NCEER-93-0011.

NCEER-89-0020 "Structural Control Considering Time-Rate of Control Forces and Control Rate Constraints," by F.Y. Cheng and C.P. Pantelides, 8/3/89, (PB90-120445, A04, MF-A01).

NCEER-89-0021 "Subsurface Conditions of Memphis and Shelby County," by K.W. Ng, T-S. Chang and H-H.M. Hwang, 7/26/89, (PB90-120437, A03, MF-A01).

NCEER-89-0022 "Seismic Wave Propagation Effects on Straight Jointed Buried Pipelines," by K. Elhmadi and M.J. O'Rourke, 8/24/89, (PB90-162322, A10, MF-A02).

NCEER-89-0023 "Workshop on Serviceability Analysis of Water Delivery Systems," edited by M. Grigoriu, 3/6/89, (PB90-127424, A03, MF-A01).

NCEER-89-0024 "Shaking Table Study of a 1/5 Scale Steel Frame Composed of Tapered Members," by K.C. Chang, J.S. Hwang and G.C. Lee, 9/18/89, (PB90-160169, A04, MF-A01).

NCEER-89-0025 "DYNA1D: A Computer Program for Nonlinear Seismic Site Response Analysis - Technical Documentation," by Jean H. Prevost, 9/14/89, (PB90-161944, A07, MF-A01). This report is available only through NTIS (see address given above).

NCEER-89-0026 "1:4 Scale Model Studies of Active Tendon Systems and Active Mass Dampers for Aseismic Protection," by A.M. Reinhorn, T.T. Soong, R.C. Lin, Y.P. Yang, Y. Fukao, H. Abe and M. Nakai, 9/15/89, (PB90-173246, A10, MF-A02). This report is available only through NTIS (see address given above).

NCEER-89-0027 "Scattering of Waves by Inclusions in a Nonhomogeneous Elastic Half Space Solved by Boundary Element Methods," by P.K. Hadley, A. Askar and A.S. Cakmak, 6/15/89, (PB90-145699, A07, MF-A01).

NCEER-89-0028 "Statistical Evaluation of Deflection Amplification Factors for Reinforced Concrete Structures," by H.H.M. Hwang, J-W. Jaw and A.L. Ch'ng, 8/31/89, (PB90-164633, A05, MF-A01).

NCEER-89-0029 "Bedrock Accelerations in Memphis Area Due to Large New Madrid Earthquakes," by H.H.M. Hwang, C.H.S. Chen and G. Yu, 11/7/89, (PB90-162330, A04, MF-A01).

NCEER-89-0030 "Seismic Behavior and Response Sensitivity of Secondary Structural Systems," by Y.Q. Chen and T.T. Soong, 10/23/89, (PB90-164658, A08, MF-A01).

NCEER-89-0031 "Random Vibration and Reliability Analysis of Primary-Secondary Structural Systems," by Y. Ibrahim, M. Grigoriu and T.T. Soong, 11/10/89, (PB90-161951, A04, MF-A01).

NCEER-89-0032 "Proceedings from the Second U.S. - Japan Workshop on Liquefaction, Large Ground Deformation and Their Effects on Lifelines, September 26-29, 1989," Edited by T.D. O'Rourke and M. Hamada, 12/1/89, (PB90-209388, A22, MF-A03).

NCEER-89-0033 "Deterministic Model for Seismic Damage Evaluation of Reinforced Concrete Structures," by J.M. Bracci, A.M. Reinhorn, J.B. Mander and S.K. Kunnath, 9/27/89, (PB91-108803, A06, MF-A01).

NCEER-89-0034 "On the Relation Between Local and Global Damage Indices," by E. DiPasquale and A.S. Cakmak, 8/15/89, (PB90-173865, A05, MF-A01).

NCEER-89-0035 "Cyclic Undrained Behavior of Nonplastic and Low Plasticity Silts," by A.J. Walker and H.E. Stewart, 7/26/89, (PB90-183518, A10, MF-A01).

NCEER-89-0036 "Liquefaction Potential of Surficial Deposits in the City of Buffalo, New York," by M. Budhu, R. Giese and L. Baumgrass, 1/17/89, (PB90-208455, A04, MF-A01).

NCEER-89-0037 "A Deterministic Assessment of Effects of Ground Motion Incoherence," by A.S. Veletsos and Y. Tang, 7/15/89, (PB90-164294, A03, MF-A01).

NCEER-89-0038 "Workshop on Ground Motion Parameters for Seismic Hazard Mapping," July 17-18, 1989, edited by R.V. Whitman, 12/1/89, (PB90-173923, A04, MF-A01).

NCEER-89-0039 "Seismic Effects on Elevated Transit Lines of the New York City Transit Authority," by C.J. Costantino, C.A. Miller and E. Heymsfield, 12/26/89, (PB90-207887, A06, MF-A01).

NCEER-89-0040 "Centrifugal Modeling of Dynamic Soil-Structure Interaction," by K. Weissman, Supervised by J.H. Prevost, 5/10/89, (PB90-207879, A07, MF-A01).

NCEER-89-0041 "Linearized Identification of Buildings With Cores for Seismic Vulnerability Assessment," by I-K. Ho and A.E. Aktan, 11/1/89, (PB90-251943, A07, MF-A01).

NCEER-90-0001 "Geotechnical and Lifeline Aspects of the October 17, 1989 Loma Prieta Earthquake in San Francisco," by T.D. O'Rourke, H.E. Stewart, F.T. Blackburn and T.S. Dickerman, 1/90, (PB90-208596, A05, MF-A01).

NCEER-90-0002 "Nonnormal Secondary Response Due to Yielding in a Primary Structure," by D.C.K. Chen and L.D. Lutes, 2/28/90, (PB90-251976, A07, MF-A01).

NCEER-90-0003 "Earthquake Education Materials for Grades K-12," by K.E.K. Ross, 4/16/90, (PB91-251984, A05, MF-A05). This report has been replaced by NCEER-92-0018.

NCEER-90-0004 "Catalog of Strong Motion Stations in Eastern North America," by R.W. Busby, 4/3/90, (PB90-251984, A05, MF-A01).

NCEER-90-0005 "NCEER Strong-Motion Data Base: A User Manual for the GeoBase Release (Version 1.0 for the Sun3)," by P. Friberg and K. Jacob, 3/31/90 (PB90-258062, A04, MF-A01).

NCEER-90-0006 "Seismic Hazard Along a Crude Oil Pipeline in the Event of an 1811-1812 Type New Madrid Earthquake," by H.H.M. Hwang and C-H.S. Chen, 4/16/90, (PB90-258054, A04, MF-A01).

NCEER-90-0007 "Site-Specific Response Spectra for Memphis Sheahan Pumping Station," by H.H.M. Hwang and C.S. Lee, 5/15/90, (PB91-108811, A05, MF-A01).

NCEER-90-0008 "Pilot Study on Seismic Vulnerability of Crude Oil Transmission Systems," by T. Ariman, R. Dobry, M. Grigoriu, F. Kozin, M. O'Rourke, T. O'Rourke and M. Shinozuka, 5/25/90, (PB91-108837, A06, MF-A01).

NCEER-90-0009 "A Program to Generate Site Dependent Time Histories: EQGEN," by G.W. Ellis, M. Srinivasan and A.S. Cakmak, 1/30/90, (PB91-108829, A04, MF-A01).

NCEER-90-0010 "Active Isolation for Seismic Protection of Operating Rooms," by M.E. Talbott, Supervised by M. Shinozuka, 6/8/9, (PB91-110205, A05, MF-A01).

NCEER-90-0011 "Program LINEARID for Identification of Linear Structural Dynamic Systems," by C-B. Yun and M. Shinozuka, 6/25/90, (PB91-110312, A08, MF-A01).

NCEER-90-0012 "Two-Dimensional Two-Phase Elasto-Plastic Seismic Response of Earth Dams," by A.N. Yiagos, Supervised by J.H. Prevost, 6/20/90, (PB91-110197, A13, MF-A02).

NCEER-90-0013 "Secondary Systems in Base-Isolated Structures: Experimental Investigation, Stochastic Response and Stochastic Sensitivity," by G.D. Manolis, G. Juhn, M.C. Constantinou and A.M. Reinhorn, 7/1/90, (PB91-110320, A08, MF-A01).

NCEER-90-0014 "Seismic Behavior of Lightly-Reinforced Concrete Column and Beam-Column Joint Details," by S.P. Pessiki, C.H. Conley, P. Gergely and R.N. White, 8/22/90, (PB91-108795, A11, MF-A02).

NCEER-90-0015 "Two Hybrid Control Systems for Building Structures Under Strong Earthquakes," by J.N. Yang and A. Danielians, 6/29/90, (PB91-125393, A04, MF-A01).

NCEER-90-0016 "Instantaneous Optimal Control with Acceleration and Velocity Feedback," by J.N. Yang and Z. Li, 6/29/90, (PB91-125401, A03, MF-A01).

NCEER-90-0017 "Reconnaissance Report on the Northern Iran Earthquake of June 21, 1990," by M. Mehrain, 10/4/90, (PB91-125377, A03, MF-A01).

NCEER-90-0018 "Evaluation of Liquefaction Potential in Memphis and Shelby County," by T.S. Chang, P.S. Tang, C.S. Lee and H. Hwang, 8/10/90, (PB91-125427, A09, MF-A01).

NCEER-90-0019 "Experimental and Analytical Study of a Combined Sliding Disc Bearing and Helical Steel Spring Isolation System," by M.C. Constantinou, A.S. Mokha and A.M. Reinhorn, 10/4/90, (PB91-125385, A06, MF-A01). This report is available only through NTIS (see address given above).

NCEER-90-0020 "Experimental Study and Analytical Prediction of Earthquake Response of a Sliding Isolation System with a Spherical Surface," by A.S. Mokha, M.C. Constantinou and A.M. Reinhorn, 10/11/90, (PB91-125419, A05, MF-A01).

NCEER-90-0021 "Dynamic Interaction Factors for Floating Pile Groups," by G. Gazetas, K. Fan, A. Kaynia and E. Kausel, 9/10/90, (PB91-170381, A05, MF-A01).

NCEER-90-0022 "Evaluation of Seismic Damage Indices for Reinforced Concrete Structures," by S. Rodriguez-Gomez and A.S. Cakmak, 9/30/90, PB91-171322, A06, MF-A01).

NCEER-90-0023 "Study of Site Response at a Selected Memphis Site," by H. Desai, S. Ahmad, E.S. Gazetas and M.R. Oh, 10/11/90, (PB91-196857, A03, MF-A01).

NCEER-90-0024 "A User's Guide to Strongmo: Version 1.0 of NCEER's Strong-Motion Data Access Tool for PCs and Terminals," by P.A. Friberg and C.A.T. Susch, 11/15/90, (PB91-171272, A03, MF-A01).

NCEER-90-0025 "A Three-Dimensional Analytical Study of Spatial Variability of Seismic Ground Motions," by L-L. Hong and A.H.-S. Ang, 10/30/90, (PB91-170399, A09, MF-A01).

NCEER-90-0026 "MUMOID User's Guide - A Program for the Identification of Modal Parameters," by S. Rodriguez-Gomez and E. DiPasquale, 9/30/90, (PB91-171298, A04, MF-A01).

NCEER-90-0027 "SARCF-II User's Guide - Seismic Analysis of Reinforced Concrete Frames," by S. Rodriguez-Gomez, Y.S. Chung and C. Meyer, 9/30/90, (PB91-171280, A05, MF-A01).

NCEER-90-0028 "Viscous Dampers: Testing, Modeling and Application in Vibration and Seismic Isolation," by N. Makris and M.C. Constantinou, 12/20/90 (PB91-190561, A06, MF-A01).

NCEER-90-0029 "Soil Effects on Earthquake Ground Motions in the Memphis Area," by H. Hwang, C.S. Lee, K.W. Ng and T.S. Chang, 8/2/90, (PB91-190751, A05, MF-A01).

NCEER-91-0001 "Proceedings from the Third Japan-U.S. Workshop on Earthquake Resistant Design of Lifeline Facilities and Countermeasures for Soil Liquefaction, December 17-19, 1990," edited by T.D. O'Rourke and M. Hamada, 2/1/91, (PB91-179259, A99, MF-A04).

NCEER-91-0002 "Physical Space Solutions of Non-Proportionally Damped Systems," by M. Tong, Z. Liang and G.C. Lee, 1/15/91, (PB91-179242, A04, MF-A01).

NCEER-91-0003 "Seismic Response of Single Piles and Pile Groups," by K. Fan and G. Gazetas, 1/10/91, (PB92-174994, A04, MF-A01).

NCEER-91-0004 "Damping of Structures: Part 1 - Theory of Complex Damping," by Z. Liang and G. Lee, 10/10/91, (PB92-197235, A12, MF-A03).

NCEER-91-0005 "3D-BASIS - Nonlinear Dynamic Analysis of Three Dimensional Base Isolated Structures: Part II," by S. Nagarajaiah, A.M. Reinhorn and M.C. Constantinou, 2/28/91, (PB91-190553, A07, MF-A01). This report has been replaced by NCEER-93-0011.

NCEER-91-0006 "A Multidimensional Hysteretic Model for Plasticity Deforming Metals in Energy Absorbing Devices," by E.J. Graesser and F.A. Cozzarelli, 4/9/91, (PB92-108364, A04, MF-A01).

NCEER-91-0007 "A Framework for Customizable Knowledge-Based Expert Systems with an Application to a KBES for Evaluating the Seismic Resistance of Existing Buildings," by E.G. Ibarra-Anaya and S.J. Fenves, 4/9/91, (PB91-210930, A08, MF-A01).

NCEER-91-0008 "Nonlinear Analysis of Steel Frames with Semi-Rigid Connections Using the Capacity Spectrum Method," by G.G. Deierlein, S-H. Hsieh, Y-J. Shen and J.F. Abel, 7/2/91, (PB92-113828, A05, MF-A01).

NCEER-91-0009 "Earthquake Education Materials for Grades K-12," by K.E.K. Ross, 4/30/91, (PB91-212142, A06, MF-A01). This report has been replaced by NCEER-92-0018.

NCEER-91-0010 "Phase Wave Velocities and Displacement Phase Differences in a Harmonically Oscillating Pile," by N. Makris and G. Gazetas, 7/8/91, (PB92-108356, A04, MF-A01).

NCEER-91-0011 "Dynamic Characteristics of a Full-Size Five-Story Steel Structure and a 2/5 Scale Model," by K.C. Chang, G.C. Yao, G.C. Lee, D.S. Hao and Y.C. Yeh," 7/2/91, (PB93-116648, A06, MF-A02).

NCEER-91-0012 "Seismic Response of a 2/5 Scale Steel Structure with Added Viscoelastic Dampers," by K.C. Chang, T.T. Soong, S-T. Oh and M.L. Lai, 5/17/91, (PB92-110816, A05, MF-A01).

NCEER-91-0013 "Earthquake Response of Retaining Walls; Full-Scale Testing and Computational Modeling," by S. Alampalli and A-W.M. Elgamal, 6/20/91, to be published.

NCEER-91-0014 "3D-BASIS-M: Nonlinear Dynamic Analysis of Multiple Building Base Isolated Structures," by P.C. Tsopelas, S. Nagarajaiah, M.C. Constantinou and A.M. Reinhorn, 5/28/91, (PB92-113885, A09, MF-A02).

NCEER-91-0015 "Evaluation of SEAOC Design Requirements for Sliding Isolated Structures," by D. Theodossiou and M.C. Constantinou, 6/10/91, (PB92-114602, A11, MF-A03).

NCEER-91-0016 "Closed-Loop Modal Testing of a 27-Story Reinforced Concrete Flat Plate-Core Building," by H.R. Somaprasad, T. Toksoy, H. Yoshiyuki and A.E. Aktan, 7/15/91, (PB92-129980, A07, MF-A02).

NCEER-91-0017 "Shake Table Test of a 1/6 Scale Two-Story Lightly Reinforced Concrete Building," by A.G. El-Attar, R.N. White and P. Gergely, 2/28/91, (PB92-222447, A06, MF-A02).

NCEER-91-0018 "Shake Table Test of a 1/8 Scale Three-Story Lightly Reinforced Concrete Building," by A.G. El-Attar, R.N. White and P. Gergely, 2/28/91, (PB93-116630, A08, MF-A02).

NCEER-91-0019 "Transfer Functions for Rigid Rectangular Foundations," by A.S. Veletsos, A.M. Prasad and W.H. Wu, 7/31/91, to be published.

NCEER-91-0020 "Hybrid Control of Seismic-Excited Nonlinear and Inelastic Structural Systems," by J.N. Yang, Z. Li and A. Danielians, 8/1/91, (PB92-143171, A06, MF-A02).

NCEER-91-0021 "The NCEER-91 Earthquake Catalog: Improved Intensity-Based Magnitudes and Recurrence Relations for U.S. Earthquakes East of New Madrid," by L. Seeber and J.G. Armbruster, 8/28/91, (PB92-176742, A06, MF-A02).

NCEER-91-0022 "Proceedings from the Implementation of Earthquake Planning and Education in Schools: The Need for Change - The Roles of the Changemakers," by K.E.K. Ross and F. Winslow, 7/23/91, (PB92-129998, A12, MF-A03).

NCEER-91-0023 "A Study of Reliability-Based Criteria for Seismic Design of Reinforced Concrete Frame Buildings," by H.H.M. Hwang and H-M. Hsu, 8/10/91, (PB92-140235, A09, MF-A02).

NCEER-91-0024 "Experimental Verification of a Number of Structural System Identification Algorithms," by R.G. Ghanem, H. Gavin and M. Shinozuka, 9/18/91, (PB92-176577, A18, MF-A04).

NCEER-91-0025 "Probabilistic Evaluation of Liquefaction Potential," by H.H.M. Hwang and C.S. Lee," 11/25/91, (PB92-143429, A05, MF-A01).

NCEER-91-0026 "Instantaneous Optimal Control for Linear, Nonlinear and Hysteretic Structures - Stable Controllers," by J.N. Yang and Z. Li, 11/15/91, (PB92-163807, A04, MF-A01).

NCEER-91-0027 "Experimental and Theoretical Study of a Sliding Isolation System for Bridges," by M.C. Constantinou, A. Kartoum, A.M. Reinhorn and P. Bradford, 11/15/91, (PB92-176973, A10, MF-A03).

NCEER-92-0001 "Case Studies of Liquefaction and Lifeline Performance During Past Earthquakes, Volume 1: Japanese Case Studies," Edited by M. Hamada and T. O'Rourke, 2/17/92, (PB92-197243, A18, MF-A04).

NCEER-92-0002 "Case Studies of Liquefaction and Lifeline Performance During Past Earthquakes, Volume 2: United States Case Studies," Edited by T. O'Rourke and M. Hamada, 2/17/92, (PB92-197250, A20, MF-A04).

NCEER-92-0003 "Issues in Earthquake Education," Edited by K. Ross, 2/3/92, (PB92-222389, A07, MF-A02).

NCEER-92-0004 "Proceedings from the First U.S. - Japan Workshop on Earthquake Protective Systems for Bridges," Edited by I.G. Buckle, 2/4/92, (PB94-142239, A99, MF-A06).

NCEER-92-0005 "Seismic Ground Motion from a Haskell-Type Source in a Multiple-Layered Half-Space," A.P. Theoharis, G. Deodatis and M. Shinozuka, 1/2/92, to be published.

NCEER-92-0006 "Proceedings from the Site Effects Workshop," Edited by R. Whitman, 2/29/92, (PB92-197201, A04, MF-A01).

NCEER-92-0007 "Engineering Evaluation of Permanent Ground Deformations Due to Seismically-Induced Liquefaction," by M.H. Baziar, R. Dobry and A-W.M. Elgamal, 3/24/92, (PB92-222421, A13, MF-A03).

NCEER-92-0008 "A Procedure for the Seismic Evaluation of Buildings in the Central and Eastern United States," by C.D. Poland and J.O. Malley, 4/2/92, (PB92-222439, A20, MF-A04).

NCEER-92-0009 "Experimental and Analytical Study of a Hybrid Isolation System Using Friction Controllable Sliding Bearings," by M.Q. Feng, S. Fujii and M. Shinozuka, 5/15/92, (PB93-150282, A06, MF-A02).

NCEER-92-0010 "Seismic Resistance of Slab-Column Connections in Existing Non-Ductile Flat-Plate Buildings," by A.J. Durrani and Y. Du, 5/18/92, (PB93-116812, A06, MF-A02).

NCEER-92-0011 "The Hysteretic and Dynamic Behavior of Brick Masonry Walls Upgraded by Ferrocement Coatings Under Cyclic Loading and Strong Simulated Ground Motion," by H. Lee and S.P. Prawel, 5/11/92, to be published.

NCEER-92-0012 "Study of Wire Rope Systems for Seismic Protection of Equipment in Buildings," by G.F. Demetriades, M.C. Constantinou and A.M. Reinhorn, 5/20/92, (PB93-116655, A08, MF-A02).

NCEER-92-0013 "Shape Memory Structural Dampers: Material Properties, Design and Seismic Testing," by P.R. Witting and F.A. Cozzarelli, 5/26/92, (PB93-116663, A05, MF-A01).

NCEER-92-0014 "Longitudinal Permanent Ground Deformation Effects on Buried Continuous Pipelines," by M.J. O'Rourke, and C. Nordberg, 6/15/92, (PB93-116671, A08, MF-A02).

NCEER-92-0015 "A Simulation Method for Stationary Gaussian Random Functions Based on the Sampling Theorem," by M. Grigoriu and S. Balopoulou, 6/11/92, (PB93-127496, A05, MF-A01).

NCEER-92-0016 "Gravity-Load-Designed Reinforced Concrete Buildings: Seismic Evaluation of Existing Construction and Detailing Strategies for Improved Seismic Resistance," by G.W. Hoffmann, S.K. Kunnath, A.M. Reinhorn and J.B. Mander, 7/15/92, (PB94-142007, A08, MF-A02).

NCEER-92-0017 "Observations on Water System and Pipeline Performance in the Limón Area of Costa Rica Due to the April 22, 1991 Earthquake," by M. O'Rourke and D. Ballantyne, 6/30/92, (PB93-126811, A06, MF-A02).

NCEER-92-0018 "Fourth Edition of Earthquake Education Materials for Grades K-12," Edited by K.E.K. Ross, 8/10/92, (PB93-114023, A07, MF-A02).

NCEER-92-0019 "Proceedings from the Fourth Japan-U.S. Workshop on Earthquake Resistant Design of Lifeline Facilities and Countermeasures for Soil Liquefaction," Edited by M. Hamada and T.D. O'Rourke, 8/12/92, (PB93-163939, A99, MF-E11).

NCEER-92-0020 "Active Bracing System: A Full Scale Implementation of Active Control," by A.M. Reinhorn, T.T. Soong, R.C. Lin, M.A. Riley, Y.P. Wang, S. Aizawa and M. Higashino, 8/14/92, (PB93-127512, A06, MF-A02).

NCEER-92-0021 "Empirical Analysis of Horizontal Ground Displacement Generated by Liquefaction-Induced Lateral Spreads," by S.F. Bartlett and T.L. Youd, 8/17/92, (PB93-188241, A06, MF-A02).

NCEER-92-0022 "IDARC Version 3.0: Inelastic Damage Analysis of Reinforced Concrete Structures," by S.K. Kunnath, A.M. Reinhorn and R.F. Lobo, 8/31/92, (PB93-227502, A07, MF-A02).

NCEER-92-0023 "A Semi-Empirical Analysis of Strong-Motion Peaks in Terms of Seismic Source, Propagation Path and Local Site Conditions, by M. Kamiyama, M.J. O'Rourke and R. Flores-Berrones, 9/9/92, (PB93-150266, A08, MF-A02).

NCEER-92-0024 "Seismic Behavior of Reinforced Concrete Frame Structures with Nonductile Details, Part I: Summary of Experimental Findings of Full Scale Beam-Column Joint Tests," by A. Beres, R.N. White and P. Gergely, 9/30/92, (PB93-227783, A05, MF-A01).

NCEER-92-0025 "Experimental Results of Repaired and Retrofitted Beam-Column Joint Tests in Lightly Reinforced Concrete Frame Buildings," by A. Beres, S. El-Borgi, R.N. White and P. Gergely, 10/29/92, (PB93-227791, A05, MF-A01).

NCEER-92-0026 "A Generalization of Optimal Control Theory: Linear and Nonlinear Structures," by J.N. Yang, Z. Li and S. Vongchavalitkul, 11/2/92, (PB93-188621, A05, MF-A01).

NCEER-92-0027 "Seismic Resistance of Reinforced Concrete Frame Structures Designed Only for Gravity Loads: Part I - Design and Properties of a One-Third Scale Model Structure," by J.M. Bracci, A.M. Reinhorn and J.B. Mander, 12/1/92, (PB94-104502, A08, MF-A02).

NCEER-92-0028 "Seismic Resistance of Reinforced Concrete Frame Structures Designed Only for Gravity Loads: Part II - Experimental Performance of Subassemblages," by L.E. Aycardi, J.B. Mander and A.M. Reinhorn, 12/1/92, (PB94-104510, A08, MF-A02).

NCEER-92-0029 "Seismic Resistance of Reinforced Concrete Frame Structures Designed Only for Gravity Loads: Part III - Experimental Performance and Analytical Study of a Structural Model," by J.M. Bracci, A.M. Reinhorn and J.B. Mander, 12/1/92, (PB93-227528, A09, MF-A01).

NCEER-92-0030 "Evaluation of Seismic Retrofit of Reinforced Concrete Frame Structures: Part I - Experimental Performance of Retrofitted Subassemblages," by D. Choudhuri, J.B. Mander and A.M. Reinhorn, 12/8/92, (PB93-198307, A07, MF-A02).

NCEER-92-0031 "Evaluation of Seismic Retrofit of Reinforced Concrete Frame Structures: Part II - Experimental Performance and Analytical Study of a Retrofitted Structural Model," by J.M. Bracci, A.M. Reinhorn and J.B. Mander, 12/8/92, (PB93-198315, A09, MF-A03).

NCEER-92-0032 "Experimental and Analytical Investigation of Seismic Response of Structures with Supplemental Fluid Viscous Dampers," by M.C. Constantinou and M.D. Symans, 12/21/92, (PB93-191435, A10, MF-A03). This report is available only through NTIS (see address given above).

NCEER-92-0033 "Reconnaissance Report on the Cairo, Egypt Earthquake of October 12, 1992," by M. Khater, 12/23/92, (PB93-188621, A03, MF-A01).

NCEER-92-0034 "Low-Level Dynamic Characteristics of Four Tall Flat-Plate Buildings in New York City," by H. Gavin, S. Yuan, J. Grossman, E. Pekelis and K. Jacob, 12/28/92, (PB93-188217, A07, MF-A02).

NCEER-93-0001 "An Experimental Study on the Seismic Performance of Brick-Infilled Steel Frames With and Without Retrofit," by J.B. Mander, B. Nair, K. Wojtkowski and J. Ma, 1/29/93, (PB93-227510, A07, MF-A02).

NCEER-93-0002 "Social Accounting for Disaster Preparedness and Recovery Planning," by S. Cole, E. Pantoja and V. Razak, 2/22/93, (PB94-142114, A12, MF-A03).

NCEER-93-0003 "Assessment of 1991 NEHRP Provisions for Nonstructural Components and Recommended Revisions," by T.T. Soong, G. Chen, Z. Wu, R-H. Zhang and M. Grigoriu, 3/1/93, (PB93-188639, A06, MF-A02).

NCEER-93-0004 "Evaluation of Static and Response Spectrum Analysis Procedures of SEAOC/UBC for Seismic Isolated Structures," by C.W. Winters and M.C. Constantinou, 3/23/93, (PB93-198299, A10, MF-A03).

NCEER-93-0005 "Earthquakes in the Northeast - Are We Ignoring the Hazard? A Workshop on Earthquake Science and Safety for Educators," edited by K.E.K. Ross, 4/2/93, (PB94-103066, A09, MF-A02).

NCEER-93-0006 "Inelastic Response of Reinforced Concrete Structures with Viscoelastic Braces," by R.F. Lobo, J.M. Bracci, K.L. Shen, A.M. Reinhorn and T.T. Soong, 4/5/93, (PB93-227486, A05, MF-A02).

NCEER-93-0007 "Seismic Testing of Installation Methods for Computers and Data Processing Equipment," by K. Kosar, T.T. Soong, K.L. Shen, J.A. HoLung and Y.K. Lin, 4/12/93, (PB93-198299, A07, MF-A02).

NCEER-93-0008 "Retrofit of Reinforced Concrete Frames Using Added Dampers," by A. Reinhorn, M. Constantinou and C. Li, to be published.

NCEER-93-0009 "Seismic Behavior and Design Guidelines for Steel Frame Structures with Added Viscoelastic Dampers," by K.C. Chang, M.L. Lai, T.T. Soong, D.S. Hao and Y.C. Yeh, 5/1/93, (PB94-141959, A07, MF-A02).

NCEER-93-0010 "Seismic Performance of Shear-Critical Reinforced Concrete Bridge Piers," by J.B. Mander, S.M. Waheed, M.T.A. Chaudhary and S.S. Chen, 5/12/93, (PB93-227494, A08, MF-A02).

NCEER-93-0011 "3D-BASIS-TABS: Computer Program for Nonlinear Dynamic Analysis of Three Dimensional Base Isolated Structures," by S. Nagarajaiah, C. Li, A.M. Reinhorn and M.C. Constantinou, 8/2/93, (PB94-141819, A09, MF-A02).

NCEER-93-0012 "Effects of Hydrocarbon Spills from an Oil Pipeline Break on Ground Water," by O.J. Helweg and H.H.M. Hwang, 8/3/93, (PB94-141942, A06, MF-A02).

NCEER-93-0013 "Simplified Procedures for Seismic Design of Nonstructural Components and Assessment of Current Code Provisions," by M.P. Singh, L.E. Suarez, E.E. Matheu and G.O. Maldonado, 8/4/93, (PB94-141827, A09, MF-A02).

NCEER-93-0014 "An Energy Approach to Seismic Analysis and Design of Secondary Systems," by G. Chen and T.T. Soong, 8/6/93, (PB94-142767, A11, MF-A03).

NCEER-93-0015 "Proceedings from School Sites: Becoming Prepared for Earthquakes - Commemorating the Third Anniversary of the Loma Prieta Earthquake," Edited by F.E. Winslow and K.E.K. Ross, 8/16/93, (PB94-154275, A16, MF-A02).

NCEER-93-0016 "Reconnaissance Report of Damage to Historic Monuments in Cairo, Egypt Following the October 12, 1992 Dahshur Earthquake," by D. Sykora, D. Look, G. Croci, E. Karaesmen and E. Karaesmen, 8/19/93, (PB94-142221, A08, MF-A02).

NCEER-93-0017 "The Island of Guam Earthquake of August 8, 1993," by S.W. Swan and S.K. Harris, 9/30/93, (PB94-141843, A04, MF-A01).

NCEER-93-0018 "Engineering Aspects of the October 12, 1992 Egyptian Earthquake," by A.W. Elgamal, M. Amer, K. Adalier and A. Abul-Fadl, 10/7/93, (PB94-141983, A05, MF-A01).

NCEER-93-0019 "Development of an Earthquake Motion Simulator and its Application in Dynamic Centrifuge Testing," by I. Krstelj, Supervised by J.H. Prevost, 10/23/93, (PB94-181773, A-10, MF-A03).

NCEER-93-0020 "NCEER-Taisei Corporation Research Program on Sliding Seismic Isolation Systems for Bridges: Experimental and Analytical Study of a Friction Pendulum System (FPS)," by M.C. Constantinou, P. Tsopelas, Y-S. Kim and S. Okamoto, 11/1/93, (PB94-142775, A08, MF-A02).

NCEER-93-0021 "Finite Element Modeling of Elastomeric Seismic Isolation Bearings," by L.J. Billings, Supervised by R. Shepherd, 11/8/93, to be published.

NCEER-93-0022 "Seismic Vulnerability of Equipment in Critical Facilities: Life-Safety and Operational Consequences," by K. Porter, G.S. Johnson, M.M. Zadeh, C. Scawthorn and S. Eder, 11/24/93, (PB94-181765, A16, MF-A03).

NCEER-93-0023 "Hokkaido Nansei-oki, Japan Earthquake of July 12, 1993, by P.I. Yanev and C.R. Scawthorn, 12/23/93, (PB94-181500, A07, MF-A01).

NCEER-94-0001 "An Evaluation of Seismic Serviceability of Water Supply Networks with Application to the San Francisco Auxiliary Water Supply System," by I. Markov, Supervised by M. Grigoriu and T. O'Rourke, 1/21/94, (PB94-204013, A07, MF-A02).

NCEER-94-0002 "NCEER-Taisei Corporation Research Program on Sliding Seismic Isolation Systems for Bridges: Experimental and Analytical Study of Systems Consisting of Sliding Bearings, Rubber Restoring Force Devices and Fluid Dampers," Volumes I and II, by P. Tsopelas, S. Okamoto, M.C. Constantinou, D. Ozaki and S. Fujii, 2/4/94, (PB94-181740, A09, MF-A02 and PB94-181757, A12, MF-A03).

NCEER-94-0003 "A Markov Model for Local and Global Damage Indices in Seismic Analysis," by S. Rahman and M. Grigoriu, 2/18/94, (PB94-206000, A12, MF-A03).

NCEER-94-0004 "Proceedings from the NCEER Workshop on Seismic Response of Masonry Infills," edited by D.P. Abrams, 3/1/94, (PB94-180783, A07, MF-A02).

NCEER-94-0005 "The Northridge, California Earthquake of January 17, 1994: General Reconnaissance Report," edited by J.D. Goltz, 3/11/94, (PB94-193943, A10, MF-A03).

NCEER-94-0006 "Seismic Energy Based Fatigue Damage Analysis of Bridge Columns: Part I - Evaluation of Seismic Capacity," by G.A. Chang and J.B. Mander, 3/14/94, (PB94-219185, A11, MF-A03).

NCEER-94-0007 "Seismic Isolation of Multi-Story Frame Structures Using Spherical Sliding Isolation Systems," by T.M. Al-Hussaini, V.A. Zayas and M.C. Constantinou, 3/17/94, (PB94-193745, A09, MF-A02).

NCEER-94-0008 "The Northridge, California Earthquake of January 17, 1994: Performance of Highway Bridges," edited by I.G. Buckle, 3/24/94, (PB94-193851, A06, MF-A02).

NCEER-94-0009 "Proceedings of the Third U.S.-Japan Workshop on Earthquake Protective Systems for Bridges," edited by I.G. Buckle and I. Friedland, 3/31/94, (PB94-195815, A99, MF-A06).

NCEER-94-0010 "3D-BASIS-ME: Computer Program for Nonlinear Dynamic Analysis of Seismically Isolated Single and Multiple Structures and Liquid Storage Tanks," by P.C. Tsopelas, M.C. Constantinou and A.M. Reinhorn, 4/12/94, (PB94-204922, A09, MF-A02).

NCEER-94-0011 "The Northridge, California Earthquake of January 17, 1994: Performance of Gas Transmission Pipelines," by T.D. O'Rourke and M.C. Palmer, 5/16/94, (PB94-204989, A05, MF-A01).

NCEER-94-0012 "Feasibility Study of Replacement Procedures and Earthquake Performance Related to Gas Transmission Pipelines," by T.D. O'Rourke and M.C. Palmer, 5/25/94, (PB94-206638, A09, MF-A02).

NCEER-94-0013 "Seismic Energy Based Fatigue Damage Analysis of Bridge Columns: Part II - Evaluation of Seismic Demand," by G.A. Chang and J.B. Mander, 6/1/94, (PB95-18106, A08, MF-A02).

NCEER-94-0014 "NCEER-Taisei Corporation Research Program on Sliding Seismic Isolation Systems for Bridges: Experimental and Analytical Study of a System Consisting of Sliding Bearings and Fluid Restoring Force/Damping Devices," by P. Tsopelas and M.C. Constantinou, 6/13/94, (PB94-219144, A10, MF-A03).

NCEER-94-0015 "Generation of Hazard-Consistent Fragility Curves for Seismic Loss Estimation Studies," by H. Hwang and J-R. Huo, 6/14/94, (PB95-181996, A09, MF-A02).

NCEER-94-0016 "Seismic Study of Building Frames with Added Energy-Absorbing Devices," by W.S. Pong, C.S. Tsai and G.C. Lee, 6/20/94, (PB94-219136, A10, A03).

NCEER-94-0017 "Sliding Mode Control for Seismic-Excited Linear and Nonlinear Civil Engineering Structures," by J. Yang, J. Wu, A. Agrawal and Z. Li, 6/21/94, (PB95-138483, A06, MF-A02).

NCEER-94-0018 "3D-BASIS-TABS Version 2.0: Computer Program for Nonlinear Dynamic Analysis of Three Dimensional Base Isolated Structures," by A.M. Reinhorn, S. Nagarajaiah, M.C. Constantinou, P. Tsopelas and R. Li, 6/22/94, (PB95-182176, A08, MF-A02).

NCEER-94-0019 "Proceedings of the International Workshop on Civil Infrastructure Systems: Application of Intelligent Systems and Advanced Materials on Bridge Systems," Edited by G.C. Lee and K.C. Chang, 7/18/94, (PB95-252474, A20, MF-A04).

NCEER-94-0020 "Study of Seismic Isolation Systems for Computer Floors," by V. Lambrou and M.C. Constantinou, 7/19/94, (PB95-138533, A10, MF-A03).

NCEER-94-0021 "Proceedings of the U.S.-Italian Workshop on Guidelines for Seismic Evaluation and Rehabilitation of Unreinforced Masonry Buildings," Edited by D.P. Abrams and G.M. Calvi, 7/20/94, (PB95-138749, A13, MF-A03).

NCEER-94-0022 "NCEER-Taisei Corporation Research Program on Sliding Seismic Isolation Systems for Bridges: Experimental and Analytical Study of a System Consisting of Lubricated PTFE Sliding Bearings and Mild Steel Dampers," by P. Tsopelas and M.C. Constantinou, 7/22/94, (PB95-182184, A08, MF-A02).

NCEER-94-0023 “Development of Reliability-Based Design Criteria for Buildings Under Seismic Load,” by Y.K. Wen, H. Hwang and M. Shinozuka, 8/1/94, (PB95-211934, A08, MF-A02).

NCEER-94-0024 “Experimental Verification of Acceleration Feedback Control Strategies for an Active Tendon System,” by S.J. Dyke, B.F. Spencer, Jr., P. Quast, M.K. Sain, D.C. Kaspari, Jr. and T.T. Soong, 8/29/94, (PB95-212320, A05, MF-A01).

NCEER-94-0025 “Seismic Retrofitting Manual for Highway Bridges,” Edited by I.G. Buckle and I.F. Friedland, published by the Federal Highway Administration (PB95-212676, A15, MF-A03).

NCEER-94-0026 “Proceedings from the Fifth U.S.-Japan Workshop on Earthquake Resistant Design of Lifeline Facilities and Countermeasures Against Soil Liquefaction,” Edited by T.D. O’Rourke and M. Hamada, 11/7/94, (PB95-220802, A99, MF-E08).

NCEER-95-0001 “Experimental and Analytical Investigation of Seismic Retrofit of Structures with Supplemental Damping: Part 1 - Fluid Viscous Damping Devices,” by A.M. Reinhorn, C. Li and M.C. Constantinou, 1/3/95, (PB95-266599, A09, MF-A02).

NCEER-95-0002 “Experimental and Analytical Study of Low-Cycle Fatigue Behavior of Semi-Rigid Top-And-Seat Angle Connections,” by G. Pekcan, J.B. Mander and S.S. Chen, 1/5/95, (PB95-220042, A07, MF-A02).

NCEER-95-0003 “NCEER-ATC Joint Study on Fragility of Buildings,” by T. Anagnos, C. Rojahn and A.S. Kiremidjian, 1/20/95, (PB95-220026, A06, MF-A02).

NCEER-95-0004 “Nonlinear Control Algorithms for Peak Response Reduction,” by Z. Wu, T.T. Soong, V. Gattulli and R.C. Lin, 2/16/95, (PB95-220349, A05, MF-A01).

NCEER-95-0005 “Pipeline Replacement Feasibility Study: A Methodology for Minimizing Seismic and Corrosion Risks to Underground Natural Gas Pipelines,” by R.T. Eguchi, H.A. Seligson and D.G. Honegger, 3/2/95, (PB95-252326, A06, MF-A02).

NCEER-95-0006 “Evaluation of Seismic Performance of an 11-Story Frame Building During the 1994 Northridge Earthquake,” by F. Naeim, R. DiSulio, K. Benuska, A. Reinhorn and C. Li, to be published.

NCEER-95-0007 “Prioritization of Bridges for Seismic Retrofitting,” by N. Basöz and A.S. Kiremidjian, 4/24/95, (PB95-252300, A08, MF-A02).

NCEER-95-0008 “Method for Developing Motion Damage Relationships for Reinforced Concrete Frames,” by A. Singhal and A.S. Kiremidjian, 5/11/95, (PB95-266607, A06, MF-A02).

NCEER-95-0009 “Experimental and Analytical Investigation of Seismic Retrofit of Structures with Supplemental Damping: Part II - Friction Devices,” by C. Li and A.M. Reinhorn, 7/6/95, (PB96-128087, A11, MF-A03).

NCEER-95-0010 “Experimental Performance and Analytical Study of a Non-Ductile Reinforced Concrete Frame Structure Retrofitted with Elastomeric Spring Dampers,” by G. Pekcan, J.B. Mander and S.S. Chen, 7/14/95, (PB96-137161, A08, MF-A02).

NCEER-95-0011 “Development and Experimental Study of Semi-Active Fluid Damping Devices for Seismic Protection of Structures,” by M.D. Symans and M.C. Constantinou, 8/3/95, (PB96-136940, A23, MF-A04).

NCEER-95-0012 “Real-Time Structural Parameter Modification (RSPM): Development of Innervated Structures,” by Z. Liang, M. Tong and G.C. Lee, 4/11/95, (PB96-137153, A06, MF-A01).

NCEER-95-0013 “Experimental and Analytical Investigation of Seismic Retrofit of Structures with Supplemental Damping: Part III - Viscous Damping Walls,” by A.M. Reinhorn and C. Li, 10/1/95, (PB96-176409, A11, MF-A03).

NCEER-95-0014 “Seismic Fragility Analysis of Equipment and Structures in a Memphis Electric Substation,” by J-R. Huo and H.H.M. Hwang, 8/10/95, (PB96-128087, A09, MF-A02).

NCEER-95-0015 “The Hanshin-Awaji Earthquake of January 17, 1995: Performance of Lifelines,” Edited by M. Shinozuka, 11/3/95, (PB96-176383, A15, MF-A03).

NCEER-95-0016 “Highway Culvert Performance During Earthquakes,” by T.L. Youd and C.J. Beckman, available as NCEER-96-0015.

NCEER-95-0017 “The Hanshin-Awaji Earthquake of January 17, 1995: Performance of Highway Bridges,” Edited by I.G. Buckle, 12/1/95, to be published.

NCEER-95-0018 “Modeling of Masonry Infill Panels for Structural Analysis,” by A.M. Reinhorn, A. Madan, R.E. Valles, Y. Reichmann and J.B. Mander, 12/8/95, (PB97-110886, MF-A01, A06).

NCEER-95-0019 “Optimal Polynomial Control for Linear and Nonlinear Structures,” by A.K. Agrawal and J.N. Yang, 12/11/95, (PB96-168737, A07, MF-A02).

NCEER-95-0020 "Retrofit of Non-Ductile Reinforced Concrete Frames Using Friction Dampers," by R.S. Rao, P. Gergely and R.N. White, 12/22/95, (PB97-133508, A10, MF-A02).

NCEER-95-0021 "Parametric Results for Seismic Response of Pile-Supported Bridge Bents," by G. Mylonakis, A. Nikolaou and G. Gazetas, 12/22/95, (PB97-100242, A12, MF-A03).

NCEER-95-0022 "Kinematic Bending Moments in Seismically Stressed Piles," by A. Nikolaou, G. Mylonakis and G. Gazetas, 12/23/95, (PB97-113914, MF-A03, A13).

NCEER-96-0001 "Dynamic Response of Unreinforced Masonry Buildings with Flexible Diaphragms," by A.C. Costley and D.P. Abrams," 10/10/96, (PB97-133573, MF-A03, A15).

NCEER-96-0002 "State of the Art Review: Foundations and Retaining Structures," by I. Po Lam, to be published.

NCEER-96-0003 "Ductility of Rectangular Reinforced Concrete Bridge Columns with Moderate Confinement," by N. Wehbe, M. Saiidi, D. Sanders and B. Douglas, 11/7/96, (PB97-133557, A06, MF-A02).

NCEER-96-0004 "Proceedings of the Long-Span Bridge Seismic Research Workshop," edited by I.G. Buckle and I.M. Friedland, to be published.

NCEER-96-0005 "Establish Representative Pier Types for Comprehensive Study: Eastern United States," by J. Kulicki and Z. Prucz, 5/28/96, (PB98-119217, A07, MF-A02).

NCEER-96-0006 "Establish Representative Pier Types for Comprehensive Study: Western United States," by R. Imbsen, R.A. Schamber and T.A. Osterkamp, 5/28/96, (PB98-118607, A07, MF-A02).

NCEER-96-0007 "Nonlinear Control Techniques for Dynamical Systems with Uncertain Parameters," by R.G. Ghanem and M.I. Bujakov, 5/27/96, (PB97-100259, A17, MF-A03).

NCEER-96-0008 "Seismic Evaluation of a 30-Year Old Non-Ductile Highway Bridge Pier and Its Retrofit," by J.B. Mander, B. Mahmoodzadegan, S. Bhadra and S.S. Chen, 5/31/96, (PB97-110902, MF-A03, A10).

NCEER-96-0009 "Seismic Performance of a Model Reinforced Concrete Bridge Pier Before and After Retrofit," by J.B. Mander, J.H. Kim and C.A. Ligozio, 5/31/96, (PB97-110910, MF-A02, A10).

NCEER-96-0010 "IDARC2D Version 4.0: A Computer Program for the Inelastic Damage Analysis of Buildings," by R.E. Valles, A.M. Reinhorn, S.K. Kunnath, C. Li and A. Madan, 6/3/96, (PB97-100234, A17, MF-A03).

NCEER-96-0011 "Estimation of the Economic Impact of Multiple Lifeline Disruption: Memphis Light, Gas and Water Division Case Study," by S.E. Chang, H.A. Seligson and R.T. Eguchi, 8/16/96, (PB97-133490, A11, MF-A03).

NCEER-96-0012 "Proceedings from the Sixth Japan-U.S. Workshop on Earthquake Resistant Design of Lifeline Facilities and Countermeasures Against Soil Liquefaction, Edited by M. Hamada and T. O'Rourke, 9/11/96, (PB97-133581, A99, MF-A06).

NCEER-96-0013 "Chemical Hazards, Mitigation and Preparedness in Areas of High Seismic Risk: A Methodology for Estimating the Risk of Post-Earthquake Hazardous Materials Release," by H.A. Seligson, R.T. Eguchi, K.J. Tierney and K. Richmond, 11/7/96, (PB97-133565, MF-A02, A08).

NCEER-96-0014 "Response of Steel Bridge Bearings to Reversed Cyclic Loading," by J.B. Mander, D-K. Kim, S.S. Chen and G.J. Premus, 11/13/96, (PB97-140735, A12, MF-A03).

NCEER-96-0015 "Highway Culvert Performance During Past Earthquakes," by T.L. Youd and C.J. Beckman, 11/25/96, (PB97-133532, A06, MF-A01).

NCEER-97-0001 "Evaluation, Prevention and Mitigation of Pounding Effects in Building Structures," by R.E. Valles and A.M. Reinhorn, 2/20/97, (PB97-159552, A14, MF-A03).

NCEER-97-0002 "Seismic Design Criteria for Bridges and Other Highway Structures," by C. Rojahn, R. Mayes, D.G. Anderson, J. Clark, J.H. Hom, R.V. Nutt and M.J. O'Rourke, 4/30/97, (PB97-194658, A06, MF-A03).

NCEER-97-0003 “Proceedings of the U.S.-Italian Workshop on Seismic Evaluation and Retrofit,” Edited by D.P. Abrams and G.M. Calvi, 3/19/97, (PB97-194666, A13, MF-A03).

NCEER-97-0004 "Investigation of Seismic Response of Buildings with Linear and Nonlinear Fluid Viscous Dampers," by A.A. Seleemah and M.C. Constantinou, 5/21/97, (PB98-109002, A15, MF-A03).

NCEER-97-0005 "Proceedings of the Workshop on Earthquake Engineering Frontiers in Transportation Facilities," edited by G.C. Lee and I.M. Friedland, 8/29/97, (PB98-128911, A25, MR-A04).

NCEER-97-0006 "Cumulative Seismic Damage of Reinforced Concrete Bridge Piers," by S.K. Kunnath, A. El-Bahy, A. Taylor and W. Stone, 9/2/97, (PB98-108814, A11, MF-A03).

NCEER-97-0007 "Structural Details to Accommodate Seismic Movements of Highway Bridges and Retaining Walls," by R.A. Imbsen, R.A. Schamber, E. Thorkildsen, A. Kartoum, B.T. Martin, T.N. Rosser and J.M. Kulicki, 9/3/97, (PB98-108996, A09, MF-A02).

NCEER-97-0008 "A Method for Earthquake Motion-Damage Relationships with Application to Reinforced Concrete Frames," by A. Singhal and A.S. Kiremidjian, 9/10/97, (PB98-108988, A13, MF-A03).

NCEER-97-0009 "Seismic Analysis and Design of Bridge Abutments Considering Sliding and Rotation," by K. Fishman and R. Richards, Jr., 9/15/97, (PB98-108897, A06, MF-A02).

NCEER-97-0010 "Proceedings of the FHWA/NCEER Workshop on the National Representation of Seismic Ground Motion for New and Existing Highway Facilities," edited by I.M. Friedland, M.S. Power and R.L. Mayes, 9/22/97, (PB98-128903, A21, MF-A04).

NCEER-97-0011 "Seismic Analysis for Design or Retrofit of Gravity Bridge Abutments," by K.L. Fishman, R. Richards, Jr. and R.C. Divito, 10/2/97, (PB98-128937, A08, MF-A02).

NCEER-97-0012 "Evaluation of Simplified Methods of Analysis for Yielding Structures," by P. Tsopelas, M.C. Constantinou, C.A. Kircher and A.S. Whittaker, 10/31/97, (PB98-128929, A10, MF-A03).

NCEER-97-0013 "Seismic Design of Bridge Columns Based on Control and Repairability of Damage," by C-T. Cheng and J.B. Mander, 12/8/97, (PB98-144249, A11, MF-A03).

NCEER-97-0014 "Seismic Resistance of Bridge Piers Based on Damage Avoidance Design," by J.B. Mander and C-T. Cheng, 12/10/97, (PB98-144223, A09, MF-A02).

NCEER-97-0015 “Seismic Response of Nominally Symmetric Systems with Strength Uncertainty,” by S. Balopoulou and M. Grigoriu, 12/23/97, (PB98-153422, A11, MF-A03).

NCEER-97-0016 “Evaluation of Seismic Retrofit Methods for Reinforced Concrete Bridge Columns,” by T.J. Wipf, F.W. Klaiber and F.M. Russo, 12/28/97, (PB98-144215, A12, MF-A03).

NCEER-97-0017 “Seismic Fragility of Existing Conventional Reinforced Concrete Highway Bridges,” by C.L. Mullen and A.S. Cakmak, 12/30/97, (PB98-153406, A08, MF-A02).

NCEER-97-0018 “Loss Asssessment of Memphis Buildings,” edited by D.P. Abrams and M. Shinozuka, 12/31/97, (PB98-144231, A13, MF-A03).

NCEER-97-0019 “Seismic Evaluation of Frames with Infill Walls Using Quasi-static Experiments,” by K.M. Mosalam, R.N. White and P. Gergely, 12/31/97, (PB98-153455, A07, MF-A02).

NCEER-97-0020 “Seismic Evaluation of Frames with Infill Walls Using Pseudo-dynamic Experiments,” by K.M. Mosalam, R.N. White and P. Gergely, 12/31/97, (PB98-153430, A07, MF-A02).

NCEER-97-0021 “Computational Strategies for Frames with Infill Walls: Discrete and Smeared Crack Analyses and Seismic Fragility,” by K.M. Mosalam, R.N. White and P. Gergely, 12/31/97, (PB98-153414, A10, MF-A02).

NCEER-97-0022 "Proceedings of the NCEER Workshop on Evaluation of Liquefaction Resistance of Soils," edited by T.L. Youd and I.M. Idriss, 12/31/97, (PB98-155617, A15, MF-A03).

MCEER-98-0001 "Extraction of Nonlinear Hysteretic Properties of Seismically Isolated Bridges from Quick-Release Field Tests," by Q. Chen, B.M. Douglas, E.M. Maragakis and I.G. Buckle, 5/26/98, (PB99-118838, A06, MF-A01).

MCEER-98-0002 "Methodologies for Evaluating the Importance of Highway Bridges," by A. Thomas, S. Eshenaur and J. Kulicki, 5/29/98, (PB99-118846, A10, MF-A02).

MCEER-98-0003 "Capacity Design of Bridge Piers and the Analysis of Overstrength," by J.B. Mander, A. Dutta and P. Goel, 6/1/98, (PB99-118853, A09, MF-A02).

MCEER-98-0004 "Evaluation of Bridge Damage Data from the Loma Prieta and Northridge, California Earthquakes," by N. Basoz and A. Kiremidjian, 6/2/98, (PB99-118861, A15, MF-A03).

MCEER-98-0005 "Screening Guide for Rapid Assessment of Liquefaction Hazard at Highway Bridge Sites," by T. L. Youd, 6/16/98, (PB99-118879, A06, not available on microfiche).

MCEER-98-0006 "Structural Steel and Steel/Concrete Interface Details for Bridges," by P. Ritchie, N. Kauhl and J. Kulicki, 7/13/98, (PB99-118945, A06, MF-A01).

MCEER-98-0007 "Capacity Design and Fatigue Analysis of Confined Concrete Columns," by A. Dutta and J.B. Mander, 7/14/98, (PB99-118960, A14, MF-A03).

MCEER-98-0008 "Proceedings of the Workshop on Performance Criteria for Telecommunication Services Under Earthquake Conditions," edited by A.J. Schiff, 7/15/98, (PB99-118952, A08, MF-A02).

MCEER-98-0009 "Fatigue Analysis of Unconfined Concrete Columns," by J.B. Mander, A. Dutta and J.H. Kim, 9/12/98, (PB99-123655, A10, MF-A02).

MCEER-98-0010 "Centrifuge Modeling of Cyclic Lateral Response of Pile-Cap Systems and Seat-Type Abutments in Dry Sands," by A.D. Gadre and R. Dobry, 10/2/98, (PB99-123606, A13, MF-A03).

MCEER-98-0011 "IDARC-BRIDGE: A Computational Platform for Seismic Damage Assessment of Bridge Structures," by A.M. Reinhorn, V. Simeonov, G. Mylonakis and Y. Reichman, 10/2/98, (PB99-162919, A15, MF-A03).

MCEER-98-0012 "Experimental Investigation of the Dynamic Response of Two Bridges Before and After Retrofitting with Elastomeric Bearings," by D.A. Wendichansky, S.S. Chen and J.B. Mander, 10/2/98, (PB99-162927, A15, MF-A03).

MCEER-98-0013 "Design Procedures for Hinge Restrainers and Hinge Sear Width for Multiple-Frame Bridges," by R. Des Roches and G.L. Fenves, 11/3/98, (PB99-140477, A13, MF-A03).

MCEER-98-0014 "Response Modification Factors for Seismically Isolated Bridges," by M.C. Constantinou and J.K. Quarshie, 11/3/98, (PB99-140485, A14, MF-A03).

MCEER-98-0015 "Proceedings of the U.S.-Italy Workshop on Seismic Protective Systems for Bridges," edited by I.M. Friedland and M.C. Constantinou, 11/3/98, (PB2000-101711, A22, MF-A04).

MCEER-98-0016 "Appropriate Seismic Reliability for Critical Equipment Systems: Recommendations Based on Regional Analysis of Financial and Life Loss," by K. Porter, C. Scawthorn, C. Taylor and N. Blais, 11/10/98, (PB99-157265, A08, MF-A02).

MCEER-98-0017 "Proceedings of the U.S. Japan Joint Seminar on Civil Infrastructure Systems Research," edited by M. Shinozuka and A. Rose, 11/12/98, (PB99-156713, A16, MF-A03).

MCEER-98-0018 "Modeling of Pile Footings and Drilled Shafts for Seismic Design," by I. PoLam, M. Kapuskar and D. Chaudhuri, 12/21/98, (PB99-157257, A09, MF-A02).

MCEER-99-0001 "Seismic Evaluation of a Masonry Infilled Reinforced Concrete Frame by Pseudodynamic Testing," by S.G. Buonopane and R.N. White, 2/16/99, (PB99-162851, A09, MF-A02).

MCEER-99-0002 "Response History Analysis of Structures with Seismic Isolation and Energy Dissipation Systems: Verification Examples for Program SAP2000," by J. Scheller and M.C. Constantinou, 2/22/99, (PB99-162869, A08, MF-A02).

MCEER-99-0003 "Experimental Study on the Seismic Design and Retrofit of Bridge Columns Including Axial Load Effects," by A. Dutta, T. Kokorina and J.B. Mander, 2/22/99, (PB99-162877, A09, MF-A02).

MCEER-99-0004 "Experimental Study of Bridge Elastomeric and Other Isolation and Energy Dissipation Systems with Emphasis on Uplift Prevention and High Velocity Near-source Seismic Excitation," by A. Kasalanati and M. C. Constantinou, 2/26/99, (PB99-162885, A12, MF-A03).

MCEER-99-0005 "Truss Modeling of Reinforced Concrete Shear-flexure Behavior," by J.H. Kim and J.B. Mander, 3/8/99, (PB99-163693, A12, MF-A03).

MCEER-99-0006 "Experimental Investigation and Computational Modeling of Seismic Response of a 1:4 Scale Model Steel Structure with a Load Balancing Supplemental Damping System," by G. Pekcan, J.B. Mander and S.S. Chen, 4/2/99, (PB99-162893, A11, MF-A03).

MCEER-99-0007 "Effect of Vertical Ground Motions on the Structural Response of Highway Bridges," by M.R. Button, C.J. Cronin and R.L. Mayes, 4/10/99, (PB2000-101411, A10, MF-A03).

MCEER-99-0008 "Seismic Reliability Assessment of Critical Facilities: A Handbook, Supporting Documentation, and Model Code Provisions," by G.S. Johnson, R.E. Sheppard, M.D. Quilici, S.J. Eder and C.R. Scawthorn, 4/12/99, (PB2000-101701, A18, MF-A04).

MCEER-99-0009 "Impact Assessment of Selected MCEER Highway Project Research on the Seismic Design of Highway Structures," by C. Rojahn, R. Mayes, D.G. Anderson, J.H. Clark, D'Appolonia Engineering, S. Gloyd and R.V. Nutt, 4/14/99, (PB99-162901, A10, MF-A02).

MCEER-99-0010 "Site Factors and Site Categories in Seismic Codes," by R. Dobry, R. Ramos and M.S. Power, 7/19/99, (PB2000-101705, A08, MF-A02).

MCEER-99-0011 "Restrainer Design Procedures for Multi-Span Simply-Supported Bridges," by M.J. Randall, M. Saiidi, E. Maragakis and T. Isakovic, 7/20/99, (PB2000-101702, A10, MF-A02).

MCEER-99-0012 "Property Modification Factors for Seismic Isolation Bearings," by M.C. Constantinou, P. Tsopelas, A. Kasalanati and E. Wolff, 7/20/99, (PB2000-103387, A11, MF-A03).

MCEER-99-0013 "Critical Seismic Issues for Existing Steel Bridges," by P. Ritchie, N. Kauhl and J. Kulicki, 7/20/99, (PB2000-101697, A09, MF-A02).

MCEER-99-0014 "Nonstructural Damage Database," by A. Kao, T.T. Soong and A. Vender, 7/24/99, (PB2000-101407, A06, MF-A01).

MCEER-99-0015 "Guide to Remedial Measures for Liquefaction Mitigation at Existing Highway Bridge Sites," by H.G. Cooke and J. K. Mitchell, 7/26/99, (PB2000-101703, A11, MF-A03).

MCEER-99-0016 "Proceedings of the MCEER Workshop on Ground Motion Methodologies for the Eastern United States," edited by N. Abrahamson and A. Becker, 8/11/99, (PB2000-103385, A07, MF-A02).

MCEER-99-0017 "Quindío, Colombia Earthquake of January 25, 1999: Reconnaissance Report," by A.P. Asfura and P.J. Flores, 10/4/99, (PB2000-106893, A06, MF-A01).

MCEER-99-0018 "Hysteretic Models for Cyclic Behavior of Deteriorating Inelastic Structures," by M.V. Sivaselvan and A.M. Reinhorn, 11/5/99, (PB2000-103386, A08, MF-A02).

MCEER-99-0019 "Proceedings of the 7th U.S.- Japan Workshop on Earthquake Resistant Design of Lifeline Facilities and Countermeasures Against Soil Liquefaction," edited by T.D. O'Rourke, J.P. Bardet and M. Hamada, 11/19/99, (PB2000-103354, A99, MF-A06).

MCEER-99-0020 "Development of Measurement Capability for Micro-Vibration Evaluations with Application to Chip Fabrication Facilities," by G.C. Lee, Z. Liang, J.W. Song, J.D. Shen and W.C. Liu, 12/1/99, (PB2000-105993, A08, MF-A02).

MCEER-99-0021 "Design and Retrofit Methodology for Building Structures with Supplemental Energy Dissipating Systems," by G. Pekcan, J.B. Mander and S.S. Chen, 12/31/99, (PB2000-105994, A11, MF-A03).

MCEER-00-0001 "The Marmara, Turkey Earthquake of August 17, 1999: Reconnaissance Report," edited by C. Scawthorn; with major contributions by M. Bruneau, R. Eguchi, T. Holzer, G. Johnson, J. Mander, J. Mitchell, W. Mitchell, A. Papageorgiou, C. Scaethorn, and G. Webb, 3/23/00, (PB2000-106200, A11, MF-A03).

MCEER-00-0002 "Proceedings of the MCEER Workshop for Seismic Hazard Mitigation of Health Care Facilities," edited by G.C. Lee, M. Ettouney, M. Grigoriu, J. Hauer and J. Nigg, 3/29/00, (PB2000-106892, A08, MF-A02).

MCEER-00-0003 "The Chi-Chi, Taiwan Earthquake of September 21, 1999: Reconnaissance Report," edited by G.C. Lee and C.H. Loh, with major contributions by G.C. Lee, M. Bruneau, I.G. Buckle, S.E. Chang, P.J. Flores, T.D. O'Rourke, M. Shinozuka, T.T. Soong, C-H. Loh, K-C. Chang, Z-J. Chen, J-S. Hwang, M-L. Lin, G-Y. Liu, K-C. Tsai, G.C. Yao and C-L. Yen, 4/30/00, (PB2001-100980, A10, MF-A02).

MCEER-00-0004 "Seismic Retrofit of End-Sway Frames of Steel Deck-Truss Bridges with a Supplemental Tendon System: Experimental and Analytical Investigation," by G. Pekcan, J.B. Mander and S.S. Chen, 7/1/00, (PB2001-100982, A10, MF-A02).

MCEER-00-0005 "Sliding Fragility of Unrestrained Equipment in Critical Facilities," by W.H. Chong and T.T. Soong, 7/5/00, (PB2001-100983, A08, MF-A02).

MCEER-00-0006 "Seismic Response of Reinforced Concrete Bridge Pier Walls in the Weak Direction," by N. Abo-Shadi, M. Saiidi and D. Sanders, 7/17/00, (PB2001-100981, A17, MF-A03).

MCEER-00-0007 "Low-Cycle Fatigue Behavior of Longitudinal Reinforcement in Reinforced Concrete Bridge Columns," by J. Brown and S.K. Kunnath, 7/23/00, (PB2001-104392, A08, MF-A02).

MCEER-00-0008 "Soil Structure Interaction of Bridges for Seismic Analysis," I. PoLam and H. Law, 9/25/00, (PB2001-105397, A08, MF-A02).

MCEER-00-0009 "Proceedings of the First MCEER Workshop on Mitigation of Earthquake Disaster by Advanced Technologies (MEDAT-1), edited by M. Shinozuka, D.J. Inman and T.D. O'Rourke, 11/10/00, (PB2001-105399, A14, MF-A03).

MCEER-00-0010 "Development and Evaluation of Simplified Procedures for Analysis and Design of Buildings with Passive Energy Dissipation Systems, Revision 01," by O.M. Ramirez, M.C. Constantinou, C.A. Kircher, A.S. Whittaker, M.W. Johnson, J.D. Gomez and C. Chrysostomou, 11/16/01, (PB2001-105523, A23, MF-A04).

MCEER-00-0011 "Dynamic Soil-Foundation-Structure Interaction Analyses of Large Caissons," by C-Y. Chang, C-M. Mok, Z-L. Wang, R. Settgast, F. Waggoner, M.A. Ketchum, H.M. Gonnermann and C-C. Chin, 12/30/00, (PB2001-104373, A07, MF-A02).

MCEER-00-0012 "Experimental Evaluation of Seismic Performance of Bridge Restrainers," by A.G. Vlassis, E.M. Maragakis and M. Saiid Saiidi, 12/30/00, (PB2001-104354, A09, MF-A02).

MCEER-00-0013 "Effect of Spatial Variation of Ground Motion on Highway Structures," by M. Shinozuka, V. Saxena and G. Deodatis, 12/31/00, (PB2001-108755, A13, MF-A03).

MCEER-00-0014 "A Risk-Based Methodology for Assessing the Seismic Performance of Highway Systems," by S.D. Werner, C.E. Taylor, J.E. Moore, II, J.S. Walton and S. Cho, 12/31/00, (PB2001-108756, A14, MF-A03).

MCEER-01-0001 “Experimental Investigation of P-Delta Effects to Collapse During Earthquakes,” by D. Vian and M. Bruneau, 6/25/01, (PB2002-100534, A17, MF-A03).

MCEER-01-0002 “Proceedings of the Second MCEER Workshop on Mitigation of Earthquake Disaster by Advanced Technologies (MEDAT-2),” edited by M. Bruneau and D.J. Inman, 7/23/01, (PB2002-100434, A16, MF-A03).

MCEER-01-0003 “Sensitivity Analysis of Dynamic Systems Subjected to Seismic Loads,” by C. Roth and M. Grigoriu, 9/18/01, (PB2003-100884, A12, MF-A03).

MCEER-01-0004 “Overcoming Obstacles to Implementing Earthquake Hazard Mitigation Policies: Stage 1 Report,” by D.J. Alesch and W.J. Petak, 12/17/01, (PB2002-107949, A07, MF-A02).

MCEER-01-0005 “Updating Real-Time Earthquake Loss Estimates: Methods, Problems and Insights,” by C.E. Taylor, S.E. Chang and R.T. Eguchi, 12/17/01, (PB2002-107948, A05, MF-A01).

MCEER-01-0006 “Experimental Investigation and Retrofit of Steel Pile Foundations and Pile Bents Under Cyclic Lateral Loadings,” by A. Shama, J. Mander, B. Blabac and S. Chen, 12/31/01, (PB2002-107950, A13, MF-A03).

MCEER-02-0001 “Assessment of Performance of Bolu Viaduct in the 1999 Duzce Earthquake in Turkey” by P.C. Roussis, M.C. Constantinou, M. Erdik, E. Durukal and M. Dicleli, 5/8/02, (PB2003-100883, A08, MF-A02).

MCEER-02-0002 “Seismic Behavior of Rail Counterweight Systems of Elevators in Buildings,” by M.P. Singh, Rildova and L.E. Suarez, 5/27/02. (PB2003-100882, A11, MF-A03).

MCEER-02-0003 “Development of Analysis and Design Procedures for Spread Footings,” by G. Mylonakis, G. Gazetas, S. Nikolaou and A. Chauncey, 10/02/02, (PB2004-101636, A13, MF-A03, CD-A13).

MCEER-02-0004 “Bare-Earth Algorithms for Use with SAR and LIDAR Digital Elevation Models,” by C.K. Huyck, R.T. Eguchi and B. Houshmand, 10/16/02, (PB2004-101637, A07, CD-A07).

MCEER-02-0005 “Review of Energy Dissipation of Compression Members in Concentrically Braced Frames,” by K.Lee and M. Bruneau, 10/18/02, (PB2004-101638, A10, CD-A10).

MCEER-03-0001 “Experimental Investigation of Light-Gauge Steel Plate Shear Walls for the Seismic Retrofit of Buildings” by J. Berman and M. Bruneau, 5/2/03, (PB2004-101622, A10, MF-A03, CD-A10).

MCEER-03-0002 “Statistical Analysis of Fragility Curves,” by M. Shinozuka, M.Q. Feng, H. Kim, T. Uzawa and T. Ueda, 6/16/03, (PB2004-101849, A09, CD-A09).

MCEER-03-0003 “Proceedings of the Eighth U.S.-Japan Workshop on Earthquake Resistant Design f Lifeline Facilities and Countermeasures Against Liquefaction,” edited by M. Hamada, J.P. Bardet and T.D. O’Rourke, 6/30/03, (PB2004-104386, A99, CD-A99).

MCEER-03-0004 “Proceedings of the PRC-US Workshop on Seismic Analysis and Design of Special Bridges,” edited by L.C. Fan and G.C. Lee, 7/15/03, (PB2004-104387, A14, CD-A14).

MCEER-03-0005 “Urban Disaster Recovery: A Framework and Simulation Model,” by S.B. Miles and S.E. Chang, 7/25/03, (PB2004-104388, A07, CD-A07).

MCEER-03-0006 “Behavior of Underground Piping Joints Due to Static and Dynamic Loading,” by R.D. Meis, M. Maragakis and R. Siddharthan, 11/17/03, (PB2005-102194, A13, MF-A03, CD-A00).

MCEER-04-0001 “Experimental Study of Seismic Isolation Systems with Emphasis on Secondary System Response and Verification of Accuracy of Dynamic Response History Analysis Methods,” by E. Wolff and M. Constantinou, 1/16/04 (PB2005-102195, A99, MF-E08, CD-A00).

MCEER-04-0002 “Tension, Compression and Cyclic Testing of Engineered Cementitious Composite Materials,” by K. Kesner and S.L. Billington, 3/1/04, (PB2005-102196, A08, CD-A08).

MCEER-04-0003 “Cyclic Testing of Braces Laterally Restrained by Steel Studs to Enhance Performance During Earthquakes,” by O.C. Celik, J.W. Berman and M. Bruneau, 3/16/04, (PB2005-102197, A13, MF-A03, CD-A00).

MCEER-04-0004 “Methodologies for Post Earthquake Building Damage Detection Using SAR and Optical Remote Sensing: Application to the August 17, 1999 Marmara, Turkey Earthquake,” by C.K. Huyck, B.J. Adams, S. Cho, R.T. Eguchi, B. Mansouri and B. Houshmand, 6/15/04, (PB2005-104888, A10, CD-A00).

MCEER-04-0005 “Nonlinear Structural Analysis Towards Collapse Simulation: A Dynamical Systems Approach,” by M.V. Sivaselvan and A.M. Reinhorn, 6/16/04, (PB2005-104889, A11, MF-A03, CD-A00).

MCEER-04-0006 “Proceedings of the Second PRC-US Workshop on Seismic Analysis and Design of Special Bridges,” edited by G.C. Lee and L.C. Fan, 6/25/04, (PB2005-104890, A16, CD-A00).

MCEER-04-0007 “Seismic Vulnerability Evaluation of Axially Loaded Steel Built-up Laced Members,” by K. Lee and M. Bruneau, 6/30/04, (PB2005-104891, A16, CD-A00).

MCEER-04-0008 “Evaluation of Accuracy of Simplified Methods of Analysis and Design of Buildings with Damping Systems for Near-Fault and for Soft-Soil Seismic Motions,” by E.A. Pavlou and M.C. Constantinou, 8/16/04, (PB2005-104892, A08, MF-A02, CD-A00).

MCEER-04-0009 “Assessment of Geotechnical Issues in Acute Care Facilities in California,” by M. Lew, T.D. O’Rourke, R. Dobry and M. Koch, 9/15/04, (PB2005-104893, A08, CD-A00).

MCEER-04-0010 “Scissor-Jack-Damper Energy Dissipation System,” by A.N. Sigaher-Boyle and M.C. Constantinou, 12/1/04 (PB2005-108221).

MCEER-04-0011 “Seismic Retrofit of Bridge Steel Truss Piers Using a Controlled Rocking Approach,” by M. Pollino and M. Bruneau, 12/20/04 (PB2006-105795).

MCEER-05-0001 “Experimental and Analytical Studies of Structures Seismically Isolated with an Uplift-Restraint Isolation System,” by P.C. Roussis and M.C. Constantinou, 1/10/05 (PB2005-108222).

MCEER-05-0002 “A Versatile Experimentation Model for Study of Structures Near Collapse Applied to Seismic Evaluation of Irregular Structures,” by D. Kusumastuti, A.M. Reinhorn and A. Rutenberg, 3/31/05 (PB2006-101523).

MCEER-05-0003 “Proceedings of the Third PRC-US Workshop on Seismic Analysis and Design of Special Bridges,” edited by L.C. Fan and G.C. Lee, 4/20/05, (PB2006-105796).

MCEER-05-0004 “Approaches for the Seismic Retrofit of Braced Steel Bridge Piers and Proof-of-Concept Testing of an Eccentrically Braced Frame with Tubular Link,” by J.W. Berman and M. Bruneau, 4/21/05 (PB2006-101524).

MCEER-05-0005 “Simulation of Strong Ground Motions for Seismic Fragility Evaluation of Nonstructural Components in Hospitals,” by A. Wanitkorkul and A. Filiatrault, 5/26/05 (PB2006-500027).

MCEER-05-0006 “Seismic Safety in California Hospitals: Assessing an Attempt to Accelerate the Replacement or Seismic Retrofit of Older Hospital Facilities,” by D.J. Alesch, L.A. Arendt and W.J. Petak, 6/6/05 (PB2006-105794).

MCEER-05-0007 “Development of Seismic Strengthening and Retrofit Strategies for Critical Facilities Using Engineered Cementitious Composite Materials,” by K. Kesner and S.L. Billington, 8/29/05 (PB2006-111701).

MCEER-05-0008 “Experimental and Analytical Studies of Base Isolation Systems for Seismic Protection of Power Transformers,” by N. Murota, M.Q. Feng and G-Y. Liu, 9/30/05 (PB2006-111702).

MCEER-05-0009 “3D-BASIS-ME-MB: Computer Program for Nonlinear Dynamic Analysis of Seismically Isolated Structures,” by P.C. Tsopelas, P.C. Roussis, M.C. Constantinou, R. Buchanan and A.M. Reinhorn, 10/3/05 (PB2006-111703).

MCEER-05-0010 “Steel Plate Shear Walls for Seismic Design and Retrofit of Building Structures,” by D. Vian and M. Bruneau, 12/15/05 (PB2006-111704).

MCEER-05-0011 "The Performance-Based Design Paradigm," by M.J. Astrella and A. Whittaker, 12/15/05 (PB2006-111705).

MCEER-06-0001 "Seismic Fragility of Suspended Ceiling Systems," H. Badillo-Almaraz, A.S. Whittaker, A.M. Reinhorn and G.P. Cimellaro, 2/4/06 (PB2006-111706).

MCEER-06-0002 "Multi-Dimensional Fragility of Structures," by G.P. Cimellaro, A.M. Reinhorn and M. Bruneau, 3/1/06 (PB2007-106974, A09, MF-A02, CD A00).

MCEER-06-0003 "Built-Up Shear Links as Energy Dissipators for Seismic Protection of Bridges," by P. Dusicka, A.M. Itani and I.G. Buckle, 3/15/06 (PB2006-111708).

MCEER-06-0004 "Analytical Investigation of the Structural Fuse Concept," by R.E. Vargas and M. Bruneau, 3/16/06 (PB2006-111709).

MCEER-06-0005 "Experimental Investigation of the Structural Fuse Concept," by R.E. Vargas and M. Bruneau, 3/17/06 (PB2006-111710).

MCEER-06-0006 "Further Development of Tubular Eccentrically Braced Frame Links for the Seismic Retrofit of Braced Steel Truss Bridge Piers," by J.W. Berman and M. Bruneau, 3/27/06 (PB2007-105147).

MCEER-06-0007 "REDARS Validation Report," by S. Cho, C.K. Huyck, S. Ghosh and R.T. Eguchi, 8/8/06 (PB2007-106983).

MCEER-06-0008 "Review of Current NDE Technologies for Post-Earthquake Assessment of Retrofitted Bridge Columns," by J.W. Song, Z. Liang and G.C. Lee, 8/21/06 (PB2007-106984).

MCEER-06-0009 "Liquefaction Remediation in Silty Soils Using Dynamic Compaction and Stone Columns," by S. Thevanayagam, G.R. Martin, R. Nashed, T. Shenthan, T. Kanagalingam and N. Ecemis, 8/28/06 (PB2007-106985).

MCEER-06-0010 "Conceptual Design and Experimental Investigation of Polymer Matrix Composite Infill Panels for Seismic Retrofitting," by W. Jung, M. Chiewanichakorn and A.J. Aref, 9/21/06 (PB2007-106986).

MCEER-06-0011 "A Study of the Coupled Horizontal-Vertical Behavior of Elastomeric and Lead-Rubber Seismic Isolation Bearings," by G.P. Warn and A.S. Whittaker, 9/22/06 (PB2007-108679).

MCEER-06-0012 "Proceedings of the Fourth PRC-US Workshop on Seismic Analysis and Design of Special Bridges: Advancing Bridge Technologies in Research, Design, Construction and Preservation," Edited by L.C. Fan, G.C. Lee and L. Ziang, 10/12/06 (PB2007-109042).

MCEER-06-0013 "Cyclic Response and Low Cycle Fatigue Characteristics of Plate Steels," by P. Dusicka, A.M. Itani and I.G. Buckle, 11/1/06 06 (PB2007-106987).

MCEER-06-0014 "Proceedings of the Second US-Taiwan Bridge Engineering Workshop," edited by W.P. Yen, J. Shen, J-Y. Chen and M. Wang, 11/15/06 (PB2008-500041).

MCEER-06-0015 "User Manual and Technical Documentation for the REDARS^{TM} Import Wizard," by S. Cho, S. Ghosh, C.K. Huyck and S.D. Werner, 11/30/06 (PB2007-114766).

MCEER-06-0016 "Hazard Mitigation Strategy and Monitoring Technologies for Urban and Infrastructure Public Buildings: Proceedings of the China-US Workshops," edited by X.Y. Zhou, A.L. Zhang, G.C. Lee and M. Tong, 12/12/06 (PB2008-500018).

MCEER-07-0001 "Static and Kinetic Coefficients of Friction for Rigid Blocks," by C. Kafali, S. Fathali, M. Grigoriu and A.S. Whittaker, 3/20/07 (PB2007-114767).

MCEER-07-0002 "Hazard Mitigation Investment Decision Making: Organizational Response to Legislative Mandate," by L.A. Arendt, D.J. Alesch and W.J. Petak, 4/9/07 (PB2007-114768).

MCEER-07-0003 "Seismic Behavior of Bidirectional-Resistant Ductile End Diaphragms with Unbonded Braces in Straight or Skewed Steel Bridges," by O. Celik and M. Bruneau, 4/11/07 (PB2008-105141).

MCEER-07-0004 “Modeling Pile Behavior in Large Pile Groups Under Lateral Loading,” by A.M. Dodds and G.R. Martin, 4/16/07(PB2008-105142).

MCEER-07-0005 “Experimental Investigation of Blast Performance of Seismically Resistant Concrete-Filled Steel Tube Bridge Piers,” by S. Fujikura, M. Bruneau and D. Lopez-Garcia, 4/20/07 (PB2008-105143).

MCEER-07-0006 “Seismic Analysis of Conventional and Isolated Liquefied Natural Gas Tanks Using Mechanical Analogs,” by I.P. Christovasilis and A.S. Whittaker, 5/1/07.

MCEER-07-0007 “Experimental Seismic Performance Evaluation of Isolation/Restraint Systems for Mechanical Equipment – Part 1: Heavy Equipment Study,” by S. Fathali and A. Filiatrault, 6/6/07 (PB2008-105144).

MCEER-07-0008 “Seismic Vulnerability of Timber Bridges and Timber Substructures,” by A.A. Sharma, J.B. Mander, I.M. Friedland and D.R. Allicock, 6/7/07 (PB2008-105145).

MCEER-07-0009 “Experimental and Analytical Study of the XY-Friction Pendulum (XY-FP) Bearing for Bridge Applications,” by C.C. Marin-Artieda, A.S. Whittaker and M.C. Constantinou, 6/7/07 (PB2008-105191).

MCEER-07-0010 “Proceedings of the PRC-US Earthquake Engineering Forum for Young Researchers,” Edited by G.C. Lee and X.Z. Qi, 6/8/07.

MCEER-07-0011 “Design Recommendations for Perforated Steel Plate Shear Walls,” by R. Purba and M. Bruneau, 6/18/07, (PB2008-105192).

MCEER-07-0012 “Performance of Seismic Isolation Hardware Under Service and Seismic Loading,” by M.C. Constantinou, A.S. Whittaker, Y. Kalpakidis, D.M. Fenz and G.P. Warn, 8/27/07, (PB2008-105193).

MCEER-07-0013 “Experimental Evaluation of the Seismic Performance of Hospital Piping Subassemblies,” by E.R. Goodwin, E. Maragakis and A.M. Itani, 9/4/07, (PB2008-105194).

MCEER-07-0014 “A Simulation Model of Urban Disaster Recovery and Resilience: Implementation for the 1994 Northridge Earthquake,” by S. Miles and S.E. Chang, 9/7/07, (PB2008-106426).

MCEER-07-0015 “Statistical and Mechanistic Fragility Analysis of Concrete Bridges,” by M. Shinozuka, S. Banerjee and S-H. Kim, 9/10/07, (PB2008-106427).

MCEER-07-0016 “Three-Dimensional Modeling of Inelastic Buckling in Frame Structures,” by M. Schachter and AM. Reinhorn, 9/13/07, (PB2008-108125).

MCEER-07-0017 “Modeling of Seismic Wave Scattering on Pile Groups and Caissons,” by I. Po Lam, H. Law and C.T. Yang, 9/17/07 (PB2008-108150).

MCEER-07-0018 “Bridge Foundations: Modeling Large Pile Groups and Caissons for Seismic Design,” by I. Po Lam, H. Law and G.R. Martin (Coordinating Author), 12/1/07 (PB2008-111190).

MCEER-07-0019 “Principles and Performance of Roller Seismic Isolation Bearings for Highway Bridges,” by G.C. Lee, Y.C. Ou, Z. Liang, T.C. Niu and J. Song, 12/10/07.

MCEER-07-0020 “Centrifuge Modeling of Permeability and Pinning Reinforcement Effects on Pile Response to Lateral Spreading,” by L.L Gonzalez-Lagos, T. Abdoun and R. Dobry, 12/10/07 (PB2008-111191).

MCEER-07-0021 “Damage to the Highway System from the Pisco, Perú Earthquake of August 15, 2007,” by J.S. O’Connor, L. Mesa and M. Nykamp, 12/10/07, (PB2008-108126).

MCEER-07-0022 “Experimental Seismic Performance Evaluation of Isolation/Restraint Systems for Mechanical Equipment – Part 2: Light Equipment Study,” by S. Fathali and A. Filiatrault, 12/13/07 (PB2008-111192).

MCEER-07-0023 “Fragility Considerations in Highway Bridge Design,” by M. Shinozuka, S. Banerjee and S.H. Kim, 12/14/07 (PB2008-111193).

MCEER-07-0024 “Performance Estimates for Seismically Isolated Bridges,” by G.P. Warn and A.S. Whittaker, 12/30/07 (PB2008-112230).

MCEER-08-0001 “Seismic Performance of Steel Girder Bridge Superstructures with Conventional Cross Frames,” by L.P. Carden, A.M. Itani and I.G. Buckle, 1/7/08, (PB2008-112231).

MCEER-08-0002 “Seismic Performance of Steel Girder Bridge Superstructures with Ductile End Cross Frames with Seismic Isolators,” by L.P. Carden, A.M. Itani and I.G. Buckle, 1/7/08 (PB2008-112232).

MCEER-08-0003 “Analytical and Experimental Investigation of a Controlled Rocking Approach for Seismic Protection of Bridge Steel Truss Piers,” by M. Pollino and M. Bruneau, 1/21/08 (PB2008-112233).

MCEER-08-0004 “Linking Lifeline Infrastructure Performance and Community Disaster Resilience: Models and Multi-Stakeholder Processes,” by S.E. Chang, C. Pasion, K. Tatebe and R. Ahmad, 3/3/08 (PB2008-112234).

MCEER-08-0005 “Modal Analysis of Generally Damped Linear Structures Subjected to Seismic Excitations,” by J. Song, Y-L. Chu, Z. Liang and G.C. Lee, 3/4/08 (PB2009-102311).

MCEER-08-0006 “System Performance Under Multi-Hazard Environments,” by C. Kafali and M. Grigoriu, 3/4/08 (PB2008-112235).

MCEER-08-0007 “Mechanical Behavior of Multi-Spherical Sliding Bearings,” by D.M. Fenz and M.C. Constantinou, 3/6/08 (PB2008-112236).

MCEER-08-0008 “Post-Earthquake Restoration of the Los Angeles Water Supply System,” by T.H.P. Tabucchi and R.A. Davidson, 3/7/08 (PB2008-112237).

MCEER-08-0009 “Fragility Analysis of Water Supply Systems,” by A. Jacobson and M. Grigoriu, 3/10/08 (PB2009-105545).

MCEER-08-0010 “Experimental Investigation of Full-Scale Two-Story Steel Plate Shear Walls with Reduced Beam Section Connections,” by B. Qu, M. Bruneau, C-H. Lin and K-C. Tsai, 3/17/08.

MCEER-08-0011 “Seismic Evaluation and Rehabilitation of Critical Components of Electrical Power Systems,” S. Ersoy, B. Feizi, A. Ashrafi and M. Ala Saadeghvaziri, 3/17/08 (PB2009-105546).

MCEER-08-0012 “Seismic Behavior and Design of Boundary Frame Members of Steel Plate Shear Walls,” by B. Qu and M. Bruneau, 4/26/08.

MCEER-08-0013 “Development and Appraisal of a Numerical Cyclic Loading Protocol for Quantifying Building System Performance,” by A. Filiatrault, A. Wanitkorkul and M. Constantinou, 4/27/08.

MCEER-08-0014 “Structural and Nonstructural Earthquake Design: The Challenge of Integrating Specialty Areas in Designing Complex, Critical Facilities,” by W.J. Petak and D.J. Alesch, 4/30/08.

MCEER-08-0015 “Seismic Performance Evaluation of Water Systems,” by Y. Wang and T.D. O’Rourke, 5/5/08.

MCEER-08-0016 “Seismic Response Modeling of Water Supply Systems,” by P. Shi and T.D. O’Rourke, 5/5/08.

MCEER-08-0017 “Numerical and Experimental Studies of Self-Centering Post-Tensioned Steel Frames,” by D. Wang and A. Filiatrault, 5/12/08.

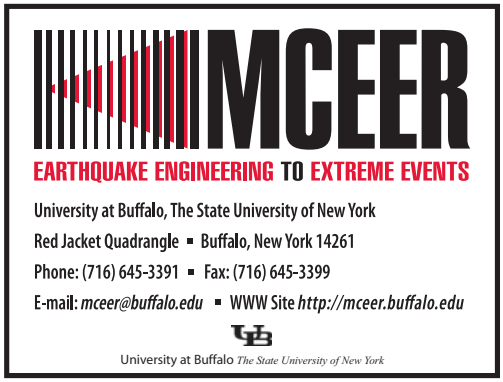

ISSN 1520-295X